

ECHANGES DE VOLATILS ENTRE SURFACE ET ATMOSPHÈRE SUR MARS

Frédéric Schmidt

▶ **To cite this version:**

Frédéric Schmidt. ECHANGES DE VOLATILS ENTRE SURFACE ET ATMOSPHÈRE SUR MARS. Planétologie. Paris-Sud XI, 2014. ⟨tel-01085029⟩

HAL Id: tel-01085029

https://theses.hal.science/tel-01085029v1

Submitted on 20 Nov 2014

HAL is a multi-disciplinary open access archive for the deposit and dissemination of scientific research documents, whether they are published or not. The documents may come from teaching and research institutions in France or abroad, or from public or private research centers.

L'archive ouverte pluridisciplinaire **HAL**, est destinée au dépôt et à la diffusion de documents scientifiques de niveau recherche, publiés ou non, émanant des établissements d'enseignement et de recherche français ou étrangers, des laboratoires publics ou privés.



HAL Authorization

HABILITATION À DIRIGER DES RECHERCHES
DE L'UNIVERSITÉ PARIS SUD

spécialité : Planétologie

LABORATOIRE GÉOSCIENCES PARIS SUD

par

Frédéric Schmidt

ECHANGES DE VOLATILS ENTRE SURFACE ET ATMOSPHÈRE SUR MARS

présentée et soutenue publiquement

le 29 Janvier 2014

devant le jury composé de :

M. Hermann Zeyen	Président du jury
M. Pascal Allemand	Rapporteur
M. Stéphane Erard	Rapporteur
M. Patrick Launeau	Rapporteur
M. Serge Chevrel	Examinateur
M. Wojciech Markiewicz	Examinateur
M. Ali Mohammad-Djafari	Examinateur

Cette Habilitation à Diriger des Recherches a été préparée au Laboratoire “Interaction et Dynamique des Environnements de Surface” IDES (UMR 8148), qui est devenu le Laboratoire “Géosciences Paris Sud” (UMR 8148) au 1er Janvier 2014.









ADRESSE POSTALE

GEOPS Batiment 504/509
Université Paris-Sud
91405 Orsay FRANCE

SITE WEB

http ://geops.geol.u-psud.fr/
http ://planeto.geol.u-psud.fr/-Equipe-Geomorphologie-planetaire-.html

INFORMATIONS SUR LE PRÉSENT DOCUMENT

Ce tapuscrit a été produit sous Lyx et contient des liens hypertextes internes et externes.

JE SOUHAITE REMERCIER...

◁ Les membres du jury :

HERMANN ZEYEN, PASCAL ALLEMAND, STÉPHANE ERARD, PATRICK LAUNEAU, SERGE CHEVREL, WOJCIECH MARKIEWICZ ET ALI MOHAMMAD-DJAFARI pour avoir accepté cette invitation, pour avoir commenté ce tapuscrit et pour avoir éclairé mon travail avec de nouvelles perspectives.

◎ L'équipe de Géomorphologie Planétaire et Interactions Subsurface-Atmosphère :

JACQUES-MARIE BARDINTZEFF, MARC BIANCHERI-ASTIER, BERNARD BONIN, SYLVAIN BOULEY, ERIC CHASSEFIÈRE, FRANÇOIS COSTARD, LUCE DELABESSE, LAURE DUPEYRAT, JULIEN GARGANI, CHIARA MARMO, HÉLÈNE MASSOL, BÉATE OBERGER, BERNARD PLATEVOET, PHILIPPE SARDA, ALBANE SAINTENOY et ANTOINE SÉJOURNÉ pour leurs discussions ressourçantes dans les canapés bleus.

JENNIFER FERNANDO, FRANÇOIS ANDRIEU, FRANÇOIS LANDAIS, IRINA SHATALINA, GWENAEL JOUANNIC, ANTHONY LAGAIN, KELLY PASQUON et les étudiants en stage court dans l'équipe pour m'avoir aidé à "putcher" à 12h précise.

⊛ Les membres du laboratoire GEOPS :

CHANTAL ROCK ET GEORGETTE RABOUX pour leur gestion à la baguette des crédits pas toujours récurrents. LES GÉOLOGUES pour leurs missions enthousiasmantes. LES ORCÉENS FOOTANTS pour jouer jusqu'au bout de la nuit.

⊞ Les planétologues Martiens et autres traiteurs du signal :

SYLVAIN DOUTÉ, BERNARD SCHMITT pour leur collaboration non volatile. XAVIER CEAMANOS, PATRICK PINET ET YVES DAYDOU pour leurs tenues toujours photométriquement correcte. JEAN-PIERRE BIBRING, YVES LANGEVIN, MATHIEU VINCENDON ET L'ÉQUIPE DE L'IAS pour leur magnifique instrument OMEGA. NICOLAS GAC, MATTHIEU KOWALSKI ET L'ÉQUIPE DU L2S, intrétables sur le signal. SAÏD MOUSSAOUI ET MAXIME LEGENDRE pour les escapades mathématiques nantaises. ALBERT SCHMIDT pour son expertise sur l'implémentation tout azimut. MARCO GIURANNA ET BORTOLINO SAGGIN pour leurs explications sur les arcanes du traitement des données PFS.

Ⓢ Les relecteurs :

FRANÇOIS COSTARD, qui m'a titillé la plume. AURÉLIE, qui m'a supporté, soutenu et surtout beaucoup aidé pendant toute la rédaction. LOUISE, qui a égayé mes jours et EMILE, qui a égayé mes nuits.

⊟ Vous, lecteurs francophones de remerciements :

Parce que cette HDR est écrite pour VOUS, je vous remercie de la lire (même une toute petite partie !), de la commenter, de la critiquer, de la dépasser...

A propos du *CIR* et de l'*UPSy*, je dirais : "Quels sinistres mots !".

Maintenant que vous savez tout, bonne lecture !

Table des matières

Remerciements **ii**

Introduction **1**

I Analyse de données de télédétection **3**

1 Imagerie hyperspectrale **5**
1.1 Contexte . . . 6
1.1.1 Capteur . . . 6
1.1.2 Images hyperspectrales . . . 8
1.1.2.1 OMEGA . . . 9
1.1.2.2 CRISM . . . 10
1.1.3 Analyse de données . . . 11
1.1.3.1 Correction atmosphérique . . . 11
1.1.3.2 Détection de composés . . . 12
1.2 Contributions . . . 14
1.2.1 WAVANGLET . . . 14
1.2.2 Séparation de source en aveugle . . . 15
1.2.3 Démélange linéaire . . . 16
1.3 Perspectives . . . 18
1.3.1 Perspectives méthodologiques . . . 18
1.3.2 Perspectives planétologiques . . . 20
1.4 Publications . . . 20
1.4.1 WAVANGLET . . . 20
1.4.2 Séparation de source en aveugle . . . 33
1.4.3 LinMin . . . 45

2 Imagerie spectro-photométrique **75**
2.1 Contexte . . . 76
2.1.1 Modèle de BRDF de régolite . . . 78
2.1.1.1 Lambert . . . 78
2.1.1.2 Minnaert . . . 78
2.1.1.3 Noyaux . . . 78
2.1.1.4 Modèle de Hapke pour les matériaux granulaires . . . 79
2.1.1.5 Autres expressions analytiques . . . 80
2.1.2 Effet de l'atmosphère . . . 80
2.2 Contributions . . . 81
2.2.1 Mars-REcO . . . 82

2.2.2 Inversion bayésienne et comparaison avec les données in situ . . . 83
2.3 Perspectives . . . 84
2.3.1 Perspectives méthodologiques . . . 84
2.3.2 Perspectives planétologiques . . . 84
2.4 Publications . . . 84
2.4.1 Mars-ReCO . . . 85
2.4.2 Photométrie MER . . . 106

3 Spectroscopie haute résolution 133
3.1 Contexte . . . 134
3.1.1 Le méthane sur Mars . . . 134
3.1.2 Etude de la surface avec PFS . . . 134
3.1.3 Microvibrations de PFS . . . 135
3.2 Contributions . . . 138
3.2.1 Modélisation analytique des vibrations . . . 138
3.2.2 Traitement des données réelles de PFS . . . 139
3.3 Perspectives . . . 141
3.3.1 Perspectives méthodologiques . . . 141
3.3.2 Perspectives planétologiques . . . 143
3.4 Publications . . . 143
3.4.1 Modélisation analytique des vibrations . . . 143
3.4.2 Correction des données PFS . . . 164

II Echanges de volatils sur Mars 185

4 La calotte saisonnière sud de Mars 187
4.1 Contexte . . . 188
4.1.1 Histoire des observations des calottes martiennes . . . 188
4.1.2 La calotte saisonnière sud de Mars . . . 190
4.1.2.1 Observations . . . 190
4.1.2.2 Modélisations . . . 194
4.1.3 Incomplétudes . . . 195
4.1.3.1 Incomplétudes 1 : asymétrie de la récession . . . 195
4.1.3.2 Incomplétudes 2 : Région cryptique . . . 196
4.1.3.3 Incomplétudes 3 : Spiders, geysers et écoulement sombre . . . 197
4.2 Contributions . . . 207
4.2.1 Cartographie de présence des glaces par spectro-imagerie . . . 207
4.2.2 Modélisation des échanges de glace . . . 208
4.2.3 Spectroscopie . . . 208
4.2.4 Géomorphologie . . . 208
4.3 Perspectives . . . 212
4.4 Publications . . . 213
4.4.1 Asymétrie de la calotte saisonnière Sud de Mars . . . 213
4.4.2 Sublimation de la calotte saisonnière Sud de Mars . . . 235
4.4.3 Glace d'eau sur la dune de Richardson . . . 246

5 Les clathrates dans l'histoire de Mars 265
5.1 Contexte . . . 266
5.1.1 Indices géomorphologiques . . . 266
5.1.1.1 Terrains chaotiques et vallées de débâcle . . . 266
5.1.1.2 Volcans de boue . . . 268

5.1.2 Indices de clathrate actuel . . . 268
5.2 Contributions . . . 270
5.3 Perspectives . . . 275
5.4 Publications . . . 276
5.4.1 Clathrate de CO_2/SO_2 sur Mars . . . 276

III Projet de recherche **291**

6 Projet de recherche : interaction surface-atmosphère **293**
6.1 Geysers et spiders . . . 294
6.2 Source d'eau atmosphérique sur Mars . . . 295
6.3 Dégradation des surfaces planétaires par étude photométrique . . . 296
6.3.1 Observation . . . 296
6.3.1.1 Mars . . . 296
6.3.1.2 Lune . . . 297
6.3.2 Expérience de laboratoire . . . 297
6.4 Clathrate sur Mars . . . 298
6.4.1 Clathrate de CH_4 actuel . . . 298
6.4.2 Clathrates passés . . . 298

Conclusion et perspectives **300**

IV Annexes **303**

7 Annexe 1 : Curriculum Vitae detaillé **305**
7.1 Emplois dans la recherche : . . . 305
7.2 Enseignements : . . . 305
7.3 Jury et commission de recrutement : . . . 305
7.4 Encadrement d'étudiants : . . . 306
7.5 Instruments spatiaux : . . . 307
7.6 Responsabilité : . . . 307
7.7 Expert pour les revues suivantes : . . . 307
7.8 Financements : . . . 307
7.9 Publications . . . 308
7.9.1 Publications de rang A : . . . 308
7.9.2 Résumé de congrès : . . . 309
7.9.3 Autres publications : . . . 309

Bibliographie **311**

Table des figures **340**

Liste des tableaux **344**

Introduction

Ce manuscrit d'Habilitation à Diriger des Recherches (HDR) est composé de deux parties : une première partie méthodologique qui concerne le développement d'outils numériques d'analyse de données, et une seconde partie qui se rapporte à l'étude des échanges de volatils sur Mars avec les outils précédemment décrit.

Le premier objectif de ce manuscrit est de réaliser un bilan des outils d'analyse de plusieurs techniques d'imagerie et de spectroscopie pour l'étude de la surface de Mars. Cette première partie méthodologique sera développée en trois chapitres, concernant les images hyperspectrales, l'imagerie photométrique et la spectroscopie à haute résolution.

Les images hyperspectrales martiennes, qui consistent à enregistrer plusieurs images à une centaine de longueurs d'onde, ont été produites par les instruments OMEGA et CRISM dans le visible et l'infrarouge. Ces instruments ont produit plusieurs dizaine de To de données, sous forme de ~100 000 images hyperspectrales. Ce volume de données mais aussi la structuration en cube spectro-spatial posent un véritable défi au traitement et à la visualisation des résultats.

L'imagerie photométrique martienne, qui consiste à observer la même zone sous diverses géométries, est produite en routine grâce à l'instrument HRSC mais surtout CRISM. Le défi d'analyse de ces données concerne la prise en compte de l'effet des aérosols en utilisant un modèle de transfert radiatif, à la fois précis et rapide, pour estimer la photométrie de la surface pour plusieurs pixels de l'image.

La spectroscopie à haute résolution en orbite autour de Mars, est produite par l'instrument PFS, qui souffre malheureusement des effets de micro-vibrations de la plateforme Mars Express. Le défi technique de correction de ces données relève de la mise en place d'un outil aveugle, car les micro-vibrations ne sont pas bien caractérisées. Face à la quantité de données PFS de l'ordre d'un milliard de spectres, le défi de rapidité de traitement est aussi très important dans cette problématique.

Dans ces trois chapitres, nous dresserons le panorama actuel des méthodes d'analyse et leurs limitations. Puis, mes diverses contributions et améliorations méthodologiques seront développées. Enfin, des perspectives à la fois méthodologiques mais également planétologiques seront proposées.

La première partie de ce document propose de répondre à ces défis techniques à l'aide d'outils novateurs et récents issus de la communauté des Sciences et Technologies de l'Information et de la Communication (STIC). Les domaines d'application qui nous concernent sont la Planétologie et les Sciences de la Terre.

Le second objectif de ce manuscrit est de faire la synthèse de notre compréhension des interactions entre surface et atmosphère sur Mars sous forme d'échange de volatils. Cette seconde partie planétologique sera développée en deux chapitres concernant la calotte saisonnière sud de Mars et les clathrates dans l'histoire de Mars.

La calotte saisonnière sud de Mars est majoritairement composée de glace de CO_2, contrairement à la calotte saisonnière nord, composée d'eau et de CO_2. Le pôle sud est un bon laboratoire pour la compréhension des échanges uniquement de CO_2 . Néanmoins, la complexité des échanges CO_2 pose un défi

dans leur compréhension car plusieurs phénomènes aux échelles microscopiques (sublimation, métamorphisme,...), macroscopiques (geysers, écoulement sombre, ...), régionales (région cryptique, précipitation de neige,...) ont lieu en même temps.

Les clathrates sont une structure cristalline de glace d'eau sous forme de cage, pouvant piéger des molécules hôtes. Si les conditions de stabilité thermodynamiques de ces espèces sont possibles aujourd'hui sur Mars au niveau des calottes, leur cinétique de formation est en générale très lente. En revanche, leurs propriétés de métastabilité ou préservation anormale, pourraient permettre aux clathrates d'être présents actuellement sur Mars. Aussi, dans le passé de Mars, les clathrates ont pu être stables. Pour dresser l'histoire des échanges de volatils sur Mars, il est nécessaire de réaliser une synthèse entre différentes sources d'informations indépendantes : les observations géomorphologiques, les équilibres thermodynamiques et les principes physiques du climat.

Pour chacun des chapitres, une synthèse bibliographique sera exposée dans un premier temps. Puis, mes travaux personnels seront détaillés. Enfin, des perspectives seront dressées.

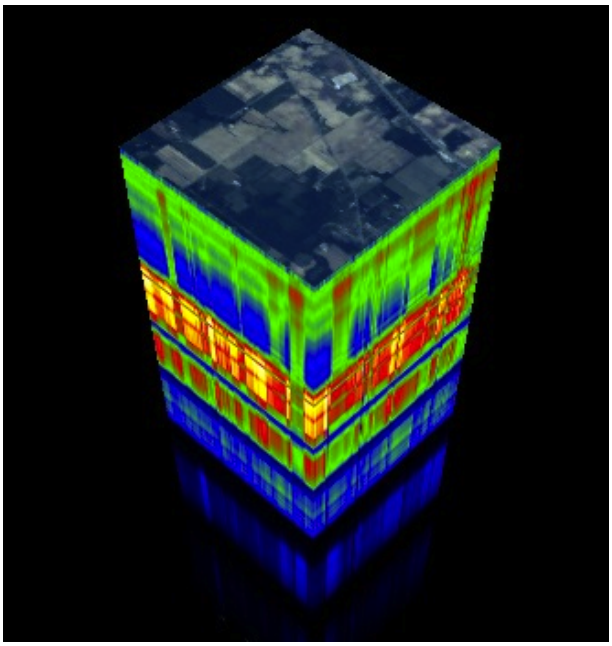
Ce manuscrit se conclu par une synthèse des perspectives concernant l'ensemble de ces thématiques. Les articles scientifiques correspondants à ces différentes thématiques sont disponibles au sein de chaque chapitre. Les références bibliographiques sont données en fin de document.

Première partie

Analyse de données de télédétection

Chapitre 1

Imagerie hyperspectrale



Représentation d'un cube de données hyperspectral

L'imagerie classique comporte une seule gamme de longueur d'onde voir trois pour l'imagerie couleur. L'imagerie "multispectrale" en comporte une dizaine et l'imagerie "hyperspectrale" plus d'une centaine (voir illustration page 5). Un élément dans la dimension spectrale est nommé *spectel*, tandis que dans la dimension spatiale, il est nommé *pixel*. Pour mes travaux de recherche, j'ai utilisé l'imagerie hyperspectrale qui consiste en l'obtention d'une information de radiance lumineuse (en W.m^{-2}.sr^{-1}), à la fois dans le domaine spectral et dans le domaine spatial. L'intérêt de ces données "hyperspectrales" réside dans le fait qu'à la fois les images seules et les spectres seuls contiennent de l'information scientifique pertinente mais que la combinaison de ces deux aspects (images et spectres) amène à élaborer des cartes de composition chimique ou de paramètres physiques, permettant une analyse scientifique sans précédent, comme en témoigne l'explosion du développement de ces technologies (voir tableau 1.1). Les premiers spectro-imageurs terrestres datent du début des années 1980-1990, avec notamment AVIRIS [323], le premier système développé au Jet Propulsion Laboratory (JPL). Le tableau 1.1 dresse la liste des instruments majeurs. Nous allons surtout décrire ici, les deux instruments majeurs pour l'étude de Mars : OMEGA et CRISM.

Dans un premier temps, il sera décrit brièvement le contexte de l'imagerie hyperspectrale pour l'observation de la Terre et des corps planétaires, la technologie des capteurs (voir section 1.1.1), la structure des images hyperspectrales (voir section 1.1.2) et les traitements associés (voir section 1.1.2). Dans un second temps, je détaillerai mes contributions personnelles (voir section 1.2) développées durant ma thèse, mon post-doctorat et dans les travaux méthodologiques de Maxime Legendre et François Andrieu que j'ai encadrés. Les perspectives de ces travaux seront présentées à la section 1.3 page 18.

Les nouvelles générations d'instruments incorporent un aspect d'échantillonnage "multi-angulaire", qui consiste à observer un même site à une dizaine de géométries différentes. L'instrument CRISM de la mission Mars Reconnaissance Orbiter (NASA) cumule, notamment, l'aspect hyperspectral et multi-angulaire qui sera traité dans le chapitre suivant.

1.1 Contexte

1.1.1 Capteur

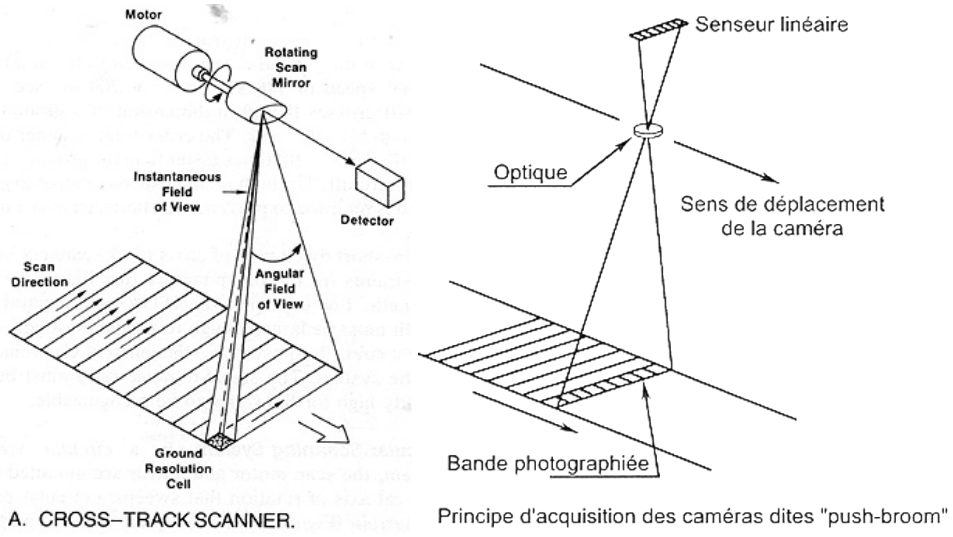
Un instrument produisant des images hyperspectrales est qualifié de spectro-imageur. Il comporte un système optique, un dispositif de sélection des longueurs d'onde qui peut être un prisme ou un réseau, un capteur numérique (équivalent au type CCD, Charge Coupled Device).

Les spectro-imageurs embarqués fonctionnent de deux façons différentes : "whisk-broom" ou "push-broom" qui sont deux types de balais. Le principe de fonctionnement consiste en l'acquisition des données simultanément pour toutes les longueurs d'onde et de réaliser un balayage de la zone observée, le long de la trace au sol du satellite ou de l'avion (voir figure 1.1).
Le mode whisk-broom est le plus ancien mode de fonctionnement. Il est à l'oeuvre lorsque le détecteur est une barrette CCD, l'acquisition de plusieurs spectres à la fois est alors impossible. Il s'agit de balayer avec un système optique la direction perpendiculaire à la trace au sol par un mouvement oscillant similaire à celui d'un balai pendulaire.
Le mode le plus récent est le push-broom, possible avec des matrices CCD. Il consiste à enregistrer une ligne au sol dans la direction perpendiculaire à la fauchée. Par analogie avec un balai à pousser, l'image se construit par juxtaposition des lignes acquises successivement.

Les capteurs convertissent le flux lumineux en signal numérique qui est stocké puis envoyé sur Terre. L'étalonnage des données hyperspectrales se fait en corrigeant le signal des différentes réponses instrumentales.
La réponse en intensité de l'instrument est fortement dépendante de la fréquence, il faut donc étalonner radiométriquement les données. Le niveau de bruit du détecteur est différent pour chaque élément du capteur (pour le whisk-broom, pixel et spectel pour le push-broom). De plus, la détérioration du détecteur dans l'espace, essentiellement par des rayons cosmiques, peut produire une altération ou une destruction de certains spectels. Ces spectels inutilisables sont dit *spectels chauds* (plus bruités) ou *spectels morts*,

Nom	Date	Mission	Corps	Longueur d'onde (μm)	Nb canaux maximum
ISM [16]	1989	Phobos2	Mars	0.76-3.14	128
TES[50]	1992	Mars Global Surveyor	Mars	5.8 - 150	286
NIMS[30]	1992	Galileo	Jupiter	0.7 - 5.2	408
AVIRIS[323]	1993	Aéroporté	Terre	0.400 - 2.500	224
VIRTIS[59]	1998	Rosetta	67P/Churyumov-Gerasimenko	0.25 - 5.0	388
Hyperion[252]	2003	Earth Observing 1	Terre	0.400 - 2.500	242
OMEGA[17]	2004	Mars Express	Mars	0.38– 5.1	352
VIMS[25]	2004	Cassini	Saturne	0.3– 5.1	352
CRISM[235]	2007	Mars Reconnaissance Orbiter	Mars	0.362 – 3.920	544
VIRTIS[1]	2007	Venus Express	Vénus	0.28 - 5.0	432
M^3[255]	2009	Chandrayaan-1	Lune	0.430 - 3.000	260
SIMBIO-SYS [88]	2010	BepiColombo	Mercure	0.4-2.0	256
MERTIS [131]	2010	BepiColombo	Mercure	7-14	78
VIR[277]	2011	DAWN	Cérès	0.25 - 5.0	-
MAJIS	?	Juice	Jupiter 2022	?	?

TABLE 1.1: Liste des instruments spectro-imageurs hyperspectraux (plus d'une centaine de canaux spectraux) majeurs, terrestres et en Planétologie en vol et sélectionné, avec leur couverture spectrale totale et leur nombre totale de longueurs d'ondes. Les autres caractéristiques de ces instruments sont disponibles dans les références.



(a) Principe du whisk-broom

(b) Principe du push-broom

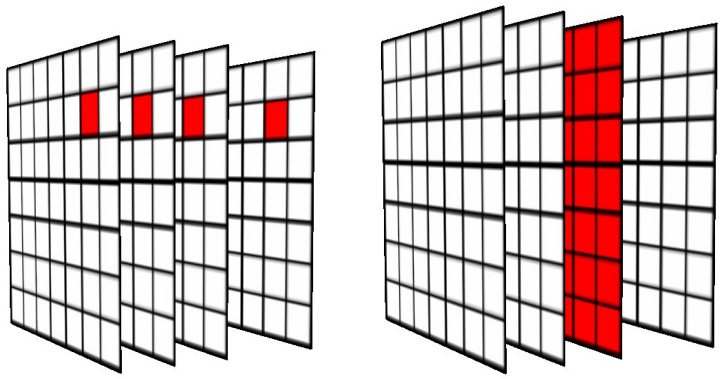
FIGURE 1.1: Principe d'acquisition des spectro-imageurs

respectivement.
Il est essentiel de connaître la réponse spectrale de l'instrument pour la modélisation, en particulier en cas de sous-échantillonnage spectral comme pour les glaces d'eau et de CO_2 avec OMEGA et CRISM. Nous pouvons reproduire les signaux observés grâce à une convolution entre le signal à haute résolution spectrale et la réponse spectrale.
La réponse de l'instrument dans le domaine spatial est le *champ de vue* associé à chaque pixel : c'est à dire l'étendue exacte au sol de la zone de chaque pixel. Nous pouvons reproduire les signaux observés grâce à une convolution entre une carte à haute résolution spatiale et le champ de vue.
Avec la connaissance des réponse spectrales et spatiales, il est possible d'appliquer une correction, spécifique au mode d'acquisition push-broom ou whisk-broom. Connaître ces fonctions de réponse instrumentale est d'autant plus important qu'elles peuvent changer au cours du temps.

1.1.2 Images hyperspectrales

Nous allons nous focaliser sur des données de télédétection hyperspectrale, c'est à dire sur des données agencées en cubes : un tenseur d'ordre 3 dont 2 directions spatiales : la direction de défilement du point de visée au dessus de la planète notée x, et la direction orthogonale notée y, alignée avec la *fauchée*. Un élément du plan spatial est appelé *pixel* de coordonnées (x, y). Un ensemble de pixels forme un *canal* ou *canal spectral*. La troisième est la direction spectrale, notée λ, qui correspond à la décomposition de la lumière à des longueurs d'onde précises. Un élément de la direction spectrale est appelé *spectel*. Un ensemble de spectels forme un *spectre* (voir figure 1.2). Les données sont donc agencées en cube noté $\mathbf{C}_{x,y,\lambda}$. Lorsque le cube est en unité de réflectance et que l'ordonnancement des pixels n'est pas utilisé (c'est à dire que la contigüité des pixels est ignorée, ce qui est le cas de la quasi-majorité des traitements), il est noté $\mathbf{R}(\lambda)$.

Chaque direction du tenseur a une dimension, c'est à dire un nombre de pixel/spectel associé. Le nombre de pixel dans la direction x, respectivement y, est noté N_x, respectivement N_y. Le nombre de spectel total dans la direction λ est noté N_λ.
L'imagerie "multi-spectrale" se contente d'une dizaine de canaux ($N_\lambda \simeq 10$) tandis que l'imagerie "hyperspectrale" dépasse la centaine de canaux (N_λ>100).



(a) Spectre (b) Canal spectral

FIGURE 1.2: Schéma d'un cube hyperspectral.

TABLE 1.2: Caractéristiques spectrales de l'instrument OMEGA à bord de Mars Express.

	Voie V	Voie C	Voie L
Domaine spectral (μm)	0,38 à 1,05	0,93 à 2,73	2,55 à 5,1
Nombre de spectels	96 ou 144	128	128
Pas spectral (μm)	0,007 ou 0,0045	0,013	0,020

1.1.2.1 OMEGA

L'instrument OMEGA à bord de la plateforme Mars Express (ESA) a été développé par l'IAS (Institut d'Astrophysique Spatiale, Orsay) en collaboration avec le LESIA (Laboratoire d'Etudes Spatiales et d'Instrumentation en Astrophysique, Paris/Meudon), IFSI (Instituto di Fisica dello Spazio Interplanetario, Rome) et IKI (Institute for Space Research, Moscou) [17]. Il contient trois voies distinctes : V dans le visible en mode push-broom ; C dans les "courtes" longueurs d'onde de l'infra-rouge proche en mode whisk-broom ; L dans les "larges" ou grandes longueurs d'onde de l'infra-rouge proche en mode whisk-broom. Les caractéristiques spectrales des trois détecteurs sont détaillées dans le tableau 1.2. Dans la suite de ce manuscrit, nous allons uniquement utiliser la partie infra-rouge proche (voies C et L) d'une part, parce que l'étalonnage radiométrique dans le visible est plus difficile, d'autre part, parce que les glaces martiennes comportent des signatures spectrales univoques essentiellement dans le proche infra-rouge. La résolution spatiale d'OMEGA, entre 350 m et 4 km, dépend fortement de l'altitude de la plateforme Mars Express qui gravite sur une orbite très elliptique.

Base de données OMEGA Cette base de données est disponible pour les Co-Investigateurs mais aussi publiquement sur le site internet de l'archive du PSA (Planetary System Archive, ESA, ESAC). Il existe plusieurs produits pour chacune des observations infra-rouges proche OMEGA. Pour chaque observation, un étalonnage est proposé, puis un assemblage des voies C et L. Tous ces produits sont indexés par des noms du type ORBXXXX_Y.ZZZ avec : XXXX le numéro de l'orbite, Y l'index de la session sur l'orbite, ZZZ le produit en question spatialement conforme à l'observation.

Exposons ici brièvement les différents produits :

- CUB : cube hyperspectral en I/F (facteur de radiance sauf pour la partie d'émission thermique dominante), noté $\mathbf{L}(\lambda)$.
- GEO : cube de données auxiliaires contenant les informations géographiques déterminées grâce à la position et à l'orientation de Mars Express sur son orbite lors de l'acquisition (coordonnées géographiques des pixels, angles d'incidence et d'émergence, topographie MOLA rééchantillonnée, ...). Il existe des biais systématiques dans l'estimation de ces métadonnées.

TABLE 1.3: Caractéristiques spectrales de l'instrument CRISM à bord de Mars Reconnaissance Orbiter.

	Voie VNIR	Voie IR
Domaine spectral (μm)	0,362 à 1,053	1,002 à 3,920
Nombre de spectels	96 ou 144	480
Pas spectral (μm)	0,00655	0,00655

- REF : cube hyperspectral en réflectance, noté $\mathbf{R}(\lambda)$. On divise simplement le CUB par l'angle d'incidence inclus dans le GEO. Si la position du satellite est mal connue et si la surface a une pente, le facteur de réflectance REF est incorrect.
- ATM : cube hyperspectral de transmission atmosphérique calculé en utilisant un modèle de transfert radiatif uniquement pour les gaz. La méthodologie utilisée à l'IPAG (Grenoble) peut être qualifiée d'ab initio, c'est à dire qu'elle est basée uniquement sur des données d'état atmosphérique issues du GCM Mars Climate Database [74].
- RAC : cube hyperspectral de la réflectance au sol, corrigé des absorptions atmosphériques des gaz du produit ATM.
- LRAC : cube hyperspectral de la réflectance au sol, corrigé des absorptions atmosphériques des gaz grâce à la méthode dite de "volcano-scan" [84, 177, 216].

1.1.2.2 CRISM

L'instrument CRISM à bord de la plateforme Mars Reconnaissance Orbiter (NASA) a été développé par un consortium de laboratoires américains [235].

Il contient deux voies distinctes, en mode push-broom : (i) VNIR (Visible and Near Infra-Red) dans le visible et proche infra-rouge, basée sur une matrice de détecteurs photodiodes de Silicium dopé à l'Indium et (ii) IR (Infra-Red) dans l'infrarouge, basée sur une matrice HgCdTe dopé à l'Indium. Les caractéristiques spectrales des deux détecteurs sont détaillées dans le tableau 1.3. Ce type de détecteur est sujet à des aberrations appelées "spectral smile" : dû aux imperfections du réseau, la même ligne du détecteur n'enregistre pas à la même longueur d'onde. Cependant, les spécifications techniques de l'instrument prétendent un décalage inférieur à 1,3 pixels. Une méthode a été proposée pour corriger cet artefact [33].

La résolution spatiale de CRISM est de 15 à 19 mètres pour l'image centrale nadir en mode «targeted observations» (voir chapitre suivant pour le mode "Emission Phase Function"). Le mode multispectral comporte 72 longueurs d'onde choisies avec une dégradation de la résolution spatiale à 100 ou 200 m/pixel.

Base de données CRISM Tous les produits CRISM sont indexés par des noms du type suivant :
FRT00007F49_07_IF163L_TRR2_???.IMG

- FRT : type d'observation
  - FRT : Full Resolution Targeted Observation
  - HRL : Half Resolution Large Targeted Observation
  - HRS : Half Resolution short Targeted Observation
- 00007F49 : Numéro d'observation en 8-digit hexadecimal
- 07 : Compteur hexadecimal pour le numéro de l'image :
  - 00, 06, 08 et 0E : 4 images du courant d'obscurité pour la calibration
  - 01 à 05, 09 et 0A à 0D : 10 images à basses résolutions en mode EPF (Emission Phase Function : configurations différentes)
  - 07 : 1 image à haute résolution qui constitue l'image centrale en mode "targeted mode"
- IF163 : Index des commandes internes et mode de l'instrument
  - IF : I/F

  - RA : radiance
- L : sensor ID
  - S : VNIR - visible and near infrared
  - L : IR - infrared
- TRR2 :
  - TRR2 : Calibration (TRDR pour “Targered Reduced Data Record”) version 2
  - TRR3 : Calibration (TRDR) version 3
  - DDR1 : Données géométriques additionnelles (DDR pour “Derived Data Record”) version 1 contenant les latitudes, longitudes, angles photométriques, ...
- ? ? ? : correction atmosphérique
  - néant : sans correction atmosphérique
  - LRAC : cube hyperspectral de la réflectance au sol, corrigé des absorptions atmosphériques des gaz grâce à la méthode dite de “volcano-scan” [84, 177, 216].
- IMG : extension du fichier
  - IMG : image data
  - LBL : PDS label
  - TAB : table instrument housekeeping

1.1.3 Analyse de données

Dès les débuts de AVIRIS [108], les aspects d’analyse des images hyperspectrales ont été abordés : simulation d’une observation, correction atmosphérique, algorithme de détection et de traitement.

Dans le domaine de la planétologie, la simulation d’observation hyperspectrale n’est pas très utilisée. Plusieurs modélisations analytiques [82] ou numériques [77, 73] de la réflectance observée sont disponibles. Récemment, un effort a été fait pour intégrer les caractéristiques de l’instrument CRISM afin de créer une simulation d’observation réaliste [251].

1.1.3.1 Correction atmosphérique

L’atmosphère martienne, bien que ténue, absorbe les photons solaires essentiellement à cause du gaz de CO_2 et, dans une moindre mesure, de H_2O, CO et OH. Aussi, l’atmosphère contient des aérosols en suspension qui absorbent et diffusent le rayonnement.

Les méthodes de corrections atmosphériques les plus basiques consistent à ignorer les effets de diffusion. Ces méthodes considèrent uniquement la transmittance atmosphérique [18, 218, 238], et éventuellement la composante de réflexion diffuse supposée de forme connue [56]. Des méthodes de corrections plus raffinées supposent que la couche d’aérosols est confinée proche de la surface, ce qui permet de découpler la correction des gaz et des aérosols [74, 329].

Correction des absorptions des gaz La méthode la plus utilisée est celle dite du “volcano-scan” qui consiste à utiliser une observation de Olympus Mons pour estimer la transmittance atmosphérique moyenne martienne, puis d’ajuster cette transmittance à chacun des spectres observés sur la base d’une bande de CO_2 atmosphérique [84, 177, 216]. Cependant, cette méthode ne fonctionne pas en présence de glace de CO_2 à la surface car les longueurs d’onde du CO_2 gazeux et solides se recouvrent.

Une autre solution consiste à utiliser les informations des simulations numériques du climat des Global Climate Model (GCM), notamment la Mars Climate Database (MCD) [191], pour créer des spectres de transmittance atmosphérique ab initio dépendant des conditions locales de prise de vue [218, 75]. D’après la structure horizontale en composition, pression et température des GCM, on estime la transmittance atmosphérique avec un code de transfert radiatif ligne-par-ligne. Ce type d’approche est plus lourd à mettre en place mais permet d’être utilisé même sur les terrains de glace de CO_2. On note généralement un bon ajustement des données et du GCM à un facteur d’échelle près (dû aux perturbations météorologiques non modélisées par le GCM)

Correction des aérosols La composante diffuse peut alors être estimée par méthode Monte Carlo [329]. Pour plus d'efficacité numérique [74], il est possible d'estimer la contribution de transmission diffuse et de réflexion diffuse analytiquement [208] et d'appliquer la méthode de Green [201], comme développé dans la section 2.1.2 page 80.

Ces approches nécessitent de connaître les propriétés optiques des aérosols mais aussi leur contenu τ_{aero} (épaisseur optique). Les propriétés optiques des aérosols martiens ont été estimées lors des épisodes de tempêtes de poussières globales, lorsque l'épaisseur optique était très grande [247, 329, 340, 239].

Au delà des estimations in situ de τ_{aero} par les rovers Spirit et Opportunity [148, 147], il est possible d'estimer la quantité d'aérosols d'après les bandes de glace de CO_2 saturées [330] mais aussi en utilisant les observations EPF [340, 76].

1.1.3.2 Détection de composés

La détection de composés minéraux ou glace à la surface de Mars est une étape importante dans l'interprétation des images hyperspectrales. Plusieurs types d'approches ont été proposés dans la littérature [283].

Manuelle Les classifications manuelles s'opèrent sur un graphe en nuage de points (scatterplot) sur des informations spectrales/spatiales en général faites après une réduction de dimensionnalité de type Analyse en Composante Principale [44, 288].

Un autre type d'approche concerne le calcul de dérivé du spectre pour estimer les bandes d'absorption très fines [212, 209]. Dans ce cas, il faut identifier manuellement chacune des bandes d'absorptions pour réaliser une détection, puis éventuellement une opération de seuillage pour obtenir une carte de détection.

Profondeur de bande Les classifications automatiques peuvent s'opérer grâce à des seuils sur des ratios de profondeur de bande. Cette technique a été beaucoup employée dans la détection des minéraux et glaces sur les instruments OMEGA [19] et CRISM [254]. Voici par exemple un seuil de détection de la glace d'eau [179] :

$$\begin{cases} \mathrm{R}_{\mathrm{H_2O}} = \frac{\mathbf{R}(1{,}500\mu m)}{(\mathbf{R}(1{,}385\mu m))^{0.7}.(\mathbf{R}(1{,}770\mu m))^{0.3}} \\ \mathrm{B}_{\mathrm{H_2O}}(1,5\mu m) = 1 - (\mathrm{R}_{\mathrm{H_2O}}) \end{cases} \tag{1.1}$$

L'avantage de cette approche est l'extrême simplicité, le temps de calcul très court et la sensibilité très importante. Cependant, si les longueurs d'ondes d'appui sont détériorées ou contiennent une information non souhaitée (par exemple, une absorption d'un autre composé), les ratios ne sont plus utilisables. Aussi, cette approche est très sensible au bruit.

Dans le cadre de la détection de minéraux, certains auteurs proposent de réaliser une opération de mise à l'échelle des spectres en réalisant un ratio entre la zone d'intérêt et une zone interprétée comme "neutre" [18, 32]. Ceci permet de s'affranchir d'éventuels artefacts de calibration de l'instrument et les non-linéarités, en supposant qu'ils soient identiques pour tous les spectres. En revanche, si la zone neutre contient des informations spectrales, cette opération pourrait créer des structures artificielles sur les données.

Plus récemment, des opérations de moyennage, de filtrage et de pré-traitement ont permis de repousser les limites de détection [32].

Automatique supervisée Les méthodes automatiques supervisées nécessitent une base de données de spectres de références, de laboratoire et/ou synthétiques. Il est aussi possible d'extraire des "endmembers" de l'image grâce à des algorithmes comme Pixel Purity Index [23], N-FINDR [339], ou grâce à une segmentation sur un graphe [316]. Ces méthodes vont alors faire une comparaison avec les spectres réellement observés, par exemple le coefficient de corrélation [176] ou l'angle spectral [160]. Il est possible d'effectuer cette comparaison dans l'espace usuel ou aussi dans un espace plus adéquat, comme dans

l'espace des coefficients d'ondelette, comme l'algorithme WAVANGLET, développé durant ma thèse (voir 1.2.1).

Les méthodes dites de "démélange linéaire" font l'hypothèse que chaque spectre observé est un mélange linéaire des spectres de références :

$$\mathbf{R}(\lambda) = \sum_{\mathrm{i}=1}^{N_s} \alpha_\mathrm{i}.\mathbf{R}_\mathrm{i}(\lambda) + \varepsilon(\lambda) \tag{1.2}$$

Avec, $\mathbf{R}(\lambda)$: spectre de l'image hyperspectrale (en général mesuré en facteur de réflectance).
α_i : coefficient de mélange ou proportion de mélange de la source "i"
$\mathbf{R}_\mathrm{i}(\lambda)$: spectre associé à la référence "i" (en général mesuré en facteur de réflectance)
N_s : nombre de sources
$\varepsilon(\lambda)$: erreur à minimiser (bruits + incohérences du modèle)

Il s'agit d'estimer α_i en incorporant ou non plusieurs types de contraintes, comme la positivité $\alpha_\mathrm{i} > 0$, la somme à un $\sum \alpha_\mathrm{i} = 1$, la parcimonie. Une synthèse concernant les méthodes de démélange a été faite récemment [22].

La méthode la plus simple consiste à ajuster les α_i tel que $\|\varepsilon(\lambda)\|$ soit minimisé. Elle est utilisée sur les données TES, sur Mars Global Surveyor/NASA [300, 12, 273]. Pour garantir la positivité, il est possible d'éliminer itérativement les spectres ayant des coefficients négatifs [56]. L'affectation d'un coefficient négatif est improbable si le spectre de référence est présent dans le mélange. Cette hypothèse peut être invalidée dans un mélange linéaire en cas de recouvrements.
La méthode "non negatively constrained least squares" suppose que les coefficients soient positifs ou nuls. Elle est basée sur les multiplicateurs de Lagrange. Elle semble efficace dans l'estimation de l'abondance de certains composants chimiques par spectroscopie [174].
En imposant à la fois la positivité de façon mathématique et la somme des proportions égale à un, le problème est connu sous le nom de "Fully Constrained Least Squares" (FCLS) [182, 123]. Il est utilisé dans le domaine de la télédétection [107] mais aussi dans mes travaux personnels de détection de glaces sur les dark spots [158]. Ce problème peut aussi être résolu de manière géométrique, en approximant la dimensionnalité, en considérant le simplex [130]. L'approche bayésienne permet une estimation robuste des coefficients de mélanges, comme proposé par "Maximum A Posteriori" (MAP) [312]. Ces algorithmes sont rapides, comportent des résultats parcimonieux mais aussi des problèmes de convergence et sont incompatibles avec des spectres de références fortement corrélés.

Grâce à FCLS, j'ai pu montrer qu'il n'y avait pas de signature d'eau liquide dans les spectres CRISM associés aux écoulements des "darks spots" [158] (voir section 4.2.3 page 208).

Au cours d'une collaboration avec le groupe d'Athènes, nous avons pu montrer que l'algorithme MAP a les aptitudes pour la détection de glaces et de minéraux mafiques sur des images OMEGA [311] avec un temps de calcul très intéressant.

J'ai continué à développer cette voie, en collaboration avec Saïd Moussaoui [46, 47, 45], pour créer un outil ayant les propriétés nécessaires à son utilisation dans le traitement des images hyperspectrales : positivité, somme à une, rapidité, unicité de la solution, aptitude à traiter des spectres fortement corrélés (voir section 1.4.3).

Automatique non-supervisée Les méthodes non-supervisées ne nécessitent pas de spectres de références et sont basées uniquement sur des considérations statistiques, c'est à dire les informations des nombreux spectres contenus dans une image hyperspectrale.

En général, les méthodes non-supervisées sont basées sur l'équation de mélange linéaire (eq 1.2), il s'agit d'estimer les coefficients de mélange α_i et les spectres extrêmes $\mathbf{R}_\mathrm{i}(\lambda)$.
La méthode la plus simple est l'Analyse en Composante Principale (ACP) qui suppose une décorrélation des sources. Cependant, cette hypothèse n'est pas adaptée aux images hyperspectrales car il y a de fortes corrélations spectrales entre composés chimiques et de forte corrélation spatiale entre classes [283]. L'Analyse en Composante Indépendante (ACI), [175, 137], recherche les sources les plus indépendantes entre elles, avec un critère de non-gaussianité ou d'information mutuelle. Les algorithmes les plus connus

sont Fast-ICA [136] et JADE [29], utilisés en Planétologie [95, 233, 83, 239]. Cependant, ces approches autorisent des abondances α_i et des spectres $\mathbf{R}_i(\lambda)$ négatifs, ce qui est une aberration.

Une autre approche consiste à utiliser uniquement les informations de positivité et de somme à un. C'est à dire l'équation 1.2 avec $\alpha_i > 0$ et $\sum \alpha_i = 1$. Ce nouveau problème est résolu soit avec des méthodes d'optimisation (minimisation d'une fonction coût) [184], soit de manière bayésienne [232]. La seconde approche comporte des problèmes d'unicité de solutions, corrigés par des termes additionnels de la fonction coût à minimiser [135]. La troisième, développée en partie par mes travaux, a pour limitation le temps de calcul (voir section 1.4.2).

1.2 Contributions

Au cours de mes recherches, j'ai développé trois types d'outils complémentaires pour la détection et l'analyse des spectro-images : "WAVANGLET" basée sur les ondelettes pour limiter les effets géométriques, "Séparation de sources en aveugle" basée sur l'inférence bayesienne pour une robustesse d'estimation non supervisée, "LinMin" basée sur le démélange linéaire avec l'algorithme en point intérieur pour une efficacité de détection supervisée. Les trois prochains sous-chapitres décrivent ces outils, leurs développements, leurs utilités et leurs complémentarités. Les articles scientifiques décrivant ces méthodes sont disponibles dans les sous-chapitres suivant.

1.2.1 WAVANGLET

La présence de glaces autour des pôles de Mars, observées avec des conditions extrêmes de géométrie en incidence et parfois en émergence, rend nécessaire le développement d'outils spécifiques de détection indépendants de la géométrie. Les outils de type rapports de bandes sont très dépendants de la géométrie, car la BRDF des glaces est très anisotrope. J'ai développé au cours de ma thèse un outil de détection supervisée (voir paragraphe 1.1.3.2) qui permet de s'affranchir des conditions d'illumination, en réalisant la détection dans un sous-espace d'ondelettes. Les ondelettes sont particulièrement adaptées aux spectres en réflectance car quelques coefficients suffisent pour décrire une bande d'absorption spécifique.

Dans un premier temps, la phase d'apprentissage consiste en la détermination d'une base de coefficient d'ondelette spécifique aux spectres de références du problème (choisi comme étant des spectres de glace de CO_2, d'eau et de minéraux dans notre cas). Nous déterminons ainsi un sous-espace d'ondelettes utiles (voir figure 1.3).
Dans un second temps, on se place dans ce sous-espace utile pour les observations réelles (après une transformée en ondelette) et on calcule un simple coefficient de corrélation entre les spectres de référence et les spectres observés. Un seuillage du coefficient de corrélation permet de réaliser la classification. Nous avons déterminé le seuil d'après des tests synthétiques d'observations.

La simplicité de la méthode et le choix d'utiliser la transformée en ondelette de Daubechies, sont à l'origine d'une grande efficacité numérique de la méthode. La relative indépendance aux conditions d'illumination réside dans : (i) l'utilisation d'un coefficient de corrélation, indépendant de l'intensité, (ii) le fait d'utiliser des coefficients d'ondelettes à échelles petite et moyenne, car les grandes échelles sont les plus sensibles à la géométrie.

Tous les détails de cette méthode sont décrits dans l'article, publié dans IEEE Transactions on Geoscience and Remote Sensing, disponible à la section 1.4.1.

Cette méthode a permis la détection de glace de CO_2, et d'eau sur la base de données OMEGA, sur deux années martiennes, représentant des milliers d'images et des centaines de milliards de spectres. Ces cartes de détection sont la sources de deux articles d'interprétation des processus martiens (voir section 4.2.1 page 207 et section 4.2.2 page 208). La détection de fortes signatures de glaces et de minéraux est possible grâce à WAVANGLET, mais la plupart des minéraux sur Mars ne peuvent pas être détectés avec cette approche car les signatures sont trop faibles [283].

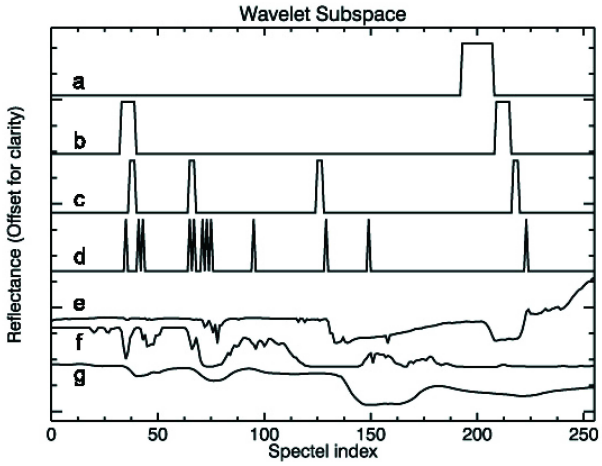


FIGURE 1.3: Sélection des coefficients d'ondelettes utiles (sous-espace utile) pour la séparation des trois spectres de références. (a)-(d) Représentation des coefficients d'ondelette des échelles 1 à 5 (voir article pour le détail de la méthode de représentation), (e) spectre typique de poussière et de contenu atmosphérique (f) spectre synthétique de glace de CO_2 (g) spectre synthétique de glace d'eau. La figure est issue de l'article de Schmidt et al. [284].

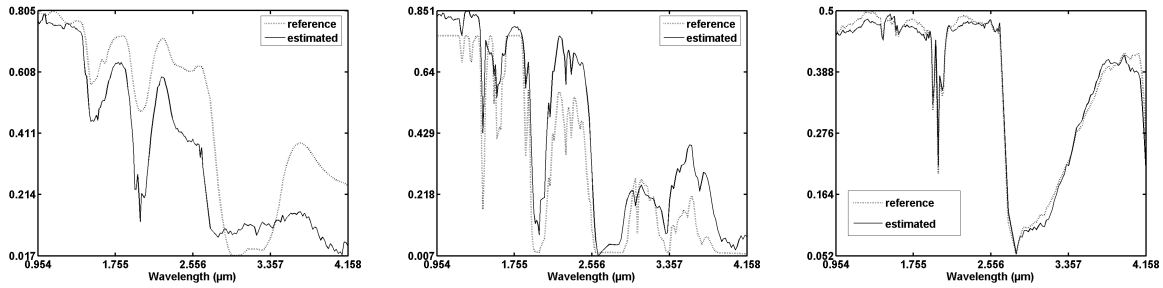


FIGURE 1.4: Comparaison entre l'estimation des sources d'après la méthode BPSS avec pré-sélection JADE. Les figures sont issues de l'article de Moussaoui et al. [233].

1.2.2 Séparation de source en aveugle

La séparation de source en aveugle en mélange linéaire consiste à estimer à la fois les coefficients de mélange (abondances) et les spectres pures (endmembers). Bien que très difficile, cette estimation est possible dans le cas linéaire grâce aux approches méthodologiques récentes (voir paragraphe 1.1.3.2), incluant la positivité et la somme à un.

En fin de thèse, nous avions pu montrer que l'approche bayésienne de l'algorithme BPSS [232] comportait toutes les propriétés utiles pour réaliser une séparation de source dans les bonnes conditions : positivité des spectres, positivité des abondances, robustesse. Une nouvelle version, notée BPSS2 [68], a été proposée incluant la positivité et la somme à un. Pour résoudre le problème du temps de calcul, la solution présentée était de sélectionner des pixels les plus extrêmes de l'image grâce à l'algorithme JADE [233] puis de calculer les sources avec BPSS sur un ensemble réduit de spectres ($\sim$ 100 au lieu de 100 000 sur une image). J'ai aussi contribué à la validation de cette approche sur des données réelles. La méthode de séparation de source en aveugle, avec pré-sélection de pixels a été validée sur des données OMEGA de la calotte permanente sud de Mars. Pour la première fois, nous avons pu montrer qu'une approche de ce type permettait d'estimer des spectres réalistes de glaces pures de CO_2, d'eau et de minéraux, sans aucune information a priori, alors que les pixels de la scène contiennent des mélanges de ces trois composants (voir figure 1.4). Cette solution n'est pourtant pas totalement satisfaisante d'un point de vue méthodologique car le résultat est fortement dépendant de la sélection de pixels.

L'objectif de mon travail de post-doc a été d'optimiser l'algorithme BPSS [232] et BPSS2 [68] pour

permettre un calcul sur la totalité des spectres d'une image typique OMEGA. Nous avons réalisé des optimisations algorithmiques, des optimisations de gestion de mémoire de Matlab et des optimisations numériques (calcul en simple précision) pour obtenir une nouvelle version de l'algorithme.

Grâce à cette version intégrale, nous avons pu montrer que l'opération de sélection de pixel par la méthode de l'enveloppe convexe était bénéfique dans des cas spécifiques : une distribution asymétrique d'abondance parmi les pixels, c'est à dire la présence de certaines sources sur un faible nombre de pixels seulement. Dans ce cas, la sélection de pixels permet de corriger l'effet du nombre et de produire un jeu de données réduit avec un nombre de pixels identique pour chacune des sources. D'autre part, nous avons démontré que la séparation de source en aveugle avec BPSS/BPSS2 était sensible au maximum d'abondance d'une certaine source. Autrement dit, plus le spectre pur est présent dans la scène, plus il est facile de l'estimer. Aussi, un fort rapport signal sur bruit et une grand nombre de canaux spectraux tendent à améliorer le résultat, tandis que respectivement un grand nombre total de sources donne de moins bons résultats.

L'article d'optimisation, publié dans IEEE Transactions on Geoscience and Remote Sensing, est disponible à la section 1.4.2.

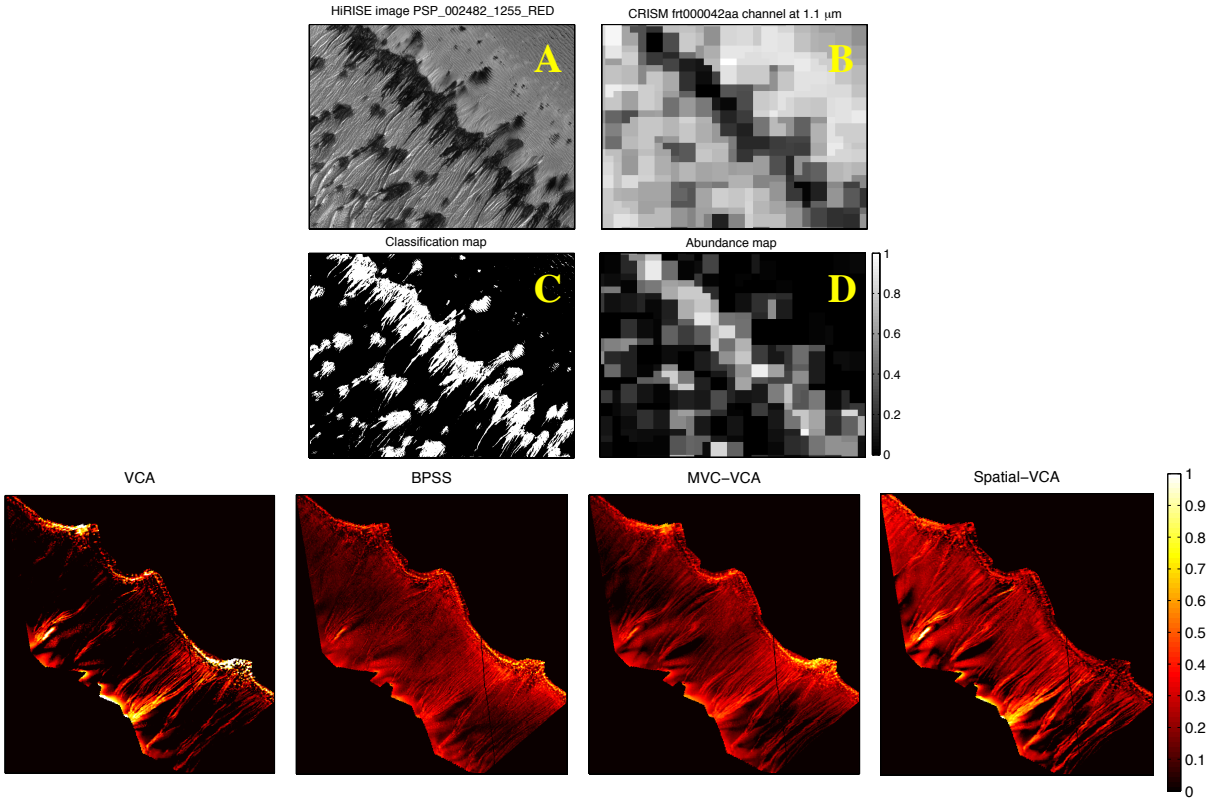
Depuis mon arrivée à IDES, j'ai appliqué cette méthode optimisée sur le cas de la dune de Russel pour valider l'approche sur des données réelles planétologiques face à la "vérité terrain" [34]. Grâce aux images HiRISE à haute résolution spatiale (50 cm), nous avons pu observer un mélange de type "poivre et sel" entre deux types de terrains à l'échelle de l'ordre de quelques mètres. Sur les images hyperspectrales CRISM à résolution spatiale de 18 m, prises au même moment que l'image HiRISE, ces deux composants sont mélangés géographiquement de manière linéaire. Nous sommes donc en présence d'un cas de test pour les algorithmes de séparation de sources. Nous avons estimé la "vérité terrain" des abondances relatives d'après une classification des images HiRISE, dégradées à l'échelle CRISM. Nous avons montré que les algorithmes de séparation de sources en aveugle sont capables d'estimer correctement les abondances, validant ainsi la méthode et l'estimation des spectres source (voir figure 1.5). Néanmoins, la contribution des aérosols n'étant pas uniforme sur la scène, dû à des différences de géométrie, chacune des sources est estimée en double avec une contribution forte/faible des aérosols. Cette validation confirme que ce type de méthode ouvre la voie d'un traitement des mélanges géographiques sub-pixel dans le cas d'un mélange géographique uniquement (pas de mélange intime, à l'échelle granulaire).

Jusqu'à présent, la détection non-supervisée des glaces ayant des fortes signatures a été validée mais ce type d'approche se révèle insuffisant pour la détection de minéraux car les signatures spectrales sont trop faibles par rapport au niveau de bruit et d'autre part, il n'y a souvent pas de spectres d'un composé pur dans la scène. L'approche supervisée de démélange linéaire développée dans ce chapitre tente de réaliser la détection de minéraux.

1.2.3 Démélange linéaire

Le démélange linéaire supervisée (eq.1.2) est un outil intéressant pour la détection d'espèce minéralogique dû à la rapidité d'exécution (voir paragraphe 1.1.3.2). En revanche, la quantification est très difficile car les mélanges intimes (mélange granulaire) sont fortement non-linéaires et peuvent conduire à des estimations équivalentes-linéaires erronées. Néanmoins, l'application à des données martiennes est possible. Dans un soucis d'efficacité, il est possible d'appliquer l'opération de démélange sans correction atmosphérique, en utilisant des "spectres additionnels" (plat, pente) pour simuler le comportement des aérosols [56]. MELSUM a été le premier outil de démélange linéaire supervisé appliqué à OMEGA [56] et consiste en l'estimation des abondances sans contraintes de positivité, sur un jeu de spectres de référence dont on retire les spectres d'abondances négatives. L'algorithme MELSUM a convergé lorsque tous les spectres ont une abondance positive. Bien que l'outil MELSUM parvienne à estimer des abondances, le traitement des conditions de positivité, de somme à un, la convergence et l'efficacité numérique ne sont pas optimales pour l'utilisation sur des images hyperspectrales et j'ai alors cherché à améliorer cette approche.

Depuis ma prise de poste à IDES, j'ai participé aux tests de la méthode MAP [312], plus robuste que MELSUM car l'estimation se fait en une seule étape, avec un outil bayésien. J'ai appliqué MAP sur



Method	VCA		BPSS		MVC-NMF		spatial VCA	
Indicator	r	ϵ	r	ϵ	r	ϵ	r	ϵ
1: All pixels	0.68	0.08	0.57	0.10	0.69	0.09	0.50	0.14
2: Accurate registration	0.73	0.08	0.59	0.09	0.72	0.08	0.56	0.13
3: Best registration	0.81	0.19	0.80	0.13	0.83	0.14	0.77	0.33

FIGURE 1.5: Comparaison entre l'estimation des méthodes de séparation de source en aveugle sur les données CRISM (au milieu) et la carte de classification HiRISE (en haut). Le tableau représente la corrélation r et l'erreur ε entre les deux, pour les différentes méthodes. Les figures sont issues de l'article de Ceamanos et al. [34].

des observations OMEGA des hautes latitudes sud mais aussi sur la zone de Syrtis Major comportant des minéraux mafiques [311]. Nous avons montré que cette méthode est plus rapide (~ 5s) que les outils proposés (~ 30s) par défauts dans les logiciels commerciaux ENVI et Matlab. Par ailleurs, ses propriétés de positivité, de somme à un et de robustesse, rendent l'outil MAP intéressant pour une application à un large jeux de données.

De récentes avancées dans le domaine du traitement du signal, utilisant une optimisation en point intérieur, ont permis de résoudre le problème de démélange supervisé sous contrainte, de manière efficace, grâce à l'algorithme IPLS [46, 47, 45].

De plus, cet algorithme ne fait pas intervenir d'inversion de matrice de spectres observés et de ce fait, permet d'utiliser de nombreux spectres additionnels "plats" et de "pente" fortement corrélés. Enfin, cet algorithme a été implémenté pour utiliser les calculateurs Graphics Processing Units (GPU), qui sont des cartes permettant d'accélérer le calcul parallèle à un coût très modeste. Notre laboratoire s'est doté d'un tel outil informatique pour l'utilisation massive sur de grands jeux de données. Dans ce contexte, j'ai proposé la stratégie LinMin, utilisant l'agorithme IPLS, pour les détections de minéraux martiens. LinMin repose sur l'utilisation de spectres additionnels (plats, pentes, sinus/cosinus) et sur des contraintes de positivités/somme-à-un des abondances. LinMin permet d'*altérer* la base de données de manière linéaire pour accommoder les effets à grandes échelles sur le continuum (effet des aérosols, des tailles de grains, ...). La puissance de l'algorithme IPLS permet de résoudre ce nouveau problème de manière non-dégénérée avec une solution unique. J'ai effectué des tests de LinMin sur des situations synthétiques d'un réalisme sans précédent (effet des aérosols calculé par transfert radiatif, effet des tailles de grains, bruit corrélé) pour montrer l'intérêt de cette approche (voir figure 1.6 page suivante).

L'article, publié dans la revue ICARUS, est disponible à la section 1.4.3.

1.3 Perspectives

1.3.1 Perspectives méthodologiques

Les méthodologies d'analyse des images hyperspectrales se classent en général en deux grandes catégories : les méthodes rapides de détection, et les méthodes d'estimation quantitative, plus longues et basées sur l'inversion du transfert radiatif. Ce premier chapitre traite essentiellement de la première catégorie.

Les outils utilisant les ondelettes, comme WAVANGLET, sont très intéressants car les ondelettes forment l'espace naturel d'analyse. Il serait intéressant de développer des outils non-supervisés pour détecter et caractériser la présence statistique de toutes les bandes d'absorption de l'image.
Les outils de type séparation de sources en aveugle sont très intéressants en présence de glace mais le développement de méthodes pouvant être appliquées aux minéraux serait très pertinent. Une amélioration serait de limiter la dépendance au niveau global.
Les outils de type démélange linéaire supervisé sont bien adaptés à la détection de minéraux mais souffrent d'une limitation concernant l'effet de la taille de grain. La perspective de limiter cet effet, par exemple en utilisant un sous espace non-linéaire particulier, rendrait ce type d'approche encore plus attrayant. D'autre part l'incorporation d'une contrainte de parcimonie pourrait se révéler judicieuse pour utiliser une base de spectre de référence plus grande.

Concernant les méthodes d'inversion quantitative, je souhaite développer des outils performants numériquement pour permettre l'inversion massive de spectres et estimer des paramètres de surfaces de manières quantitatives (taille de grain, proportion, rugosité, compacité, ...). Ce travail a commencé avec la thèse de François Andrieu, durant laquelle nous développons une méthode d'inversion bayésienne basée sur une table de référence pour accélérer le calcul. Ce travail a déjà été effectué avec une méthode bayesienne dans la dimension angulaire durant la thèse de Jennifer Fernando, voir section 2.2 page 81.

Enfin, la perspective d'une application massive de ces outils à grande échelle sur l'ensemble des jeux de données hyperspectraux OMEGA, CRISM, M^3, ... soulève des problématiques d'implémentation des algorithmes mais aussi des questions de visualisation. A plus long terme, je souhaite développer ces

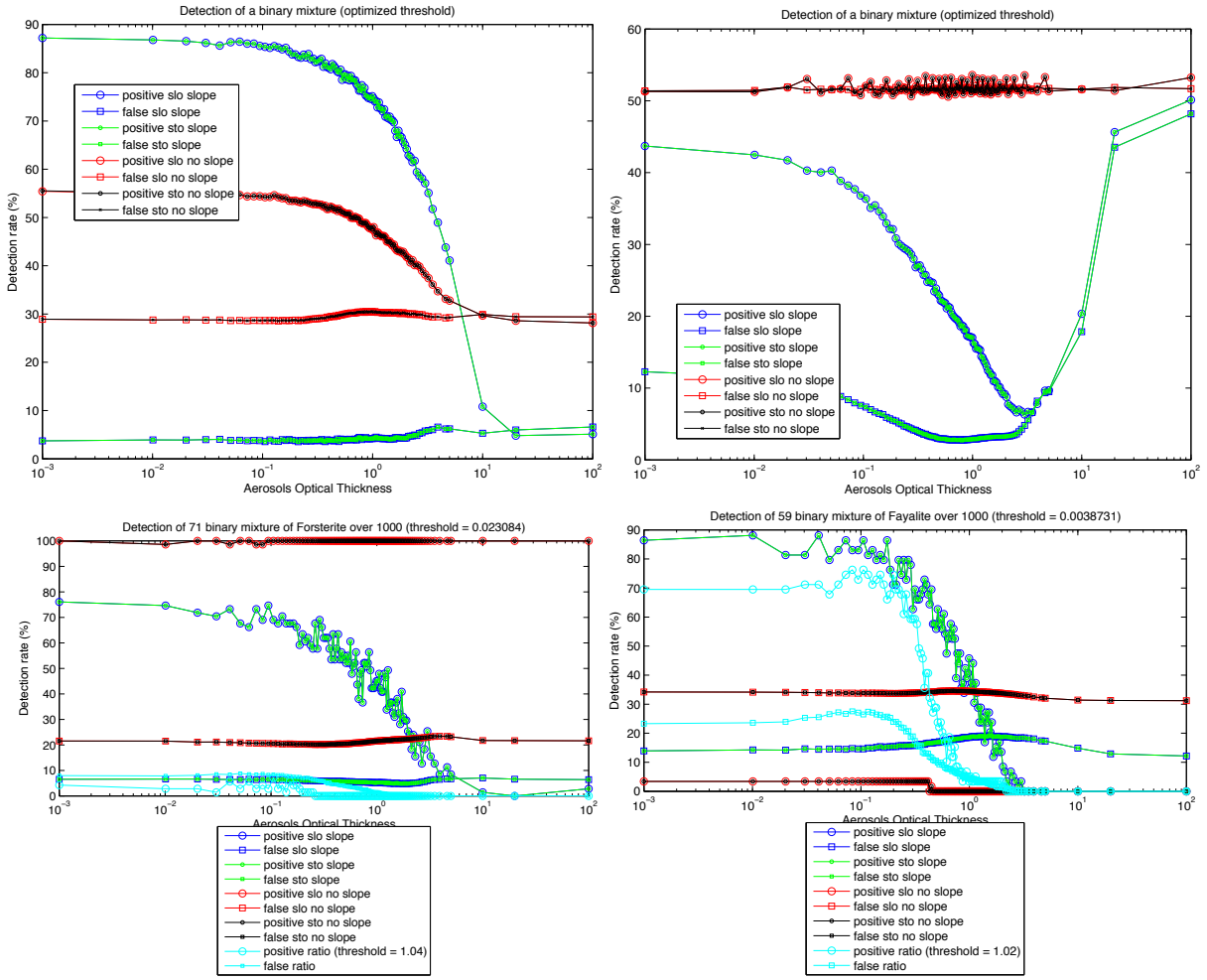


FIGURE 1.6: Précision de la détection pour plusieurs algorithmes sur un jeu de données de 1000 spectres synthétiques simulant Mars pour différentes valeurs de contenu en aérosols. Les ronds représentent les bonnes détections, les carrés les fausses détections. “slope” signifie avec l’ajout des spectres additionnels de la stratégie LinMin (en haut, à gauche) algorithme IPLS (en haut, à droite) algorithme BIICE (en bas à gauche) détection des 71 spectres contenant de l’olivine forsterite uniquement en utilisant IPLS et le rapport de bande (en bas à gauche). Détection des 59 spectres d’olivine fayalite uniquement en utilisant IPLS et le rapport de bande (voir l’article disponible à la section 1.4.3 page 45).

thématiques pour extraire l'information très riche contenue dans ces jeux de données. Cette perspective permettrait aussi l'intégration dans un Système d'Information Géographique pour une analyse multi-instrument.

1.3.2 Perspectives planétologiques

Les perspectives planétologiques se déclinent aux divers contextes géologiques des surfaces planétaires. Dans un premier temps, je souhaite appliquer ces outils aux problématiques des glaces Martiennes mais aussi contribuer à analyser surfaces lunaires et des autres corps, grâce à des collaboration au sein de la communauté scientifique.

1.4 Publications

Co-encadrement de thèses de Doctorat :
- M. Legendre
- F. Andrieu
- J. Fernando

Publications scientifiques :
- **Schmidt F.** ; Douté S. and Schmitt B., "WAVANGLET : an efficient supervised classifier for hyperspectral images" ; IEEE Transactions on Geoscience and Remote Sensing, 2007, 45, 1374-1385 (voir section 1.4.1).
- Moussaoui, S. ; Hauksdóttir, H. ; **Schmidt, F.** ; Jutten, C. ; Chanussot, J. ; Brie, D. ; Douté, S. & Benediktsson, J., "On the Decomposition of Mars Hyperspectral data by ICA and Bayesian positive source separation" ; Neurocomputing, Neurocomputing for Vision Research ; Advances in Blind Signal Processing, 2008, 71, 2194-2208
- **Schmidt, F.** ; Schmidt, A. ; Tréguier, E. ; Guiheneuf, M. and Moussaoui, S. & Dobigeon, N., Implementation strategies for hyperspectral unmixing using Bayesian source separation, IEEE Transaction on Geoscience and Remote Sensing, 2010, 48, 4003-4013 (voir section 1.4.2 page 33).
- Ceamanos, X. ; Douté ;, S. ; Luo, B. ; **Schmidt, F.** ; Jouannic, G. & Chanussot, J., "Intercomparison and Validation of Techniques for Spectral Unmixing of Hyperspectral Images : A Planetary Case Study", IEEE Transaction on Geoscience and Remote Sensing, 2011, 49, 4341-4358
- Themelis, K. E. ; **Schmidt, F.** ; Sykioti, O. ; Rontogiannis, A. A. ; Koutroumbas, K. D. & Daglis, I. A., "On the unmixing of MEx/OMEGA hyperspectral data", Planetary and Space Science, 2012, 68, 34-41
- Schmidt, F. ; Legendre, M., and et Le Mouelic, S., Minerals detection for hyperspectral images, LinMin, en révision à ICARUS 2013 (voir section 1.4.3 page 45).

Abstracts :
- F. Andrieu et al., EPSC 2013

1.4.1 WAVANGLET

Cette section contient l'article suivant :

Schmidt F. ; Douté S. and Schmitt B., "WAVANGLET : an efficient supervised classifier for hyperspectral images" ; IEEE Transactions on Geoscience and Remote Sensing, 2007, 45, 1374-1385

1374 IEEE TRANSACTIONS ON GEOSCIENCE AND REMOTE SENSING, VOL. 45, NO. 5, MAY 2007

WAVANGLET: An Efficient Supervised Classifier for Hyperspectral Images

Frédéric Schmidt, Sylvain Douté, and Bernard Schmitt

***Abstract*—The new generation of imaging spectrometers onboard planetary missions usually produce hundreds to thousands of images a year, each made up of a thousand to a million spectra with typically several hundred wavelengths. Such huge datasets must be analyzed by efficient yet accurate algorithms. A supervised automatic classification method (hereafter called "*wavanglet*") is proposed to identify spectral features and classify images in spectrally homogeneous units. It uses four steps: 1) selection of a library composed of reference spectra; 2) application of a Daubechies wavelet transform to referenced spectra and determination of the wavelet subspace that best separates all referenced spectra; and 3) in this selected subspace, determination of the best threshold on the spectral angle to produce detection masks. This application is focused on the Martian polar regions that present three main types of terrains: H_2O ice, CO_2 ice, and dust. The wavanglet method is implemented to detect these major compounds on near-infrared hyperspectral images acquired by the OMEGA instrument onboard the Mars Express spacecraft. With an overall accuracy of 89%, wavanglet outperforms two generic methods: band ratio (57% accuracy) and spectral feature fitting (83% accuracy). The quantitative detection limits of wavanglet are also evaluated in terms of abundance for H_2O and CO_2 ices in order to improve the interpretation of the masks.**

***Index Terms*—Automatic detection, automatic supervised classification, hyperspectral images, mass treatment, pattern recognition, remote sensing, spectral feature recognition and extraction, wavelet filtering.**

I. Introduction

In order to understand the current climate on Mars, it is necessary to detect, characterize, and monitor CO_2 and H_2O ices at its surface (permanent and seasonal deposits) and in its atmosphere (vapor, clouds). The series of images acquired above medium latitudes and the poles by the OMEGA [1] imaging spectrometer onboard the Mars Express (MEX) mission [European Space Agency (ESA)] represents a unique opportunity to achieve these objectives. Currently, it contains more than a hundred visible and near-infrared hyperspectral images taken during different seasons above the north and south polar regions with usually $\sim$100 000 spectra for each image.

Manuscript received May 12, 2006; revised September 23, 2006. This work was supported in part by a Ph.D. Grant from the "Ministère délégué à l'Enseignement supérieur et à la Recherche" and in part by a contract with CNES through its "Groupe Système Solaire" programs.

The authors are with the Laboratoire de Planétologie de Grenoble—CNRS/UJF, Bâtiment D de Physique, 38041 Grenoble Cedex 09, France.

Color versions of one or more of the figures in this paper are available online at http://ieeexplore.ieee.org.

Digital Object Identifier 10.1109/TGRS.2006.890577

We aim to do the following:

1) evaluate the relevance of each image for volatile molecule studies in terms of fractions covered by CO_2 and H_2O ices;
2) generate CO_2 and H_2O ice distribution maps;
3) automatically determine the seasonal condensation and defrost lines and their temporal evolution;
4) define spectrally homogeneous units of terrain as detection masks, each undergoing a specific physical modeling of the spectra in order to evaluate their surface properties.

Because of the huge volume of data, we need an automatic and efficient algorithm to achieve these goals in a reasonably short calculation time. In supervised classification, the usual way to compare each spectra X of a hyperspectral image and a well-known reference spectrum E is to calculate their spectral angle (SA) [2] in the n-dimensional base ($n =$ the number of channels) which is equivalent to the correlation coefficient. However, this method is not robust enough to classify the polar terrains because of the slightly degraded signal-to-noise ratio of the spectra mostly acquired at high incidence angles. Furthermore, gaseous CO_2 and H_2O present in the atmosphere add absorption features that sometimes partly overlap their solid counterparts. Finally, variations of the physical properties of the ices (e.g., grain size) and variations of geometrical illumination conditions induce nonlinear variations of the absorption band intensity across the studied scene that are impossible to unravel using a linear SA method. Therefore, we propose a supervised classification method called wavanglet. It defines a more effective way of measuring the SA between the image spectrum X and the reference spectrum E in a wavelet transform (WT) domain. The reference is usually an image endmember or a synthetic spectrum that nonambiguously characterizes the compound to be detected, e.g., CO_2 or H_2O ice owing to their distinctive absorption bands. Similar methods have already been evaluated in remote sensing. The use of wavelets for pattern recognition was already proposed by [3] and [4], and their efficiency is better than that provided by other techniques such as principal component analysis (PCA) and Fourier transforms [5]. Experimental studies have shown that the performance of wavelets in classification is very good for vegetation detection with Airborne Visible/Infrared Imaging Spectrometer data [6] and hyperspectral data collected at ground level [7].

The use of unsupervised classification methods like PCA [8] or hierarchical clustering [9] is limited when processing large

0196-2892/$25.00 © 2007 IEEE

TABLE I
BASIC SPECTRAL CHARACTERISTICS OF THE OMEGA INSTRUMENT ONBOARD MEX

	V channel	C channel	L channel
Spectral Range (μm)	0.38 to 1.05	0.93 to 2.73	2.55 to 5.1
Number of Samples	96 or 144	128	128
Spectral Resolution (μm)	0.007 or 0.0045	0.013	0.020

datasets because such methods are computer intensive. Furthermore, they do not take advantage of the *a priori* knowledge we may have concerning planetary surfaces and atmospheres. Finally, they classify an image according to multiple chemical, physical, and structural information that are combined. Thus, the classification can be difficult to interpret in terms of chemical composition only, a problem that we do not encounter with wavanglet.

This paper is divided into four sections. In the first, we provide background information necessary to introduce the wavanglet method and the OMEGA dataset on which we will base our classification experiments. We also describe comparable standard methods that already exist: band ratio (BR) [10], [11], Spectral Angle Mapper (SAM) [2], and spectral feature fitting (SFF) [12]. The second section presents the different steps followed by our method. Next, we will perform a comparative experiment between wavanglet and two standard methods based on performance (overall accuracy, separability between classes, multiple endmembers and possible overlapping signatures, mass processing feasibility, and calculation time). Finally, in the particular case of the OMEGA polar images, we evaluate quantitative detection limits in terms of abundance for H_2O and CO_2 ices. We also determine how these limits vary with the coexistence mode of the ices, their main physical parameters (e.g., granularity) and the incidence angle of the observation. For this, we use synthetic data.

II. BACKGROUND INFORMATION

A. OMEGA Instrument

The OMEGA instrument [1] is an imaging spectrometer onboard the MEX—ESA. Its spatial resolution varies from 350 m up to 4 km depending on the observation altitude. The instrument has three distinct spectral channels designated V, C, and L. Table I summarizes the spectral range, number of spectels, and spectral resolution for each. Unlike the V channel, the C and L channels are particularly relevant to our studies since they sample numerous absorption bands distinctive of CO_2 and H_2O in their solid state. After calibration, the dimensionless physical unit used to express the spectra is the reflectance: the irradiance leaving each pixel toward the sensor divided by the solar irradiance at the ground. Each pixel is characterized by a spectrum of 256 spectels organized according to increasing wavelength, the corresponding index going from 0 to 255. The name of each observation is coded as ORBXXXX_Y where XXXX is the orbit number and Y the observation number.

B. Wavelet Transform

Our signals are modeled by finite energy functions of the $\mathbf{H}$ Hilbert space with the usual norm of the $L^2(\mathbb{R})$ Banach space and the usual inner product $\langle ; \rangle$. As the Fourier transform is a projection on an orthogonal base made of orthogonal sine and cosine functions, the WT is a projection into a new base made of orthogonal wavelets. Each wavelet is built by scaling and shifting a single "mother" wavelet [13]. Consequently, a wavelet is defined by a mother pattern, a scale "s," and a position "p."

The mother wavelet is as follows:

1) a function
$$\Psi \in L^2(\mathbb{R}) \tag{1}$$
2) with a zero average
$$\int_{-\infty}^{+\infty} \Psi(x)dx = 0 \tag{2}$$
3) centered in the neighborhood of $t = 0$
4) normalized such that
$$\|\Psi\| = 1. \tag{3}$$

It is used to generate a family of functions: $\Psi_{s,p}(x) = (1/\sqrt{s})\Psi((x-p)/s)$

1) which could be a base of $L^2(\mathbb{R})$;
2) which could have the orthonormal property: $\forall(s,p,s',p')$, $\langle \Psi_{s,p}; \Psi_{s',p'} \rangle = \delta_{s,s'} \cdot \delta_{p,p'}$.

The originality of wavelets compared to the usual sine and cosine functions is that each base function is localized. A cosine function, instead, is defined by its period and its phase, and is present throughout the entire signal.

The WT of the signal-vector $E(x)$ is:

$$\mathrm{WE}(s,p) = \langle E, \Psi_{s,p} \rangle = \int_{-\infty}^{+\infty} E(x) \frac{1}{\sqrt{s}} \Psi^* \left(\frac{x-p}{s} \right) dx. \tag{4}$$

This transformation is linear and can be written by the usual convolution product:

$$\mathrm{WE}(s,p) = \int_{-\infty}^{+\infty} E(x) \frac{1}{\sqrt{s}} \Psi^* \left(\frac{x-p}{s} \right) dx = f \star \Psi_s \tag{5}$$

with $\Psi_s = (1/\sqrt{s})\Psi^*(-x/s)$.

In signal processing, several classes of mother wavelets exist, each with different properties (including nonbase and nonorthogonality). We build our wavanglet method on an orthonormal base made using the Daubechies wavelet family. The corresponding transform algorithm was specially developed for fast numerical calculation [14]. Faster than the usual WTs [4], this particular WT is particularly suitable for the detection and classification of spectral features on large datasets. The morphology of the Daubechies mother wavelet can be tuned by a parameter—with 4, 16, or 20 as possible values—that depends on the regularity of the signal. If the latter is undersampled, the regularity is low and the best suited mother wavelet must be highly irregular and as short as possible (value 4). If sampling

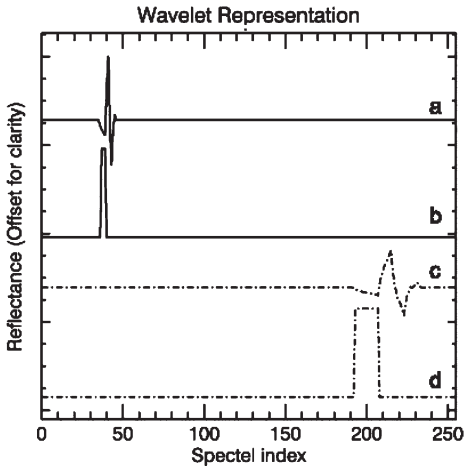


Fig. 1. (a) Daubechies wavelet representation. Wavelet No 28 (Scale 5 Position 13) and (b) its representation. (c) Wavelet No 73 (Scale 7 Position 10) and (d) its representation.

is sufficient, the mother wavelet must be smooth and long (value 20). The OMEGA data correspond to the first case. The discrete WT algorithm transforms a 2^k element vector into a vector of the same length. The counterpart of the spectel index in the wavelet domain will be called the wavelet index. The length 2^k of the vector determines the number of scales k, 8 for OMEGA, due to a spectral dimension of 256. The scale s and position p are not explicitly specified in the output vector but can be easily reconstructed. Each wavelet index corresponds to a unique wavelet with scale s and position p. Different representations of the vector can be used in the wavelet space: for instance the primary output vector or a scale/position scheme. We will use a convenient representation with each scale represented by a 2^k element vector resulting from the superposition of gate functions, one for each wavelet, with a width equal to the scale s, a localization equal to position p, and a depth equal to the projection coefficient (see Fig. 1).

WTs can be used in spectral pattern recognition as proposed several years ago [3], [4]. The idea is that the wavelet localization and scale, respectively, correspond to the position and width of a particular spectral feature. Furthermore, the projection coefficient is linked to feature depth. In the case of a hyperspectral planetary image, each absorption band can be represented by the sum of a limited number of wavelets. In an ideal case, only the projection coefficients for this group of wavelets would differ from zero.

C. Usual Classification Methods

Many different methods of detection and classification are used in the domain of planetary sciences. We will only summarize three among the most popular.

1) BR Method: A ratio between two channels of interest can be calculated for all the spectra of an image. For instance, one channel can be chosen in the middle of an absorption band and the other on its far wing (local continuum). In this case, the ratio is straightforwardly linked to the relative band depth. a detection mask can be computed by applying a fixed threshold on the image ratio, above which we consider that the band exists. The threshold can be calibrated by a visual inspection of representative spectra. Sometimes the definition of the BR is slightly more refined, e.g., the area sustained by the absorption band divided by its continuum. The main advantage of the ratio method is its simplicity. Nevertheless, this method is only used for preliminary investigations because of a number of limitations: dependence of hot spectels and sensitivity to nonmultiplicative noise, instrumental artifacts, and frequent superposition of different absorption bands. This method has already been applied to MEX OMEGA data [10], [11].

TABLE II
WAVELENGTHS USED IN THE BR METHOD

Spectel index	35	40	60	75
Wavelength (μm)	1.4286	1.5004	1.7860	1.9973

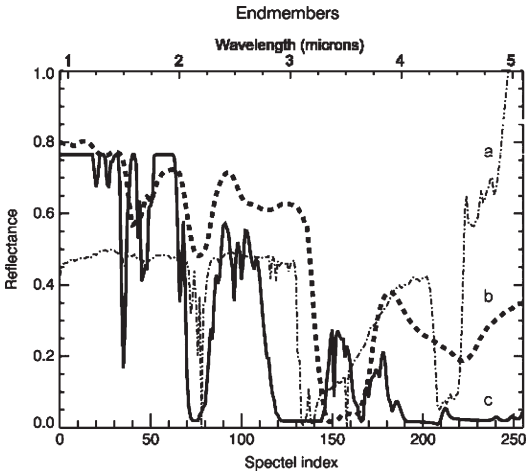


Fig. 2. Spectral endmembers. (a) Dust + atmosphere spectrum, (b) synthetic spectrum of H_2O ice, and (c) synthetic spectrum of CO_2 ice.

The BR we used for our classification experiments (see Section IV-B) is $(S(40)/S(35))(1-(S(75)/S(60)))$ with the associated wavelengths listed in Table II. Spectel index 35 corresponds to a CO_2 solid absorption band and spectel index 40 to a water ice absorption. Spectel index 60 is the continuum, and spectel index 75 corresponds to both CO_2 and H_2O absorption bands (see Fig. 2 for the reference spectra). Terrains with a minimum value of the ratio are composed of dust. CO_2-ice-rich terrains are represented by pixels with a high ratio. In between, water-ice-rich terrains have intermediate values (see Fig. 4 for the BR distribution in one OMEGA observation). An overview of the properties of this method and the results from experiments are reported (later) in Table IX.

2) SA: A collection of spectra produced by a given instrument can be represented by a series of vectors each anchored at the origin of an n-dimensional space (n being the number of channels of the instrument). In a usual 3-D Euclidean space, the SA corresponds to the real angle between the two directions defined by two vectors [2]. In a general $n-d$ space, the SA is a coefficient α between 0 and π radians which determines the proximity of the directions of two vectors E and X.

The SA:

$$\alpha(E;X) = \arccos\left(\frac{\langle E;X\rangle}{\|E\|\cdot\|X\|)}\right) = \arccos(\mathrm{cor}(E;X))$$

The SA is not sensitive to a multiplication factor because it is normalized. This method is often used in remote sensing analysis to compare two spectra (vectors) because the photometric effect is not taken into account. Another way to introduce the SA is to present it as a correlation coefficient between two random vectors (the spectra) combined with an arc-cosine. As the arc-cosine is a monotonically declining function in the [0, 1] interval, the SA decreases as the normalized correlation increases. In the extreme case, when the two directions are similar, SA tends to 0 and the normalized correlation tends to 1. When the two vectors are anticorrelated, the correlation coefficient is close to -1, and thus the SA is close to π radians. The intermediary situation is when the angle is $\pi/2$ and the correlation is null.

The value of the SA does not depend on the base used for the vector representation if the new base is orthogonal for the usual scalar product. This means that if the scalar product between two vectors is preserved, the SA is also preserved.

If Φ is a self-adjoint linear operator such as WT, e.g., the projection into an orthonormal base of the $\mathbf{H}$ Hilbert space, we can write the following:

The Parseval formula

$$\langle\Phi(E);\Phi(X)\rangle = \langle E;X\rangle \tag{6}$$

and the Plancherel formula

$$\|\Phi(X)\| = \langle\Phi(X);\Phi(X)\rangle = \langle X;X\rangle = \|X\| \tag{7}$$

and thus

$$\alpha\left\{\Phi(E);\Phi(X)\right\} = \arccos\left(\frac{\langle\Phi(E);\Phi(X)\rangle}{\|\Phi(E)\|\cdot\|\Phi(X)\|}\right) \tag{8}$$

$$\alpha\left\{\Phi(E);\Phi(X)\right\} = \arccos\left(\frac{\langle E;X\rangle}{\|E\|\cdot\|X\|}\right) \tag{9}$$

$$\alpha\left\{\Phi(E);\Phi(X)\right\} = \alpha(E;X). \tag{10}$$

SA is an algorithm already implemented in the environment for visualizing images (ENVI) environment [15].

3) Spectral Feature Fitting: SFF is a method that compares the spectrum of an image X to a selected reference spectrum E in a least-squares sense [12]. The reference spectrum is scaled to match the image spectrum after continuum removal for both spectra and the root mean square (rms) error is determined. We choose to express the similarity between X and E by calculating the combined ratio: scale/rms. The scale and the rms are, respectively, an estimation of the strength of the searched absorption features and of the quality of the fit. A simple threshold can be applied to the ratio to decide if the observed spectrum belongs to the class of the reference spectrum or not.

An overview of the properties of this method and the results from experiments are also reported in Table IX. SFF is also an algorithm included in the ENVI environment [15].

III. Proposed Method: Wavanglet, SA Classification in a Wavelet Filtered Space

The proposed wavanglet method is a succession of four steps. Step A is the determination of significant reference spectra E characteristic of the different types of terrains present in the scene (the set is called the "reference base"). Step B is the choice of the most discriminating wavelet subspace for SA classification of the observed spectra X. Step C is the determination of the best threshold for the SA to produce detection masks $(0 = \text{nondetection}; 1 = \text{detection})$. Step D is the automatic mass classification for the complete dataset.

A. Step A: Choice of Relevant Reference Spectra

This first step is crucial in the process because it will strongly affect the validity of the detection. If some species are not represented in the reference base, they will be misclassified in the dataset. If other species are represented in the base but are not present in the observation, the classification will not be optimized. This method is supervised because the *a priori* knowledge used to perform the classification is strong: number of present compounds in the image, nature of the compounds, etc. The user must supply a reference base that can be a set of endmembers extracted from the hyperspectral images and/or a set of synthetic spectra generated by a physical model. Endmembers can be extracted manually or automatically, for instance by a pixel purity index routine [16], after a dimension reduction performed by different techniques such as PCA or minimum noise fraction [17]. The synthetic spectra can be calculated with a bidirectional reflectance model adapted to the type of planetary surfaces observed [18]. A single chemical species with homogeneous physical properties (grain size, roughness, etc.) or a geographical/granular mixture of different chemical species with different surface properties may be used under certain circumstances. We will denote the ith spectra of the reference base as E_i. Our algorithm will detect a reference spectrum E_i in an observed spectrum X when the signatures of the former are found in the latter with similar position, width, and relative depth. However, this method will neither be sensitive to the general level of the spectra nor to the absolute depth of bands for a particular species.

B. Step B: Determination of the Best Subspace

Several methods have been proposed to reduce the dimension, such as band selection on a well-documented learning dataset using discriminant analysis [19], or directly on the hyperspectral image avoiding correlation [20]. We will use the discrete WT, which is already used to increase the classification accuracy [21], in a alternative way.

1) Step B1—Continuum Removal: Real observed spectra commonly result from the superposition of multiple absorption bands due to several pure compounds mixed at different spatial scales. Such absorption bands undergo nonlinear variations when the physical properties of the materials present in the scene change [22]. Moreover, these bands appear on a continuum that is highly variable due to changes of illumination and global albedo. These are the main limiting effects when

comparing the observed spectra with the image or synthetic endmembers. In order to reduce the sensitivity of our algorithm to such variations—which cannot be taken into account by our fixed reference endmembers—we perform the comparison only at medium and small wavelet scales ($s \in [5-8]$ for OMEGA classification). In this first filtered space, all wavelet coefficients mainly depend on the absorption band positions, widths, and relative depths. They are only moderately affected by noise in the spectra as shown by the experiments we carried out (see Section IV-C). One specific absorption band is usually represented by several wavelets.

2) Step B2—Best Discrimination: Additionally, we have to select the ideal subspace that allows the best discrimination among the different endmembers. It is possible to separate overlapping signatures during the decomposition process if they have different positions or widths, i.e., if we can find one wavelet at medium or small scale, specific to one absorption band but not polluted by another absorption band.

Qualitatively speaking, this subspace is composed of wavelets on which the reference spectra show the greatest differences. We propose three simple methods to carry out the selection.

$\mathrm{WE}_i(s,p)$ denotes the projection of the ith spectrum of the reference base on the wavelet $\Psi_{s,p}$ at scale s and position p.

1) Threshold for only one single reference spectra in the base:
   Keep $\Psi_{s,p}$ if $\exists i$ such that

$$\|\mathrm{WE}_i(s,p)\| > \mathrm{thres}(s). \tag{11}$$

2) Threshold for an extended spectral base:
   Keep $\Psi_{s,p}$ if $\exists(i,j)$ such that

$$\|\mathrm{WE}_i(s,p) - \mathrm{WE}_j(s,p)\| > \mathrm{thres}(s,i,j) \tag{12}$$

   with

$$\mathrm{thres}(s,i,j) = \mathrm{const}. \tag{13}$$

3) Automatic threshold method, same as method 2) above with

$$\mathrm{thres}(s,i,j) = \mathrm{mean}_{i,j}\left\{\|\mathrm{WE}_i(s,p) - \mathrm{WE}_j(s,p)\|\right\} + c * \mathrm{std}_{i,j}\left\{\|\mathrm{WE}_i(s,p) - \mathrm{WE}_j(s,p)\|\right\}. \tag{14}$$

   Both mean $\mathrm{mean}_{i,j}$ and standard deviation $\mathrm{std}_{i,j}$ are calculated for combinations of i and j for a given s. The coefficient c is determined by the user.

The norm $\|\ \|$ can be L^1, L^2, or any other norm definition. We choose L^2 to be consistent with previous considerations concerning WTs in a $\mathbf{H}$ Hilbert space (see Section II-B).

Methods 1) and 2) cannot easily be carried out if the number of reference spectra is high because the number of thresholds becomes excessive. An alternative is method 3) which automatically determines the threshold. Other more complicated automatic methods have already been proposed in the literature, for example selection of the maximum by scale instead of a threshold criterion [3] or the best basis algorithm [23], [24].

3) Step B3—Circularity, Noise, and Dead Channels: The first problem that arises when analyzing numerical data by a WT is the edge effect. The circularity of the sampling creates false information symmetrically before and after the measured signal. All wavelets near the edge are polluted by this construction. To solve such a problem, we eliminate all wavelets containing information inherited from the first or last instrument spectels. For the OMEGA images, this method is valid because no features of interest are located near the edge of the signal.

Also, wavelets corresponding to spectels affected by instrumental defects or noise can reduce the accuracy of the classification algorithm. These wavelets are determined by the following method. First, we built a null-vector with a length equal to the number of spectels in an OMEGA spectrum. Second, we change the value of the vector from zero to one only at the rank of a defective spectel in order to simulate the defect with a normalized energy of one. The base of the modeled defect is denoted D_i. Then, we perform a WT on this signal D_i and eliminate all wavelets with a coefficient higher than a threshold, i.e., the wavelets most affected by the defect. If we choose a typical value of $D_i(s,p) > 0.5$, we eliminate only the wavelets that receive more than 50% of the defect energy. This operation should be performed for all potential defects i.

C. Step C: SA Thresholds

The calculation of the SA between the reference spectrum E and the observation spectrum X gives the correlation coefficient between these two spectra in a determined space. The characteristics of an appropriate subspace are the following. The belonging wavelets must be corrected from continuum effect (Step B1), form a part of an absorption band and be discriminating for at least one reference spectrum (Step B2), and be almost free of noise and numerical problems (Step B3). The SA in this subspace can be interpreted as a measurement of the agreement between distinctive spectral features of a reference spectrum and those of an observed spectrum. A small value indicates a good match of spectral features whereas a value close to π indicates total disagreement. Some analysis procedures we use subsequently in wavanglet require that we decide from the SA if a given compound, characterized by its associated reference spectrum, is present or absent in a pixel. In this case, after processing the whole image, we obtain detection masks for the compounds that indicate if a given treatment is to be applied or not for a given pixel.

To declare positive detection, the correlation coefficient must be higher than a certain threshold, or in an analogous manner, the SA must be lower than a limiting angle. Ideally, to build our detection algorithm, a unique limiting angle, one per compound, must be detected and valid for all observations. This limiting angle can be interpreted as a limiting condition adapting the mathematical problem to a physical one. Two methods can be performed to determine the series of thresholds: calibration using a controlled database of synthetic spectra—modeling approach [C1]—and/or an empirical approach based on an already analyzed subset of real data [C2]. The choice of the threshold must maximize the detection limit of each pure

compound in the image, regardless of its physical properties, and and must minimize false detections.

As the SA calculation is invariant with any linear orthonormal transformation, such as the Daubechies WT, we have the choice to perform the SA mapping of all the pixels in the filtered wavelet base or in the filtered spectral space. The latter is reconstructed by the inverse transform of the filtered wavelet base. The calculation of the SA is faster in the filtered wavelet base than in the complete spectral space because the dimensions of the former are lower. We therefore choose to perform the calculation in the filtered wavelet base.

D. Step D: Automatic Mass Classification With SAs in This Subspace

All the parameters are now adjusted to perform the automated classification. For each image and each spectrum of the reference base, a detection mask will be created. For datasets spanning a long time range (several months to years), many parameters can vary. For instance, the bad channel list can change with time thus affecting Steps B2 and B3. If this happens, then Step C should be adapted according to the former steps.

IV. EXPERIMENTS

We will now apply this general wavanglet method to a series of OMEGA/MEX hyperspectral images and compare the obtained classifications with the ones produced by two alternative methods: BR and SFF (Section II-C1 and -C3). We also evaluate quantitative detection limits for H_2O and CO_2 ices in terms of abundance. We use synthetic spectra for this. This paper consists of five tests: classification accuracy, separability between classes, multiple endmembers and possible overlapping signatures, mass processing feasibility, and calculation time.

A. Application of the Wavanglet Method to the Omega Dataset

We follow the four steps described in Section III to apply the method to a collection of OMEGA/MEX images covering the polar regions of Mars.

1) Step A—Choice of Relevant "Endmembers" (Reference Spectra): The OMEGA spectra display signatures characteristic of both the atmosphere and the surface. The atmospheric contribution is due to gaseous CO_2 and, depending on weather conditions, to clouds of dust, CO_2, and H_2O ices. The spectral effect of the clouds can often be neglected for a first-order approximation. The surface contribution is due to a mixture of H_2O ice, CO_2 ice, and dust in various proportions. In the images, we try to detect the last three compounds to which we attribute reference spectra (see Fig. 2). Pure H_2O and CO_2 are represented by synthetic spectra computed by a reflectance model [18] using the physical parameters listed in Table III and an optical constant measured in the laboratory [25]–[27]. These parameters have been chosen to be compatible with recent studies of both south and north Martian polar regions [10], [11], [28], [29]. On the other hand, the third reference spectrum representing polar dust is extracted from a single OMEGA image covering the southern high latitudes by averaging all spectra within a relatively homogeneous region near 70° longitude and $-77°$ latitude. Note that this spectrum is almost featureless in the near-infrared range except for the 3-μm band due to the hydration of the minerals and the absorption bands of atmospheric CO_2. Globally, the dust spectrum does not display much spatial variation in this spectral range. Indeed, it is well mixed by winds and spread over wide areas. Thus, we can assume that our reference spectrum is representative of most areas of both polar regions. Our Martian studies focus mainly on the two first endmembers while the third endmember represents spectral features that appear in the data but which are not of interest to us.

TABLE III
SYNTHETIC ENDMEMBER PARAMETERS

	pure H_2O ice	pure CO_2 ice
Grain size (μm)	10	100 000
Incidence angle (°)	85	85
Emergence Angle (°)	0	0

TABLE IV
LIST OF ELIMINATED WAVELETS

Spectel indexes of dead spectels	34	78	158
Wavelet indexes of eliminated wavelets	35, 71, 144	82, 166	102, 206

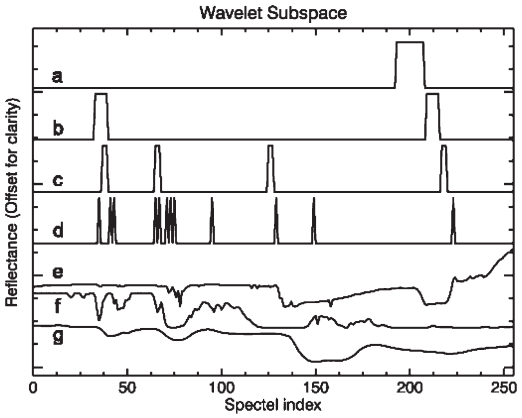


Fig. 3. Representation of the selected subspace of (upper part) wavelets that best discriminate the endmembers (lower part). (a)–(d) Wavelets selected in scales 5 to 8. (e) Observed dust and atmosphere spectra, (f) synthetic CO_2 ice, and (g) synthetic H_2O ice. See Section II-B for wavelet representation.

2) Step B—Determination of the Best Subspace:

Step B1—Continuum removal: We use only the last four scales (from 5 to 8) in order to remove the contribution of the continuum.

Step B2—Best discrimination: We prefer the automatic threshold method [method 3)], with norm L^2 and the value $c = 2.5$ to select the best subspace. This threshold criterion optimizes the classification.

Step B3—Circularity, noise, and dead spectels: We eliminate all wavelets containing a nonzero contribution from the last spectel number 255.

We eliminate wavelets polluted by damaged spectels (number 34, 78, and 158) with an energy criterion $(D = 0.45)$. Table IV lists the indexes of the eliminated wavelets.

Finally, the selected subspace is formed by the 12 wavelets shown in Fig. 3 and summarized in Table V.

TABLE V
LIST OF SELECTED WAVELETS

Scale	Indexes of selected wavelets
5	28
6	36, 58
7	73, 80, 95, 118
8	145, 148, 149, 160, 161, 163, 164, 165, 175, 192, 202, 239

3) Step C—Threshold Determination: We use two different procedures to constrain the SA threshold: numerical calibration [C1] and image calibration [C2]

C1—Numerical calibration: The idea is to generate a database of synthetic spectra that simulates the OMEGA dataset by varying the relative abundances of ices and dust as well as other physical parameters over realistic ranges of values. Then, we can apply the wavanglet method on this controlled data and adjust the angle threshold so as to maximize the detection sensitivity for H_2O and CO_2 ices while minimizing false detections.

The synthetic spectra are calculated by SPECTRIMAG, a bidirectional reflectance model that solves the radiative transfer of solar light through granular icy media [18]. The input data are the spectral optical constants of ice crystals and dust measured in the laboratory [25]–[27]. Each compound is also characterized by parameters such as grain size and porosity. A real OMEGA spectrum measures the surface reflectance of a geographical and/or granular mixture of H_2O ice, CO_2 ice, and dust at, or under, the pixel scale. In the first case, the resulting spectrum is a linear combination of the spectral reflectance signatures of the individual compounds. In the second case, the spectrum results from nonlinear physics aspects implemented in the model. In order to simulate as realistically as possible a Martian spectrum acquired by OMEGA, we also take into account the atmosphere and the instrumental noise contributions. The first contribution is introduced by multiplying each simulated spectrum by a constant atmospheric transmission spectrum calculated for an altitude of -4800 m and typical Martian weather conditions by a line-by-line radiative transfer model [30]. We simulate the instrumental noise by a Gaussian process using statistics coming from dark current measurements of OMEGA observation 41_1 acquired during orbit 41.

C2—Image calibration: We carry out the training phase of the wavanglet and SFF methods using observation 41_1 that covers the south polar region during local summer ($\mathrm{Ls} = 337.9^\circ$).

A careful visual interpretation of observation 41_1 was carried out in order to select samples of pixels that we can define as "ground truth" regions of interest (GTROI). Dust, H_2O, and CO_2 ices are identified on the basis of their distinct absorption bands. Nevertheless, this operation is very time consuming, and we need as many GTROIs as possible to carry out the training and subsequent testing (see Section IV-B) of the classification methods evaluated in this paper. Furthermore, the sensitivity of the brain/eye system is sometimes insufficient to recognize relevant spectral features in circumstances such as a very small amount of water ice mixed with solid CO_2. As a consequence we use the limited ($\approx$30) manually obtained set of GTROIs for 41_1 in order to train the BR method, which is always more sensitive than the human eye. We obtain two detection thresholds that, respectively, separate the CO_2 class from the H_2O class and the latter from the dust class. These thresholds are optimized for observation 41_1 or any other visually interpreted image. Then, we consider that the classification maps obtained with this optimized BR method (hereafter named BR_opt) constitute a reference for the training (observation 41_1) and testing (observation 231_1, see Section IV-B) of wavanglet as well as other classification methods.

Since our detection classes can overlap because both CO_2 and H_2O ices as well as dust can be detected in the same pixel, the training and testing are performed separately for the three compounds. In each case, we consider two classes: pixels with positive detection and pixels with negative detection. For a range of proposed SA thresholds (see Table VII), we calculate the overall accuracy and the kappa statistics [31] given by wavanglet by comparing its classification map with the reference map (BR_opt). The production and user accuracies are also calculated. We retain the threshold that maximizes the kappa factor. The training of SFF is performed in the same manner.

Both numerical and image calibrations converge on threshold angles of 1.54 rad for H_2O ice, 1.48 rad for CO_2 ice, and 0.34 for dust. Note that the threshold value is close to $\pi/2$ for the ices whereas it is much lower for dust. Our reference spectra for H_2O and CO_2 do not contain any atmospheric contribution as opposed to the dust reference and to the images we classify. As a consequence, the observed spectra over icy terrains differ more from their reference spectra than those observed over the dusty terrains. In Section IV-C, we present the detection limits we achieve on the synthetic spectra in more detail.

4) Step D—Classification Using the Complete Dataset: The presentation and discussion of the results obtained by applying the wavanglet method to the complete OMEGA dataset are not the subject of this paper. We only discuss the ability of our algorithm to analyze a selection of representative observations. For that purpose, we carry out a comparative study with the BR, SAM, and SFF methods (see Section II-C).

B. Comparison With Other Methods

In this paper, we illustrate our tests with observation 231_1 of the north polar region recorded during local springtime (Mars solar longitude, $\mathrm{Ls} = 8.6^\circ$). This observation presents different H_2O and CO_2 ice properties than observation 41_1, such as grain size and dust content [10], [11], [28].

All the results are summarized in Table IX.

1) Classification Accuracy: We admit that the optimized BR method (BR_opt for 231_1) is the best classification method and thus constitutes a reference (see Section IV-A3b). Yet, we cannot use it to classify the whole OMEGA dataset since it requires the manual constitution of GTROIs and subsequent manual training. As a consequence we only test and compare classification methods that could be used to process a large number of images automatically:

1) non-optimized BR method (hereafter called BR_fix);
2) SFF method;
3) "Wavanglet" method.

TABLE VI
CLASSIFICATION ACCURACY FOR A POLAR OBSERVATION (231_1) ACQUIRED BY OMEGA. THE REFERENCE METHOD IS THE BR METHOD OPTIMIZED FOR 231_1. THE DEFINITION OF THE KAPPA PARAMETER AND THE OVERALL AND USER ACCURACY CAN BE FOUND IN [31]

Method	Threshold	Kappa	Overall accuracy (%)	user accuracy (%) detection	user accuracy (%) no detection
BR_fix - H_2O	0.36 - 0.664	0.071	35.6	16.8	97.0
SFF^{TM}- H_2O	5.534	0.583	86.0	49.3	99.9
Wavanglet - H_2O	1.54	0.538	83.7	45.3	100.0
BR_fix - CO_2	0.467	0.576	80.2	54.6	100.0
SFF^{TM}- CO_2	3.716	0.572	80.0	54.4	99.9
Wavanglet - CO_2	1.48	0.793	93.2	100	92.0

All three methods use fixed detection thresholds to classify the dataset. For BR_fix, the thresholds equal those of BR_opt for observation 41_1.

Table VI shows the overall accuracy of the classifications achieved by wavanglet, SFF, and BR_fix using the optimized thresholds listed in Section IV-A3. In Table VI, note that for the detection of water ice terrains, SFF and wavanglet show similar detection capabilities with an overall accuracy of 86% and 84%, respectively. On the other hand, BR_fix misclassifies 64% of the pixels spectrally dominated by H_2O. For CO_2 terrains, wavanglet clearly outperforms SFF and BR_fix with an overall accuracy of 93% versus 80%.

2) Separability Between Classes: Class separability must be considered to evaluate the robustness of a classification algorithm. In our case, each class corresponds to the positive detection of H_2O ice, CO_2 ice, and dust. First, we must consider a space in which the data can be represented. For wavanglet, this space is the SA in the wavelet filtered subspace, one for each endmember E_i. For the BR method, this space is the ratio, unique for all endmembers. In these representation spaces, a hyperspectral image is a collection of values, each representing one spectrum. The classification consists in defining a threshold in the distribution of SAs or a ratio for the whole population of spectra of a hyperspectral image. The distribution may have three types of groups: first with a dominant presence of the reference material corresponding to E_i (group #1), second with the presence of the same material mixed with other components (group #2), third without the presence of the selected material corresponding to E_i (group #3). In the distribution, each group can be identified, and usually multiple peaks correspond to a single group. In our case, the intersection between materials are non-null: for instance, we can find materials with both H_2O ice and CO_2 ice (group #2).

The less the intersection between group #2 and group #3 contains pixels, the more the classification will be reliable. One way to estimate the class separability is to evaluate the range of thresholds that give reasonably accurate detections. Robustness is ensured when the range of possible values is relatively wide compared to the width of the groups. This corresponds to a large distance between pixels from groups #2 and #3 in the representative space.

For the BR method (Fig. 4), the H_2O, CO_2, and dust groups strongly overlap, and thus the range of possible thresholds is very limited. On the other hand, for the wavanglet method (Fig. 5), the SA distribution plots of the different materials, measured in their relative representing space, display well-separated groups.

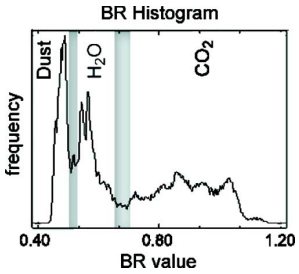


Fig. 4. BR value distribution for the 231_1 image. The gray boxes represent the range of thresholds possible for Dust/H_2O detection on the right and H_2O/CO_2 detection on the left.

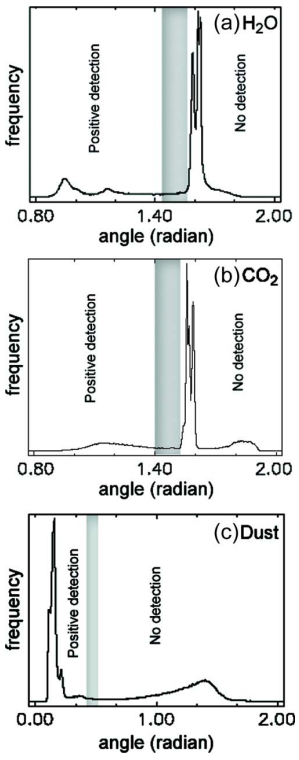


Fig. 5. SA distributions from the wavanglet method applied to the 231_1 image for (a) H_2O ice, (b) CO_2 ice, and (c) dust endmembers. The gray box represents the range of acceptable thresholds for reliable detection.

3) Multiple Endmembers and Possible Overlapping Signatures: When an increasing number of endmembers is required to classify a large dataset, it must still be possible to separate

TABLE VII
THRESHOLD RANGE OF POSITIVE DETECTION FOR THE BR AND WAVANGLET METHODS BASED ON 41_1 AND 231_1 OBSERVATIONS

Threshold	H_2O ice	CO_2 ice	dust
BR_opt on 41_1	<0.360 (*<0.398*) to >0.467 (>0.664)	>0.467 to >0.664	<0.360 to *<0.398*
BR_opt on 231_1	*<0.507* (<0.532) to >0.651 (>0.695)	>0.651 to >0.695	*<0.507* to <0.532
wavanglet opt. on 41_1	<1.5 to <1.56	<1.4 to <1.53	<0.3 to <0.6
wavanglet opt. on 231_1	<1.45 to <1.57	<1.43 to <1.52	<0.32 to <0.58
operational wavanglet	<1.54	<1.48	<0.34

classes. The BR method, as presented above, does not work for the detection of more than a few species because it becomes impossible to find a ratio that ensures class separability, especially when the spectral signatures overlaps. On the other hand, the SFF and wavanglet methods are more suitable for the classification of large spectral datasets with multiple endmembers because they perform the classification based on an automatically defined spectral subspace. The user only needs to define the endmember collection.

4) Mass Processing Feasibility: Application of a classification method with a threshold (like wavanglet, BR, SFF) to a huge dataset requires a constant threshold from one image to the other. Table VII shows the acceptable range of thresholds for the BR and wavanglet methods based on observations 41_1 and 231_1. For BR, the threshold range between dust and H_2O is strongly variable, and automation is therefore not possible. For the wavanglet method, the threshold range for a given compound varies only slightly, and a single constant value can be selected for optimized detection. The final thresholds determined in Section IV-A3 for H_2O, CO_2, and dust are also reported in Table VII.

5) Calculation Time: We measured the computation time necessary to complete the classification of observation 41_1 (111 616 spectra of 256 spectels) with the BR, SFF, and wavanglet methods. A complete process consists of opening files, running the classification algorithm, creating regions of interest, and saving product files. Each type of processing was performed in the ENVI environment on a LINUX workstation with the following characteristics: Intel Xeon 2.40-GHz biprocessor with a 512-KB cache memory for each processor, hyperthreading active technology, 6 GB of RAM, OS Linux with kernel 2.6 SMP. Results of the tests are given in Table IX. Wavanglet is the slowest method, but its run-time is comparable to SFF.

C. Evaluating Detection Limits With Synthetic Data

We now evaluate the sensitivity of wavanglet for the detection of H_2O and CO_2 ices using synthetic data. For this, we consider that solid H_2O, CO_2, and dust form a granular mixture with different mass proportions and grain sizes. For given observation conditions, we calculate the reflectance spectra that OMEGA would measure including the atmosphere contribution and the instrument noise (as explained in Section IV-A3-C1). We use different sets of parameters in the simulation. We span the whole range of mass proportions in a relatively continuous manner and use a limited set of values for the other parameters: atmospheric path, grain sizes, and incidence angle. The latter values, listed in Table VIII, are characteristics of polar ices [10], [11], [28], [29]. For each combination of parameters,

TABLE VIII
SET OF PHYSICAL AND OBSERVATION PARAMETER VALUES USED TO GENERATE THE TERNARY COMPOSITION DIAGRAMS

	Figure 6 and 7	Figure 8	Figure 9
Grain size H_2O ice (μm)	100	100	**1000**
Grain size CO_2 ice (μm)	45 000	45 000	45 000
Grain size dust (μm)	30	30	30
Incidence angle (°)	85 and 15	85 and 15	85 and 15
Emergence angle (°)	0	0	0
Atmosphere	South	**North (deeper)**	South

we perform automatic detection of the ices using wavanglet. The reference base is composed of the three spectra described in Section IV-A1 (see Fig. 2). The results are represented in ternary diagrams with the three poles (H_2O, CO_2, and dust) at the edges of the triangle, one point inside the triangle corresponding to a triplet of mass proportions (their sum being always equal to unity). Each symbol represents a positive detection for a triplet. The absence of a symbol means no detection. At one triplet location two symbols can be superimposed on the triangular diagram: the inner and outer symbols correspond to incidence angles of 85° and 15°, respectively. We can thus assess the effect of changing the atmospheric path, grain size, and incidence angle on the detection limits.

1) General Result: The detection limit for physical parameters of the typical surface (see Table VIII) of the permanent south polar cap is plotted in Fig. 6 and zoomed in Fig. 7. First, note that the general detection of H_2O ice is good until near the dust corner and near the CO_2 corner. Second, the detection of CO_2 ice is only present near the pure CO_2 ice pole. The difference between these two situations is related to the grain size effect. The grain size of CO_2 ice is almost 500 times greater than the grain size of H_2O ice and 1000 times greater than that of dust. In our case of granular mix, the mean free path is smaller inside CO_2 ice than inside H_2O ice or dust. The result is that even with a similar proportion of H_2O, CO_2, and dust, the CO_2 absorption bands will be smaller than the H_2O and dust absorption bands. The presence of significant CO_2 absorption bands in the spectra requires a high relative weight proportion of CO_2 in order to balance this grain size effect.

2) Atmospheric Path: We generate two ternary diagrams for an atmosphere extending from space to an altitude of, respectively, $+4800$ m (a situation typical of south polar region of Mars, Fig. 6) and -4800 m (a situation typical of the northern lowland region, Fig. 8). We see in the figures that, despite a large atmosphere thickness difference, the atmospheric path has only a minor effect on our detection limits. The detection of ice with the wavanglet method is thus only slightly disturbed by the atmosphere contribution.

3) Grain Size Effect: Two ternary diagrams are calculated, one with a water ice grain size of 100 μm (Fig. 6), a value

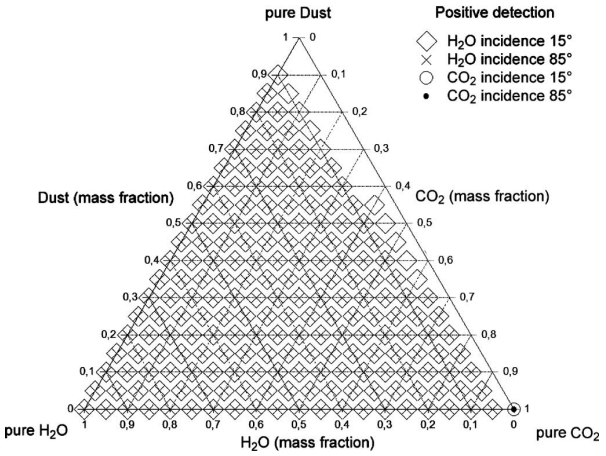


Fig. 6. Detection limits for H_2O and CO_2 for physical parameters of the typical surface (see Table VIII) of the permanent south polar cap. The atmosphere is typical for these conditions. The type of mixing is granular. Each symbol corresponds to positive detection of H_2O ice (square and cross) and CO_2 ice (circle and dot).

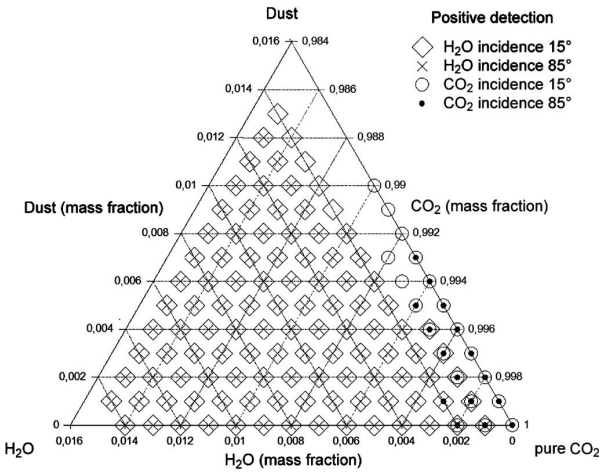


Fig. 7. Zoom on the lower right corner (pure CO_2) of Fig. 6. Each symbol corresponds to positive detection of H_2O ice (square and cross) and CO_2 ice (circle and dot).

characteristics of the permanent south polar cap [10], [28], [29], and a second with a much higher value (1000 μm, north polar cap [11], Fig. 9). Comparison of the two figures shows that the detection capacity strongly decreases as the grain size departs from the one used to generate the reference spectrum (10 μm). This effect is due to the high nonlinear dependence of the H_2O and CO_2 spectral signatures with grain size that wavanglet cannot handle. In conclusion, for efficient detection, the real grain size on the site must not be too different from the value used for the endmember reference. Otherwise, we must modify or complete our reference base with more relevant spectra (simulated, measured, or observed) in order to improve the detection limit.

4) Incidence Angle: For a first approximation, the observation parameters (incidence, emergence, and azimuth angles) only influence the absolute band depth of the spectral features.

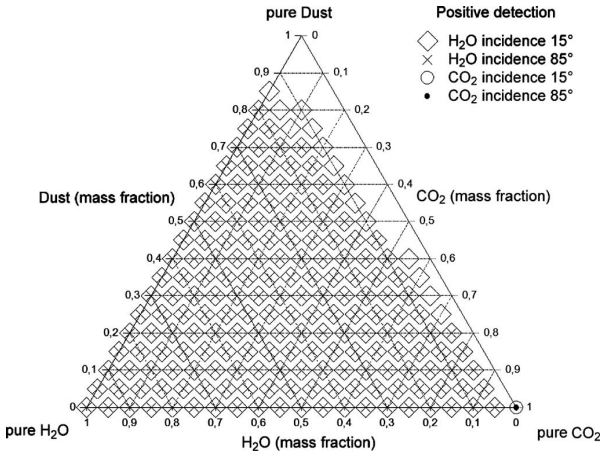


Fig. 8. Same conditions as in Fig. 6 except for a larger atmospheric path. Each symbol correspond to a positive detection of H_2O ice (square and cross) and CO_2 ice (circle and dot). Table VIII summarizes all parameters.

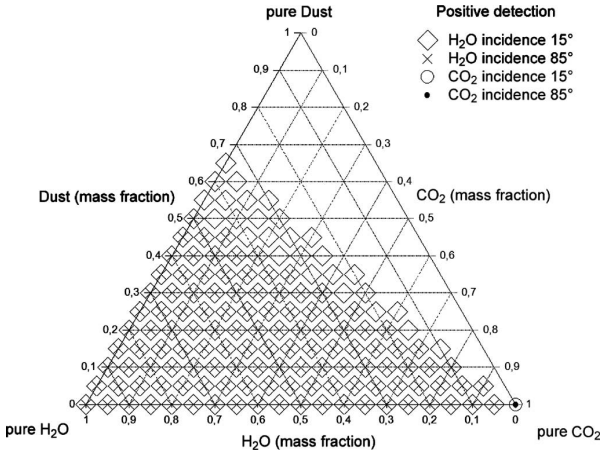


Fig. 9. Same conditions as in Fig. 6 except for a larger water grain size (1000 μm) compared to the reference on the detection limits (100 μm). Each symbol corresponds to positive detection of H_2O ice (square and cross) and CO_2 ice (circle and dot). Table VIII summarizes all parameters.

Since the wavanglet classification method is mostly sensitive to relative band depth, it may be fairly independent with respect to the illumination and observation conditions. The effect of the incidence angle has been tested for two extreme values: 85° (inner symbols) and 15° (outer symbols) for all the previous parameter sets (Figs. 6–9). The relative positioning of the inner and outer symbols for H_2O and CO_2 in all figures shows a very slightly better detection limit for 15° incidence. Other calculations on the emergence angle near the nadir support the same conclusion. The wavanglet method appears to be independent of the geometrical conditions of the observation.

V. Discussion and Conclusion

We have conducted a comparative study between two generic methods—the BR method and SFF—and wavanglet, our wavelet-based procedure. For this, we have considered

TABLE IX
COMPARISON OF BR, SFF, AND WAVANGLET METHODS

	Band Ratio (BR_fix)	Spectral Feature Fitting	*Wavanglet*
Overall accuracy (mean for H_2O and CO_2)	57%	83%	**89%**
Class separability	Low	Overlap	**High**
Large end-member dataset	Difficult	**Possible**	**Possible**
Mass processing	Yes (No for BR_opt)	-	**Yes**
Calculation time (s)	**11**	41	54
Noise dependence	High and localized	-	**Low**

five criteria pertaining to automatic compound detection and classification of spectra: overall accuracy, separability between classes, multiple endmembers and possible overlapping signatures, mass processing feasibility, and calculation time. Table IX shows that only wavanglet possesses all the desired properties. Furthermore, it has the highest overall accuracy, outperforming SFF for the CO_2 terrains. The BR_fix method usually misclassified a large fraction of the OMEGA images, and unfortunately BR_opt is not suitable for mass processing of complete datasets because a unique single detection threshold cannot be determined and applied to all OMEGA images. Also, BR is potentially very sensitive to noise for some spectels. Furthermore, wavanglet has two interesting properties for classifying our dataset: a reasonable calculation time and possible multidetections with a large endmember dataset. We demonstrated that the wavanglet method is able to discriminate between various spectral patterns that sometimes differ insufficiently and strongly overlap. We have also evaluated the sensitivity of wavanglet for the detection of H_2O and CO_2 ices as a function of certain physical as well as geometrical parameters using synthetic data. Thanks to the selection of medium and small-scale wavelets, the sensitivity of wavanglet is not hampered by variations of the incidence and emergence angles or by noise. Furthermore, the presence of atmospheric CO_2 bands has a minor influence on detection. On the other hand, the nonlinear effect of grain size variability on the spectral signatures is difficult to handle with only one reference spectrum per material. To improve detectability over a wide range of surface textures, we propose selection of one endmember per terrain and per characteristic grain size in the reference base.

ACKNOWLEDGMENT

The authors would like to thank the two anonymous reviewers for interesting remarks. The authors would also like to thank the OMEGA team at Institut d'Astrophysique Spatiale for support with sequencing and data downloading activities, and also to M. Lonjaret, F. Madec, and T. Questier for usefull discussions.

REFERENCES

[1] J.-P. Bibring, A. Soufflot, M. Berthé, Y. Langevin, B. Gondet, P. Drossart, M. Bouyé, M. Combes, P. Puget, A. Semery, G. Bellucci, V. Formisano, V. Moroz, V. Kottsov, G. Bonello, S. Erard, O. Forni, A. Gendrin, N. Manaud, F. Poulet, G. Poulleau, T. Encrenaz, T. Fouchet, R. Melchiori, F. Altieri, N. Ignatiev, D. Titov, L. Zasova, A. Coradini, F. Capacionni, P. Cerroni, S. Fonti, N. Mangold, P. Pinet, B. Schmitt, C. Sotin, E. Hauber, H. Hoffmann, R. Jaumann, U. Keller, R. Arvidson, J. Mustard, and F. Forget, "OMEGA: Observatoire pour la Minéralogie, l'Eau, les Glaces et l'Activité," in *Mars Express: The Scientific Payload*. Noordwijk, Netherlands: ESA SP-1240, Aug. 2004, pp. 37–49.

[2] F. A. Kruse, A. B. Lefkoff, J. W. Boardman, K. B. Heidebrecht, A. T. Shapiro, P. J. Barloon, and A. F. H. Goetz, "The spectral image processing system (SIPS)—Interactive visualization and analysis of imaging spectrometer data," *Remote Sens. Environ.*, vol. 44, no. 2/3, pp. 145–163, May/Jun. 1993.

[3] N. S. Subotic, J. D. Gorman, and B. J. Thelen, "Wavelet techniques for band selection and material classification from hyperspectral data," in *Proc. SPIE—Imaging Spectrometry*, M. R. Descour, J. M. Mooney, D. L. Perry, and L. R. Illing, Eds., Jun. 1995, vol. 2480, pp. 426–434.

[4] L. M. Bruce, and J. Li, "Fast wavelet-based algorithms for multiresolutional decomposition and feature extraction of hyperspectral signatures," in *Proc. SPIE—Algorithms for Multispectral and Hyperspectral Imagery V*, S. S. Shen and M. R. Descour, Eds., Jul. 1999, vol. 3717, pp. 72–81.

[5] L. M. Bruce, C. H. Koger, and J. Li, "Dimensionality reduction of hyperspectral data using discrete wavelet transform feature extraction," *IEEE Trans. Geosci. Remote Sens.*, vol. 40, no. 10, pp. 2331–2338, Oct. 2002.

[6] S. Kaewpijit, J. Le Moigne, and T. El-Ghazawi, "Automatic reduction of hyperspectral imagery using wavelet spectral analysis," *IEEE Trans. Geosci. Remote Sens.*, vol. 41, no. 4, pp. 863–871, Apr. 2003.

[7] C. H. Koger, L. M. Bruce, D. R. Shaw, and K. N. Reddy, "Wavelet analysis of hyperspectral reflectance data for detecting pitted morning glory (ipomoea lacunosa) in soybean (glycine max)," *Remote Sens. Environ.*, vol. 86, no. 1, pp. 108–119, Jun. 2003.

[8] H. Wu, G. Kuang, and W. Yu, "Unsupervised classification method for hyperspectral image combining PCA and Gaussian mixture model," in *Proc. 3rd Int. Symp. Multispectr. Image Process. and Pattern Recognit.*, H. Lu and T. Zhang, Eds., Sep. 2003, vol. 5286, pp. 729–734.

[9] J. E. Pinzon, S. L. Ustin, C. M. Castaneda, J. F. Pierce, and L. A. Costick, "Robust spatial and spectral feature extraction for multispectral and hyperspectral imagery," in *Proc. SPIE—Algorithms for Multispectral and Hyperspectral Imagery IV*, S. S. Shen and M. R. Descou, Eds., Jul. 1998, vol. 3372, pp. 199–210.

[10] J. Bibring, Y. Langevin, F. Poulet, A. Gendrin, B. Gondet, M. Berthé, A. Soufflot, P. Drossart, M. Combes, G. Bellucci, V. Moroz, N. Mangold, and B. Schmitt, "Perennial water ice identified in the south polar cap of Mars," *Nature*, vol. 428, no. 6983, pp. 627–630, Apr. 2004.

[11] Y. Langevin, F. Poulet, J.-P. Bibring, B. Schmitt, S. Douté, and B. Gondet, "Summer evolution of the north polar cap of Mars as observed by OMEGA/Mars express," *Science*, vol. 307, no. 5715, pp. 1581–1584, Mar. 2005.

[12] R. N. Clark, A. J. Gallagher, and G. A. Swayze, "Material absorption band depth mapping of imaging spectrometer data using the complete band shape least squares algorithm simultaneously fit to multiple spectral features from multiple materials," in *Proc. 3rd AVIRIS Workshop*, 1990, pp. 176–186.

[13] S. Mallat, *A Wavelet Tour of Signal Processing*. New York: Academic, 1999, ch. 4, pp. 107–121.

[14] W. H. Press, B. P. Flannery, S. A. Teukolsky, and W. T. Vetterling, *Numerical Recipes in Fortran 77 : The Art of Scientific Computing*. Cambridge, U.K.: Cambridge Univ. Press, 1986–1992, ch. 13.10, pp. 584–599.

[15] Research Systems, Inc., "Spectral tools," in *ENVI User's Guide*, Research Systems, Boulder, CO, 2000, ch. 9, pp. 615–686.

[16] J. Boardman, F. A. Kruse, and R. O. Green, "Mapping target signatures via partial unmixing of AVIRIS data: In summaries," in *Proc. 5th JPL Airborne Earth Sci. Workshop*, JPL Publication 95-1, Mar. 1995, vol. 1, pp. 23–26.

[17] A. Green, M. Berman, P. Switzer, and M. Craig, "A transformation for ordering multispectral data in terms of image quality with implications for noise removal," *IEEE Trans. Geosci. Remote Sens.*, vol. 26, no. 1, pp. 65–74, Jan. 1988.

[18] S. Douté and B. Schmitt, "A multilayer bidirectional reflectance model for the analysis of planetary surface hyperspectral images at visible and near-infrared wavelengths," *J. Geophys. Res.*, vol. 103, no. 12, pp. 31 367–31 390, Dec. 1998.

[19] L. Renzullo, A. Blanchfield, and K. Powell, "A method of wavelength selection and spectral discrimination of hyperspectral reflectance spectrometry," *IEEE Trans. Geosci. Remote Sens.*, vol. 44, no. 7, pp. 1986–1994, Jul. 2006.
[20] C.-I Chang and S. Wang, "Constrained band selection for hyperspectral imagery," *IEEE Trans. Geosci. Remote Sens.*, vol. 44, no. 6, pp. 1575–1585, Jun. 2006.
[21] J. Li, "Wavelet-based feature extraction for improved endmember abundance estimation in linear unmixing of hyperspectral signals," *IEEE Trans. Geosci. Remote Sens.*, vol. 42, no. 3, pp. 644–649, Mar. 2004.
[22] S. Liangrocapart and M. Petrou, "Feasibility study on the use of nonlinear spectral unmixing," in *Proc. SPIE—Image and Signal Processing for Remote Sensing V,* S. B. Serpico, Ed., Dec. 1999, vol. 3871, pp. 159–168.
[23] R. R. Coifman and M. V. Wickerhauser, "Entropy-based algorithms for best basis selection," *IEEE Trans. Inf. Theory*, vol. 38, no. 2, pp. 713–718, Mar. 1992.
[24] N. Saito and R. R. Coifman, "Local discriminant bases," in *Proc. SPIE—Wavelet Applications in Signal and Image Processing II*, A. F. Laine and M. A. Unser, Eds., Oct. 1994, vol. 2303, pp. 2–14.
[25] E. Quirico and B. Schmitt, "Near-infrared spectroscopy of simple hydrocarbons and carbon oxides diluted in solid N_2 and as pure ices: Implications for Triton and Pluto," *Icarus*, vol. 127, no. 2, pp. 354–378, Jun. 1997.
[26] W. M. Grundy and B. Schmitt, "The temperature-dependent near-infrared absorption spectrum of hexagonal H_2O ice," *J. Geophys. Res.*, vol. 103, no. E11, pp. 25 809–25 822, Nov. 1998.
[27] B. Schmitt, E. Quirico, F. Trotta, and W. M. Grundy, "Optical properties of ices from UV to infrared," in *Proc. ASSL—Solar System Ices*, 1998, vol. 227, pp. 199–240.
[28] S. Douté, B. Schmitt, Y. Langevin, J.-P. Bibring, F. Altieri, G. Bellucci, and B. Gondet, "South pole of Mars: Nature and composition of the icy terrains from Mars express OMEGA observations," *Planet. Space Sci.*, vol. 55, no. 1–2, pp. 113–133, Jan. 2007.
[29] D. A. Glenar, G. Hansen, G. Bjoraker, M. Smith, J. Pearl, and D. Blaney, , "Bright-region radiative properties within the Mars south polar cap ($Ls = 231$) from near-infrared spectroscopic imaging," *Icarus*, vol. 174, no. 2, pp. 600–603, Apr. 2005.
[30] S. A. Clough, M. W. Shephard, E. J. Mlawer, J. S. Delamere, M. J. Iacono, K. Cady-Pereira, S. Boukabara, and P. D. Brown, "Atmospheric radiative transfer modeling: a summary of the AER codes," *J. Quant. Spectrosc. Radiat. Transf.*, vol. 91, no. 2, pp. 233–244, Mar. 2005.
[31] R. Congalton and K. Green, *Assessing the Accuracy of Remotely Sensed Data: Principles and Practices*, J. Lyon, Ed. New York: Lewis, 1999.



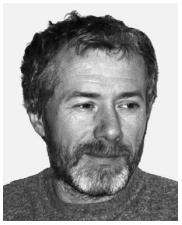
Frédéric Schmidt received the two-years degree in physics from the Université Louis Pasteur, Strasbourg, France, in 2001, the B.S. degree in earth science from the Ecole Normale Supérieure, Lyon, France, in 2003, and the M.S. degree in earth science from the Université Joseph Fourier (UJF), Grenoble, France, in 2004. He is currently working toward the Ph.D. degree at the Laboratoire de Planétologie de Grenoble (Centre National de la Recherche Scientifique-UJF), Grenoble.

His research interests are analysis of hyperspectral data, statistics in geophysical fields, ices on planet Mars, and Martian climate. In particular, he is working on hyperspectral images produced by the OMEGA imaging spectrometer (MEX, ESA).



Sylvain Douté received the B.S. and M.S. degrees from the Université Joseph Fourier (UJF), Grenoble, France, in 1991 and 1994, respectively, and the Ph.D. degree from the Université Denis Diderot, Paris, France, after working three years at the Laboratoire de Glaciologie et Géophysique de l'Environnement, Grenoble.

He held a postdoctoral position for two years at the Institute of Geophysics and Planetary Physics (University of California, Los Angeles) to analyze images of the near-infrared mapping spectrometer (Galileo, NASA). He is currently a Researcher with the Laboratoire de Planétologie de Grenoble (CNRS-UJF), Grenoble. His research interests include remote sensing of planetary surfaces by hyperspectral imaging, theoretical as well as experimental study of solar light radiative transfer in geophysical media. In particular, he is working on images produced by the OMEGA imaging spectrometer (MEX, ESA).



Bernard Schmitt received the Ingenieur degree (material sciences) from the Institut National Polytechnique de Grenoble, Grenoble, France, in 1983, and the Ph.D. degree in physics (material sciences) from the University J. Fourier, Grenoble, in 1986.

From 1988 to 1999, he was affiliated with the Laboratoire de Glaciologie et Géophysique de l'Environnement (CNRS) and contributed to create in 1999 the Laboratoire de Planétologie de Grenoble (CNRS—University J. Fourier) where he is currently Research Director of a group working on solid-matter spectroscopy and remote sensing of solar system surfaces. His research interests include visible to infrared laboratory spectroscopy and radiometry of ices and molecular solids, and hyperspectral remote sensing of planetary surfaces. He is Coinvestigator of several imaging spectrometers onboard space missions (OMEGA/MEX, DISR/Casini-Huygens, VIRTIS/Rosetta, etc.).

1.4.2 Séparation de source en aveugle

Cette section contient l'article suivant :

Schmidt, F. ; Schmidt, A. ; Tréguier, E. ; Guiheneuf, M. and Moussaoui, S. & Dobigeon, N., Implementation strategies for hyperspectral unmixing using Bayesian source separation, IEEE Transaction on Geoscience and Remote Sensing, 2010, 48, 4003-4013.

IEEE TRANSACTIONS ON GEOSCIENCE AND REMOTE SENSING, VOL. 48, NO. 11, NOVEMBER 2010 4003

Implementation Strategies for Hyperspectral Unmixing Using Bayesian Source Separation

Frédéric Schmidt, Albrecht Schmidt, Erwan Tréguier, Maël Guiheneuf,
Saïd Moussaoui, and Nicolas Dobigeon, *Member, IEEE*

***Abstract*—Bayesian positive source separation (BPSS) is a useful unsupervised approach for hyperspectral data unmixing, where numerical nonnegativity of spectra and abundances has to be ensured, such as in remote sensing. Moreover, it is sensible to impose a sum-to-one (full additivity) constraint to the estimated source abundances in each pixel. Even though nonnegativity and full additivity are two necessary properties to get physically interpretable results, the use of BPSS algorithms has so far been limited by high computation time and large memory requirements due to the Markov chain Monte Carlo calculations. An implementation strategy that allows one to apply these algorithms on a full hyperspectral image, as it is typical in earth and planetary science, is introduced. The effects of pixel selection and the impact of such sampling on the relevance of the estimated component spectra and abundance maps, as well as on the computation times, are discussed. For that purpose, two different data sets have been used: a synthetic one and a real hyperspectral image from Mars.**

***Index Terms*—Bayesian estimation, computation time, hyperspectral imaging, implementation strategy, source separation.**

I. Introduction

In VISIBLE and near-infrared hyperspectral imaging, each image recorded by the sensor is the solar light reflected and diffused back from the observed planet surface and atmosphere at a particular spectral band. Under some assumptions related to surface and atmosphere properties—e.g., Lambertian surface, no intimate mixture, no diffusion terms in the atmosphere, and homogeneous geometry in the scene—each measured spectrum—i.e., each pixel of the observed image for several spectral bands—is modeled as a linear mixture of the scene component spectra (*endmembers*) [1]–[3]. In this model, the weight of each component spectrum is linked to its abundance in the surface area, which corresponds to the underlying pixel. The main goal of hyperspectral unmixing is to identify the components of the imaged surface and to estimate their respective abundances [4], [5].

By considering P pixels of a hyperspectral image acquired in L frequency bands, the observed spectra are gathered in a $P \times L$ data matrix $\mathbf{X}$, potentially ignoring spatiality. Each row of this matrix contains a measured spectrum at a pixel with spatial index $p = 1, \ldots, P$. According to the linear mixing model, the pth spectrum, i.e., $1 \leq p \leq P$, can be expressed as a linear combination of R pure spectra of the surface components. Using matrix notations, this linear spectral mixing model can be written as

$$\mathbf{X} \approx \mathbf{AS} \tag{1}$$

where nonnegative matrices $\mathbf{A} \in \mathbb{R}_+^{P \times R}$ and $\mathbf{S} \in \mathbb{R}_+^{R \times L}$ approximate $\mathbf{X} \in \mathbb{R}_+^{P \times L}$ in the sense that $1/2\|\mathbf{AS} - \mathbf{X}\|^2$ is minimized ($\mathbb{R}_+^{\cdot \times \cdot}$ denotes the space of matrices with only nonnegative entries of respective dimensions). The rows of matrix $\mathbf{S}$ now contain the pure surface spectra of the R components, and each element a_{pr} of matrix $\mathbf{A}$ corresponds to the abundance of the rth component in pixel with spatial index p. For the qualitative and quantitative descriptions of the observed scene composition, the estimation problem consists of finding matrices $\mathbf{S}$ and $\mathbf{A}$ that allow one to explain the data matrix $\mathbf{X}$ and have a coherent physical interpretation. This approach casts the hyperspectral unmixing as a *source separation* problem under a linear instantaneous mixing model [6]. Source separation is a statistical multivariate data processing problem whose aim is to recover unknown signals (called *sources*) from noisy and mixed observations of these sources [7], [8].

This problem has been studied in-depth in recent years, starting with pioneer work more than 15 years ago [9], [10]. From a statistical point of view, the problem is also related to principal component analysis (PCA) and k-means clustering (see [11] for an overview). Also note that the factorization $\mathbf{AS}$ is not uniquely defined. For instance, for any matrices $\mathbf{Z} \in \mathbb{R}_+^{R \times \cdot}$ such that $\mathbf{ZZ}^{-1} = \mathbf{I}$, then $\mathbf{AZZ}^{-1}\mathbf{S} = (\mathbf{AZ})(\mathbf{Z}^{-1}\mathbf{S}) = \mathbf{A}'\mathbf{S}'$ is a solution as well; this holds even if the minimization is able to find a global minimum. However, when solving this separation problem with hyperspectral data, several constraints can be considered to reduce the set of admissible solutions. A first hard constraint is the nonnegativity of the elements of both

Manuscript received December 14, 2009; revised April 9, 2010. Date of publication September 13, 2010; date of current version October 27, 2010.

F. Schmidt was with the European Space Astronomy Centre, European Space Agency, 28692 Madrid, Spain. He is now with the Laboratoire des Intéractions et Dynamique des Environnements de Surface, UMR 8148, University Paris-Sud, 91405 Orsay, France, and also with the Centre National de la Recherche Scientifique, Université Paris-Sud, 91405 Orsay, France (e-mail: frederic.schmidt@u-psud.fr).

A. Schmidt, E. Tréguier, and M. Guiheneuf are with European Space Astronomy Center, European Space Agency, 28692 Madrid, Spain (e-mail: Albrecht.Schmidt@esa.int; mael.guiheneuf@gmail.com; erwan.treguier@sciops.esa.int).

S. Moussaoui is with the Institut de Recherche en Communication et Cybernétique de Nantes (IRCCyN), Centre National de la Recherche, UMR 6597, École Centrale Nantes, 44321 Nantes Cedex 3, France (e-mail: said.moussaoui@irccyn.ec-nantes.fr).

N. Dobigeon is with the Institut de Recherche en Informatique de Toulouse (IRIT), and with the Institut National Polytechnique de Toulouse, and the Ecole Nationale Supérieure d'Electrotechnique, d'Electronique, d'Hydraulique et d'Informatique, et des Télécommunications (ENSEEIHT), and also with the Telecommunications for Space and Aeronautics TeSA, University of Toulouse, 31071 Toulouse Cedex 7, France (e-mail: Nicolas.Dobigeon@enseeiht.fr).

Color versions of one or more of the figures in this paper are available online at http://ieeexplore.ieee.org.

Digital Object Identifier 10.1109/TGRS.2010.2062190

0196-2892/$26.00 © 2010 IEEE

matrices $\mathbf{S}$ and $\mathbf{A}$ since they correspond to pure spectra and abundances of the surface components, respectively. A second constraint that may be imposed is the sum-to-one (additivity) constraint of the abundances. Indeed, the abundance weights correspond to proportions and should therefore sum to unity.

Several algorithms have been proposed in the literature to solve fully constrained unmixing problems, i.e., handling both of the constraints imposed on the spectra and abundances. Specifically, an iterative algorithm called iterated constrained endmembers (ICE) has been proposed in [12] to minimize the size of the simplex formed by the estimated endmembers. However, as noted in [13], results provided by ICE strongly depend on the choice of the algorithm parameters. More recently, Jia and Qian have developed in [14] complexity-based BSS algorithms that exploit pixel correlations to recover endmember signatures. In [15], Miao and Qi have introduced a nonnegative matrix factorization (NMF) algorithm with an additivity penalty on the abundance coefficients. Similarly, other constrained NMF approaches exploiting smoothness and sparseness features have been considered in [16]. Note that all the strategies described earlier are based on an optimization scheme to minimize a penalty criterion. Consequently, they may suffer from convergence issues, e.g., due to the presence of local maxima and the large number of parameters to be estimated.

Alternatively, the constrained separation problem can be conveniently addressed in a Bayesian framework. Two algorithms that perform unsupervised separation under positivity and sum-to-one constraints have been recently proposed [17], [18]. These algorithms are based on hierarchical Bayesian modeling to encode prior information regarding the observation process the parameters of interest and include the positivity and full additivity constraints. The complexity of the inference from the posterior distribution of the parameters of interest is tackled using Markov chain Monte Carlo (MCMC) methods [19], [20], which has been proposed to analyze hyperspectral images [21]. The algorithmic details are not described here. The reader is invited to read the pseudocodes summarized in algorithms 1 and 2 and to consult [17] and [18] for further details. The only difference between the two Bayesian positive source separation (BPSS) algorithms is the sampling of the abundance vectors $\mathbf{a}_p$ $(p = 1, \ldots, P)$. However, since these algorithms rely on MCMC methods, the computation time drastically increases with the image size, and these algorithms have not been applied for large-scale data processing in spite of their high effectiveness.

The aim of this paper is to discuss some implementation strategies that allow one to apply these algorithms to real hyperspectral data even if images are large. Previous works about blind source separation of hyperspectral images have been proposed [22]–[24], but only few use positivity/sum-to-unity constraints [25]. To overcome this difficulty, a first approach has been proposed in [25] to combine independent component analysis (ICA) and BPSS. First, applying an ICA algorithm (such as JADE [26] or FastICA [27]) to hyperspectral images is applied to get a rough spatial classification of the scene and to sample relevant pixels (i.e., from each *class*, the pixels whose spectra are mostly uncorrelated are selected). Second, the spectra associated to these pixels will serve in the Bayesian separation algorithm to estimate the endmember spectra. Finally, the abundances can then be estimated on the whole image using the estimated spectra. However, this strategy presents a limitation related to the difficulty to determine the number of pixels to retain from each independent component class. In this paper, another pixel selection strategy based on the computation of the convex hull of the hyperspectral data is introduced. Its influence on separation performances is also discussed. The issue of estimating the number of sources, or "intrinsic dimension" [28], will not be addressed in this paper. Several methods have been proposed in the literature [29], [30].

This paper is organized as follows. Section II describes the proposed implementation strategies adopted for this paper. Section III summarizes the improvements related to the technical aspects of memory storage and computation issues. Section IV discusses the performances of the resulting algorithms when the pixel selection preprocessing step is introduced.

Algorithm 1 BPSS algorithm

for $i = 1, \ldots, N_{\mathrm{MC}}$ **do**
% sampling the abundance hyperparameters
for $p = 1, \ldots, P$ **do**
Draw λ_p from the pdf

$$f(\lambda_p|\mathbf{a}_{p:}, \gamma_p) \propto \prod_{r=1}^{R} \left[\frac{\gamma_p^{\lambda_p}}{\Gamma(\lambda_p)} a_{p,r}^{\lambda_p}\right] e^{-\epsilon\lambda_p} \mathbf{1}_{\mathbb{R}^+}(\lambda_p).$$

end for
% sampling the abundance hyperparameters
for $p = 1, \ldots, P$ **do**
Draw γ_p from the gamma distribution

$$\gamma_p|\lambda_p, \mathbf{a}_{p:} \sim \mathcal{G}\left(1 + R\lambda_p + \epsilon, \sum_{r=1}^{R} a_{p,r} + \epsilon\right).$$

end for
% sampling the abundance vectors
for $p = 1, \ldots, P$ and $r = 1, \ldots, R$ **do**
Draw $a_{p,r}$ from the pdf

$$f\left(a_{p,r}|\lambda_p, \gamma_p, \mathbf{S}, \boldsymbol{\sigma}_{\mathrm{e}}^2, \mathbf{X}\right) \propto a_{p,r}^{\lambda_r - 1} \mathbf{1}_{\mathbb{R}^+}(a_{p,r}) \exp\left[-\frac{(a_{p,r} - \mu_{p,r})^2}{2\delta_p^2} - \gamma_p a_{p,r}\right]$$

end for
% sampling the noise hyperparameters
Draw ψ_{e} from the inverse-gamma distribution

$$\psi_{\mathrm{e}}|\boldsymbol{\sigma}_{\mathrm{e}}^2, \rho_{\mathrm{e}} \sim \mathcal{IG}\left(\frac{P\rho_{\mathrm{e}}}{2}, \frac{1}{2}\sum_{p=1}^{P} \frac{1}{\sigma_{\mathrm{e},p}^2}\right).$$

% sampling the noise variances
for $p = 1, \ldots, P$ **do**
Draw $\sigma_{\mathrm{e},p}^2$ from the inverse-gamma distribution

$$\sigma_{\mathrm{e},p}^2|\psi_{\mathrm{e}}, \mathbf{a}_{p:}, \mathbf{S}, \mathbf{x}_{p:} \sim \mathcal{IG}\left(\frac{\rho_{\mathrm{e}} + L}{2}, \frac{\psi_{\mathrm{e}} + \|\mathbf{x}_{p:} - \mathbf{S}\mathbf{a}_{p:}\|^2}{2}\right).$$

end for
% sampling the source hyperparameters
for $r = 1, \ldots, R$ **do**

Draw α_r from the pdf

$$f(\alpha_r|\mathbf{s}_{r:},\beta_r) \propto \prod_{l=1}^{L}\left[\frac{\beta_r^{\alpha_r}}{\Gamma(\alpha_r)}s_{r,l}^{\alpha_r}\right]e^{-\epsilon\alpha_r}\mathbf{1}_{\mathbb{R}^+}(\alpha_r).$$

end for
% sampling the source hyperparameters
for $r = 1,\ldots,R$**do**
Draw β_r from the gamma distribution

$$\beta_r|\alpha_r,\mathbf{s}_{r:} \sim \mathcal{G}\left(1+L\alpha_r+\epsilon, \sum_{l=1}^{L}s_{r,l}+\epsilon\right).$$

end for
% sampling the source spectra
for $r = 1,\ldots,R$ and $l = 1,\ldots,L$**do**
Draw $s_{r,l}$ from the pdf

$$f\left(s_{r,l}|\alpha_r,\beta_r,\mathbf{A},\boldsymbol{\sigma}_{\mathrm{e}}^2,\mathbf{X}\right) \propto s_{r,l}^{\alpha_r-1}\mathbf{1}_{\mathbb{R}^+}(s_{r,l})\exp\left[-\frac{(s_{r,l}-\mu_{r,l})^2}{2\delta_r^2}-\beta_r s_{r,l}\right]$$

end for
end for

Algorithm 2 Fully constrained BPSS algorithm (BPSS2)

for $i = 1,\ldots,N_{\mathrm{MC}}$**do**
% sampling the abundance vectors
for $p = 1,\ldots,P$**do**
Draw $\mathbf{a}_{p:}$ from the pdf

$$f\left(\mathbf{a}_{p:}|\mathbf{A},\boldsymbol{\sigma}_{\mathrm{e}}^2,\mathbf{X}\right) \propto \exp\left[-\frac{1}{2}(\mathbf{a}_{p:}-\boldsymbol{\mu}_p)^{\mathsf{T}}\boldsymbol{\Lambda}_p^{-1}(\mathbf{a}_{p:}-\boldsymbol{\mu}_p)\right]\mathbf{1}_{\mathbb{S}}(\mathbf{a}_{p:})$$

with

$$\mathbb{S} = \left\{\mathbf{a}_{p:}a_{p,r} \geq 0,\ \forall r = 1,\ldots,R,\ \sum_{r=1}^{R}a_{p,r} = 1\right\}.$$

end for
% sampling the noise hyperparameters
Draw ψ_{e} from the inverse-gamma distribution

$$\psi_{\mathrm{e}}|\boldsymbol{\sigma}_{\mathrm{e}}^2,\rho_{\mathrm{e}} \sim \mathcal{IG}\left(\frac{P\rho_{\mathrm{e}}}{2},\frac{1}{2}\sum_{p=1}^{P}\frac{1}{\sigma_{\mathrm{e},p}^2}\right).$$

% sampling the noise variances
for $p = 1,\ldots,P$**do**
Draw $\sigma_{\mathrm{e},p}^2$ from the inverse-gamma distribution

$$\sigma_{\mathrm{e},p}^2|\psi_{\mathrm{e}},\mathbf{a}_{p:},\mathbf{S},\mathbf{x}_{p:} \sim \mathcal{IG}\left(\frac{\rho_{\mathrm{e}}+L}{2},\frac{\psi_{\mathrm{e}}+\|\mathbf{x}_{p:}-\mathbf{S}\mathbf{a}_{p:}\|^2}{2}\right).$$

end for
% sampling the source hyperparameters
for $r = 1,\ldots,R$ **do**
Draw α_r from the pdf

$$f\left(\alpha_r|\mathbf{s}_{r:},\beta_r\right) \propto \prod_{l=1}^{L}\left[\frac{\beta_r^{\alpha_r}}{\Gamma(\alpha_r)}s_{r,l}^{\alpha_r}\right]e^{-\epsilon\alpha_r}\mathbf{1}_{\mathbb{R}^+}(\alpha_r).$$

end for
% sampling the source hyperparameters
for $r = 1,\ldots,R$**do**
Draw β_r from the gamma distribution

$$\beta_r|\alpha_r,\mathbf{s}_{r:} \sim \mathcal{G}\left(1+L\alpha_r+\epsilon, \sum_{l=1}^{L}s_{r,l}+\epsilon\right).$$

end for
% sampling the source spectra
for $r = 1,\ldots,R$ and $l = 1,\ldots,L$**do**
Draw $s_{r,l}$ from the pdf

$$f\left(s_{r,l}|\alpha_r,\beta_r,\mathbf{A},\boldsymbol{\sigma}_{\mathrm{e}}^2,\mathbf{X}\right) \propto s_{r,l}^{\alpha_r-1}\mathbf{1}_{\mathbb{R}^+}(s_{r,l})\exp\left[-\frac{(s_{r,l}-\mu_{r,l})^2}{2\delta_r^2}-\beta_r s_{r,l}\right]$$

end for
end for

II. Optimization Strategies

The optimization consists of two independent parts, which will be referred to as follows: 1) *technical optimization (TO)* to reduce the memory footprint, lower the average cost of algorithmic operations, and make smarter reuse of memory, and 2) *convex hull optimization (CHO)* to reduce the number of spectra to be processed.

Both parts enabled us to analyze hyperspectral images that so far were not open to analysis. The authors stress that the techniques applied in 1) do not alter the results of the original algorithm (see Section III). On the other hand, the optimization strategy 2) only selects a subset of the original input and may therefore change the results. The impact of the strategy 2) needs to be evaluated, which will be presented in Section IV.

A. TO

The algorithms introduced in [17] and [18] and referred to as BPSS and BPSS2, respectively, could be successfully launched on an image of a restricted size, typically of a few thousand pixels. The main goal of this paper is to optimize the memory requirement of these algorithms to process a whole hyperspectral image of 100 000 spectra, as it typically occurs in earth and planetary science. Since the time requirements of the computation increase drastically for a larger number of pixels and a larger number of sources, another challenging objective is to reduce as much as possible the computation time. In that respect, our proposal is to discuss the memory storage, the data representation, the operating system (OS) architecture, and the computing parallelization. These algorithms have been implemented in MATLAB for this paper, but future implementations will be done in other languages as well.

1) Memory: Thanks to the MATLAB profiler, it can be noticed that the main limitation of the BPSS implementation is the contiguous memory. Fragmentation may occur when variables are resized after memory allocation. In this case, the memory management might not be able to allocate a chunk of memory that is large enough to hold the new variable.

TABLE I
SUMMARY OF MEMORY LIMITATION, DEPENDING ON THE OS

Operating System	Memory Limitation
32-bit Microsoft Windows XP Windows Vista	2GB
32-bit Windows XP with 3 GB *boot.ini* switch 32-bit Windows Vista with *increaseuserva* set	3GB
32-bit LINUX	3GB
64-bit Windows XP, Linux, Apple Macintosh OS X or SunSolaris running 32-bit MATLAB©	4GB
64-bit Windows XP, Windows Vista, Linux, or Solaris running 64-bit MATLAB©	8GB

TABLE II
COMPUTATION TIMES (AFTER TO) IN SECONDS, FOR A SYNTHETIC DATA SET WITH THREE ENDMEMBERS (NO CUTOFF, NO NOISE), FOR BOTH BPSS AND BPSS2, WITH AND WITHOUT CHO. IN THIS EXAMPLE, 944 PIXELS WERE SELECTED FORTHE CHO AMONG A TOTAL OF 100 000. THE NAME OFTHE RUN OF TABLE III AND TABLE IV IS NOTED IN PARENTHESIS

Algorithm	Without CHO	With CHO	Time ratio
BPSS	71463 (BPSS-2)	2205 (BPSS-1)	32.41
BPSS2	530654 (BPSS2-2)	7133 (BPSS2-1)	74.39

Significant garbage collection may set in, which may have a significant performance impact. In our case, to reduce the impact of garbage collection, preallocating the matrices and work with global variables has been found to be useful.

2) Precision: MATLAB, by default, computes on double precision. However, computing with single data type saves a lot of computation time while providing sufficient arithmetic precision. It has been estimated to win up to 60% computation time on an x86 processor architecture, while the changes to the code have been minimal. Furthermore, most data sets come as single precision.

3) OS Architecture: It is interesting to note that MATLAB is limited in terms of memory usage (regardless of the size of physical memory). This depends on the OS and the MATLAB version (see Table I).

Therefore, a 32-bit LINUX architecture has been chosen.

4) Parallelization: MATLAB contains libraries dedicated to automatically parallelize parts of the algorithms on a single computer. BPSS has been run on a four-core machine. The underlying matrix libraries already provide a certain level of parallelism, depending on the number of available cores. However, in the future, parts of the code could be parallelized, and the jobs could be submitted to a grid in order to speed up the calculation process.

B. CHO

The proposed pixel selection strategy is based on the convex hull of the data matrix projection into the subspace spanned by the principal components. The convex hull of a point set is the smallest convex set that includes all the points [31]. The pixels associated to the vertices of the convex hull are selected [32] and are expected, despite their limited number, to exhibit the main spectral features of the whole data set. In terms of abundances, this sample of points should contain the pixels with the highest abundances of the components that contribute to the investigated hyperspectral image (i.e., the purest pixels or most extreme pixels). It can be used as a concise representation of the data set that still features the strongest spectral signatures available in the original image. This strategy is also used as a first step in endmember extraction algorithms for dimension reduction and purest pixel determination [32]–[37]. Pixel selection has the advantage to reduce the number of mixture spectra to unmix and to enforce the sparsity of the mixing coefficients to be estimated. Note that the spectral dimension of the selected spectra is not changed; only the spatial dimension is reduced since only a few pixels are selected.

The convex hull selection has been implemented after seven spectral components have been selected through PCA, which turned out to be a good compromise between resource consumption and accuracy.

III. PERFORMANCE AND ACCURACY OF TO

All the following runs are performed on a Quad-Core AMD Opteron Processor 8384 at 2.7 GHz with 2 GB of memory.

1) Performance: Computation times between the previous version of BPSS and the TO version have been compared when processing a synthetic data set of 1052 spectra of 128 bands and 3 sources. For a run attempting at estimating three sources, the computation time has decreased from 1106 s (previous version) to 724 s (TO version), i.e., by a factor of about 1.5. In addition, the total memory consumption is nearly half for the TO version of the algorithm.

2) Accuracy: Due to the stochastic nature of the BPSS algorithms, it is difficult to demonstrate that two algorithms are semantically identical. In order to check that no significant loss of accuracy has been induced by TO and, in particular, by the change from double to single precision, several tests have been performed with different random seeds χ_1 and χ_2, which are used for the initialization step of the MCMC. The sources $S_{\chi 1}$ and $S_{\chi 2}$ estimated with and without TO have been compared.

The average correlations between $S_{\chi 1}$ and $S_{\chi 2}$ are 0.9816 ± 0.0315 and 0.9818 ± 0.0255 without and with TO, respectively. These correlations are due to the stochastic approach in the Bayesian framework. Correlation values are similar, indicating that the stochastic variance has not been affected by TO.

The average cross correlation between $S_{\chi 1}$ and $S_{\chi 2}$ with and without TO is 0.9760 ± 0.0388. This value is similar to the correlation due to the stochastic process, demonstrating that the TO version is equivalent to the original version of BPSS.

No significant differences have been observed, confirming that the TO version is equivalent to the original version of BPSS.

IV. PERFORMANCE AND ACCURACY OF CHO

The impact of the convex hull pixel selection preprocessing step has been evaluated on two data sets: 1) synthetic data generated from linear mixtures of known materials and 2) an Observatoire pour la Minéralogie, l'Eau, les Glaces et l'Activité (OMEGA) hyperspectral image of the south polar cap of Mars as an example from planetology. Since the BPSS with TO has been shown to be semantically equivalent to the previous version, the TO approach is used in the rest of this paper.

TABLE III
RESULTS OBTAINED FOR DIFFERENT SYNTHETIC DATA SETS WITH THE BPSS ALGORITHM. THE CHARACTERISTICS OF EACH DATA SET ARE SHOWN: NUMBER OF ENDMEMBERS, CUTOFF, AND NOISE. EACH DATA SET HAS BEEN ANALYZED WITH A NUMBER OF SOURCES TO BE ESTIMATED EQUAL TO THE NUMBER OF ENDMEMBERS USED TO GENERATE THE ARTIFICIAL DATA SET, WITH AND WITHOUT PIXEL SELECTION. THE QUALITY OF THE ESTIMATION IS EXPRESSED THROUGH THE NUMBER OF WELL-ESTIMATED SOURCES AND THE MEAN ABSOLUTE EXPRESSION, AS EXPLAINED IN THE TEXT

Run Id	Cutoff (%)	Nb of endmembers	Noise	Pixel selection	Nb of well-estimated sources	Mean correlation (%)
BPSS-1	100%	3	no	yes	2/3	99.9441
BPSS-2	100%	3	no	no	2/3	99.9963
BPSS-3	80%	3	no	yes	2/3	98.5826
BPSS-4	80%	3	no	no	2/3	99.9286
BPSS-5	60%	3	no	yes	2/3	98.2135
BPSS-6	60%	3	no	no	2/3	99.2499
BPSS-7	100%	5	no	yes	2/5	92.0689
BPSS-8	100%	5	no	no	3/5	92.5181
BPSS-9	100%	10	no	yes	5/10	88.3081
BPSS-10	100%	10	no	no	6/10	94.2996
BPSS-11	100%	3	OMEGA	yes	2/3	99.9067
BPSS-12	100%	3	OMEGA	no	2/3	99.9961
BPSS-13	100%	3	10xOMEGA	yes	2/3	99.8927
BPSS-14	100%	3	10xOMEGA	no	2/3	99.9976
BPSS-15	100%	3	100xOMEGA	yes	2/3	98.8182
BPSS-16	100%	3	100xOMEGA	no	2/3	98.2574
BPSS-17	ices: 100%, alb.: 35%	3	no	yes	2/3	99.9811
BPSS-18	ices: 100%, alb.: 35%	3	no	no	2/3	98.9855

A. Synthetic Data

1) Description: Several synthetic data sets have been generated by mixing a known number of endmembers, with abundances simulated with uniform distribution. The generated data sets are of size 200 $\times$ 500 pixels, which is a spatial size similar to the one of a typical hyperspectral image. For the endmembers, the following spectra have been used: H_2O and CO_2 ice spectra [38], [39] and mineral spectra from the U.S. Geological Survey Digital Spectral Library splib06a [40], resampled to match the 128 wavelengths of OMEGA C Channel [41]. To ensure the sum-to-one constraint on the R endmember abundances, a uniform distribution on the simplex has been used following a well-established scheme [42]. Synthetic data sets have been generated with three, five, and ten endmembers. Based on this method, data sets for which the maximum abundance of each single endmember was limited to certain values (100%, 80%, and 60%) have also been considered. These latter data, which are called "cutoff" in the sequel, allow one to test the method efficiency face to various conditions in terms of purity of the samples (in cases where pure—to a certain degree—components occur in the data set or not). In addition, a three-component asymmetric data set has been investigated, with one of the component abundances (albite) being limited to a cutoff of 35% and the abundances of the two others (ices) not being limited. In addition, data sets with some added OMEGA-like Gaussian noise, amplified or not, have also been generated and investigated. The noise estimation on the dark currents of the OMEGA instruments for observation 41_1 has been used [39]. Note that, for all the considered simulation scenarios, the number of sources to be estimated has been tuned to the actual number of endmembers used to produce the artificial data set.

2) Performance: Computation times are about 50 times shorter when pixel selection by convex hull (CHO) is performed as a preprocessing step (see Table II).

3) Accuracy:

a) Analysis of the results: The spectrum of each estimated source has been compared to the spectra from the spectral library containing the pure endmembers used to produce the synthetic data set. The absolute value of the correlation has been used as a similarity measurement (thus as a criterion for the determination of the best spectral match). In Fig. 1, each source is represented along with its best match, according to the aforementioned criterion. Table III (resp. Table IV) shows the results for BPSS (resp. BPSS2).

A source is considered a good estimation of a certain endmember if both spectrally match each other best and if their absolute correlation is greater than 80%. For each run, the number of well-estimated sources is mentioned in Tables III and IV. Note that endmembers matched by several sources, in case it happens, are only counted once. Along with the number of well-estimated sources, the mean value of the correlations between (only) the well-estimated sources and their best spectral match also helps for the assessment of the accuracy for the estimation of the whole set of sources for each run. Simple distance could not be used here because the scale in usual blind source separation is undetermined [8].

b) BPSS versus BPSS2: In most of the tested cases, the quality of estimation is unambiguously better with BPSS2 than that with BPSS (see Tables III and IV). The improvement appears to be even more significant when the number of endmembers is increasing. Our three-endmember test data set is a mixture of two endmembers with strong spectral signatures (CO_2 and H_2O ices) and a third one with weaker signatures (albite), as often with minerals. Interestingly, while using BPSS allows one to correctly estimate the ice spectra but not albite, BPSS2 is actually able to correctly estimate the three endmembers. This confirms that adding the sum-to-one constraint is necessary when dealing with such a data set, which is important regarding the analysis of other data set.

c) Effect of the pixel selection (CHO): With the exception of the asymmetric data set (see in the following), the endmembers are less well estimated when a pixel selection has been performed, with the loss appearing to be less significant when the number of endmembers is low.

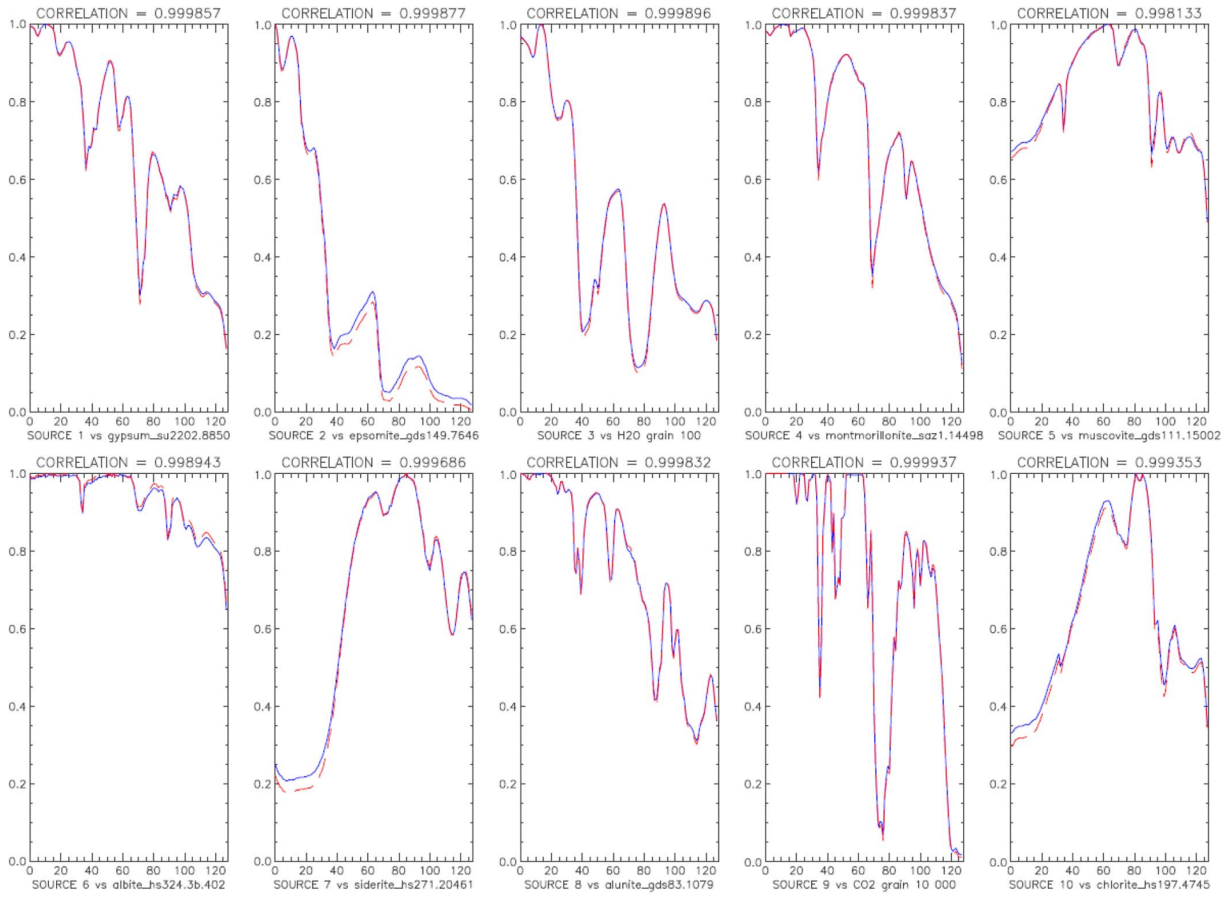


Fig. 1. (Blue lines) Sources estimated by BPSS2 and (red dotted lines) their spectral matches for an artificial data set with ten endmembers (no cutoff, no noise).

TABLE IV
RESULTS OBTAINED FOR DIFFERENT SYNTHETIC DATA SET WITH THE BPSS2 ALGORITHM. THE CHARACTERISTICS OF EACH DATA SET ARE SHOWN: NUMBER OF ENDMEMBERS, CUTOFF, AND NOISE. EACH DATA SET HAS BEEN ANALYZED WITH A NUMBER OF SOURCES TO BE ESTIMATED EQUAL TO THE NUMBER OF ENDMEMBERS USED TO GENERATE THE ARTIFICIAL DATA SET, WITH AND WITHOUT PIXEL SELECTION. THE QUALITY OF THE ESTIMATION IS EXPRESSED THROUGH THE NUMBER OF WELL-ESTIMATED SOURCES AND THE MEAN ABSOLUTE EXPRESSION, AS EXPLAINED IN THE TEXT

Run Id	Cutoff (%)	Nb of endmembers	Noise	Pixel selection	Nb of well estimated sources	Mean correlation (%)
BPSS2-1	100%	3	no	yes	3/3	99.8923
BPSS2-2	100%	3	no	no	**3**/3	99.9222
BPSS2-3	80%	3	no	yes	2/3	95.8934
BPSS2-4	80%	3	no	no	**3**/3	99.9200
BPSS2-5	60%	3	no	yes	2/3	95.2965
BPSS2-6	60%	3	no	no	3/3	97.5408
BPSS2-7	100%	5	no	yes	3/5	99.2821
BPSS2-8	100%	5	no	no	**5**/5	99.9174
BPSS2-9	100%	10	no	yes	5/10	98.9439
BPSS2-10	100%	10	no	no	10/10	99.9535
BPSS2-11	100%	3	OMEGA	yes	3/3	99.8726
BPSS2-12	100%	3	OMEGA	no	3/3	99.9955
BPSS2-13	100%	3	10xOMEGA	yes	3/3	99.7298
BPSS2-14	100%	3	10xOMEGA	no	3/3	99.9962
BPSS2-15	100%	3	100xOMEGA	yes	2/3	95.4706
BPSS2-16	100%	3	100xOMEGA	no	3/3	98.5647
BPSS2-17	ices: 100%, alb.: 35%	3	no	yes	3/3	95.9402
BPSS2-18	ices: 100%, alb.: 35%	3	no	no	2/3	99.7202

Also note that the results with pixel selection do not appear to be very sensitive to the cutoff variations: The loss of quality (between runs performed with and without pixel selection) is similar for cutoffs of 60%, 80%, and 100%, which can be explained by the pixel selection's ability to extract the purest available pixels.

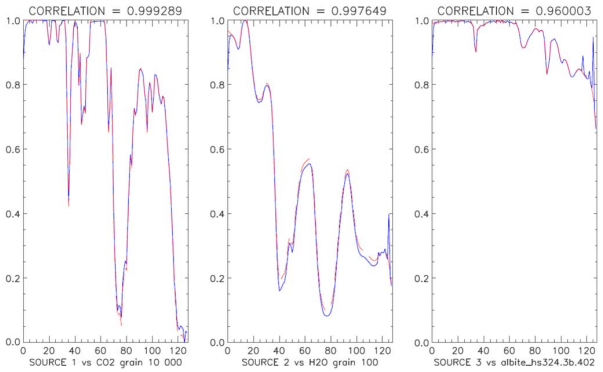


Fig. 2. (Blue lines) Sources estimated by BPSS2 and (red dotted lines) their spectral matches for an artificial data set with three endmembers and 100-times amplified OMEGA-like noise (no cutoff).

d) Effect of the number of endmembers: Due to the curse of dimensionality, the higher the number of endmembers to be estimated with a fixed number of wavelengths, the more difficult the estimation becomes [43], [44]. Still, BPSS2 gives excellent results even for ten sources, as all spectra are estimated with a correlation coefficient higher than 99% (see Fig. 1).

e) Effect of the maximum abundance cutoff: The cutoff affects the quality of estimation, which is clearly better, for BPSS and BPSS2, when pure components occur in the data set. This has to be remembered when dealing with real data sets.

f) Effect of noise: The results clearly show that the method is very robust to noise, as the estimation of the sources does not appear to be significantly affected by the addition of a Gaussian OMEGA-like noise to the synthetic data set. BPSS2 (without pixel selection) even manages to successfully overcome the addition of a 100-times amplified OMEGA-like noise (see Table II and Fig. 2).

g) Effect of asymmetry in maximum abundance cutoff: In this case, the results are better with pixel selection rather than without. BPSS2 with pixel selection is the only run (performed on this synthetic data set) that allows one to successfully estimate the three endmembers that have been used to generate the data set, including albite, whose abundances have been limited to a cutoff of 35% and whose spectral signature is weaker than the ones of the other endmembers (ices). This result can be explained by the fact that pixel selection is able to extract the pixels with the strongest available albite signature, and consequently overcomes the blinding effect of the ices occurring in the whole data set, which has affected the results when no pixel selection has been performed.

B. OMEGA Data

1) Presentation: The OMEGA instrument is a spectrometer onboard Mars Express (European Space Agency), which provides hyperspectral images of the Mars surface, with a spatial resolution from 300 m to 4 km, 96 channels in the visible range, and 256 wavelength channels in the near infrared [45]. In this paper, 184 spectral bands have been selected according to the best signal-to-noise ratio. Conversely, spectral bands that contain thermal emission have been removed.

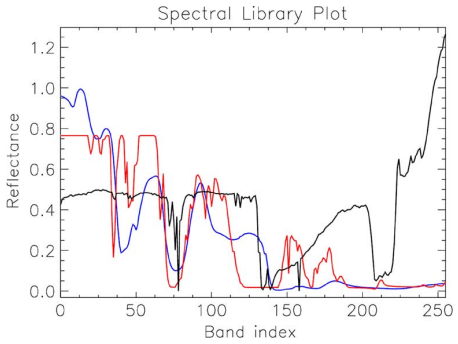


Fig. 3. Reference spectra of the OMEGA hyperspectral image 41_1: (i) in blue: synthetic H_2O ice with a grain size of 100 μm, (ii) in red: synthetic CO_2 ice with a grain size of 10 cms, and (iii) in black: OMEGA typical dust materials with atmosphere absorption.

TABLE V
COMPUTATION TIMES IN SECONDS, FOR THE OMEGA 41_1 IMAGE WITH THREE ENDMEMBERS, FOR BOTH BPSS AND BPSS2, WITH AND WITHOUT CHO. IN THIS EXAMPLE, 670 PIXELS HAVE BEEN SELECTED WITH THE CHO, AMONG A TOTAL OF 111 488. THE NAME OF THE RUN OF TABLE VI IS NOTED IN PARENTHESES

Algorithm	Without CHO	With CHO	Time ratio
BPSS	166 400 (OMEGA-5)	1 468 (OMEGA-7)	113.28
BPSS2	332 680 (OMEGA-6)	3 176 (OMEGA-8)	104.71

TABLE VI
RESULTS ON ALGORITHMS BPSS AND BPSS2 ON A PORTION OF THE OMEGA IMAGE (41_1.CUT) AND ON THE ENTIRE IMAGE (41_1). FOR 41_1.CUT, THE PROPORTION OF PIXELS WITH DETECTED CO_2 IS 48.72%, AND IT IS 63.48% FOR H_2O [39]. FOR 41_1, THE PROPORTIONS OF PIXELS FOR CO_2 AND H_2O ARE 16.76% AND 21.84%, RESPECTIVELY. THE COLUMNS H_2O, CO_2, AND DUST INDICATE THE CORRELATIONS COEFFICIENT BETWEEN THE ESTIMATED SOURCES AND THE REFERENCE SPECTRA. (−) INDICATES NO IDENTIFICATION OF H_2O NEITHER FROM SPECTRAL NOR SPATIAL RESULTS. THIS SOURCE HAS BEEN DETECTED TO BE CO_2 ICE (CORRELATION OF 0.911)

Run Id	Image	Algo	pixel selection	H_2O	CO_2	dust
OMEGA-1	41_1.CUT	BPSS	no	0.883	0.955	0.542
OMEGA-2	41_1.CUT	BPSS2	no	0.823	0.958	0.980
OMEGA-3	41_1.CUT	BPSS	yes	0.956	0.951	0.766
OMEGA-4	41_1.CUT	BPSS2	yes	0.894	0.910	0.975
OMEGA-5	41_1	BPSS	no	0.773	0.957	0.555
OMEGA-6	41_1	BPSS2	no	-	0.953	0.512
OMEGA-7	41_1	BPSS	yes	0.940	0.953	0.372
OMEGA-8	41_1	BPSS2	yes	0.450	0.954	0.982

Blind source separation on this data set has been initiated by using the JADE algorithm [46]. In particular, the 41_1 image of the permanent south polar region has been used for the supervised classification approach with WAVANGLET [39], unsupervised classification approach [47], and unsupervised blind source separation using BPSS [25]. Since no ground truth is available, the results from physical nonlinear inversion have been considered as a reference [39], [48], [49]. In this image, the surface is dominated by dust, and some spectra contain CO_2 and water ices (see Fig. 3). This reference data set for hyperspectral classification is available online.[1] The Luo *et al.* method introduced in [30] has estimated two sources

[1] http://sites.google.com/site/fredericschmidtplanets/Home/hyperspectral-reference

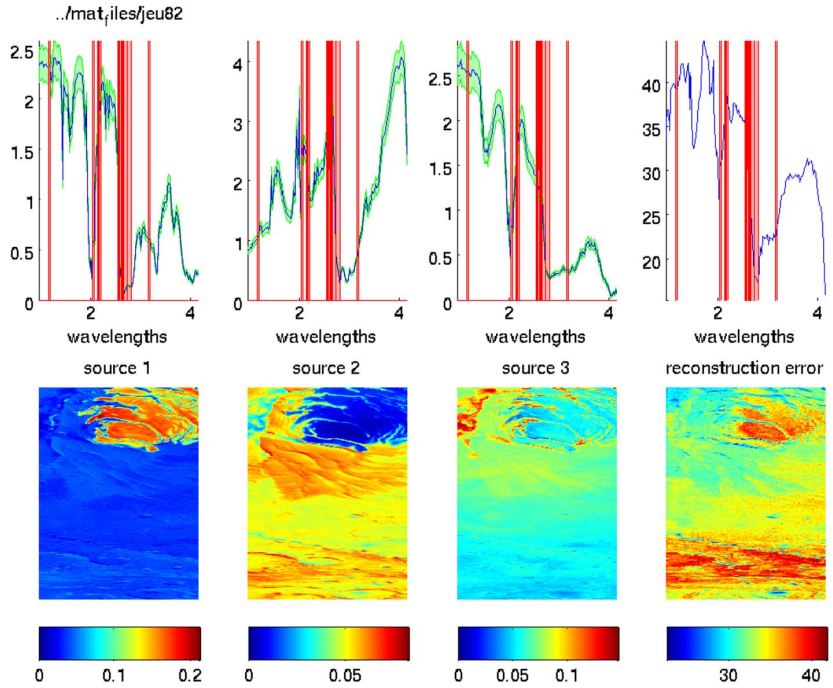


Fig. 4. Estimation of three sources of the entire OMEGA image 41_1 with BPSS using a preprocessing step of pixel selection employing the convex hull method. The first and third sources are clearly identified as CO_2 and H_2O ices (see Fig. 3) with correlation coefficients of 0.953 and 0.940, respectively (see run OMEGA-7 of Table VI). The spatial abundances are well estimated regarding the WAVANGLET classification method [39], [25]. The second source is identified as dust with a lower correlation coefficient (0.372).

for both 41_1 and 41_1.CUT images. From previous work using band ratio detection [41], physical inversion of the radiative transfer [48], [49], supervised classification approach using WAVANGLET [39], and unsupervised classification [47], three endmembers have been detected: dust, CO_2, and water ice. The number of sources has been tuned to three in our study.

The proportions of pixels containing CO_2 and H_2O ices on the 41_1 image are estimated to be 16.76% and 21.84%, respectively [39]. The first 300 lines of the 41_1 image (subset named 41_1.CUT) contain all spectra having ices. For this subset, the proportions of pixels with detected CO_2 and H_2O are 48.72% and 63.48%, respectively.

2) Performance: Computation times are about 100 times shorter when pixel selection by convex hull (CHO) has been performed as a preprocessing step (see Table V).

3) Accuracy: Table VI reports the results from different tests; each run is defined by a number. To estimate the quality of estimation, the correlation between the reference spectra and the estimated sources has been computed. The attribution of each source has been done *ad hoc* using both spectral source and spatial abundances.

a) Asymmetric abundances of the sources: The quality of estimation with both BPSS and BPSS2 is significantly lower for data set 41_1 (runs OMEGA-5 to OMEGA-8) in comparison with 41_1.CUT (runs OMEGA-1 to OMEGA-4). This result suggests that both BPSS and BPSS2 are less efficient in a case of an asymmetric distribution of the sources.

b) BPSS versus BPSS2: The BPSS algorithm gives significantly better results than the BPSS2 one (for instance, run OMEGA-3 versus OMEGA-4). This is due to nonlinearity in the radiative transfer and noise in the data set in contradiction with the full additivity constraint.

c) Effect of pixel selection: When convex hull selection has been used as a preprocessing step to BPSS/BPSS2, the estimation is significantly better (see Fig. 4 for run OMEGA-5 and Fig. 5 for run OMEGA-7). These results show that pixel selection is a way to better take into account the occurrence of rare endmembers and is thus an interesting method to provide better results.

V. Discussion and Conclusion

For the first time, an MCMC-based blind source separation strategy with positivity and sum-to-one constraints has been effectively applied on a complete hyperspectral image with a typical size frequently encountered in earth and planetary science. The optimization of BPSS [17] and BPSS2 [18] presented in this paper consists of two independent parts: 1) *TO* reduces the memory footprint, lowers the average cost of algorithmic operations, and makes smart reuse of memory, and 2) *CHO* reduces the number of spectra to process.

Fig. 6 summarizes the following results in a schematic form.

1) TO, for both BPSS and BPSS2, allows one to decrease the computation times by a factor of 1.5, without altering the accuracy of the results. Memory consumption has also been reduced by a significant factor. With such unambiguous advantages, the TO versions of BPSS and BPSS2 can be rather used than the original implementations.

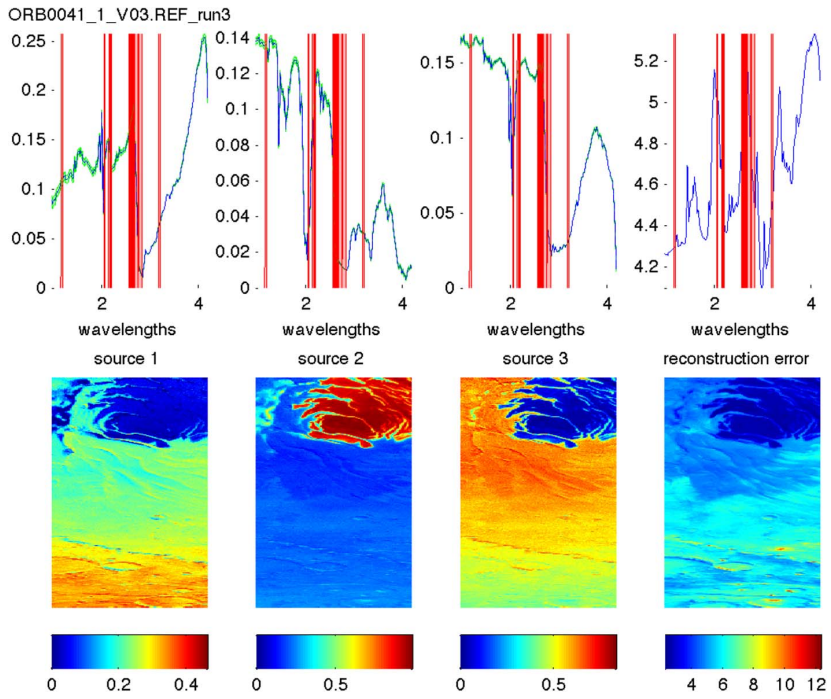


Fig. 5. Estimation of three sources of the entire OMEGA image 41_1 with BPSS without pixel selection. The second source is clearly identified as CO_2 ice (see Fig. 3) with a correlation coefficient of 0.957 (see run OMEGA-5 of Table VI). The first and third sources are identified as dust and water ice with lower correlation coefficients of 0.555 and 0.773, respectively. The spatial abundances of water ice are not well estimated regarding the WAVANGLET classification method [39].

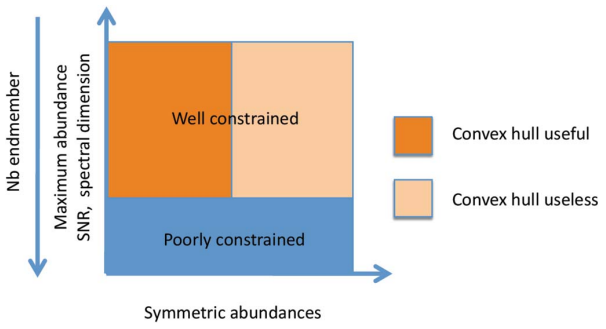


Fig. 6. Schematic of source separation estimation and usefulness of convex hull pixel selection for hyperspectral images.

2) Trivially, the results obtained for linear artificial data set (with uniform abundance distributions identical for each endmember with abundances until 100%) have demonstrated that the sources estimated by the TO strategy are equivalent to that by the CHO strategy (for instance, runs BPSS-1 to BPSS-2 in Table III and runs BPSS2-1 to BPSS2-2 in Table IV). In this case, pixel selection is still relevant to reduce the computation time by about 50 times (Table II).
3) The results obtained for the artificial data set with uniform abundance distributions and identical cutoffs for all endmembers have shown that the estimation of the sources is less accurate when a pixel selection (CHO) has been performed (runs BPSS-3 to BPSS-6 in Table III and runs BPSS2-3 to BPSS2-6 in Table IV). In this case, despite 50-times shorter computation times, using pixel selection as a preprocessing step seems to be inadequate.
4) For OMEGA data, the computation time reduction due to CHO has been around 100 (Table V). Abundance distributions can be significantly imbalanced (some endmembers are significantly less present in the scene). In that case, pixel selection by convex hull (CHO) is a way to overcome the bias caused by the overwhelming endmembers. This has been supported by the results obtained for the synthetic data set of linear mixture using imbalanced uniform distribution.
5) BPSS2 seems to better estimate the sources in the artificial data set but not in the real case. This is probably due to nonlinearity or the non-Gaussian noise effect.
6) The method BPSS2 appears to be very robust to Gaussian noise, as shown by the results obtained on the synthetic data set, even with 100-times actual OMEGA noise.
7) Sometimes, some sources have been well estimated but anticorrelated with the real spectra. This behavior has been interpreted to be due to the linearly dependent endmembers. In that case, spectra built by a linear combination of all sources except the considered source already contain spectral signatures of the considered source. The last source is then anticorrelated with the corresponding endmember to decrease his contribution. This behavior has to be studied in further detail because it is clearly a limitation of blind source separation.

In the future, the choice of the number of sources, which is an input in the current implementation, should be automated to allow one batch processing without human intervention. A methodology of pixel selection for use across data sets should also be established to enable integration of source separation techniques into larger systems and aim at the generation of catalogs and maps.

ACKNOWLEDGMENT

The authors would like to thank J. P. Bibring and the OMEGA Team for providing the OMEGA data set; S. Douté and B. Schmitt for their ice spectral library; the faculty of the European Space Astronomy Centre for the support; the Centre National d'Etudes Spatiales (CNES); the Programme National de Planétologie (CNRS/INSU); and the two anonymous reviewers for their valuable comments and suggestions that enabled significant improvements to this paper.

REFERENCES

[1] D. Tanre, M. Herman, P. Y. Deschamps, and A. de Leffe, "Atmospheric modeling for space measurements of ground reflectances, including bidirectional properties," *Appl. Opt.*, vol. 18, no. 21, pp. 3587–3594, Nov. 1979.

[2] G. Healey and D. Slater, "Models and methods for automated material identification in hyperspectral imagery acquired under unknown illumination and atmospheric conditions," *IEEE Trans. Geosci. Remote Sens.*, vol. 37, no. 6, pp. 2706–2717, Nov. 1999.

[3] N. Keshava and J.-F. Mustard, "Spectral unmixing," *IEEE Signal Process. Mag.*, vol. 19, no. 1, pp. 44–57, Jan. 2002.

[4] J. Scott, *Remote Sensing: The Image Chain Approach*. New York: Oxford Univ. Press, 1997.

[5] C.-I Chang, *Hyperspectral Data Exploitation: Theory and Applications*. New York: Wiley-Interscience, 2007.

[6] P. Comon, C. Jutten, and J. Hérault, "Blind separation of sources, Part II: Problems statement," *Signal Process.*, vol. 24, no. 1, pp. 11–20, Jul. 1991.

[7] A. Cichocki and S.-I. Amari, *Adaptive Blind Signal and Image Processing—Learning Algorithms and Applications*. New York: Wiley-Interscience, 2002.

[8] A. Hyvärinen, J. Karhunen, and E. Oja, *Independent Component Analysis*. New York: Wiley, 2001, ser. Adaptive and Learning Systems for Signal Processing, Communications, and Control.

[9] P. Paatero and U. Tapper, "Positive matrix factorization: A non-negative factor model with optimal utilization of error estimates of data values," *Environmetrics*, vol. 5, no. 2, pp. 111–126, Jun. 1994.

[10] D. D. Lee and H. S. Seung, "Learning the parts of objects by non-negative factorization," *Nature*, vol. 401, no. 6755, pp. 788–791, Oct. 1999.

[11] M. W. Berry, A. N. Langville, V. P. Pauca, and R. J. Plemmons, "Algorithms and applications for approximate nonnegative matrix factorization," *Comput. Stat. Data Anal.*, vol. 52, no. 1, pp. 155–173, Sep. 2007.

[12] M. Berman, H. Kiiveri, R. Lagerstrom, A. Ernst, R. Dunne, and J. F. Huntington, "ICE: A statistical approach to identifying endmembers in hyperspectral images," *IEEE Trans. Geosci. Remote Sens.*, vol. 42, no. 10, pp. 2085–2095, Oct. 2004.

[13] J. M. P. Nascimento and J. M. Bioucas-Dias, "Hyperspectral unmixing algorithm via dependent component analysis," in *Proc. IEEE IGARSS*, Jul. 2007, pp. 4033–4036.

[14] S. Jia and Y. Qian, "Spectral and spatial complexity-based hyperspectral unmixing," *IEEE Trans. Geosci. Remote Sens.*, vol. 45, no. 12, pp. 3867–3879, Dec. 2007.

[15] L. Miao and H. Qi, "Endmember extraction from highly mixed data using minimum volume constrained nonnegative matrix factorization," *IEEE Trans. Geosci. Remote Sens.*, vol. 45, no. 3, pp. 765–777, Mar. 2007.

[16] S. Jia and Y. Qian, "Constrained nonnegative matrix factorization for hyperspectral unmixing," *IEEE Trans. Geosci. Remote Sens.*, vol. 47, no. 1, pp. 161–173, Jan. 2009.

[17] S. Moussaoui, D. Brie, A. Mohammad-Djafari, and C. Carteret, "Separation of non-negative mixture of non-negative sources using a Bayesian approach and MCMC sampling," *IEEE Trans. Signal Process.*, vol. 54, no. 11, pp. 4133–4145, Nov. 2006.

[18] N. Dobigeon, S. Moussaoui, J.-Y. Tourneret, and C. Carteret, "Bayesian separation of spectral sources under non-negativity and full additivity constraints," *Signal Process.*, vol. 89, no. 12, pp. 2657–2669, Dec. 2009.

[19] W. Gilks, S. Richardson, and D. Spiegehalter, *Markov Chain Monte Carlo in Practice*. London, U.K.: Chapman & Hall, 1999.

[20] A. E. Gelfand and A. F. M. Smith, "Sampling based approaches to calculating marginal densities," *J. Amer. Stat. Assoc.*, vol. 85, no. 410, pp. 398–409, Jun. 1990.

[21] N. Bali and A. Mohammad-Djafari, "Bayesian approach with hidden Markov modeling and mean field approximation for hyperspectral data analysis," *IEEE Trans. Image Process.*, vol. 17, no. 2, pp. 217–225, Feb. 2008.

[22] M. Naceur, M. Loghmari, and M. Boussema, "The contribution of the sources separation method in the decomposition of mixed pixels," *IEEE Trans. Geosci. Remote Sens.*, vol. 42, no. 11, pp. 2642–2653, Nov. 2004.

[23] J. Nascimento and J. Dias, "Does independent component analysis play a role in unmixing hyperspectral data?" *IEEE Trans. Geosci. Remote Sens.*, vol. 43, no. 1, pp. 175–187, Jan. 2005.

[24] J. Wang and C.-I Chang, "Applications of independent component analysis in endmember extraction and abundance quantification for hyperspectral imagery," *IEEE Trans. Geosci. Remote Sens.*, vol. 44, no. 9, pp. 2601–2616, Sep. 2006.

[25] S. Moussaoui, H. Hauksdottir, F. Schmidt, C. Jutten, J. Chanussot, D. Brie, S. Douté, and J. Benediktsson, "On the decomposition of Mars hyperspectral data by ICA and Bayesian positive source separation," *Neurocomputing*, vol. 71, no. 10–12, pp. 2194–2208, Jun. 2008.

[26] J.-F. Cardoso and A. Souloumiac, "Blind beamforming for non Gaussian signals," *Proc. Inst. Elect. Eng.—F*, vol. 140, no. 6, pp. 362–370, Dec. 1993.

[27] A. Hyvarinen and E. Oja, "A fast fixed-point algorithm for independent component analysis," *Neural Comput.*, vol. 9, no. 7, pp. 1483–1492, Oct. 1997.

[28] C.-I Chang and Q. Du, "Estimation of number of spectrally distinct signal sources in hyperspectral imagery," *IEEE Trans. Geosci. Remote Sens.*, vol. 42, no. 3, pp. 608–619, Mar. 2004.

[29] J. M. Bioucas-Dias and J. M. P. Nascimento, "Hyperspectral subspace identification," *IEEE Trans. Geosci. Remote Sens.*, vol. 46, no. 8, pp. 2435–2445, Aug. 2008.

[30] B. Luo and J. Chanussot, "Unsupervised classification of hyperspectral images by using linear unmixing algorithm," in *Proc. IEEE ICIP*, Cairo, Egypt, 2009, pp. 2877–2880.

[31] C. B. Barber, D. Dobkin, and H. Huhdanpaa, "The quickhull algorithm for convex hulls," *ACM Trans. Math. Softw.*, vol. 22, no. 4, pp. 469–483, Dec. 1996.

[32] J. W. Boardman, "Analysis, understanding, and visualization of hyperspectral data as convex sets in n-space," *Proc. SPIE*, vol. 2480, pp. 14–22, 1995.

[33] C.-I Chang, C.-C. Wu, W.-M. Liu, and Y.-C. Ouyang, "A new growing method for simplex-based endmember extraction algorithm," *IEEE Trans. Geosci. Remote Sens.*, vol. 44, no. 10, pp. 2804–2819, Oct. 2006.

[34] J. Nascimento and J. Dias, "Vertex component analysis: A fast algorithm to unmix hyperspectral data," *IEEE Trans. Geosci. Remote Sens.*, vol. 43, no. 4, pp. 898–910, Apr. 2005.

[35] A. Ifarraguerri and C.-I Chang, "Multispectral and hyperspectral image analysis with convex cones," *IEEE Trans. Geosci. Remote Sens.*, vol. 37, no. 2, pp. 756–770, Mar. 1999.

[36] A. Plaza, P. Martinez, R. Perez, and J. Plaza, "A quantitative and comparative analysis of endmember extraction algorithms from hyperspectral data," *IEEE Trans. Geosci. Remote Sens.*, vol. 42, no. 3, pp. 650–663, Mar. 2004.

[37] M. Craig, "Minimum-volume transforms for remotely sensed data," *IEEE Trans. Geosci. Remote Sens.*, vol. 32, no. 3, pp. 542–552, May 1994.

[38] S. Douté and B. Schmitt, "A multilayer bidirectional reflectance model for the analysis of planetary surface hyperspectral images at visible and near-infrared wavelengths," *J. Geophys. Res.*, vol. 103, no. 12, pp. 31 367–31 390, Dec. 1998.

[39] F. Schmidt, S. Douté, and B. Schmitt, "WAVANGLET: An efficient supervised classifier for hyperspectral images," *IEEE Trans. Geosci. Remote Sens.*, vol. 45, no. 5, pp. 1374–1385, May 2007.

[40] R. N. Clark, G. A. Swayze, R. Wise, E. Livo, T. Hoefen, R. Kokaly, and S. J. Sutley, USGS Digital Spectral Library splib06a, U.S. Geological Survey, Reston, VA, 2007, [Online]. Available: http://speclab.cr.usgs.gov

[41] J.-P. Bibring, Y. Langevin, F. Poulet, A. Gendrin, B. Gondet, M. Berthé, A. Soufflot, P. Drossart, M. Combes, G. Bellucci, V. Moroz, N. Mangold, and B. Schmitt, "Perennial water ice identified in the south polar cap of Mars," *Nature*, vol. 428, no. 6983, pp. 627–630, Apr. 2004.

[42] S. Onn and I. Weissman, "Generating uniform random vectors over a simplex with implications to the volume of a certain polytope and to multivariate extremes," *Ann. Oper. Res.*, pp. 1–12, 2009. DOI: 10.1007/s10479-009-0567-7.
[43] G. Hughes, "On the mean accuracy of statistical pattern recognizers," *IEEE Trans. Inf. Theory*, vol. IT-14, no. 1, pp. 55–63, Jan. 1968.
[44] C. Lee and D. Landgrebe, "Analyzing high-dimensional multispectral data," *IEEE Trans. Geosci. Remote Sens.*, vol. 31, no. 4, pp. 792–800, Jul. 1993.
[45] J.-P. Bibring, A. Soufflot, M. Berthé, Y. Langevin, B. Gondet, P. Drossart, M. Bouyé, M. Combes, P. Puget, A. Semery, G. Bellucci, V. Formisano, V. Moroz, V. Kottsov, G. Bonello, S. Erard, O. Forni, A. Gendrin, N. Manaud, F. Poulet, G. Poulleau, T. Encrenaz, T. Fouchet, R. Melchiori, F. Altieri, N. Ignatiev, D. Titov, L. Zasova, A. Coradini, F. Capacionni, P. Cerroni, S. Fonti, N. Mangold, P. Pinet, B. Schmitt, C. Sotin, E. Hauber, H. Hoffmann, R. Jaumann, U. Keller, R. Arvidson, J. Mustard, and F. Forget, "OMEGA: Observatoire pour la Minéralogie, l'Eau, les Glaces et l'Activité," in *Mars Express: The Scientific Payload*. Noordwijk, The Netherlands: ESA Publications Division, Aug. 2004, pp. 37–49, ESA SP-1240.
[46] O. Forni, F. Poulet, J.-P. Bibring, S. Erard, C. Gomez, Y. Langevin, and B. Gondet, "Component separation of OMEGA spectra with ICA," in *Proc. 36th Annu. Lunar Planet. Sci. Conf.*, pp. 1623, S. Mackwell and E. Stansbery, Eds., Mar. 2005.
[47] L. Galluccio, O. J. J. Michel, P. Comon, E. Slezak, and A. O. Hero, "Initialization free graph based clustering," *IEEE Trans. Pattern Anal. Mach. Intell.*, 2009, submitted for publication.
[48] S. Douté, B. Schmitt, Y. Langevin, J.-P. Bibring, F. Altieri, G. Bellucci, B. Gondet, and F. Poulet, "South Pole of Mars: Nature and composition of the icy terrains from Mars Express OMEGA observations," *Planet. Space Sci.*, vol. 55, no. 1/2, pp. 113–133, Jan. 2007.
[49] C. Bernard-Michel, S. Douté, M. Fauvel, L. Gardes, and S. Girard, "Retrieval of mars surface physical properties from OMEGA hyperspectral images using regularized sliced inverse regression," *J. Geophys. Res.*, vol. 114, no. E6, p. E06 005, Jun. 2009.



Frédéric Schmidt received the Ph.D. degree from the Laboratoire de Planétologie de Grenoble (Centre National de la Recherche Scientifique (CNRS)–Université Joseph-Fourrier), Grenoble, France, in 2007.

He spent two years at the European Space Astronomy Centre, European Space Agency (ESA), Madrid, Spain, as a Postdoctoral Fellow. Since 2009, he has been an Assistant Professor with the Laboratoire Intéractions et Dynamique des Environnements de Surface, University Paris-Sud, Orsay, France, and is also with the Centre National de la Recherche Scientifique. He is a Coinvestigator of the OMEGA imaging spectrometer onboard Mars Express (ESA). His research interests are in analysis of hyperspectral data, ices, and polar processes on planet Mars.



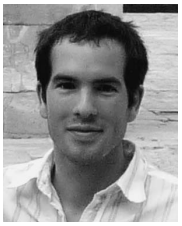
Albrecht Schmidt received the Ph.D. degree from the University of Amsterdam, Amsterdam, The Netherlands, in 2002.

After working for three years at the University of Aalborg, Aalborg, Denmark, he joined the European Space Astronomy Centre, European Space Agency, Madrid, Spain, where he is currently a Computer Scientist with the Solar System Operations Division. His research interests are in data management and data analysis.



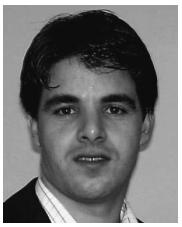
Erwan Tréguier received the Engineer degree from the École Nationale Supérieure d'Ingénieurs en Constructions Aéronautiques (currently part of the Institut Supérieur de l'Aéronautique et de l'Espace), Toulouse, France, in 2001 and the Ph.D degree from Université Paul Sabatier, Toulouse, in 2008, after defending his thesis in the Centre d'Étude Spatiale des Rayonnements.

He is currently holding a postdoctoral position at the European Space Astronomy Centre, European Space Agency, Madrid, Spain. His main field of research is planetary science. His research interests include the composition of the Martian surface (from both *in situ* and orbital data), geochemical modeling of alteration, and investigation of multidimensional data sets through statistical approaches.



Maël Guiheneuf received the M.S. degree in signal processing from the École Centrale de Nantes, Nantes, France, in 2009.

He was a Student Fellow with the European Space Astronomy Centre, European Space Agency, Madrid, Spain, for six months in 2009 on the following subject: "Optimization strategies for hyperspectral unmixing using Bayesian source separation."



Saïd Moussaoui received the State Engineering degree from the École Nationale Polytechnique, Algiers, Algeria, in 2001 and the Ph.D. degree in automatic control and signal processing from Université Henri Poincaré, Nancy, France, in 2005.

He is currently an Associate Professor with the École Centrale de Nantes, Nantes, France, and since September 2006, he has been with the Institut de Recherche en Communication et Cybernétique de Nantes (IRCCyN), UMR CNRS 6597. His research interests are in statistical signal and image processing, including source separation, Bayesian estimation, and their applications.



Nicolas Dobigeon (S'05–M'08) was born in Angoulême, France, in 1981. He received the Engineering degree in electrical engineering from the Ecole Nationale Supérieure d'Electrotechnique, d'Electronique, d'Hydraulique et d'Informatique, et des Télécommunications, Toulouse, France, in 2004, and the M.Sc. and Ph.D. degrees in signal processing from the National Polytechnic Institute of Toulouse, Toulouse, in 2004 and 2007, respectively.

From 2007 to 2008, he was a Postdoctoral Research Associate with the Department of Electrical Engineering and Computer Science, University of Michigan, Ann Arbor. Since 2008, he has been an Assistant Professor with the National Polytechnic Institute of Toulouse (ENSEEIHT, University of Toulouse), within the Signal and Communication Group of the IRIT Laboratory. His research interests are focused on statistical signal and image processing, with particular interest in Bayesian inference and Markov chain Monte Carlo methods.

1.4.3 LinMin

Cette section contient l'article suivant :

Schmidt, F. ; Legendre, M., and Le Mouelic, S., Minerals detection for hyperspectral images, LinMin, submitted to ICARUS 2013.

Minerals detection for hyperspectral images using adapted linear unmixing : LinMin

Schmidt Frédéric[1,2], Maxime Legendre[3], Stéphane Le Mouëlic[4]

[1] *Univ Paris-Sud, Laboratoire IDES, UMR8148, Orsay, F-91405; (frederic.schmidt@u-psud.fr)* [2] *CNRS, Orsay, F-91405.Université Paris Sud* [3] *IRCCyN (CNRS UMR 6597), Ecole Centrale Nantes, France,* [4] *LPGN, CNRS UMR 6112, Université de Nantes, France*

Abstract

Minerals detection over large volume of spectra is the challenge addressed by current hyperspectral imaging spectrometer in Planetary Science. Instruments such OMEGA (Mars Express), CRISM (Mars Reconnaissance Orbiter), M^3 (Chandrayaan-1), VIRTIS (Rosetta) and many more, have been producing very large datasets since one decade. We propose here a fast supervised detection algorithm called LinMin, in the framework of linear unmixing, with innovative arrangement in order to treat non-linear cases due to radiative transfer in both atmosphere and surface. We use reference laboratory and synthetic spectral library. Additional spectra are used in order to mimic the effect of Martian aerosols, grain size, and observation geometry discrepancies between reference and observed spectra. The proposed algorithm estimates the uncertainty on "mixing coefficient" from the uncertainty of observed spectra. Both numerical and observational tests validate the approach. Fast parallel implementation of the best algorithm (IPLS) on Graphics Processing Units (GPU) allows to significantly reduce the computation cost by a factor of ˜40.

Key words: spectroscopy, hyperspectral, supervised detection, linear unmixing under constraint, sum to one, positivity, GPU, LinMin

1. Introduction

Various methods have been proposed to detect surface chemical species (minerals, ice) on large dataset of hyperspectral images. Supervised methods (knowing the spectra of the chemical species you want to detect) are widely used, for instance : band ratio techniques (Poulet et al., 2007; Ehlmann et al., 2011; Carter et al., 2013), linear unmixing (Combe et al., 2008; Themelis et al., 2012b), wavelet based detection (Schmidt et al., 2007; Gendrin et al., 2006), correlation based detection - Spectral Angle Mapper (Kruse et al., 1993). Other linear non-supervised techniques (estimating the spectra directly from the scene) have been proposed, using Independent Component Analysis ICA (Forni et al., 2005; Erard et al., 2009) or Bayesian methods under constrained (Moussaoui et al.,

2008; Schmidt et al., 2010). Also some algorithms only extract the endmember spectra such: Pixel Purity Index (Boardman et al., 1995), N-FINDR (Winter, 1999), or graph-based segmentation (Gilmore et al., 2011) .

The linear mixture is still valid in non-linear intimate mixture, but with significant difference between retrieved "mixing coefficient" and actual abundance (Mustard and Pieters, 1989; Mustard et al., 1998). Nevertheless, linear unmixing is satisfactory for mineral detection (Combe et al., 2008; Themelis et al., 2012b). It has the significant advantage to deal with complex mixture of a large variety of candidate minerals (see fig. 2), whereas band ratio methods fails, due to the lack of defined reference "continuum" wavelength channel. In such situation each wavelength may sample an absorption band of a particular mineral and no reference wavelength can be found. If band ratio's are adapted to detect minerals over flat spectra, methods using the entire wavelength channels (such linear unmixing) are adapted to detect minerals over a complex variety of background. Specifically, we draw attention that the band ratio's of the CRISM summary products are only relevant in case of a pure mineral detection but may be irrelevant in case of a mixture.

Linear unmixing is relatively simple enough to provide a fast implementation. Furthermore supervised linear unmixing has the advantage that its interpretation is directly and automatically provided in terms of mineralogical class on the bulk hyperspectral image. Dimensionality reduction methods, such unsupervised algorithms or endmember extractions are not required in linear unmixing. Also linear unmixing does not require manual interpretation and identification of spectra.

Previous linear unmixing algorithms have proposed to optimize the reference spectral library in order to solve positivity (Combe et al., 2008), forcing for sum-to-one constraints on the mixing coefficients (Roberts et al., 1998). Roberts et al., 1998 discusses the benefits of constraining the number of endmembers from the spectral library. They have shown that the solutions with a mixture of two endmembers have less overlap that three endmembers mixtures, probably due to the dimension space. In our article, we focus on the interest of both positivity and sum-to-one constraints, that allow to estimate the optimum of all possibility of mixtures. Without positivity and sum-to-one constraints, singularities may arise due "linear dependance" of endmember spectra (Roberts et al., 1998; Dalton et al., 2013). We show that most recent algorithms, including both positivity and sum-to-one constraints, handle this difficulty, thus simplifying tremendously the treatment.

Our aim is to show that additional spectra (flat, slope) minimize the differences between reference laboratory spectra and actually observed spectra, by reducing the effect of grain size and continuum level (photometry, surface roughness, compaction). Some differences between observations and reference endmembers may still be present due to variations in composition, texture,... The selection of the reference spectra database requires always special care and depends on the scientific questions addressed, but at least this database is explicitly known.

Once detection has been performed, time consuming inversions must be

applied in order to retrieve quantitative estimate of surface properties (exact mineralogy, abundances, grain size, porosity, ...) as proposed by different techniques such MGM (Sunshine and Pieters, 1993; Kanner et al., 2007) or radiative transfer inversion (Douté et al., 2007; Poulet et al., 2009a). Also the particular mineral type, for instance Al/Fe or Mg/Fe phyllosilicate, must be addressed by additional work using specific spectral library.

We propose here to extend the linear supervised detection technique using a new set of constraint (positivity and sum to unity) and a new set of additional spectra in order to improve the "mixing coefficient" estimation. We also introduce a new renormalization with the goal to fit the signal, even in the case of very low signal to noise ratio.

We propose to call LinMin our strategy of using:

1. linear unmixing technique under constraints (positivity, sum to unity/sum lower than unity)
2. additional spectra made of flat and slope (also possibly cosine functions)
3. renormalization by the variance/covariance noise matrix
4. estimation of the error on the "mixing coefficient

In order to validate the LinMin approach, we test the detection limits on synthetic data simulating a regolith mixture, the grain size effect and the Martian aerosols effect. We also validate the method on actual hyperspectral dataset of OMEGA, CRISM and M^3. Quantitative estimate of the detection limits are computed.

2. Method

2.1. Linear unmixing

The linear mixing model of hyperspectral reflectance is usually written as:

$$X = A.S + E \tag{1}$$

with the collection of observed spectra X ($M \times N_\lambda$ matrix), the reference spectra S ($N \times N_\lambda$ matrix), the unknown mixing coefficients A ($M \times N$ matrix) and the additive noise error E ($M \times N_\lambda$ matrix), assumed to be gaussian with zero mean. N_λ is the number of wavelength, N the number of reference spectra, M the number of observed spectra.

The unmixing problem then consists in the estimation of the mixing coefficients A that minimize the error E. Considering the least squares error minimization, it is written:

$$\min_{A \in \Re^{M \times N}} F(A) \quad \text{with} \quad F(A) = \sum_{m=1}^{M} \sum_{\lambda=1}^{N_\lambda} (X_{m\lambda} - (A.S)_{m\lambda})^2 \tag{2}$$

The unconstrained solution $A = X.S^T.\left(S.S^T\right)^{-1}$ has been used the in previous detection methods (Boardman et al., 1995; Combe et al., 2008) but the retrieved mixing coefficient A may be negative. One solution is to test all combination of reference spectra S in order to keep only positive case (Roberts et al., 1998; Combe et al., 2008), but the computation cost is very high.

2.2. Linear unmixing under constraint

The previous formulation is not sufficient to describe physical constraints on the mixing coefficients. Indeed, the mixing coefficients must satisfy non-negativity :

$$\forall m \in \{1, \ldots, M\} \; \forall n \in \{1, \ldots, N\} \; A_{mn} \geq 0 \tag{3}$$

and sum-to-one constraints:

$$\forall m \in \{1, \ldots, M\} \; \sum_{n=1}^{N} A_{mn} = 1 \tag{4}$$

Non-Negative Least Squares (NNLS) algorithms(Lawson and Hanson, 1995; Bro and De Jong, 1997) aim at solving the problem 2 subject to constraint 3. *Sum-to-one Constrained Least Squares* (SCLS) methods Settle and Drake, 1993 solve the same problem with constraint 4. Eventually, *Fully Constrained Least Squares* (FCLS) algorithms (Heinz and Chein-I-Chang, 2001; Dobigeon et al., 2008) solve the problem 2 subject to both constraints 3 and 4. In this article, two FCLS methods are considered: (i) IPLS based on primal dual interior point optimization (Chouzenoux et al., 2011) that benefits from GPU implementation (Chouzenoux et al., 2013), (ii) BI-ICE in the bayesian framework (Themelis et al., 2012a).

As stated in Chouzenoux et al., 2013, the convexity of the criterion F is sufficient to establish the convergence of IPLS when constraints 3 and 4 are considered. Hence, the unmixing estimation can be performed even with correlated reference spectra, such in fig. 1. Next sections will describe the results on actual data.

2.3. Measurement uncertainty consideration

In some cases, the level of uncertainty is known and can be modeled by a gaussian probability density function with zero mean and the covariance C ($N_\lambda \times N_\lambda$ matrix). C^{-1} being a symmetric positive definite matrix, it can be factorized using the Cholesky decomposition:

$$C^{-1} = L.L^T \tag{5}$$

with L lower triangular. Thus, noting $X = [X_1, \ldots, X_M]^T$ and $A = [A_1, \ldots, A_M]^T$, the least squares criterion becomes:

$$\min_{A \in \Re^{M \times N}} F(A) \quad \text{with} \quad F(A) = \sum_{m=1}^{M} (X'_m - A_m.S')(X'_m - A_m.S')^T \tag{6}$$

with $X' = X.L$ and $S' = S.L$. Thereby, the measurement uncertainty is handled by modifying the observation matrix X and the reference spectra S before the unmixing process.

An estimation of the error on the mixing coefficient A is directly provided by the Hessian (Chouzenoux et al., 2013).

2.4. Reference spectra database

As stated in introduction, the reference spectra database depends on the scientific goal of the detection. The total number of spectra is limited to the number of wavelength. In the following, we used 32 spectra of the main minerals type proposed to be present at the surface of Mars and the Moon (see fig. 2). More endmembers can be used but with increasing computation time (Chouzenoux et al., 2013).

2.5. Benefits of additional spectra

In order to model the effect of shading, grain size and aerosols, Combe et al., 2008 propose to add a positive and a negative linear slope, and also a flat spectrum in order to correct for the Mie scattering of the aerosols particles (see fig. 2 in Combe et al., 2008).

This strategy can be extended in the case of linear unmixing under constraints. Since mixing coefficients are positive and constrained to one, the flat spectra split in two : flat near zero level and also near 1 level (see fig. 1). Those 4 additional spectra allows to model the difference of level and slope between X and S.

In order to model more complex continuum shape such aerosols, we could also add cosine function with periods x2 and x4 of the spectral domain (Schmidt et al., 2011, 2012). Similarly to Fourier transform, those cosine functions are orthogonal and linearly independent, allowing unique mixing coefficient. In the framework of linear unmixing under positivity and sum to one constraint, 12 additional spectra are required. Those 12 additional spectra allow to model the large scale difference between X and S, similar to Fourier filtering. In particular the aerosols contribution that peak at the wavelength similar to the grain size may be fitted by large scale cosine. Figure 4 (b) show a pure aerosol spectra (aot=100), that could be modeled by level/slope/sine/cosine functions. Since the aerosols grain size may change, leading to an unknown peak over the wavelength, our approach will be able to fit it.

Since those 4 (or 12) additional spectra are highly correlated, from algorithmic point of view it may hard to estimate the mixing coefficient. To our knowledge, the only algorithms that are able to estimate the unmixing under constraints and high correlated reference spectra are IPLS (Chouzenoux et al., 2011) and BI-ICE (Themelis et al., 2012a). Next section will describe the results on actual data.

3. Synthetic tests

In order to test the effect of various discrepancies between observation and reference spectra on detection accuracy, we propose to simulate 3 cases: linear random mixture at the surface without atmosphere, linear random mixture at the surface observed trough a diffusive atmosphere, grain size change.

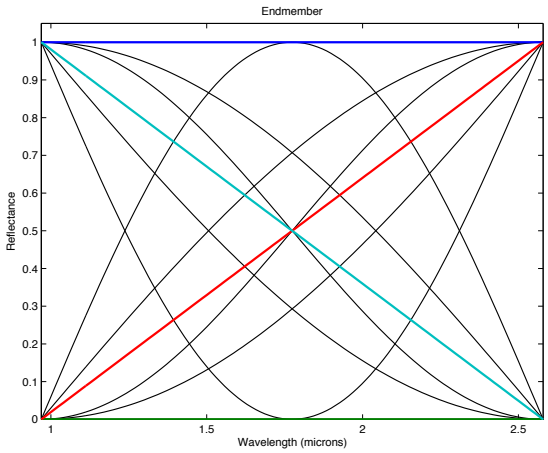


Figure 1: thick color lines : 4 additional spectra to fit difference of level and slope between X and S. thin black lines : 8 cosine/sine function to model the large scale difference between X and S.

3.1. Surface mixture

In order to simulate a realistic set of spectra, we create a random set of 1000 binary mixture spectra from our 32 reference spectra database (see fig. 2) from USGS catalog (Clark et al., 2003), the CRISM Analysis Tool (CAT), synthetic spectra from radiative transfer model (Douté and Schmitt, 1998). Each simulated spectra are composed of:

- 90% is a flat component at reflectance 0.35 in agreement with OMEGA studies Vincendon, 2013 in order to reproduce the low level and flatness of actual Martian spectra. The flatness is also representative of the Moon or other planetary surface.

- 10% of a random mixture of two over 32 reference spectra with random uniform mixing coefficients, noted as A_0. For each endmember i, there is ˜30 spectral mixture with non-null mixing coefficient (noted $A^{positive}$) and ˜970 with null mixing coefficient (A^{false}).

We add synthetic noise, simulating the noise level of a typical OMEGA observation after gas correction. We estimate the noise covariance matrix from dark current noise of ORB41_1, transferred into the gas corrected calibrated observation space. The noise has a wavelength-average standard deviation of 1.3×10^{-3}. Other noise statistics can be used, such MNF shift difference from ENVI software, but we point the fact that OMEGA dark current is archived, estimating the minimum noise statistics (excluding spike and other non-linear effects).

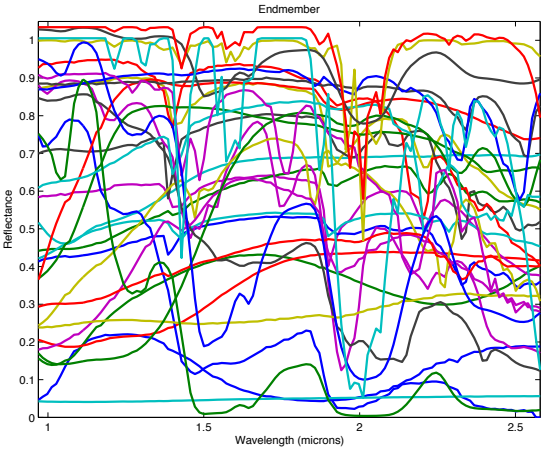


Figure 2: 32 Reference spectra of minerals, ice and atmospheric gas representing major classes of contributions of surface spectra. See Appendix for the names.

The estimated mixing coefficients are noted A_{IPLS}, A_{BI-ICE} and $A_{IPLS,cov}$ for the renormalized problem.

Examples of fits are shown in fig. 4 on left with AOT=0.

Figure 3 compares estimated $A_{IPLS,cov}$ and actual A_0 mixing coefficients, for the IPLS algorithm using 32 and the 4 additional spectra, on the 1000 binary mixture, with the renormalized unmixing problem. Usually, $A_{IPLS,cov}$ for actually present endmember ($A^{positive}_{IPLS,cov}$ in green), are well separated from the absent endmember ($A^{false}_{IPLS,cov}$ in red), showing that a simple threshold can be used to detect the endmember. Endmember No 18 (Magnetite) is not detectable because there is no difference between $A^{positive}_{IPLS,cov}$ and $A^{false}_{IPLS,cov}$. Please note that $A^{positive}_{IPLS,cov}$ and $A^{positive}_{0}$ are very close, the mean absolute difference is 0.0142, one order of magnitude lower than the mixing coefficients (up to 10%), showing that when linear mixing is true, the estimated mixing coefficients are validated as real abundances. Also, the root-mean-square (RMS) error is compatible with the level of noise (1.2×10^{-3}).

In order to estimate the best threshold $C^i_{IPLS,cov}$, avoiding the maximum number of false detection but keeping the maximum positive detection, we propose the following formulation, for each endmember i:

$$C^i_{IPLS,cov} = \frac{1}{2}\left(mean(A^{positive}_{IPLS,cov}) - 2.std(A^{positive}_{IPLS,cov}) + mean(A^{false}_{IPLS,cov}) + 6.std(A^{false}_{IPLS,cov})\right) \quad (7)$$

Figure 3 shows these threshold for all endmembers. It confirms that some endmembers can be detected with a larger detection limits than other, depending

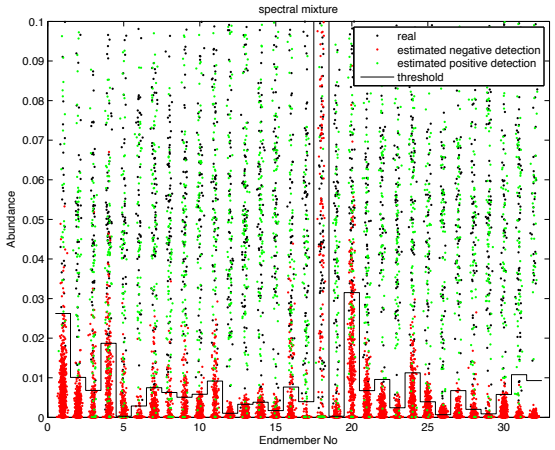


Figure 3: Mixing coefficient for 32 spectra (see fig. 2) for the IPLS algorithm on 1000 binary mixture, solving the renormalized unmixing problem (eq. 6), using 36 endmembers (32 spectra and the 4 additional spectra). black points: actual mixing coefficient A_0, generated randomly. green points: estimated mixing coefficient $A^{positive}_{IPLS,cov}$ in the case of positive detection. red points: estimated mixing coefficient $A^{false}_{IPLS,cov}$ in the case of false detection. black line: best threshold $C^i_{IPLS,cov}$ to detect the endmember. Please note that artificial dispersion around the endmember No has been added in order to increase the clarity of the figure.

on their relative similarities. Endmember No 18 (Magnetite) is not detectable because its spectral shape is too close to a combination of the 4 artificial spectra, because its spectra is featureless.

Actual positive detection and false detection rates without atmosphere are shown in figure 6 at the AOT=10^{-3} for IPLS with/without renormalization, for IPLS and BI-ICE, for 32 or 36 or 44 endmembers. For all algorithms the 4 additional spectra (called slope), clearly improve the classification over the 32 endmembers case (called no slope). Without renormalization, IPLS shows the best results ($>$ 70% of positive detection, $<$ 20% of false detection) over BI-ICE. With renormalization, the detection rates is improved ($>$ 85% of positive detection, $<$ 5% of false detection) for IPLS. For non-renormalized IPLS, the sum-to-one (sto) seems slightly better than sum-lower-than-one (slo).

The use of 12 additional spectra (including the sine/cosine), seems to be less efficient that 4 additional spectra (83 % of positive detection, 5% of false detection). It appears that the accuracy of detection slightly decreases for some minerals with large scale feature such olivines or pyroxenes. Since, those phases are major ones, we decide to focus on the 4 additional spectra.

As a summary, the best algorithm to detect linear mixture is clearly IPLS with renormalization and 4 additional spectra. Please note that a different threshold may change the positive/false detection rates but not change the relative accuracy of the classification. Estimating the threshold for real case images is more difficult due to the possible differences between observation and reference spectra. Please note that our test uses the same spectra in the spectral library and in the mixture.

3.2. Aerosols

In order to test if our methodology is able to reduce the effect of the non linear surface-atmosphere coupling due to aerosols, we modified the previous surface spectra by non linear radiative transfer using aerosol properties from Vincendon et al., 2007. These authors propose a parameterization of the dust aerosol properties in form of a single scattering albedo and a shape of optical thickness as a function of wavelength, rescaled to a Aerosols Optical Thickness at 1 micron (AOT). The reflectance of a semi-infinite aerosol media is plotted in figure 4 b, for AOT=100. The simulation uses the DISORT algorithm (Stamnes et al., 1988) with the bottom condition as lambertian surface with the previous surface mixture spectra. We took into account the reflection and absorption of the aerosols but also the multiple reflection between surface and atmosphere. We used the following geometry, typical of hyperspectral observation: emergence angle 0°, incidence angle 76°, azimuth angle 60°. Other optical properties and/or geometries may be used but we assume that the chosen properties are reasonable to simulate aerosols effects. We sample 104 values of AOT (Aerosols Optical Thickness):

- The value 0 for no aerosols, identical to surface only (noted 10^{-3} in the log scale graphs)

- 99 value in a logarithm from 0.01 to 4.6 using $-\log(\frac{100-[1:99]}{100})$.
- Four values : 5, 10, 20 and 100 to sample the optically thick cases.

We obtain a set of 104 000 spectra simulating the space-borne Martian observation from the top of the atmosphere. We also add the synthetic OMEGA noise in order to simulate a realistic observation using the same approach that previously described.

On a desktop with Dual Core at 2.53 Ghz with 4Go RAM memory, the typical computation time to solve the non-normalized problem of eq. 2 on $M = 104000$ spectra with $N_\lambda = 110$, $N = 36$ are : 3.3 h for BI-ICE, 4.5 min for IPLS. The estimated mixing coefficients are noted A_{IPLS}, A_{BI-ICE}. Since IPLS is the fastest algorithm, we also tried the solve the harder renormalized problem of eq. 6 and found a computation time of 1.2h. We also use IPLS to solve the renormalized problem using 12 additional spectra. The estimated mixing coefficients are noted $A_{IPLS,cov}$. Also GPU implementation on a TESLA C 2050 (448 core at 1.15 GHz) may solve the problem with a computation time of several 10s. The GPU implementation efficiency dependance on spectral/spatial size and number of endmember is discussed in Chouzenoux et al., 2013.

In order to illustrate the effect of AOT on the detection limits, figure 5 shows the same than figure 3 but for AOT=1. The positive detection mixing coefficients endmembers ($A^{positive}_{IPLS,cov}$ in green) are well separated from the absent endmember ($A^{false}_{IPLS,cov}$ in red), showing again that a simple threshold can be used to detect the endmember. Endmember No 18 (Magnetite) is still not detectable. Please note that $A^{positive}_{IPLS,cov}$ and $A^{positive}_{0}$ are getting far, the mean absolute difference is 0.0310, showing that when linear mixing is not true, the estimated mixing coefficient may differ from the true abundances. The estimated mixing coefficients $A^{positive}_{IPLS,cov}$ are systematically lower than the "true" $A^{positive}_{0}$ because of the effect of aerosols, removing the minerals signature (see fig. 4).

Results on actual positive detection and false detection rates are shown in figure 6 as a function of AOT. The positive detection rates of all algorithms drop for AOT$> 10^{-1}$. For IPLS with renormalization, the positive detection rates is 70 % at AOT=10^0 and 10 % at AOT=10^1, showing again that it is the best algorithm. IPLS with renormalization is also the only providing a constant low false detection rate (<5 %), independent of the AOT. The RMS error for IPLS with renormalization and additional spectra is still very low and compatible with the actual level of noise (at maximum 1.7×10^{-3} for AOT=10^2), showing that the non-linearity of the radiative transfer due aerosols can be fitted with our model. Examples of fits are shown in fig. 4 b) demonstrating the effect of decreasing mixing coefficient as a function of increasing AOT.

Figures 4 c) and d) show the effect of 4 additional spectra (level and slope) or 12 additional spectra (level, slope, cosine) on the detection of pure diopside. In the case of AOT=1 using 12 additional spectra, the mixing coefficient is estimated to be $0.7 \pm 2\%$, showing a non-probable detection in spite of the actual 10% abundance. In the same case using 4 additional spectra, the mixing

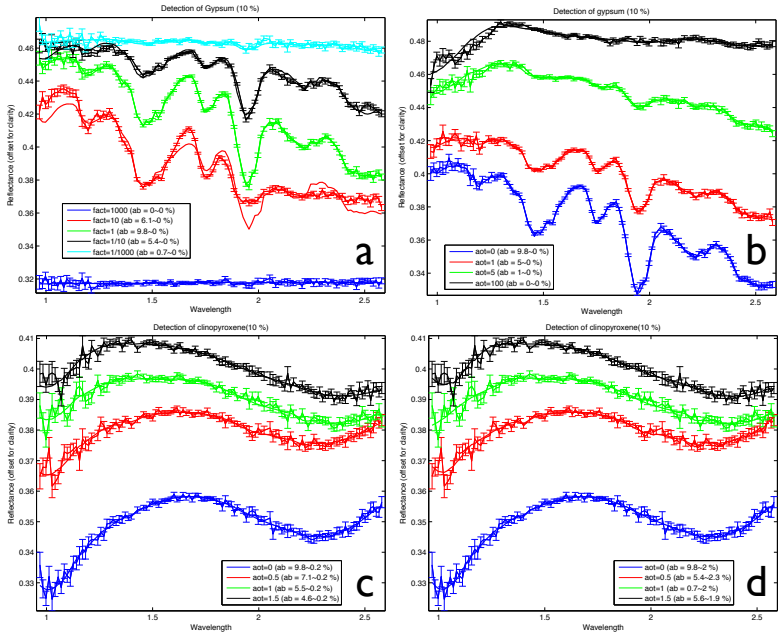


Figure 4: Examples of results using the IPLS algorithm: a) and b) with renormalization and 12 additional spectra (flat and slope) in the case of a pure gypsum spectra (10% in abundance). a) with different grain size factor, from x1000 to x1/1000, b) with different atmospheric load from AOT=0 to AOT=100. ; c) and d) with renormalization in the case of diopside (clinopyroxene). c) using 4 additional spectra (flat and slope), d) using 12 additional spectra (flat, slope and cosine).

coefficient is estimated to $5.5 \pm 0.2\%$, showing a clear positive good detection. We argue that all endmember with large scale absorption bands could have the same behavior and thus, we prefer to use 4 additional spectra to detect them. Users focused on spectra endmember with small scale features only, such phyllosilicate, could use the 12 additional spectra.

As a summary, the best algorithm to detect non-linear coupling of a linear mixture under increasing aerosols content is IPLS with renormalization and additional spectra. Please note that a different threshold may change the positive/false detection rates but not change the relative accuracy of the classification. Estimating the threshold for real case images is more difficult due to the possible differences between observation and reference spectra. Please note that our test uses the same spectra in the spectral library and in the mixture.

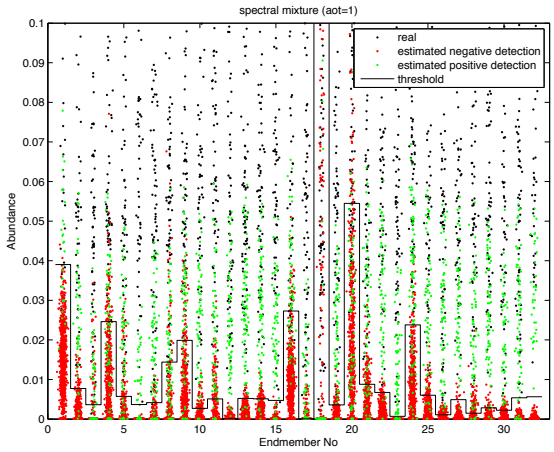


Figure 5: Same fig. as 3 but with AOT=1 instead of AOT=0.

3.3. Grain size

We choose the first 26 minerals spectra (see Appendix) with following parameter to retrieve the optical index of the grain material using the inverse Shkuratov theory (Shkuratov et al., 1999): real optical constant=1.7, volume fraction filled by particles=0.8, grain size=100 microns. This approach has been widely used in hyperspectral data analysis (Poulet et al., 2002; Douté et al., 2007; Poulet et al., 2009b).

We then regenerate the reflectance spectra using the direct Shkuratov theory but with 9 different grain size factor x1000, x100, x10, x5, x1, x$\frac{1}{5}$, x$\frac{1}{10}$, x$\frac{1}{100}$, x$\frac{1}{1000}$ of the original 100 microns. We obtain a set of 234 synthetic spectra.

In order to simulate a realistic observation we use the same approach that previously described for the surface mixture using flattening of the spectra and OMEGA noise addition (see section 3.1).

We do not claim that all reference spectra have been recorded at a grain size of 100 microns so that the generated dataset has a determined accurate grain size. Nevertheless, this manner allows us to generate synthetic spectra simulating a grain size factor change.

Since IPLS with renormalization is obviously the best algorithm, we only tested this approach for the grain size. We used again the same threshold strategy explained earlier in eq. 7. Here positivity constraint only may be relevant in the case of higher grain size than the endmember, since the signature are stronger and may imply mixing coefficient larger than 1.

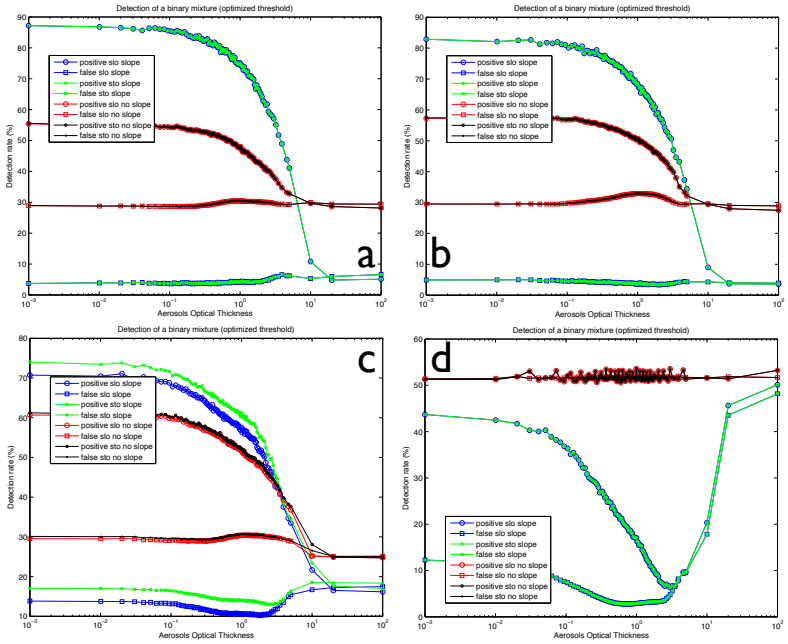


Figure 6: Positive detection rate (circle) and false detection rates (square) with optimized threshold as a function of AOT for (a) IPLS with renormalization and 36 endmembers (b) IPLS with renormalization and 44 endmembers (c), IPLS without renormalization and 36 endmembers (d) BI-ICE without renormalization and 36 endmembers. For each algorithm, the positive/false detection rates are computed using 32 endmember spectra only (no slope), or 36/44 endmember spectra (slope). IPLS has an option of sum-lower-than-one (slo) or sum-to-one (sto) that is not relevant for other algorithms. The case without aerosols is plotted at AOT=10^{-3}.

Positive and negative detection rates are plotted in fig. 7 for 36 or 32 spectra, for three constraints of IPLS : sum-lower-than-one (slo), sum-to-one (sto) and positivity only (pos). First of all, the detection is nearly perfect (>90%) for the grain size factor of x1, x5 and x1/5 using additional 4 spectra. The false detection rate is very low (<2%). For 32 spectra, the positive detection is around 60% for factor x1 to x10, and false detection is around 20%. Using the 4 additional spectra clearly improves the detection rates but slo, sto and pos are equivalent in this case. For a factor of x$\frac{1}{10}$ to x10, the detection rate is higher than 65%. It then decreases, moving away from factor x1. The detection rates are quiet symmetrical in respect to increasing and decreasing grain size, with a slightly lower detection rates for the increasing grain size. Examples of fits are shown in fig. 4 demonstrating the effect of decreasing mixing coefficient as a function of increasing/decreasing grain size factor. This plot clearly shows that increasing grain sizes are more difficult to handle with our strategy because the error between estimated spectra and true one is higher. The main solution is to provide the endmembers with grain size higher than expected.

The RMS error is still very low and compatible with the actual level of noise (at maximum 2.1×10^{-3}), showing that the main non-linearity effects due grain size factor can be fitted with our model.

As a summary, the best endmembers to detect mineral species in case of a non-linear grain size effect again with the 4 additional spectra. Please note that a different threshold may change the positive/false detection rates but not change the relative accuracy of the classification. Estimating the threshold for real case images is more difficult due to the possible differences between observation and reference spectra. Please note that our test uses the same spectra in the spectral library and in the mixture. Intimate mixture may be generated from the Shkuratov theory but the detection limits may be forecast from this discussion, knowing that the largest grain size species is spectrally dominant (as computed for ices in Schmidt et al., 2007 for instance).

4. Real case

We propose to test our automatic algorithm to three different real case from OMEGA, CRISM and M^3 instrument. For all cases, we will compare our results with other detection from the literature, mainly based on band ratio followed by ratio of the region of interest spectra over a manually selected "flat" spectra. For all cases, we do not test that the exact minerals types could be detected since many equivalent spectra can be identified (clays, olivine, pyroxene, ...). The names are the names of the material from laboratory spectra. For instance "goethite" is an example of iron oxide. Since all mineral inside a class are spectrally close (like for iron-oxides), it may be not possible to distinguish the precise mineral. We decided to keep magnetite since it has been detected on Mars (Chevrier and Mathe, 2007) but estimated mixing coefficients are not relevant due to the featureless spectra. More accurate detections are possible by adapting and improving the endmember spectra database. All maps, spectral

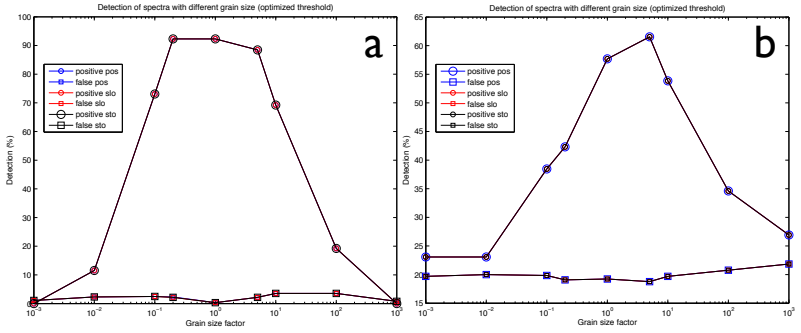


Figure 7: Positive detection rate (circle) and false detection rates (square) with optimized threshold as a function of grain size factor for IPLS with renormalization: (a) using 36 endmember spectra (using additional flat and slope endmember), (b) using 32 endmember spectra only (no slope). IPLS has options of constraints: sum-lower-than-one (slo), sum-to-one (sto) and positivity only (pos).

fits of the maximum mixing coefficient and average of each compounds are available in supplementary material.

From previous section, IPLS seems the best algorithm to solve the LinMin problem so that we will exclusively use it on the real case hyperspectral images.

The detection of minerals requires different conditions of good behavior of the solution:

- The maximum mixing coefficient of the mineral should be higher than a certain threshold. This condition permits to focus on the main spectral component but component with smaller contribution can be present.
- The error on mixing coefficient should be lower than the mixing coefficient, in order to have a significant detection.
- The RMS should be lower than the noise, basically estimated at 10 times the dark current noise.

4.1. OMEGA

We select the observation ORB422_4 of Observatoire pour la Minéralogie, l'Eau, les Glaces et l'Activité (OMEGA) onboard Mars Express (MEx) (Bibring et al., 2004) of Syrtis Major as a test case because this single cube contains well identified areas with very strong signatures of mafic minerals (pyroxenes, olivines) and phyllosilicates (Mustard et al., 2005; Combe et al., 2008; Ehlmann and Mustard, 2012). The data cube has been radiometrically calibrated and the atmospheric gas transmission has been empirically corrected using the volcano scan method (Erard and Calvin, 1997; Langevin et al., 2005). We estimated the noise covariance matrix on the calibrated and atmosphere corrected cube from

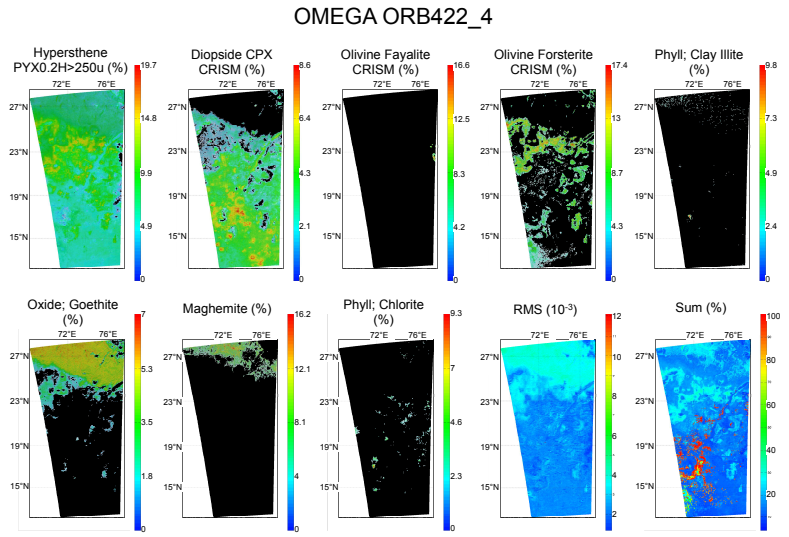


Figure 8: Detection of 8 minerals over 36 spectra on OMEGA image ORB422_4 of Syrtis Major using IPLS in the hue-saturation-value color system. The hue (color) represents the mixing coefficient. The saturation (color or b/w) represents the error. The value (intensity of color or b/w) represents the rms. Spectral mixing coefficient map are shown with following conditions : (i) maximum mixing coefficient $> 5\%$, (ii) error on mixing coefficient $<$ mixing coefficient, and (iii) RMS $<$ 10x the dark current noise (see text). Pyroxenes, olivines, phyllosilicates and oxides are detected and the corresponding "mixing coefficient" are mapped (color refer to the online version of the article).

the dark current. We then applied the renormalized IPLS algorithm using 36 spectra and sum-lower-than-one constraint.

The mixing coefficient results, plotted in figure 8, shows that orthopyroxene, clinopyroxene, olivine, goethite, clays and maghemite are detected, in agreement with previous detection (Mustard et al., 2005; Combe et al., 2008; Ehlmann and Mustard, 2012). The fit of the spectra with highest mixing coefficient are available in supplementary material. The estimated noise standard deviation is 3.3×10^{-4} from dark current but 5.0×10^{-3} using the MNF shift difference from ENVI software. The lack of fit estimated by the RMS error is 2.1×10^{-3} , in agreement with the previous two extreme values. Using the fast GPU implementation, the computation time is only 4 minutes for the complete OMEGA image of M =128x366 pixels, $N_\lambda = 110$ bands. The computation time can can be reduced to 0.3 min without any significant change in case of a recalibration with $C \times 100$.

4.2. CRISM

We propose to use the Compact Reconnaissance Imaging Spectrometer for Mars (CRISM) onboard Mars Reconnaissance Orbiter (MRO) image frt0000A09C (Murchie et al., 2007) of Nili Fossae where carbonate has been detected using manual band ratio's technique on stacked denoise spectra, divided by a spectrally flat component (Ehlmann et al., 2009). We estimate the SNR=400 from the calibration at the ground (Murchie et al., 2007). We did not correct for spectral smile (Murchie et al., 2007) unless this artifact can be corrected (Ceamanos and Doute, 2010). Since the algorithm is comparing observed spectra to a single reference spectra that cannot be shifted in wavelength, results may be affected by the smile artifact. Nevertheless, the absorption bands of minerals are often large and very insensitive to spectral smile, which is not the case for gas and ices.

The results in fig. 9 and 10 confirm the detection of carbonate. We stress the fact that our approach has been applied on raw image, without stacking, neither dividing by a spectrally flat component, in contrary to published detection.The algorithm also detects monohydrated sulfate kieserite, than has not been described in Ehlmann et al., 2009 (see fig. 11). The broad absorption band at 2 microns, and the small absorption band at 2.3 microns are present in the CRISM image. Nevertheless the large absorption band at 1.5 microns that should be seen is absent in the CRISM spectra. Our algorithm proposes that a mixture with olivine could erase significantly this absorption band. All spectra are polluted by an artifact at 2.1 microns. As a summary, the clear detection of kieserite is not established but at least, the kieserite map in fig. 9Fig6 should be interpreted as a map of the maximum probability of kieserite in the scene.

The estimated noise standard deviation is 3.5×10^{-4} from SNR but 3.4×10^{-3} using the MNF shift difference from ENVI software. The lack of fit estimated by the RMS error is 1.0×10^{-3} , in agreement with the previous two extreme values. Using the fast GPU implementation, the computation time is 20 minutes for M =600x478 pixels, $N_\lambda = 56$ bands. The computation time can can be reduced to 2.7 min without any significant change in case of a recalibration with $C\times100$.

4.3. M^3

We propose to use the Moon Mineralogy Mapper (M^3) onboard Chandrayaan-1 image G20090209T054031 (Pieters et al., 2009) of Aristarchus, where peculiar olivines has been detected (Le Mouëlic et al., 1999; Chevrel et al., 2009; Mustard et al., 2011).

We estimate the SNR=400 from the calibration at the ground (Green et al., 2011),

The results in fig. 12 also confirms that the South East of Aristarchus is olivine rich but without any spectral signature of pyroxene (Le Mouëlic et al., 1999; Chevrel et al., 2009; Mustard et al., 2011).

The estimated noise standard deviation is 5.4×10^{-5} from SNR but 1.6×10^{-3} using the MNF shift difference from ENVI software. The lack of fit estimated by the RMS error is 2.1×10^{-4}, in agreement with the previous two extreme values.

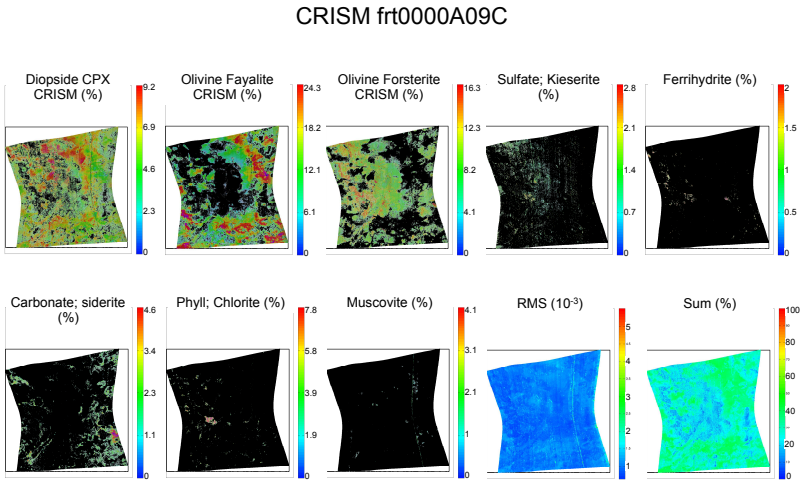


Figure 9: Detection of 8 minerals over 36 spectra on CRISM image frt0000A09C of Nili Fossae (21.3°N, 78.5°E) using IPLS in the hue-saturation-value color system. The hue (color) represents the mixing coefficient. The saturation (color or b/w) represents the error. The value (intensity of color or b/w) represents the rms. Spectral mixing coefficient map are shown with following conditions : (i) maximum mixing coefficient $> 2\%$, (ii) error on mixing coefficient $<$ mixing coefficient, and(iii) RMS $<$ 10x the dark current noise (see text). Pyroxenes, olivines, phyllosilicates, sulfate and carbonate are detected and the corresponding "mixing coefficient" are mapped (color refer to the online version of the article).

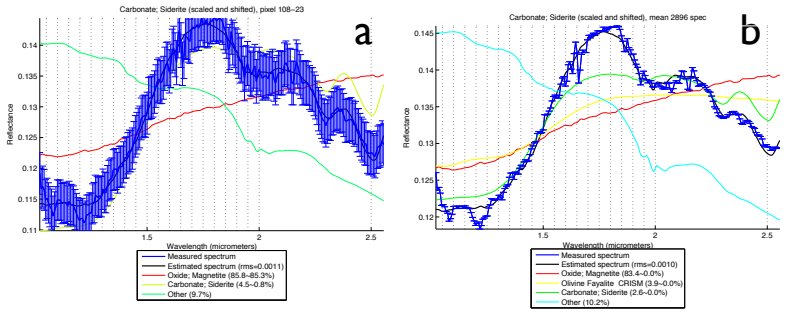


Figure 10: Example of spectra fit for the carbonate component (siderite in our spectral database). All spectral endmember with significant mixing coefficients (>2%) are plotted but the other component are retrieved by the algorithm (spectra called "Other"), mainly due to atmospheric transmission and water ice most probably in form of clouds. a) maximum mixing coefficients spectra (pixel coordinates is line No 108, row No 23), b) average value of 2896 spectra of the CRISM observation frt0000A09C.

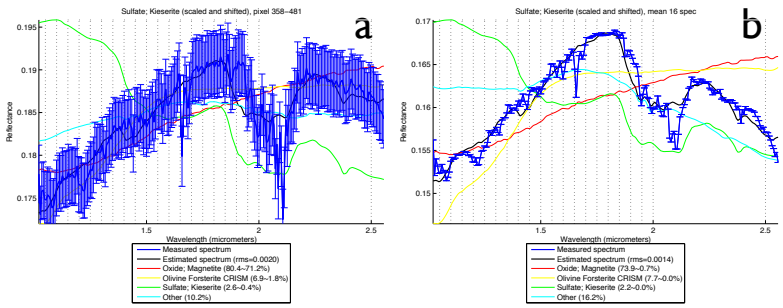


Figure 11: Example of spectra fit for the monohydrate sulfate (kieserite) component. All spectral endmember with significant mixing coefficients (>2%) are plotted but the other component are retrieved by the algorithm (spectra called "Other"), mainly due to atmospheric transmission and water ice most probably in form of clouds. a) maximum mixing coefficient spectra (pixel coordinates is line No 358, row No 481), b) average value of 16 spectra of the CRISM observation frt0000A09C.

Using the fast GPU implementation, the computation time is 13 minutes for M =304x500 pixels, $N_\lambda = 56$ bands due to the very small noise level expected from the SNR (5.4×10^{-5}). The computation time can can be reduced to 1.6 min without any significant change in case of a recalibration with $C \times 100$.

5. Conclusion

We propose to incorporate additional spectra (constant, slope, and cosine functions) to build a new supervised algorithm, called LinMin, based on linear unmixing under positivity and sum-to-one constraints in the goal to detect minerals at the planetary surfaces. The main novelty of this approach is to treat "linearly dependent spectra" (such constant, slope and cosine functions) that create degeneracies in usual unconstraints unmixing algorithms, because under our constraints, they are not linearly dependent anymore.

We validated the usefulness of LinMin to estimate mixing coefficients in the case of linear mixture on synthetic examples. We also tested numerically the most important non-linear effects on the detection limits : aerosols content and grain size change. Both cases are well treated with our modeling. Some minerals with large scale feature, such olivines and pyroxenes, cannot be detected in the case of additional cosine function because their spectral signature can be also fitted with a mixture of cosine. Nevertheless, the use of additional spectra made of constant and slope components improve the detection of all minerals, including olivines and pyroxenes in comparison with no additional spectra Our approach permits to save the continuum fitting step since it is incorporated in the linear unmixing. We also showed that the knowledge of the noise covariance matrix, that can be estimated from dark current or using other techniques is

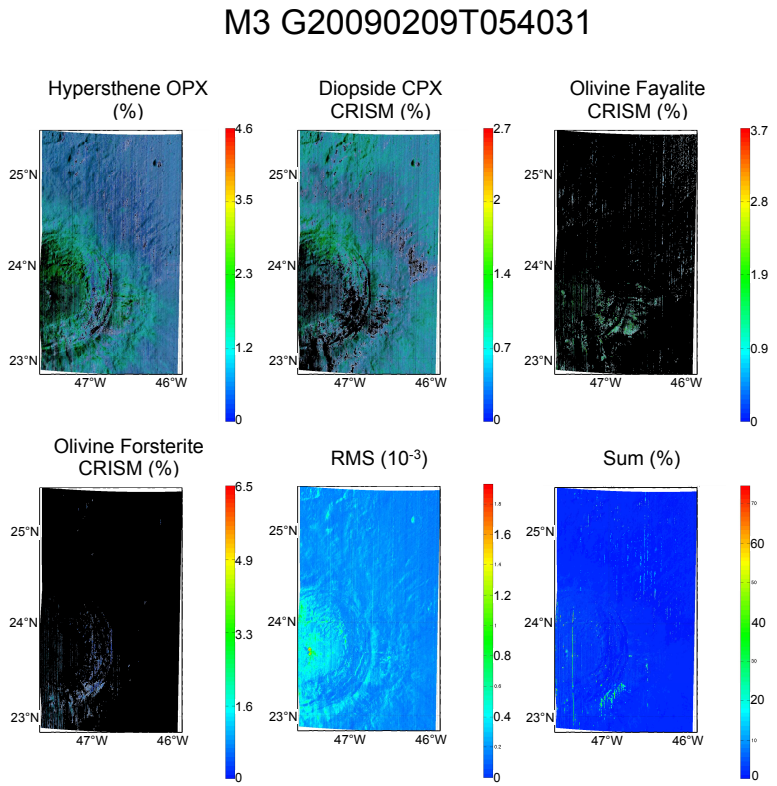


Figure 12: Detection of 4 minerals over 36 spectra on M^3 image G20090209T054031 of Aristarchus using IPLS in the hue-saturation-value color system. The hue (color) represents the mixing coefficient. The saturation (color or b/w) represents the error. The value (intensity of color or b/w) represents the rms. Spectral mixing coefficient map are shown with following conditions : (i) maximum mixing coefficient $> 2\%$, (ii) error on mixing coefficient $<$ mixing coefficient, and (iii) RMS $<$ 10x the dark current noise (see text). Pyroxenes and olivines are detected and the corresponding "mixing coefficient" are mapped (color refer to the online version of the article).

important to assess the detection limits, and in particular the error on mixing coefficients.

We also tested LinMin on three real cases of hyperspectral images from OMEGA, CRISM and M^3 instruments. All three cases show detections in agreement with previous analysis, validating the LinMin with approach. The main difficulty of this approach, that is also present in band ratio and other detection method, is to optimize the threshold for detection. Nevertheless, this problem is partly tackled by the estimation of the error on the mixing coefficients. A combination of threshold on RMS residues, error on mixing coefficients, and maximum mixing coefficients seems to be the best compromise to ensure automatic detection. This strategy has to be fully validated on large dataset.

IPLS is shown to be the best numerical algorithm to solve the LinMin problem. Its fast GPU implementation is particularly relevant for the treatment of large dataset of hyperspectral images. In the future, this methodology should be applied in various planetary cases in order to study the surface geology, especially in more challenging detection situation such complex mafics and anorthosites assemblage on the Moon (Ohtake et al., 2009), or mixture of hydrous sulfates, hydrated acid and water ice on Europa (McCord et al., 2010; Dalton et al., 2013). Also a significant improvement of the mineral detection may be addressed by using spectral database adapted to the context.

Acknowledgement

We acknowledge support from the "Institut National des Sciences de l'Univers" (INSU), the "Centre National de la Recherche Scientifique" (CNRS) and "Centre National d'Etude Spatiale" (CNES) and through the "Programme National de Planétologie".

Appendix

Name of the 32 spectra:

1 Inosilicate (Hypersthene OPX PYX02.h >250u)	12 Sulfate; Gypsum	23 Carbonate; Siderite
2 Inosilicate (Diopside CPX CRISM)	13 Sulfate; Jarosite	24 Phyllosilicate (Chlorite)
3 Olivine Fayalite CRISM	14 Sulfate; Kieserite	25 Muscovite GDS116 Tanzania
4 Olivine Forsterite CRISM	15 Epsomite USGS GDS149	26 Alunite GDS83 Na63
5 Phyllosilicate (Clay Montmorillonite Bentonite)	16 Oxide; Goethite	27 Atmospheric Transmission
6 Phyllosilicate (Clay Illite Smectite)	17 Oxide; Hematite	28 H2O grain 1
7 Phyllosilicate (Serpentine Chrysotile Clinochry.)	18 Oxide; Magnetite	29 H2O grain 100
8 Phyllosilicate (Serpentine Lizardite)	19 Ferrihydrite USGS GDS75 Sy F6	30 H2O grain 1000
9 Phyllosilicate (Clay Illite)	20 Maghemite USGS GDS81 Sy (M-3)	31 CO2 grain 100
10 Phyllosilicate (Clay Kaolinite)	21 Carbonate; Calcite	32 CO2 grain 10 000
11 Phyllosilicate (Nontronite)	22 Carbonate; Dolomite	

Name of the 12 additional spectra:

33 Flat 1	37 cos 1/4	41 cos 1/2
34 Flat 0.0001	38 sin 1/4	42 sin 1/2
35 Slope Increasing	39 -cos 1/4	43 -cos 1/2
36 Slope Decreasing	40 -sin 1/4	44 -sin 1/2

References

Bibring, J.-P., Soufflot, A., Berthé, M., Langevin, Y., Gondet, B., Drossart, P., Bouyé, M., Combes, M., Puget, P., Semery, A., Bellucci, G., Formisano, V., Moroz, V., Kottsov, V., Bonello, G., Erard, S., Forni, O., Gendrin, A., Manaud, N., Poulet, F., Poulleau, G., Encrenaz, T., Fouchet, T., Melchiori, R., Altieri, F., Ignatiev, N., Titov, D., Zasova, L., Coradini, A., Capacionni, F., Cerroni, P., Fonti, S., Mangold, N., Pinet, P., Schmitt, B., Sotin, C., Hauber, E., Hoffmann, H., Jaumann, R., Keller, U., Arvidson, R., Mustard, J., Forget, F., Aug. 2004. OMEGA: Observatoire pour la Minéralogie, l'Eau, les Glaces et l'Activité. ESA SP-1240: Mars Express: the Scientific Payload, pp. 37–49.

Boardman, J., Kruse, F. A., Green, R. O., Mar. 1995. Mapping target signatures via partial unmixing of AVIRIS data: in Summaries. In: Fifth JPL Airborne Earth Science Workshop, JPL Publication 95-1. Vol. 1. pp. 23–26.

Bro, R., De Jong, S., 1997. A fast non-negativity-constrained least squares algorithm. Journal of chemometrics 11 (5), 393–401.

Carter, J., Poulet, F., Murchie, S., Bibring, J., 2013. Automated processing of planetary hyperspectral datasets for the extraction of weak mineral signatures and applications to {CRISM} observations of hydrated silicates on mars. Planetary and Space Science 76 (0), 53 – 67.
URL http://www.sciencedirect.com/science/article/pii/S0032063312003625

Ceamanos, X., Doute, S., 2010. Spectral smile correction of crism/mro hyperspectral images. Geoscience and Remote Sensing, IEEE Transactions on DOI - 10.1109/TGRS.2010.2064326 48 (11), 3951–3959.

Chevrel, S., Pinet, P., Daydou, Y., Le Mouëlic, S., Langevin, Y., Costard, F., Erard, S., Jan. 2009. The aristarchus plateau on the moon: Mineralogical and structural study from integrated clementine uv-vis-nir spectral data. Icarus 199 (1), 9–24.
URL http://www.sciencedirect.com/science/article/pii/S0019103508002935

Chevrier, V., Mathe, P., Feb. 2007. Mineralogy and evolution of the surface of mars: A review. Planetary and Space Science 55 (3), 289–314.
URL http://www.sciencedirect.com/science/article/B6V6T-4KST3NG-4/2/57ccbb298d799322cad03ca5fedc2e26

Chouzenoux, E., Legendre, M., Moussaoui, S., Idier, J., 2013. Fast constrained least squares spectral unmixing using primal-dual interior-point optimization. SUBMITTED TO THE IEEE JOURNAL OF SELECTED TOPICS IN APPLIED EARTH OBSERVATIONS AND REMOTE SENSING.

Chouzenoux, E., Moussaoui, S., Idier, J., Sep. 2011. Algorithme primal-dual de points interieurs pour l'estimation penalisee des cartes d'abondances en imagerie hyperspectrale. In: Actes de GRETSI 2011. Bordeaux, France, p. ID290.
URL http://hal.archives-ouvertes.fr/hal-00625893

Clark, R. N., Swayze, G. A., Wise, R., Livo, K. E., Hoefen, T. M., Kokaly, R. F., Sutley, S. J., 2003. Usgs digital spectral library splib05a. Tech. rep., U.S. Geological Survey.
URL http://speclab.cr.usgs.gov/spectral-lib.html

Combe, J.-P., Le Mouélic, S., Sotin, C., Gendrin, A., Mustard, J. F., Le Deit, L., Launeau, P., Bibring, J.-P., Gondet, B., Langevin, Y., Pinet, P., the OMEGA Science team, May 2008. Analysis of OMEGA/Mars Express data hyperspectral data using a Multiple-Endmember Linear Spectral Unmixing Model (MELSUM): Methodology and first results. Planetary and Space Science 56, 951–975.

Dalton, J. I., Cassidy, T., Paranicas, C., Shirley, J., Prockter, L., Kamp, L., Mar. 2013. Exogenic controls on sulfuric acid hydrate production at the surface of europa. Planetary and Space Science 77 (0), 45–63.
URL http://www.sciencedirect.com/science/article/pii/S0032063312001262

Dobigeon, N., Tourneret, J.-Y., Chang, C.-I., 2008. Semi-supervised linear spectral unmixing using a hierarchical bayesian model for hyperspectral imagery. Signal Processing, IEEE Transactions on 56 (7), 2684–2695.

Douté, S., Schmitt, B., Dec. 1998. A multilayer bidirectional reflectance model for the analysis of planetary surface hyperspectral images at visible and near-infrared wavelengths. Journal of Geophysical Research 103, 31367–31390.

Douté, S., Schmitt, B., Langevin, Y., Bibring, J.-P., Altieri, F., Bellucci, G., Gondet, B., Poulet, F., the MEX OMEGA team, Jan. 2007. South Pole of Mars: Nature and composition of the icy terrains from Mars Express OMEGA observations. Planetary and Space Science 55, 113–133.

Ehlmann, B. L., Mustard, J. F., Jun. 2012. An in-situ record of major environmental transitions on early mars at northeast syrtis major. Geophys. Res. Lett. 39 (11), L11202–.
URL http://dx.doi.org/10.1029/2012GL051594

Ehlmann, B. L., Mustard, J. F., Murchie, S. L., Bibring, J.-P., Meunier, A., Fraeman, A. A., Langevin, Y., Nov. 2011. Subsurface water and clay mineral formation during the early history of mars. Nature 479 (7371), 53–60.
URL http://dx.doi.org/10.1038/nature10582

Ehlmann, B. L., Mustard, J. F., Swayze, G. A., Clark, R. N., Bishop, J. L., Poulet, F., Des Marais, D. J., Roach, L. H., Milliken, R. E., Wray, J. J.,

588 Barnouin-Jha, O., Murchie, S. L., Oct. 2009. Identification of hydrated sili-
589 cate minerals on mars using mro-crism: Geologic context near nili fossae and
590 implications for aqueous alteration. J. Geophys. Res. 114, E00D08–.
591 URL http://dx.doi.org/10.1029/2009JE003339

592 Erard, S., Calvin, W., Dec. 1997. New composite spectra of mars, 0.4 microns.
593 Icarus 130 (2), 449–460.
594 URL http://www.sciencedirect.com/science/article/pii/
595 S0019103597958309

596 Erard, S., Drossart, P., Piccioni, G., Jan. 2009. Multivariate analysis of visible
597 and infrared thermal imaging spectrometer (virtis) venus express nightside
598 and limb observations. J. Geophys. Res. 114, –.
599 URL http://dx.doi.org/10.1029/2008JE003116

600 Forni, O., Poulet, F., Bibring, J.-P., Erard, S., Gomez, C., Langevin, Y.,
601 Gondet, B., The Omega Science Team, Mar. 2005. Component Separation
602 of OMEGA Spectra with ICA. In: Mackwell, S., Stansbery, E. (Eds.), 36th
603 Annual Lunar and Planetary Science Conference. pp. 1623–+.

604 Gendrin, A., Langevin, Y., Bibring, J.-P., Forni, O., Oct. 2006. A new method
605 to investigate hyperspectral image cubes: An application of the wavelet trans-
606 form. Journal of Geophysical Research (Planets) 111, 10004–+.

607 Gilmore, M. S., Thompson, D. R., Anderson, L. J., Karamzadeh, N., Mandrake,
608 L., Castao, R., Jul. 2011. Superpixel segmentation for analysis of hyperspec-
609 tral data sets, with application to compact reconnaissance imaging spectrom-
610 eter for mars data, moon mineralogy mapper data, and ariadnes chaos, mars.
611 J. Geophys. Res. 116 (E7), E07001–.
612 URL http://dx.doi.org/10.1029/2010JE003763

613 Green, R. O., Pieters, C., Mouroulis, P., Eastwood, M., Boardman, J., Glavich,
614 T., Isaacson, P., Annadurai, M., Besse, S., Barr, D., Buratti, B., Cate, D.,
615 Chatterjee, A., Clark, R., Cheek, L., Combe, J., Dhingra, D., Essandoh, V.,
616 Geier, S., Goswami, J. N., Green, R., Haemmerle, V., Head, J., Hovland,
617 L., Hyman, S., Klima, R., Koch, T., Kramer, G., Kumar, A. S. K., Lee, K.,
618 Lundeen, S., Malaret, E., McCord, T., McLaughlin, S., Mustard, J., Nettles,
619 J., Petro, N., Plourde, K., Racho, C., Rodriquez, J., Runyon, C., Sellar,
620 G., Smith, C., Sobel, H., Staid, M., Sunshine, J., Taylor, L., Thaisen, K.,
621 Tompkins, S., Tseng, H., Vane, G., Varanasi, P., White, M., Wilson, D., Oct.
622 2011. The moon mineralogy mapper (m3) imaging spectrometer for lunar
623 science: Instrument description, calibration, on-orbit measurements, science
624 data calibration and on-orbit validation. J. Geophys. Res. 116 (E10), E00G19–
625 .
626 URL http://dx.doi.org/10.1029/2011JE003797

627 Heinz, D., Chein-I-Chang, 2001. Fully constrained least squares linear spectral
628 mixture analysis method for material quantification in hyperspectral imagery.
629 Geoscience and Remote Sensing, IEEE Transactions on 39 (3), 529–545.

Kanner, L. C., Mustard, J. F., Gendrin, A., Apr. 2007. Assessing the limits of the modified gaussian model for remote spectroscopic studies of pyroxenes on mars. Icarus 187 (2), 442–456.
URL http://www.sciencedirect.com/science/article/B6WGF-4MK615R-3/2/38f09266a273ce0b9f2df7c7848f9515

Kruse, F. A., Lefkoff, A. B., Boardman, J. W., Heidebrecht, K. B., Shapiro, A. T., Barloon, P. J., Goetz, A. F. H., May 1993. The spectral image processing system (sips)–interactive visualization and analysis of imaging spectrometer data. Remote Sensing of Environment 44, 145–163.

Langevin, Y., Poulet, F., Bibring, J.-P., Gondet, B., Mar. 2005. Sulfates in the North Polar Region of Mars Detected by OMEGA/Mars Express. Science 307, 1584–1586.

Lawson, C. L., Hanson, R. J., Jul. 1995. Solving Least Squares Problems. SIAM (Society for Industrial and Applied Mathematics).
URL http://link.aip.org/link/?SIR/18/518/1

Le Mouëlic, S., Langevin, Y., Erard, S., May 1999. The distribution of olivine in the crater aristarchus inferred from clementine nir data. Geophys. Res. Lett. 26 (9), 1195–1198.
URL http://dx.doi.org/10.1029/1999GL900180

McCord, T. B., Hansen, G. B., Combe, J.-P., Hayne, P., Oct. 2010. Hydrated minerals on europa's surface: An improved look from the galileo nims investigations. Icarus 209 (2), 639–650.
URL http://www.sciencedirect.com/science/article/pii/S0019103510002186

Moussaoui, S., Hauksdóttir, H., Schmidt, F., Jutten, C., Chanussot, J., Brie, D., Douté, S., Benediktsson, J., Jun. 2008. On the decomposition of mars hyperspectral data by ica and bayesian positive source separation. Neurocomputing 71 (10-12), 2194–2208.
URL http://www.sciencedirect.com/science/article/B6V10-4RV17HX-4/1/739950d227add850ec0720718c1c2362

Murchie, S., Arvidson, R., Bedini, P., Beisser, K., Bibring, J.-P., Bishop, J., Boldt, J., Cavender, P., Choo, T., Clancy, R. T., Darlington, E. H., Des Marais, D., Espiritu, R., Fort, D., Green, R., Guinness, E., Hayes, J., Hash, C., Heffernan, K., Hemmler, J., Heyler, G., Humm, D., Hutcheson, J., Izenberg, N., Lee, R., Lees, J., Lohr, D., Malaret, E., Martin, T., McGovern, J. A., McGuire, P., Morris, R., Mustard, J., Pelkey, S., Rhodes, E., Robinson, M., Roush, T., Schaefer, E., Seagrave, G., Seelos, F., Silverglate, P., Slavney, S., Smith, M., Shyong, W.-J., Strohbehn, K., Taylor, H., Thompson, P., Tossman, B., Wirzburger, M., Wolff, M., May 2007. Compact reconnaissance imaging spectrometer for mars (crism) on mars reconnaissance orbiter (mro). J. Geophys. Res. 112 (E5), E05S03–.
URL http://dx.doi.org/10.1029/2006JE002682

672 Mustard, J. F., Li, L., He, G., Aug. 1998. Nonlinear spectral mixture modeling
673 of lunar multispectral data: Implications for lateral transport. Journal of
674 Geophysical Research 103, 19419–19426.

675 Mustard, J. F., Pieters, C. M., 1989. Photometric phase functions of common
676 geologic minerals and applications to quantitative analysis of mineral mixture
677 reflectance spectra. J. Geophys. Res. 94, –.
678 URL http://dx.doi.org/10.1029/JB094iB10p13619

679 Mustard, J. F., Pieters, C. M., Isaacson, P. J., Head, J. W., Besse, S., Clark,
680 R. N., Klima, R. L., Petro, N. E., Staid, M. I., Sunshine, J. M., Runyon,
681 C. J., Tompkins, S., Jun. 2011. Compositional diversity and geologic insights
682 of the aristarchus crater from moon mineralogy mapper data. J. Geophys.
683 Res. 116 (E6), E00G12–.
684 URL http://dx.doi.org/10.1029/2010JE003726

685 Mustard, J. F., Poulet, F., Gendrin, A., Bibring, J.-P., Langevin, Y., Gondet,
686 B., Mangold, N., Bellucci, G., Altieri, F., Mar. 2005. Olivine and Pyroxene
687 Diversity in the Crust of Mars. Science 307, 1594–1597.

688 Ohtake, M., Matsunaga, T., Haruyama, J., Yokota, Y., Morota, T., Honda, C.,
689 Ogawa, Y., Torii, M., Miyamoto, H., Arai, T., Hirata, N., Iwasaki, A., Naka-
690 mura, R., Hiroi, T., Sugihara, T., Takeda, H., Otake, H., Pieters, C. M., Saiki,
691 K., Kitazato, K., Abe, M., Asada, N., Demura, H., Yamaguchi, Y., Sasaki,
692 S., Kodama, S., Terazono, J., Shirao, M., Yamaji, A., Minami, S., Akiyama,
693 H., Josset, J.-L., Sep. 2009. The global distribution of pure anorthosite on
694 the moon. Nature 461 (7261), 236–240.
695 URL http://dx.doi.org/10.1038/nature08317

696 Pieters, C. M., Boardman, J., Buratti, B., Chatterjee, A., Clark, R., Glavich,
697 T., Green, R., Head III, J., Isaacson, P., Malaret, E., et al., 2009. The moon
698 mineralogy mapper (m3) on chandrayaan-1. Curr. Sci 96 (4), 500–505.

699 Poulet, F., Bibring, J.-P., Langevin, Y., Mustard, J., Mangold, N., Vincendon,
700 M., Gondet, B., Pinet, P., Bardintzeff, J.-M., Platevoet, B., May 2009a.
701 Quantitative compositional analysis of martian mafic regions using the
702 mex/omega reflectance data 1. methodology, uncertainties and examples of
703 application. Icarus 201 (1), 69–83.
704 URL http://www.sciencedirect.com/science/article/
705 B6WGF-4V8GB7J-7/2/2e4599e5853cac2cdc431481fefbbbf0

706 Poulet, F., Cuzzi, J. N., Cruikshank, D. P., Roush, T., Dalle Ore, C. M., Dec.
707 2002. Comparison between the Shkuratov and Hapke Scattering Theories for
708 Solid Planetary Surfaces: Application to the Surface Composition of Two
709 Centaurs. Icarus 160, 313–324.

710 Poulet, F., Gomez, C., Bibring, J.-P., Langevin, Y., Gondet, B., Pinet, P.,
711 Belluci, G., Mustard, J., Jul. 2007. Martian surface mineralogy from Ob-
712 servatoire pour la Minéralogie, l'Eau, les Glaces et l'Activité on board the

Mars Express spacecraft (OMEGA/MEx): Global mineral maps. Journal of Geophysical Research (Planets) 112, 8–+.

Poulet, F., Mangold, N., Platevoet, B., Bardintzeff, J.-M., Sautter, V., Mustard, J., Bibring, J.-P., Pinet, P., Langevin, Y., Gondet, B., Alon-Toppani, A., May 2009b. Quantitative compositional analysis of martian mafic regions using the mex/omega reflectance data: 2. petrological implications. Icarus 201 (1), 84–101.
URL http://www.sciencedirect.com/science/article/B6WGF-4VD9X90-2/2/33d7e179b191694bac08cc430f1ddf5f

Roberts, D., Gardner, M., Church, R., Ustin, S., Scheer, G., Green, R., Sep. 1998. Mapping chaparral in the santa monica mountains using multiple endmember spectral mixture models. Remote Sensing of Environment 65 (3), 267–279.
URL http://www.sciencedirect.com/science/article/pii/S0034425798000376

Schmidt, F., Bourguignon, S., Le Mouelic, S., Dobigeon, N., Theys, C., Treguier, E., 2011. Accuracy and performance of linear unmixing techniques for detecting minerals on omega/mars express. In: Hyperspectral Image and Signal Processing: Evolution in Remote Sensing (WHISPERS), 2011 3rd Workshop on DOI - 10.1109/WHISPERS.2011.6080858. pp. 1–4.

Schmidt, F., Douté, S., Schmitt, B., 2007. Wavanglet: An efficient supervised classifier for hyperspectral images. Geoscience and Remote Sensing, IEEE Transactions on 45 (5), 1374–1385.

Schmidt, F., Schmidt, A., Treguier, E., Guiheneuf, M., Moussaoui, S., Dobigeon, N., 2010. Implementation strategies for hyperspectral unmixing using bayesian source separation. Geoscience and Remote Sensing, IEEE Transactions 48 (11), 4003–4013.

Schmidt, F., Verdier, M., Legendre, M., Schmidt, A., Moussaoui, S., 2012. Accurate database for linear unmixing under constraints. In: EPSC (Madrid, 23-28 September 2012).
URL http://meetingorganizer.copernicus.org/EPSC2012/EPSC2012-887-1.pdf

Settle, J., Drake, N., 1993. Linear mixing and the estimation of ground cover proportions. International Journal of Remote Sensing 14 (6), 1159–1177.

Shkuratov, Y., Starukhina, L., Hoffmann, H., Arnold, G., Feb. 1999. A model of spectral albedo of particulate surfaces: Implications for optical properties of the moon. Icarus 137 (2), 235–246.
URL http://www.sciencedirect.com/science/article/B6WGF-45GMFKB-5T/2/2b056567d27e74edbaf976c01f89d10f

Stamnes, K., Tsay, S.-C., Jayaweera, K., Wiscombe, W., Jun. 1988. Numerically stable algorithm for discrete-ordinate-method radiative transfer in multiple scattering and emitting layered media. Appl. Opt. 27, 2502–2509.

Sunshine, J. M., Pieters, C. M., May 1993. Estimating modal abundances from the spectra of natural and laboratory pyroxene mixtures using the modified Gaussian model. Journal of Geophysical Research 98, 9075–9087.

Themelis, K. E., Rontogiannis, A. A., Koutroumbas, K. D., Feb. 2012a. A Novel Hierarchical Bayesian Approach for Sparse Semisupervised Hyperspectral Unmixing. IEEE Transactions on Signal Processing 60, 585–599.

Themelis, K. E., Schmidt, F., Sykioti, O., Rontogiannis, A. A., Koutroumbas, K. D., Daglis, I. A., Aug. 2012b. On the unmixing of mex/omega hyperspectral data. Planetary and Space Science 68 (1), 34–41.
URL http://www.sciencedirect.com/science/article/pii/S0032063311003497

Vincendon, M., 2013. Mars surface phase function constrained by orbital observations. Planetary and Space Science 76 (0), 87 – 95.
URL http://www.sciencedirect.com/science/article/pii/S0032063312003820

Vincendon, M., Langevin, Y., Poulet, F., Bibring, J.-P., Gondet, B., Jul. 2007. Recovery of surface reflectance spectra and evaluation of the optical depth of aerosols in the near-IR using a Monte Carlo approach: Application to the OMEGA observations of high-latitude regions of Mars. Journal of Geophysical Research (Planets) 112, 8–+.

Winter, M. E., 1999. N-findr: an algorithm for fast autonomous spectral end-member determination in hyperspectral data, 266–275.
URL http://dx.doi.org/10.1117/12.366289

Chapitre 2

Imagerie spectro-photométrique

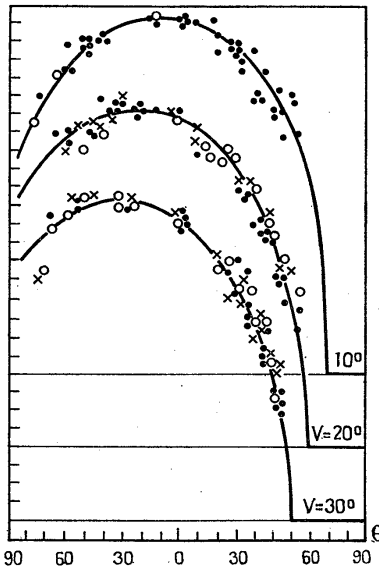


Figure 5

Réflectance de la région claire “Amazonis” de Mars en fonction de V l’angle de phase Soleil-Mars-Terre (changeant au fil des mois) et de θ l’angle de position par rapport au centre du disque martien observé (changeant au fil de la journée) (D’après *“Propriétés photométriques des contrées désertiques sur la planète Mars.”* d’Audouin Dollfus en 1957 *[69])*

La photométrie concerne l'étude du comportement de la réflectance d'une surface en fonction de la géométrie d'observation. En général, les angles sont notés comme la figure 2.1.

Le cosinus des angles d'incidence/émergence est noté $\mu = \cos(\theta)$ and $\mu' = \cos(\theta')$.

La manière dont l'énergie réfléchie est distribuée, est décrite par la réflectance bi-directionnelle ρ, c'est à dire le rapport des radiances incidentes I et émergentes I' en W.m^{-2}.sr^{-1}, dépendant à la fois de la direction d'incidence s et d'émergence s'. Cette quantité est notée BRDF pour "Bidirectional Reflectance Distribution Function" :

$$\rho(s,s') = \frac{I'}{\pi I \mu} \tag{2.1}$$

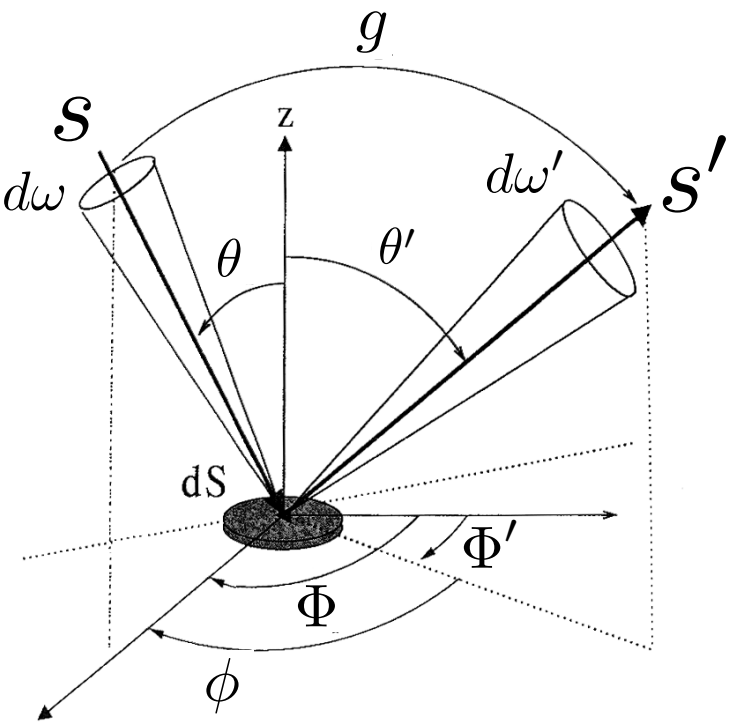


FIGURE 2.1: Définition des angles en photométrie : angle solide d'incidence $d\omega$ dans la direction s, angle solide d'émergence $d\omega'$ dans la direction s', direction normale à la surface z, angle d'incidence θ, angle d'émergence θ', angle de phase g, angle d'azimut d'incidence Φ par rapport à la direction du Nord, angle d'azimut d'émergence Φ' par rapport à la direction du Nord, angle d'azimut relatif ϕ (figure d'après [77]).

Les propriétés physiques de la surface comme la rugosité, la compacité, la taille et la forme des grains déterminent la BRDF. De ce fait, l'étude de la BRDF permet d'estimer les propriétés des régolites planétaires et les processus qui les façonnent.

Le premier sous-chapitre décrit le contexte des observations de BRDF martiennes, sans atmosphère (voir section 2.1.1), puis avec atmosphère (voir section 2.1.2). Dans un second temps, je décrierai mes contributions personnelles, essentiellement développées au cours de la thèse de Jennifer Fernando (voir section 2.2). Enfin, les perspectives de ces travaux seront dressées dans la section 2.3 page 84.

2.1 Contexte

Les observations photométriques d'une même surface, vues sous différents angles sont très récentes dans l'exploration martienne et font l'objet de mes investigations personnelles. Historiquement, les études photométriques ont toujours considéré l'observation une étendue supposée homogène (la planète

entière ou une portion de terrain vu des rovers) géométriques. L'observation la plus facilement accessible depuis un télescope ou depuis une sonde en orbite, est l'assombrissement centre-bord de la planète entière. Les premières mesures photométriques télescopiques de Mars datent des années 1950 [69] (voir illustration page 75). Pour Mars, les 7300 observations de la sonde Mariner 9 ont permis une estimation de la réflectance de surface en utilisant un modèle de Minnaert, et une modélisation de l'atténuation par les aérosols [317]. En utilisant 9000 images Viking, les études suivantes ont découvert que l'effet d'opposition est omniprésent, plus marqué et de largeur angulaire plus faible pour les terrains brillants [318]. Des études photo-polarimétriques au sol [70], mais aussi grâce à l'instrument VPM de Mars-5 [71] ont permis de déterminer des tailles de grains très faibles (<50 microns) sur Mars.

Plus récemment, de nombreux travaux théoriques ont permis d'établir, puis de résoudre, l'équation du transfert radiatif dans le cadre d'un régolite granulaire compact [119, 115, 116, 117, 118, 121, 122, 297, 73].

Grâce aux rovers, l'accès à la photométrie locale est possible, même si en général l'étude se fait sur des zones spatialement étendues, supposées homogènes mais ayant des conditions d'observations différentes, par exemple Viking [7] et Pathfinder [146]. L'analyse, in situ des rovers MER Spirit [148] et Opportunity [147], ont montré des terrains globalement rétrodiffusants dû à la présence de poussière atmosphérique. Ces études ont montré une diversité photométrique plutôt diffusante vers l'avant (roche grise sur Spirit) ou rétrodiffusante (sphérules formés de couches concentriques sur Opportunity [106]).

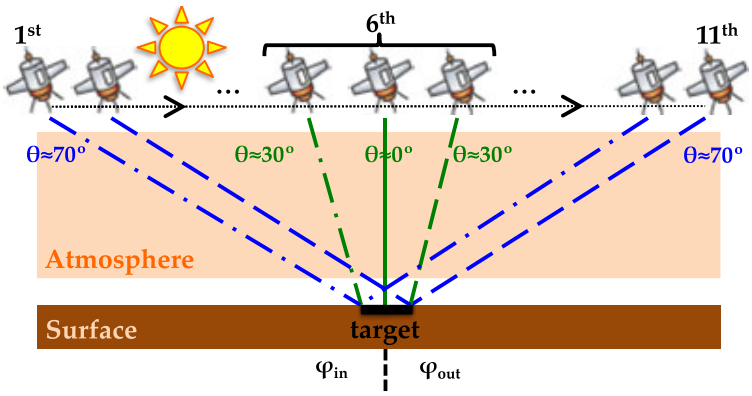


FIGURE 2.2: Géométrie d'observation de l'instrument CRISM en mode FRT (figure d'après [35]).

Des instruments spatiaux en mode "Emission Phase Function" (EPF) ont permis pour la première fois d'enregistrer la réflectance de la même zone, vue sous des conditions d'illumination identique, mais avec des directions d'observations différentes. A partir des observations en orbite grâce à l'instrument TES dans l'infrarouge thermique, à bord de Mars Global Surveyor en mode EPF une étude couplée surface et atmosphère a été réalisée [48, 51]. Aussi, l'instrument HRSC dans le visible a montré que la surface de Mars avait des comportements photométriques spatialement hétérogènes [145]. Dans l'infrarouge proche, l'instrument OMEGA a fonctionné ponctuellement en mode EPF [257]. Des analyses plus récentes, compilant un grand jeux de données OMEGA avec des observations essentiellement au nadir, corrigées des aérosols ont estimé la BRDF moyenne de Mars, légèrement rétrodiffusante [331]. Cependant, cette approche est incohérente car la correction atmosphérique se fait sous l'hypothèse d'une surface lambertienne. Entre Octobre 2006 et Septembre 2010, l'instrument CRISM a fonctionné de manière nominale en mode EPF, nommé FRT, avec 11 géométries d'observation pour chaque séquence, 5 observations en avant d'émergence ~70° à ~30° à 180 m/pixel, puis une observation centrale à 18 m/pixel d'incidence $\pm 30°$, puis 5 observations en arrière de ~30° à ~70° à 180 m/pixel (voir figure 2.2). Depuis Septembre 2010, un problème technique de rotation du cardan du miroir empêche l'acquisition dans ce mode FRT mais plusieurs milliers d'images ont été acquises.

De précédentes études suggèrent que les corrections atmosphériques ne sont pas nécessaires dans le cas d'un faible contenu d'aérosols, ou qu'au moins, l'effet de l'atmosphère est mineur de manière à identifier les changements de propriétés photométriques en surface [257, 145]. Néanmoins, nous avons

développé une méthode pour corriger les effets des aérosols basés sur le formalisme de Green et une inversion bayesienne (voir chapitre 2.2). D'autres études d'inversion couplées surface-atmosphère des images CRISM ont abouti à la BRDF de surface [293] en utilisant le code de transfert radiatif DISORT, avec une version simplifiée de la BRDF de Hapke sans rugosité et un modèle à 15 couches atmosphériques. Cette étude a utilisé une stratégie d'inversion de type moindre carré de Levenberg-Marquardt. Ce travail sur le site d'Opportunity a montré que les éjectas du cratère sont plus rétrodiffusants, bien qu'une comparaison avec les données in situ soit difficile à cause de l'absence de rugosité.

Les deux prochaines sections décrivent les différents modèles analytiques de la BRDF et la formulation analytique de Green qui nous ont amené à établir notre méthode d'analyse des images CRISM.

2.1.1 Modèle de BRDF de régolite

2.1.1.1 Lambert

Le modèle de BRDF le plus simple est le modèle de Lambert, supposant l'isotropie totale :

$$\rho(s,s') = \frac{\rho_L \mu}{\pi} \tag{2.2}$$

Dans ce cas, le terme ρ_L est noté albédo lambertien.

2.1.1.2 Minnaert

L'approximation de Minnaert [224, 82] dépend de deux paramètres : la réflectance normale ρ_M et l'exposant k :

$$\rho(s,s') = \frac{\rho_M}{\pi} \mu^k \mu'^{k-1} \tag{2.3}$$

Bien que plus précise que le modèle lambertien, la limitation majeure de l'approximation de Minnaert concerne le manque de réalisme des effets de surface, comme la rugosité. Par ailleurs, l'exposant k n'a pas de signification physique.

2.1.1.3 Noyaux

Pour faciliter l'inversion des paramètres photométriques [199], la BRDF peut être décomposée dans une somme semi-empirique de termes connus : les noyaux. Par exemple, la forme de la BRDF, développée initialement pour des zones de végétation [275], peut s'écrire de la manière suivante :

$$\rho(s,s') = \rho_{iso} + \rho_{vol}.K_{vol}(s,s') + \rho_{geo}.K_{geo}(s,s') \tag{2.4}$$

avec un terme isotrope, un terme de diffusion en volume K_{vol} et un terme géométrique de rugosité de surface K_{geo}, tous trois pondérés par des facteurs ρ_{iso}, ρ_{vol} et ρ_{geo} , dépendants de la nature de la surface.

Le noyau de diffusion en volume K_{vol} le plus utilisé est le modèle de "RossThick" [274, 275] :

$$K_{vol}(s,s') = \frac{4}{3\pi} \frac{1}{\mu + \mu'} \left[\left(\frac{\pi}{2} - g \right) \cos g + \sin g \right] - \frac{1}{3} \tag{2.5}$$

Le noyau de surface K_{geo} peut être écrit de la manière suivante dans le modèle "Li-Sparse" :

$$\begin{aligned} K_{geo}(s,s') &= \frac{1}{2\pi} \left[(\pi - \phi) \cos\phi + \sin\phi \right] - \frac{1}{\pi} \left(\tan\theta + \tan\theta' \right) \\ &\quad - \frac{1}{\pi} \sqrt{\tan^2\theta + \tan^2\theta' - 2\tan\theta \tan\theta' \cos\phi}\, \Phi' \Phi \end{aligned} \tag{2.6}$$

Dans le modèle "LiSparse-R" [192, 335], le noyau K_{geo} est défini de manière non-analytique par son expression inverse.

2.1.1.4 Modèle de Hapke pour les matériaux granulaires

La forme analytique de BRDF la plus utilisée est la théorie phénoménologique de Hapke, basée sur la théorie du transfert radiatif, adaptée pour les matériaux granulaires compacts [117] :

$$\rho(s,s') = \frac{\omega}{4\pi}\frac{\mu}{\mu+\mu'}\left\{(1+B(g))\,p(g)+M(s,s',\omega)\right\}S(s,s',\bar{\Theta}) \tag{2.7}$$

Dans le cadre de Hapke, le matériau granulaire est décrit par des paramètres dépendants de la longueur d'onde (au travers de leur dépendance dans les parties réelles n et imaginaires des κ des indices de réfractions des matériaux spécifiques) et de la géométrie des grains (taille, forme, irrégularités) : le coefficient de diffusion Q_S, le coefficient d'extinction Q_E et la fonction de phase $p(g)$. Aussi, la surface du matériau granulaire est décrite par deux quantités : l'angle moyen des pentes $\bar{\Theta}$ indiquant la rugosité, et le paramètre de compacité de l'effet d'opposition h. On note qu'en absence de diffusion multiple, de masquage des ombres et d'effet d'opposition, ce modèle est équivalent à celui de Lommel-Seeliger $\rho(s,s') = \frac{\omega}{4\pi}\frac{\mu}{\mu+\mu'}\{p(g)\}$ [290].

2.1.1.4.1 Fonction de phase La fonction de diffusion moyenne des grains, ou fonction de phase, décrit la fraction d'énergie diffusée dans la direction g par rapport à un flux incident. La fonction de Henyey-Greenstein à double lobe semble le meilleur compromis entre complexité et adéquation avec les observations des grains naturels [124] :

$$p(g) \quad = \quad \frac{1-f}{2}\frac{1-a^2}{(1+a^2+2\cos g)^{3/2}} + \frac{1+f}{2}\frac{1-a^2}{(1+a^2-2\cos g)^{3/2}} \tag{2.8}$$

Le paramètre f décrit la diffusion, vers l'avant ou l'arrière. Le paramètre a, décrit la largeur du lobe.

2.1.1.4.2 Diffusion multiple La fonction de diffusion multiple $M(s,s',\omega)$ peut être évaluée numériquement pour des matériaux isotropes [36] et anisotropes [117]. Une expression analytique a été proposée dans le cadre isotrope [119] :

$$M(s,s',\omega) = H(\mu)H(\mu') - 1 \tag{2.9}$$

avec $H(x) = \frac{1+2x}{1+2x\sqrt{1-\omega}}$

Plus récemment, Hapke a proposé une forme plus précise pour des diffuseurs non isotropes [118] :

$$M(s,s',\omega) = P^{\downarrow\downarrow}(\mu)[H(\mu')-1] + P^{\uparrow\uparrow}(\mu')[H(\mu)-1] + P^{\uparrow\downarrow}[H(\mu')-1][H(\mu)-1] \tag{2.10}$$

avec $H(x) = \left[1-\omega x\left(r_0 + \frac{1-2r_0x}{2}\ln\frac{1+x}{x}\right)\right]^{-1}$

2.1.1.4.3 Masquage des ombres dû à la rugosité macroscopique Selon le modèle de Hapke [115], la rugosité de surface, caractérisée par sa pente moyenne $\bar{\Theta}$, est à l'origine d'une fonction de masquage des ombres $S(\mu,\mu',\bar{\Theta})$ dans l'équation 2.7. Il s'agit de modéliser comment se forme une ombre sur une surface rugueuse en fonction des conditions d'éclairement. Aussi, cette fonction modélise la fraction de surface éclairée vu de l'observation. La formulation explicite est donnée dans les équations (57)-(58) de son livre [115].
Aussi, Hapke définit deux nouvelles directions équivalentes $(s'_{eq}, s'_{eq}) = f(s,s',\bar{\Theta})$ de manière à échantillonner la BRDF équivalente pour une surface plane. La forme mathématique complexe est défini dans les équations (32), (46)-(49) de [115].

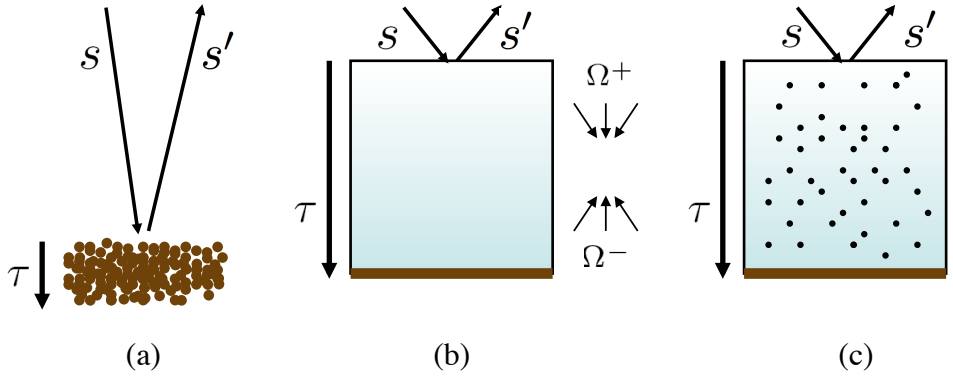


FIGURE 2.3: Schéma du transfert radiatif : (a) pas d'atmosphère (b) atmosphère non diffusante (c) atmosphère diffusante 1-d plan parallèle

2.1.1.4.4 Effet d'opposition L'effet d'opposition est l'augmentation de la réflectance lorsque l'angle de phase est très faible. Il est décrit par la fonction $B(g)$ [116] :

$$B(g) \quad = \quad B_0/[1+\tan(g/2)/h)] \tag{2.11}$$

avec h qui représente la compacité et B_0 l'intensité de cet effet.

2.1.1.5 Autres expressions analytiques

D'autres expressions analytiques de la BRDF ont été proposées dans la littérature, cependant, elles ne justifient pas d'être décrites dans ce manuscrit. Par exemple, citons des approximations pour les sols granulaires [200, 244] ou la végétation [306, 274, 325, 244, 27, 258, 66, 327, 193, 194].

2.1.2 Effet de l'atmosphère

L'effet de l'atmosphère peut être approximé à un problème de transfert radiatif en géométrie plan parallèle" (voir fig. 2.3 (b)). La diffusion dans l'atmosphère change les directions d'incidence et ajoute un parcours optique plus grand, ce qui amène un degré de complexité supplémentaire dans la résolution du transfert radiatif. Ce problème a été défini dans le livre de Chandrasekhar, il y a plus de 50 ans [36] et a été résolu pour une surface lambertienne. Durant des dizaines d'années, plusieurs auteurs ont étudié ce problème[309, 269] mais la solution générale, tenant compte d'une BRDF de surface quelconque n'a été proposée que récemment grâce au formalisme de Green [201].

Pour une atmosphère plan-parallèle, Lyapustin et co-auteurs [201] proposent d'introduire les fonctions de Green suivantes : la réponse impulsionnelle de l'atmosphère illuminée du haut dans la direction s, observée au niveau optique τ dans la direction s', : $G^{\downarrow}(\tau,s,s')$, respectivement, avec une illumination d'en bas $G^{\uparrow}(\tau,s,s')$. La profondeur optique de l'atmosphère est notée τ_0.

En utilisant le formalisme de Chandrasekhar, nous pouvons introduire : S la fonction de diffusion décrivant la réflexion diffuse, T la fonction de transmission décrivant la transmission diffuse, et A la fonction d'atténuation décrivant l'atténuation du trajet direct. La fonction de Green s'écrit :

$$G^{\downarrow}(\tau,s,s') = A^{\downarrow\downarrow}(\tau,s,s') + T^{\downarrow\downarrow}(\tau,s,s') + S^{\downarrow\uparrow}(\tau,s,s') \tag{2.12}$$

La première flèche de l'exposant décrit la direction incidente, la seconde la direction émergente.

Au sommet de l'atmosphère, le seul terme non nul correspond à la réflexion diffuse : $G^{\downarrow}(0,s,s') = S^{\downarrow\uparrow}(0,s,s')$.

A la base de l'atmosphère, la fonction de Green vaut : $G^{\downarrow}(\tau_0,s,s') = A^{\downarrow\downarrow}(\tau_0,s,s') + T^{\downarrow\downarrow}(\tau_0,s,s')$.

Pour une atmosphère non diffusante, l'atténuation s'écrit [36] :

$$A^{\downarrow\downarrow}(\tau,s,s') = \delta(s-s').\exp^{-\tau/\mu'} \tag{2.13}$$

Les fonctions S et T dépendent des diffuseurs dans l'atmosphère (quantité, distribution, taille de grain, forme de grain, composition, ...) et peuvent être modélisées par des méthodes de type transfert radiatif ou Monte Carlo. En négligeant les effets de diffusions multiples, une approximation semi-analytique a été proposée en utilisant les diffusions de Mie and Rayleigh diffusion [82]. Aussi, un modèle empirique comportant les diffusions de Rayleigh a été publié [326].

La source solaire est décrit comme la fonction suivante : $S_\lambda = F_\lambda.\delta(s-s_0)$ à $\tau = 0$.

L'opérateur de propagation de la radiance dans toutes les directions vers le bas (Ω^+) est :

$$\Gamma_\tau^{\downarrow+}... = \int_{\Omega^+} dsG^{\downarrow}(\tau,s,s')... \tag{2.14}$$

Par exemple, la radiance de sortie vers le haut, au sommet de l'atmosphère dû à la réflexion diffuse, est : $I(0,s,s') = \Gamma_0^{\downarrow+}.S_\lambda = G^{\downarrow}(0,s,s').F_\lambda = S^{\downarrow\uparrow}(0,s,s').F_\lambda$

Nous définissons de la même manière, l'opérateur de propagation de la radiance dans toutes les directions vers le haut (Ω^-) $\Gamma_\tau^{\uparrow-}$ et l'opérateur de réflexion en surface (à $\tau = \tau_0$) comme $R^{\downarrow\uparrow}$.

La radiance montante, qui quitte la surface avant les interactions multiples entre surface et atmosphère, est :

$$J_-^0(\tau_0,s) = R^{\downarrow\uparrow}.\Gamma_{\tau=\tau_0}^{\downarrow+}.S_\lambda \tag{2.15}$$

La radiance observée au sommet de l'atmosphère, est la somme des contributions suivantes :

$$\begin{aligned} I(0,s,s') &= \Gamma_{\tau=0}^{\downarrow+}.S_\lambda + \Gamma_{\tau=0}^{\uparrow-}.J_-^0(\tau,s) + \\ &\quad \Gamma_{\tau=0}^{\uparrow-}.\left[R^{\downarrow\uparrow}.\Gamma_{\tau=\tau_0}^{\uparrow-}\right]^1.J_-^0(\tau_0,s) + ... \end{aligned} \tag{2.16}$$

Le premier terme représente la réflexion diffuse de l'atmosphère, le second terme, la lumière qui se réfléchit qu'une fois en surface. Les autres termes représentent les différents ordres d'interactions multiples entre surface et atmosphère. Dans le cas général, la solution est :

$$\begin{aligned} I(0,s,s') &= \Gamma_{\tau=0}^{\downarrow+}.S_\lambda + \\ &\quad \Gamma_{\tau=0}^{\uparrow-}.\left[Id - R^{\downarrow\uparrow}.\Gamma_{\tau=\tau_0}^{\uparrow-}\right]^{-1}.R^{\downarrow\uparrow}.\Gamma_{\tau=\tau_0}^{\downarrow+}.S_\lambda \end{aligned} \tag{2.17}$$

Dans le cas d'une atmosphère non diffusante, cette équation se simplifie en :

$$I(0,s,s') = F_\lambda e^{-\tau_0/\mu}\mu\rho(s,s')e^{-\tau_0/\mu'} \tag{2.18}$$

Les termes additionnelles dus à la diffusion sont : $\Gamma_{\tau=0}^{\downarrow+}.S_\lambda$ qui représente la lumière diffusée dans l'atmosphère et $\left[Id - R^{\downarrow\uparrow}.\Gamma_{\tau=\tau_0}^{\uparrow-}\right]^{-1}$ qui est l'opérateur des interactions multiples entre surface et atmosphère.

2.2 Contributions

Mes contributions majeures dans l'estimation des propriétés photométriques de la surface de Mars concernent la mise en place d'une inversion bayesienne. Le but est de maîtriser la propagation des erreurs et de valider la méthode sur les données in-situ. Ces contributions ont été réalisées au cours de la thèse de Jennifer Fernando.

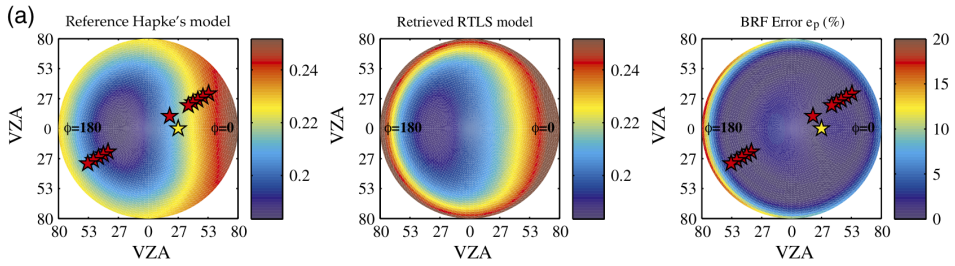


FIGURE 2.4: Exemple de résultats de Mars-ReCO d'après [35]. A gauche : la BRDF de surface, généré d'après le modèle de Hapke. Au centre : l'estimation de la BRDF de surface avec Mars-ReCO, dans le cas de $\tau = 0.5$. A droite : l'erreur, exprimé en %

J'ai également développé des outils d'inversion de type Monte Carlo par chaîne de Markov (MCMC), suffisamment rapides pour estimer les paramètres des modèles photométriques et leurs incertitudes. Cette approche a nécessité la prise en compte de la propagation des erreurs de mesure au sommet de l'atmosphère, à la BRDF de surface, jusqu'aux paramètres de photométriques de Hapke. Dans un premier temps, nous décrirons la méthode de correction atmosphérique, appelée Mars RecO, développée au cours de la thèse de Xavier Ceamanos. Puis, nous détaillerons l'inversion bayesienne et la comparaison avec les données in situ des rovers MER, développées au cours de la thèse de Jennifer Fernando.

Récemment, d'autres études d'inversion couplés surface-atmosphère des images CRISM ont analysé la BRDF de surface [293] en utilisant, la BRDF de Hapke sans rugosité et un modèle à 15 couches atmosphériques, avec une stratégie d'inversion de type moindre carré de Levenberg-Marquardt. Notre approche permet de propager les incertitudes de mesure de manière plus précises et plus rapides, d'estimer la BRDF de surface et son incertitude, et d'analyser les résultats avec un modèle de Hapke complet. Notre approche repose sur l'hypothèse d'une BRDF à noyau qui pourrait être limitante, néanmoins, nos différents tests synthétiques ont montré la validité pour plusieurs surfaces de propriétés photométriques différentes, caractéristiques de Mars. Nous nous sommes limité à une seule longueur d'onde alors que l'étude de Shaw et al. a utilisé plusieurs longueurs d'onde [293].

2.2.1 Mars-REcO

La stratégie Mars-RecO, inspiré de la méthode MAIAC [202], fait l'hypothèse que la BRDF de surface peut être décrite par un modèle à noyaux de type "Ross-Thick Li-Sparse" à trois paramètres ρ_{iso}, ρ_{vol}, ρ_{geo} (voir équation 2.4 et section 2.1.1.3). Le transfert radiatif dans l'atmosphère est décrit grâce à la formulation de Green (voir équation 2.17) qui exprime de manière analytique la BRDF au sommet de l'atmosphère, en fonction des trois paramètres :

$$R(s_i,s_r) = R^D(s_i,s_r) + \rho_{iso}F^{iso}(s_i,s_r) + \rho_{vol}.R^{vol}(s_i,s_r) + \rho_{geo}.R^{geo}(s_i,s_r) + R^{nl}(s_i,s_r) \tag{2.19}$$

La modélisation directe du transfert radiatif est une simple multiplication matricielle, car les termes non-linéaire R^{nl} sont très faibles pour les situations les plus caractéristiques de Mars $\tau < 2$. Les différents termes R^D, F^{iso}, R^{vol}, R^{geo} et R^{nl} sont estimés dans une table en fonction de τ en utilisant les propriétés optiques des aérosols déterminés par Wolff et al. [340] dans le code numérique DISORT [305]. L'inversion bayesienne est réalisée itérativement [202], de manière à estimer les valeurs de ρ_{iso}, ρ_{vol}, ρ_{geo} mais aussi leurs incertitudes. La BRDF de surface est tout simplement le modèle de noyau de l'équation 2.4 avec les valeurs de la solution bayesienne. En supposant les incertitudes initiales de forme gaussienne et comme le modèle est pseudo linéaire, les incertitudes finales sont aussi gaussiennes [310]. Les tests synthétiques ont montré qu'il est possible de corriger les effets de l'atmosphère avec les conditions suivantes $\tau < 2$, incidence $\theta < 60°$, azimut relatif $\phi < 60°$ (voir figure 2.4).

Dans le cadre du traitement des données CRISM, nous avons choisi de ré-échantillonner la BRDF de surface estimée par Mars-ReCO aux géométries initiales CRISM, car il s'agit de nos données initiales

et les résultats dans d'autres géométries peuvent être hasardeuses, comme l'ont montrés nos tests synthétiques. D'autre part, le modèle à noyau décrit la BRDF de surface avec seulement trois paramètres, ce qui facilite son estimation d'après les 11 géométries d'acquisition CRISM. Cependant, le modèle à noyau ne permet pas une interprétation des propriétés de surface, et ses possibilités de BRDF sont plus réduites qu'un modèle plus précis, comme celui de Hapke. Le but final de Mars-RECO est d'estimer la réflectance, corrigée des effets des aérosols, de manière à réaliser une seconde inversion, en utilisant par exemple le modèle de Hapke (voir section suivante).

Cette méthode est pour l'instant établie pour une seule longueur d'onde (750 nm) mais les calculs peuvent être facilement étendus à plusieurs longueurs d'ondes. La méthode nécessite une estimation de l'opacité de l'atmosphère (avec son incertitude, propagée dans l'incertitude de la BRDF de surface). Nous avons choisi d'utiliser les données de Wolff et al., bien que leur estimation se fait pour des surfaces lambertiennes [340]. D'autres nouvelles méthodes sont en cours pour une estimation de l'opacité [76].

Pour plus d'information, l'article est disponible à la section 2.4.1.

2.2.2 Inversion bayésienne et comparaison avec les données in situ

L'analyse de la BRDF de surface, directement accessible depuis l'espace sur un corps sans atmosphère comme la Lune, ou depuis les rovers in-situ, ou après une correction atmosphérique comme Mars-ReCO, peut se faire grâce à un outil rapide de modélisation du transfert radiatif dans les milieux granulaires. Les méthodes de type tracé de rayons [109, 140], ou de résolution de la propagation des ondes électromagnétiques [321], bien qu'intéressants pour étudier le transfert radiatif dans les milieux compacts denses, ne sont pas adaptés pour l'analyse de données car leur temps de calcul est trop long. Nous avons choisi d'utiliser le modèle de Hapke (voir section 2.1.1.4) car il a été largement utilisé pour l'analyse des données in-situ de Mars [148, 147]. Cependant, ce modèle est vivement critiqué pour ces simplifications abusives [297] et les interprétations des paramètres sont difficiles. Des études de laboratoires sont nécessaires pour aider à comprendre les observations [215, 302].

Dans le but d'une validation de l'approche Mars-ReCO, nous souhaitons comparer les BRDF in-situ avec les BRDF estimées par Mars-ReCO. Pour cela, la seule solution possible est d'utiliser le modèle de Hapke de 1994 (voir section 2.1.1.4). Ce modèle non-linéaire analytique est suffisamment simple pour réaliser une inversion de type bayésienne par méthode Monte Carlo, la solution étant décrite par une chaîne de Markov [229]. L'intérêt de cette méthode est de propager très précisément les incertitudes de mesures de la BRDF de surface vers les paramètres du modèle de Hapke. Les résultats sont tout simplement des densités de probabilités pour chacun des paramètres, comme présentés à la figure 2.5. Cette figure montre l'intérêt de fusionner plusieurs observations CRISM de la même zone, lorsqu'il n'y a pas de changement majeur d'état de surface, pour mieux contraindre les propriétés photométriques de la surface. Les études précédentes utilisaient des méthodes d'analyse de type moindre-carré [148, 147] ou algorithme génétique [145] qui ne donnaient pas accès aux incertitudes avec autant de précision. C'est le cas, notamment, de plusieurs solutions qui n'étaient pas correctement gérées avec ces outils.

De manière générale, les estimations des paramètres de Hapke sont compatibles avec les données in-situ des rovers à la fois sur les sites de Meridiani et de Gusev. Les albédos de diffusion simples sont compatibles avec l'unité géologique dominante à l'échelle des observations CRISM : les sols. La différence majeure concerne la rugosité qui est plus importante d'après nos analyses, à 400 m de résolution, dû à la présence de blocs en surface, non inclus dans les analyses in-situ à plus petite échelle. D'autre part, nous avons démontré que sur ces sites, une image CRISM seule n'a pas suffisamment d'information pour contraindre les paramètres photométriques. Le site du rover Spirit à Gusev a été couvert par 3 observations CRISM, comportant des échantillonnages angulaires complémentaires, suffisant pour bien contraindre les paramètres photométriques. Le site d'Opportunity à Meridiani est plus difficile à étudier car la combinaison des données CRISM disponibles (3 observations sur le trajet du rover) ne permet pas de contraindre les paramètres photométriques très précisément. Nos travaux en cours permettront de réaliser des cartes photométriques autour du site des rovers pour aboutir à des interprétations plus précises des processus géologiques à la surface de Mars.

Pour plus d'information, l'article est disponible à la section 2.4.2.

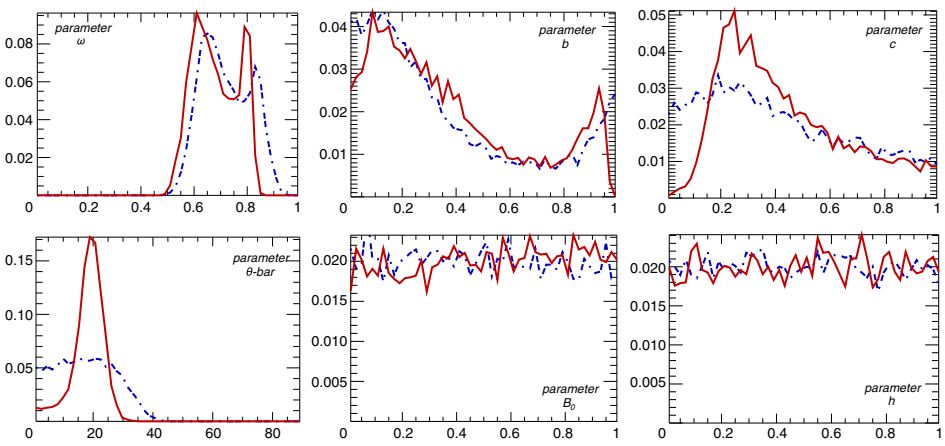


FIGURE 2.5: Exemple de résultats de l'inversion bayésienne pour les 6 paramètres de Hapke, dans le cas d'une seule observation CRISM (10 géométries en bleu) et de la fusion de 3 observations CRISM (27 géométries en rouge)

2.3 Perspectives

2.3.1 Perspectives méthodologiques

La perspective à court terme la plus intéressante est l'extension de Mars ReCO sur plusieurs pixels, car la méthode est très rapide (<1seconde/pixel). L'inversion bayésienne du modèle de Hapke est plus lent (~1 minute/pixel), mais permet le traitement d'une image complète. Des travaux en cours dans la thèse de Jennifer Fernando vont dans ce sens.

A moyen terme, la réalisation de l'inversion sur plusieurs longueurs d'onde est extrêmement intéressante car elle permettra d'estimer les propriétés photométriques qui peuvent dépendre de la longueur d'onde [263].

A plus long terme, le développement d'une méthode d'inversion de l'opacité des aérosols et de la BRDF de surface directement sur les observations CRISM est envisageable et elle s'affranchirait de l'éventuel biais actuel de l'estimation préalable de l'opacité des aérosols de Wolff et al., déterminée sous l'hypothèse de surface lambertienne.

2.3.2 Perspectives planétologiques

Les perspectives planétologiques sont nombreuses, car autant la dimension spectrale de la réflectance a été très largement étudiée, autant la dimension photométrique est très peu utilisée, car plus difficile d'accès à la fois en termes de mesure (surtout dans le cas d'une carte photométrique), mais aussi en termes d'analyse. Nous avons développé des outils novateurs qui contribuent à des nouvelles interprétations des données de spectro-photo-imagerie. L'instrument CRISM a acquis plusieurs milliers d'images dans des régions très différentes de Mars en contextes sédimentaire, volcanique, de dépôts éoliens ou de dépôts de glace. Après la phase de validation de l'approche, nous souhaitons maintenant déterminer les propriétés micro-physiques des surfaces afin d'étudier les processus de surface.

De manière générale, il serait intéressant d'étendre ce type d'analyse à d'autre corps, comme sur la Lune ou sur les satellites de glaces, afin d'étudier les processus de surface. La dégradation sous l'effet du bombardement de météorites et de particules solaires, appelée "space weathering", pourrait notamment, être caractérisée par photométrie des surfaces planétaires (voir section6.3)

2.4 Publications

Co-encadrement de thèses de Doctorat :

– J. Fernando

Publications scientifiques :

– Ceamanos, X., Doute, S., Fernando, J., **Schmidt, F.**, Pinet, P. & Lyapustin, A. (2013), « Surface reflectance of Mars observed by CRISM/MRO : 1. Multi-angle Approach for Retrieval of Surface Reflectance from CRISM Observations (MARS-ReCO) », Journal of Geophysical Research, 118, 1-20 (voir section 2.4.1).
– Fernando, J., **Schmidt, F.**, Ceamanos, X., Pinet, P., Douté, S. & Daydou, Y. (2013), « Surface reflectance of Mars observed by CRISM/MRO : 2. Estimation of surface photometric properties in Gusev Crater and Meridiani Planum », Journal of Geophysical Research, 118, 1-26 (voir section 2.4.2 page 106).

2.4.1 Mars-ReCO

Cette section contient l'article suivant :

Ceamanos, X., Doute, S., Fernando, J., Schmidt, F., Pinet, P. & Lyapustin, A. (2013), « Surface reflectance of Mars observed by CRISM/MRO : 1. Multi-angle Approach for Retrieval of Surface Reflectance from CRISM Observations (MARS-ReCO) », Journal of Geophysical Research, 118, 1-20

JOURNAL OF GEOPHYSICAL RESEARCH: PLANETS, VOL. 118, 1–20, doi:10.1029/2012JE004195, 2013

Surface reflectance of Mars observed by CRISM/MRO: 1. Multi-angle Approach for Retrieval of Surface Reflectance from CRISM observations (MARS-ReCO)

X. Ceamanos,[1,2] S. Douté,[1] J. Fernando,[3,4] F. Schmidt,[3,4] P. Pinet,[5,6] and A. Lyapustin[7]

Received 9 July 2012; revised 11 December 2012; accepted 13 December 2012.

[1] This article addresses the correction for aerosol effects in near-simultaneous multi-angle observations acquired by the Compact Reconnaissance Imaging Spectrometer for Mars (CRISM) aboard the Mars Reconnaissance Orbiter. In the targeted mode, CRISM senses the surface of Mars using 11 viewing angles, which allow it to provide unique information on the scattering properties of surface materials. In order to retrieve these data, however, appropriate strategies must be used to compensate the signal sensed by CRISM for aerosol contribution. This correction is particularly challenging as the photometric curve of these suspended particles is often correlated with the also anisotropic photometric curve of materials at the surface. This article puts forward an innovative radiative transfer-based method named Multi-angle Approach for Retrieval of Surface Reflectance from CRISM Observations (MARS-ReCO). The proposed method retrieves photometric curves of surface materials in reflectance units after removing aerosol contribution. MARS-ReCO represents a substantial improvement regarding previous techniques as it takes into consideration the anisotropy of the surface, thus providing more realistic surface products. Furthermore, MARS-ReCO is fast and provides error bars on the retrieved surface reflectance. The validity and accuracy of MARS-ReCO is explored in a sensitivity analysis based on realistic synthetic data. According to experiments, MARS-ReCO provides accurate results (up to 10% reflectance error) under favorable acquisition conditions. In the companion article, photometric properties of Martian materials are retrieved using MARS-ReCO and validated using in situ measurements acquired during the Mars Exploration Rovers mission.

Citation: Ceamanos, X., S. Douté, J. Fernando, F. Schmidt, P. Pinet, and A. Lyapustin (2013), Surface reflectance of Mars observed by CRISM/MRO: 1. Multi-angle Approach for Retrieval of Surface Reflectance from CRISM observations (MARS-ReCO), *J. Geophys. Res. Planets*, *118*, doi:10.1029/2012JE004195.

1. Introduction

[2] Imaging spectroscopy is a key remote sensing technique to study the composition, the mineralogy, and the physical state of planetary surfaces. A new generation of imaging spectrometers has recently emerged in the field of space exploration by incorporating an angular dimension of measurement. Multi-angle imaging spectroscopy is conceived to provide a more accurate characterization of planetary materials from orbit and a higher success in separating the signals coming from the atmosphere and the surface [*Martonchik et al.*, 2009]. The Compact Reconnaissance Imaging Spectrometer for Mars (CRISM) aboard the Mars Reconnaissance Orbiter (MRO) is a visible/short-wave infrared hyperspectral camera that can operate systematically in multi-angle mode from space [*Murchie et al.*, 2007]. In the targeted mode, CRISM measures radiative energy coming from the planet Mars within 0.36–3.92 microns using 544 spectral bands. As shown in Figure 1, CRISM targeted observations are composed of a quasi-nadir hyperspectral image at a spatial resolution of up to 18 m/pixel accompanied by ten 10× spatially binned hyperspectral images which are captured before and after the central scan. This sequence of off-nadir scans called emission phase function (EPF) encompasses view zenith angles up to 70° and two modes of relative azimuth, corresponding to the inbound and outbound portions of the satellite flyby. CRISM targeted observations can sense a given Martian site using different atmospheric paths and thus have proved to be of great value in atmospheric studies [*Smith et al.*, 2009; *Wolff et al.*, 2009]. In addition, this multi-angle data may be exploited to separate atmospheric and surface contributions when analyzed

[1]Université Joseph Fourier/CNRS, Institut de Planétologie et d'Astrophysique de Grenoble (IPAG), UMR 5274, Grenoble, France.
[2]Météo-France/CNRS, CNRM/GAME, Toulouse, France.
[3]Université Paris-Sud, Laboratoire IDES, UMR 8148, Orsay, France.
[4]CNRS, Orsay, France.
[5]Université de Toulouse, UPS-OMP, IRAP, Toulouse, France.
[6]CNRS, IRAP, Toulouse, France.
[7]NASA GSFC, Greenbelt, Maryland, USA.

Corresponding author: X. Ceamanos, GAME, CNRM, Météo-France, CNRS, 42 avenue Gaspard Coriolis, 31057 Toulouse, France. (xavier.ceamanos@meteo.fr)

©2012. American Geophysical Union. All Rights Reserved.
2169-9097/13/2012JE004195

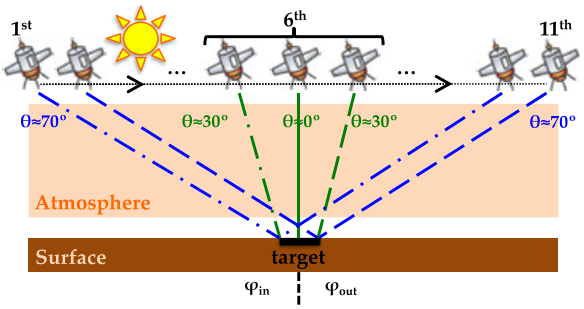


Figure 1. Schema of a CRISM targeted observation. Only three images out of 11 are shown. The central scan at full spatial resolution is drawn in green, while the most extreme scans of the EPF are pictured in blue. Dash-dotted and dashed lines depict the first and last scanned lines of each single image, respectively. All scans are acquired as a combination of the gimbal and the motion of MRO which results in a VZA range of $\theta \in [0°, 30°]$ for the quasi-nadir central scan. The two modes in relative azimuth ($\varphi_{in} + \varphi_{out} \approx 180°$) are shown.

using a radiative transfer model accounting for surface scattering and atmospheric extinction [*Murchie et al*., 2007]. The combination of an adequate atmospheric correction and the multi-angle capabilities of CRISM may make possible the retrieval of photometric properties of the surface according to observation geometry and wavelength. These surface products are essential to characterize the physical state of Martian materials as well as to distinguish between different types of terrains [*Johnson et al*., 2006a, 2006b; *Jehl et al*., 2008].

[3] The atmosphere of Mars is quite thin and mainly composed of carbon dioxide (CO_2) gas and suspended mineral and water ice particles named aerosols [*Barlow*, 2008]. These components represent an obstacle to remotely sensing the Martian surface as extinction of solar irradiance in the visible/short-wave infrared range happens by gaseous absorption and aerosol scattering and absorption. The modeling of the radiation reaching the top-of-atmosphere (TOA) level therefore demands an adequate characterization of both components [*Clancy and Lee*, 1991; *Drossart et al*., 1991; *Erard et al*., 1994; *Ockert-Bell et al*., 1997; *Tomasko et al*., 1999; *Korablev et al*., 2005; *Wolff et al*., 2009]. Atmospheric correction algorithms compensate the sensed TOA radiances for atmospheric contribution through the inversion of such atmosphere/surface models in order to retrieve surface quantities. One of the main hurdles to achieve an accurate correction is that aerosols and materials at the surface scatter light anisotropically depending on illumination and viewing conditions and are rarely spectrally distinct. Retrieval of accurate estimates of surface reflectance therefore requires the consideration, in the radiative transfer model, of the scattering phase function of aerosols as well as the bidirectional reflectance distribution function (BRDF) of the surface. In this context, the availability of multiple TOA measurements with different angular configurations, together with the implementation of appropriate techniques, becomes necessary to solve as accurately as possible the inverse problem [*Martonchik*, 1994]. In practice, atmospheric correction strategies are devised to retrieve the surface BRDF assuming an aerosol phase function.

[4] While correction for atmospheric gases is generally possible for non-icy surfaces [*Langevin et al*., 2005; *McGuire et al*., 2009], compensation for aerosol contribution represents a major challenge. Aerosol content on Mars is very variable as these particles are highly mobilized during storms which range from local events to global storms covering the entire planet. The variability of aerosol content in time and space is generally overcome by estimating, for each spacecraft orbital path, the local atmospheric opacity or the aerosol optical depth (AOD). For instance, *Vincendon et al*. [2007] propose to retrieve surface reflectance from observations taken by the hyperspectral imager "Observatoire pour la Minéralogie, l'Eau, les Glaces, et l'Activité" (OMEGA) aboard the Mars Express orbiter after quantifying the contribution of atmospheric aerosols using a Monte Carlo method. In that study, the need of multi-angle data is satisfied by processing several nadir observations acquired over the same target at different times, resulting in different solar zenith angles, and assuming that the AOD remains constant along the time span (up to several days). Besides this supposition, the surface is assumed to be characterized by a wavelength-dependent angular-independent single reflectance value called Lambertian albedo. The Lambertian assumption supposes that variations of TOA radiance with geometry are exclusively related to aerosols. This hypothesis is also adopted by *McGuire et al*. [2008] to process the central scan of CRISM targeted observations by a radiative transfer approach that computes surface spectra in Lambertian albedo units after correction for gaseous and aerosol contributions. Alternatively, *Brown and Wolff* [2009] propose to exploit the multi-angle information enclosed in CRISM targeted observations by modeling the remotely sensed signal at a single wavelength. Three parameters (surface Lambertian albedo, mineral aerosol opacity, and water ice aerosol opacity) are iteratively adjusted to fit the multi-angle CRISM data. Similarly, a Lambertian surface is also considered by the radiative transfer-based procedure developed by *Wiseman et al*. [2012] to retrieve atmospherically corrected CRISM surface spectra.

[5] In planetary remote sensing, the Lambertian assumption is generally adopted by atmospheric correction techniques, even when multi-angle measurements are available. This supposition substantially simplifies the radiative transfer modeling and reduces the size of the look-up table used in the inversion. The Lambertian hypothesis seems intuitively appropriate in some cases (e.g., turbid atmosphere). However, it has been proved that non-Lambertian, or anisotropic, scattering properties play a significant role for most mineral and icy surfaces [*de Grenier and Pinet*, 1995; *Pinet and Rosemberg*, 2001; *Johnson et al*., 2006a, 2006b; *Lyapustin et al*., 2010]. As a consequence, the adoption of a Lambertian assumption can create significant angle-dependent biases in derived surface reflectances [*Lyapustin*, 1999]. To our knowledge, *Cull et al*. [2010] are pioneers in performing surface retrievals from CRISM targeted observations considering a non-Lambertian surface. In that work, the inversion for the surface properties is achieved using a Hapke's model for the surface BRDF and a radiative transfer-simulated look-up table that stores TOA spectra corresponding to multiple atmospheric situations. Nevertheless, the algorithm of *Cull et al*. [2010] is restricted to a few CRISM targeted observations as it assumes that the sensed surface has similar

photometric properties than the materials characterized by the Mars Exploration Rovers (MER) mission at the Gusev crater of Mars.

[6] In the field of Earth remote sensing, some efforts have been done towards the mitigation or the elimination of the Lambertian assumption. *Guanter et al*. [2005] address the atmospheric correction of multi-angle observations acquired by the Compact High Resolution Imaging Spectrometer (CHRIS) aboard the PRoject for On-Board Autonomy (PROBA) under a Lambertian constraint with relaxation. An iterative strategy for surface retrieval is defined by assuming a Lambertian surface on the first iteration and injecting the inferred BRDF into the radiative transfer-based inversion on subsequent iterations until convergence is reached. Although this method improves the quality of the finally estimated BRDF, it may become problematic for highly anisotropic surfaces for which the initial assumption may greatly impact the succeeding retrievals. The incorporation of the BRDF into the atmospheric correction of remotely sensed data is also considered for processing multi-temporal data collected by the MODerate resolution Imaging Spectroradiometer (MODIS) aboard the Terra and Aqua spacecrafts [*Schaaf et al*., 2002] and the Multi-angle Imaging SpectroRadiometer (MISR) aboard the Terra spacecraft [*Diner et al*., 2005]. Recently, surface retrievals are carried out for series of multi-temporal images acquired by MODIS by the Multi-angle Implementation of Atmospheric Correction (MAIAC) algorithm *Lyapustin et al*. [2011a, 2011b, 2012]. Contrary to the previous methods, MAIAC solves the aerosol/surface coupling problem without strong reductionist assumptions using an innovative radiative transfer-based formulation of the TOA radiance. The mathematical properties of this formulation combined with the consideration of an advantageous surface BRDF model enable a fast and efficient inversion for the surface reflectance.

[7] To our knowledge, a method to compensate CRISM targeted observations for aerosol contribution considering an unknown non-Lambertian surface is not available in the literature. This article puts forward such a method through an innovative radiative transfer-based strategy that inherits some basis from the MAIAC algorithm. The method under the name of Multi-angle Approach for Retrieval of Surface Reflectance from CRISM Observations (hereafter referred to as MARS-ReCO) is proposed to retrieve surface reflectance from CRISM targeted observations. The major innovation is the consideration of an anisotropic surface, thanks to an accurate quasi-linear parametrization of the TOA radiance. In addition, the algorithm is endowed with a formalism integrating several sources of uncertainty into the inversion process and propagating them to the solution. MARS-ReCO transforms a CRISM targeted observation, originally in units of TOA radiance, into a set of photometric curves with error bars in units of surface reflectance depending on acquisition geometry. MARS-ReCO addresses the correction for mineral aerosols exclusively, thus not dealing with water ice aerosols nor atmospheric gases. The mineral aerosol particle size distribution and refractive index, as well as the AOD of each observation, must be provided beforehand.

[8] The article is organized as follows. The MARS-ReCO approach is detailed in Section 2 as well as the preprocessing of CRISM targeted observations. Section 3 describes the tests conducted to evaluate the performance of MARS-ReCO on CRISM-like synthetic data. Eventually, Section 4 discusses the benefits and limitations of the proposed approach. The capabilities of MARS-ReCO are tested on real CRISM data and validated against MER in situ measurements in the companion article [*Fernando et al*., 2013]. Note that the present work as well as the companion article restricts the use of MARS-ReCO to spectral bands without gaseous absorption.

2. Methods

[9] MARS-ReCO compensates CRISM targeted observations for mineral aerosol effects. The proposed method inherits the basis from the method named MAIAC [*Lyapustin et al*., 2012] while adding some functionalities. Contrary to MAIAC, which works with multi-temporal series of images, MARS-ReCO is devised to process near-simultaneous multi-angle CRISM observations. Furthermore, MARS-ReCO takes care of propagating several sources of errors to the end products. Before applying MARS-ReCO, CRISM targeted observations are transformed into appropriate products for multi-angular data processing.

2.1. Preliminaries

2.1.1. Integrated Multi-angle Product

[10] The 11 hyperspectral images forming a CRISM targeted observation are released individually in units of I/F, the ratio of measured intensity to solar flux. Note that the dependency on wavelength of all radiometric quantities in this article is omitted for simplicity. In order to facilitate the simultaneous processing of the multi-angle information associated to each terrain unit, the spectra corresponding to the 10 scans are rearranged in a common geographical grid of super-pixels (i.e., terrain units sensed at more than one geometry) to create a single data set named SPC cube (for SpectroPhotometric Curve). This is done after degrading the spatial resolution of the central scan in coherence with the properties of the EPF. SPC cubes are multi-angle integrated products which facilitate the access to photometric curves. A photometric curve is a series of radiometric measurements at a given wavelength acquired from a specific super-pixel with different angular configurations. The stacking of several photometric curves corresponding to consecutive wavelengths forms a spectrophotometric set. Figure 2 (left) illustrates the typical degree of overlapping by projecting the footprints of the 11 hyperspectral images onto the common geographical space. Note that the overlap is non-optimal, as typically only ~30% of all super-pixels are sensed by four or more angular measurements. Figure 2(center) shows the regular grid that is defined over the resulting mosaic such that each element (i.e., a super-pixel) corresponds to a single terrain unit typically measuring $\sim 450 \times 450$ m^2. This value takes into account the decrease in spatial resolution at the edges of the central and EPF images. Under this configuration, each band of a SPC cube contains about 2300 photometric curves, many of them made of less than four measurements. Note that a higher spatial resolution can be achieved only by tossing out the largest EPF super-pixels. Figure 2(right) details the structure of a SPC cube in which each spectrum of a targeted observation is arranged according to its angular configuration (up to 11) along the x axis and according to its spatial location, or super-pixel, along the y axis. For simplicity, super-pixels are arranged according to the number of available

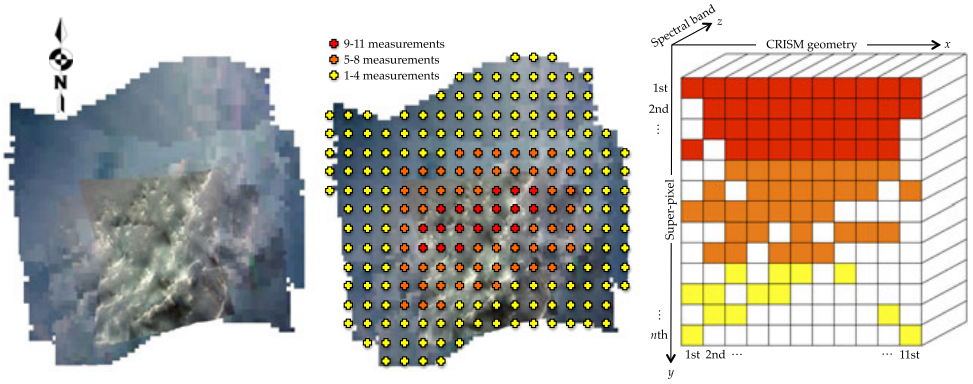


Figure 2. (left) Footprints of the 11 scans of a CRISM observation in a common geographical space. Note the different extent and shape of each image. In this example, the spatial resolution of the central scan has not been degraded for clarity. (center) Schema of the approximative overlaying grid of super-pixels. Each cross indicates the center of the associated super-pixel, while its color is coded according to the number of available angular measurements. (right) Schema of a SPC cube. Each row stores the information belonging to a same super-pixel. Photometric curves follow the same color code that in Figure 2 (center). Blank positions mean absence of angular measurement.

measurements. Under this configuration, each row at a specific spectral band contains a photometric curve while a *x*-*z* plane includes a spectrophotometric set, both products being in *I*/*F* units. Note that MARS-ReCO processes one spectral band at a time.

2.1.2. Retrieval of Aerosol Content

[11] MARS-ReCO must be fed with an estimate of the AOD associated to the CRISM observation to be processed. In the literature, many authors address this issue with a direct application to CRISM data [*Lemmon et al*., 2004; *Wolff et al*., 2009; *Douté and Ceamanos*, 2010]. Note that the performance of MARS-ReCO is sensitive to the accuracy of the AOD estimate. Furthermore, methods avoiding or minimizing the Lambertian surface assumption should be prioritized for consistency with MARS-ReCO.

2.2. Description of the MARS-ReCO Approach

[12] MARS-ReCO is conceived to infer photometric curves of the Martian surface from CRISM multi-angle orbital imagery. The contribution of mineral aerosols to the remotely sensed signal is compensated based on a radiative transfer-based algorithm which is fed by the scattering properties of these atmospheric particles. After fitting a model of the TOA signal to the CRISM measurements, the surface bidirectional reflectance associated to each super-pixel in a SPC cube is retrieved at the acquisition geometries. The theoretical background and the technical aspects of the proposed approach are detailed in the following. The notation used in this article is listed at the end of this document.

[13] The MARS-ReCO algorithm is based on a coupled surface-atmosphere radiative transfer formulation of the TOA signal originally proposed by *Lyapustin and Knyazikhin* [2001] and adapted by *Lyapustin et al*. [2011a] for the MAIAC algorithm. The major keystone of this accurate semi-analytical formulation is the consideration in the radiative transfer equation of a Green's function to model the intrinsic diffuse scattering responses of the atmosphere and a kernel-based scattering model for the surface.

2.2.1. Green's Function of the Atmosphere

[14] Many codes solving the radiative transfer of solar light in the surface-atmosphere interface are not suitable for simulating large collections of spectra because of their large computational requirements. The condition for the lower limit of the radiative transfer (i.e., the surface reflectance) is usually part of the calculation which must be performed for each combination of physical parameters related to the surface and the atmosphere. The Green's function method allows us to circumvent these drawbacks by a partial decoupling of the surface and the atmosphere. *Lyapustin and Knyazikhin* [2001] proved that this method makes possible the analytical combination of the atmospheric reflectivity and transmissivity with the surface reflectance to calculate TOA radiances for an arbitrary aerosol optical depth and acquisition geometry. This is achieved at the price of a small degradation of accuracy coming from two simplifications. Details on the use of a Green's function in the radiative transfer equation and the related assumptions can be found in Appendix A.

2.2.2. Expression for the TOA Reflectance

[15] The radiance reaching the CRISM instrument (L) can be decomposed as a sum of the atmospheric path radiance (D), and the radiance reflected by the surface before being directly (L_s) and diffusely (L_s^d) transmitted through the atmosphere,

$$L(s_0,s) = D(s_0,s) + L_s(s_0,s)e^{-\tau_0/|\mu|} + L_s^d(s_0,s), \quad (1)$$

where s_0 and s are the incidence and view directions. The first term of the surface-reflected radiance can be written as

$$L_s(s_0,s) \cong S\mu_0 e^{-\tau_0/\mu_0}\{\rho(s_0,s) + \alpha c_0 \rho_1(\mu)\rho_2(\mu_0)\} + \frac{\alpha}{\pi}\int_{\Omega^+} D_s\left(s_0,s'\right)\rho\left(s',s\right)\mu' ds', \quad (2)$$

where πS is the extraterrestrial solar spectral irradiance, ρ is the bidirectional reflectance factor (BRF) ($\rho = \pi f$, where f is the BRDF as defined by *Nicodemus et al*. [1977]), c_0 is the spherical albedo of the atmosphere, D_s is the path radiance

incident on the surface, and ρ_1 and ρ_2 are BRF-derived functions described in Appendix A. Parameter α is a multiple reflection factor that depends on the surface albedo $q(\mu_0)$ such that $\alpha = (1 - q(\mu_0)c_0)^{-1}$.

[16] The diffusely transmitted surface-reflected radiance at the TOA can be calculated from L_s with the help of the one-dimensional diffuse Green's function of the atmosphere (G^d) as it is demonstrated in Appendix A,

$$L_s^d(s_0, s) = \int_{\Omega^-} G^d(s_1, s) L_s(s_0, , s_1) ds_1. \tag{3}$$

[17] The quantity πG_d is also called bidirectional upward diffuse transmittance of the atmosphere. The surface albedo is defined as a ratio of reflected and incident radiative fluxes at the surface,

$$\begin{aligned} q(\mu_0) &= F^{Up}(\mu_0)/F^{Down}(\mu_0), \\ F^{Down}(\mu_0) &= F_s(\mu_0) + F_s^d(\mu_0) = \pi S \mu_0 e^{-\frac{\tau_0}{\mu_0}} + \int_{\Omega^+} D_s\left(s_0, s'\right)\mu' ds', \\ F^{Up}(\mu_0) &= \pi S \mu_0 e^{-\frac{\tau_0}{\mu_0}} q_2(\mu_0) + \int_{\Omega^+} \mu' q_2\left(\mu'\right) D_s\left(s_0, s'\right) ds', \\ q_2(\mu_0) &= \frac{1}{\pi}\int_{\Omega^-} \rho(s_0, s)\mu ds. \end{aligned} \tag{4}$$

[18] These formulas give an explicit expression for the TOA radiance as a function of the surface BRF. Their accuracy is high, usually within a few tenths of a percent [*Lyapustin and Knyazikhin*, 2001]. In the following, we work with units of top-of-atmosphere reflectance which is defined as $R = L/(S\mu_0) = (I/F)/\mu_0$. Note that MARS-ReCO processes SPC cubes which have been previously transformed into units of top-of-atmosphere reflectance. For simplicity, we use the symbol R to refer to units of TOA reflectance in a gas-free atmosphere populated by aerosols.

2.2.3. Surface Scattering Model

[19] The anisotropy of the surface is taken into account through its BRF modeled using a semi-empirical kernel-based Ross-Thick Li-Sparse (RTLS) model [*Lucht et al*., 2000]. The RTLS model expands the bidirectional reflectance distribution of the surface into a linear sum of terms (the so-called kernels) characterizing different scattering modes. The kernels in the RTLS model are derived from physical theory through simplifying assumptions and approximations. In particular, the surface bidirectional reflectance is decomposed as the sum of (i) a Lambertian—or isotropic—contribution, (ii) a geometric component modeling the diffuse reflection taking into account the 3D geometrical structure of opaque reflectors on the surface and shadowing phenomena, and (iii) a volume scattering contribution simulated by a collection of dispersed facets. In this way the BRF is written as

$$\rho(\mu_0, \mu, \varphi) = k^L + k^G f_G(\mu_0, \mu, \varphi) + k^V f_V(\mu_0, \mu, \varphi), \tag{5}$$

where subscripts refer to Lambertian (L), geometric (G), and volumetric (V) components, and f_G, f_V are predefined geometric kernels. More details on the RTLS kernels can be found in Appendix B.

[20] The RTLS model is very advantageous to shape efficient inversion algorithms based on radiative transfer [*Schaaf et al*., 2002; *Lyapustin et al*., 2012] as the surface bidirectional reflectance is characterized by a linear combination of three invariant kernels scaled by their corresponding kernels weights $\mathbf{k} = \{k^L, k^G, k^V\}$. While they are not perfectly orthogonal functions, they are sufficiently independent to allow stable recovery of the parameters for many angular sampling distributions [*Lucht et al*., 2000]. Furthermore, the RTLS model has proved to be accurate in recreating many types of natural surface ranging from highly anisotropic snow-covered terrains [*Lyapustin et al*., 2010] to backscattering surfaces such as those found in vegetation [*Schaaf et al*., 2002]. In particular, the geometric kernel models the backscattering features at the smallest CRISM phase angles ($g \approx 30°$).

2.2.4. Expression for the TOA Reflectance Using the RTLS Surface Model

[21] The substitution of equation (5) into equations (1)–(4) (after normalization to reflectance units and separation of the kernel weights) provides the following quasi-linear expression for the TOA reflectance:

$$\begin{aligned} R(\mu_o, \mu, \varphi) = R^D(\mu_o, \mu, \varphi) + k^L F^L(\mu_o, \mu) \\ + k^G F^G(\mu_o, \mu, \varphi) \quad + k^V F^V(\mu_o, \mu, \varphi) + R^{nl}(\mu_o, \mu), \end{aligned} \tag{6}$$

where R^D stands for the atmospheric path reflectance coming from photons scattered by aerosols without interacting with the surface. Quantities $\{F^L, F^G, F^V\}$, on the one hand, and R^{nl}, on the other hand, are multiplicative factors for the kernel weights $\mathbf{k}$ and a nonlinear term, respectively,

$$F^L(\mu_o, \mu) = \left(e^{-\tau_0/\mu_0} + \alpha\mu_0^{-1} F_s^d(\mu_0)/(\pi S)\right)\left(e^{-\tau_0/|\mu|} + G^{av}(\mu)\right), \tag{7}$$

$$\begin{aligned} F^k(\mu_o, \mu, \varphi) = \left\{e^{-\tau_0/\mu_0} f_k(\mu_0, \mu, \varphi) + \alpha\mu_0^{-1} D_k^1(\mu_0, \mu, \varphi)\right\} e^{-\tau_0/|\mu|} \\ + e^{-\tau_0/\mu_0} G_k^1(\mu_0, \mu, \varphi) + \alpha\mu_0^{-1} H_k^1(\mu_0, \mu, \varphi), \end{aligned} \tag{8}$$

$$\begin{aligned} R^{nl}(\mu_o, \mu) = \alpha c_0 \rho_2(\mu_o) e^{-\tau_0/\mu_0} \{e^{-\tau_0/|\mu|}\rho_1(\mu) + k^L G^{av}(\mu) \\ + k^G G_G^{11}(\mu) + k^V G_V^{11}(\mu)\}, \end{aligned} \tag{9}$$

where the subscript k refers to either geometric (G) or volumetric (V) kernels. Quantities D_G^1, D_V^1, G^{av}, G_G^1, G_V^1, G_G^{11}, G_V^{11}, H_G^1, and H_V^1 represent different integrals of the incident path radiance (D_s) and/or the atmospheric Green's function (G^d) with the RTLS kernels (f_G,f_V). The integral expression for these functions can be found in *Lyapustin and Wang* [2005]. Contrary to R^{nl}, which strongly depends on the surface by means of functions ρ_1 and ρ_2, quantities $\{F^L, F^G, F^V\}$ depend only weakly through the multiple reflection factor (α). Equation 6 describes the TOA reflectance as an explicit quasi-linear function of the RTLS kernel weights, thus provides the means for an efficient inversion.

2.2.5. Look-up Table

[22] As it will be explained, the retrieval of the surface kernel weights $\mathbf{k}$ is possible through the inversion of equation (6) subject to the availability of quantities R^D, $\{F^L, F^G, F^V\}$, and R^{nl}. A look-up table is generated to store R^D and all surface-independent radiometric quantities allowing us to calculate $\{F^L, F^G, F^V\}$ and R^{nl}. In particular, the look-up table includes the basic quantities R^D, D_s, c_0, and G^d as well as the intermediate quantities D_G^1, D_V^1, G^{av}, G_G^1, G_V^1, G_G^{11}, G_V^{11}, H_G^1, and H_V^1.

[23] Basic quantities are computed using the radiative transfer program named Discrete Ordinates Radiative Transfer Program for a Multi-layered Plane-Parallel Medium

(DISORT) [*Stamnes et al*., 1988]. For a homogeneous aerosol layer with opacity τ_0, the atmospheric reflected path reflectance (R^D) is computed considering a dark surface (surface albedo set to 0) and simulating the radiation at the sensor level. The path radiance incident on the surface (D_s) is computed similarly but considering this time the downward radiance at the lower interface. The spherical albedo of the atmosphere (c_0) is obtained after integration of its directional-hemispherical version which is directly provided by DISORT. Eventually, the diffuse Green's function of the atmosphere (G^d) is calculated similarly to D_s but reversing the direction of light propagation. In other words, the atmospheric layers must be set in reverse order and the result must be normalized by πS_λ [*Lyapustin and Knyazikhin*, 2001]. In the case of an homogeneous atmosphere, the problem for the Green's function becomes identical to the problem for D_s provided the substitution $s_0 \rightarrow s$. A completely dark surface is also considered to avoid multiple reflections between the surface and the atmosphere. The calculation of the intermediate quantities from the basic functions and the RTLS kernels is explained in *Lyapustin and Wang* [2005].

[24] A homogeneous atmosphere made of a single layer of mineral aerosols is used to compute the basic quantities look-up table. Besides its simplicity, this atmospheric model is appropriate to compute a "universal" look-up table representing the average Martian atmosphere. This model supposes that uncertainties related to mineral aerosols (i.e., AOD estimate, particle size, and refractive indexes) are negligible and that water clouds are not present. If the latter particles become significant, a stratified atmosphere should be considered. However, the correction for atmospheric water ice is out of the scope of this work. The radiative properties of the mineral aerosol particles (phase function and single-scattering albedo) are taken from the work of *Wolff et al*. [2009] in which Martian aerosols are modeled as cylindrical particles with an effective radius of 1.5 μm.

[25] All radiometric quantities stored in the look-up table are computed for several values of τ_0 and $\{\mu_0,\mu,\varphi\}$ to encompass different scenarios regarding atmospheric conditions and acquisition geometry, respectively. The angular grid density of the look-up table is selected empirically based on a trade-off between inversion accuracy and required memory. The angular range encompassed by CRISM targeted observations is taken into account by computing the look-up table at $\theta_0 \in [14°, 81°]$, $\theta \in [0°, 70°]$, and $\varphi \in [0°, 180°]$, with $\Delta\mu_0 = \Delta\mu = 0.02$ and $\Delta\varphi = 3°$. A nearest neighbor technique is selected to fit CRISM observations to the pre-computed look-up table. In this way, we avoid a costly interpolation in the angular triplet $\{\mu_0,\mu,\varphi\}$ that should be done for each CRISM angular measurement otherwise. On the other hand, the look-up table is computed for a set of 12 atmospheric opacities values, namely, $\tau_0(1\ \mu m) = \{0,0.05,0.1,0.2,0.33,0.5,0.75,1,1.4,2.0,2.8,4.0\}$. The look-up table is not homogeneously sampled in terms of AOD since the contribution of a changing aerosol content to the remotely sensed signal is more variable for a low AOD. A linear interpolation is used to obtain the look-up table values for a specific AOD. Under this configuration, the size of the look-up table is low (~50 megabytes per spectral band) due to its independence on the surface kernel weights **k**. Note that the look-up table is computed only once and can be then used for any CRISM observation.

2.2.6. Inversion Strategy for Surface Reflectance

[26] MARS-ReCO retrieves the photometric curve in BRF units corresponding to each super-pixel of a SPC cube by inverting the TOA reflectance model in equation (6). This is done based on the look-up table described above. An iterative inversion strategy is proposed based on a formalism borrowed from *Tarantola* [2005], which integrates several sources of uncertainty in the inversion process and propagates them to the solution.

2.2.6.1. Basis and Objective of the Inversion

[27] Let $\mathbf{R}^C = \left\{R_1^C, \ldots, R_{Ng}^C\right\}$ be the photometric curve in units of TOA reflectance measured by CRISM at a given gas-free spectral band. The term Ng is the number of available angular measurements, where $Ng \leq 11$ in the case of CRISM targeted observations. Let $\mathbf{R}^C$ be associated to a given super-pixel of the SPC cube which corresponds to a portion of Martian surface characterized by the state vector $\mathbf{k} = \{k^L, k^G, k^V\}$, whose elements are unknown at first. Let $\mathbf{k}_{sol}$ be the RTLS kernel weights that provide the best fit between the observed data $\mathbf{R}^C$ and the predicted photometric curve $\mathbf{R} = \{R_1, \ldots, R_{Ng}\}$, which is built using equation (6). The comparison is done by means of the root mean square error (RMSE) as follows:

$$RMSE = \sqrt{\frac{1}{N_g}\sum_{j=1}^{Ng}\left(R_j^C - R_j\right)^2}. \tag{10}$$

[28] The solution $\mathbf{k}_{sol}$ is therefore the set of kernel weights that minimizes the RMSE such that $\mathbf{k}_{sol} = \arg_{\mathbf{k}} \min\ RMSE$. MARS-ReCO addresses the obtention of the triplet $\mathbf{k}_{sol}$ for every photometric curve in a CRISM targeted observation. This triplet allows us to compute the surface BRF at the N_g sampled geometries by means of the RTLS model (equation (5)). Also, the existing uncertainties are taken into account and propagated to put error bars to the retrieved solution $\mathbf{k}_{sol}$ and the associated surface reflectance values.

2.2.6.2. Composition of the Inversion Matrix and Assumptions on the First Iteration

[29] The model relating the state vector **k** to the TOA reflectances **R** (i.e., equation (6)) is initially dependent on the surface properties due to the nonlinear term R^{nl} and, to a lesser extent, the quantities $\{F^L, F^G, F^V\}$. As a solution, we follow *Lyapustin et al*. [2012] who propose to retrieve $\mathbf{k}_{sol}$ through an iterative inversion algorithm. Let $\mathbf{r}^{(0)} = \left\{r_1^{(0)}, \ldots r_{Ng}^{(0)}\right\}$ be a set of reduced measurements on the first iteration $n = 0$ where $r_j^{(0)} = R_j - R_j^D - R_j^{nl(0)}$. Using equation (6) and a matrix form, we read

$$\mathbf{r}^{(0)} = \mathbf{F}^{(0)}\mathbf{k}, \qquad \mathbf{F}^{(0)} = \begin{bmatrix} F_1^{L(0)} & F_1^{G(0)} & F_1^{V(0)} \\ F_j^{L(0)} & F_j^{G(0)} & F_j^{V(0)} \\ F_{N_g}^{L(0)} & F_{N_g}^{G(0)} & F_{N_g}^{V(0)} \end{bmatrix}. \tag{11}$$

[30] *Lyapustin et al*. [2012] remove the dependence on the surface by assuming a black surface on the first iteration, that is, $\mathbf{k}^{(0)} = \{0,0,0\}$. This supposition, however, results in longer convergence times for bright surfaces such as those found on the high latitudes of Mars. As a consequence, MARS-ReCO

assumes an isotropic surface on the first iteration $\mathbf{k}^{(0)} = \left\{R^C_{bck}, 0, 0\right\}$, where the subscript *bck* corresponds to the CRISM geometry in which aerosols are less predominant, that is, the backscattering direction. This assumption is generally possible because the majority of CRISM targeted observations are split into two modes of relative azimuth (review Figure 1), one of them corresponding to low φ values.

[31] This assumption allows the iterative process to start by computing $\mathbf{F}^{(0)}$ through the evaluation of the look-up table at the angular triplet $\{\mu_{0j},\mu_j,\varphi_j\}$ of each measurement R^C_j and at the atmospheric input τ_0. We remember that the look-up table is linearly interpolated according to τ_0 and a nearest neighbor method is used in the geometric dimension. Similarly, the quantity $R^D_j(\tau_0) + R^{nl}_j\left(\mathbf{k}^{(0)}, \tau_0\right)$ is computed knowing τ_0 and $\mathbf{k}^{(0)}$.

2.2.6.3. Characterizing the Uncertainties

[32] In order to propagate the existing uncertainties, the a posteriori covariance matrix of the state vector ($\mathbf{C}_k$) is calculated. The state vector $\mathbf{k}$ is considered a random variable. For this purpose, we use the formalism of *Tarantola* [2005] in the framework of (i) a linear model that relates $\mathbf{k}$ to the set of reduced measurements $\mathbf{r}^{(0)}$ and (ii) a set of Gaussian probability distribution functions (PDFs) pertaining to the input and output parameters of the inversion problem. Each PDF expresses different information at different steps of the process (i.e., evaluation of the most probable AOD and its related uncertainty, a priori knowledge on the state of the system, CRISM measurements, and the top-of-atmosphere reflectance model). We note two types of uncertainties on vector $\mathbf{r}^{(0)}$:

1. The error on the CRISM measurements R^C_j, which is assumed to be independent on the state of the system and the other geometries, with a diagonal covariance matrix $\mathbf{C}_C$ with elements $\sigma^2_1, \ldots, \sigma^2_{N_g}$.
2. The error on the AOD estimation τ_0, which induces an error on $R^D_j + R^{nl(0)}_j$. In this case, we also assume the independence regarding the state of the system and the other geometries. We evaluate the elements of the covariance matrix experimentally by generating a random series of values according to a Gaussian PDF with mean τ_0 and variance $\sigma^2_{\tau_0}$. We then calculate, based on the TOA reflectance model in equation (6), the population of samples $R^D_j(\tau_0) + R^{nl}_j\left(\mathbf{k}^{(0)}, \tau_0\right)$ for each geometry $j \in [1,N_g]$. Likewise, the covariance matrix $\mathbf{C}^{(0)}_{\tau_0}$ is computed using a classical estimator.

[33] The total covariance matrix for the reduced measurements is $\mathbf{C}^{(0)}_r = \mathbf{C}_C + \mathbf{C}^{(0)}_{\tau_0}$. Last but not least, we have some a priori information on the solution in the form of a PDF characterized by its mean $\mathbf{k}^{(0)}$ and a covariance matrix $\mathbf{C}_k$ that we suppose to be diagonal with elements σ^2_L, σ^2_V, and σ^2_G taking large values.

2.2.6.4. Retrieval of Surface Reflectance and Propagation of Errors

[34] In the framework of the linear model and the Gaussian PDFs, the most likely a posteriori state vector $\mathbf{k}^{(1)}$ and the a posteriori covariance matrices $\mathbf{C}_{kp}$ and $\mathbf{C}_{rp}$—respectively associated to $\mathbf{k}^{(1)}$ and the model of TOA reflectance—are retrieved through the explicit least-squares solution proposed by *Tarantola* [2005]:

$$\mathbf{k}^{(1)} = \mathbf{k}^{(0)} + \mathbf{C}_k\mathbf{F}^{(0)T}\left(\mathbf{F}^{(0)}\mathbf{C}_k\mathbf{F}^{(0)T} + \mathbf{C}^{(0)}_r\right)^{-1}\left(\mathbf{r}^{(0)} - \mathbf{F}^{(0)}\mathbf{k}^{(0)}\right), \quad (12)$$

$$\mathbf{C}_{kp} = \mathbf{C}_k - \mathbf{C}_k\mathbf{F}^{(0)T}\left(\mathbf{F}^{(0)}\mathbf{C}_k\mathbf{F}^{(0)T} + \mathbf{C}^{(0)}_r\right)^{-1}\mathbf{F}^{(0)}\mathbf{C}_k, \quad (13)$$

$$\mathbf{C}_{rp} = \mathbf{F}^{(0)}\mathbf{C}_{kp}\mathbf{F}^{(0)T} + \mathbf{C}^{(0)}_\tau. \quad (14)$$

[35] Vector $\mathbf{k}^{(1)}$ provides a refined estimate of the surface BRF and, consequently, of the model $\mathbf{F}^{(1)}$. These two quantities are used in the upcoming iteration $n = 1$. Furthermore, the reduced measurement vector and its associated covariance matrix are updated through the calculation of $R^{nl(1)}$ to give $\mathbf{r}^{(1)}$ and $\mathbf{C}^{(1)}_r$. This iterative process is repeated for several iterations before stopping on the iteration m after MARS-ReCO decides that the triplet of weights is satisfactory (i.e., $\mathbf{k}^{(m)} \sim \mathbf{k}_{sol}$). As it is explained below, the number of iterations is set automatically according to the goodness of the retrieved surface BRF model.

2.2.6.5. Refinement of Surface Solution by Iterative Method

[36] A convergence criterion is defined to refine the surface solution through several iterations. However, the physical sense of the retrieved BRF is not always assured. Indeed, the retrieved BRF model can be related to an incorrect shape (e.g., negative BRF values at some angles) despite a high goodness of fit at the measurement angles. This situation is likely to happen due to a deficient radiometric quality, a limited angular sampling, or a high aerosol content. For this reason, the quality of the input TOA photometric curve and the output retrieved surface solution is assured on each iteration by a set of rejection criteria. These criteria (see Appendix C for details) prove to reject the majority of unphysical BRF solutions. Convergence usually occurs after four to five iterations resulting in a computational time of 1 minute to process one spectral band of a SPC cube at 450 m/pixel on a regular computer (i.e., dual 2.66 GHz quad-core processor, 6 GB RAM).

2.2.6.6. Characterizing the Solution

[37] After reaching convergence on iteration m, the quality of the solution is characterized by a series of indicators. First, the root mean square error is computed to express the adequacy between the CRISM measurements and the retrieved BRF model such that

$$RMSE^{(m)} = \sqrt{\frac{1}{N_g}\sum_{j=1}^{Ng}\left(r^{(m)}_j - F^{L(m)}_j k^{L(m)} - F^{V(m)}_j k^{V(m)} - F^{G(m)}_j k^{G(m)}\right)^2}, \quad (15)$$

[38] Second, we compute the a posteriori variance on the estimated surface reflectance for each geometry $j = 1, \ldots, N_g$ as the trace of the a posteriori covariance matrix $\mathrm{tr}(\mathbf{C}_{\rho p})$ where $\mathbf{C}_{\rho p} = \mathbf{Q}\mathbf{C}_{kp}\mathbf{Q}^T$. Term $\mathbf{Q}$ is the linear operator relating the state vector to the surface BRF values $\rho^{(m)} = \left\{\rho^{(m)}_1, \ldots \rho^{(m)}_{Ng}\right\}$ (computed using equation (5)) such that

$$\rho^{(m)} = \mathbf{Q}\mathbf{k}^{(m)}, \qquad \mathbf{Q} = \begin{bmatrix} 1 & f^G_1 & f^V_1 \\ & \cdots & \\ 1 & f^G_j & f^V_j \\ & \cdots & \\ 1 & f^G_{N_g} & f^V_{N_g} \end{bmatrix}. \quad (16)$$

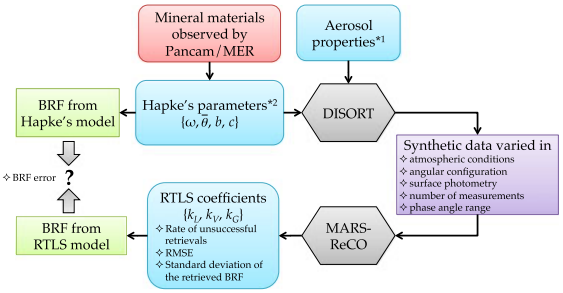


Figure 3. Schema of the sensitivity analysis based on synthetic CRISM-like data. *Aerosol properties are provided by *Wolff et al*. [2009]. *Hapke's parameters of the minerals found in the Gusev crater are borrowed from *Johnson et al*. [2006a].

[39] Finally, the a posteriori standard deviation of a predicted BRF photometric curve is

$$\sigma_\rho = \sqrt{\frac{1}{N_g}\mathrm{tr}\left(\mathbf{C}_{\rho\rho}\right)}. \tag{17}$$

[40] In the following, this parameter proves to be an accurate indicator of the quality of the retrieved surface BRF. Indeed, it helps to flag those surface solutions which are wrong but physical and thus more difficult to detect by the rejection and convergence criteria.

3. Sensitivity Analysis

[41] In this section, the capabilities of MARS-ReCO are tested on simulated data following the sensitivity analysis depicted in Figure 3. Such task is achieved at the CRISM spectral band centered at $\lambda = 755.3$ nm where gas absorption is negligible. The present research also aims at studying the correlation of the a posteriori standard deviation σ_ρ with the quality of the retrieved surface reflectances. First, a CRISM-like synthetic data set is generated for test in Section 3.1 based on the optical properties of Martian aerosols and the photometric properties of some surface materials. Second, Section 3.2 evaluates the performance of MARS-ReCO on photometric curves with different angular configurations, atmospheric conditions, and surface photometric properties. Third, the requirements to process CRISM multi-angle data with a limited angular diversity are given in Section 3.3. Fourth, the stability of the inversion performed by MARS-ReCO is studied in Section 3.4. Lastly, the impact on MARS-ReCO of the uncertainties of the input aerosol content is explored in Section 3.5.

3.1. Synthetic Data Set

[42] The sensitivity analysis is performed on a controlled synthetic data set formed by CRISM-like photometric curves which are simulated in I/F units using DISORT. We consider a coupled atmosphere/surface system that is fed by the scattering properties of Martian dust aerosols from *Wolff et al*. [2009] and by photometric properties of Martian minerals. The reflectances of several surface materials found in the Gusev crater were measured on ground by the Pancam instrument aboard the MER Spirit. These data were fitted by *Johnson et al*. [2006a] to a Hapke's BRDF model with a two-lobed Henyey-Greenstein phase function [*Hapke*, 1993]. In this research, we select four mineral materials, which belong to two endmembers referred by *Johnson et al*. [2006a] to as (i) endmember "Soil", which corresponds to typical soils being dominant at the spatial scale accessible to CRISM, and (ii) endmember "Red rock", which is related to rocky facets with higher anisotropic photometric properties than soils. Table 1 details two different Pancam measurements of the same endmember at 753 nm, the first one corresponding to a brighter sample of the endmember (subindex 1) and the second one belonging to a darker sample (subindex 2). By selecting these photometrically distinct materials, the sensitivity analysis aims at assessing the capabilities of MARS-ReCO against the variability of Martian mineral surfaces.

[43] Based on Table 1, a TOA photometric curve is simulated by DISORT at 753 nm for each combination of the atmospheric/angular configurations summarized in Table 2. Each photometric curve is made of 11 I/F measurements at constant solar zenith angle and varying view zenith angle, thus mimicking the acquisition of targeted observations by CRISM. A single combination of 11 view zenith angles, one for each measurement, is selected for all synthetic photometric curves as the view angle is quite constant for all CRISM targeted observations. By contrast, six solar zenith angles are considered to embrace the angular range in which CRISM works, going from equatorial ($\theta_0 < 60°$) to polar observations ($\theta_0 > 60°$). Four archetypal configurations are selected in terms of relative azimuth according to the typical functioning of MRO, each one linked to a specific couple of φ_1 and φ_2 values. The fourth configuration represents the extreme case when the direction of the Sun and the direction of the MRO flyby are orthogonal ($\varphi_1 = \varphi_2 = 90°$), resulting in the most limited phase angle range. Note that in this extreme configuration half of the angular measurements are identical to the other half due to the symmetry in view zenith angle. As regards atmospheric opacity, a set of nine AOD values

Table 1. Photometric Parameters at 753 nm of the Four Surface Materials Considered in the Sensitivity Analysis

Endmember\Hapke's Parameters at 753 nm	ω	$\bar{\theta}$	b	c
Soil-1 (Table 4c in *Johnson et al*. [2006a])	0.69	11	0.241	0.478
Soil-2 (Table 6c in *Johnson et al*. [2006a])	0.65	12	0.170	0.547
Red rock-1 (Table 4b in *Johnson et al*. [2006a])	0.83	19	0.450	0.255
Red rock-2 (Table 8b in *Johnson et al*. [2006a])	0.65	14	0.166	0.801

A Hapke's model with a two-lobed Henyey-Greenstein phase function is used. Parameters ω, $\bar{\theta}$, b, and c correspond to the single-scattering albedo, the macroscopic roughness, the asymmetry parameter, and the backward scattering fraction of the phase function, respectively [*Hapke*, 1993]. Note that a bright backscattering highly anisotropic surface corresponds to $\omega \to 1$, $c > 0.5$, and $b \to 1$.

Table 2. Angular and Atmospheric Ranges Encompassed by the TOA Photometric Curves of the Synthetic Data Set[a]

Parameter	Acquisition and Atmospheric Configurations
θ (°)	1 config.: 70, 63.5, 57.5, 52, 46.5, 25, 46.5, 52, 57.5, 63.5, 70
θ_0 (°)	6 config.: 30; 40; 50; 60; 70; 80
φ_1, φ_2 (°)	4 config.: 0, 180; 30, 150; 60, 120; 90, 90
τ_0	9 config.: 0; 0.1; 0.33; 0.5; 1; 1.5; 2; 2.5; 3

[a]Only one configuration is considered in terms of view zenith angle as this angle is quite constant among the 11 images of all CRISM targeted observations. For the central scan, we choose $\theta = 25°$ as this is the typical average value in real CRISM targeted observations.

at 1 μm is considered to test MARS-ReCO under clear and turbid conditions. The resulting synthetic data set contains 216 configurations for each surface material, making a total of 864 CRISM-like photometric curves.

[44] Lastly, noise is added to the synthetic data set to mimic the signal-to-noise ratio of CRISM observations. An additive Gaussian noise with a noise figure of 1/50 is added to each simulated *I*/*F* value (i.e., the standard deviation of a given *I*/*F* measurement R_j^C being equal to $R_j^C/50$). Note that this noise level is higher than the one claimed by *Murchie et al.* [2007], that is, a signal-to-noise ratio of 450 dB at 750 nm. In this way we assess MARS-ReCO under less favorable and more realistic conditions.

3.2. Study on the Acquisition Geometry, Atmospheric Opacity and Surface Type

3.2.1. MARS-ReCO Performance Based on Built-in Indicators

[45] Each TOA photometric curve in the synthetic data set is compensated for aerosol contribution by MARS-ReCO. In the case of convergence, the corresponding surface RTLS weights $\mathbf{k}_{sol}$ are retrieved. According to the noise attributes of the synthetic data set, each photometric curve $\mathbf{R}^C = \left\{R_1^C, \ldots, R_j^C, \ldots, R_{Ng}^C\right\}$ is assumed to have a diagonal covariance matrix $\mathbf{C}_C$ with elements $\sigma_j^2 = \left(R_j^C/50\right)^2$. In order to determinate the intrinsic limitations of MARS-ReCO, we first consider the ideal case in which the exact optical depth (the AOD values used for the data simulation) is known. Accordingly, parameter $\sigma_{\tau_0}^2$ is set to zero. The performance of the surface inversion is illustrated in Figure 4 in terms of (i) unsuccessful retrievals (i.e., the percentage of photometric curves that have been discarded for inversion), (ii) RMSE, and (iii) standard deviation of the retrieved BRF (σ_ρ).

[46] Figure 4(top) illustrates the percentage of unsuccessful retrievals according to atmospheric conditions (set by τ_0), angular configuration (set by θ_0 and $\{\varphi_1,\varphi_2\}$), and type of material. As it can be seen, the rate of unsuccessful retrievals is about 15% for all TOA photometric curves not sampling the solar cross-principal plane ($\varphi_1, \varphi_2 = \{90°, 90°\}$). This specific azimuthal configuration is related to the most limited phase angle range and does not encompass enough angular diversity for a satisfactory inversion. Likewise, unsuccessful retrievals increase significantly for turbid atmospheres and extreme solar zenith angle, reaching a 40% rate of rejection when $\tau_0 \geq 2$ and $\theta_0 \geq 80°$. Regarding the solar angle, the RTLS model becomes less accurate at extreme illumination conditions due to the divergence of the geometric kernel [*Lucht et al.*, 2000] and the higher anisotropy of surfaces in this angular range. The success of MARS-ReCO is, by contrast, less dependent on the properties of the surface materials. In particular, MARS-ReCO performs slightly worse when dealing with bland materials such as Soil-2, which may be too dark and too isotropic to be accurately separated from the aerosol photometric curve.

[47] Figure 4(middle) illustrates the quality of the fit between the synthetic data set and the TOA reflectance model by means of the RMSE (see equation (15)). Only the successfully inverted photometric curves are considered in this experiment. The RMSE is generally equal to a few tenths of 1% reflectance, and while it logically increases according to solar zenith angle and AOD, it decreases for reduced phase angle ranges. This result is, however, reasonable since photometric curves along the solar cross-principal plane are easier to fit as they do not sample the aerosol photometric curve spanning the solar principal plane ($\varphi_1, \varphi_2 = \{0°, 180°\}$). Contrary to the lower RMSE, the retrieved BRF model in this case is likely to be wrong. Therefore, the RMSE cannot be considered as a reliable indicator of the quality of MARS-ReCO as the surface/atmosphere model can satisfactorily fit a photometric curve while providing a physically incorrect solution. By contrast, the RMSE coherently increases according to solar zenith angle due to the combined effect of a stronger surface anisotropy at extreme angular configurations and the limitations of the RTLS model. Note that inaccuracies at extreme angles also come from small differences between the Hapke's and the RTLS models as well as the use of a plane-parallel radiative transfer code such as DISORT. Lastly, the RMSE also depends slightly on the type of surface, being higher for anisotropic surfaces.

[48] Finally, Figure 4(bottom) explores the average a posteriori standard deviation of the surface photometric curves (σ_ρ) as defined in equation (17). Again, only the successfully inverted photometric curves are considered. The standard deviation is generally lower than 0.1 for favorable conditions and, contrary to the previous indicators, clearly increases according to AOD, solar zenith angle, and limited phase angle range, which typically correspond to the most challenging scenarios.

3.2.2. MARS-ReCO Performance Based on the Pancam Reference

3.2.2.1. BRF Error in the 11 Acquisition Geometries

[49] The accuracy of the retrieved surface BRF is evaluated using the surface data derived from Pancam. Note that these data are used in the simulation of the synthetic data set. This experiment is done exclusively for those photometric curves for which MARS-ReCO converges. We define the BRF error of a given photometric curve (e_ρ) as the average of the difference between (i) the surface photometric curve retrieved by MARS-ReCO in BRF units and (ii) the same curve reconstructed using the Hapke's model and Table 1

$$e_\rho = \frac{100}{Ng}\sum_{j=1}^{Ng}\frac{\left|\rho_j^{\text{MARS-ReCO}} - \rho_j^{\text{Hapke}}\right|}{\rho_j^{\text{Hapke}}}. \quad (18)$$

[50] Figure 5 shows the result of averaging the BRF error of all photometric curves associated to a given AOD, solar

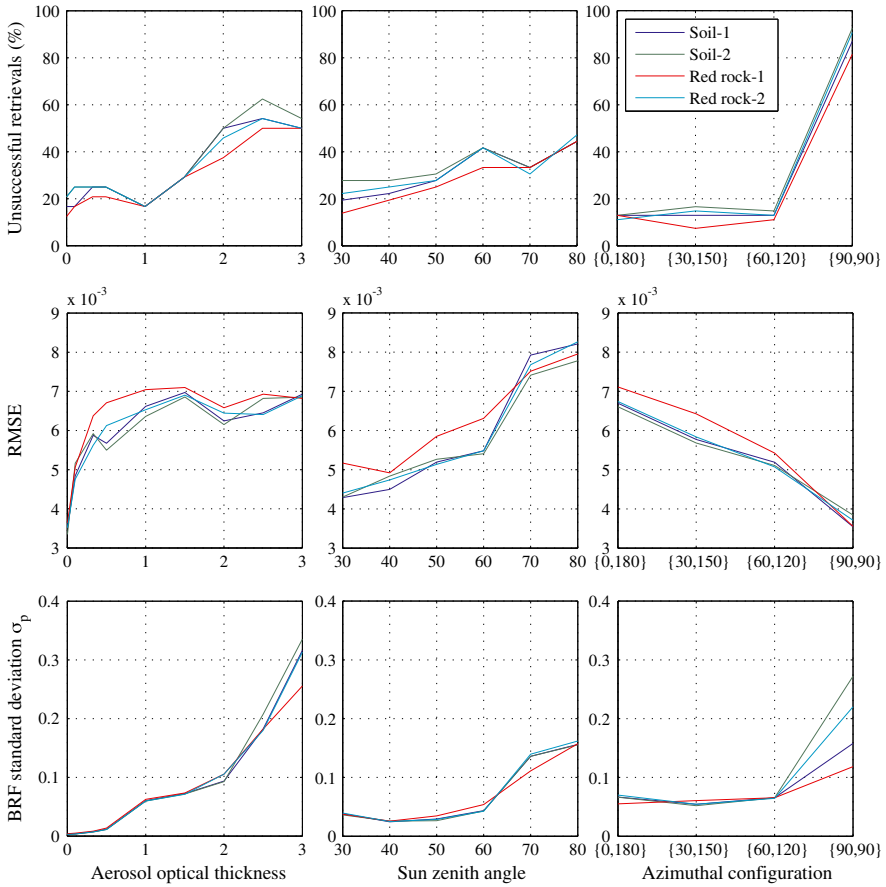


Figure 4. (top) Percentage of unsuccessful retrievals, (middle) RMSE, and (bottom) a posteriori standard deviation of the retrieved BRF for the processed synthetic data set. All parameters are averaged according to the AOD, the solar zenith angle, and the azimuthal configuration that correspond to each synthetic photometric curve. The RMSE and the standard deviation are computed based only on successfully inverted curves.

zenith angle, or azimuthal configuration. As it can be seen, the accuracy of the retrieved BRF decreases under unfavorable conditions, that is, high AOD, extreme solar zenith angle, and limited phase angle range. The average BRF error is lower than 20% when $\tau_0 \leq 1$, $\theta_0 \leq 60°$, and $\varphi_1, \varphi_2 \neq \{90°, 90°\}$ despite the unfavorable configurations of the other parameters (e.g., $e_\rho > 20\%$ when $\tau_0 \leq 1$ and $\theta_0 = 80°$). By contrast, it is important to remark that ranges of validity with higher average BRF errors contain configurations with acceptable accuracies (e.g., for Soil-2, while the average e_ρ is up to 38% when $\tau_0 = 2$, the individual e_ρ is 5.6% for the configuration when $\tau_0 = 2$, $\theta_0 = 30°$, and $\varphi_1, \varphi_2 = \{30°, 150°\}$). Note the high correlation between the BRF error and the a posteriori standard deviation (σ_ρ) in Figure 4(bottom). Lastly, we remark the continuity of the error curves when $\tau_0 = 1.5$. Contrary to the adjacent situations ($\tau_0 = 1$ and $\tau_0 = 2$), this particular aerosol content is not considered in the look-up table, and therefore, the inversion of the associated curves is made after interpolation of the pre-computed atmospheric quantities (see Section 2.2.5). According to results, the performance of MARS-ReCO is robust against this interpolation.

3.2.2.2. BRF Error in the Complete Upper Hemisphere

[51] The capabilities of MARS-ReCO are further validated by evaluating the retrieved surface BRF model out of the 11 acquisition geometries. This time we use a dense angular grid to explore the whole upper hemisphere in view zenith angle and relative phase angle. The evaluation is, however, restricted to the illumination conditions of acquisition (θ_0) as the investigation of other angular ranges becomes unpredictable. Figures 6 and 7 assess a couple of surface models that have been retrieved under varied acquisition conditions. The BRF models are evaluated at the defined angular grid and plotted in polar coordinates, where the radial and angular coordinates correspond to the view zenith angle and the relative azimuth of evaluation, respectively. Note that while the case illustrated in Figure 6 corresponds to very favorable conditions, the examples in Figure 7 are increasingly challenging in terms of AOD, solar zenith angle, azimuthal configuration, and surface anisotropy.

[52] Figure 6 illustrates the evaluation of the retrieved BRF model for a surface made of material Soil-1 in the absence of atmosphere ($\tau_0 = 0$). The Sun position is at $\theta_0 = 30°$ (see yellow star) and the MRO flyby results in a relative

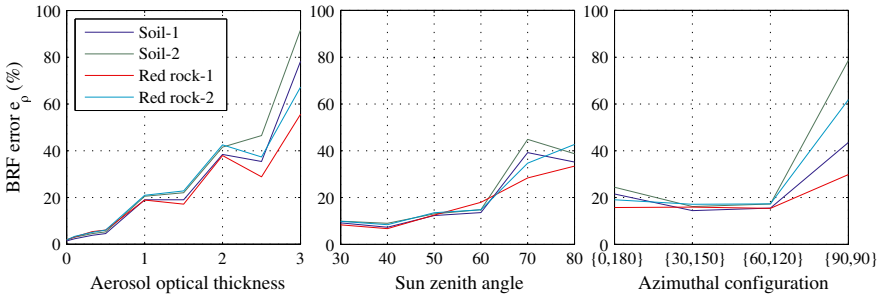


Figure 5. BRF error in percent (e_ρ) between the BRF curve retrieved by MARS-ReCO and the reference data constructed from a Hapke's model fed by Table 1. The plotted BRF errors are the result of averaging each combination of (left) AOD, (center) solar zenith angle, and (right) azimuthal configuration. Only successful retrievals are considered.

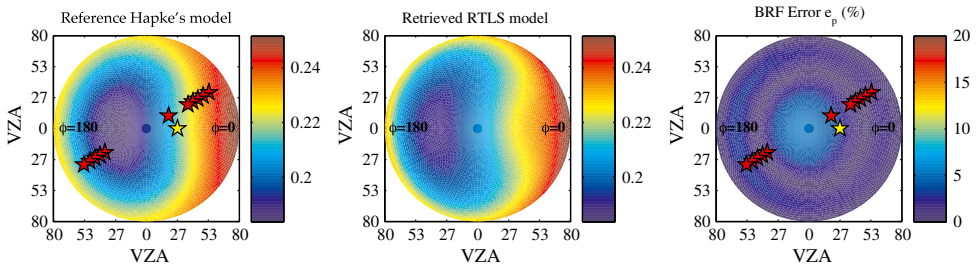


Figure 6. Surface BRF corresponding to material Soil-1 generated using (left) the reference Hapke's model and (center) the RTLS model retrieved by MARS-ReCO from a TOA photometric curve defined by $\tau_0 = 0$ (i.e., no atmospheric effects), $\theta_0 = 30°$, and $\varphi_1, \varphi_2 = \{30°, 150°\}$. (right) BRF error ($e_\rho$) between the BRF calculated from the Hapke's model and that from the RTLS model. Red stars show the geometry of the 11 measurements of the synthetic photometric curve. The Sun position is marked with a yellow star. Note that the backscattering direction is situated at the right-hand side of the plot.

azimuthal angle configuration of $\varphi_1, \varphi_2 = \{30°, 150°\}$. Red stars represent the 11 CRISM-like measurements. This angular configuration results in a phase angle range of acquisition where $g \in [14°, 96°]$. Figure 6(left) shows the surface BRF calculated using the Hapke's model fed by the reference photometric data in Table 1 and evaluated at $\theta_0 = 30°$. Similarly, Figure 6(center) shows the surface BRF calculated using the RTLS model fed by the $\mathbf{k}_{sol}$ retrieved by MARS-ReCO. Figure 6(right) expresses the quality of the retrieval by plotting the relative difference between both BRF data sets. A low error ($e_\rho = 0.8\%$) underlines the compatibility of the RTLS and the Hapke's models even with a few available measurements and despite the additive noise. This result is in agreement with the low BRF standard deviation ($\sigma_\rho = 0.002$) given by MARS-ReCO.

[53] The same experiment is repeated in Figure 7a for a typical atmospheric opacity on Mars, that is, $\tau_0 = 0.5$. Despite the aerosol effects, the BRF error and the standard deviation are very low ($e_\rho = 1.6\%$ and $\sigma_\rho = 0.004$), mainly due to the favorable angular and atmospheric conditions. As it can be seen, MARS-ReCO satisfactorily retrieves a surface model with two scattering lobes in the backward and forward directions. The sole dissimilarity is observed in the forward direction when $\theta \approx 80°$ where the differences between the two surface models become significant.

[54] In Figure 7b, the aerosol contribution is severely increased ($\tau_0 = 2$) to recreate very turbid conditions. This configuration results in a higher BRF error ($e_\rho = 5.6\%$), which is well correlated with a higher standard deviation ($\sigma_\rho = 0.027$). Note that the BRF error is relatively moderate since strong inaccuracies mainly happen at high view zenith angles (errors up to 50%), which are not sampled by the CRISM geometries.

[55] Figure 7c repeats the same experiment with $\tau_0 = 0.5$ and $\theta_0 = 70°$ ($g \in [28°, 130°]$). Although the retrieved backscattering lobe is accurate, the extreme illumination conditions result in a somewhat incorrect forward scattering feature. Nonetheless, similar to Figure 7b, the average BRF error along the 11 geometries is moderate ($e_\rho = 3.0\%$) as well as the associated standard deviation ($\sigma_\rho = 0.011$). Note that the BRF error is expected to increase for higher values of solar zenith angle due to limitations of both surface models.

[56] The experiment in Figure 6 is repeated with $\tau_0 = 0.1$ and $\varphi_1, \varphi_2 = \{90°, 90°\}$, resulting in a very limited phase angle range of acquisition ($g \in [38°, 73°]$). The inversion of this photometric curve is one of the few that converges under this azimuthal configuration [Figure 4(top right)], probably because the rest of acquisition conditions are favorable. Nonetheless, Figure 7d shows that the shape of the retrieved surface model is strongly inaccurate (error up to 80%). This result comes from the restriction of the TOA measurements

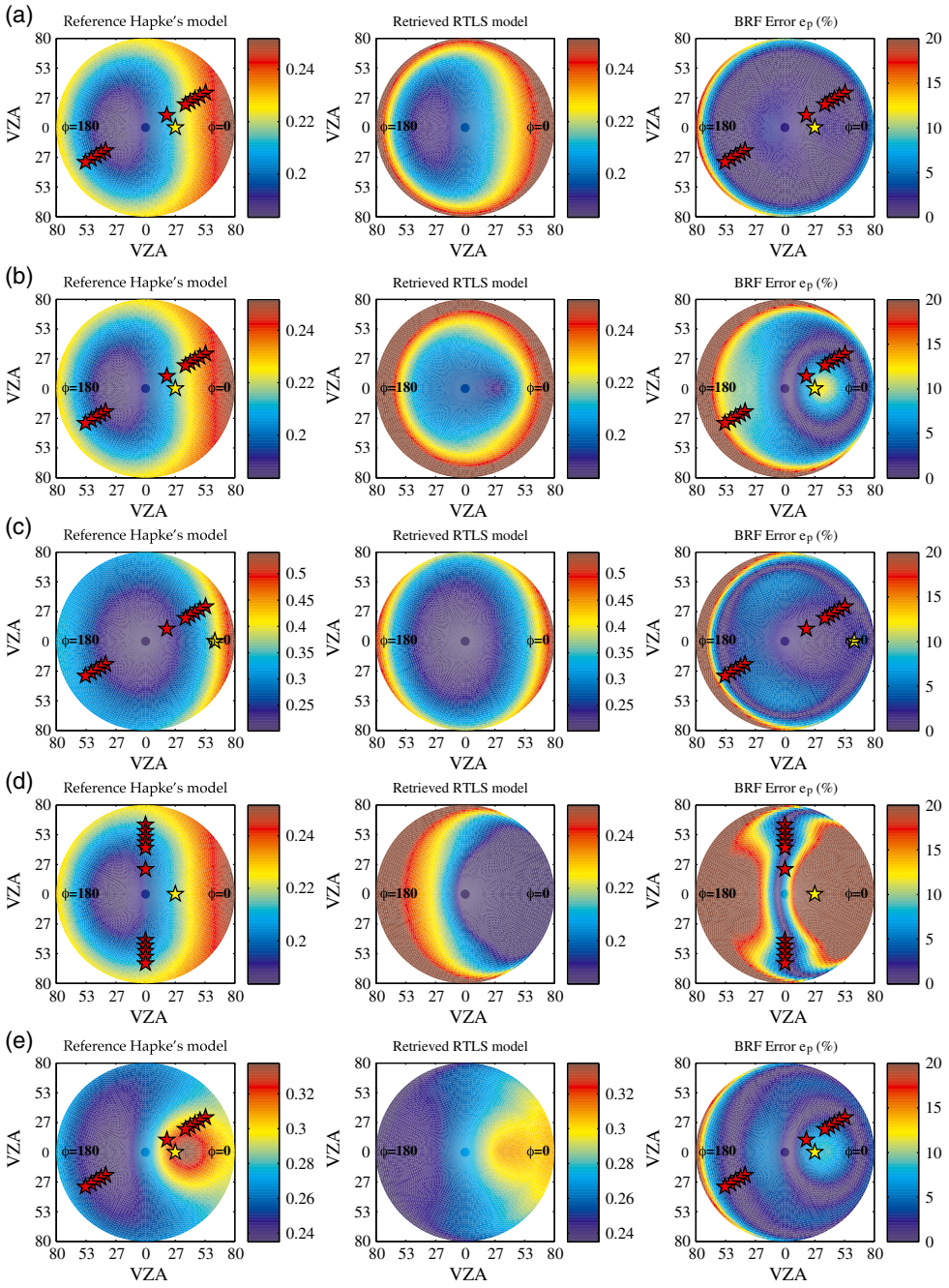


Figure 7. From top to bottom, same as Figure 6 when (a) $\tau_0 = 0.5$, (b) $\tau_0 = 2$, (c) $\tau_0 = 0.5$ and $\theta_0 = 70°$, (d) $\tau_0 = 0.1$ and $\varphi_1, \varphi_2 = \{90°, 90°\}$, and (e) $\tau_0 = 0.5$ and surface made of material Red rock-1.

to the solar cross-principal plane where the main surface scattering features of Soil-1 cannot be sampled. Note, however, that the average BRF error and the standard deviation are quite low ($e_\rho = 1.8\%$ and $\sigma_\rho = 0.003$) as inaccuracies are found out of the 11 sensing geometries. This example highlights the differences between the quality of the retrieved photometric curve, which is quite high in this case, and that of the complete BRF model, which is very poor.

[57] The last experiment summarized in Figure 7e considers $\tau_0 = 0.5$ and material Red rock-1, which is related to a higher albedo, a higher anisotropy, and a higher surface roughness (Table 1). As it can be seen, the retrieved BRF model is rather accurate and reproduces accurately the main narrow backscattering lobe (i.e., the scattering feature in the forward direction of Red rock-1 is smoothed by the surface roughness $\bar{\theta}$), except for a slight underestimation of 7%. The smoothness of narrow

and strong lobes is a typical limitation of the RTLS model [*Roujean et al.*, 1992]. Again, the highest BRF error is obtained in the forward direction for extreme viewing geometries ($\theta > 70°$). This configuration is associated to a low average BRF error and a low standard deviation ($e_\rho = 2.5\%$ and $\sigma_\rho = 0.005$), indicating the goodness of the retrieval.

3.3. Study on Observations with Restricted Geometry

[58] Up to this point MARS-ReCO has been applied to photometric curves made of 11 measurements. Unfortunately, this situation does not correspond to reality since less than 20% of the area encompassed by CRISM targeted observations is typically sensed by more than seven geometries (see Figure 2). The following experiments aim at assessing MARS-ReCO against a reduced number of measurements and thus a restricted geometry.

3.3.1. Number of Angular Measurements and Phase Angle Range

[59] The synthetic data set defined in Section 3.1 is iteratively degraded by removing an increasing number of measurements from each photometric curve. The position of the removed measurements in terms of view zenith angle is chosen randomly. MARS-ReCO is applied to the resulting data set on each iteration until only three measurements are available. Note that the inversion for the RTLS kernel weights with less than three measurements becomes unconstrained. The performance of MARS-ReCO is assessed according to the number of measurements and the phase angle range encompassed by each photometric curve. Note that a high number of measurements within a narrow phase angle range may be less appropriate than few measurements and a broad phase angle range [*Souchon et al.*, 2011].

[60] According to Figure 8(top left), the rate of unsuccessful retrievals remains rather acceptable except for photometric curves with a phase angle range lower than 40°. In this case, photometric curves do not contain enough angular diversity to separate the photometric curve of aerosols from that of the surface, regardless of the number of geometries. Note how the performance of MARS-ReCO decreases for a reduced number of geometries as the inversion becomes progressively unconstrained. However, the number of available geometries is less crucial than the phase angle diversity in terms of convergence.

[61] Figures 8(bottom left) and 8(bottom right) explore the a posteriori standard deviation (σ_ρ) and the error (e_ρ) of the retrieved BRF, respectively. Again, the phase angle range appears as the most critical parameter to perform an accurate atmospheric correction. In fact, Figure 8(bottom right) shows the decrease of the retrieved BRF accuracy for limited phase angle ranges combined with a few available geometries. These unfavorable situations can be detected when processing real CRISM observations based on the a posteriori standard deviation. Indeed, this parameter shows a strong correlation with the BRF error, thus confirming its pertinence as an indicator of the accuracy of the retrieved surface. By contrast, Figure 8(top right) proves that the RMSE is not correlated with the accuracy of MARS-ReCO. For instance, contrary to the BRF error, the RMSE is minimum when only three geometries are available as photometric curves are easier to fit in this case. Lastly, note that the

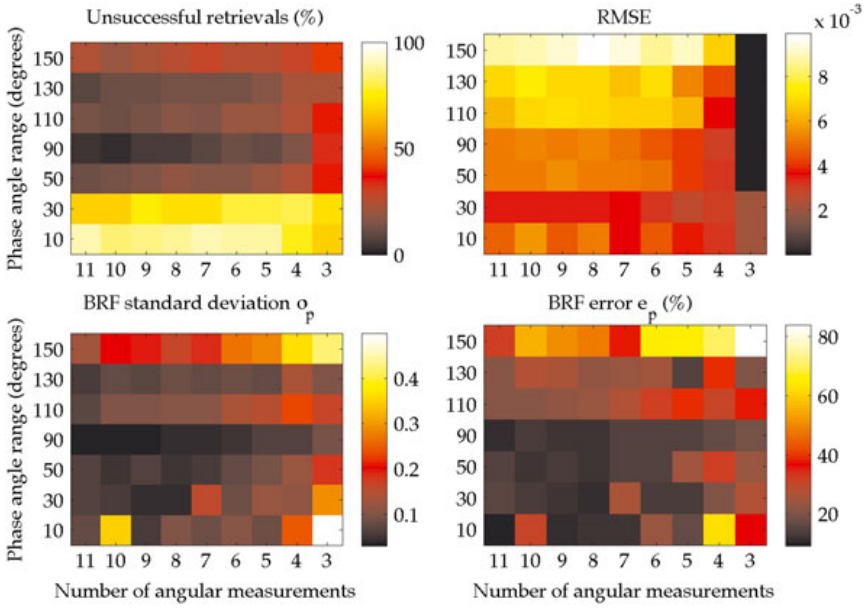


Figure 8. (top left) Percentage of unsuccessful retrievals, (top right) RMSE, (bottom left) a posteriori standard deviation of the retrieved BRF surface σ_ρ, and (bottom right) average BRF error (e_ρ) computed along the acquisition geometries according to the number of measurements and the phase angle range (Δg). The RMSE, BRF error, and parameter (σ_ρ) are computed only for the successfully processed photometric curves. The y axis of the figures is defined such that the row associated to a phase angle range of 110° encompasses the photometric curves within $100° < \Delta g \leq 120°$. Results when $\Delta g = 70°$ and $\Delta g = 170°$ are not shown due to the absence of photometric curves at these configurations.

rather inaccurate results obtained when dealing with very broad phase angle ranges (larger than 140°) are misleading. In fact, this situation encompasses the most extreme illumination conditions ($\theta_0 > 70°$).

3.3.2. Distribution of the Phase Angle

[62] The previous experiment does not take into account which phase angles are sampled by the photometric curves. Although broad sampled phase angle range are usually beneficial, not all ranges of a given magnitude are equally useful. Furthermore, since the end of 2010, CRISM is acquiring targeted observations without inbound portion due to gimbal stickiness [*Murchie*, 2012]. These restricted range observations sample either small phase angles (when the Sun is "behind" MRO) or large phase angles (when the Sun is "in front" of MRO) while corresponding to similar magnitudes of phase angle range.

[63] In order to assess the performance of MARS-ReCO according to the sampled phase angles, two synthetic data sets are built based on the data set described in Section 3.1. Both data sets mimic the latest restricted range observations by containing photometric curves with only five measurements corresponding to a single mode of azimuth, φ_1 or φ_2 (see Table 1). The first data set simulates no inbound observations sampling small phase angles, while the second one favors larger phase angles. The BRF error at the acquisition geometries e_ρ resulting from the inversion of these two data sets is explored according to the type of material in Figure 9. Two cases are defined to study the sampled phase angles. The first case computes the average BRF error of all "backward" photometric curves ($g \in [0°, 90°]$), while the second case considers all "forward" curves ($g \in [90°, 180°]$). Note that there are approximately 30% less photometric curves in the second case as the phase angle becomes quite small for $\varphi_2 = 120°$ or 90°, especially when solar zenith angle is small.

[64] According to Figure 9, the predominance of aerosol contribution results in larger BRF errors for "forward" photometric curves. Also, the BRF error is larger where there is less signal coming from the surface as it happens for backscattering surface materials when $g \in [90°, 180°]$. Contrarily, the BRF error related to Red rock-1 is larger when $g \in [0°, 90°]$ as this material is forward scattering. The BRF error decreases for large reflectances and sharp scattering lobes (e.g., Red rock-1) as the surface signal is easier to retrieve in this case. In opposite, flat scattering lobes result in higher BRF errors (e.g., Soil-2 obtains a higher error than Soil-1 since the latter has a sharper lobe) even for highly anisotropic materials (e.g., Red rock-2). In conclusion, while the BRF error for no inbound observations is somewhat higher than for complete observations (see Figure 5), it is still reasonable ($e_\rho \approx 20\%$). This result underlines that MARS-ReCO is appropriate to process restricted range CRISM observations provided that five angular measurements are available. In particular, backscattering surfaces are prone to be retrieved more accurately when the outbound images have the Sun in the back (i.e., small phase angles), that is, when MRO in is the north (south) hemisphere in its descending (ascending) node. Finally, it should be remarked that the retrieved BRF model is likely to be less accurate out of the acquisition geometries than for complete targeted observations.

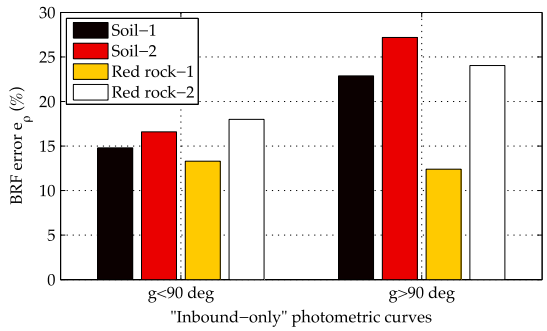


Figure 9. Average BRF error at the acquisition geometries (e_ρ) for a set of photometric curves without the inbound portion found in CRISM targeted observations. Two classes are defined according to the distribution of the phase angle, those sensing the surface of Mars exclusively (i) in the backward direction ($g \in [0°, 90°]$) and those (ii) in the forward direction ($g \in [90°, 180°]$).

3.4. Study on the Stability of the Surface Solution

[65] This experiment explores the robustness of MARS-ReCO by assessing the stability of the retrieved surface solution for a set of similar photometric curves. With this aim, MARS-ReCO is run on a set of photometric curves deriving from a particular configuration defined by material Soil-1, $\tau_0 = 0.5$, $\theta_0 = 30°$, and $\varphi_1, \varphi_2 = \{30°, 150°\}$. Figure 10 shows the evolution of the retrieved RTLS kernel weights according to a varying AOD, solar zenith angle, and azimuthal configuration. In Figure 10(left), for instance, the AOD associated to the set of photometric curves varies in contrast to the solar zenith angle and the azimuthal configuration, which remain at their initial values. According to results, the surface BRF models provided by MARS-ReCO for material Soil-1 are quite alike despite the variability encompassed by the data set of study. Only extreme configurations such as $\varphi_1, \varphi_2 = \{90°, 90°\}$ or $\theta_0 = 80°$ result in a significantly different RTLS triplet $\mathbf{k}_{sol}$. As for the aerosol content, Figure 10(left) shows that an increasing AOD results in a slight variation of all RTLS kernel weights (note that the geometric kernel function F^G is much larger than the volumetric one F^V, and therefore, the associated weights k^G are respectively smaller). The increase in k^V is compensated by the decrease in k^G, so the anisotropy of the surface is maintained. This result underlines that two slightly different combinations of the RTLS weights can provide two satisfactory surface fits at the acquisition geometries. Note, however, that when $\tau_0 > 2$ the retrieved BRF models are certainly incorrect.

3.5. Study on the Aerosol Content Uncertainty

[66] Up to now MARS-ReCO has been fed with the exact aerosol content that is used for the data simulation. In reality, however, the actual optical depth of a given observation can be known only with a given uncertainty. *Clancy et al*. [2003] find a ±0.05 uncertainty for retrieved optical depths between 0.20 and 0.50 using EPF observations taken by the Thermal Emission Spectrometer aboard Mars Global Surveyor. *Lemmon et al*. [2004] determine typical uncertainties between ±0.02 and ±0.04 when measuring the AOD with the MER rovers. *Vincendon et al*. [2009] find uncertainties

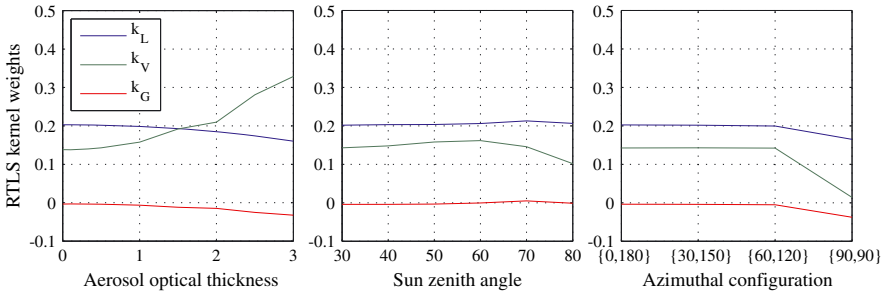


Figure 10. RTLS kernel weights retrieved from a set of photometric curves initially defined by material Soil-1, $\tau_0 = 0.5$, $\theta_0 = 30°$, and $\varphi_1, \varphi_2 = \{30°, 150°\}$. The AOD, solar zenith angle, and azimuthal configuration vary in the left, center, and right figures, respectively.

of ±10% for moderate aerosols loading ($\tau_0(1\mu m) = 0.5$) and of ±20% for high aerosols contribution ($\tau_0(1\ \mu m) = 1$) using OMEGA observations. Similarly, *Wolff et al.* [2009] obtain uncertainties of ±10–20% for aerosol depths measured with CRISM EPF data.

[67] The last experiment of the sensitivity analysis investigates the impact of these uncertainties on the MARS-ReCO capabilities. We now consider that the actual optical depth is affected by an unknown additive bias such that $\tau'_0 = \tau_0 + b_{\tau_0}$. According to the studies cited above, the bias affecting aerosol content is modeled with a normal distribution that introduces an average bias of ±15% (standard deviation of 5%). In this way, a vector of 216 different biases b_{τ_0}—negative and positive with different magnitudes—is generated, one for each synthetic photometric curve. The suite of inversions performed in Section 3.2.1 is repeated using the biased optical depths (τ'_0). The error on the latter estimates is considered by setting the parameter characterizing the AOD uncertainty to $\sigma^2_{\tau_0} = \left(0.15 * \tau'_0\right)^2$ (see Section 2.2.6).

[68] Figure 11 illustrates the inversion quality by means of the typical MARS-ReCO indicators. Only the dependence on aerosol optical depth is shown as the relation between the inversion quality, and all acquisition parameters is very similar to that observed for the ideal case (see Figures 4 and 5). In fact, only the average value of the quality indicators suffers significant variations. In particular, the RMSE and the BRF error (e_ρ) undergo an increase of 30% and 9%, respectively. This decrease in the quality of the retrieved surface reflectance results in an increase of the evaluated uncertainty of the surface BRF (σ_ρ) by a factor 2. Higher inaccuracies for $\tau_0 = 2$ are explained by the higher bias that affects the photometric curves typically related to the greatest errors (e.g., $\theta_0 = 80°$) in this AOD interval. Likewise, remember that the CRISM-like data are affected by random noise. Lastly, the rate of unsuccessful retrievals is not shown for this experiment as results are very similar to those in Figure 4. Although the rate of successful retrievals decreases due to the error on the AOD estimates, the relaxation introduced in the inversion by considering $\sigma^2_{\tau_0} \neq 0$ helps MARS-ReCO fitting the TOA photometric curves.

4. Discussion

[69] According to the sensitivity analysis described in the previous section, MARS-ReCO proves to be appropriate to process real CRISM targeted observations. Surface reflectance curves provided by MARS-ReCO are physically plausible and mostly accurate. The few inaccurate surface solutions can be detected by examining the a posteriori standard deviation of the estimated BRF (σ_ρ) provided by MARS-ReCO. This output has proved to be a satisfactory indicator of the quality of the retrieved surface reflectance according to its high correlation with the BRF error. Note that the latter indicator is

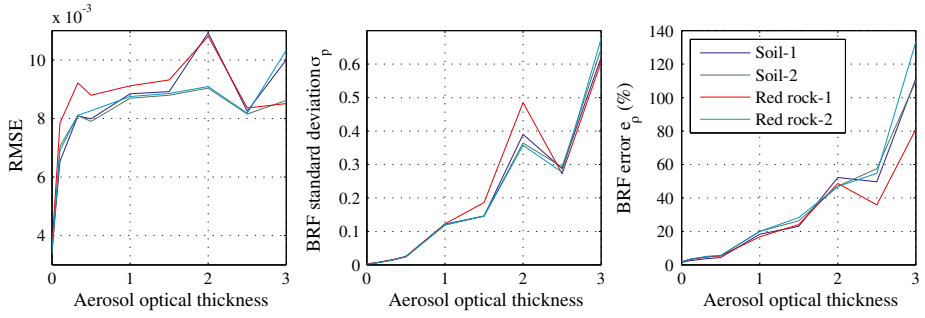


Figure 11. RMSE, a posteriori standard deviation of the retrieved BRF, and BRF error when a 10% uncertainty is considered for the aerosol content estimate. Note the different vertical axis range with respect to Figures 4 and 5.

accessible only if ground truth data are available. Based on the sensitivity analysis, this section establishes the range of conditions over which MARS-ReCO is able to confidently retrieve surface properties from CRISM targeted observations.

[70] Table 3 summarizes the main results obtained by the sensitivity analysis. In particular, retrievals of surface reflectance are possible (unsuccessful retrievals lower than 5%) and relatively accurate (BRF error lower than 20%) when TOA photometric curves are related to (i) an appropriate angular configuration set by a moderate solar zenith angle ($\theta_0 < 70°$) and an azimuthal configuration ensuring a broad phase angle range ($\Delta g \in [40°, 140°]$), and (ii) a surface signal which is significant compared to the aerosol contribution, that is, a moderate AOD ($\tau_0 \leq 1.5$). Accuracy can be increased ($e_\rho < 10\%$) by restricting the validity ranges to $\theta_0 \leq 60°$ and $\tau_0 \leq 0.9$. Furthermore, results show that surfaces combining a low albedo and a low anisotropy (e.g., Soil-2 with $\omega = 0.65$ and $c = 0.17$) lead to slightly worse retrievals (accuracy decrease of 10%). The previous range of conditions is subject to the availability of the aerosol content over CRISM observations. An average decrease of 9% of the quality of the retrieved surface reflectance must be expected for AOD estimates with a 15% error.

[71] In practice, the range of conditions providing inaccurate surface solutions is limited. First, the inversion of CRISM observations with restricted phase angle range (e.g., $\varphi_1, \varphi_2 = \{90°, 90°\}$) is discarded by the criteria of MARS-ReCO (90% of rejection in this case). In this matter, experiments underline that the reflectance accuracy remains acceptable ($e_\rho \lesssim 20\%$) even against a reduced number of angular measurements (down to 5–6 geometries) as long as a broad phase angle range is available ($\Delta g \in [40°, 140°]$). Configurations out of these bounds make the separation between aerosol and surface signals not possible due to the lack of angular diversity, when $\Delta g < 40°$, or the scarcity of available geometries, when $\Delta g > 140°$. Second, opacities on Mars are often rather low ($\tau_0 < 1$ long-ward of one micron [*Smith*, 2009]). However, precaution must be taken when processing CRISM observations from the high latitudes of Mars as they can be acquired with solar zenith angles around 70°. Besides the limitations of the RTLS surface model at these angles, the plane-parallel approximation used by DISORT may affect the surface retrievals. In this situation (and other unfavorable cases), the a posteriori standard deviation of the estimated BRF (σ_ρ) must be inspected in order to detect incorrect surface retrievals. Experiments prove that surface solutions with $\sigma_\rho \lesssim 0.08$ are related to errors greater than 20%.

[72] It is important to remark that despite a low standard deviation ($\sigma_\rho < 0.08$), the retrieved BRF surface model must be handled with care when it is evaluated out of the CRISM acquisition geometries (Figure 7d). Also, MARS-ReCO has proved to be stable (variability of ~10% of the retrieved surface model) when dealing with a group of adjacent CRISM-like super-pixels belonging to the same surface material but observed with slightly different geometric configurations.

5. Conclusions

[73] A radiative transfer-based algorithm for atmospheric correction is put forward to retrieve surface reflectance from CRISM multi-angle imagery. The method referred to as MARS-ReCO transforms a set of gas-free TOA radiances, which correspond to the same terrain unit observed at different geometries, into a photometric curve in units of surface reflectance. MARS-ReCO represents a substantial improvement regarding the state of the art in atmospheric correction of Martian data as it considers a non-Lambertian surface along with the photometric curve of the aerosols. The latter data are an input of the proposed technique as well as the aerosol optical depth. Although being based on a radiative transfer model, MARS-ReCO is very fast as it is based on an efficient formulation of the TOA signal and a linear model for the surface reflectivity. In addition, MARS-ReCO integrates a statistical formalism that propagates several uncertainties to the solution, thus providing an accurate indicator of the quality of the retrieved surface reflectance. These statements are confirmed by the sensitivity analysis that is presented in this article and that has proven the validity, the accuracy, and the stability of the surface solutions retrieved from realistic synthetic data (CRISM-like geometric configuration and noise) under realistic conditions (Martian optical depths associated to the typical uncertainties provided by aerosol retrieval methods). This is further proved in the companion article [*Fernando et al*., 2013] where MARS-ReCO processes real CRISM observations and retrieves surface reflectance curves, which are highly accurate (maximum error of 5%) when compared to in situ measurements.

[74] MARS-ReCO is subject to some limitations when processing CRISM multi-angle data acquired under unfavorable acquisition conditions, that is, turbid atmospheres, extreme illumination conditions, and restricted phase angle ranges. The uncertainties on the surface reflectance retrieved under these situations are, however, quantified by the a posteriori standard deviation provided by MARS-ReCO. It is important to note that the potential of MARS-ReCO to map the photometric properties of the surface of Mars is subject to the degree of overlap among the individual images composing a CRISM targeted observation. In this matter, MARS-ReCO has proved to be robust against observations with restricted geometry such as those acquired by CRISM from late 2010. Furthermore, restricted geometry diversity can be overcome by combining different CRISM observations

Table 3. Performance of MARS-ReCO in Terms of Unsuccessful Retrievals and BRF Error (e_ρ) According to Acquisition Configuration

Convergence and BRF Error	Optical Depth	Solar Zenith Angle	Phase Angle Range
Unsuccessful retrievals < 5%	$\tau_0 \leq 2.0$	$\theta_0 < 70°$	$\Delta g \geq 40°$
Unsuccessful retrievals > 5%	$\tau_0 > 2.0$	$\theta_0 \geq 70°$	$\Delta g < 40°$
$e_\rho < 10\%$, ($\sigma_\rho \lesssim 0.04$)	$\tau_0 \leq 0.9$	$\theta_0 \leq 60°$	$\Delta g < 100°$[a]
$e_\rho < 20\%$, ($\sigma_\rho \lesssim 0.08$)	$\tau_0 \leq 1.5$	$\theta_0 < 70°$	$\Delta g \in [100°, 140°]$
$e_\rho > 20\%$, ($\sigma_\rho \gtrsim 0.08$)	$\tau_0 > 1.5$	$\theta_0 \geq 70°$	$\Delta g > 140°$

[a]The few photometric curves satisfying $\Delta g < 40°$ that pass the inversion criteria (see in Appendix C) lead to physically plausible surface reflectance curves (low e_ρ) but strongly incorrect BRF models (see Figure 7d).

of the same target acquired under different angular configurations. Eventually, note that this article assesses the performance of MARS-ReCO on gas-free wavelengths. In order to process the whole CRISM spectral range, gaseous contribution must be previously compensated [*McGuire et al*., 2009; *Douté*, 2009]. In this case, testing must be carried out to evaluate the impact of the uncertainties coming from a faulty gas correction on the retrieved surface reflectance.

[75] One major advantage of MARS-ReCO is that its look-up table can be easily adapted to accommodate different scenarios. In this article, the look-up table considers only mineral aerosols, making MARS-ReCO suitable to process most CRISM observations acquired over the equatorial regions of Mars. Future versions of the look-up table may, however, consider other atmospheric situations such as the presence of water ice aerosols, mineral aerosols with different grain size, or even gases. Further testing should be performed to test the performance of MARS-ReCO in this case. Likewise, limitations found at extreme zenith angles may be mitigated using a look-up table calculated by a radiative transfer code considering the sphericity of Mars.

[76] Further research will be conducted on the exploitation of the complete surface reflectance model retrieved by MARS-ReCO to calculate directional-hemispherical albedos of the surface as it is done with in situ measurements in *Bell et al*. [2008]. Also, we will address the processing of the whole spectral dimension of CRISM. The resulting increase of the input data, together with the consideration of appropriate techniques, may allow us to retrieve simultaneously the surface BRF and the aerosol optical depth as it is done by *Lyapustin et al*. [2011b].

Appendix A: Green's Function Method for the Radiative Transfer Problem

[77] *Lyapustin and Knyazikhin* [2001] address the use of the Green's function method for the radiative transfer problem. The surface is considered to be non-Lambertian and spatially homogeneous, and the atmosphere is vertically stratified with a plan parallel geometry and τ_0 being the integrated optical depth. The atmosphere is illuminated at the TOA by a quasi collimated solar beam of flux πS with incident direction $s_0=(\theta_0,0)$. The direction of radiation propagation within the atmosphere is noted $s=(\theta,\varphi)$. The vertical axis z points downward so that downward directions of propagation ($\mu>0$) are indicated by a plus sign (+) while the upward direction ($\mu<0$) corresponds to a minus sign (−). The wavelength of measurement of the sensor λ is omitted for clarity. The method is based on the additive properties of the radiative transfer equation and on three ideas.

1. First, the total radiance at a given level of optical depth τ and direction of propagation s is decomposed into the radiance corresponding to the photons that never interacted with the surface and a term corresponding to the radiance carried by all other photons

$$L(\tau;s_0,s)=D(\tau;s_0,s)+J(\tau;s_0,s), \tag{A1}$$

where the first term depends only on the properties of the atmosphere and obeys the radiative transfer equation with the boundary conditions $D_+(0)=0$ and $D(\tau_0)=0$.

2. Second, the determination of the radiative response of the atmosphere to a given field of upward radiance at the surface-atmosphere interface $L_-(\tau_0,s')$ requires the calculation of the atmospheric response $G^d(\tau;s',s)$ if the atmosphere is illuminated from below with an elementary collimated flux beam $\pi S=1$ in the direction s'. This diffuse Green's function $G^d(\tau;s',s)$ is a solution to the radiative transfer problem adjoint to the standard radiative transfer equation which solution is $D(\tau;s_0,s)$. By adjoint, we mean reversing the order of the atmospheric layers ($\tau\rightarrow\tau_0-\tau$) but with the same boundary conditions, that is, $G^d_+(0)=0$ and $G^d_-(\tau_0)=0$. Similar to $D(\tau;s_0,s)$, the term $G^d(\tau;s',s)$ depends only on the properties of the atmosphere. We define the operator

$$\hat{\Gamma}^-_{\tau,s}L_-=\int_{\Omega^-}ds'\,G^d\left(\tau,s',s\right)L_-\left(\tau_0,s'\right), \tag{A2}$$

which transforms $L_-(\tau_0,s')$ into the atmospheric response.

3. Third, the radiance field $J(\tau;s_0,s)$ is considered as a series of converging terms $J^{(j)}(\tau;s_0,s)$ that quantify the radiative flux of photons which have undergone a number j of surface-atmosphere round trips. On the surface-atmosphere interface, it is possible to formalize the physical interaction that binds a term $j-1$ to the next j such that

$$J^{(j)}_-(\tau_0)=\hat{R}\hat{\Gamma}^+_{\tau_0}J^{(j-1)}_-(\tau_0), \tag{A3}$$

and, at this level, the series converges to

$$J_-(\tau_0)=\sum_{j\geq1}J^{(j)}_-(\tau_0)=\left[\hat{I}-\hat{R}\cdot\Gamma^+_{\tau_0}\right]^{-1}\hat{R}L^{(0)}_+(\tau_0), \tag{A4}$$

the zeroth-order illumination of the surface being

$$L^{(0)}_+(\tau_0 s)=\pi S e^{-\tau_0/\mu_0}\delta(s-s_0)+D\left(\tau_{0;}s_{0,}s\right),\qquad \mu>0. \tag{A5}$$

[78] In all cases, the operator $\hat{R}$ expresses the reflection by the surface of a downward radiance field into a upward radiance field

$$J^{(j)}_-(\tau_0)=\hat{R}J^{(j-1)}_+(\tau_0)=\int_{\Omega^+}ds'\rho\left(s',s\right)\mu' J^{(j-1)}_+\left(\tau_0,s'\right). \tag{A6}$$

[79] Transferring the total radiance exiting the surface to the TOA and adding the additive contribution of the latter, the TOA radiation measured by the instrument becomes

$$L(\tau=0;s_0,s)=D(0;s_0,s)+\hat{\Gamma}^-{}_{0,s}\left[\hat{I}-\hat{R}\cdot\Gamma^+_{\tau_0}\right]^{-1}\hat{R}L^{(0)}_+(\tau_0),\quad \mu<0. \tag{A7}$$

A1. Practical Resolution

[80] In order to achieve the calculation, it is necessary to calculate each term $J^{(j)}_-(\tau_0;s)$, $j\geq1$ using equation (A3) resulting in a quadruple numerical integration. In the case of a surface and/or atmosphere high albedo, the series can be long to converge and the number of terms required in the summation becomes important. Two main assumptions

become therefore necessary to circumvent the prohibitive computation time in this case.

1. After a sufficiently large number of atmosphere-surface round trips, two successive terms of the series become proportional; that is, the angular structure of the radiance field is preserved at the interface ($\tau = \tau_0$), the absolute level becoming weaker and weaker:

$$J_-^{(j+1)}(\tau_0) = \hat{R}\hat{\Gamma}^+_{\tau_0} J_-^{(j)}(\tau_0) \simeq \eta J_-^{(j)}(\tau_0). \tag{A8}$$

For many natural surfaces that are reasonably anisotropic, this number is very small $j = 2$. Then we only need to calculate the terms $J_-^{(j)}(\tau_0), j = 2, 3$ with equation (A3) starting with

$$J_-^{(1)}(\tau_0; s) = S\mu_0 e^{-\tau_0/\mu_0}\rho(s_0, s) + \frac{1}{\pi}\int_{\Omega^+} ds'\rho(s', s)\mu' D(\tau_{0;} s_0, s'). \tag{A9}$$

Quantity $\eta \simeq \frac{J_-^{(3)}(\tau_0;s)}{J_-^{(2)}(\tau_0;s)}$ can be now evaluated, allowing a simplified expression of the upward radiance field requiring the computation of only two successive quadruple integrations

$$J_-(\tau_0; s) = J_-^{(1)}(\tau_0; s) + \frac{J_-^{(2)}(\tau_0; s)}{1 - \eta}. \tag{A10}$$

2. Assuming that radiation is enough isotropic so that multiple surface-atmosphere reflections occur according to a Lambertian law, factor η is the product of two bihemispherical albedos $\eta = c_0\rho_0$, the surface and atmospheric albedos (ρ_0 and c_0) being

$$\rho_0 = \frac{1}{\pi}\cdot\int_{\Omega^-} ds'\mu' \int_{\Omega^+} ds\cdot\rho(s, s'), \tag{A11}$$

$$c_0 = \frac{1}{\pi}\cdot\int_{\Omega^+} ds'\mu' \int_{\Omega^-} dsG^d(\tau_0; s, s').$$

[81] The resolution proceeds with the simplification of term $J_-^{(2)}(\tau_0; s) = \hat{R}\hat{\Gamma}^+_{\tau_0} J_-^{(1)}(\tau_0; s)$, which is the diffuse and direct solar illumination reflected once by the surface, then undergoing one surface-atmosphere round trip. As the first diffuse contribution is already a slowly changing function with respect to direction, the angular structure is conserved in the operation which reduces to a multiplication by η. The second contribution can also be approximated but less drastically. This step gives the final expression for the upward radiance rising at the surface-atmosphere interface

$$J_-(\tau_0; s) = S\mu_0 e^{-\tau_0/\mu_0}\left[\rho(s_0, s) + \frac{c_0\rho_1(s)\rho_2(s_0)}{1 - c_0\rho_0}\right] + \frac{1}{\pi[1 - c_0\rho_0]}\int_{\Omega^+} ds'\rho(s', s)\mu' D(\tau_0, ; s_0, s'), \tag{A12}$$

where

$$\rho_1(s) = \frac{1}{2\pi}\int_{\Omega^+} ds'\rho(s', s), \qquad \rho_2(s_0) = \frac{1}{2\pi}\int_{\Omega^-} ds'\rho(s_0, s'). \tag{A13}$$

[82] The last step consists in transferring the radiance to the TOA, thanks to the direct and diffuse term of the Green's function as it is done in equations (1)–(4).

Appendix B: Ross-Thick and Li-Sparse Kernels

[83] The volumetric or Ross-Thick kernel is a single-scattering approximation of radiative transfer theory consisting of a Lambertian background and a layer of small scatterers with uniform angle distribution and equal transmittance and reflectance [*Roujean et al.*, 1992]. The form of this kernel, normalized to zero for $\theta_0 = 0°$, $\theta = 0°$, is

$$f_V(\theta_0, \theta, g) = \frac{(\pi/2 - g)\cos g + \sin g}{\cos\theta_0 + \cos\theta} - \frac{\pi}{4}. \tag{B1}$$

[84] The geometric or Li-Sparse kernel assumes a sparse ensemble of randomly located spheroids casting shadows on the background, which is assumed Lambertian [*Wanner et al.*, 1995]. This geometric term is given by the proportions of sunlit and shaded scene components in a scene consisting of randomly located spheroids of height-to-center-of-crown h and crown vertical-to-horizontal radius ratio b/r. For CRISM processing, we take $b/r = 1$ and $b/r = 2$ as it is done for MODIS processing [*Lucht et al.*, 2000]. If the sunlit component is simply assumed to vary as $1/\cos\theta_0$, the kernel takes on the reciprocal form

$$f_G(\theta_0, \theta, \varphi) = O(\theta_0, \theta, \varphi) - \sec\theta'_0 - \sec\theta' + \frac{1}{2}\left(1 + \cos g'\right)\sec\theta'_0\sec\theta', \tag{B2}$$

where

$$\begin{aligned} O &= \frac{1}{\pi}(t - \sin t\cos t)\left(\sec\theta'_0 + \sec\theta'\right), \\ \cos t &= \frac{h}{b}\frac{\sqrt{D^2 + \left(\tan\theta'_0\tan\theta'\sin\varphi\right)^2}}{\sec\theta'_0 + \sec\theta'}, \\ D &= \sqrt{\tan^2\theta'_0 + \tan^2\theta' - 2\tan\theta'_0\tan\theta'\cos\varphi}, \\ \cos g' &= \cos\theta'_0\cos\theta' + \sin\theta'_0\sin\theta'\cos\varphi, \\ \theta_0 &= \tan^{-1}\left(\frac{b}{r}\tan\theta_0\right), \theta' = \tan^{-1}\left(\frac{b}{r}\tan\theta\right). \end{aligned} \tag{B3}$$

Appendix C: Rejection and Convergence Criteria

[85] The quality of the surface solutions provided by MARS-ReCO is assured by the following set of rejection criteria adopted from *Lyapustin et al.* [2012]:

1. Before inversion, we check if the photometric curve to be processed satisfies a minimum phase angle sampling, namely, $\max(g_j) - \min(g_j) \geq 20°$, $\forall j \in [1, N_g]$. Inversion is aborted otherwise. Additionally, MARS-ReCO is run only if there are at least three angular measurements as the inversion problem becomes unconstrained otherwise (note the three unknown variables **k**).

2. After retrieving the surface solution $\mathbf{k}^{(n+1)}$ on iteration n, the angular measurements R_j^C that satisfy $\left|R_j^C - R_j^{(n+1)}\right| > 4\sigma_{Rj} = 4\sqrt{C_{pr}^{jj}}$ are excluded. The inversion is restarted on iteration $n+1$ with a reduced number of geometries. Note that σ_{Rj} is the a posteriori 1σ error bar on the modeled TOA reflectance for each geometry. Testing proved that a 4σ threshold is a good trade-off between rejection of wrong solutions and limitations of the inversion method. This criterion is especially useful for challenging CRISM observations such as those acquired over the polar regions or under turbid atmospheric conditions.
3. The physical sense of the retrieved kernel weights $\mathbf{k}^{(n+1)}$ is verified by checking that the associated surface albedo $q^{(n+1)}(\theta_0)$ is positive and lower than unity when $\theta_0 = 15°$, $45°$, $60°$. The inversion of the current photometric curve is aborted otherwise.

[86] At the end of each iteration, the retrieved surface solution is evaluated for convergence by the following convergence criterion:

1. The quality of the derived surface BRF is assessed by a confidence index that is initially low ($flag = 0$, when $n = 0$). The retrieved solution $\mathbf{k}^{(n+1)}$ obtained on iteration n is compared with the previous solution $\mathbf{k}^{(n)}$ as follows $|q^{(n+1)}(\theta_0) - q^{(n)}(\theta_0)| < 0.001$, where $\theta_0 = 15°$, $45°$, $60°$. Each time a new retrieval agrees with the previous solution according to this criterion, *flag* is increased by 1 and the inversion is repeated on next iteration $n+1$ using $\mathbf{k}^{(n+1)}$. The retrieval is considered to be reliable when $flag = 4$. This criterion is useful for CRISM polar observations for which the nonlinear term R^{nl} becomes larger due to the high brightness of the surface and the extreme acquisition geometry.

C1. Notation

C1.1. Spectral and Directional Parameters

θ, θ_0: view and solar zenith angle
μ, μ_0: cosine of view and solar zenith angle
φ, g: view-sun relative azimuth and phase angle
s, s_0: view and sun directions defined by (θ,φ) and (θ_0,φ_0). In this work, $\varphi_0 = 0°$
λ: wavelength

C2. Atmospheric Parameters

$\tau_0(\lambda)$: aerosol optical depth
$c_0(\lambda)$: spherical albedo of the atmosphere
$G^d(s_0,s,\lambda)$: diffuse Green's function of the atmosphere
$D(s_0,s,\lambda)$, $R^D(s_0,s,\lambda)$: atmospheric reflected path radiance and reflectance
$D_s(s_0,s,\lambda)$: path radiance incident on the surface
$F_s(s_0,\lambda)$, $F_s^d(s_0,\lambda)$: direct and diffuse radiative fluxes incident on the surface
$F^{Down}(s_0,\lambda)$, $F^{Up}(s_0,\lambda)$: downwelling and upwelling radiative fluxes at the surface
$\mathrm{L_s}(\mathrm{s_0,s},\lambda)$, $\mathrm{L_s^d}(\mathrm{s_0,s},\lambda)$: direct and diffuse upwelling radiance after surface reflection
$\alpha(\mathrm{s_0},\lambda)$: multiple reflection factor

C3. Top-of-atmosphere Parameters

$I(s_0,s,\lambda)/F(s_0,\lambda)$: ratio of measured intensity to solar flux
$L(s_0,s,\lambda)$, $R(s_0,s,\lambda)$: gas-free radiance and reflectance
$\pi S(s_0,\lambda)$: extraterrestrial solar spectral irradiance

C4. Surface-related Parameters

$\rho(s_0,s,\lambda)$: bidirectional reflectance factor
$q(s_0,\lambda)$: directional-hemispherical surface albedo
$f_G(s_0,s,\lambda)$, $f_V(s_0,s,\lambda)$: RTLS geometric and volumetric kernels
$\mathbf{k} = \{k^L(\lambda), k^G(\lambda), k^V(\lambda)\}$: weights for the RTLS kernels

C5. Inversion Parameters

$\mathbf{k}_{sol}$: weights providing the best fit between the model and the CRISM measurements
$\{F^L,F^G,F^V\}$: multiplicative factors for the kernel weights
$R^{nl}(\mu_o,\mu)$: nonlinear term comprising the surface dependence of the TOA reflectance
$r(s_0,s,\lambda)$: reduced measurements such that $\mathrm{r = R - R^D - R^{nl}}$
$\mathbf{C}_C$, $\mathbf{C}_{\tau_0}$, $\mathbf{C}_k$, $\mathbf{C}_r$: covariance matrix of the CRISM measurements, the AOD estimate, the RTLS weights, and the reduced measurements
$\mathbf{C}_{pr}$, $\mathbf{C}_{pk}$, $\mathbf{C}_{p\rho}$: a posteriori covariance matrix of the reduced measurements, the RTLS weights, and the retrieved BRF
RMSE: root mean square error between the sensed and the modeled TOA reflectances
σ_ρ: a posteriori standard deviation of a retrieved photometric curve in BRF units
e_ρ: relative error of the retrieved BRF photometric curve as regards the synthetic data

[87] **Acknowledgments.** This work was done within the framework of the Vahiné project funded by the "Agence Nationale de la Recherche" (ANR) and the "Centre National d'Études Spatiales" (CNES). This work has benefited from the scientific environment of Paul Sabatier University. We also acknowledge support from the "Centre National de la Recherche Scientifique" (CNRS) through the "Programme National de Planétologie". The authors would like to thank Michael J. Wolff for making his aerosol properties available to the authors for this study. The authors would like to thank the anonymous reviewers for their constructive comments that helped improving this paper.

References

Barlow, N. (2008), *Mars: An Introduction to its Interior, Surface and Atmosphere*, Cambridge University Press, Cambridge, U.K., doi:10.1017/CBO9780511536069.

Bell, J. F., III, M. S. Rice, J. R. Johnson, and T. M. Hare (2008), Surface albedo observations at Gusev Crater and Meridiani Planum, Mars, *J. Geophys. Res.*, *113*(E06S18), doi:10.1029/2007JE002976.

Brown, A. J., and M. J. Wolff (2009), Atmospheric modeling of the Martian polar regions: One Mars year of CRISM EPF observations of the south pole, in *Lunar and Planetary Science Conference*, 1675.

Clancy, R. T., and S. W. Lee (1991), A new look at dust and clouds in the Mars atmosphere: Analysis of emission-phase-function sequences from global Viking IRTM observations, *Icarus*, *93*, 135–158.

Clancy, R. T., M. J. Wolff, and P. R. Christensen (2003), Mars aerosol studies with the MGS TES emission phase function observations: Optical depths, particle sizes, and ice cloud types versus latitude and solar longitude, *J. Geophys. Res.*, *108*(E9), 5098, doi:10.1029/2003JE002058.

Cull, S., R. E. Arvidson, M. Mellon, S. Wiseman, R. Clark, T. Titus, R. V. Morris, and P. McGuire (2010), Seasonal H2O and CO2 ice cycles at the Mars Phoenix landing site: 1. Prelanding CRISM and HiRISE observations, *J. Geophys. Res.*, *115*(E00D16), doi:10.1029/2009JE003340.

Diner, D. J., J. V. Martonchik, R. A. Kahn, B. Pinty, N. Gobron, D. L. Nelsonc, and B. N. Holben (2005), Using angular and spectral shape similarity constraints to improve MISR aerosol and surface retrievals over land, *Remote Sens. Environ.*, *94*, 155–171, doi:10.1016/j.rse.2004.09.009.

Douté, S. (2009), Retrieving Mars surface reflectance from OMEGA/MEX imagery, in *IEEE Workshop on Hyperspectral Image and Signal Processing: Evolution in Remote Sensing*.

Douté, S., and X. Ceamanos (2010), Retrieving Mars aerosol optical depth from CRISM/MRO imagery, in *IEEE Workshop on Hyperspectral Image and Signal Processing: Evolution in Remote Sensing*, Reykjavik.

Drossart, P., J. Rosenqvist, S. Erard, Y. Langevin, J.-P. Bibring, and M. Combes (1991), Martian aerosol properties from the Phobos/ISM experiment, *Ann. Geophys.*, *9*(11), 754–760.

Erard, S., J. Mustard, S. Murchie, and J.-P. Bibring (1994), Martian aerosols: Near-infrared spectral properties and effects on the observation of the surface, *Icarus*, *111*, 317–337.

Fernando, J., X. Ceamanos, F. Schmidt, S. Douté, P. Pinet, and Y. Daydou (2013), Surface reflectance of Mars observed by CRISM/MRO: 2. Estimation of surface photometric properties in Gusev Crater and Meridiani Planum, *J. Geophys. Res.*, *118*, doi:10.1029/2012JE004194, in press.

de Grenier, M., and P. C. Pinet (1995), Near-opposition Martian limb-darkening: quantification and implication for visible-near-infrared bidirectional reflectance studies, *Icarus*, *115*, 354–368, doi:10.1016/j.icarus.2008.05.022.

Guanter, L., L. Alonso, and J. Moreno (2005), A method for the surface reflectance retrieval from PROBA/CHRIS data over land: Application to ESA SPARC campaigns, *IEEE Trans. Geosci. Remote Sens.*, *43*(12), doi:10.1109/TGRS.2005.857915.

Hapke, B. (1993), *Theory of Reflectance and Emittance Spectroscopy*, pp. 2908–2917, Cambridge University Press, Cambridge, U. K.

Jehl, A., et al. (2008), Gusev photometric variability as seen from orbit by HRSC/Mars-express, *Icarus*, *197*, 403–428.

Johnson, J. R., W. M. Grundy, M. T. Lemmon, J. F. Bell III, M. J. Johnson, et al. (2006a), Spectrophotometric properties of materials observed by Pancam on the Mars Exploration Rovers: 1. Spirit, *J. Geophys. Res.*, *111*(E02S14), doi:10.1029/2005JE002494.

Johnson, J. R., et al. (2006b), Spectrophotometric properties of materials observed by Pancam on the Mars Exploration Rovers: 2. Opportunity, *J. Geophys. Res.*, *111*(E12S16), doi:10.1029/2006JE002762.

Korablev, O., V. Moroz, E. Petrova, and A. Rodin (2005), Optical properties of dust and the opacity of the Martian atmosphere, *Adv. Space Res.*, *35*(1), 21–30, doi:10.1016/j.asr.2003.01.061.

Langevin, Y., F. Poulet, J.-P. Bibring, and B. Gondet (2005), Sulfates in the north polar region of Mars detected by OMEGA/Mars Express, *Science*, *307*(5715), 1584–1586, doi:10.1126/science.1109091.

Lemmon, M. T., et al. (2004), Atmospheric imaging results from the Mars Exploration Rovers: Spirit and Opportunity, *Science*, *306*, 1753–1756, doi:10.1126/science.1104474.

Lucht, W., C. B. Schaaf, and A. H. Strahler (2000), An algorithm for the retrieval of albedo from space using semiempirical BRDF models, *IEEE Trans. Geosci. Remote Sens.*, *38*(2), 977–998.

Lyapustin, A., Y. Wang, I. Laszlo, R. Kahn, S. Korkin, L. Remer, R. Levy, and J. S. Reid (2010), Analysis of snow bidirectional reflectance from ARCTAS spring-2008 campaign, *Atmos. Chem. Phys.*, *10*, 4359–4375, doi:10.5194/acp-10-4359-2010.

Lyapustin, A., and Y. Knyazikhin (2001), Green's function method for the radiative transfer problem. I. Homogeneous non-Lambertian surface, *Appl. Opt.*, *40*(21), 3495–3501.

Lyapustin, A., J. Martonchik, Y. Wang, and I. Laszlo (2011a), Multiangle implementation of atmospheric correction (MAIAC): 1. Radiative transfer basis and look-up tables, *J. Geophys. Res.*, *116*(D03210), doi:10.1029/2010JD014985.

Lyapustin, A., and Y. Wang (2005), Parameterized code SHARM-3D for radiative transfer over inhomogeneous surfaces, *Appl. Opt.*, *44*(35), 7602–7610, doi:10.1364/AO.44.007602.

Lyapustin, A., Y. Wang, I. Laszlo, R. A. Kahn, S. Korkin, et al. (2011b), Multiangle implementation of atmospheric correction (MAIAC): 2. Aerosol algorithm, *J. Geophys. Res.*, *116*(D03211), doi:10.1029/2010JD014986.

Lyapustin, A. I. (1999), Atmospheric and geometrical effects on land surface albedo, *J. Geophys. Res.*, *104*(D4), 4127–4143.

Lyapustin, A. I., Y. Wang, I. Laszlo, T. Hilker, F. G. Hall, P. J. Sellers, C. J. Tucker, and S. V. Korkin (2012), Multi-angle implementation of atmospheric correction for MODIS (MAIAC): 3. Atmospheric correction, *Remote Sens. Environ.*, doi:10.1016/j.rse.2012.09.002.

Martonchik, J. V. (1994), Retrieval of surface directional reflectance properties using ground level multiangle measurements, *Remote Sens. Environ.*, *50*, 303–316.

Martonchik, J. V., R. A. Kahn, and D. J. Diner (2009), Retrieval of aerosol properties over land using MISR observations, in *Satellite Aerosol Remote Sensing Over Land*, pp. 267–293, Springer Praxis Books, Heidelberg.

McGuire, P. C., et al. (2009), An improvement to the volcano-scan algorithm for atmospheric correction of CRISM and OMEGA spectral data, *Planet. Space Sci.*, *57*, 809–815, doi:10.1016/j.pss.2009.03.007.

McGuire, P. C., M. J. Wolff, M. D. Smith, R. E. Arvidson, S. L. Murchie, et al. (2008), MRO/CRISM retrieval of surface Lambert Albedos for multispectral mapping of Mars with DISORT-based radiative transfer modeling: Phase 1—Using historical climatology for temperatures, aerosol optical depths, and atmospheric pressures, *IEEE Trans. Geosci. Remote Sens.*, *46*(12), 4020–4040, doi:10.1109/TGRS.2008.2000631.

Murchie, S. (2012), CRISM on MRO—Instrument and investigation overview, in *MRO/CRISM Data Users' Workshop*, The Woodlands, TX.

Murchie, S., et al. (2007), Compact Reconnaissance Imaging Spectrometer for Mars (CRISM) on Mars Reconnaissance Orbiter (MRO), *J. Geophys. Res.*, *112*(E05S03), doi:10.1029/2006JE002682.

Nicodemus, F. E., J. C. Richmond, J. J. Hsia, I. W. Ginsberg, and T. Limperis (1977), Geometrical considerations and nomenclature for reflectance, *National Bureau of Standards*, *160*.

Ockert-Bell, M. E., J. F. Bell III, J. B. Pollack, C. P. McKay, and F. Forget (1997), Absorption and scattering properties of the Martian dust in the solar wavelengths, *J. Geophys. Res.*, *102*(E4), 9039–9050.

Pinet, P., and C. Rosemberg (2001), Regional photometry and spectral albedo of the eastern hemisphere of Mars in the 0.7–1 micron domain, in *Lunar and Planetary Science Conference*, 1640.

Roujean, J.-L., M. Leroy, and P.-Y. Deschamps (1992), A bidirectional reflectance model of the Earth's surface for the correction of remote sensing data, *J. Geophys. Res.*, *97*(D18), 20,455–20,468, doi:10.1029/92JD001411.

Schaaf, C. B., et al. (2002), First operational BRDF, albedo nadir reflectance products from MODIS, *Remote Sens. Environ.*, *83*, 135–148.

Smith, M. D. (2009), THEMIS observations of Mars aerosol optical depth from 2002–2008, *Icarus*, *202*(2), 444–452, doi:10.1016/j.icarus.2009.03.027.

Smith, M. D., M. J. Wolff, R. T. Clancy, and S. L. Murchie (2009), Compact Reconnaissance Imaging Spectrometer observations of water vapor and carbon monoxide, *J. Geophys. Res.*, *114*(E00D03), doi:10.1029/2008JE003288.

Souchon, A. L., P. C. Pinet, S. D. Chevrel, Y. H. Daydou, D. Baratoux, K. Kurita, M. K. Shepard, and P. Helfenstein (2011), An experimental study of Hapke's modeling of natural granular surface samples, *Icarus*, *215*, 313–331, doi:10.1016/j.icarus.2011.06.023.

Stamnes, K., S.-C. Tsay, W. Wiscombe, and K. Jayaweera (1988), Numerically stable algorithm for discrete-ordinate-method radiative transfer in multiple scattering and emitting layered media, *Appl. Opt.*, *27*(12), 2502–2509.

Tarantola, A. (2005), *Inverse Problem Theory and Methods for Model Parameter Estimation*, Society for Industrial and Applied Mathematics, Philadelphia.

Tomasko, M. G., L. R. Doose, M. Lemmon, P. H. Smith, and E. Wegryn (1999), Properties of dust in the Martian atmosphere from the Imager on Mars Pathfinder, *J. Geophys. Res.*, *104*, 8987–9008.

Vincendon, M., Y. Langevin, F. Poulet, J.-P. Bibring, and B. Gondet (2007), Recovery of surface reflectance spectra and evaluation of the optical depth of aerosols in the near-IR using a Monte Carlo approach: Application to the OMEGA observations of high-latitude regions of Mars, *J. Geophys. Res.*, *112*(E08S13), doi:10.1029/2006JE002845.

Vincendon, M., Y. Langevin, F. Poulet, A. Pommerol, M. Wolff, J.-P. Bibring, B. Gondet, and D. Jouglet (2009), Yearly and seasonal variations of low albedo surfaces on Mars in the OMEGA/MEx dataset: Constraints on aerosols properties and dust deposits, *Icarus*, *200*, 395–405, doi:10.1016/j.icarus.2008.12.012.

Wanner, W., X. Li, and A. H. Strahler (1995), On the derivation of kernels for kernel-driven models of bidirectional reflectance, *J. Geophys. Res.*, *100*, 21,077–21,090.

Wiseman, S., R. E. Arvidson, M. J. Wolff, R. V. Morris, F. P. Seelos, M. D. Smith, D. Humm, S. L. Murchie, and J. F. Mustard (2012), Retrieval of atmospherically corrected CRISM spectra using radiative transfer modeling, in *Lunar and Planetary Science Conference*, 2146.

Wolff, M. J., M. D. Smith, R. T. Clancy, R. Arvidson, M. Kahre, F. Seelos IV, S. Murchie, and H. Savijärvi (2009), Wavelength dependence of dust aerosol single scattering albedo as observed by the Compact Reconnaissance Imaging Spectrometer, *J. Geophys. Res.*, *114*(E00D04), doi:10.1029/2009JE003350.

2.4.2 Photométrie MER

Cette section contient l'article suivant :

Fernando, J., Schmidt, F., Ceamanos, X., Pinet, P., Douté, S. & Daydou, Y. (2013), « Surface reflectance of Mars observed by CRISM/MRO : 2. Estimation of surface photometric properties in Gusev Crater and Meridiani Planum », Journal of Geophysical Research, 118, 1-26

JOURNAL OF GEOPHYSICAL RESEARCH: PLANETS, VOL. 118, 1–26, doi:10.1029/2012JE004194, 2013

Surface reflectance of Mars observed by CRISM/MRO: 2. Estimation of surface photometric properties in Gusev Crater and Meridiani Planum

J. Fernando,[1,2] F. Schmidt,[1,2] X. Ceamanos,[3,4] P. Pinet,[5,6] S. Douté,[4] and Y. Daydou[5,6]

Received 9 July 2012; revised 30 November 2012; accepted 12 December 2012.

[1] The present article proposes an approach to analyze the photometric properties of the surface materials from multi-angle observations acquired by the Compact Reconnaissance Imaging Spectrometer for Mars (CRISM) on-board the Mars Reconnaissance Orbiter. We estimate photometric parameters using Hapke's model in a Bayesian inversion framework. This work also represents a validation of the atmospheric correction provided by the Multi-angle Approach for Retrieval of Surface Reflectance from CRISM Observations (MARS-ReCO) proposed in the companion article. The latter algorithm retrieves photometric curves of surface materials in reflectance units after removing the aerosol contribution. This validation is done by comparing the estimated photometric parameters to those obtained from in situ measurements by Panoramic Camera instrument at the Mars Exploration Rover (MER) Spirit and MER Opportunity landing sites. Consistent photometric parameters with those from in situ measurements are found, demonstrating that MARS-ReCO gives access to accurate surface reflectance. Moreover, the assumption of a non-Lambertian surface as included in MARS-ReCO is shown to be significantly more precise to estimate surface photometric properties from space in comparison to methods based on a Lambertian surface assumption. In the future, the presented method will allow us to map from orbit the surface bidirectional reflectance and the related photometric parameters in order to characterize the Martian surface.

Citation: Fernando, J., F. Schmidt, X. Ceamanos, P. Pinet, S. Douté, and Y. Daydou (2013), Surface reflectance of Mars observed by CRISM/MRO: 2. Estimation of surface photometric properties in Gusev Crater and Meridiani Planum, *J. Geophys. Res. Planets*, *118*, doi:10.1029/2012JE004194.

1. Introduction

[2] Reflectance of the planetary surfaces is not only tightly controlled by the composition of the materials present but also by their granularity, the internal heterogeneities, porosity, and roughness. The reflectance can be characterized by measurements at different wavelengths, viewing geometries (emergence direction), and solar illuminations (incidence direction). Such investigations have been conducted for Mars using telescopes, instruments on-board spacecrafts, and rovers. A summary of these studies is available in the *Johnson et al.* [2008] review chapter. One can find studies related to the Viking Landers [*Guinness et al.*, 1997], the Pathfinder Lander [*Johnson et al.*, 1999], the Hubble Space Telescope [*Bell et al.*, 1999], the Panoramic Camera (Pancam) instrument on-board Mars Exploration Rovers (MER) [*Johnson et al.*, 2006a, 2006b], the Observatoire pour la Minéralogie, l'Eau, les Glaces et l'Activité (OMEGA) instrument on-board Mars Express (MEx) [*Pinet et al.*, 2005], and the High Resolution Stereo Camera (HRSC) instrument on-board MEx [*Jehl et al.*, 2008]. Recently, *Shaw et al.* [2012] derived maps of millimeter- to centimeter-scale surface roughness at MER Opportunity landing site by using multi-angle hyperspectral imager spectrometer called Compact Reconnaissance Imaging Spectrometer for Mars (CRISM) on-board Mars Reconnaissance Orbiter (MRO).

[3] In order to derive compositional and structural information from reflectance measurements, physical models describing the interaction of light with natural media are needed. *Chandrasekhar* [1960] proposed the radiative transfer equation describing the loss and gains of multidirectional streams of radiative energy within media considered as continuously absorbing and scattering where grains are separated by a distance greater than the wavelength (e.g., atmospheres). In the case of a dense medium (e.g., surfaces), two different solutions are developed.

All Supporting Information may be found in the online version of this article.

[1]Univ. Paris-Sud, Laboratoire IDES, UMR, 8148, Orsay, F-91405, France.
[2]CNRS, Orsay, F-91405, France.
[3]Météo-France/CNRS, CNRM/GAME, Toulouse, France.
[4]Université Joseph Fourier/CNRS and, Institut de Planétologie et d'Astrophysique de Grenoble (IPAG), Grenoble, France.
[5]Université de Toulouse, UPS-OMP, Toulouse, France.
[6]CNRS, IRAP, Toulouse, France.

Corresponding author: J. Fernando, Laboratoire IDES, Batiment 504, Rue du Belvédère, Campus Universitaire d'Orsay, 91405 Orsay, France. (jennifer.fernando@u-psud.fr)

©2012. American Geophysical Union. All Rights Reserved.
2169-9097/13/2012JE004194

First, solutions based on Monte Carlo ray tracing methods handled the medium complexity [e.g., *Grynko and Shkuratov*, 2007]. Unfortunately, this direct approach requires large computing times and large parameter space, limiting the inversion. Second, solutions based on an empirical or semi-empirical approach were proposed by adapting the radiative transfer equation to granular media [e.g., *Hapke*, 1981; *Hapke and Wells*, 1981; *Hapke*, 1986, 1993, 2002; *Shkuratov and Starukhina*, 1999; *Douté and Schmitt*, 1998]. These techniques are more relevant for inversion. Several parameters characterize natural surfaces such as roughness and compaction, while other parameters characterize an average grain, such as the single scattering albedo or the phase function.

[4] Previous photometric studies suggest that variations in scattering properties are controlled by local processes. For example, the photometric variations observed by Pancam at Columbia Hills and the cratered plains of Gusev Crater are mainly caused by aeolian and impact cratering processes [*Johnson et al*., 2006a]. These conclusions encourage us to expand the estimation of photometric properties from in situ observations to the entire planet using orbital data to go further in the interpretations.

[5] Observations acquired from space, however, require the correction for atmospheric contribution (i.e., gases and aerosols) in the remotely sensed signal prior to the estimation of the bidirectional reflectance of the surface materials. Previous orbital photometric studies of Martian surfaces were conducted without atmospheric correction but using the lowest aerosols content observations [e.g., *Jehl et al*., 2008; *Pinet et al*., 2005]. Using the data acquired by the multi-angle hyperspectral imaging spectrometer called CRISM on-board MRO [*Murchie et al*., 2007], our objective is to estimate accurately (i) surface bidirectional reflectance of the surface of Mars and (ii) photometric parameters associated with the materials. *Ceamanos et al*. [2013] present a method referred to as Multi-angle Approach for Retrieval of Surface Reflectance from CRISM Observations (MARS-ReCO). This original technique takes advantage of the multi-angular capabilities of CRISM to determine the bidirectional reflectance of the Martian surface. This is done through the atmospheric correction of the signal sensed at the top of atmosphere (TOA). We propose an approach to analyze the photometric parameters of the surface materials in terms of structural information by inverting Hapke's photometric model in a Bayesian framework, as discussed below. The validation of the methods proposed in this work and in the companion article [*Ceamanos et al*., 2013] is performed by comparing the estimated photometric parameters to those obtained from in situ measurements by Pancam instrument at the MER Spirit and MER Opportunity landing sites (respectively at Gusev Crater and Meridiani Planum) [*Johnson et al*., 2006a, 2006b].

[6] This article is organized as follows. First, the methodology to obtain photometric surface parameters is described in Section 2. Second, the estimated photometric parameters are presented in Section 3. Third, results are compared to experimental studies, independent orbital measurements and in situ measurements in Section 4. The significance of the photometric results shall be discussed in Section 5.

2. Methodology

[7] This article and its companion take advantage of the multi-angular capabilities of the CRISM instrument to correct for atmospheric contribution in order to estimate the surface bidirectional reflectance [*Ceamanos et al*., 2013] and to determine the surface photometric parameters (this work). The approach presented in this article includes the following steps: (i) the selection of appropriate CRISM observations at both MER landing sites for the photometric study, (ii) the determination of the surface bidirectional reflectance by correcting for aerosol contributions, (iii) the combination of several CRISM observations for a better sampling of the surface bidirectional reflectance, and (iv) the estimation of the associated surface photometric parameters. The detailed scheme of the procedure is illustrated in Figure 1. One should note that, in order to test the performance of the method presented throughout this article and its companion paper, the study is only conducted at one wavelength and for some spatial pixels. We choose to work at 750 nm where (i) the contribution of gases is minimal and thus the retrieval of photometric properties is likely to be more accurate and (ii) in situ photometric measurements from Pancam instrument are available for the comparison to the estimated photometric parameters.

2.1. CRISM Data Sets

2.1.1. The CRISM Instrument and Targeted Observations

[8] The CRISM instrument on-board MRO is a visible and infrared hyperspectral imager (i.e., 362 to 3920 nm at 6.55 nm/channel) that operates from a sun-synchronous, near-circular (255 × 320 km altitude), near-polar orbit since November 2006. The appropriate mode to estimate surface spectrophotometric properties is the so-called targeted mode providing Full Resolution Targeted (FRT) observations consisting of a sequence of 11 hyperspectral images from a single region acquired at different emission angles. The solar incidence angle is almost constant during the MRO flyby of a targeted observation. A typical targeted sequence is composed of a nadir image (~10 × 10 km) at high spatial resolution (15–19 m/pixel) and 10 off-nadir images with a ×10 spatial binning (resulting in a resolution of 150–200 m/pixel) taken before and after the nadir image. The latter sequence constitutes the so-called Emission Phase Function (EPF) sequence. The pointing of CRISM can rotate (gimbal) ±60° [*Murchie et al*., 2007].

2.1.2. Selection of Targeted Observations

[9] As explained in the companion paper [*Ceamanos et al*., 2013], the accuracy of the surface reflectance provided by MARS-ReCO when dealing with a single targeted observation highly depends on the combination of a moderate atmospheric opacity (i.e., aerosol optical thickness less than or equal to 2), reasonable illumination conditions (i.e., incidence angle less than or equal 60°), an appropriate phase domain (i.e., significant difference between the available maximum and minimum phase angles up to 40°) and on the number and diversity of angular measurements. The combination of several targeted observations, since it enables a better sampling of the bidirectional reflectance, could therefore significantly improve the reflectance estimation as it provides more regular angular sampling of the surface target. *Pinet et al*. [2005] and *Jehl et al*. [2008] proved the benefits of using different spaceborne observations under varied illumination conditions (OMEGA and HRSC). The principal requirement to combine targeted observations is the absence of seasonal changes among the selected observations.

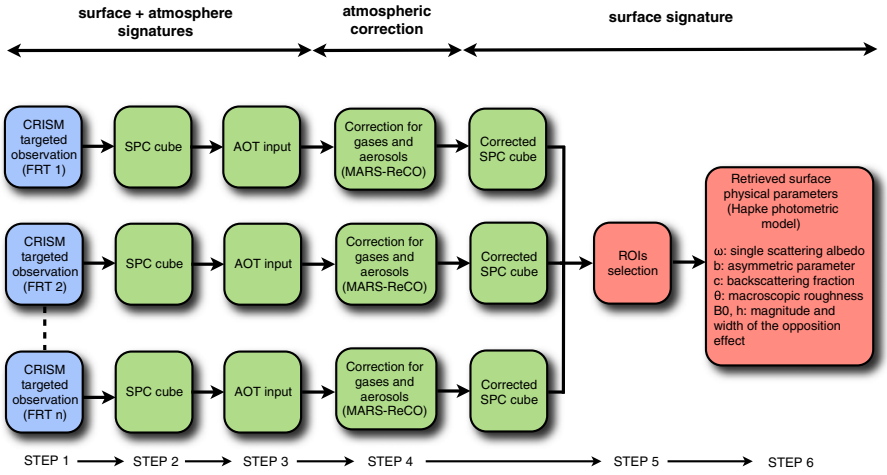


Figure 1. Detailed scheme of the estimation of surface photometric properties. The blue blocks represent the initial FRT CRISM observations (from $i = 1$ to n). The green blocks represent the aerosol optical thickness retrieval and the correction for atmospheric contribution for the determination of the surface bidirectional reflectance, which is carried out by the methodology described in the companion paper [*Ceamanos et al*., 2013]. The red blocks correspond to the work presented in this article, that is, the estimation of surface photometric properties.

[10] Several CRISM observations have been acquired over the MER landing sites since the beginning of the mission. In particular, up to 16 and 10 CRISM full targeted observations (FRT) are available in the MER Spirit and MER Opportunity landing sites, respectively. In this article, we select CRISM observations according to several criteria: (i) the quality of overlap among the observations (above 70%), (ii) the variation of the solar incidence angle implying a widening of the phase angle domain (note that only the variation of the seasonal solar longitude (*Ls*) can provide different incidence angles due to the sun-synchronous orbit of MRO, and (iii) the absence of surface changes (e.g., seasonal phenomena) as they can jeopardize the determination of the surface photometric properties. Taking into account these criteria, three CRISM observations acquired over Gusev Crater (i.e., FRT3192, FRT8CE1, and FRTCDA5) and over Meridiani Planum (i.e., FRT95B8, FRT334D, and FRTB6B5) are selected, respectively. We note that the selected observations have quite different phase angle ranges as shown in Table 1.

[11] Targeted observations are archived in the Planetary Data System (PDS) and are composed of the following: (i) targeted reduced data records (TRDR), which store the calibrated data in units of I/F (radiance factor, RADF; see Table 2), the ratio of measured intensity to solar flux, and (ii) derived data records, which store the ancillary data such as the spatial coordinates (latitude and longitude) and the geometric configurations of each pixel by means of the incidence, emission, and phase angles. In the present study, CRISM products are being released with the TRDR2 version of CRISM calibration (TRR2 for brevity).

2.1.3. SPC Cubes: Integrated Multi-Angle Product

[12] To facilitate the access to the multi-angular information pertaining to each terrain unit, the 11 hyperspectral images corresponding to a single targeted observation were spatially rearranged into data set named spectro-photometric curve (SPC) cube (see *Ceamanos et al*. [2013] for more detail). The SPC cube is composed of the following:

Table 1. Selected CRISM Observations Focused on the Spirit and Opportunity Landing Sites, Respectively at Gusev Crater and Meridiani Planum[a]

	Gusev Crater (MER Spirit)			Meridiani Planum (MER Opportunity)		
	FRT3192	FRT8CE1	FRTCDA5	FRT95B8	FRT334D	FRTB6B5
Acquisition date	22 Nov 2006	17 Dec 2007	07 Oct 2008	11 Jan 2008	30 Nov 2006	08 Jul 2008
Ls (deg)	139.138	4.040	138.333	16.223	142.975	96
θ_0 (deg)	60.4	40.02	62.8	39.3	55.4	56.4
g (deg)	~56–112	~41–90	~46–106	~41–86	~41–106	~40–106
$AOT_{mineral}$ (1 μm)	0.33 ± 0.04	0.98 ± 0.15	0.32 ± 0.04	0.56 ± 0.09	0.35 ± 0.04	0.35 ± 0.04
AOT_{water} (320 nm)	0.08 ± 0.03	0.07 ± 0.03	0.03 ± 0.03	0.12 ± 0.05	0.12 ± 0.03	0.14 ± 0.03

[a] *Ls* stands for the solar longitude, θ_0 is the incidence angle, *g* is the phase angle range. $AOT_{mineral}$ stands for the mineral aerosol optical thickness at 1 µm from Wolff's estimates [*Wolff et al*., 2009, M. Wolff, personal communication] and AOT_{water} is the water aerosol optical thickness at 320 nm by MARs color imager instrument (M. Wolff, personal communication, 2011).

Table 2. Photometric Units Derived From the Bidirectional Reflectance r[a]

	Unit	Symbol	Name	Expression
reflectance	sr^{-1}	r	bidirectional reflectance	$r(\theta_0,\theta,g)=\frac{I}{\pi\times F}$
		BRDF	bidirectional reflectance distribution function	$BRDF=r(\theta_0,\theta,g)/cos(\theta_0)$
		RADF	radiance factor	$RADF=\pi\times r(\theta_0,\theta,g)=\frac{I}{F}$
		BRF	bidirectional reflectance factor	$\rho=BRF=\pi\times r(\theta_0,\theta,g)/cos(\theta_0)$

[a] I, intensity; F, solar flux; θ_0, incidence angle; θ, emergence angle; g, phase angle. The CRISM observations are released in RADF unit and the SPC cubes in BRF units.

[13] 1. x dimension (horizontal) corresponding to angular configurations (up to 11) grouping all reflectance values at different geometric views,

[14] 2. y dimension (vertical) corresponding to the spatial coordinate defining a super-pixel. The super-pixels are rearranged as function of the number of available angular configurations, and

[15] 3. z dimension corresponding to the spectral sampling.

The photometric curves, stored in a SPC cube are in units of RADF (see Table 2), correspond to the signals TOA. In the present work, all selected FRT observations are binned at 460 m/pixel (the spatial resolution of each super-pixel). This is done (i) to cope with the geometric deformation inaccuracies in the case of an oblique view with pointing errors, (ii) to minimize on poorly known topography (a CRISM pixel is smaller than MOLA resolution), (iii) to reduce local seasonal variations, and (iv) to minimize local slopes effects. We found that binning at 460 m is a good compromise.

2.2. Estimation of Surface Bidirectional Reflectance: Correction for Atmospheric Contribution

[16] The radiative transfer in the Martian atmosphere is dominated by CO_2 and H_2O gases and mineral and ice aerosols which are an obstacle for the studies of the surface properties. Indeed, the extinction of radiative fluxes, in particular the solar irradiance in the wavelength range of CRISM observations, is mostly due to absorption by gases and scattering by aerosols. Also, aerosols produce an additive signal by scattering of the solar light. As a result, a spectrum collected by the CRISM instrument at the TOA is a complex signal determined by both the surface and the atmospheric components (gases and aerosols). The atmospheric correction chain proposed for CRISM observations is composed of the following: (i) the retrieval of aerosol optical thickness (AOT), (ii) the correction for gases, and (iii) the correction for aerosols resulting in the estimation of the surface reflectance. The last step is carried out by the technique referred to as the MARS-ReCO [*Ceamanos et al*., 2013]. In the following, a short summary of the methodology is provided.

2.2.1. Retrieval of AOT

[17] The AOT is defined as the aerosol optical depth along the vertical of the atmosphere layer and is related to the aerosol content.

[18] The retrieval of AOT from orbit is difficult because of the coupling of signals between the aerosols and the surface. Over the last decades, EPF sequences of Mars were obtained and were used to separate the atmospheric and surface contributions. Significant progresses have resulted from the pioneer works of *Clancy and Lee* [1991] based on Viking Orbiter InfraRed Thermal Mapper EPF observations and *Clancy et al*. [2003] from Mars Global Surveyor Thermal Emission Spectrometer (TES) EPF observations 10 years later.

[19] For our study, we decided to use Michael Wolff's AOT estimates for atmospheric correction purposes (personal communication, 2011). This parameter is available for each CRISM observation and is derived from the work of *Wolff et al*. [2009]. This method is based on the analysis of CRISM EPF sequences combined with information provided by "ground truth" results at both MER landing sites which allow isolating the single scattering albedo. This method carries out a minimization of the mean square error between measured and predicted TOA radiance based on the previously estimated aerosol single scattering albedo and scattering phase function.

[20] Some assumptions regarding the aerosol properties (i.e., phase function, mixing ratio, column optical depth, etc.) and the surface properties (i.e., phase function) must have been accounted for to separate the atmospheric and surface contributions. Concerning the surface properties, this method assumes a non-Lambertian surface to estimate the AOT by using a set of surface photometric parameters that appears to describe the surface phase function adequately for both MER landing sites [*Johnson et al*., 2006a, 2006b]. This assumption is qualitative but reasonable for several reasons enumerated by *Wolff et al*. [2009]. For both MER landing sites, it seems from the work of *Wolff et al*. [2009] that the AOT retrievals are overall consistent with optical depths returned by the Pancam instrument (available via PDS). Consequently, Wolff's AOT estimates are suitable for our study at both MER landing sites. Concerning the aerosol properties, some uncertainties may exist especially for the aerosol scattering phase function which is related to the aerosol particle size and shape. First, this method assumes a mean particle aerosol but variations are observed as a function of solar longitude and spatial location (latitude, longitude, and altitude) [*Wolff et al*., 2006]. Second, the mean aerosol particle size is derived from CRISM observations acquired during planet-encircling dust event in 2007. During a large dust event, the aerosol particle size is larger than those found under clear atmospheric conditions. Third, the hypothesis of the particle shape used in the study of *Wolff et al*. [2009] contains a wrong backscattering part in the scattering phase function [*Wolff et al*., 2010]. Thus, all points previously enumerated may bias the AOT estimation and must be taken into account during the analysis of the robustness of results (the surface bidirectional reflectance and the surface photometric parameters). However, the performance of MARS-ReCO is sensitive to the accuracy of the AOT estimate [*Ceamanos et al*., 2013] (see section 2.2.2). Note that the AOT is calculated at 1 μm where the absorption of gases is almost null.

2.2.2. Correction for Gases and Aerosols

[21] In order to test the performances of the methodology presented in this article and its companion paper, the present

study is only conducted at a single wavelength. We choose to work exclusively at 750 nm where the contribution of gases is low and thus the retrieval of photometric properties is likely to be sufficiently accurate. Furthermore, photometric properties retrieved from in situ measurements taken by Pancam are available at this wavelength and our photometric properties can be validated. Note, however, that the presented methodology can be applied to any CRISM wavelength provided the contribution of gases is corrected previously.

[22] MARS-ReCO is devised to compensate for mineral aerosol effects considering the anisotropic scattering properties of the surface and the aerosols. This method is suitable for any CRISM multi-angle observation within some atmospheric and geometrical constraints (AOT ≤ 2, incidence angle $\theta_0 < 60°$, phase angle range $g_{max} - g_{min} > 40°$). MARS-ReCO is based on a coupled surface-atmosphere radiative transfer formulation using a kernel-driven scattering model for the surface and a Green's function to model the diffuse response of the atmosphere (please refer to *Ceamanos et al*. [2013] for more detail). The AOT of each observation is an input of MARS-ReCO. Table 1 presents the AOT_{water} and $AOT_{mineral}$ for each selected CRISM observation. We can note that AOT_{water} is negligible in front of the $AOT_{mineral}$ and consequently, the photometric effects from aerosol water ice can be considered negligible in this study.

[23] The uncertainties pertaining to the AOT estimates (personal communication of Michael Wolff, [*Wolff et al*., 2009]) and to the TOA measurements by CRISM are integrated and propagated in the estimation of the surface bidirectional reflectance in BRF units (cf. Table 2).

[24] Besides the retrieval of the surface bidirectional reflectance, MARS-ReCO also provides an indicator of the quality of the estimated solution in a standard deviation sense, noted by parameter σ_ρ (in BRF units) and computed as $\sigma_\rho = \sqrt{\frac{1}{Ng}\sum_{j=1}^{Ng} \mathrm{tr}(\mathbf{C}_{\rho\rho})}$, where $\mathrm{tr}(\mathbf{C}_{\rho\rho})$ is the a posterior covariance matrix and *Ng* the available geometries [*Ceamanos et al*., 2013]. In systematic test presented in the companion article, the parameter σ_ρ has proved to be highly correlated with the bidirectional reflectance error from MARS-ReCO and thus provides us with reliable information on the accuracy of the estimated surface bidirectional reflectance.

2.3. Estimation of Surface Photometric Properties: Bayesian Inversion Based on a Hapke's Photometric Model

2.3.1. Defining Regions of Interest and Selection

[25] We now discuss the improvement that results when combining different CRISM targeted observations based on their spatial coherence and thus a better sampling of the surface bidirectional reflectance and a maximization of the phase angle range. We defined in Subsection 2.1.3 a super-pixel as the combination of all reflectance value corresponding to a same location unit coming from an individual CRISM sequence or SPC cube. The combination of each super-pixel from each selected CRISM targeted observation is performed when their central coordinates (latitude and longitude) differ less than a half super-pixel size (460/2 = 230 meters). This is done to ensure maximum overlap. We choose same combined super-pixels called regions of interest (ROI) in following for the photometric study using the several criteria. First, the different ROIs must be located close to the MER Spirit and Opportunity rover's path, specifically to the location of spectrophotometry measurements by Pancam and in the same geological unit (i.e., presenting same materials). Second, the local topography makes the photometric study more challenging when it is poorly known because it controls to a large extent the incidence, emergence, and azimuth local angles. Besides, in the case of an oblique illumination (i.e., up to 70°), shadows decrease the signal/noise ratio. In this study, ROIs were therefore selected only in flat areas. Third, ROIs are chosen to have the richest angular configurations and the best angular sampling in terms of phase angle range in order to constrain as much as possible the photometric properties. Figure 2 presents the selected ROIs for this photometric study at Gusev Crater and Meridiani Planum. Four ROIs are selected for Gusev Crater study while only one is chosen for Meridiani Planum study. The limited number of selected ROIs is explained by the fact that few ROIs in both cases respect the combination of criteria previously mentioned. In order to improve the number of ROIs, an improved pointing of each CRISM targeted observation could be envisaged.

2.3.2. Direct Surface Model: Hapke's Photometric Model

[26] Models describing the photometry of discrete granular media have been proposed to express the surface bidirectional reflectance using semi-empirical analytical approaches [e.g., *Hapke*, 1981; *Hapke and Wells*, 1981; *Hapke*, 1984, 1986, 1993, 2002] and numerical approaches [e.g., *Cheng and Domingue*, 2000; *Douté and Schmitt*, 1998; *Mishchenko et al*., 1999].

[27] Hapke's modeling [*Hapke*, 1993] is widely used in the planetary community due to the simplicity of its expression and due to the fact that it introduces photometric parameters claimed to have physical relevance. Previous Martian photometric studies have been conducted based on orbital HRSC measurements [*Jehl et al*., 2008] and based on the analysis of in situ MER measurements [*Johnson et al*., 2006a, 2006b] using the Hapke's 1993 version model [*Hapke*, 1993]. For this study, since we use the in situ investigation as ground truth in order to validate the MARS-ReCO approach, we have to use Hapke's 1993 version model.

[28] More recent Hapke models [*Hapke*, 2002, 2008] are available improving the original formulation [*Hapke*, 1981, 1993] and can be used for future photometric studies. First, the model [*Hapke*, 2002] includes the following: (1) a more accurate analytic approximation for isotropic scatterers, (2) a better estimation of the bidirectional reflectance when the scatterers are anisotropic, and (3) the incorporation of coherent backscattering. Second, the model [*Hapke*, 2008] overcomes the limitations of the original model in order to predict porosity dependence of the bidirectional reflectance, in case of a particulate medium such as a planetary regolith. For that purpose the treatment of light is propagating through the particle spacing.

[29] Following Johnson et al.'s works [*Johnson et al*. 2006a, 2006b] and for the sake of the comparison coherence we use the expression of *Hapke* [1993] as follows:

$$r(\theta_0,\theta,g) = \frac{\omega}{4\pi}\,\frac{\mu_{0e}}{(\mu_{0e}+\mu_e)}\,\Big\{[1+B(g)]P(g) + H(\mu_{0e})H(\mu_e) - 1\Big\}S(\theta_0,\theta,g), \quad (1)$$

where

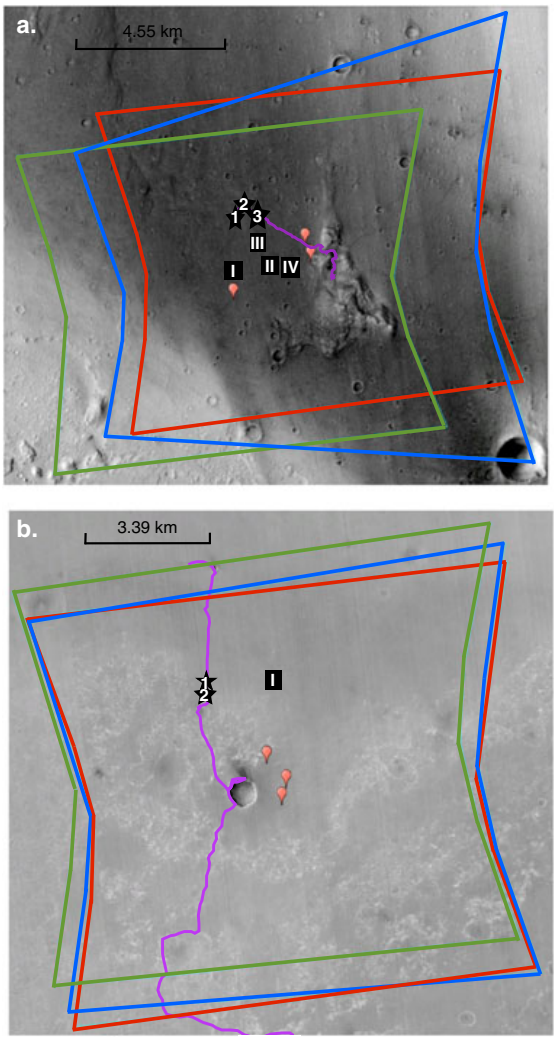


Figure 2. a. Image from Context camera (CTX) of the Spirit landing site at Gusev Crater with the rover path across the plain up to the Columbia hill in purple. The footprint of each selected CRISM observations (only the nadir image) is represented here (blue: FRT3192, green: FRT8CE1 and red: FRTCDA5). Full black stars point to the locations of the photometric measurements in the Gusev plains (1. Landing site, 2. Bonneville rim, 3. NW of Missoula) taken by instrument onboard Spirit [*Johnson et al.*, 2006a]. Full black squares represent the four ROIs that have been selected for our photometric study (ROI from I to IV). b. Image from CTX camera of the Opportunity landing site at Meridiani Planum with the rover path in purple. The footprint of each selected CRISM observations (only the nadir image) is represented here (blue: FRT95B8, green: FRT334D, and red: FRTB6B5). Full black stars represent the locations of photometric measurements (1. South of Voyager, 2. Purgatory region) taken by Pancam instrument onboard Opportunity [*Johnson et al.*, 2006b]. Full black square represents the selected ROI for our photometric study (ROI I).

[30] 1. Geometry θ_0, θ, and g: The refer to the incidence, emergence and phase angles, respectively.

[31] 2. Single scattering albedo ω: Factor ω ($0 \leq \omega \leq 1$) depends on wavelength and represents the fraction of scattered light to incident light by a single particle [*Chandrasekhar*, 1960].

[32] 3. Particle scattering phase function *P(g)*: Function *P (g)* characterizes the angular distribution of an average particle. The empirical 2-term Henyey-Greenstein function (hereafter referred to as HG2) is used commonly for studying planetary surfaces [e.g., *Cord et al.*, 2003; *Hartman and Domingue*, 1998; *Jehl et al.*, 2008; *Johnson et al.*, 2006a, 2006b; *Souchon et al.*, 2011]. It reads as follows:

$$P(g) = (1-c)\,\frac{1-b^2}{\left(1+2b\cos(g)+b^2\right)^{3/2}} + c\,\frac{1-b^2}{\left(1-2b\cos(g)+b^2\right)^{3/2}}, \quad (2)$$

where the asymmetric parameter b ($0 \leq b \leq 1$) characterizes the anisotropy of the scattering lobe (from $b=0$, which corresponds to the isotropic case, to $b=1$, which corresponds to a particle which diffuses light in a single direction). The backscattering fraction c ($0 \leq c \leq 1$) characterizes the main direction of the diffusion ($c < 0.5$ corresponding to forward scattering and $c > 0.5$ corresponding to backward scattering).

[33] 4. Multiple scattering function *H(x)*. The exact values of the H function for isotropic scatterers were given by *Chandrasekhar* [1960]. For consistency we use the approximation of isotropic scattering named H93 in the following [*Hapke*, 1993] as was done for the estimation of the surface photometric parameters by [*Johnson et al.*, 2006a, 2006b]. The H93 differs by a relative error on H lower than 1% and a relative error on the bidirectional reflectance of a regolith lower than 2% [*Cheng and Domingue*, 2000]. Defining $y=(1-\omega^{1/2}$, the multiple scattering function becomes the following:

$$H(x) = \left\{1-[1-y]x\left[\left(\frac{1-y}{1+y}\right)+\left(1-\frac{1}{2}\left(\frac{1-y}{1+y}\right)-x\left(\frac{1-y}{1+y}\right)\right)ln\left(\frac{1+x}{x}\right)\right]\right\}^{-1} \quad (3)$$

[34] 5. Shadow hiding opposition effect (SHOE) and Coherent backscatter opposition effect (CBOE). *B(g)* is a function designed to model the sharp increase of brightness around the zero-phase angle often observed in the case of particulate media, the so-called opposition effect. The *B(g)* function is given by *Hapke* [1993] as follows:

$$B(g) = \frac{B_0}{1+\frac{1}{h}\tan\left(\frac{g}{2}\right)}. \quad (4)$$

Parameters h and B_0 are, respectively, the angular width and the amplitude of the opposition effect. Factor h (ranging from 0 to 1) is physically related to compaction and particle size distribution and B_0 (ranging from 0 to 1) is an empirical parameter which is related to the particle transparency

[*Hapke*, 1993]. It is important to mention that the Ross-thick Li-sparse (RTLS) model for the surface reflectivity employed by MARS-ReCO [*Ceamanos et al*., 2013] is able to describe a backscattering lobe by means of its geometrical kernel. Nevertheless, its angular width is more characteristic of photometric effects linked with shadows cast by macroscopic roughness than those occurring at the grain scale such as the SHOE and the CBOE [*Lucht et al*., 2000]. Furthermore, the radiative transfer algorithm that is used to calculate the atmospheric quantities at the core of the MARS-ReCO procedure through the atmosphere cannot propagate properly the narrow backscattering lobes of the SHOE and CBOE. Finally, CRISM orbital measurements never reach the small phase angle domain ($<5°$) where the previous phenomena are expressed. Consequently, MARS-ReCO is never in the position of retrieving accurate values for B_0 and h.

[35] 6. Macroscopic roughness factor S. We note that planetary regoliths present roughness driven by grain clusters to the pixel scale. In the Hapke's surface model this phenomena is described by a Gaussian distribution of slopes at a single spatial scale under the pixel size which is not explicitly given. The mean slope angle $\bar{\theta}$ is the only required parameter [*Hapke*, 1993]. Surface roughness involves several radiative phenomena: (i) multiple reflection of light between facets, (ii) shadows depending on the geometry, (iii) bias on the incidence and emergence angles, and (iv) increase of the multiple scattering component. In order to quantify their influence on the bidirectional reflectance, Hapke's model introduces a simple multiplicative factor S depending on μ_{0e} and μ_e whose expressions are given in *Hapke* [1993].

2.3.3. Bayesian Inversion of the Surface Model

[36] The "inverse problem" consists in estimating the model parameters that best explain the observations. Unfortunately, inverse problems do not have a unique solution if the direct model is nonlinear, as does the Hapke's model. *Tarantola and Valette* [1982] proposed to solve inverse problems in a general nonlinear case based on the concept of the state of information which is characterized by a probability density function (PDF). The PDF is defined over both the parameter space and the observed space. The formalism of a PDF is used to define the initial state of information (i.e., a priori knowledge on the parameters, the uncertainties on the observation and on the model). To infer the solution, the Bayes' theorem is applied. Key points concerning the Bayesian inversion concept and framework assumptions are presented in the following:

[37] 1. Data, model parameters and theoretical relationship. The direct model consists of computing the simulated data d from model parameters m:

$$d = F(m) \tag{5}$$

[38] 2. Prior information on the model. The prior information on model parameters $\rho_m(m)$ in the parameter space *(M)* is independent with the data and corresponds to the state of null information. For the Hapke model parameters ω, b, c, $\bar{\theta}$, B_0, and h, we consider a uniform PDF, different from zero on an interval that insures their physical relevance (between 0 and 1 for ω, b, c, B_0, and h and between 0° and 90° for $\bar{\theta}$). Outside the intervals, the PDF is null, avoiding unphysical solution to appear. As discussed in Subsection 2.3.2 in real planetary situations, the SHOE and the CBOE phenomena are only expressed for phase angles $g < 5°$ out of the range encompassed by typical CRISM observations ($g \gtrsim 30°$). Thus, a priori, neglecting both phenomena should not influence the retrieval of the other parameters. However, following *Souchon et al*. [2011], the model can still be profitably inverted on the data by keeping parameters B_0 and h since they will compensate for discrepancies between the model and the measurements in some situations. Consequently in the present work, we first chose to invert the parameters B_0 and h to systematically control if they are constrained or not by the CRISM data set. However, in a second phase we also tested the inversion by setting B_0 and h to zero, and no change was observed on the determination of the other parameters (ω, $\bar{\theta}$, b, and c).

[39] 3. Prior information on the data. The prior information on data $\rho_d(d)$ in the observation space *(D)* is assumed to be a Gaussian PDF according to the MARS-ReCO formalism and retrieval strategy. Note that the error σ on a CRISM measurement at one geometry is assumed to be independent on the state of the surface and on the other geometries (i.e., the PDF has a diagonal covariance matrix with elements $\sigma_1^2, \ldots, \sigma_{N_g}^2$, where N_g is the number of available geometries, up to 11). At 750 nm, the signal to noise ratio was estimated before launch to be equal to 450 [*Murchie et al*., 2007]; but due to additional artifacts such as spikes and calibration issues [*Seelos et al*., 2011], we evaluated the uncertainty σ of the reflectance measurement (ρ) at each geometry j to be of the order of $\sigma_j = (1/50) \times \rho_j$, where $j = 1,\ldots,N_g$ and ρ_j is the CRISM dataset at the jth angular configuration [*Ceamanos et al*., 2013]. Moreover, MARS-ReCO takes into account the uncertainty of the AOT input. Figure 3 presents a typical TOA photometric curve collected by the CRISM instrument (green plus) and the bidirectional reflectance curve produced by the MARS-ReCO algorithm (red crosses). For each geometry the bidirectional reflectance value is accompanied by its 1σ uncertainty. Those means and root mean square errors are used to build $\rho_d(d)$ that serves as an input PDF of the Bayesian inversion.

[40] 4. Posterior probability density function and resolution of inverse problems. Inversion problems correspond to the particular case where information from the data space *(D)* is translated into the model space *(M)*. The posterior PDF in the model space $\sigma_M(m)$ as defined by *Tarantola and Valette* [1982] reads

$$\sigma_M(m) = k\ \rho_M(m)\ L(m), \tag{6}$$

where k is a constant and *L(m)* is the likelihood function

$$L(m) = \int_D \partial d \frac{\rho_D(d)\ \theta(d|m)}{\mu_D(d)}, \tag{7}$$

where $\theta(d|m)$ is the theoretical relationship of the PDF for d given m, and $\mu_D(d)$ is null information PDF for the data d. The solution of the general inverse problem is given by the PDF $\sigma_M(m)$ from which any information on the model parameter can be obtained such as mean values and uncertainty bars. Please refer to *Tarantola and Valette* [1982] for more details.

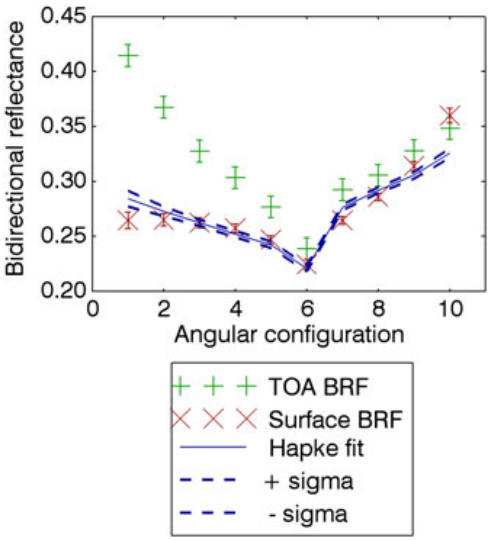


Figure 3. Reflectance values (in BRF units) corresponding to the photometric curve of the ROI I from FRT3192 observation composed of 10 angular configurations at the TOA (green plus) and at the surface after the correction for atmospheric contribution carried out by MARS-ReCO (red crosses). In both cases the 1σ uncertainty is expressed as a function of angular configuration (the 11 geometric views of one CRISM EPF scans from first to fifth corresponds to the inbound direction, sixth is the central scan and from seventh to eleventh are related to the outbound direction). The latter data are used in the Bayesian inversion. The blue solid and dashed lines represent the Hapke's best fit and their 1σ uncertainties, respectively.

[41] 5. Sampling of solutions to inverse problems. In our case, the relationship between model parameters and observed data through Hapke's modeling is nonlinear. While it is not possible to describe the posterior PDF analytically, it can be sampled using a Monte Carlo approach and a Markov chain [*Mosegaard and Tarantola*, 1995]. After a sufficient number of steps, the state of the chain corresponds to the desired distribution. According to our tests, the best trade-off between computation time and accuracy is a burn-in phase (phase in which the Markov chain approaches a stationary state after a certain number of runs) of 500 steps. The next 500 iterations are used to estimate the posterior PDF allowing the determination of the mean and standard deviation of each parameter. Note that a posteriori PDF of a retrieved parameter is not necessarily a Gaussian distribution but can be a square function or multi-modal as seen in Figures 4 and 5. To describe the results of each parameter, we choose to compute the mean of the posterior PDF. To describe the uncertainties, we choose to compute the standard deviation. We warn the reader because sometimes these estimators can be inappropriate to describe the PDF. In the following graphs, 2σ error bars are plotted to describe more accurately the PDFs.

[42] 6. Root mean square residual RMS. In order to estimate the difference between the fit and the observed bidirectional reflectance, the root mean square residual (noted RMS) is given for each Bayesian inversion as follows:

$$\mathrm{RMS} = \sqrt{\frac{\sum_{N_g} (\rho_{obs} - \rho_{mod})^2}{N_g}} \tag{8}$$

where N is the available geometric configurations, ρ_{obs} the CRISM bidirectional reflectance corrected for atmosphere and ρ_{mod} the modeled bidirectional reflectance taken as the mean of the 500 iterations used to estimate the posterior PDF.

[43] 7. Nonuniformity of criterion k. Photometric parameters m is constrained if their marginal posterior PDF differs from the prior state of information (i.e., a null information

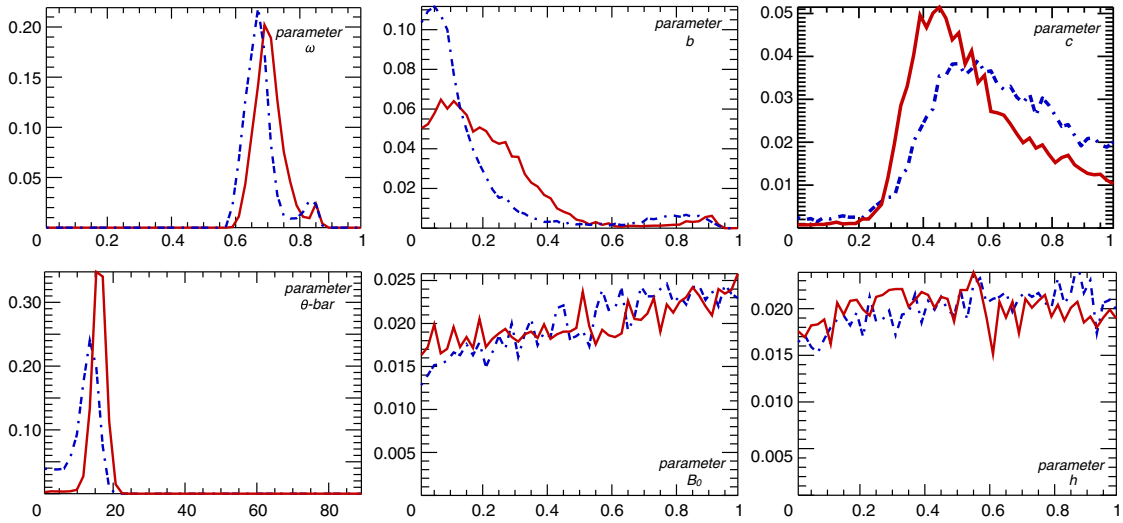


Figure 4. The PDF of each of the six photometric parameters retrieved for ROI I. Two cases are considered: the inversion of a single CRISM FRT observation (i.e., FRT3192 in blue line) and the inversion of three combined CRISM FRT observations (in red line).

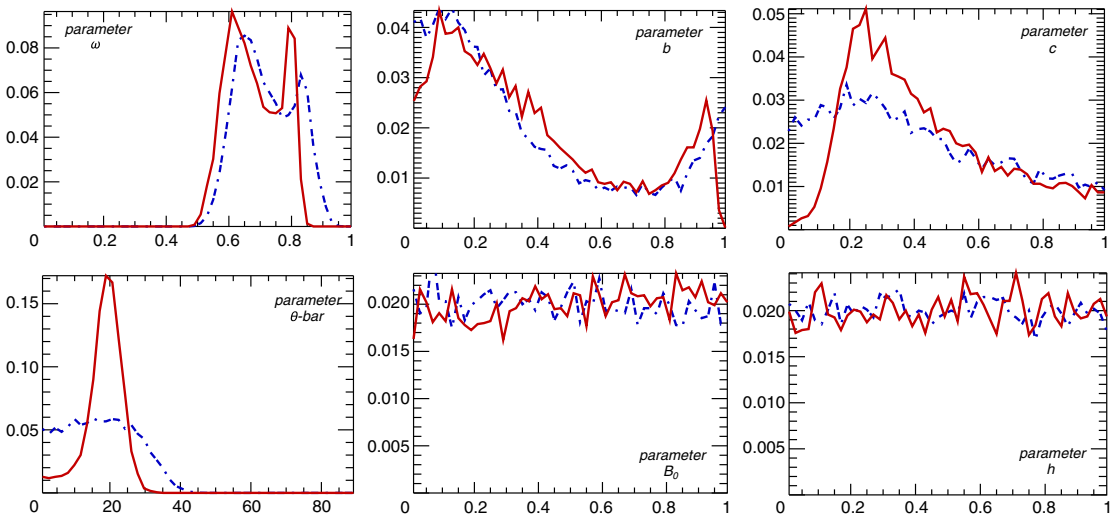


Figure 5. The PDF of each of the six photometric parameters retrieved for ROI I of Meridiani Planum. Two cases are considered: the inversion of a single CRISM FRT observation (i.e., FRT95B8 in blue line) and the inversion of three combined CRISM FRT observations (in red line).

taken as a uniform distribution, in our case). In order to distinguish if a given parameter has a solution, we perform a statistical test leading to a nonuniformity criterion k (see Appendix A). For $k > 0.5$, the marginal posterior PDF is considered to be nonuniform and thus, we consider that the mean and standard deviation of the PDF satisfactorily describe the solution(s).

3. Analysis of Retrieved Photometric Parameters

[44] As mentioned in Subsection 2.1.2, we selected three CRISM targeted observations from Gusev Crater and from Meridiani Planum (cf. Table 1). All observations were individually corrected for aerosols using MARS-ReCO, knowing the respective AOT values (cf. Table 1). Based on the corrected bidirectional reflectance, we use the proposed methodology described in section 2.3.3 to estimate the photometric parameters of the materials encompassed by four ROIs in the case of Gusev Crater (ROI I to ROI IV) and by one ROI in the case of Meridiani Planum (ROI I).

[45] For each ROI, we determine the surface photometric parameters at 750 nm from (i) a single CRISM FRT observation or (ii) a combination of all selected FRT observations (i.e., FRT3192, FRT8CE1, and FRTCDA5 in the case of Gusev Crater; and FRT95B8, FRT334D, and FRTB6B5 in the case of Meridiani Planum). Remember that the chosen targeted observations are complementary in terms of phase angle range (cf. Table 1).

[46] For each parameter of the photometric Hapke's model (i.e., ω, b, c, $\bar{\theta}$, B_0, and h) we determine its mean value and standard deviation by running the proposed Bayesian inversion procedure. The nonuniform criterion-noted k is conjointly computed and detailed in Tables 3 and 4 for Gusev Crater and Table 5 for Meridiani Planum. In the following, we have two criteria that help us estimate the existence and the quality of a solution. On the one hand, the nonuniform criteria k allows us to reject posterior PDFs that do not carry a solution. On the other hand, the standard deviation allows us to quantify to which extent a given parameter is constrained by the current solution.

3.1. Results on Gusev Crater

[47] The quality of the surface bidirectional reflectance estimated by MARS-ReCO is given by the standard deviation σ_ρ. This quality parameter is available for each ROI of each CRISM targeted observation of the present study (cf. Tables 3 and 4). The highest σ_ρ value is observed for FRT8CE1 which can be explained by a wrong AOT estimation (highest AOT value) in this case (i.e., FRT8CE1: $\sigma_\rho = 0.03$–0.04 for AOT = 0.98). The positive correlation of this uncertainty and the AOT are also observed in the sensitivity study led by *Ceamanos et al.* [2013]. Indeed the error computed for the synthetic reference data mimicking the photometric properties of the planet Mars increases with AOT (i.e., for AOT = 1, $\sigma_\rho \sim 0.05$ and error is ~10% while for AOT = 1.5, $\sigma_\rho \sim 0.10$, and error is ~20%; see *Ceamanos et al.* [2013] for more detail).

[48] Tables 3 and 4 present results regarding the Hapke's model parameters for the different ROIs of Gusev Crater.

[49] The goodness of fit is estimated through the absolute quadratic residual RMS value (cf. Tables 3 and 4). For all Bayesian inversions, the estimates are less than 0.02 which mean that the inversions are deemed satisfactory.

[50] Figure 4 represents the PDF of each parameter considering the inversion of a single FRT observation as well as the inversion of the three combined observations. According to results, a solution exists for parameters ω, b, c, and $\bar{\theta}$ (because the PDF is nonuniform) whereas no solution exists for parameters B_0 and h (uniform PDF). Several conclusions can be drawn when using a single targeted observation such as the following:

[51] 1. Solutions exist for parameter ω in all cases ($k \sim 1$). The standard deviation shows that the single scattering albedo

Table 3. Retrieved Hapke's Parameters (ω, b, c, $\bar{\theta}$ in Degrees, B_0, h) and Their Standard Deviation in Parentheses[a]

FRT	Latitude (°N)	Longitude (°E)	AOT	σ_ρ, RMS	ω k	b k	c k	$\bar{\theta}$ k	B_0 k	h k	nb	g
3192	−14.603	175.478	0.33 ± 0.04	0.01	0.68 (0.06)	0.17 (0.20)	0.62 (0.20)	11.62 (3.98)	0.52 (-)	0.52 (-)	10	~56–112
				0.01	1.00	1.92	0.96	1.00	0.24	0.12		
8CE1	−14.606	175.478	0.98 ± 0.15	0.03	0.77 (0.07)	0.30 (0.28)	0.42 (0.27)	17.23 (9.64)	0.47 (-)	0.50 (-)	9	~37–79
				0.01	1.00	1.47	0.60	0.98	0.20	0.12		
CDA5	−14.604	175.481	0.32 ± 0.04	0.01	0.78 (0.08)	0.44 (0.32)	0.54 (0.23)	16.71 (4.64)	0.51 (-)	0.52 (-)	8	~46–107
				0.00	0.99	0.91	0.70	1.00	0.05	0.30		
ROI I - 3 FRTs	-	-	-	-	0.71 (0.05)	0.22 (0.18)	0.54 (0.18)	15.78 (2.65)	0.49 (-)	0.54 (-)	27	~37–112
				0.01	1.00	1.45	0.95	1.00	0.28	0.23		
3192	−14.599	175.499	0.33 ± 0.04	0.01	0.72 (0.08)	0.29 (0.31)	0.59 (0.20)	12.32 (5.26)	0.52 (-)	0.52 (-)	9	~55–112
				0.01	1.00	1.69	0.92	1.00	0.23	0.16		
8CE1	−14.603	175.500	0.98 ± 0.15	0.03	0.76 (0.08)	0.34 (0.29)	0.44 (-)	17.58 (9.91)	0.48 (-)	0.48 (-)	7	~36–90
				0.02	0.99	1.42	0.41	0.98	0.08	0.09		
CDA5	−14.602	175.498	0.32 ± 0.04	0.01	0.74 (0.07)	0.37 (0.28)	0.65 (0.20)	14.62 (4.97)	0.53 (-)	0.51 (-)	8	~46–107
				0.01	1.00	1.06	0.81	1.00	0.14	0.10		
ROI II - 3 FRTs	-	-	-	-	0.72 (0.05)	0.27 (0.15)	0.56 (0.16)	15.62 (2.43)	0.49 (-)	0.52 (-)	24	~36–112
				0.01	1.00	1.18	0.99	1.00	0.05	0.23		

[a]The underconstrained parameters are indicated by (-) corresponding to the ROI I and II from CRISM measurement at 750 nm using our Bayesian inversion as well as the nonuniform criterion k (second line of each entry) after MARS-ReCO. This analysis is done for each CRISM FRT observation (i.e., FRT3192, FRT8CE1, and FRTCDA5) or for the combination of the three observations after correction for the atmospheric effects by MARS-ReCO. The standard deviation σ_ρ (in BRF units) is a parameter provided by MARS-ReCO estimating the quality of the retrieved surface bidirectional reflectance. The absolute quadratic residual of the fit RMS (in BRF units) evaluates the deviation of the fit from observed bidirectional reflectance. (*nb*: number of angular configurations *g*: phase angle range in degree).

Table 4. Same as Table 3 but for the ROI III and ROI IV

FRT	Latitude (°N)	Longitude (°E)	AOT	σ_ρ RMS	ω k	b k	c k	$\bar{\theta}$ k	B_0 k	h k	nb	g
3192	−14.593	175.496	0.33 ± 0.04	0.01	0.72 (0.08)	0.32 (0.29)	0.58 (0.20)	10.53 (5.81)	0.50 (-)	0.50 (-)	7	~56–108
				0.01	1.00	1.12	0.94	1.00	0.15	0.10		
8CE1	−14.596	175.494	0.98 ± 0.15	0.03	0.77 (0.09)	0.35 (0.29)	0.44 (-)	19.13 (10.52)	0.49 (-)	0.51 (-)	7	~37–84
				0.01	0.99	1.36	0.39	0.98	0.02	0.06		
CDA5	−14.594	175.497	0.32 ± 0.04	0.01	0.72 (0.07)	0.26 (0.25)	0.65 (0.20)	14.21 (5.59)	0.51 (-)	0.54 (-)	7	~46–106
				0.01	1.00	1.67	0.85	1.00	0.15	0.24		
ROI III - 3 FRTs	-	-	-	-	0.69 (0.04)	0.19 (0.14)	0.66 (0.18)	13.96 (4.40)	0.50 (-)	0.53 (-)	21	~37–108
				0.01	1.00	1.43	0.87	1.00	0.08	0.11		
3192	−14.600	175.507	0.33 ± 0.04	0.01	0.68 (0.06)	0.17 (0.21)	0.61 (0.22)	11.74 (4.43)	0.53 (-)	0.56 (-)	9	~56–112
				0.01	1.00	1.80	0.97	1.00	0.28	0.39		
8CE1	−14.602	175.508	0.98 ± 0.15	0.04	0.78 (0.09)	0.38 (0.29)	0.47 (-)	20.40 (11.41)	0.51 (-)	0.50 (-)	6	~41–84
				0.01	0.99	0.80	0.24	0.97	0.22	0.12		
CDA5	−14.600	175.509	0.32 ± 0.04	0.01	0.74 (0.07)	0.35 (0.27)	0.65 (0.20)	14.55 (5.48)	0.51 (-)	0.50 (-)	8	~46–107
				0.01	1.00	1.10	0.79	1.00	0.14	0.09		
ROI IV - 3 FRTs	-	-	-	-	0.79 (0.07)	0.59 (0.27)	0.56 (0.16)	10.88 (5.11)	0.50 (-)	0.48 (-)	23	~41–112
				0.01	1.00	0.53	0.97	1.00	0.09	0.05		

Table 5. Same as Table 3 but for Meridiani Planum With CRISM FRT Observations FRT95B8, FRT334D, and FRTB6B5

FRT	Latitude (°N)	Longitude (°E)	AOT	σ_ρ RMS	ω k	b k	c k	$\bar{\theta}$ k	B_0 k	h k	nb	g
95B8	−2.000	−5.484	0.56 ± 0.09	0.02	0.72 (0.09)	0.34 (0.30)	0.42 (-)	17.32(10.33)	0.48 (-)	0.50 (-)	5	~41–86
				0.01	0.99	1.40	0.44	0.98	0.12	0.16		
334D	−2.001	−5.482	0.35 ± 0.04	0.01	0.67 (0.09)	0.38 (0.32)	0.49 (0.25)	16.65 (7.82)	0.49 (-)	0.48 (-)	5	~50–98
				0.01	0.99	1.16	0.61	1.00	0.18	0.16		
B6B5	−2.004	−5.482	0.35 ± 0.04	0.01	0.65 (0.07)	0.19 (0.20)	0.52 (-)	18.09 (5.82)	0.50 (-)	0.50 (-)	6	~41–106
				0.01	1.00	2.06	0.41	1.00	0.12	0.14		
ROI I - 3 FRTs	-	-	-	-	0.68 (0.08)	0.36 (0.26)	0.41 (0.21)	18.37 (5.20)	0.51 (-)	0.52 (-)	16	~41–106
				0.02	0.99	0.82	0.95	1.00	0.15	0.24		

is the most constrained parameter (i.e., $0.06 < \sigma < 0.09$). Examples of a posteriori PDFs are plotted in Figures 4 and 6.

[52] 2. Although solutions exist for parameter b in all cases ($k >> 0.5$), the standard deviation shows that it is poorly constrained (i.e., $0.25 < \sigma < 0.32$) except for the ROI I and ROI IV using the CRISM observation FRT3192. This discrepancy can be explained by the higher number of available geometric configurations, respectively 10 and 9. Examples of a posteriori PDFs are plotted in Figures 4 and 7.

[53] 3. We find meaningful values for parameter c only when we use FRT3192 or FRTCDA5 ($k > 0.5$). The standard deviation is relatively low (i.e., $0.20 < \sigma < 0.23$) in this case. In the case of FRT8CE1, no solution is found for parameter c ($k < 0.5$) for ROI II, III and IV. For the ROI I, however, a solution exists but it is poorly constrained (i.e., $\sigma = 0.27$). Examples of a posteriori PDFs are plotted in Figures 4 and 7.

[54] 4. While parameter $\bar{\theta}$ has a solution in all cases ($k \sim 1$), we distinguish two types of results: (i) using FRT3192 or FRTCDA5, we note that the standard deviation is relatively low (i.e., $3.98 < \sigma < 5.81$); and (ii) using FRT8CE1, the standard deviation is relatively high (i.e., $9.64 < \sigma < 20.40$). Examples of a posteriori PDFs are plotted in Figures 4 and 8.

[55] 5. No solutions are found for parameters B_0 and h in any case ($k << 0.5$). As mentioned in Subsection 2.3.2, nor the phase domain covered by the CRISM observations nor the capabilities of MARS-ReCO allow constraining the opposition effect [*Ceamanos et al.*, 2013]. Consequently, accurate values for B_0 and h cannot be retrieved and no physical interpretation can be done in this case. Examples of a posteriori PDFs are plotted in Figure 4.

[56] Regarding the processing of a single CRISM observation, we note that parameters c and $\bar{\theta}$ are, respectively, nonconstrained and poorly constrained only when treating data from FRT8CE1. The reason to explain such a difference may be that the available maximum phase angle range is less than 90° for FRT8CE1. Indeed, *Helfenstein* [1988] underlined the necessity to have observations which extend from small phase angles out to phase angles above 90° for an accurate determination of the photometric roughness. By contrast, the phase angle range expands by more than 100° for the other observations (cf. Table 1). We note that parameter b is poorly constrained when treating data from all available observations. This result may be explained again by the available phase angle range (cf. Table 1). In conclusion, the presented study clearly demonstrates that the existence and quality of a solution for parameters b, c, and $\bar{\theta}$ is dependent on the available phase angle range. The bidirectional reflectance curve from a single CRISM observation does not contain enough phase angle information.

[57] By contrast, the combination of three targeted observations provides improved constrains on all Hapke's parameters except for B_0 and h. Indeed, the standard deviation of each estimated parameter is lower than those obtained when using only a single targeted observation. We note that for ROI IV, the Hapke's parameters are less constrained than for the other ROIs, especially for parameter b for which no solutions were found. This result can be explained by the

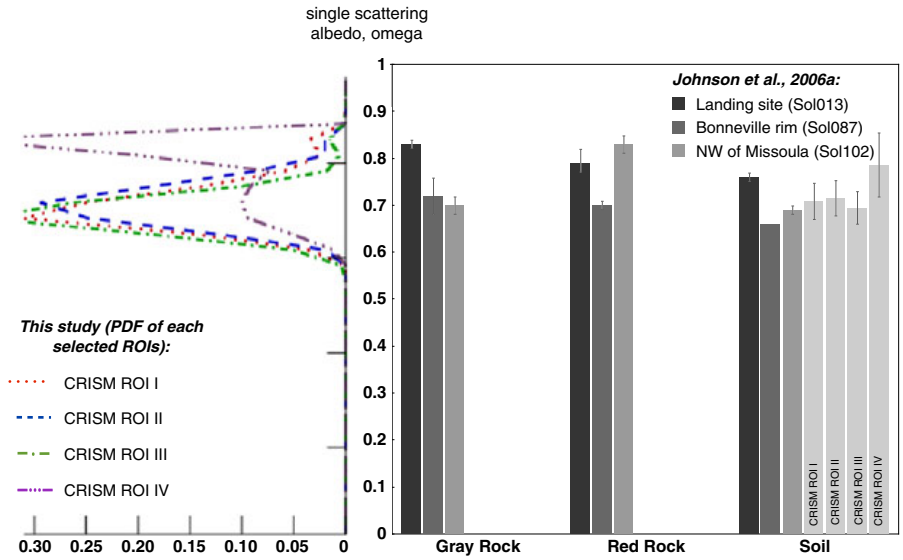


Figure 6. Mean and uncertainties of the single scattering albedo ω estimated from Pancam measurements at 753 nm for different geological units at landing site (Sol 013), Bonneville rim (Sol 087-088), and NW of Missoula (Sol 102-103) [*Johnson et al.*, 2006a] compared to those estimated from CRISM measurements at 750 nm (note that the error bar represents 2σ uncertainties) derived from 2-term HG models. The PDFs of the parameter ω estimated from the last 500 iterations of the Bayesian inversion are also represented on the left side. This is helpful when mean and uncertainties are not entirely representative of the PDF (such as the PDF of the parameter ω for the ROI IV which shows a bimodal distribution).

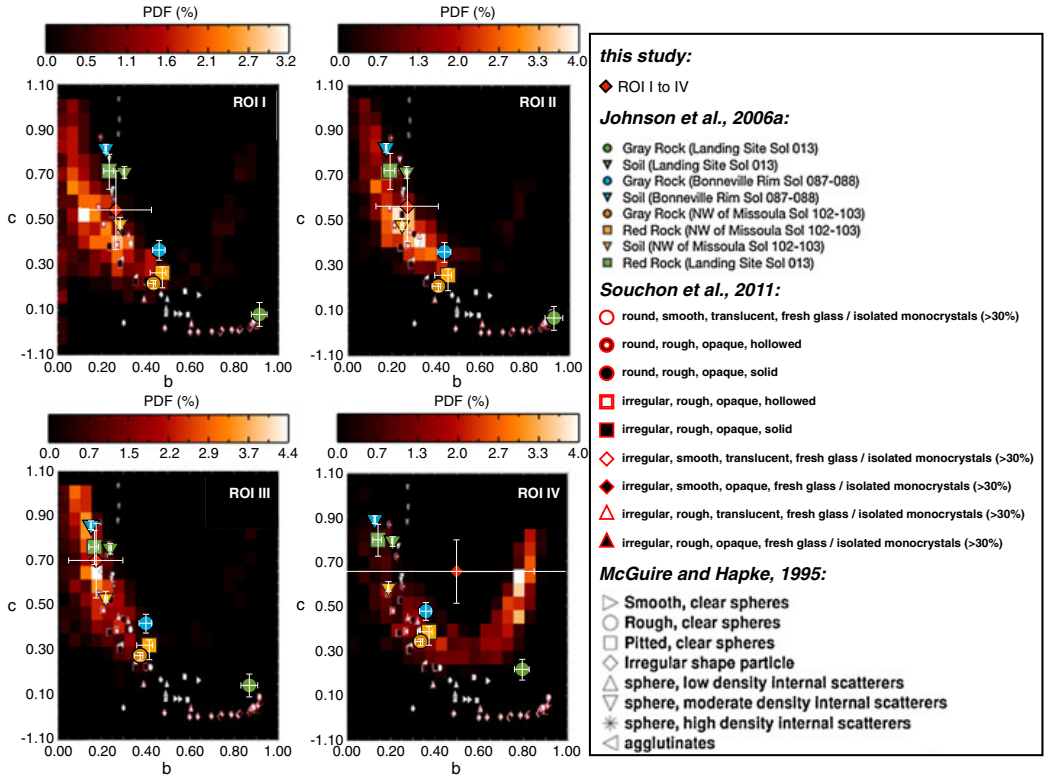


Figure 7. Probability density map of the asymmetric parameter b (horizontal axis) and the backscattering fraction c (vertical axis) solutions from the last 500 iterations of the Bayesian inversion estimated at 750 nm obtained for the four selected ROIs. The grid is divided into 24 (vertical) × 20 (horizontal) square bins. The coloring gives the probability corresponding to each bin. Means and 2σ uncertainties (red rhombus) are plotted, too. The inversion solutions are plotted against the experimental b and c values pertaining to artificial particles measured by *McGuire and Hapke* [1995] and to natural particles measured by *Souchon et al*. [2011]. The Gray Rock (circle), Red Rock (square) and Soil (triangle) units from Pancam sequences at landing site (green), Bonneville rim (blue) and NW of Missoula (orange) estimated at 753 nm (except for the Red Rock unit at the landing site which is constrained at 754 nm) [*Johnson et al*., 2006a] are plotted here.

limitation in the bidirectional sampling. In fact, we can note in Figure 9 which represents the north projection of geometric conditions for the four selected ROIs that the ROI IV misses a near-nadir geometry from the observation FRT8CE1. The latter shows a more different incidence angles (nearly 40°) than the two other CRISM FRT observations (nearly 60°) (see also Table 1) thus explaining that the parameters are less constrained for ROI IV than the other ROI.

[58] To conclude, the quality of these results shows the benefits of combining several targeted observations in constraining photometric parameters.

3.2. Results on Meridiani Planum

[59] Similar to the photometric study on the Gusev Crater, the standard deviation σ_ρ determined by MARS-ReCO is given for each CRISM observation and the ROI I used for the present study (cf. Table 5). Note that σ_ρ values are acceptable ($0.01 < \sigma_\rho < 0.02$) meaning that estimated surface bidirectional reflectance are accurate.

[60] Table 5 presents the results obtained on Meridiani Planum. Similar to Gusev Crater study, Figure 5 shows that a solution exists for the parameters ω, b, c, and $\bar{\theta}$ (i.e., nonuniform PDF) when a single CRISM FRT and in the case of three combined observations, except for parameters B_0 and h.

[61] The goodness of fit is estimated through the absolute quadratic residual RMS_{abs} value (cf. Table 5). For all Bayesian inversions, the estimates are less than 0.02 which mean that the inversions are deemed satisfactory.

[62] We note that for the parameter ω, two maximums are visible at nearly 0.6 and 0.8. In order to understand the origin of the bimodal distribution for the parameter ω in this case, the reflectance of typical Martian material was generated by using realistic photometric properties determined by the Pancam instrument aboard the MER Opportunity site in Meridiani Planum (i) at the same geometric configurations as the FRT95B8 observations, and (ii) at the same combined geometric configurations when merging the three selected observations. In both cases, the posterior PDF for the parameter ω shows a bimodal distribution. If the geometric sampling is broader

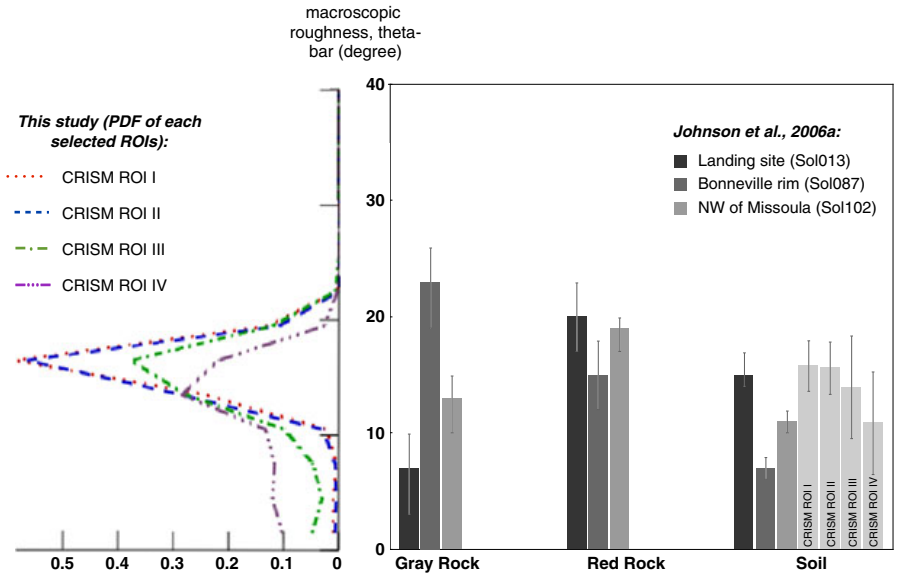


Figure 8. Mean and uncertainties of the macroscopic roughness $\bar{\theta}$ estimated from Pancam measurements at 753 nm for different geological units at landing site (Sol 013), Bonneville rim (Sol 087-088), and NW of Missoula (Sol 102-103) [*Johnson et al*., 2006a] compared to those estimated from CRISM measurements at 750 nm (note that the error bar represents 2σ uncertainties) derived from 2-term HG models. The PDFs of the parameter $\bar{\theta}$ estimated from the last 500 iterations of the Bayesian inversion are also represented on the left side. This is helpful when mean and uncertainties are not representative of the PDF.

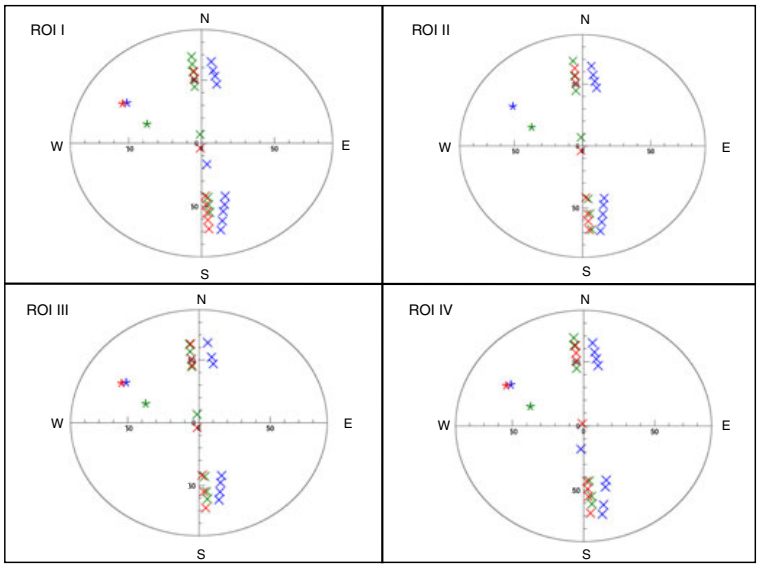


Figure 9. North projection of geometric conditions (stars: incidence rays and crosses: emergence directions) of the four selected ROIs for the Gusev Crater study (blue: FRT3192, green: FRT8CE1 and red: FRTCDA5).

(i.e., with varied incidence and emergence and phase angles), the posterior PDF of the parameter ω becomes a Gaussian with a single peak. The presence of two possible solutions is the consequence of the limitation of a sufficient geometric diversity in our selection of CRISM observations for the Meridiani Planum study to constrain the parameter ω, which is otherwise the best-constrained parameter in photometric modeling.

[63] Several conclusions can be drawn when using a single CRISM targeted observation:

[64] 1. Solutions exist for parameter ω in all cases ($k \sim 1$). The standard deviation shows that the single scattering albedo is the most constrained parameter (i.e., $0.07 < \sigma$ 0.15). Examples of a posteriori PDFs are plotted in Figures 5 and 10.

[65] 2. We find meaningful values for parameter b only when for FRT95B8 or FRT334D or FRTB6B5 ($k > 0.5$). Albeit the standard deviation is relatively high for FRT95B8 or FRT334D (i.e., $0.30 < \sigma < 0.32$), the standard deviation becomes relatively low for FRTB6B5 (i.e., $\sigma = 0.20$). Examples of a posteriori PDFs are plotted in Figures 5 and 11.

[66] 3. Solutions only exist for parameter c when using FRT334D ($k > 0.5$). However, the standard deviation is relatively high ($\sigma = 0.25$). Examples of a posteriori PDFs are plotted in Figures 5 and 11.

[67] 4. While parameter $\bar{\theta}$ has a solution in all cases ($k \sim 1$), we distinguish two types of results: (i) using FRT334D or FRTB6B5, we note that the standard deviation is relatively low (i.e., $5.82 < \sigma < 7.82$); and (ii) the standard deviation is relatively high (i.e., $\sigma = 10.33$) when using FRT95B8. Examples of a posteriori PDFs are plotted in Figures 5 and 12.

[68] 5. Similar to the Gusev study, no solution is found for parameters B_0 and h in any case ($k >> 0.5$). Examples of a posteriori PDFs are plotted in Figure 5.

[69] Dealing with single observations, we note that parameter $\bar{\theta}$ is poorly constrained when treating data from FRT95B8 and FRT334D, whereas it is highly constrained when using FRTB6B5 which can be explained by a maximum phase angle below 90° in case of FRT95B8 and FRT334D (cf. Table 1). *Helfenstein* [1988] underlined the necessity to have observations which extend from small phase angles out to phase angles above 90° for an accurate determination of the photometric roughness. Note that parameters b and c are non-constrained or poorly constrained even through solutions exist in all cases. This outcome can be explained by a worse quality of the Meridiani Planum bidirectional reflectance sampling. Indeed, we note in Figure 13 which represents the north projection of geometric conditions of each selected CRISM FRT observations that the three selected CRISM FRT (i) miss near-nadir geometries (close to emergence equal 0) and (ii) present lower number of available angular configurations compared to Gusev Crater work (lower than 6).

[70] We then improve the bidirectional reflectance sampling by combining the three selected targeted observations. We observe that parameters ω, b, and $\bar{\theta}$ become significantly more constrained. Indeed, the standard deviation of each estimated parameter is lower than those obtained when using only a single observation. However, the parameters are less constrained than those obtained for the Gusev Crater study, which can be explained by the lack of near-nadir geometry for this case (cf. Figure 13).

[71] Again, results underline the benefits of combining several observations.

4. Validation

[72] This section focuses on the validation of the estimated photometric parameters by comparing them to the previous photometric studies based on experimental, in situ, and orbital photometric studies. As the PDF of each parameter is not necessary a Gaussian, the estimated mean and the

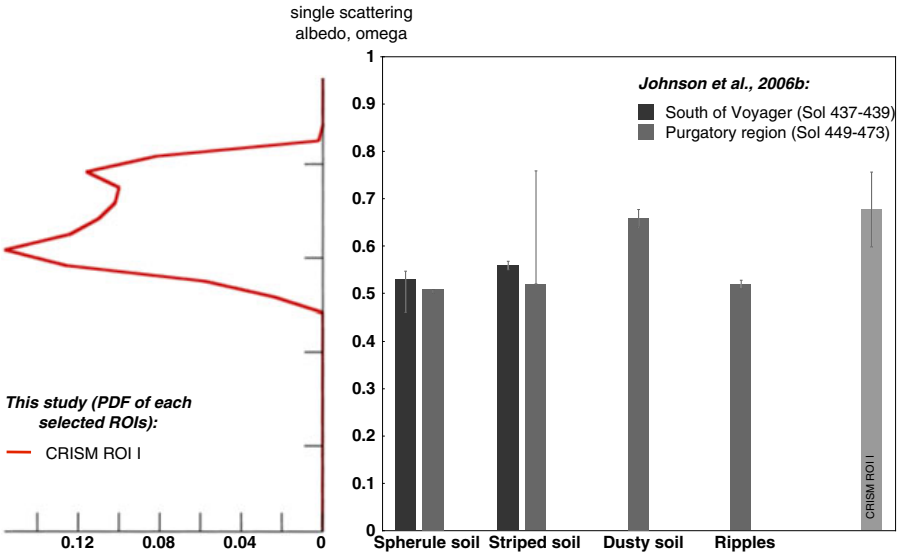


Figure 10. Mean and uncertainties of the single scattering albedo ω estimated from Pancam measurements at 753 nm for different geological units at South of Voyager (Sol 437-439) and Purgatory region (Sol 449-473) [*Johnson et al.*, 2006b] compared to those estimated from CRISM measurements at 750 nm (note that the error bar represents 2σ uncertainties) derived from 2-term HG models. The PDFs of the parameter ω estimated from the last 500 iterations of the Bayesian inversion are also represented on the left side. This is helpful when mean and uncertainties are not representative of the PDF (such as the PDF of the parameter ω for the ROI I which shows a bimodal distribution).

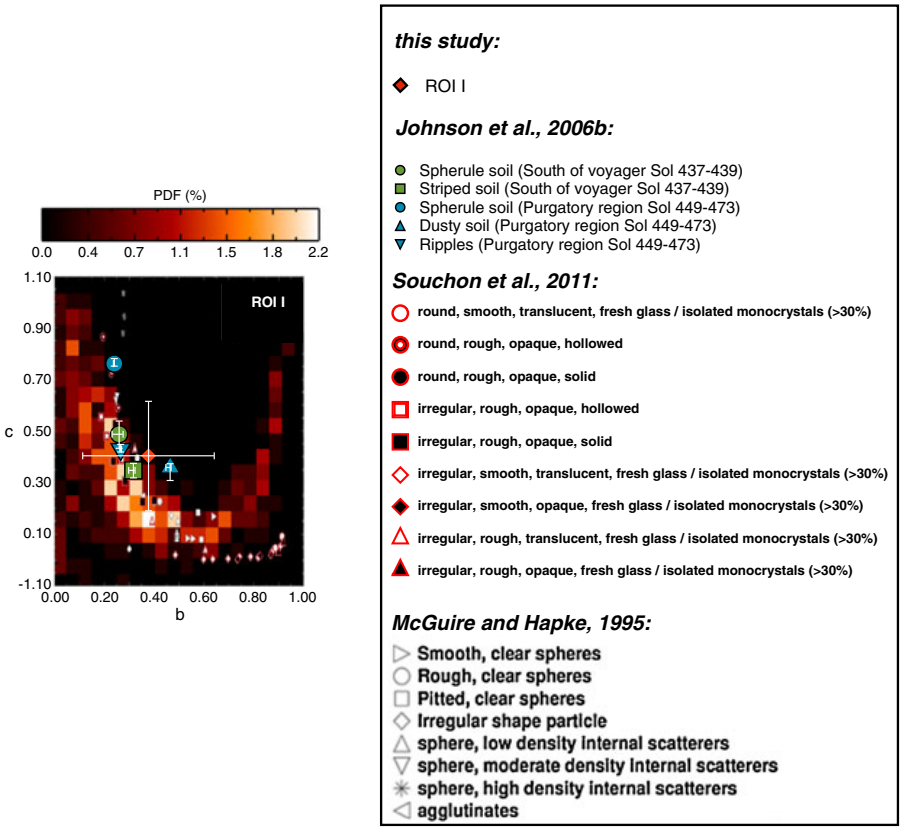


Figure 11. Probability density map of the asymmetric parameter *b* (horizontal axis) and the backscattering fraction *c* (vertical axis) solutions from the last 500 iterations of the Bayesian inversion estimated at 750 nm obtained for the selected ROI. The grid is divided into 24 (vertical) x 20 (horizontal) square bins. The coloring gives the probability corresponding to each bin. Means and 2σ uncertainties (red rhombus) are plotted too. The inversion solutions are plotted against the experimental *b* and *c* values pertaining to artificial particles measured by *McGuire and Hapke* [1995] and to natural particles measured by *Souchon et al*. [2011]. The Spherule soil (circle), Striped soil (square), Ripple (triangle), and Dusty soil (triangle) units from Pancam sequences at South of Voyager (green and Purgatory region (blue) estimated at 753 nm [*Johnson et al*., 2006b] are plotted here.

standard deviation are not always representative of the entire distribution. Consequently for each parameter, we use the PDF built from the last 500 iterations of the Markov chain process (see 2.3.1) instead of the previous statistical estimators for the comparison to the previous studies.

4.1. Validation of Results from Gusev Crater

4.1.1. Comparison to Experimental Measurements on Artificial and Natural Samples

[73] *McGuire and Hapke* [1995] studied the scattering properties of different isolated artificial particles which have different structure types (sphere/rough particles, clear/irregular shape particle, with/without internal scatterers, . . .). Their study showed that the Henyey-Greenstein function with two parameters, HG2 (backscattering fraction *c* and asymmetric parameter *b*) provided the best description of their laboratory bidirectional reflectance measurements. In short, their study shows that smooth clear spheres exhibit greater forward scattering (low values of *c*) and narrower scattering lobes (high values of *b*), whereas particles characterized by their roughness or internal scatterers exhibit greater backward scattering (high values of *c*) and broader scattering lobe (low values of *b*). In a graph mapping the *b* and *c* parameter spaces, the results exhibit a "L-shape" from particles with high density of internal scatterers to smooth, clear, spherical particles. For their study, *McGuire and Hapke* [1995] used centimeter-sized artificial particles which are larger than the light wavelength and far than typical constituents of the planetary regoliths. In order to examine the impact of particle size on the scattering phase function, *Hartman and Domingue* [1998] observed that there are no significant variations of the latter in *McGuire and Hapke* [1995] measurements when the particle size is similar to typical planetary regoliths particles. *Hartman and Domingue* [1998] concluded that *McGuire and Hapke* [1995] results could be considered to be representative of their respective particle structure types independent of particle size. However, recent experimental works have questioned the initial interpretation of the Hapke's parameters. Indeed, the Hapke's parameters seem to be more sensitive to the

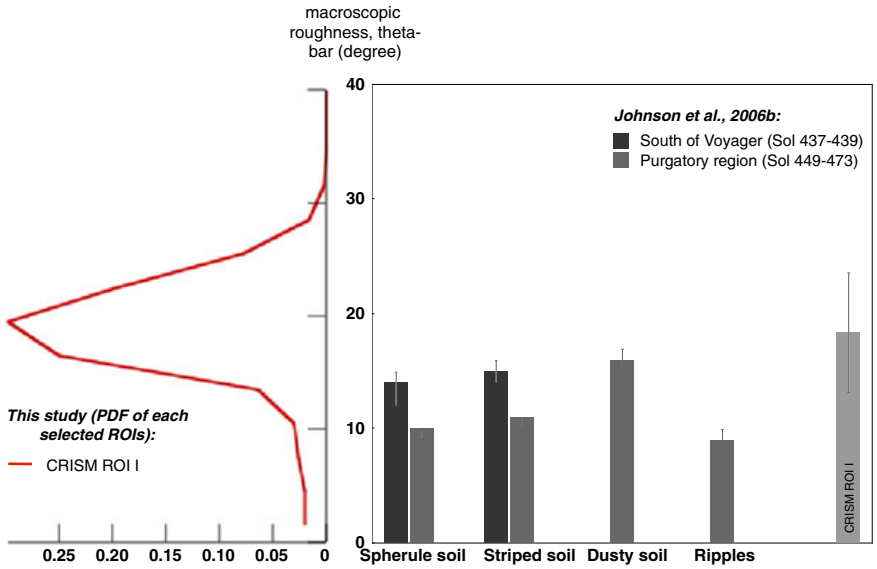


Figure 12. Mean and uncertainties of the macroscopic roughness $\bar{\theta}$ estimated from Pancam measurements at 753 nm for different geological units at the south of Voyager (Sol 437-439) and Purgatory region (Sol 449-473) [*Johnson et al*., 2006b] compared to those estimated from CRISM measurements at 750 nm (note that the error bar represents 2σ uncertainties) derived from 2-term HG models. The PDFs of the parameter $\bar{\theta}$ estimated from the last 500 iterations of the Bayesian inversion are also represented on the left side. This is helpful when mean and uncertainties are not entirely representative of the PDF.

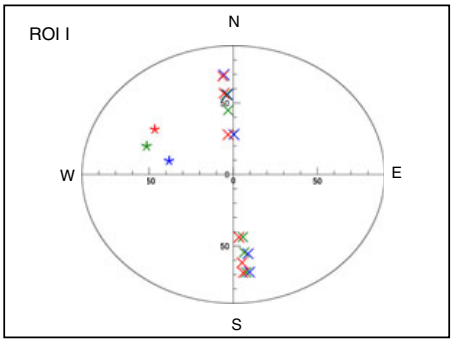


Figure 13. North projection of geometric conditions (stars: incidence directions and crosses: emergence directions) of the selected ROI for the Meridiani Planum study (blue: FRT95B8, green: FRT334D, and red: FRTB6B5).

organization of the surface material (effects of close packing, micro-roughness) than to the optical properties depending on individual particles [*Cord et al*., 2003; *Shepard and Helfenstein*, 2007]. Similarly, *Souchon et al*. [2011] measured for a comprehensive set of geometries the reflectance factor of natural granular surfaces composed of volcanic materials differing by their grain size (from the micron-scale to the millimeter-scale), shapes, surface aspect, and mineralogy (including glass and minerals). Thus, the main novelty of Souchon et al.'s experimental study [*Souchon et al*. 2011] compared to McGuire and Hapke's works [*McGuire and Hapke* 1995] is the determination of the parameters *b* and *c* for planetary analogs of basaltic granular surfaces and not isolated artificial particles. *Souchon et al*. [2011] compared the scattering parameters retrieved by inversion of Hapke's model with results on artificial materials [*McGuire and Hapke*, 1995] and a similar trend was found, though with some variations and new insights. Granular surfaces even with a moderate proportion of isolated translucent monocrystals and/or fresh glass exhibit strongly forward scattering properties, and a new part of the L-shape domain in the *b* and *c* parameter space is explored.

[74] In Figure 14 that is given as an example of similar figures, the scattering parameters (i.e., backscattering fraction *c* and asymmetric parameter *b*) of the ROI I from CRISM data (cf. Table 3) are plotted along with the scattering parameters obtained from laboratory measurements of artificial [*McGuire and Hapke*, 1995] and natural samples [*Souchon et al*., 2011]. Results show that parameters *b* and *c* retrieved from the inversion of combined CRISM FRT observations are consistent with the laboratory studies. The combination of three FRTs is necessary to constrain satisfactorily the *b* and *c* values with acceptable error bars. As it can be seen, surface materials of ROI I have high values of *c* and low values of *b*, which indicate broad backscattering properties related to artificial materials composed of spheres with a moderate density of internal scatterers and close to irregular or round rough, opaque, and solid natural particles (cf. Figure 14).

4.1.2. Comparison to In Situ Measurements Taken by Pancam/MER Spirit

[75] The Pancam instrument on-board MER Spirit acquired several spectrophotometric observations along the rover's traverse paths to determine the surface physical and chemical properties of rocks and soils encountered at the Gusev Crater. *Johnson et al*. [2006a] evaluated the parameters of Hapke's photometric model [*Hapke*, 1993] using equations 1, 2, and

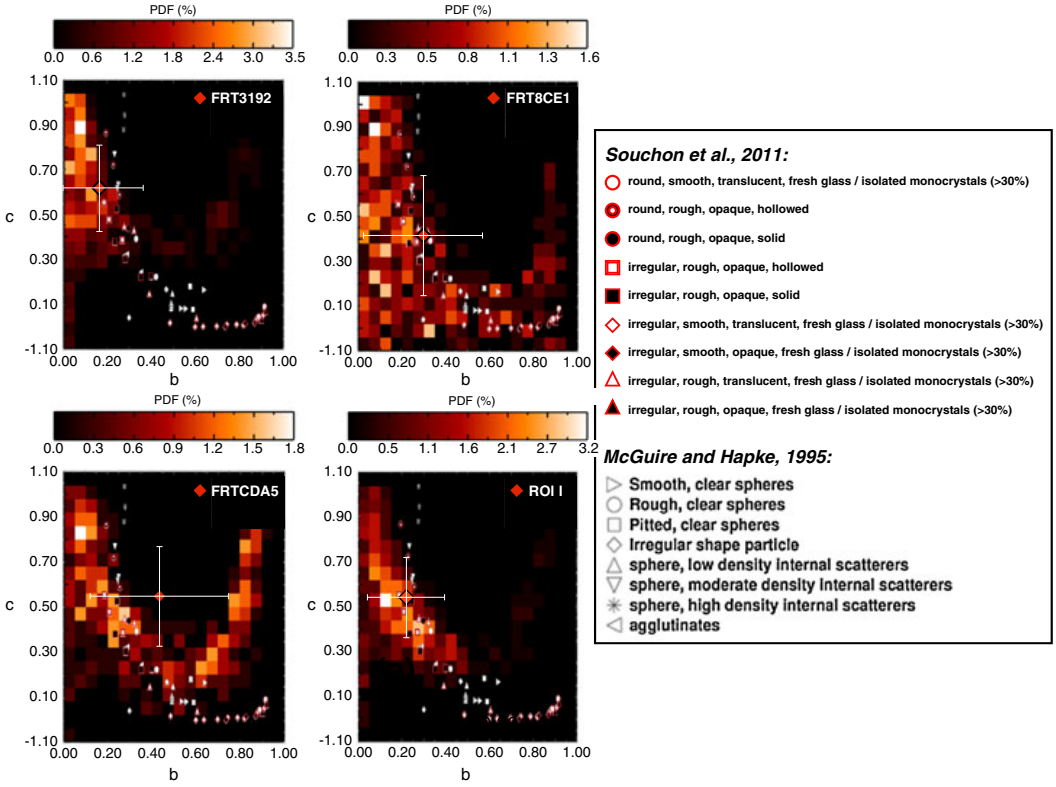


Figure 14. Probability density map of the asymmetric parameter *b* (horizontal axis) versus the backscattering fraction *c* (vertical axis) solutions retrieved at 750 nm estimated from the last 500 iterations of the Bayesian inversion for FRT3192, FRT8CE1 and FRTCDA5 observations and their combination (ROI I). The grid is divided into 24 (vertical) × 20 (horizontal) square bins. The coloring gives the probability corresponding to each bin. Means and 2σ uncertainties (red rhombus) are plotted, too. The inversion solutions are plotted against the experimental *b* and *c* values pertaining to artificial particles measured by *McGuire and Hapke* [1995] and to natural particles measured by *Souchon et al*. [2011].

3 from measured radiance for several identified units (i.e., "Gray" rocks, which are free of airfall deposit dust or other coatings, "Red" rocks, which have coating, and "Soil" unit, corresponding to unconsolidated materials). The measured radiance at the ground was first corrected for diffuse sky illumination [*Johnson et al*., 2006a] and local surface facet orientations [*Soderblom et al*., 2004].

[76] The difference of spatial resolution between CRISM and Pancam instruments must be considered prior to comparison. Indeed, a direct comparison between both sets of photometric parameters must be handled with care as Pancam provides local measurements (at a centimetric scale such as soils and rocks), whereas orbital instruments such as CRISM measure extended areas integrating different geologic units (at a pluri-decametric scale such as a landscape). In the latter case, measurements may be dominated by unconsolidated materials such as soils. As mentioned in Subsection 2.3.1, the four selected ROIs are chosen close to the MER Spirit's path. The retrieved photometric parameters for each ROI from the combination of three CRISM observations were compared to those extracted from three sequences taken by Pancam in the Gusev plains. These measurements are located near to the four ROIs in landing site (Sol 013), Bonneville rim (Sol 087-088), and Missoula (Sol 102-103) to the northwest side of Columbia Hill (cf. Figure 2) [*Johnson et al*., 2006a]. In this case the combination of three CRISM observations were treated using the H93 version of the Hapke's model in order to match the same model used in *Johnson et al*. [2006a]. Pancam results are summarized in Table 6.

[77] 1. Single scattering albedo. Figure 6 plots the means and uncertainties as well as the PDF of single scattering albedo ω estimated for the four selected ROIs against values extracted for each unit defined by *Johnson et al*. [2006a] (i. e., Gray rocks, Red rocks, and Soil) at the landing site, Bonneville rim, and NW of Missoula. The bimodality is identical to Meridiani ROI I (see subsection 3.2) and is the consequence of the lack of geometric diversity in the CRISM dataset. The estimated values of ω from CRISM are consistent with the Pancam outputs for the Soil unit.

[78] 2. Phase function. Figure 7 plots the asymmetric parameter *b* versus the backscattering fraction *c* solutions provided by the Bayesian inversion for each ROI in comparison to the photometric parameters obtained by *Johnson et al*. [2006a]. In the case of Red rock unit for landing site,

Table 6. Retrieved Hapke's Parameters and Their Standard Deviation[a]

Site	Unit	ω	$\bar{\theta}$ (deg)	b	c	Number	g (deg)
Landing Site	Bright Soil	0.75 (+0.01, −0.00)	2 (+, −)	0.243 (+0.020, −0.017)	0.625 (+0.012, −0.013)	21	~30–120
(Sol 013)	Gray Rock	0.83 (+0.01, −0.01)	7 (+3, −4)	0.931 (+0.045, −0.044)	0.065 (+0.058, −0.058)	66	~30–120
	Red Rock	0.79 (+0.03, −0.02)	20 (+3, −3)	0.187 (+0.026, −0.031)	0.720 (+0.084, −0.087)	68	~30–120
	Soil	0.76 (+0.01, −0.01)	15 (+2, −1)	0.262 (+0.010, −0.010)	0.715 (+0.029, −0.032)	51	~30–120
Bonneville Rim	Gray rock	0.72 (+0.04, −0.04)	23 (+3, −4)	0.434 (+0.035, −0.037)	0.359 (+0.048, −0.050)	63	~25–120
(Sol 087-088)	Red rock	0.70 (+0.01, −0.01)	15 (+3, −3)	0.219 (+0.017, −0.020)	1.000 (+,−)	72	~25–120
	Soil	0.66 (+0.00, −0.00)	7 (+1, −1)	0.170 (+0.008, −0.008)	0.823 (+0.025, −0.024)	54	~25–120
NW of Missoula	Gray rock	0.70 (+0.02, −0.02)	13 (+2, −3)	0.406 (+0.018, −0.032)	0.206 (+0.019, −0.025)	225	~0–125
(Sol 102-103)	Red rock	0.83 (+0.02, −0.02)	19 (+1, −2)	0.450 (+0.023, −0.064)	0.255 (+0.032, −0.072)	141	~0–125
	Soil	0.69 (+0.01, −0.00)	11 (+1, −1)	0.241 (+0.011, −0.009)	0.478 (+0.036, −0.022)	132	~0–125

[a]Underconstrained parameters are indicated by "(+,−)" from the 2-term model for Sol 13, Sol 87-88, and Sol 102-103 and each of the three considered units (Gray Rock, Red Rock, and Soil) at 753 nm (except for the parameter c of Red Rock unit for landing site which corresponds to the 754 nm model results) from Pancam onboard Spirit [*Johnson et al*., 2006a].

the parameter c is determined at 754 nm instead of usual 753 nm. Moreover, the parameter c is not constrained at both wavelengths in the case of Red Rock at Bonneville rim. Consequently, the parameters b and c are not plotted here. The b and c pairs from CRISM observations are most consistent with the Soil unit for all the studied Spirit sites and the Red Rock unit from the landing site which exhibits broad backscattering properties. Again, we note that for ROI IV, the Hapke's parameters are less constrained than for the other ROIs, especially for parameter b for which no solutions were found.

[79] 3. Macroscopic roughness. Means and uncertainties as well as the PDF of the macroscopic roughness $\bar{\theta}$ obtained for each selected ROI are presented in Figure 8. The parameter $\bar{\theta}$ of all selected ROIs, estimated from CRISM measurements is consistent with the Soil unit found at the landing site and at NW of Missoula (cf. Figure 8). By contrast, this parameter indicates a rougher surface than the soil unit found at Bonneville rim which is consistent with *Johnson et al*. [2006a]. At intercrater plains where the landing site is situated, the greater proportion of small clasts in the soil (compared to the soils near Bonneville rim and Missoula area) may explain the rougher surface texture [*Ward et al*., 2005].

[80] Two principal points from the previous comparison can be outlined. First, at the effective spatial scale achieved from space by CRISM for the photometric characterization (460 m), the surface behaves like the Soil units defined by [*Johnson et al*., 2006a] and particularly like the Soil unit observed at the landing site. Second, the values of ω and (b,c) resulting from our analysis are approximately inside the range of variation seen in Figures 6 and 7 for the Soil units at the three locations. This is not the case for the macroscopic roughness which is close to (within the error bars) the Soil unit values only for the landing site and Missoula area (cf. Figure 8). Consequently, all photometric parameters retrieved following the methodology proposed in this article are consistent with the results arising from the analysis of Pancam measurements at Gusev provided that ROIs are associated to the proper soil unit. That means that the two independent investigations (the present work and the study of *Johnson et al*. [2006a]study) are cross-validated in the Gusev case.

4.1.3. Comparison with Photometric Estimates Derived from Orbital Measurements by HRSC/MEx

[81] Using HRSC imagery, which provides multi-angle data sets (up to five angular configurations by orbit) [*McCord et al*., 2007], *Jehl et al*. [2008] determined the regional variations of the photometric properties at the kilometer spatial scale across Gusev Crater and the south flank of Apollinaris Patera using several observations in order to cover a phase angle range from 5° to 95°. The photometric study was carried out without any atmospheric correction but ensuring that the atmospheric contribution was limited by selecting HRSC observations with AOT lower than 0.9. *Jehl et al*. [2008] applied an inversion procedure developed by *Cord et al*. [2003] based on the H93 version of Hapke's model (equation 1). In the study of *Jehl* [2008], even photometric units were determined using a principal component analysis at 675 nm in which one of them corresponds to the Spirit landing site area. There is a robust overall first-order consistency between these photometric orbital estimates independently retrieved from HRSC and CRISM observations, particularly for ROIs I, II, and III (see Table 7).

[82] The principal point from the comparison between both orbital photometric results is that there is a robust overall first-order consistency between these photometric orbital estimates which reached independently from HRSC and CRISM observations, particularly for ROIs I, II, and III (see Table 7). However, in detail, two differences can be noted for the parameters ω and c (see Table 7). In fact, the parameters ω and c from CRISM measurements are respectively lower and higher than those determined from HRSC measurements. Moreover, the parameters ω and c estimated from CRISM data set are more consistent with in situ measurements. These differences are explained by the use of an aerosol correction in the CRISM data whereas no correction was made in HRSC data. As a consequence, the contribution of bright and forward scattering aerosols in the HRSC measurements appeared to increase the apparent surface single scattering albedo and to decrease the surface backscattering fraction value.

4.2. Validation of Meridiani Planum

4.2.1. Comparison to Experimental Measurements on Artificial Particles

[83] Our investigation shows that parameters b and c estimated from the inversion of both individual and combined (cf. Figure 15) CRISM FRTs are consistent with the L-shape defined from laboratory studies. However, the bidirectional reflectance sampling is not adequate to provide accurate estimation of the scattering parameters, even by combining up to three FRTs. In this case, according to parameters b and c, the surface represented by ROI I is slightly forward

Table 7. Retrieved Hapke's Parameters and Their Standard Deviation[a]

Instrument	ROI or Unit	ω	*b*	*c*	$\bar{\theta}$ (deg)	B_0	*h*
CRISM	ROI I	0.71 (0.05)	0.22 (0.18)	0.54 (0.18)	15.78 (2.65)	0.49 (-)	0.54 (-)
	ROI II	0.72 (0.05)	0.27 (0.15)	0.56 (0.16)	15.62 (2.43)	0.49 (-)	0.52 (-)
	ROI III	0.69 (0.04)	0.19 (0.14)	0.66 (0.18)	13.96 (4.40)	0.50 (-)	0.53 (-)
	ROI IV	0.79 (0.07)	0.59 (0.27)	0.56 (0.16)	10.88 (5.11)	0.50 (-)	0.48 (-)
HRSC	case 1	0.72 ± 0.02	0.06 ± 0.02	0.34 ± 0.06	18.5 ± 1.5	0.73 ± 0.07	0.75 ± 0.13
	case 2	0.80 ± 0.02	0.22 ± 0.04	0.41 ± 0.06	17.2 ± 3.0	-	-

[a]The underconstrained parameters are indicated by "(-)") from CRISM measurement at 750 nm (present results) compared to those from HRSC measurements at 675 nm [*Jehl et al*., 2008]. The Yellow Unit is associated to the Spirit landing site. The case 1 is the Hapke's parameters determination when the opposition effect parameters are set free and the case 2, when the Opposition Effect is neglected, with phase angles larger than 20° (see *Jehl et al*. [2008] for more details).

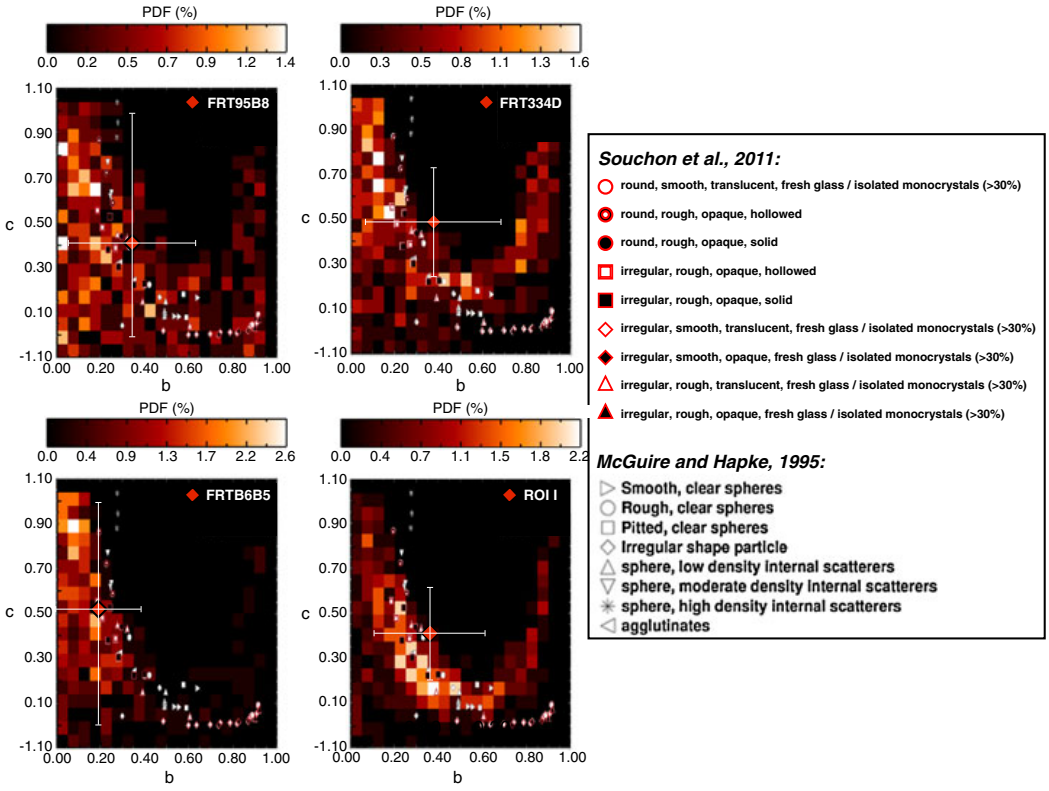


Figure 15. Same as Figure 14 for Meridiani Planum using observations FRT95B8, FRT334D, and FRTB6B5 and their combination (ROI I).

scattering with a relatively broad lobe (low *b* and *c*) which is consistent with artificial materials composed of round and clear sphere or agglutinates and close to irregular or round rough, opaque, and solid natural particles (cf. Figure 15).

4.2.2. Comparison To In Situ Measurements Taken by Pancam/MER Opportunity

[84] Similar to the work done at the Spirit's landing site, a photometric study was done at Meridiani Planum by using the Pancam instrument from Eagle crater to Purgatory ripple in *Johnson et al*. [2006b]. Units were defined, for example, as "Spherule soil" (typical soil with abundant spherules), "bounce marks" (soil compressed by the airbags at the landing site), and "outcrop rock" (bedrock). Our results are compared to the two photometric sequences taken by Pancam that are near the selected ROI: south of Voyager (Sol 437-439) and Purgatory region (Sol 449-473) (cf. Figure 2). In addition to the Spherule soil unit, *Johnson et al*. [2006b] defined the soil class "striped soil", which characterizes soils with a striped appearance on the faces of some dune forms. Especially for the Purgatory region, large ripples were present and a specific class was defined. Bright soil deposits among the striped soil unit were defined as a Dusty soil unit which was limited in spatial extent. Results are summarized in Table 8. In this article the photometric results are obtained from the combination of four FRT observations using the H93 version of the

Table 8. Retrieved Hapke's Parameters and Their Standard Deviation[a]

Site	Unit	ω	(deg)	*b*	*c*	Number	*g* (deg)
South of Voyager	Spherule soil	0.53 (+0.02, −0.07)	14 (+1, −2)	0.249 (+0.022, −0.031)	0.491 (+0.058, −0.057)	144	~5–140
(Sol 437-439)	Striped soil	0.56 (+0.01, −0.01)	15 (+1, −1)	0.305 (+0.010, −0.022)	0.353 (+0.033, −0.032)	119	~5–140
Purgatory region	Spherule soil	0.51 (+0.00, −0.01)	10 (+0, −1)	0.230 (+0.006, −0.007)	0.761 (+0.023, −0.013)	686	~0–135
(Sol 449-473)	Striped soil	0.52 (+0.24, −0.00)	11 (+0, −1)	0.117 (+0.011, −0.012)	1.000 (+,−)	104	~0–135
	Dusty soil	0.66 (+0.02, −0.02)	16 (+1, −1)	0.449 (+0.011, −0.020)	0.364 (+0.019, −0.053)	64	~0–135
	Ripples	0.52 (+0.01, −0.01)	9 (+1, −1)	0.255 (−0.008, −0.007)	0.434 (+0.023, −0.014)	234	~0–135

[a]The unconstrained parameters are indicated by "(+,−)" from the 2-term HG model for Sol 437-439 (Spherule Soil and Striped soil) and Sol 449-473 units (Spherule soil, Striped soil, Dusty soil, and Ripples) at 753 nm from Pancam onboard Opportunity [*Johnson et al*., 2006b].

Hapke's model. In this way, we use the same model as in *Johnson et al*. [2006b].

[85] 1. Single scattering albedo. Figure 10 plots means and uncertainties as well as the PDF of the single scattering albedo ω of the selected ROI against the values of the Spherule soil and Striped soil units defined by *Johnson et al*. [2006b] at south of Voyager and the additional dusty soil and ripples units in the Purgatory region. The retrieved values of ω from CRISM are higher than those estimated from Pancam measurements except for the spatially sparse dusty soil unit (first maximum of the PDF around 0.65).

[86] 2. Phase function. Figure 11 plots the asymmetric parameter *b* and the backscattering fraction *c* solutions of the Bayesian inversion for the ROI I in comparison to results of two photometric units (i.e., Spherule soil and striped soil) from south of Voyager and three photometric units (Spherule soil, Dusty soil and Ripples) for the Purgatory region. Note that the parameter *c* is underconstrained in the striped soil unit in the Purgatory region area because of the relative lack of phase angle coverage (~45–110°). As mentioned in Subsection 3.2, parameters *b* and *c* are not well constrained in the CRISM case but exhibit slightly more forward scattering properties than at Gusev crater. This results is still potentially consistent with all units in Purgatory region and south of Voyager, except for the Spherule soil which exhibits more backscattering properties.

[87] 3. Macroscopic roughness. Means and uncertainties as well as the PDF of the macroscopic roughness $\bar{\theta}$ modeled from CRISM data is higher than that retrieved at the south of Voyager and at Purgatory region (cf. Figure 12).

[88] Two principal points from the previous comparison can be outlined. First, at the effective spatial scale achieved from space by CRISM for the photometric characterization (460 m), the surface behaves particularly like the Dusty soil unit defined by *Johnson et al*. [2006b] at the Purgatory region: higher single scattering albedo, more forward scattering materials, and rougher surfaces. Second, the photometric properties estimated from CRISM data are not strongly supported by those determined from Pancam. In fact, the selected ROI and the Pancam photometric sequences (South of Voyager and Purgatory region) are located several kilometers to the south of the Opportunity landing site where a geological transition region is observed. Indeed, bright plains which exposed a smaller areal abundance of hematite, brighter fine-grained dust rich in nanophase iron oxides (such as in Gusev Crater plains), and a larger areal of bright outcrops are observed from orbital measurements (cf. see Figure S1 in the Supporting Information) compared to plains near the landing site [*Arvidson et al*., 2006]. Inside the ROI I, even if the bright material unit does not seem to be the main geological unit at centimeter spatial scale, it seems to be more abundant from the orbit.

5. Discussion

[89] The previous results show that the surface photometric parameters retrieved in this study are consistent with those derived from in situ measurements. This cross-validation demonstrates that MARS-ReCO is able to estimate accurately the surface bidirectional reflectance of Mars. Nevertheless, one could question the significance of these estimates. Therefore, this section aims at testing the non-Lambertian surface hypothesis used by MARS-ReCO and the influences of the surface bidirectional reflectance sampling on the determination of the photometric parameters.

5.1. Non-Lambertian Surface Hypothesis

[90] The compensation for aerosol contribution represents a great challenge for photometric studies. In planetary remote sensing, the Lambertian surface assumption is often adopted by the radiative atmospheric calculations that allow retrieval of surface reflectance [*Vincendon et al*., 2007; *McGuire et al*., 2008; *Brown and Wolff*, 2009; *Wiseman et al*., 2012]. The surface reflectance is then assumed to be independent on geometry (i.e., the variation of TOA radiance with geometry is supposed to exclusively relate to aerosol properties). This hypothesis is generally used as it simplifies the radiative transfer modeling. However, it has been proved that most surface materials (e.g., minerals and ices) have an anisotropic non-Lambertian scattering behaviors [*de Grenier and Pinet*, 1995; *Pinet and Rosemberg*, 2001; *Johnson et al*., 2006a, 2006b; *Johnson et al*., 2008; *Lyapustin et al*., 2010]. Consequently, we consider that a Lambertian hypothesis can potentially create biases in the determination of the surface reflectance.

[91] For the AOT estimate some assumptions regarding the surface properties were taken in Wolff et al.'s work [*Wolff et al*. 2009]. Indeed this method assumes a non-Lambertian surface to estimate the AOT by using a set of surface photometric parameters [*Johnson et al*., 2006a, 2006b] that appears to describe the surface phase function adequately for both MER landing sites (roughly associated to the brighter or dusty soils). This assumption is qualitative but reasonable for several reasons enumerated by *Wolff et al*. [2009]. However, bias in the estimation of surface bidirectional reflectance can appear. For both MER landing sites it seems from Wolff et al.'s work [*Wolff et al*. 2009] that the AOT retrievals are overall consistent with optical depths returned by the Pancam instrument (available via PDS).

[92] In order to test whether or not the non-adoption of a Lambertian hypothesis improves the quality of the retrieved

surface reflectance, we compare the surface reflectance and the surface photometric parameters retrieved by a radiative transfer-based atmospheric correction technique that adopts a Lambertian assumption for the surface [*Douté*, 2009] and those given by MARS-ReCO [*Ceamanos et al*., 2013].

[93] Figure 16 presents the initial TOA reflectance and the surface reflectance derived from both atmospheric correction techniques as a function of the phase angle. As can be seen, the main difference is observed at high phase angle (greater than 90°) where lower BRF are estimated in the case of the Lambertian method. This difference can be explained by the non-Lambertian assumption of the surface by MARS-ReCO. Table 9 presents the photometric parameters retrieved from the surface bidirectional reflectance estimated from both techniques. First, solutions are found for the parameters ω, b, c, and $\bar{\theta}$ with higher standard deviations from the Lambertian method. Second, higher b is observed from the Lambertian method which is not compatible with the in situ photometric results. This shows that the consideration of a non-Lambertian surface in the correction for aerosol contribution by MARS-ReCO is needed for the determination of accurate surface bidirectional reflectance and thus for the estimation of accurate surface photometric parameters.

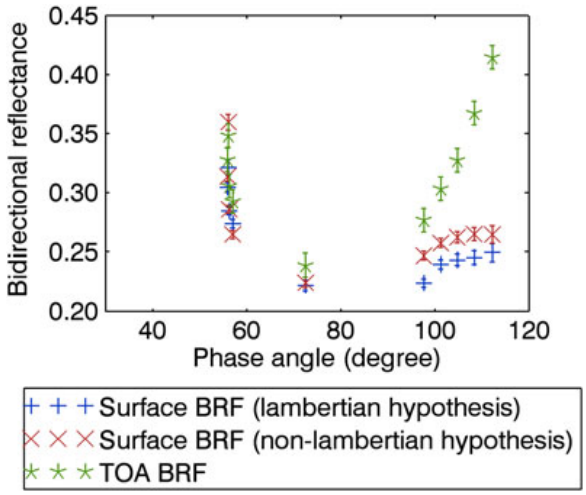


Figure 16. Photometric curves corresponding to ROI I of the FRT3192 observation and composed of 10 angular configurations. The reflectance values (in BRF units) are extracted at the TOA (green asterisk) and at the surface after correction for atmospheric contribution. The latter takes into account a non-Lambertian surface hypothesis using MARS-ReCO (red crosses) and a Lambertian surface assumption (blue plus sign; see details in section 5.1). In the three cases, we plot error bars corresponding to the 1σ uncertainty.

5.2. Influences of the Surface Bidirectional Reflectance Sampling on the Determination of the Photometric Parameters

[94] The accuracy of the determination of Hapke's parameters ω, b, c, $\bar{\theta}$, B_0, and h highly depends on the quality and the representativeness of the surface bidirectional reflectance used for their estimation. Indeed, for a given phase angle range, the estimation of all parameters is essentially controlled by the degree to which the angular space (incidence, emergence, azimuth, and consequently phase angles) is covered rather than by the number of available angular configurations [*Souchon et al*., 2011]. Also, a large phase angle domain is required. In fact, certain photometric parameter are sensitive to the availability of low and high phase angle values. First, the opposition effect is visible only with phase angle values less than 20°. Second, for an accurate determination of the macroscopic roughness, observations that span from small phase angle out to phase angle above 90° are needed [*Helfenstein*, 1988]. Finally, materials with strong backscattering or forward scattering properties require the consideration of large phase angles, ideally greater than 140° [*Kamei and Nakamura*, 2002; *Shkuratov et al*., 2007; *Shepard and Helfenstein*, 2011; *Helfenstein et al*., 1991].

[95] As presented previously (Subsection 2.1.1), CRISM targeted observations are composed of 11 images which are characterized by a constant incidence angle and 11 different emergence angles. Two modes of relative azimuth are used corresponding to the inbound and outbound portions of the spacecraft trajectory. Based on laboratory experiments performed under a given incidence angle, *Souchon* [2012] showed that the photometric parameters are determined with a good reliability under the condition of varied emergence and azimuth angles, resulting in varied phase angle values. However, each CRISM observation has intrinsically limited azimuthal and emergence coverage, which affects the determination of all the photometric parameters such as the opposition effect parameters, B_0 and h, the phase function parameters, b and c, and the macroscopic roughness, $\bar{\theta}$. The solution used in the present

Table 9. Retrieved Hapke's Parameters (ω, b, c, and $\bar{\theta}$ in degrees, B_0, h) and Their Standard Deviation[a]

ROI	FRT	AOT	ω k	b k	c k	$\bar{\theta}$ k	B_0 k	h k	nb	g
ROI I	3192 (non-lamb. hypo.)	0.33 ± 0.04	0.68 (0.06) 1.00	0.17 (0.20) 1.92	0.62 (0.20) 0.96	11.62 (3.98) 1.00	0.52 (-) 0.24	0.52 (-) 0.12	10	~56–112
	3192 (lamb. hypo.)	0.33 ± 0.04	0.74 (0.08) 0.99	0.46 (0.32) 1.12	0.64 (0.17) 0.74	12.43 (4.86) 0.98	0.52 (-) 0.25	0.50 (-) 0.03	10	~56–112

[a]The underconstrained parameters are indicated by "(-)" from CRISM measurement at 750 nm using our Bayesian Inversion assuming (i) a non-Lambertian assumption (MARS-ReCO) [*Ceamanos et al*., 2013] and (ii) a Lambertian hypothesis [*Douté*, 2009] for the surface. The Hapke's photometric parameters corresponding to the ROI I are retrieved by Bayesian Inversion as well as the nonuniform criterion k. (*nb*: number of angular configurations, g: phase angle range in degree).

study is to combine several targeted observations with different illumination conditions taken at different times in a year (because of the MRO sun-synchronous orbit) in order to enrich as much as possible the phase angle range by adding low and high phase angles. Nevertheless, low (less than 20°) and high (greater than 120°) phase angle values are not available here.

[96] Thanks to Bayesian inversion, the shape of the a posteriori PDF is known and will inform us whether the bidirectional reflectance sampling is sufficient to estimate accurate photometric parameters. In fact, a uniform or bimodal PDF are the consequence of a lack of the bidirectional reflectance sampling as confirmed by synthetic tests.

[97] Note that the surface bidirectional sampling also influences the AOT estimate notably through the determination of the single scattering albedo. Large AOT error bars are related to CRISM targeted observations presenting limited geometries [*Wolff et al*., 2009]. However, the surface bidirectional reflectance estimated by MARS-ReCO is sensitive to the accuracy of the AOT input [*Ceamanos et al*., 2013].

5.3. Comparison of Surface Photometric Results From Pancam Versus CRISM

[98] The differences regarding the acquisition geometries between Pancam and CRISM can influence the determination of the photometric properties. Ideally, in order to properly compare both results, the bidirectional reflectance sampling should be the same. However, this cannot be achieved because of the technical constraints on the acquisition of the bidirectional reflectance measurements in the case of a spaceborne instrument and an in situ vehicle, respectively. In addition, the atmospheric contribution does not affect the observation in the same manner. In the orbital case the light travels twice across the atmosphere while in the in situ case, it only travels once before reaching the sensor.

[99] Comparison of orbital photometric results to in situ photometric results demonstrates two main differences arising from different acquisition modes. The first comes from the sampling of the bidirectional reflectance. Pancam acquires a photometric sequence by varying the illumination angles (observations acquired at several times of day) and by varying the local azimuth and emission angles among similar units to order to enrich the phase angle range.

[100] The second difference comes from the spatial scale that is accessible. CRISM photometric curves are obtained at the hectometric spatial scale on an extended area whereas Pancam observes at the centimeter spatial scale. Some characteristics of the surface can be observed at a hectometric scale but not at centimeter scale and conversely. From the ground, Pancam is able to distinguish rocks and soils with relatively high variability, whereas CRISM observes extended areas for which the variability of rocks and soils may appear relatively reduced. Despite these differences, the choice is made here to consider the Pancam in situ photometric results as the ground truth, taken as a reference.

5.4. Interpretation of the Retrieved Photometric Parameters From Orbit

[101] Consistent trends were found with regard to the in situ photometric results. At the hectometer-scale, the surface behaves like the Soil unit defined by *Johnson et al*. [2006a]. The signal acquired by CRISM mixes several contributions coming from distinct surface materials occurring at the subpixel level. This mixing can be (i) linear or (ii) nonlinear. In the case of linear mixing (geographic mixing), the measured signal is a linear sum of all the radiated energy curves of materials making up the pixel. Consequently, the consistency of our results with the Soil unit behavior can be due to their dominant relative abundance within the CRISM pixel. In the case of nonlinear mixing, the signal measured is the result of a nonlinearly weighted combination of signals coming from different units. In both cases, the apparent consistency with the Soil unit could be coincidental.

[102] Previous orbital observations acquired at the MER landing sites gave several clues concerning its physical and chemical properties. This information can be used to validate the present photometric results to provide a better understanding of the geological meaning of the estimated photometric properties. First, we compare our results to the albedo estimates by the TES instrument. Spirit landed in a relatively dark streak feature which is composed of hundreds of dark-toned, small sub-parallel streaks created by dust devils, roughly oriented NW-SE. This feature is characterized by low albedo values (between 0.16 and 0.22) [*Martinez-Alonso et al*., 2005]. Pancam in situ analysis [*Bell et al*., 2004; *Farrand et al*., 2006] and coupled OMEGA measurements and Spirit data [*Lichtenberg et al*., 2007] show that the Spirit landing site is mainly composed of soil deposits sprinkled with small rocks interspersed with nanophase ferric-oxide-rich dust. These results are consistent with the intermediate single scattering albedo estimates modeled from CRISM observations ($\omega \sim 0.68$). Meridiani Planum is characterized by a low albedo estimated at 0.09–0.19 [*Mellon et al*., 2000]. Dust-free dark sand surface is mainly observed on the Meridiani Planum landing site. However, the intermediate single scattering albedo value modeled from CRISM dataset is more consistent with bright plains which exposed a smaller areal abundance of hematite, brighter fine-grained dust rich in nanophase iron oxides (such as in Gusev Crater plains) and a larger areal of bright outcrops are observed several kilometers to the south of the Opportunity landing site from orbital measurements [*Arvidson et al*., 2006].

[103] Second, we compare our results to the thermal inertia (TI) estimated by Thermal Emission Imaging System (THEMIS) images. This is a measure of the resistivity of surface materials to a change in temperature which is function of the particle size, bulk density, and cohesion. The intermediate THEMIS-derived TI at Gusev landing site (186–347 SI, 3×6 km resolution; *Martinez-Alonso et al*., 2005) suggests that the surface is dominated by unconsolidated materials (cohesionless surface) which is consistent with the photometric estimates. This shows that the surface dominantly behaves like the Soil unit, particularly those observed at the landing site which exhibit more small clasts in soil. At Meridiani landing site, lower THEMIS-derived TI is found (i.e., 175 SI, 3×6 km resolution; *Jakosky et al*., 2006) suggests that the surface is dominated by more fine-grained materials. Those pieces of information are consistent with the CRISM-derived photometric estimates showing that the area has similar properties as the Soil unit.

[104] Even if consistent trends were found, one difference is observed with regard to the in situ photometric results.

The difference concerns the macroscopic roughness $\bar{\theta}$. At Gusev Crater, the intermediate values of $\bar{\theta}$ conjugated to the presence of more small clasts on soil [*Ward et al*., 2005; *Johnson et al*., 2006a] suggest that the parameter $\bar{\theta}$ is mainly sensitive to micro-structure. In contrast, slightly rougher soil was modeled from CRISM data at Meridiani Planum. This outcome can be explained by (i) the presence of rocks but very few rocks are observed [*Golombek et al*., 2005], (ii) the presence of less than 1 cm hematite-rich concretions [*Calvin et al*., 2008] and/or (iii) the presence of morphological structures such as centimeter-high ripples [*Golombek et al*., 2010]. The second and third explanations could be responsible for the roughness measured at hectometer scale, suggesting that the parameter $\bar{\theta}$ is sensitive to both the specific local micro- and macrostructure. At the Gusev plain, it seems that the surface roughness is dominated by small clasts in soils, whereas, at Meridiani Planum it is dominated by the soil particles (concretions) and ripples.

6. Conclusions

[105] CRISM observations acquired over the MER Spirit and MER Opportunity landing sites allow us to validate the accuracy of (i) the Martian surface bidirectional reflectance estimated by the procedure named MARS-ReCO developed by *Ceamanos et al.* [2013] and (ii) the determined Martian photometric parameters, by comparing our results to the in situ photometric results modeled from data taken by the Pancam instrument on-board both rovers. Indeed, Hapke's parameters (ω, $\bar{\theta}$, *b*, and *c*) estimated from CRISM measurements (using a combination of CRISM multi-angle images after individually applying to each FRT observation the MARS-ReCO atmospheric correction procedure) are mainly consistent with parameters modeled from in situ measurements taken at the Spirit and Opportunity landing sites. The innovative assumption of a non-Lambertian surface is used in our methodology to accurately estimate intrinsic surface photometric properties from space. Our results appear to improve (i) those achieved in HRSC-based photometric studies, in which no aerosol correction was used and (ii) those estimated from surface bidirectional reflectance derived from atmospheric correction assuming a Lambertian surface, as they compare better with the in situ Pancam results. This outcome of our study shows that MARS-ReCO gives access to consistent surface bidirectional reflectance. As a consequence, surface photometric parameters can be reliably estimated from CRISM observations, provided that the atmospheric conditions are not turbid. As presented previously, the AOT values derived from Wolff et al.'s work [*Wolff et al.* 2009] are estimated with assumptions concerning the surface properties, imposed to be similar as MER observations at both landing sites. Further developments could lead to the joint estimation of AOT and surface bidirectional reflectance by considering the full spectral dimension.

[106] This presented approach may suffer from intrinsic limitations due to the scarcity of CRISM measurements with broad bidirectional reflectance sampling. However the combination of several CRISM observations alleviates this problem by improving the phase angle range thus better constraining the determination of photometric parameters. Furthermore, since September 2010, the inbound segment in targeted observations is absent due to problems of the gimbal instrument [*Murchie*, 2012]. Only six angular configurations are still available after this date. Consequently, more targeted observations must be combined in order to compensate this limitation.

[107] The presented methodology opens the possibility to map the surface bidirectional reflectance thus the spatial variations of the photometric parameters. The determination of the physical state of the surface materials (i.e., mean grain size, grain sphericity and grain heterogeneity, mean surface porosity, and surface brightness) through the study of their photometric properties (phase function of the particle, single scattering albedo, surface roughness, and opposition effects) provides complementary information to composition. It has implications for the characterization of different types of terrain over Mars (i.e., extrusive and intrusive volcanic terrains, sedimentary terrains, and impact craters) and for identification of surface temporal modifications (i.e., aeolian process and space weathering process). Moreover, the present work has implications for spectroscopic interpretation as it gives information about the particle (i.e., size) and grain organization which have significant influence on spectral properties [*Poulet and Erard*, 2004].

[108] In future work, both challenges of map creation and improvements for non-flat terrains shall be taken into account, with a particular emphasis on the complex handling of local slope effects which is not straightforward in the case of multiple reflection between surface facets. Note that MARS-ReCO may be used for mapping the photometric properties of the Martian surface even when using a single CRISM targeted observation. In this case, however, the photometric inversion should be focused to retrieve only single scattering albedo for the best surface bidirectional reflectance sampling. Furthermore, use of a single-lobed Henyey-Greenstein function would reduce the number of unknown photometric parameters and therefore could allow us to constrain the asymmetry parameter besides the single scattering albedo. Likewise, laboratory studies bearing on the photometric behavior of natural surfaces under controlled conditions and under a large range of observational geometries [*Souchon et al*., 2011] are necessary to better document and interpret the variations of the photometric parameters in relation with surface geological processes such as aeolian, aqueous, and impact processes.

Appendix A: Nonuniform PDF

[109] Central moments μ_n (such as the variance μ_2 of order two) are commonly used for statistical purpose while cumulants k_n have the advantage to present unbiased statistical estimator for all orders [*Fisher*, 1930]. Also, the first three cumulants are equivalent to the central moments. For arandom variable following the PDF *f(x)* in (0,1), the cumulant-generating function is

$$\Phi(t) = \ln TF\{f(x)\} = \ln \int_0^1 e^{itx} f(x) dx. \qquad \text{(A1)}$$

Cumulants of order *n* are defined by

$$k_n = \frac{\partial^n \Phi(t)}{\partial i t^n} + o(t). \quad \text{(A2)}$$

The first four cumulants of a uniform PDF are

$$k_1 = \frac{1}{2} = \mu_1, \quad \text{(A3)}$$

$$k_2 = \frac{1}{12} = \mu_2, \quad \text{(A4)}$$

$$k_3 = 0 = \mu_3, \quad \text{(A5)}$$

$$k_4 = -\frac{1}{120} = \mu_4 - 3(\mu_2)^2. \quad \text{(A6)}$$

Thus, we propose to estimate the nonuniformity of the results of the inversion with

$$k = max\left|\frac{k_1 - 12}{12}, \frac{k_2 - 112}{112}, \frac{k_3}{160}, \frac{k_4 + 1120}{1120}\right| \quad \text{(A7)}$$

We perform 10,000 uniform random vectors of 500 samples (identical to the inversion procedure). Since the maximum is $k = 0.47$ for the most extreme event, we propose to have nonuniform PDF for $k > 0.5$. For the inversion purpose, since the a priori PDFs on the parameters are uniform if the results of the inversion on one parameter has $k < 0.5$, we conclude that this parameters is not constrained by the observations.

[110] **Acknowledgments.** This work was supported by the French Space Agency CNES (Centre National d'Etudes Spatiales) and PNP (Programme National de Planétologie) from INSU (Institut National des Sciences de l'Univers). The authors would like to thank Michael Wolff for making his aerosol optical thickness values available for this study. We would like to gratefully thank Jeffrey Johnson, Mathieu Vincendon, and the anonymous reviewer for their constructive comments that substantially improved this article.

References

Arvidson, R. E., et al. (2006), Nature and origin of the hematite-bearing plains of terra meridiani based on analyses of orbital and mars exploration rover data sets, *J. Geophys. Res.*, *111*, E12S08, doi:10.1029/2006JE002728.

Bell, J. F., M. J. Wolff, T. C. Daley, P. B. Crisp, S. W. Lee, J. T. Trauger, and R. W. Evans (1999), Near-infrared imaging of Mars from HST: Surface reflectance, photometric properties, and implications for MOLA data, *Icarus*, *138*, 25–35, doi:10.1006/icar.1998.6057.

Bell, J. F., et al. (2004), Pancam multispectral imaging results from the Spirit rover at Gusev Crater, *Science*, *305*(5685), 800–806, doi:10.1126/science.1100175, 2004.

Brown, A. J., and M. J. Wolff (2009), Atmospheric modeling of the Martian polar regions: One Mars year of CRISM EPF observations of the South Pole, *Lunar Planet. Sci.*, abstract 1675.

Calvin, W. M., et al. (2008), Hematite spherules at Meridiani: Results from MI, Mini-TES and Pancam, *J. Geophys. Res.*, *113*, E12S37, doi:10.1029/2007JE003048.

Ceamanos, X., S. Douté, J. Fernando, F. Schmidt, P. Pinet, and A. Lyapustin (2013), Surface reflectance of mars observed by CRISM/MRO: 1. Multi-angle approach for retrieval of surface reflectance from CRISM observations (MARS-ReCO), submitted in *J. Geophys. Res.*, doi:10.1029/2012JE004195, in press.

Chandrasekhar, S. (1960), *Radiative Transfer*, Dover Publications, New York.

Cheng, A., and D. L. Domingue (2000), Radiative transfer models for light scattering from planetary surfaces., *J. Geophys. Res.*, *105*(E4), 9477–9482, doi:10.1029/1999JE001170.

Clancy, R. T., and S. W. Lee (1991), A new look at dust and clouds in the Mars atmosphere: Analysis of Emission-Phase-Function sequences from global Viking IRTM observations, *Icarus*, *93*, 135–158, doi:10.1016/0019-1035(91)90169-T.

Clancy, R. T., M. J. Wolff, and P. R. Christensen (2003), Mars aerosol studies with the MGS TES emission phase function observations: Optical depths, particle sizes, and ice cloud types versus latitude and solar longitude, *J. Geophys. Res.*, *E9 5098*, doi:10.1029/2003JE002058.

Cord, A. M., P. C. Pinet, Y. Daydou, and S. D. Chevrel (2003), Planetary regolith surface analogs: Optimized determination of Hapke parameters using multi-angular spectro-imaging laboratory data, *Icarus*, *165*, 414–427, doi:10.1016/S0019-1035(03)00204-5.

de Grenier, M., and P. C. Pinet (1995), Near-opposition Martian limb-darkening: Quantification and implication for visible-near-infrared bidirectional reflectance studies, *Icarus*, *115*, 354–368, doi:10.1006/icar.1995.1103.

Douté, S., and B. Schmitt (1998), A multilayer bidirectional reflectance model for the analysis of planetary surface hyperspectral images at visible and near-infrared wavelengths, *J. Geophys. Res.*, *103*, 31,367–31,389, doi:10.1029/98JE01894.

Douté, S. (2009), Retrieving Mars surface reflectance from OMEGA/MEx imagery, in IEEE Workshop on Hyperspectral Image and Signal Processing: Evolution in Remote Sensing.

Farrand, W. H., J. F. Bell III, J. R. Johnson, S. W. Squyres, J. Soderblom, and D. Ming (2006), Spectral variability among rocks in visible and near-infrared multispectral Pancam data collected at Gusev Crater: Examinations using spectral mixture analysis and related techniques, *J. Geophys. Res.*, *111*, E02S15, doi:10.1029/2005JE002495.

Fisher, R. A. (1930), The Genetical Theory Of Natural Selection, Clarendon Press, Oxford.

Golombek, M. P., et al. (2005), Assessment of Mars Exploration Rover landing site predictions, *Nature*, *436*, 44–48, doi:10.1038/nature03600.

Golombek, M., K. Robinson, A. McEwen, B. Bridges, N. Ivanov, L. Tornabene, and R. Sullivan (2010), Constraints on ripple migration at Meridiani Planum from Opportunity and HiRISE observations of fresh craters, *J. Geosphys. Res.*, *115*, E00F08, doi:10.1029/2010JE003628.

Grynko, Y., and Y. Shkuratov (2007), Ray tracing simulation of light scattering by spherical clusters consisting of particles with different shapes, *J. Quant. Spectrosc. Radiat. Trans.*, *106*, 56–62, doi:10.1016/j.jqsrt.2007.01.005.

Guinness, E. A., R. E. Arvidson, I. H. D. Clark, and M. K. Shepard (1997), Optical scattering properties of terrestrial varnished basalts compared with rocks and soils at the Viking Lander sites, *J. Geophys. Res.*, *102*, 28,687–28,703, doi:10.1029/97JE03018.

Hapke, B. (1981), Bidirectional reflectance spectroscopy: 1. Theory, *J. Geophys. Res.*, *86*, 3039–3054, doi:10.1029/JB086iB04p03039.

Hapke, B., and E. Wells (1981), Bidirectional reflectance spectroscopy: 2. Experiments and observations, *J. Geophys. Res.*, *86*, 3055–3060.

Hapke, B. (1984), Bidirectional reflectance spectroscopy: 3. Correction for macroscopic roughness, *Icarus*, *59*, 41–59, doi:10.1016/0019-1035(84)90054-X.

Hapke, B. (1986), Bidirectional reflectance spectroscopy: 4. The extinction coefficient and the opposition effect, *Icarus*, *67*, 264–280, doi:10.1016/0019-1035(86)90108-9.

Hapke, B. (1993), Theory of Reflectance and Emittance Spectroscopy, Cambridge University Press, New York.

Hapke, B. (2002), Bidirectional reflectance spectroscopy: 5. The coherent backscatter opposition effect and anisotropic scattering, *Icarus*, *157*, 523–534, doi:10.1006/icar.2002.6853.

Hapke, B. (2008), Bidirectional reflectance spectroscopy: 6. Effects of porosity, *Icarus*, *195*, 918–926, doi:10.1016/j.icarus.2008.01.003.

Hartman, B., and D. Domingue (1998), Scattering of light by individual particles and the implications for models of planetary surfaces, *Icarus*, *131*, 421–448, doi:10.1016/j.jqsrt.2011.04.006.

Helfenstein, P. (1988), The geological interpretation of photometric surface roughness, *Icarus*, *73*, 462–481, doi:10.1016/0019-1035(88)90056-5.

Helfenstein, P., U. A. Bonne, S. Stolovy, and J. Veverka (1991), Laboratory photometric measurements of particulate soils out to very large phase angles, in *Reports of Planetary Geology and Geophysics Program - 1990*, NASA-TM-4300, pp. 280–282.

Jakosky, B. M., et al. (2006), Thermophysical properties of the MER and Beagle II landing site regions on Mars, *J. Geophys. Res.*, *111*, E08,008, doi:10.1029/2004JE002320.

Jehl, A., et al. (2008), Gusev photometric variability as seen from orbit by HRSC/Mars-express, *Icarus*, *197*, 403–428, doi:10.1016/j.icarus.2008.05.022.

Johnson, J. R., et al. (1999), Preliminary results on photometric properties of materials at the Sagan Memorial Station, Mars, *J. Geophys. Res.*, *104*, 8809–8830, doi:doi:10.1029/98JE02247.

Johnson, J. R., et al. (2006a), Spectrophotometric properties of materials observed by Pancam on the Mars Exploration Rovers: 1. Spirit, *J. Geophys. Res.*, *111*, E02S14, doi:10.1029/2005JE002494.

Johnson, J. R., et al. (2006b), Spectrophotometric properties of materials observed by Pancam on the Mars Exploration Rovers: 2. Opportunity, *J. Geophys. Res.*, *111*, E12S16, doi:10.1029/2006JE002762.

Johnson, J. R., J. F. Bell, P. Geissler, W. M. Grundy, E. A. Guinness, P. C. Pinet, and J. Soderblom (2008), *The Martian Surface*, chap. Physical properties of the Martian surface from spectrophotometric observations, pp. 428–450, Cambridge University Press.

Kamei, A., and A. M. Nakamura (2002), Laboratory study of the bidirectional reflectance of powdered surfaces: On the asymmetry parameter of asteroid photometric data, *Icarus*, *156*, 551–561, doi:10.1006/icar.2002.6818.

Lichtenberg, K. A., et al. (2007), Coordinated analyses of orbital and Spirit Rover data to characterize surface materials on the cratered plains of Gusev Crater, Mars, *J. Geophys. Res.*, *112*, E12S90, doi:10.1029/2006JE002850.

Lucht, W., C. B. Schaaf, and A. H. Strahler (2000), An algorithm for the retrieval of albedo from space using semiempirical BRDF models, *IEEE Transact. Geosci. Remote Sens.*, *38*(2), 977–998.

Lyapustin, A., et al. (2010), Analysis of snow bidirectional reflectance from ARCTAS Spring-2008 Campaign, *Atmospheric Chem. Phys.*, *10*, 4359–4375, doi:10.5194/acp-10-4359-2010.

Martinez-Alonso, S., B. M. Jakosky, M. T. Mellon, and N. E. Putzig (2005), A volcanic interpretation of Gusev Crater surface materials from thermophysical, spectral, and morphological evidence, *J. Geophys. Res.*, *110*, E01,003, doi:10.1029/2004JE002327.

McCord, T. B., et al. (2007), The Mars Express High Resolution Stereo Camera spectrophotometric data: Characteristics and science analysis. *J. Geophys. Res.*, *112*, E06,004, doi:10.1029/2006JE002769. E06004.

McGuire, A., and B. Hapke (1995), An experimental study of light scattering by large irregular particles, *Icarus*, *113*, 134–155.

McGuire, P. C., et al. (2008), MRO/CRISM retrieval of surface Lambert albedos for multispectral mapping of Mars with DISORT-based radiative transfer modeling: Phase 1 - Using historical climatology for temperatures, aerosol optical depths, and atmospheric pressures, *IEEE Transac. Geosci. Remote Sens.*, *46*(12), 4020–4040.

Mellon, M. T., B. M. Jakosky, H. H. Kieffer, and P. R. Christensen (2000), High-resolution thermal inertia mapping from the mars global surveyor thermal emission spectrometer, *Icarus*, *148*, 437–455, doi:10.1006/icar.2000.6503.

Mishchenko, M., J. M. Dlugach, E. G. Yanovitskij, and N. T. Zakharova (1999), Bidirectional reflectance of flat, optically thick particulate layers: An efficient radiative transfer solution and applications to snow and soil surfaces., *J. Quant. Spectrosc. Radiat. Trans.*, *63*, 409–432, doi:10.1016/S0022-4073(99)00028-X.

Mosegaard, K., and A. Tarantola (1995), Monte Carlo sampling of solutions to inverse problems, *J. Geophys. Res.*, *100*, 12,431–12,447.

Murchie, S., et al. (2007), Compact Reconnaissance Imaging Spectrometer for Mars (CRISM) on Mars Reconnaissance Orbiter (MRO), *J. Geophys. Res.*, *112*, E05S03, doi:10.1029/2006JE002682.

Murchie, S. (2012), CRISM on MRO - instrument and investigation overview, in MRO/CRISM Data Users' Workshop, The Woodlands, TX.

Pinet, P., and C. Rosemberg (2001), Regional photometry and spectral albedo of the eastern hemisphere of Mars in the 0.7-1 micron domain, *Lunar Planet. Sci.*, abstract 1640.

Pinet, P. C., et al. (2005), Derivation of Mars surface scattering properties from OMEGA spot pointing, *Lunar Planet. Sci.*, *XXXVI*, abstract 1694.

Poulet, F., and S. Erard (2004), Nonlinear spectral mixing: Quantitative analysis of laboratory mineral mixtures, *J. Geophys. Res.*, *109*, E02,009, doi:10.1029/2003JE002179.

Seelos, F. P., S. Murchie, D. Humm, O. S. Barnouin, F. Morgan, H. W. Taylor, C. Hash, and T. C. Team (2011), CRISM data processing and analysis products update - calibration, correction, and visualization, *Lunar Planet. Sci.*, *XXXXII*, abstract 1438.

Shaw, A., R. E. Arvidson, M. J. Wolff, F. P. Seelos, S. M. Wiseman, and S. Cull (2012), Determining surface roughness and additional terrain properties: Unsig opportunity mars rover results to interpret orbital data for extended mapping, *Lunar Planet. Sci.*, *XXXXIII*, abstract 1644.

Shepard, M. K., and P. Helfenstein (2007), A test of the Hapke photometric model, *J. Geophys. Res.*, *112*, E03,001, doi:10.1029/2005JE002625.

Shepard, M. K., and P. Helfenstein (2011), A laboratory study of the bidirectional reflectance from particulate samples, *Icarus*, *215*, 526–533, doi:10.1016/j.icarus.2011.07.033.

Shkuratov, Y., and L. Starukhina (1999), A model of spectral albedo of particulate surfaces: Implications for optical properties of the Moon, *Icarus*, *137*, 235–246, doi:10.1006/icar.1998.6035.

Shkuratov, Y., S. Bondarenko, V. Kaydash, G. Videen, O. Munoz, and H. Volten (2007), Photometry and polarimetry of particulate surfaces and aerosol particles over a wide range of phase angles, *J. Quant. Spectrosc. Radiat. Trans.*, *106*, 487–508, doi:10.1016/j.jqsrt.2007.01.031.

Soderblom, J. M., J. F. Bell, R. E. Arvidson, J. R. Johnson, M. J. Johnson, and F. P. Seelos (2004), Mars Exploration Rover Pancam photometric data QUBs: Definition and example uses, *AGU*, *85*(47) Fall Meet, Suppl., Abstract P21A-0198.

Souchon, A. L., P. Pinet, S. Chevrel, Y. Daydou, D. Baratoux, K. Kurita, M. K. Shepard, and P. Helfenstein (2011), An experimental study of Hapke's modeling of natural granular surface samples, *Icarus*, *215*, 313–331, doi:10.1016/j.icarus.2011.06.023.

Souchon, A. (2012), Influence des phases amorphes dans la réponse optique des régolites planétaires : Caractérisation des propriétés physiques et application a l'étude géologique de la lune, Ph.D. thesis, Univ. de Toulouse, France.

Tarantola, A., and B. Valette (1982), Inverse problems = quest for information, *J. Geophys. Res.*, *50*, 159–170.

Vincendon, M., Y. Langevin, F. Poulet, J.-P. Bibring, and B. Gondet (2007), Recovery of surface reflectance spectra and evaluation of the optical depth of aerosols in the near-IR using a Monte Carlo approach: Application to the OMEGA observations of high-latitude regions of Mars, *J. Geophys. Res.*, *112*, E08S13, doi:10.1029/2006JE002845.

Ward, J. G., R. E. Arvidson, and M. Golombek (2005), The size-frequency and areal distribution of rock clasts at the Spirit landing site, Gusev Crater, Mars, *Geophys. Res. Lett.*, *32*, L11,203, doi:10.1029/2005GL022705.

Wiseman, S. M., R. E. Arvidson, M. J. Wolff, R. V. Morris, F. P. Seelos, M. D. Smith, D. Humm, S. L. Murchie, and J. F. Mustard (2012), Retrieval of atmospherically corrected CRISM spectra using radiative transfer modeling, *Lunar Planet. Sci.*, *XXXXIII*, abstract 2146.

Wolff, M. J., et al. (2006), Constraints on dust aerosols from the Mars Exploration Rovers using MGS overflights and Mini-TES, *J. Geophys. Res.*, *111*, E12S17, doi:10.1029/2006JE002786.

Wolff, M. J., et al. (2009), Wavelength dependence of dust aerosol single scaterring albedo as observed by the Compact Reconnaissance Imaging Spectrometer, *J. Geophys. Res.*, *114*, E00D64, doi:10.1029/2009JE003350.

Wolff, M. J., R. T. Clancy, J. D. Goguen, M. C. Malin, and B. A. Cantor (2010), Ultraviolet dust aerosol properties as observed by MARCI, *Icarus*, *208*, 143–155, doi:10.1016/j.icarus.2010.01.010.

Chapitre 3

Spectroscopie haute résolution



Représentation populaire des astronomes au Moyen-Age

Les identifications de matériaux en Planétologie et en Astronomie se font généralement par des méthodes spectroscopiques. La comparaison entre les positions et largeurs des bandes d'absorptions observées et mesurées en laboratoire permet de déterminer les matériaux en présence. Dans ce contexte, la spectroscopie à haute résolution spectrale (de l'ordre de 0.001 microns à 5 microns) est ~10 fois meilleure, en comparaison avec les techniques d'imageries hyperspectrales décrites précédemment (de résolution de 0.01 microns à 5 microns). Néanmoins, les instruments de spectroscopie à haute résolution ne permettent pas de réaliser une cartographie très précise car ils observent un point unique, défilant avec le trajet du satellite. Bien que la majorité des minéraux ne comportent pas de bande d'absorption nécessitant la haute résolution, l'étude précise des volatils, requiert la haute résolution.

Le premier sous-chapitre décrit le contexte actuel des observations de spectroscopie à haute résolution, au travers de la détection de méthane sur Mars et de l'instrument PFS (embarqué à bord de Mars Express). Mes contributions, développées notamment lors du séjour d'Irina Shatalina (doctorante de Bortolino Saggin de l'équipe PFS) à IDES, seront détaillées au sous-chapitre 3.2 page 138. Les perspectives de ces travaux sont décrites à la section 3.3.

3.1 Contexte

3.1.1 Le méthane sur Mars

La détection de méthane dans l'atmosphère de Mars a été suggérée par des études télescopiques [170, 171]. Cependant les attributions des bandes d'absorption au méthane martien peuvent être confondues avec la contribution terrestre. Le méthane a été détecté par le spectromètre Planetary Fourier Spectrometer (PFS) de la sonde Mars Express [93] et par les réanalyses de l'instrument Thermal Emission Spectrometer (TES) à bord de Mars Gobal Surveyor [89]. Une autre équipe d'astronome [234] a suggéré la présence de méthane mais des réanalyses de ces données ont montré que la contribution majeure de CH_4 était terrestre [343].

Ces détections de méthane suggèrent qu'il est présent à quelques dizaines de ppb (partie par milliard) et extrêmement fluctuant en fonction de la saison, de la longitude et de la latitude [100]. Ces détections ont suscité un très grand intérêt dans la communauté des planétologues et des exobiologistes. Cependant, il n'y a toujours pas actuellement de consensus sur la réalité du méthane martien, détecté néanmoins, à des niveaux comparables par trois instruments différents. Plusieurs raisons sont évoqués : (i) parce que la variabilité spatio-temporelle observé du méthane exige une durée de vie courte (~1 an), contredisant les modèles photochimiques (~300 ans) [185], (ii) parce que les concentrations sont très faibles à la limite de la résolution, (iii) parce que l'instrument in situ le plus précis, Tunable Laser Spectrometer (TLS) du rover Curosity, a montré une absence de méthane avec une limite de détection très faible (<1.3 ppb) [337]. Néanmoins, le caractère très oxydant du sol suggère une oxydation hétérogène du méthane dans le régolite [40] qui pourrait expliquer l'absence de méthane au sol et un profil en croissance verticale d'après PFS [Formisano et al., non publié].

Plusieurs scénarii de formation du méthane ont été proposés : par photochimie à partir d'eau et de CO_2 [13], par serpentinisation [8, 42], serpentinisation dans des systèmes hydrothermaux actuels ou passés [39], par la formation de clathrate en surface [43], voir métastable dans l'atmosphère [38], ou encore éventuellement dû à la présence de bactéries méthanogènes [9, 8]. Une synthèse des travaux concernant les implications géologiques de la présence méthane sur Mars a été proposé [169].

Dans ce contexte, les données de PFS sont les seules données de spectroscopie à haute résolution prises en orbite autour de Mars qui permettent d'établir une réponse claire concernant la présence de méthane et aussi de déterminer ses éventuelles variabilités spatiale et temporelle.

3.1.2 Etude de la surface avec PFS

Au delà du méthane, les données de l'instrument PFS sont les seules disponibles à haute résolution spectrale et permettent des études spectroscopiques de la surface et en particulier des glaces. La première étude spectroscopique des glaces par PFS concerne la calotte permanente sud de Mars [112]. D'après

cette étude, la calotte est composée de CO_2 pur. Les contours de la calotte comportent des impuretés d'eau. Des unités de terrains brillants, détaché de la calotte correspondent à de la glace d'eau pure. Le suivi de la calotte saisonnière sud de CO_2 a été fait grâce à l'émission thermique [103]. Aussi, une étude spectroscopique de la calotte saisonnière nord, dans le domaine proche infra-rouge [104], a permis de montrer la présence d'une couronne d'eau autour de la calotte de CO_2. Cependant, à cause des artefacts et de la relative basse résolution spatiale (>50 km), dus au traitement par stacking (voir section suivante), ce type d'analyse de spectroscopie fine est limité.

3.1.3 Microvibrations de PFS

Bien que les données de PFS soient intéressantes pour l'étude des composés atmosphériques mineurs comme le méthane ou des glaces en surfaces, leur utilisation est limitée par un niveau de bruit trop important. En effet, l'instrument a été construit pour un niveau de vibrations mécaniques nettement inférieur au bruit de la plateforme Mars Express. Certains de ces bruits sont structurés, avec des fréquences précises, comme par exemple :

- les modes propres de l'instrument PFS lui-même
- les modes propres des instruments voisins
- les générateurs de bruits structurés comme les cryocoolers
- les roues de réaction (Reaction Wheels), qui permettent d'orienter la plateforme Mars Express par effet d'inertie
- les unités de mesures inertiels (Inertia Measurement Unit), dont les détecteurs sont générateurs de bruit.

De ce fait, les mesures se trouvent polluées par des artefacts, identifiés dès la phase de croisière jusqu'à Mars [102, 101]. L'instrument PFS est un spectromètre à transformée de Fourier. En effet, il enregistre les interférences du signal avec lui-même en fonction d'un décalage entre les deux signaux [94]. Sur l'instrument PFS, le décalage est créé grâce à la rotation d'un miroir à coin cubique (voir figure 3.1). Le spectre lumineux est estimé par transformée de Fourier numérique de l'interférogramme. Pour limiter les effets des vibrations et avoir un maximum de précision, le pas du dessalage est donné par un signal laser artificiel, parcourant le même trajet optique que les signaux Martiens, dont la longueur d'onde est connue. En cas de vibrations, le décalage oscille autour de la valeur du pas laser, induisant des artefacts dans le spectre appelés fantômes ou "ghost" (voir figure 3.2). Précisons aussi que l'instrument PFS a deux canaux de sensibilité spectrale différente : Long Wavelength Channel (LWC) entre 200 et 2000 cm^{-1} (5 et 50 microns), de résolution spatiale maximum de 7 km et Short Wavelength Channel (SWC) entre 2000 et 8200 cm^{-1} (1.2 et 5 microns), de résolution spatiale maximum 12 km, avec un pas de 1.03 cm^{-1} (1.4 cm^{-1} de résolution avec apodisation).

Pour résoudre ce problème, deux stratégies ont été mises en place par l'équipe PFS :

- lors de l'acquisition, la vitesse de rotation du miroir cubique, c'est à dire la vitesse d'acquisition de l'interferogramme, a été adaptée pour minimiser les artefacts. Des tests lors de la période de navigation vers Mars ont montré que la vitesse d'acquisition de 2500 Hz (fréquence de passage des pas du laser) optimise les artefacts sur la voie SWC et LWC (voir figure 3.3).
- un effort intense de modélisations analytique [57, 276] et numérique [58] des effets des vibrations a été réalisé dans le but de comprendre en détail la formation des artefacts. Ces résultats montrent que pour une fréquence de vibration fixe, la phase, c'est à dire le décalage spatial ou temporel entre l'interférogramme et la perturbation mécanique, est aléatoire. De ce fait, un moyennage ou "stacking" d'un grand nombre de spectres permet d'éliminer les artefacts de phases aléatoires (voir figure 3.4). Néanmoins, il n'est plus possible d'analyser des spectres individuels mais seulement un grand nombre de spectres, ce qui dégrade la résolution spatiale et temporelle de l'instrument. De plus, d'autres effets instrumentaux, résultant à des phases structurées, ne sont pas corrigés par le stacking [58].

Au vu des enjeux, j'ai mis au point un programme de recherche pour améliorer la calibration de l'instrument PFS. J'ai constitué un groupe de travail comportant des spécialistes du traitement du signal à SUPELEC (Nicolas Gac et Matthieu Kowalski) et l'équipe PFS (Marco Giuranna et Bortolino Saggin).

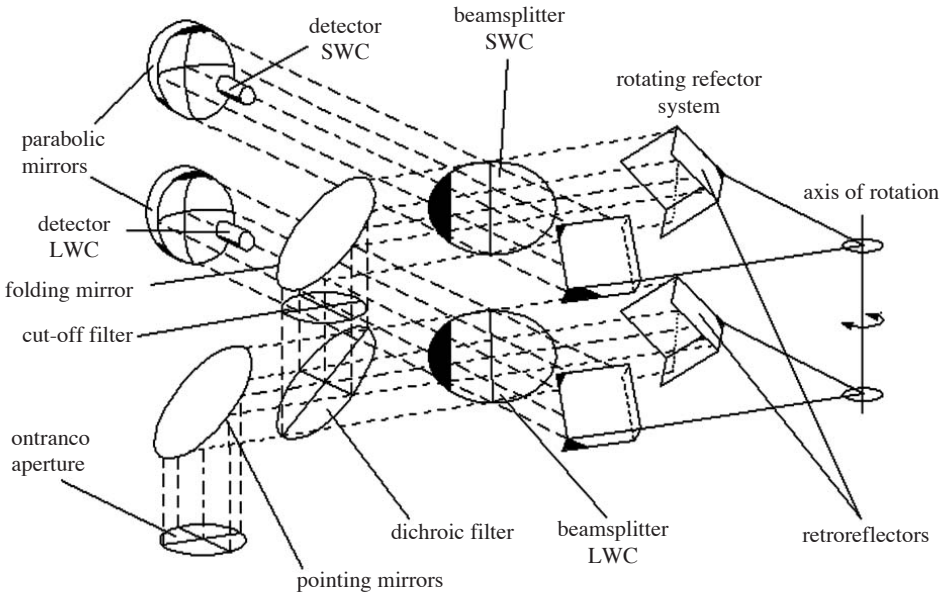


FIGURE 3.1: Schéma optique de l'instrument PFS d'après [94]

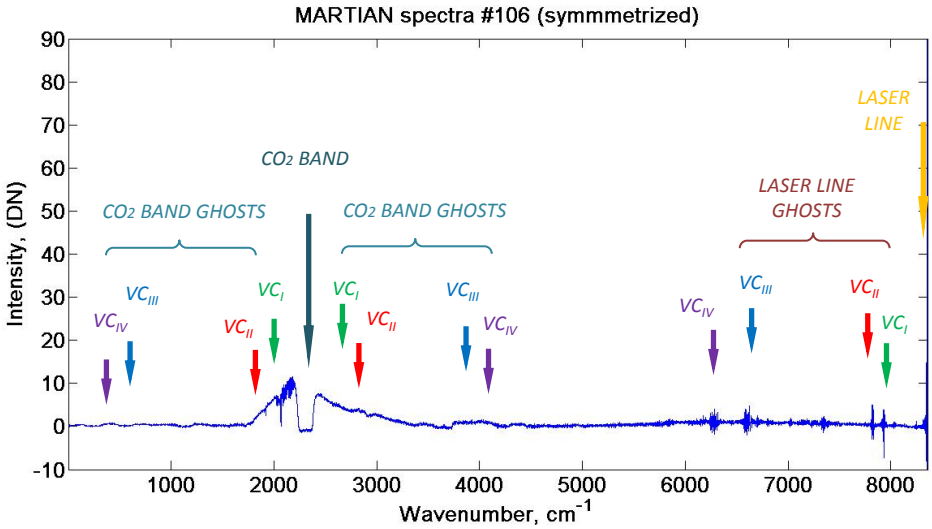


FIGURE 3.2: Exemple de fantôme (ghost) sur une observation PFS SWC en unité DN (non calibré en radiance) d'après [282]

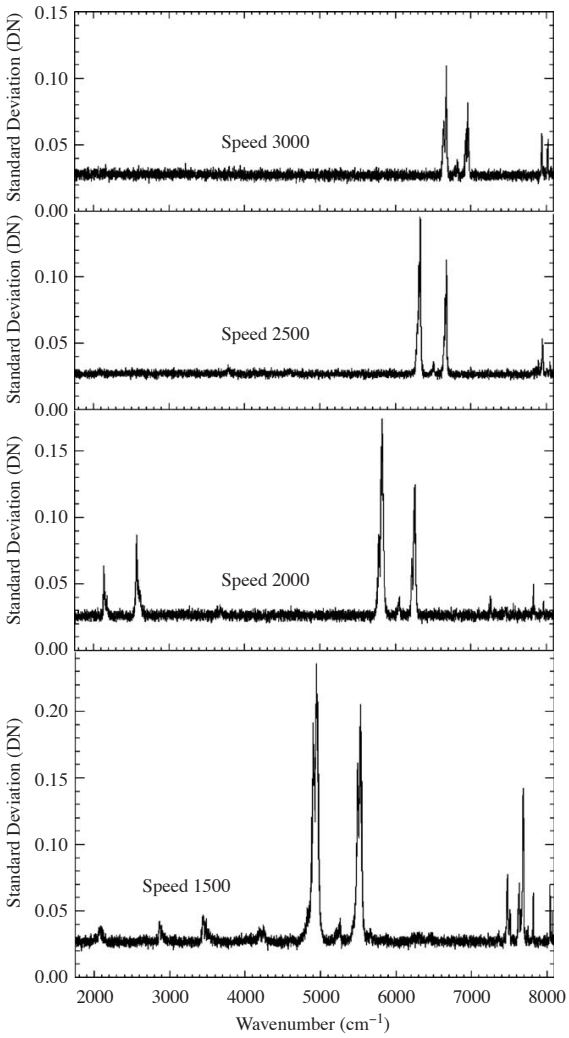


FIGURE 3.3: Effet de la vitesse d'acquisition de l'interferogramme sur les artefacts de PFS SWC, d'après [102]

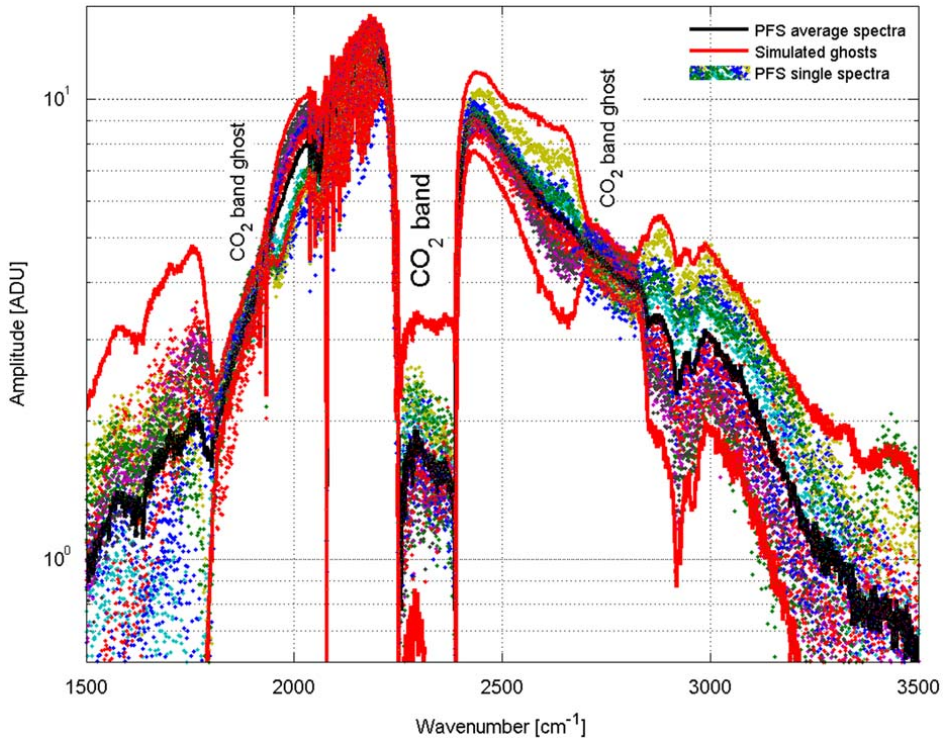


FIGURE 3.4: Comparaison entre simulation d'artefact (extrême en rouge) et les données réelles (points de couleurs), et la moyenne (en noir), d'après [58]

3.2 Contributions

Mon objectif principal est d'améliorer la calibration PFS, en estimant les effets de micro-vibrations directement sur chacun des spectres et en utilisant des méthodes de déconvolution en aveugle. Dans un premier temps, il s'agit d'établir un modèle analytique simplifié, puis, de réaliser une méthode de correction des spectres, ayant une implémentation rapide pour le traitement d'un grand jeux de données.

3.2.1 Modélisation analytique des vibrations

Des travaux de modélisations analytiques des effets des micro-vibrations ont été proposées pour plusieurs effets découplés [276] : oscillation autour du pas d'échantillonnage et oscillation du désalignement optique. D'autre part, ces auteurs proposent une modélisation des effets de non-linéarité du détecteur et de réflexions internes. Cependant, ces différents effets n'ont pas été traités analytiquement ensemble, pour plusieurs fréquences de vibrations mais de manière indépendante analytiquement. Les effets combinés ont été étudiés par modélisation numérique et validés sur des données réelles [58] (voir figure 3.4).

Nous avons réalisé une modélisation analytique de tous les effets de vibrations au premier ordre (l'article est disponible au chapitre 3.4.1) et l'expression est la suivante :

$$I_{PFS}(\sigma) = I_{Mars}(\sigma) + [\sigma . I_{Mars}(\sigma)] \star K(\sigma) \tag{3.1}$$

avec le nombre d'onde σ, le spectre de PFS en complexe $I_{PFS}(\sigma)$, le spectre de Mars en complexe $I_{Mars}(\sigma)$, le noyau de vibrations en complexe $K(\sigma)$ de forme suivante, somme de j fréquences de vibrations :

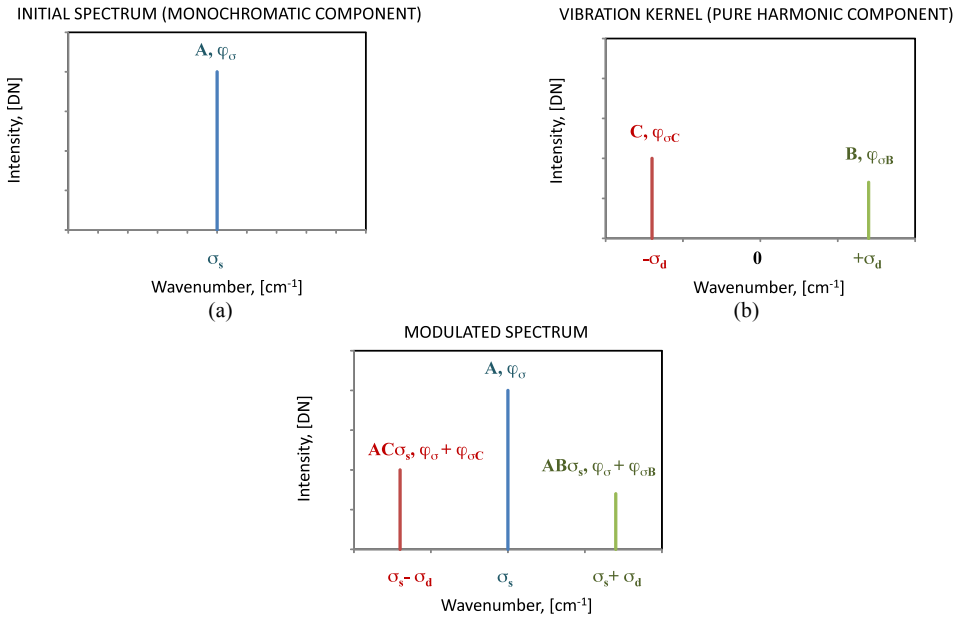


FIGURE 3.5: Schéma de l'effet d'une fréquence pure de vibration sur le spectre PFS, d'après[292].

$$K_{PFS}(\sigma) = \sum_j \{C_{1,j}\exp(i\varphi_{C_{1,j}}(\sigma))\delta(\sigma-\sigma_{d_j}) \tag{3.2}$$

$$+C_{2,j}\exp(i\varphi_{C_{2,j}}(\sigma))\delta(\sigma+\sigma_{d_j})\} \tag{3.3}$$

$$= \delta(\sigma)+A(\sigma)e^{i\varphi_A(\sigma)}+B(\sigma)e^{i\varphi_B(\sigma)} \tag{3.4}$$

avec la fonction dirac $\delta()$.

$\sigma_{d_j} = f_j/v_m$ avec f_j la fréquence de vibrations et v_m la vitesse moyenne d'acquisition de l'interferogramme. Les quantités A, B, C, φ_A, φ_B sont inconnus et ne peuvent pas être évaluées quantitativement à cause du manque d'information à propos de l'amplitude et de la phase des micro-vibrations. En pratique, les fonctions A, B, C, φ_A, φ_B sont parcimonieuses sur σ car les fréquences de vibrations sont peu nombreuses, et donc parcimonieuses. Les fonctions A, B, C, φ_A, φ_B ne sont pas symétriques autour de $\sigma = 0$ à cause de leur phase relative. La figure 3.5 illustre l'effet d'une fréquence de microvibration pure sur le spectre PFS.

Pour plus de détail, l'article est disponible au chapitre 3.4.1 page 143.

3.2.2 Traitement des données réelles de PFS

Le problème de déconvolution en aveugle est un problème jugé très difficile en traitement du signal, car il y a peu d'informations disponibles face aux inconnus. En réalité dans notre cas, les inconnus sont deux fois plus nombreuses que les données car le noyau inconnu $K(\sigma)$ et le spectre de Mars corrigé des vibrations inconnues $I_{Mars}(\sigma)$ ont la même dimension que les données $I_{PFS}(\sigma)$. Néanmoins, ce problème peut être résolu par des méthodes de minimisation, en introduisant des contraintes sous forme de termes de régularisation [138].

Notre stratégie est aveugle (ou semi-aveugle comme présentée ci-après), afin d'assurer une convergence dans toutes les situations d'observations réelles, de manière automatique et sans définir a priori un domaine valide de nombre d'onde. Malheureusement, un problème non-linéaire, comme celui de l'équation 3.1, ne permet pas de réaliser une inversion aveugle. Nous avons donc simplifié le problème en supposant pour le second terme, contenant les fantômes des vibrations, que le domaine de nombre d'onde de I_{Mars} , avec un signal significatif, est réduit à $\sigma_k \sim 2500$ cm^{-1} (il est en réalité majeure autour de $\sigma \sim 2000-3000$ cm^{-1}). Dans ce cas, l'équation 3.1 se simplifie en :

$$I_{PFS}(\sigma) = I_{Mars}(\sigma) \star [\delta(\sigma) + K(\sigma).\sigma_k] \ . \tag{3.5}$$

Puis, en redéfinissant le noyau $K_{PFS}(\sigma) = \delta(\sigma) + K(\sigma).\sigma_k$:

$$I_{PFS}(\sigma) = I_{Mars}(\sigma) \star K_{PFS}(\sigma) \tag{3.6}$$

Dans ce cas, le problème est bien celui d'une déconvolution. Il est rappelé que toutes les quantités sont complexes. L'approximation du domaine de nombre d'onde réduit est valide à cause de la sensibilité du détecteur et du signal martien typique (voir figure 3.2). Les écarts entre $\sigma_k \sim 2500$ cm^{-1} et le vrai signal $\sigma \sim 2000 - 3000$ cm^{-1} correspondent à un facteur d'erreur de x0.8 à x1.2, ce qui est raisonnable dans notre cas.

Nous avons proposé une méthode de déconvolution itérative, basée sur la minimisation d'une fonction coût $\mathscr{C}$, soit pour $\hat{I}_{Mars}$, soit pour $\hat{K}_{PFS}$:

$$\hat{I}_{Mars}, \hat{K}_{PFS} \quad = \quad \underset{I_{Mars}, K_{PFS}}{\operatorname{argmin}} \ \mathscr{C}(I_{Mars}, K_{PFS}) \tag{3.7}$$

Une fonction coût convexe assure l'existence d'une solution unique au problème de minimisation.

Les estimateurs de la solutions sont notés : $\hat{I}_{Mars}, \hat{K}_{PFS}$, et la fonction coût est la suivante :

$$\mathscr{C}(I_{Mars}, K_{PFS}) = \frac{1}{2}\|I_{PFS} - K_{PFS} \star I_{Mars}\|_2^2 + \lambda_K \|K_{PFS}\|_1 + \frac{\lambda_{Mars}}{2}\|D \star I_{Mars}\|_2^2 \tag{3.8}$$

Trois termes apparaissent dans cette fonction :

1. Le premier terme représente l'attache aux données, c'est à dire le modèle directe de l'équation 3.6. Ce terme est sensible au bruit haute fréquence et doit être balancé par des termes de régulation qui correspondent à des a priori sur la solution [138].
2. le second terme représente une contrainte de type parcimonie. La norme ℓ_1 (somme des valeurs absolues) du noyau doit être petite, en accord avec le fait que le noyau est composé d'un nombre réduit de dirac, définit à l'équation 3.4.
3. le troisième terme représente une contrainte de type lissage $\|D \star I_{Mars}\|_2^2$, avec D l'opérateur discret de dérivé au premier ordre. Cet a priori encourage des solutions lisses pour réduire l'effet d'amplification du bruit haute fréquence.

Tous ces termes sont pondérés par deux hyperparamètres positifs λ_K and λ_{Mars}. La fonction coût de l'équation 3.8 est convexe pour les variables I_{Mars} lorsque K_{PFS} est fixe et vice et versa, mais pas pour le couple (I_{Mars}, K_{PFS}). Notre stratégie est de suivre une procédure classique itérative : d'après une valeur initiale $\hat{I}^0_{Mars}$, la procédure estime successivement à l'itération n $\hat{K}^{n+1}_{PFS}$ et $\hat{I}^{n+1}_{Mars}$.

Plus précisément, l'algorithme est le suivant :

1. Première estimation du noyau $\hat{K}^1_{PFS}$ d'après les données filtrées $\hat{I}^0_{Mars}$ et I_{PFS}, avec un terme de régularisation de type parcimonie
2. Boucle itérative :
   (a) estimation du spectre de Mars $\hat{I}^{n+1}_{Mars}$ d'après les données non-filtrées $\hat{K}^n_{PFS}$ et I_{PFS}, avec un terme de régularisation de type lissage
   (b) estimation du noyau $\hat{K}^{n+1}_{PFS}$ d'après les données non-filtrées $\hat{I}^{n+1}_{Mars}$ et I_{PFS}, avec un terme de régularisation de type parcimonie
3. Dernière estimation du spectre de Mars $\hat{I}^{final}_{Mars}$ d'après les données non-filtrées $\hat{K}^{final}_{PFS}$ et I_{PFS}

Il est nécessaire de commencer cette boucle sur des données filtrées car les fonctions de Planck peuvent être estimées pour Mars (émission solaire réfléchie et émission thermique). Néanmoins, la structure fine et la composition de l'atmosphère, qui composent les hautes fréquences de I_{Mars}, sont difficiles à estimer a priori. Nous avons choisi d'ajuster plusieurs fonctions de Planck d'après les données I_{PFS}, afin d'estimer

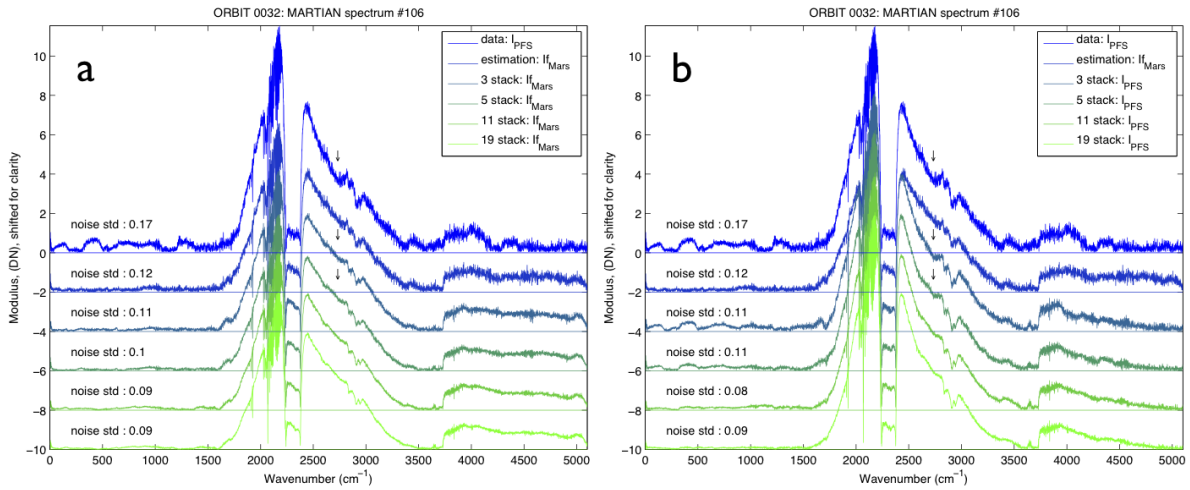


FIGURE 3.6: Comparaison du traitement entre notre algorithme (à gauche) et la méthode du stacking (à droite), d'après [282].

$\hat{I}^0_{Mars}$ pour chaque spectre observé. La méthode est dite "semi-aveugle", car il est nécessaire d'estimer une valeur initiale $\hat{I}^0_{Mars}$.

Nous avons validé cette approche sur des données réelles et synthétiques. Notre approche permet une correction de la forme générale des spectres, c'est à dire l'élimination des "fantômes", plus rapidement que la méthode de stacking (voir figure 3.6). Globalement, notre méthode permet l'utilisation des spectres uniques alors que la méthode des stackings nécessite une moyenne de 11 spectres.

D'autre part, la figure 3.7 présente une comparaison entre trois techniques d'estimation du noyau de vibration : notre méthode de déconvolution $\hat{K}^{final}_{PFS}$, une méthode approximée basée sur le laser de référence, les données ab initio des sources de vibrations de Mars Express d'après la télémétrie de l'Agence Spatiale Européenne. L'accord est relativement bon (rms=$3.1\text{x}10^{-4}$), mais le détail de tous les pics n'est pas parfait, probablement à cause des limitations de la déconvolution en aveugle.

Pour plus de détails, l'article est disponible au chapitre 3.4.2 page 164.

3.3 Perspectives

3.3.1 Perspectives méthodologiques

Pour l'instant, notre approche traite les spectres de manière indépendante. Cependant, une correction multi-spectre est envisageable pour améliorer la robustesse des estimations, car les fréquences de vibrations varient peu dans le temps. En revanche, les amplitudes complexes sont à chaque fois différentes : (i) les amplitudes sont relativement constantes mais peuvent varier dans le temps, (ii) les phases sont toujours aléatoires entre l'acquisition et la vibration.

D'autre part, nous avons établi une méthode de correction efficace pour l'instrument PFS. Sa qualité peut-être estimée lorsque le laser est allumé, c'est à dire pour les 310 premières orbites de Mars Express. Lorsque le laser est éteint, il serait judicieux de développer des tests de cohérence pour estimer la validité de la correction.

Aussi, nous avons choisi de simplifier le problème sous forme de convolution linéaire, mais à l'avenir des méthodes de corrections plus précises, basées sur le modèle non-linéaire exact au premier ordre (équation 3.1), permettraient un meilleur traitement des données.

Enfin, nous souhaitons implémenter cette approche avec des outils de calculs performants pour corriger l'intégralité des données PFS, soit près d'un milliard de spectres.

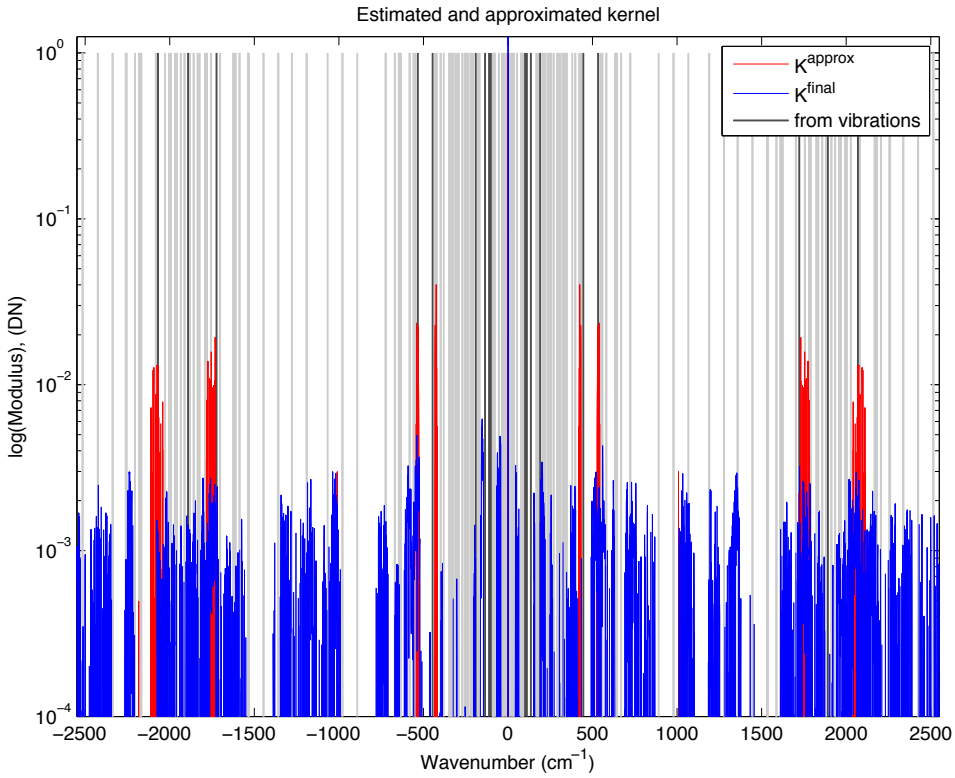


FIGURE 3.7: Comparaison entre le noyau de vibration K_{PFS} : d'après notre algorithme en bleu, d'après une méthode approximée basée sur le signal laser de référence en rouge, d'après les données ab initio de la sonde Mars Express en gris foncé, les combinaison des fréquences de vibrations ab initio en gris clair (figure d'après [282])

3.3.2 Perspectives planétologiques

Les perspectives planétologiques sont multiples, de la structure et la composition de l'atmosphère, à l'étude de la surface et notamment des glaces. Une perspective intéressante serait l'étude de la source d'eau actuelle sur Mars (voir section 6.2 page 295) ou la possibilité de présence de clathrates actuels (voir section 6.4.1 page 298). Ces perspectives seront développées dans le dernier chapitre de ce manuscrit.

3.4 Publications

Scientifique invité :

- I. Shatalina (doctorante de Politecnico di Milano sous la direction de B. Saggin) invité pendant 5 mois à IDES
- M. Giuranna, Professeur invité pendant 1 mois (PI PFS, chercheur à l'IAPS Rome)

Publications scientifiques :

- Shatalina, I., **Schmidt, F.**, Saggin, B., Kowalski, M., Gac, N., Giuranna, M. & Nhean, S. (2013), « Analytical expression of combined microvibrations effects on Fourier Spectrometer », soumis à "Aerospace Science and Technology" (voir section 3.4.1).
- **Schmidt, F.**, Shatalina, I., Kowalski, M., Gac, N., Saggin, B. & Giuranna, M. (2013), « Toward a numerical deshaker for PFS », accepté dans "Planetary and Space Science" (voir section 3.4.2 page 164).

3.4.1 Modélisation analytique des vibrations

Cette section contient l'article suivant :

- Shatalina, I., Schmidt, F., Saggin, B., Kowalski, M., Gac, N., Giuranna, M. & Nhean, S. (2013), « Analytical expression of combined microvibrations effects on Fourier Spectrometer », soumis à "Aerospace Science and Technology"

Combined microvibrations effects on Fourier Spectrometer

Shatalina[a] I., Schmidt[b,c] F., Saggin[a] B., Gac[d] N., Kowalski[d] M., Giuranna[e] M., Nhean[b,c] S.

[a]*Dipartimento di Meccanica, Politecnico di Milano, Campus of Lecco, Via M. d'Oggiono 18/a, 23900, Lecco, Italy (i-shtln@ya.ru, tel. +39 02 2399 8811)*
[b]*Univ. Paris-Sud, Laboratoire IDES, UMR 8148, Bât 509, Orsay, F-91406, France*
[c]*CNRS, Orsay, F-91405, France*
[d] *Laboratoire des Signaux et Systèmes (L2S), UMR8506 Univ Paris-Sud - CNRS – SUPELEC, SUPELEC, 3 rue Joliot Curie, Gif sur Yvette, F-91192, France*
[e]*IFSI, via del Fosso del Cavaliere 100, 00133, Roma, Italy*

Abstract.

Fourier spectrometers are strongly sensitive to mechanical vibrations. Even the implementation of the optical path sampling strategy, based on a reference laser signal used as sampling trigger, will not totally eliminate data distortion: time delays in the acquisition chains and vibration borne cyclic misalignments of optical system, result in modulation effects on the original interferogram. This article proposes an analytical expression of all combined modulation effects created on the main signal and on the laser line component. The analytical relations are illustrated and the effect highlighted on actually observed spectral features from the PFS (Planetary Fourier Spectrometer) data onboard Mars Express, ESA (European Space Agency). This complete modeling allows the development of a novel data processing techniques devoted to single spectra correction. Also, it permits to design future spaceborne high spectral resolution Fourier spectrometers tackling this difficulty, either by reducing the microvibrations environment, or directly by implementing a correction strategy.

Keywords: PFS; Fourier Transform Spectrometer; Micro-vibration; Distortions; Spectroscopy; Analytical model

1. Introduction

This study is focused on spaceborne Fourier Transform Spectrometer onboard subjected to microvibration environment. Spacecraft are usually designed to limit the onboard mechanical vibrations [1-3], but some rotating elements (such as Reaction Wheels or dithering of Inertia Measurement Units) may generate small perturbations,.
Our work is illustrated on the PFS (Planetary Fourier Spectrometer) onboard the Mars Express ESA (European Space Agency) mission. The PFS is a FTIRS (Fourier Transform InfraRed

Spectrometer) having two channels: Short Wavelength Channel (SWC) for the 1.2-5 μm range and Long Wavelength Channel (LWC) for 5-45 μm one. The interferometer scheme of PFS is a modified Michelson with swinging Cubic Corner Mirrors instead of translating flat ones. More information about PFS and its working principle can be found in [4-8]. The problem of the spectrum distortion due to vibrations has been evidenced since the instrument commissioning and is mainly concerning the SWC data [9-10]. Here we deal with the SWC measurements, affected by vibrations transmitted to the instrument by the spacecraft, and the analysis goal is assessing the distortion generated on one single measured spectrum. The general direct problem of modulations is divided into two sub problems: modulation of the continuum in the low wavenumber region (up to 5000 cm^{-1}) characterized mostly by vibration effect and, modulation in high wavenumber zone (5000 cm^{-1} up to 8330 cm^{-1} – the Nyquist limit) with significant filtering and aliasing effects along with the vibration one.

The FTIS sensitivity to vibrations and resulting ghosted features have been studied in literature [11-13] but, up to now, the usual approach for the spectra correction is based on the stacking of considerable amount of records in order to reduce the ghosts amplitude through averaging. Our aim is to propose a direct analytical model, allowing to achieve the inversion of the problem i.e: extraction of the true signal from distorted data spectrum-by-spectrum.

PFS utilizes the constant optical path difference sampling strategy based on the reference laser, a monochromatic source, sharing the optical path within the interferometer with that of one of the main IR beam. The reference laser interferogram zero crossings are used as trigger for sampling, in this way the sampling OPD (Optical Path Difference) step should be exactly half the wavelength of the reference laser. This approach theoretically should provide insensitivity of the instrument to the Cubic Corner Mirrors velocity changes (in particular those due to vibrations). In practice, however, the OPD steps will differ due to the acquisition chains [11], in particular because of the different time delays in the reference and main signal acquisition chains. Being the information on the actual step sampling not available, the spectra are determined assuming a uniform sampling step and applying the usual FT computation algorithm; this results in the distortion of the actual spectra [14-18].

Moreover, the interferogram acquired by the interferometer depends on the “modulation factor” which accounts for the deviations of the real instrument configuration from the ideal optical system [11]. This parameter is function of the instrument optical misalignments, which in turn are fluctuating periodically in presence of mechanical vibrations. This effect leads to an additional instrument sensitivity to vibrations that could not be avoided even in the ideal case of truly uniform sampling step of the interferogram.

2. Vibrations Effects Modeling.

As pointed out above the final spectrum is affected by mechanical disturbances through two main effects [11]:

- the implemented sampling system vibration borne sampling step errors due to the time delays in the acquisition systems;
- the cyclic misalignments induced by the vibrations.

In the following the effects on a monochromatic radiation entering the spectrometer subject to a purely harmonic vibration will be analyzed to derive then the effect on any complex spectrum.

The interferogram of a monochromatic source in a perfect interferometer can be represented as follows:

$$I_{\sigma_s}(x_k) = mI_s \cos(2\pi\sigma_s x_k), \quad (1)$$

where x_k is the OPD at the k^{ith} zero-crossing of the reference signal, σ_s is the wavenumber of the observed line and m is the modulation factor referred to the misalignments of the optical system from its ideal position, I_s the source half-intensity.

The pure harmonic vibration component generated at the source can be described by:

$$\mathbf{y} = \mathbf{y_d} \sin(\omega_d t + \varphi_d), \quad (2)$$

where **y** represents the vector of the vibration component generated at the source and is characterized by its angular frequency $\omega_d = 2\pi f_d$ and phase φ_d. It has to be noticed that the phase is a random variable for each interferogram (though defined for each ω_d) and usually follows a uniform distribution, in the 0-2π interval, through the set of the measurements.

Taking coordinates x and u respectively along and perpendicular to the optical axis of cube corner, we obtain the vibration components Δx and Δu responsible for the mirror speed alternations and optical misalignments in the PFS:

$$\Delta u = u_d \sin(\omega_d t + \varphi^{u*}{}_d), \quad (3)$$

$$\Delta x = x_d \sin(\omega_d t + \varphi^{x}{}_d), \quad (4)$$

where phases $\varphi^{u*}{}_d$ and $\varphi^{x}{}_d$ generally can be different, since the vector components of the transfer function of vibration propagation from the source to the interferometer in general will differ.

2.1. Combination of the vibrations effects.

As it was shown in [11] the modulation factor m is a function of Cubic Corner Mirror (CCM) position error u along any direction perpendicular to its optical axis and, as first order approximation, it can be written in the form

$$m(\sigma_s u) = m(\sigma_s u_o) + \frac{\partial m}{\partial(\sigma u)}\Big|_{\substack{u=u_o \\ \sigma=\sigma_s}} \sigma_s \Delta u + E(\sigma_s u), \quad (5.1)$$

$$m(\sigma_s, u) \cong m_o(\sigma_s, u_o) + \sigma_s a(\sigma_s, u_o) \cdot \sin(\omega_d t + \varphi^u{}_d), \quad (5.2)$$

where $E(\sigma_s u)$ is the series truncation error, a is proportional to the vibration amplitude u_d and depends on the wavenumber σ_s of the modulated component and the initial interferometer alignment quality u_o (would be zero for a perfectly aligned instrument with u_o=0). Similarly, for the effect of the "along the axis" vibration component it was shown that the sampling steps first order approximation take the expression:

$$x_k = k\frac{\lambda_r}{2} + v_m T_D + v_o T_D \cos(\omega_d t_k + \varphi^x{}_d). \quad (6)$$

Where T_D is the time delay in the sampling chain, λ_r is the reference laser wavelength, t_k is the time corresponding to the k[th] sampling while v_o is the vibration amplitude expressed as speed (i.e $v_o = \omega_d x_d$)
By substituting Eq. (5.2) and Eq. (6) in Eq. (1) one obtains:

$$I_{\sigma_s}(x_k) = [m_o(\sigma_s, u_o) + a(\sigma_s, u_o)\sigma_s \sin(\omega_d t_k + \varphi^u{}_d)] I_s$$

$$\times \cos\left[2\pi\sigma_s\left(\frac{k\lambda_r}{2} + T_D v_m\right) + 2\pi\sigma_s v_o T_D \cos(\omega_d t_k + \varphi^x{}_d)\right]. \quad (7)$$

For further simplification the following substitutions will be applied:

- the time within the sine function can be written $t_k \cong k\lambda_r/(2v_m)$;
- $\varphi_{\sigma_s} = 2\pi\sigma_s v_m T_D$;
- $\omega_d/v_m = 2\pi f_d/v_m = 2\pi\sigma_d$, $\sigma_d = f_d/v_m$.

Developing cosine into Taylor series up to 1[st] order we can rewrite Eq. (7) as:

$$I_{\sigma_s}(x_k) = \left\{m_o(\sigma_s, u_o) + a(\sigma_s, u_o)\sigma_s \sin\left[2\pi\sigma_d\left(\frac{k\lambda_r}{2}\right) + \varphi^u{}_d\right]\right\}$$

$$\times I_s\{\cos\left[2\pi\sigma_s\left(\frac{k\lambda_r}{2}\right) + \varphi_{\sigma_s}\right]$$

$$-2\pi\sigma_s v_o T_D \sin\left[2\pi\sigma_s\left(\frac{k\lambda_r}{2}\right) + \varphi_{\sigma_s}\right]\cos\left[2\pi\sigma_d\left(\frac{k\lambda_r}{2}\right) + \varphi^x{}_d\right]\}. \quad (8)$$

The ghost studies performed on PFS spectra demonstrated that the sampling error term is prevailing. Therefore as first approximation we neglect the m_o and a coefficients dependence on wavenumber σ_s. Such assumption generally can be valid or not depending on the initial misalignment u_o.

Developing the product and remembering that the factor "$2\pi\sigma_s v_o T_D a$" is a second order infinitesimal and so it is negligible with respect to the other terms, we obtain:

$$I_{\sigma_s}(x_k) = m_o I_s \cos\left[2\pi\sigma_s\left(\frac{k\lambda_r}{2}\right) + \varphi_{\sigma_s}\right]$$

$$+ a\sigma_s I_s \sin\left[2\pi\sigma_d\left(\frac{k\lambda_r}{2}\right) + \varphi^u{}_d\right]\cos\left[2\pi\sigma_s\left(\frac{k\lambda_r}{2}\right) + \varphi_{\sigma_s}\right]$$

$$-2\pi\sigma_s v_o T_D m_o I_s \sin\left[2\pi\sigma_s\left(\frac{k\lambda_r}{2}\right) + \varphi_{\sigma_s}\right]\cos\left[2\pi\sigma_d\left(\frac{k\lambda_r}{2}\right) + \varphi^x{}_d\right]. \quad (9)$$

Substituting $A_s = m_o I_s$, $A_1 = a/(2m_o)$, $A_2 = \pi v_o T_D$ and grouping the terms by the ghosts they describe, one can rewrite the Eq. (9) as follows:

$$I_{\sigma_s}(x_k) = A_s \cos\left[2\pi\sigma_s\left(\frac{k\lambda_r}{2}\right) + \varphi_{\sigma_s}\right]$$

$$+A_1\sigma_s A_s \cos\left[2\pi(\sigma_d + \sigma_s)\left(\frac{k\lambda_r}{2}\right) + (\varphi^u{}_d + \varphi_{\sigma_s} - \frac{\pi}{2})\right]$$

$$+ A_2\sigma_s A_s \cos\left[2\pi(\sigma_d + \sigma_s)\left(\frac{k\lambda_r}{2}\right) + (\varphi^x{}_d + \varphi_{\sigma_s} + \frac{\pi}{2})\right]$$

$$+A_1\sigma_s A_s \cos\left[2\pi(\sigma_s - \sigma_d)\left(\frac{k\lambda_r}{2}\right) + (\varphi_{\sigma_s} - \varphi^u{}_d + \frac{\pi}{2})\right]$$

$$+A_2\sigma_s A_s \cos\left[2\pi(\sigma_s - \sigma_d)\left(\frac{k\lambda_r}{2}\right) + (\varphi_{\sigma_s} - \varphi^x{}_d + \frac{\pi}{2})\right]$$

$$= I_{\sigma_s \text{original signal}} + I_{\sigma_s \text{right ghost}} + I_{\sigma_s \text{left ghost}} \quad (10)$$

Note: it does not change physical sense of the expression if we replace $\varphi^{u}{}_{d} - \pi/2$ by simply $\varphi^{u}{}_{d}$ as it is generally a random unknown value.

In wavenumber domain Eq. (10) can be represented as:

$$I(\sigma) = A_s \exp(i\varphi_{\sigma_s})\delta(\sigma - \sigma_s)$$

$$+ A_s \left\{ A_1 \sigma_s \exp\left[i(\varphi_{\sigma_s} + \varphi^{u}{}_{d})\right] + A_2 \sigma_s \exp\left[i(\varphi_{\sigma_s} + \varphi^{x}{}_{d} + \tfrac{\pi}{2})\right] \right\} \delta[\sigma - (\sigma_s + \sigma_d)]$$

$$+ A_s \left\{ A_1 \sigma_s \exp\left[i(\varphi_{\sigma_s} - \varphi^{u}{}_{d})\right] + A_2 \sigma_s \exp\left[i(\varphi_{\sigma_s} - \varphi^{x}{}_{d} + \tfrac{\pi}{2})\right] \right\} \delta[\sigma - (\sigma_s - \sigma_d)], \quad (11)$$

Using the $B\exp(i\varphi_{\sigma B})$ and $C\exp(i\varphi_{\sigma C})$ expressions (see Annex 1) we can rewrite Eq. (11) as following:

$$I(\sigma) = A_s \exp(i\varphi_{\sigma_s}) \delta(\sigma - \sigma_s) +$$

$$\left[\sigma_s A_s \exp(i\varphi_{\sigma_s}) \delta(\sigma - \sigma_s)\right] * \{ B\exp(i\varphi_{\sigma B})\delta[\sigma - (+\sigma_d)] + C\exp(i\varphi_{\sigma C})\delta[\sigma - (-\sigma_d)]\}$$

$$= I_{\text{signal}}(\sigma) + \left[\sigma_s I_{\text{signal}}(\sigma)\right] * K_{\sigma_d}(\sigma), \quad (12)$$

where $I_{signl}(\sigma)$ is the undistorted spectrum and $K_{\sigma d}(\sigma)$ is the single harmonic vibration kernel, "δ" and "*" are respectively the Dirac's function and the convolution operator.

The combined modulation effect can be evidenced as on Fig. 1.

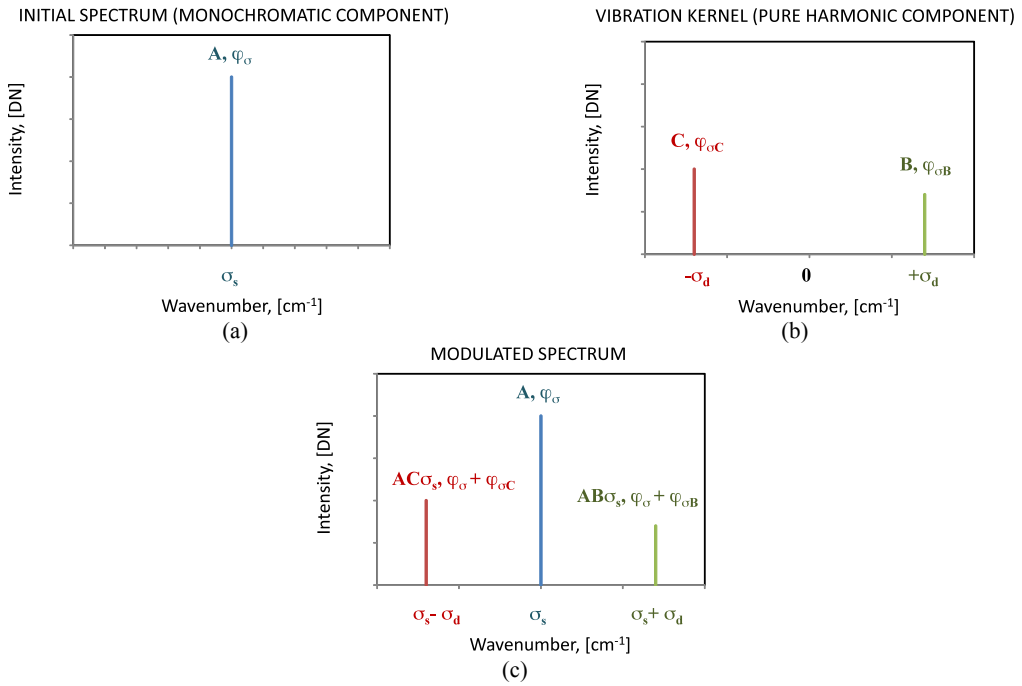


Figure 1. Monochromatic line modulation by pure harmonic vibration; (a) – initial spectrum, (b) – vibration kernel, (c) – modulated spectrum.

The above reasoning can be extended for any non-monochromatic input spectra and arbitrary vibration component shape (see Annex 2):

$$I(\sigma) = I_{\text{continuum}}(\sigma) + [\sigma I_{\text{continuum}}(\sigma)] * K(\sigma) \tag{13}$$

$$K(\sigma) = \sum_j \left\{ B_j \exp\left[i\varphi_{\sigma B_j}(\sigma)\right] \delta\left[\sigma - \left(+\sigma_{d_j}\right)\right] \right.$$

$$\left. + C_j \exp\left[i\varphi_{\sigma C_j}(\sigma)\right] \delta\left[\sigma - (-\sigma_{d_j})\right] \right\} \tag{14}$$

The last observation becomes important as the general vibration kernel does not consist of single vibration component but a whole set of them, each appearing as the bell-shaped function in the wavenumber domain, although being a pure harmonic in the time domain. This peculiarity is caused by the uneven sampling: because of non-constant mirror speed, the equal OPD step does not correspond to the equal time step.

2.2. Laser straylight modulation.

The above discussion concludes that to each harmonic of vibrations two ghosts are obtained of every spectral feature: one on its right and the other on its left. A particular case will be generated by the spectrum of the reference laser, which becomes visible in the main signal spectrum due to straylight effects. Being the laser line on the Nyquist border, its right ghost will be generated out of the instrument measurement range thus it will appear in the signal spectrum through the aliasing (Fig. 2). One must also notice that aliasing changes the phase of feature into opposite value, i.e. $\varphi_{ALIASED\ FEATURE} = -\varphi_{FEATURE}$.

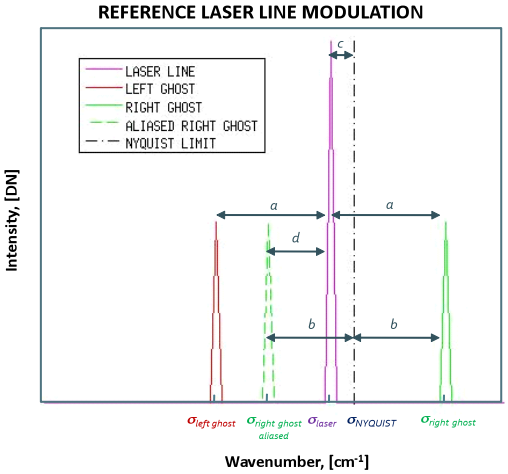
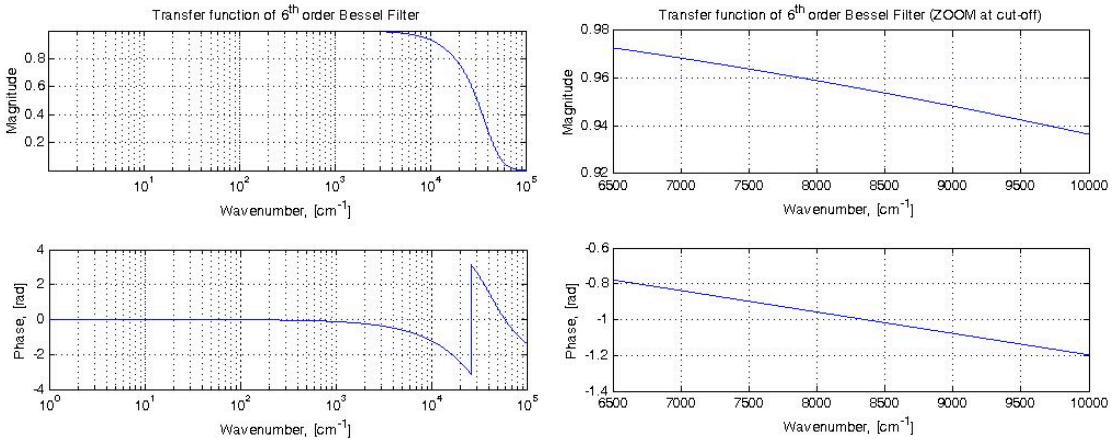


Figure 2. Aliasing of the laser line ghost

Another peculiarity of the laser line modulation refers to the anti-aliasing filter that noticeably distorts data in the high wavenumber region. For more precise information about those distortions the Transfer Function of the filter has to be discussed (Fig. 3).

It has to be noticed that the filter will affect directly the spectrum of laser line and ghosts due to misalignment as they have physical nature; the ghosts generated by sampling error due to their numerical nature will be not affected by filter directly. However those ghosts are built from already filtered laser line shape thus an indirect filtering effect will still be present.

The anti-aliasing filter implemented in PFS is the 6th order Bessel filter with cut frequency at Nyquist. Its transfer function plots are shown in Fig. 3.



(a) (b)

Figure 3. 6th order Bessel filter Transfer Function: magnitude and phase; (a) – semi log plot, (b) – zoom around cut-off wavenumber ($\sigma_{cut\text{-}off}$ = 8356 cm^{-1}).

Original signal spectrum at the Nyquist border will be distorted in amplitude and phase:

$$Y(\omega) = H(\omega) \cdot X(\omega), \tag{15.1}$$

$$H(\omega) = |H(\omega)| \exp\left[i\varphi_{H}(\omega)\right], \tag{15.2}$$

where $Y(\omega)$ and $X(\omega)$ are filtered and original signal correspondingly, and $H(\omega)$ is the filter transfer function described by its magnitude and phase.
In other words:

$$|Y(\omega)| = |H(\omega)| \cdot |X(\omega)|, \tag{16.1}$$

$$\varphi_{Y}(\omega) = \varphi_{H}(\omega) + \varphi_{X}(\omega), \tag{16.2}$$

Remembering that the pulsation can be obtained from the wavenumber by the relationship $\omega=2\pi\sigma\nu_m$, the filter transfer function can be written as a function of the wavenumber. Generally H(ω) is varying "slowly" and can be considered constant throughout the spectral width of the laser line and its ghosts as they are narrow features in the spectrum. E. g. throughout the laser spectral band $|H(\sigma_l)|$ = 0.9553± 0.02% and $\varphi_H(\sigma)$ = -1 rad ±0.04%.

Note: in the following we will use $H(\sigma)$ instead of $|H(\sigma)|$ to simplify the notation.

Now we rewrite Eq. (11) under direct and indirect filter effects, described by Eq. (15-16):

$$I_{\text{laser}}(\sigma) = A_{\text{laser}}\exp\{i[\varphi_{\sigma_l} + \varphi_H(\sigma_l)]\}H(\sigma_l)\delta(\sigma - \sigma_l)$$

$$+ A_{\text{laser}}A_1\sigma_l\exp\{i[\varphi_{\sigma_l} + \varphi^u{}_d + \varphi_H(\sigma_l + \sigma_d)]\}H(\sigma_l + \sigma_d)\delta[\sigma - (\sigma_l + \sigma_d)]$$

$$+A_{\text{laser}}A_2\sigma_l\exp\left\{i\left[\varphi_{\sigma_l} + \varphi^x{}_d + \frac{\pi}{2} + \varphi_H(\sigma_l)\right]\right\}H(\sigma_l)\delta[\sigma - (\sigma_l + \sigma_d)]$$

$$+A_{\text{laser}}A_1\sigma_l\exp\{i[\varphi_{\sigma_l} - \varphi^u{}_d + \varphi_H(\sigma_l + \sigma_d)]\}H(\sigma_l - \sigma_d)\delta[\sigma - (\sigma_l - \sigma_d)]$$

$$+A_{\text{laser}}A_2\sigma_l\exp\left\{i\left[\varphi_{\sigma_l} - \varphi^x{}_d + \frac{\pi}{2} + \varphi_H(\sigma_l)\right]\right\}H(\sigma_l)\delta[\sigma - (\sigma_l - \sigma_d)], \quad (17)$$

where σ_l is the wavenumber of the reference laser line (with nominal value of 8330 cm^{-1}).

From the Eq. (17) we can obtain right and left ghost components in analytical form:

$$I_{\text{LEFT GHOST}}(\sigma) = A_{\text{laser}}A_1\sigma_l\exp\{i[\varphi_{\sigma_l} - \varphi^u{}_d + \varphi_H(\sigma_l + \sigma_d)]\}$$

$$\times H(\sigma_l - \sigma_d)\delta[\sigma - (\sigma_l - \sigma_d)]$$

$$+A_{\text{laser}}A_2\sigma_l\exp\left\{i\left[\varphi_{\sigma_l} - \varphi^x{}_d + \frac{\pi}{2} + \varphi_H(\sigma_l)\right]\right\}$$

$$\times H(\sigma_l)\delta[\sigma - (\sigma_l - \sigma_d)], \quad (18.1)$$

$$I_{\text{RIGHT GHOST}}(\sigma) = A_{\text{laser}}A_1\sigma_l\exp\{i[\varphi_{\sigma_l} + \varphi^u{}_d + \varphi_H(\sigma_l + \sigma_d)]\}$$

$$\times H(\sigma_l + \sigma_d)\delta[\sigma - (\sigma_l + \sigma_d)]$$

$$+A_{laser}A_2\sigma_l \exp\left\{i\left[\varphi_{\sigma_l} + \varphi^x{}_d + \frac{\pi}{2} + \varphi_H(\sigma_l)\right]\right\}$$

$$\times H(\sigma_l)\delta[\sigma - (\sigma_l + \sigma_d)], \quad (18.2)$$

$$I_{\text{RIGHT GHOST ALIASED}}(\sigma) = A_{laser}A_1\sigma_l \exp\{-i[\varphi_{\sigma_l} + \varphi^u{}_d + \varphi_H(\sigma_l + \sigma_d + 2c)]\}$$

$$\times H(\sigma_l + \sigma_d)\delta[\sigma - (\sigma_l + \sigma_d)]$$

$$+A_{laser}A_2\sigma_l \exp\left\{-i\left[\varphi_{\sigma_l} + \varphi^x{}_d + \frac{\pi}{2} + \varphi_H(\sigma_l)\right]\right\}$$

$$\times H(\sigma_l)\delta[\sigma - (\sigma_l + \sigma_d + 2c)], \quad (18.3)$$

where c is the distance from the laser peak to the Nyquist limit (Fig. 2): due to divergence of the laser straylight they do not perfectly coincide.

Finally both ghosts superimpose and generate the distorted spectrum:

$$I_{LM}(\sigma) = I_{LF}(\sigma) + I_{LG}(\sigma) + I_{RGA}(\sigma), \quad (19)$$

where are $I_{LG}(\sigma)$ and $I_{RGA}(\sigma)$ the left and aliased right ghosts correspondingly, $I_{LF}(\sigma)$ is the filtered original laser line and $I_{LM}(\sigma)$ is the resulting modulated laser line spectrum.

Up to now we considered the laser line as the monochromatic feature (what is not physically true). However the obtained solution can be easily extended to the physically meaningful case through two additional statements: specifying the laser line feature shape by its modulus $A_{laser}(\sigma)$ and phase $\varphi_L(\sigma)$ as functions of wavenumber σ (as it is shown in the Eq. (20)):

$$I_{LF}(\sigma) = H(\sigma_l)(A_{laser}(\sigma)\exp\{i[\varphi_L(\sigma) + \varphi_H(\sigma_l)]\}) * \delta(\sigma - \sigma_l), \quad (20)$$

3. Testing the model.

In the previous sections an analytical formulation for the ghost features was provided, developing the analytical base. In the following we will test this vibration model on actual spaceborne data from the PFS/SWC instrument.

The typical SWC spectrum with reference laser switched on (Fig. 4) can be divided into two domains: the main signal continuum with its ghosts on the left side (up to 5000 cm^{-1}) and the modulated reference laser line on the right (region between 5000 cm^{-1} and 8330 cm^{-1}). The reason for this division is that the analytical expression of the ghosts will be different in those regions according to the scheme in the previous sections. However being referred to the same interferogram, they are modulated by the same vibration kernel; i.e. once the kernel is determined for the laser line domain, its formulation will be valid as well for the main signal one.

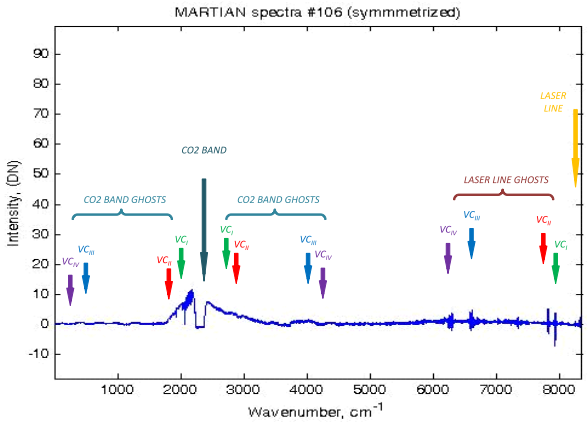


Figure 4. Typical SWC spectrum of Martian atmosphere (data from Symmetrized spectrum #106, ORBIT0032).

Ghost formation in the main signal continuum is characterized by the convolution with vibration kernel, as it is presented in Eq. (13). The complete demonstration of the direct vibration model thus would be the convolution of the "true" signal and the predicted vibration kernel, along with further comparison with the actually acquired data. The problem encountered is that there is no precise information available neither about the signal, nor about the kernel. As the first approximation of the model, the estimates of the signal and kernel are to be used.

3.1. Approximated estimation of the vibration kernel using laser line.

The estimate of the vibration kernel can be obtained from the modulated laser line domain, owing to its near monochromatic properties.

The example of the laser line shape and its ghosts in the acquired PFS spectrum is shown on the Fig. 5.

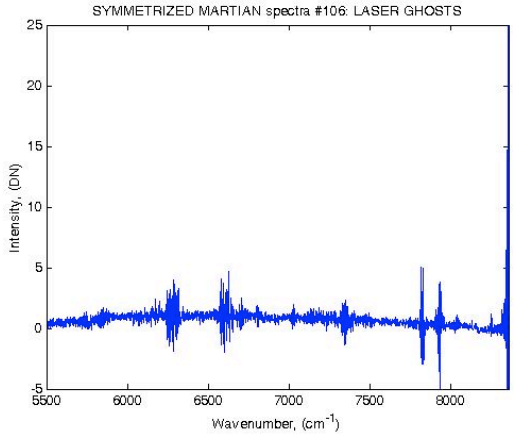


Figure 5. Modulated laser line spectrum (data from symmetrized spectrum #106, ORBIT0032).

Generally the laser line modulation is not a simple convolution problem and it is not invertible linearly (Eq. (17-20)).

Anyway it has been demonstrated in Eq. (18.1), (18.3) that the position between Laser Left Ghost and Laser Right Ghost Aliased is shifted by $2c$, where value of c can be taken from the actual spectrum (Fig. 5) as about 1 cm^{-1}. This permits retrieving from the laser ghosts the approximate vibration kernel, which is not valid for the absolute values of modulations, but provides a fair estimation of σ_d (Fig.6).

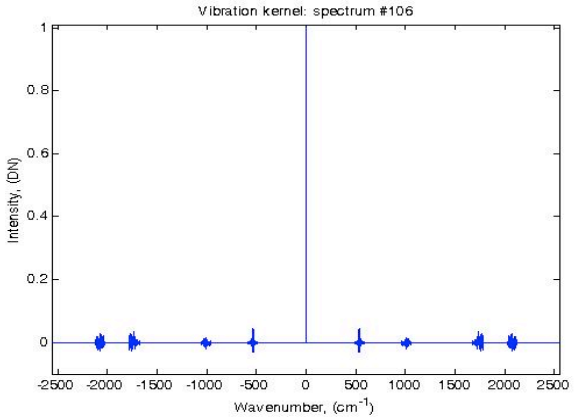


Figure 6. Estimate of vibration kernel (data from symmetrized spectrum #106, ORBIT0032).

3.2. Direct vibration model of the main signal continuum.

For the signal estimate the measured distorted spectrum (Fig. 4) can be used. In the range 2000 to 3500 cm^{-1} the content of the signal is mostly described by the real Martian spectrum with the slighter ghost impact. So this spectral region was taken as the signal estimate for the direct vibration model. The results of convolution with kernel components are presented on the Fig. 7.

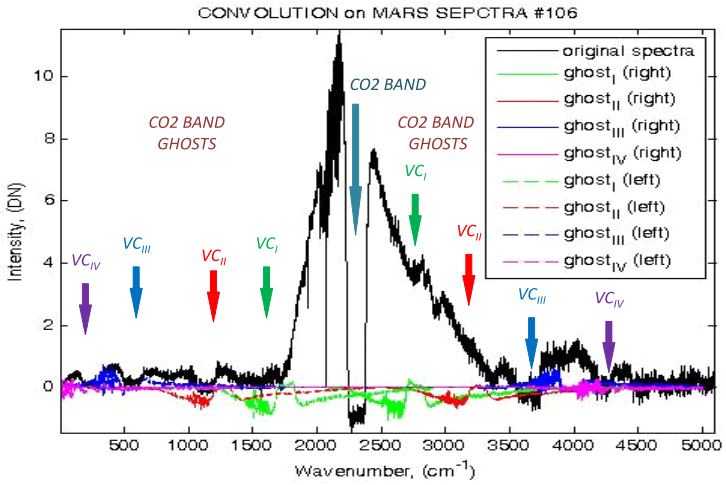


Figure 7. Direct vibration model results.

As it is seen on the previous image, some spectral features well-agree with the direct vibration model results, while others show less correspondence. This inconsistency can be explained by the fact, that the kernel estimates, used in the direct vibration model, do not recover neither actual phase nor modulus of the actual kernel.

To check the correspondence of the estimated ghost with the actual spectral feature, the correlation analysis was performed (Fig. 8). The characteristic feature to be analyzes was taken the CO_2 absorption band (2200..2300 cm^{-1}), as the one with the highest contrast in signal intensity. The resulting correlation peaks for the ghosts in the no-signal region (up to 1500 cm^{-1}) are summarized in the Table 1. The ghosts that demonstrate better correlation are the ones where "phase guess" was closer to the real situation. For the vibration component II, the large shift value is explained by the smooth variation of the signal, disabling the possibility of precise shift determination. For vibrations II and IV, the correlation is high, showing that this methodology is correct at first order.

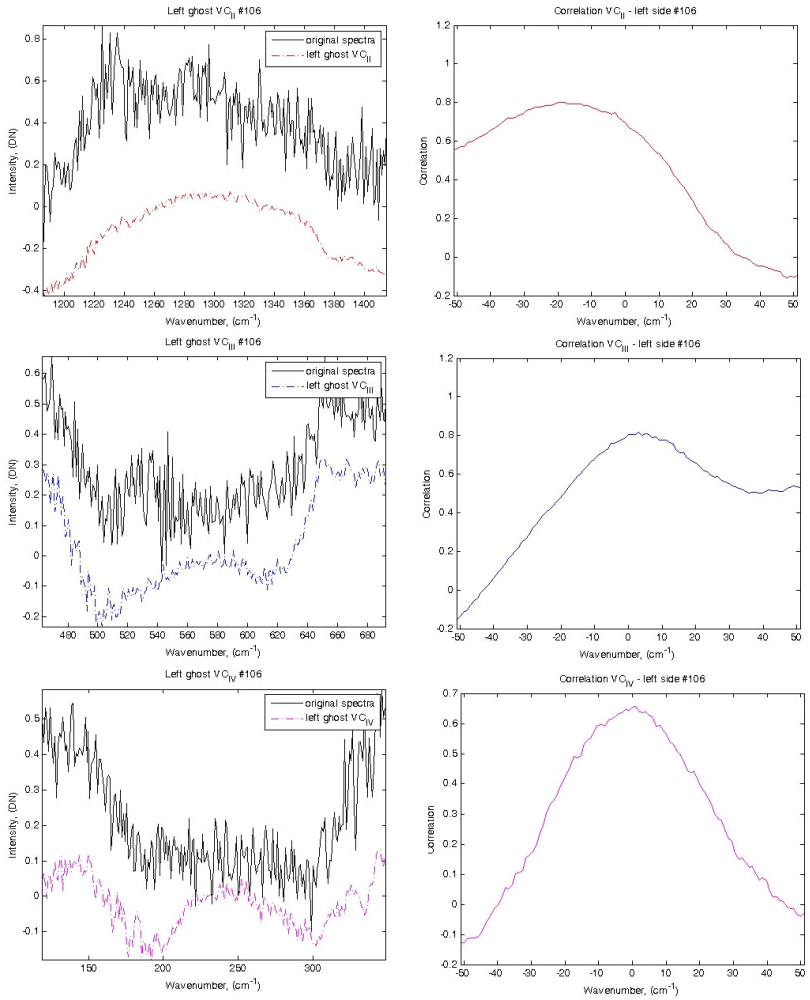


Figure 8. Direct vibration model results: correlation check.

Table 1.
Correlation analysis result: value and position of the peak.

Vibration component		Correlation peak	
number	approximate σ_d, [cm^{-1}]	shift from zero, [cm^{-1}]	value
II	1010	-18	0.79
III	1750	3	0.81
IV	2070	1	0.66

4. Conclusions.

In this work the analytical formulation of ghosts caused by mechanical disturbances has been derived. The adopted mathematical formulation is based on a simple linear convolution; this approach allows the inversion of the problem using supervised blind de-convolution techniques for the signal domain [19]. For the laser straylight, the derived non-linear mathematical formulation shows that inversion is not trivial. Leveraging on an approximated formulation of the laser line, it is possible however, to estimate the vibration kernel.

The direct vibration model has been tested using actual PFS data, by (i) estimating first the vibration kernel using the approximated formulation and then (ii) applying the convolution vibration model to the actual signal. It has been shown that, the results are in accordance with the observed spectral features in terms of wavenumber position though the amplitude estimation still need to be improved.

The future effort to correct for mechanical disturbances on Fourier Transform Spectrometers should focus on inversion of these formulations using efficient and robust algorithms to treat the dataset spectrum by spectrum. Also, the design of future spaceborne Fourier Transform Spectrometers must take into account this difficulty by innovative conception.

Acknowledgement.

We acknowledge support from the “Institut National des Sciences de l’Univers” (INSU), the "Centre National de la Recherche Scientifique" (CNRS) and "Centre National d’Etude Spatiale" (CNES) and through the "Programme National de Planétologie".

Annex 1.

Concerning the Eq. (11):

$$I(\sigma) = A_s \exp(i\varphi_{\sigma_s})\delta(\sigma - \sigma_s)$$

$$+ A_s\left\{ A_1\sigma_s \exp\left[i(\varphi_{\sigma_s} + \varphi^{u}{}_{d})\right] + A_2\sigma_s \exp\left[i(\varphi_{\sigma_s} + \varphi^{x}{}_{d} + \tfrac{\pi}{2})\right]\right\}\delta[\sigma - (\sigma_s + \sigma_d)]$$

$$+ A_s\left\{ A_1\sigma_s \exp\left[i(\varphi_{\sigma_s} - \varphi^{u}{}_{d})\right] + A_2\sigma_s \exp\left[i(\varphi_{\sigma_s} - \varphi^{x}{}_{d} + \tfrac{\pi}{2})\right]\right\}\delta[\sigma - (\sigma_s - \sigma_d)] =$$

$$A_s \exp(i\varphi_{\sigma_s})\delta(\sigma - \sigma_s)$$

$$+\left[\sigma_s A_s \exp\left(i\varphi_{\sigma_s}\right)\delta(\sigma-\sigma_s)\right] * \left\{\left[A_1\exp\left(i\,\varphi^{u}{}_{d}\right) + A_2\exp\left(i\left(\varphi^{x}{}_{d}+\frac{\pi}{2}\right)\right)\right]\delta[\sigma-(+\sigma_d)]\right.$$

$$\left. + \left[A_1\exp\left(-i\,\varphi^{u}{}_{d}\right) + A_2\exp\left(i\left(-\varphi^{x}{}_{d}+\frac{\pi}{2}\right)\right)\right]\delta[\sigma-(-\sigma_d)]\right\}$$

For the simplification reasons the following notation can be used:

$$B\exp(i\,\varphi_{\sigma B}) = A_1\exp\left(i\,\varphi^{u}{}_{d}\right) + A_2\exp\left(i\left(\varphi^{x}{}_{d}+\frac{\pi}{2}\right)\right),$$

$$C\exp(i\,\varphi_{\sigma C}) = A_1\exp\left(-i\,\varphi^{u}{}_{d}\right) + A_2\exp\left(i\left(-\varphi^{x}{}_{d}+\frac{\pi}{2}\right)\right).$$

Annex 2.

Extension of the Eq. (12) can be performed in two steps.

Step 1. Extension for the non-monochromatic input spectra.
To go to the general source case, it has to be remembered that the non-monochromatic spectrum $I_{\text{continuum}}(\sigma)$ can be expressed through its monochromatic components $I_{\text{signal }k}(\sigma)$ as following:

$$I_{\text{continuum}}(\sigma) = \sum_k I_{\text{signal}_k}(\sigma) = \sum_k A_{s_k}\exp(i\varphi_{\sigma_{s_k}})\delta(\sigma-\sigma_{s_k})$$

Modulated by single vibration component σ_d, spectrum $I_{\sigma d}(\sigma)$ in its turn can be represented as the sum of the modulated monochromatic components $I_k(\sigma)$:

$$I_{\sigma_d}(\sigma) = \sum_k I_k(\sigma)$$

where $I_k(\sigma)$ is defined in accordance with the Eq. (12) :

$$I_k(\sigma) = I_{\text{signal}_k}(\sigma) + \sigma_{s_k} I_{\text{signal}_k}(\sigma) * K_{\sigma_d}(\sigma) =$$

$$A_{s_k}\exp\left(i\varphi_{\sigma_{s_k}}\right)\delta(\sigma-\sigma_{s_k}) + \sigma_{s_k}A_{s_k}\exp\left(i\varphi_{\sigma_{s_k}}\right)\delta(\sigma-\sigma_{s_k}) * K_{\sigma_d}(\sigma) =$$

$$A_{s_k}\exp\left(i\varphi_{\sigma_{s_k}}\right)\delta(\sigma-\sigma_{s_k}) + A_{s_k}\exp\left(i\varphi_{\sigma_{s_k}}\right)[\sigma\delta(\sigma-\sigma_{s_k})] * K_{\sigma_d}(\sigma)$$

Note:

$$\sigma_{s_k}\delta(\sigma-\sigma_{s_k}) = \sigma\delta(\sigma-\sigma_{s_k}) = \begin{bmatrix}\sigma_{s_k}\delta(0), \sigma=\sigma_{s_k}\\ 0, \sigma\neq\sigma_{s_k}\end{bmatrix}$$

Thus we obtain:

$$I_{\sigma_d}(\sigma) = \sum_k \left\{A_{s_k}\exp\left(i\varphi_{\sigma_{s_k}}\right)\delta(\sigma-\sigma_{s_k}) + A_{s_k}\exp\left(i\varphi_{\sigma_{s_k}}\right)[\sigma\delta(\sigma-\sigma_{s_k})] * K_{\sigma_d}(\sigma)\right\} =$$

$$\sum_k \left\{A_{s_k} \exp\left(i\varphi_{\sigma_{s_k}}\right)\delta(\sigma-\sigma_{s_k})\right\} + \sum_k \left\{A_{s_k} \exp\left(i\varphi_{\sigma_{s_k}}\right)[\sigma\delta(\sigma-\sigma_{s_k})] * K_{\sigma_d}(\sigma)\right\} =$$

$$\sum_k I_{\text{signal}_k}(\sigma) + \left[\sum_k \sigma I_{\text{signal}_k}(\sigma)\right] * K_{\sigma_d}(\sigma) =$$

$$\sum_k I_{\text{signal}_k}(\sigma) + \left[\sigma \sum_k I_{\text{signal}_k}(\sigma)\right] * K_{\sigma_d}(\sigma) =$$

$$I_{\text{continuum}}(\sigma) + [\sigma I_{\text{continuum}}(\sigma)] * K_{\sigma_d}(\sigma)$$

Step 2. Extension for the arbitrary vibration component shape
Having the vibration kernel $K(\sigma)$ consisting of more than one harmonic, we obtain the final modulated spectrum as the combination of the modulations by each harmonic component σ_{dj}:

$$I(\sigma) = I_{\text{continuum}}(\sigma) + \sum_j \left\{[\sigma I_{\text{continuum}}(\sigma)] * K_{\sigma_{d_j}}(\sigma)\right\} =$$

$$I_{\text{continuum}}(\sigma) + [\sigma I_{\text{continuum}}(\sigma)] * \sum_j K_{\sigma_{d_j}}(\sigma) =$$

$$I_{\text{continuum}}(\sigma) + [\sigma I_{\text{continuum}}(\sigma)] * K(\sigma)$$

where $K(\sigma) = \sum_j K_{\sigma_{d_j}}(\sigma)$, or in other words:

$$\mathrm{K}(\sigma) = \sum_j \left\{B_j \exp\left[i\varphi_{\sigma B_j}(\sigma)\right]\delta\left[\sigma - \left(+\sigma_{d_j}\right)\right] + C_j \exp\left[i\varphi_{\sigma C_j}(\sigma)\right]\delta\left[\sigma - (-\sigma_{d_j})\right]\right\}$$

References.

[1] Qiu Z, Wu H, Ye C. Acceleration sensors based modal identification and active vibration control of flexible smart cantilever plate. Aerospace Science and Technology 2009;13:277-90.

[2] Oh H, Lee K, Jo M. A passive launch and on-orbit vibration isolation system for the spaceborne cryocooler. Aerospace Science and Technology; in Press.

[3] Hu Q, Ma G. Variable structure control and active vibration suppression of flexible spacecraft during attitude maneuver. Aerospace Science and Technology 2005;9:307-17.

[4] V. Formisano, F. Angrilli, G. Arnold, S. Atreya, G. Bianchini, D. Biondi, A. Blanco, M.I. Blecka, A. Coradini, L. Colangeli, A. Ekonomov, F. Esposito, S. Fonti, M. Giuranna, D. Grassi, V. Gnedykh, A. Grigoriev, G. Hansen, H. Hirsh, I. Khatuntsev, A. Kiselev, N. Ignatiev, A.

Jurewicz, E. Lellouch, J. Lopez Moreno, A. Marten, A. Mattana, A. Maturilli, E. Mencarelli, M. Michalska, V. Moroz, B. Moshkin, F. Nespoli, Y. Nikolsky, R. Orfei, P. Orleanski, V. Orofino, E. Palomba, D. Patsaev, G. Piccioni, M. Rataj, R. Rodrigo, J. Rodriguez, M. Rossi, B. Saggin, D. Titov, and L. Zasova. The Planetary Fourier Spectrometer (PFS) onboard the European Mars Express mission. Planet Space Sci 2005;53:963-74.

[5] V. Formisano, V. I. Moroz, F. Angrilli, G. Bianchini, E. Bussoletti, N. Cafaro, F. Capaccioni, M. T. Capria, P. Cerroni, G. Chionchio, L. Colangeli, A. Coradini, A. Di Lellis, S. Fonti, R. Orfei, E. Palomba, G. Piccioni, B. Saggin, A. Ekonomov, A. Grigorlev, V. Gnedykh, I. Khatuntsev, A. Kiselev, I. Matsygorin, B. Moshkin, V. Nechaev, Yu. Nikolsky, D. Patsaev, A. Russakov, D. Titov, L. Zasova, M. I. Blecka, A. Jurewicz, M. Michalska, W. Novosielski, P. Orleanski, G. Arnold, H. Hirsch, H. Driesher, J. Lopez-Moreno, R. Rodrigo, J. Rodriguez-Gomez, and G. Michel. PFS: a Fourier spectrometer for the study of Martian atmosphere. Adv Space Res 1997;19:1277-80.

[6] V. Formisano, V. I. Moroz, H. Hirsch, P. Orleanski, G. Michel, J. Lopez-Moreno, E. Amata, G. Bellucci, G. Piccioni, G. Chionchio, A. Carusi, A. Coradini, P. Cerroni, M. T. Capria, F. Capaccioni, A. Adriani, M. Vitterbini, F. Angrilli, G. Bianchini, B. Saggin, S. Fonti, E. Bussoletti, D. Mancini, L. Colangeli, A. Grigoriev, B. Moshkin, V. Gnedykh, I. A. Matsygorin, D. Patsaev, Yu. V. Nikolsky, D. V. Titov, L. V. Zasova, I. Khatuntsev, A. Kiselev, G. Arnold, H. Driesher, M. I. Blecka, R. Rodrigo, and J. Rodriguez-Gomez. Infrared spectrometer PFS for the Mars94 orbiter. Adv Space Res 1996;17:61-4.

[7] H. Hirsh, V. Formisano, V. I. Moroz, V. Arnold, A. Jurewicz, G. Michel, J. J. Lopez-Moreno, G. Piccioni, and N. Cafaro. The planetary Fourier spectrometer (PFS) for the orbiter of the spacecraft Mars96. Planet Space Sci 1996;44:889-97.

[8] V. Formisano, D. Grassi, N. Ignatiev, L. Zasova, A. Maturilli, and the PFS team. PFS for Mars Express: a new approach to study Martian atmosphere. Adv Space Res 2002;29:131-42.

[9] M. Giuranna, V. Formisano, D. Biondi, A. Ekonomov, S. Fonti, D. Grassi, H. Hirsch, I. Khatuntsev, N. Ignatiev, M. Michalska, A. Mattana, A. Maturilli, B.E. Moshkin, E. Mencarelli, F. Nespoli, R. Orfei, P. Orleanski, G. Piccioni, M. Rataj, B. Saggin, and L. Zasova. Calibration of the Planetary Fourier Spectrometer short wavelength channel. Planet Space Sci 2005;53:975-91.

[10] M. Giuranna, V. Formisano, D. Biondi, A. Ekonomov, S. Fonti, D. Grassi, H. Hirsch, I. Khatuntsev, N. Ignatiev, M. Malgoska, A. Mattana, A. Maturilli, E. Mencarelli, F. Nespoli, R. Orfei, P. Orleanski, G. Piccioni, M. Rataj, B. Saggin, and L. Zasova. Calibration of the Planetary Fourier Spectrometer long wavelength channel. Planet Space Sci 2005;53:993-1007.

[11] B. Saggin, L. Comolli, and V. Formisano. Mechanical disturbances in Fourier spectrometers. Applied Optics 2007;46:5248-56.

[12] L. Comolli, and B. Saggin. Evaluation of the sensitivity to mechanical vibrations of an IR Fourier spectrometer. Rev Sci Instrum 2005;76:123112.

[13] M. Toyoshima, T. Jono, N. Takahashi, T. Yamawaki, K. Nakagawa, and K. Arai. Transfer function of microvibrational disturbances on a satellite 2003:paper 2003-2406.

[14] Alexander S. Zachor, and Steve M. Aaronson. Delay compensation: its effect in reducing sampling errors in Fourier spectroscopy. Applied Optics 1979;18:68-75.

[15] Douglas L. Cohen. Performance Degradation of a Michelson Interferometer Due to Random Sampling Errors. Applied Optics 1999;38:139-51.

[16] E. E. Bell, and R. B. Sanderson. Spectral Errors Resulting from Random Sampling-Position Errors in Fourier Transform Spectroscopy. Applied Optics 1972;11:688-9.

[17] L. Comolli, and B. Saggin. Effetti degli errori nel passo di campionamento sulla DFT: applicazione al caso di uno spettrometro di Fourier 2005.

[18] Luca Palchetti, and Davide Lastrucci. Spectral noise due to sampling errors in Fourier-transform spectroscopy. Applied Optics 2001;40:3235-43.

[19] F. Schmidt, I. Shatalina, M. Kowalski, N. Gac, B. Saggin, and M. Giuranna. Toward a numerical deshaker for PFS. Planet Space Sci submitted 2013.

3.4.2 Correction des données PFS

Cette section contient l'article suivant :

– Schmidt, F., Shatalina, I., Kowalski, M., Gac, N., Saggin, B. & Giuranna, M. (2013), « Toward a numerical deshaker for PFS », accepté à "Planetary and Space Science"

Toward a numerical deshaker for PFS

Schmidt[1,2] F., Shatalina[3] I., Kowalski[4] M., Gac[4] N., Saggin[3] B., Giuranna[5], M.

[1] *Univ. Paris-Sud, Laboratoire IDES, UMR 8148, Bt 509, Orsay, F-91405, France (frederic.schmidt@u-psud.fr)*
[2] *CNRS, Orsay, F-91405, France*
[3] *Dipartimento di Meccanica, Politecnico di Milano, Campus of Lecco, Via M. d'Oggiono 18/a, 23900, Lecco, Italy*
[4] *Laboratoire des signaux et systemes (L2S), UMR8506 Univ Paris-Sud - CNRS – SUPELEC, SUPELEC, 3 rue Joliot Curie, Gif sur Yvette, F-91192, France*
[5] *IFSI, via del Fosso del Cavaliere, 100, 00133 Roma, Italy*

Abstract

The Planetary Fourier Spectrometer (PFS) onboard Mars Express (MEx) is the instrument with the highest spectral resolution observing Mars from orbit since 2005. It permits studying the atmospheric structure, major and minor compounds. The present time version of the calibration is limited by the effects of mechanical vibration, currently not corrected. We proposed here a new approach to correct for the vibrations based on semi-blind deconvolution of the measurements. This new approach shows that a correction can be done efficiently but not automatically due to the dependence on some regularisation parameters. It may be applied on the complete PFS dataset, correcting the large-scale perturbation due to microvibrations for each spectrum independently. This approach is validated on actual PFS data. A coherence check can be performed and also validate our approach. Unfortunately, the coherence check can be done only on the first 310 orbits of MEx only, until the laser line has been switch off. More generally, this work may apply to numerically "deshake" Fourier Transform Spectrometer, widely used in space experiments or in the laboratory.

Key words: Keyword: PFS ; Fourier Transform Spectrometer; Micro-vibration ; Calibration; Spectroscopy; Blind Inverse problem

1. Introduction

The Planetary Fourier Spectrometer (PFS) is a double pendulum Fourier transform infrared spectrometer instrument onboard MEx, operating in the 1.5 to 5.5 micrometers for the Short Wavelength Channel (SWC), and 5 to 45 microns in the Long Wavelength Channel (LWC) (Formisano et al., 2005). It is based on a modified Michelson's scheme using a double pendulum of cubic reflectors. The optical path difference is defined by the zero crossing of a laser

tacking the same optical path that the signal. The spectra presented in this article are the numerical Fourier transform of the recorded interferograms.

An experimental study of mechanical vibration impact on Fourier-transform spectrometer has been proposed based on PFS example (Comolli and Saggin, 2005). Analytical expression of all distortion effects have been formulated separately (Saggin et al., 2007): offset of the reference laser signal, mirrors speed variation, periodic misalignments, detector non linearity and internal reflections. More recently, a numerical simulation model has been proposed to explore all effects combined in order to understand the PFS signal (Comolli and Saggin, 2010). Perturbations are creating artificial features, called "ghosts", present in some spectra of the SWC. Since the amplitude of ghosts are small (few % of the original signal) and its phase has a stochastic behavior, the worst cases correspond to only few significant ghosts Shatalina et al. (2013).

Quantitatively, the ghosts are affecting few % of the total spectrum energy (3% typically; 5% maximum). When single spectra are used, the absolute radiometric calibration is degraded, and spurious spectral features may appear in the spectrum, preventing any surface-related analysis, and introducing large uncertainties in the quantitative retrievals of abundances of minor species in the atmosphere. When discussing the calibration procedure for the SCW (Giuranna et al., 2005b) and the LWC (Giuranna et al., 2005a), the authors suggest to stack the data to correct for the effects of the mechanical vibrations. The position of ghosts depends on the frequencies of the external vibrations, which have been found to be quite stable. Since the phase of ghosts is random and the external frequencies are stable, only the signal should be coherent during the stack. This idea has been confirmed by numerical modeling of the perturbations (Comolli and Saggin, 2010). Practically, averaging a few spectra (ten or so) is enough to average out the ghosts. However, this will degrade the spatial and temporal resolution of PFS measurements, limiting the interpretation of small-scale features and hampering some scientific studies (e.g., the composition of ices; detection of minerals at the surface).

Typical PFS raw measurements are shown in Fig. 1. One can identify the major signals from Mars: thermal emission and reflection of solar energy, and the laser line stray-light. Also the contribution due to mechanical vibrations are shown on the signal, leading to additional energy shifted on left and right almost symmetrically. The ghost of the laser line is only one sided due to aliasing.

Our aim is to provide a new approach to process the PFS instrument with following constraint:

1. correct the effect of mechanical vibrations due to both misalignment and optical path difference errors.
2. perform the correction on each spectrum separately.
3. validate the approach by using actual PFS observations.

In order to avoid unphysical solution, the algorithm is initialized with an priori guess of the large scale structure of the spectra, adapted to each measurement, reproducing the Martian thermal emission and the reflected solar light (see section 2.2.2).

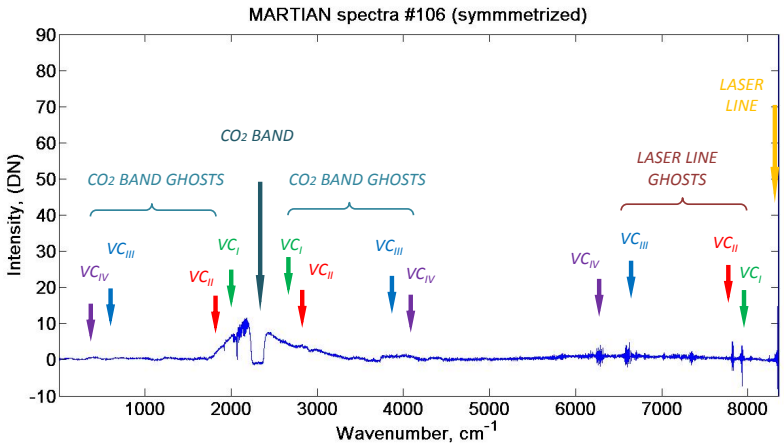


Figure 1: Typical symmetrized PFS measurement in SWC. Signal and major CO_2 band and laser lines are noted. The four main ghosts are identified as "Vibration Component" (VC) affecting both signal and laser line..

A check of the correction can be done but require the SWC laser diode switched on, to estimate the vibration kernel independently (see section 2.3).

2. Method

This section contains the direct model of the Martian spectra affected by vibrations. Then, an iterative procedure is exposed in order to invert it as well as some criteria to measure the quality of our estimation.

2.1. Analytical formulation in the signal domain (0 to 5000 cm^{-1})

As it can be seen from Fig.1, it is possible to separate the whole spectrum into two wavenumber domains to deal the effects of the mechanical vibrations apart in each of them. From 0 to 5000 points (5000*1.02 cm^{-1}), we define the signal domain, where the thermal energy from Mars and the reflected Martian energy are recorded.

The region from 1700 cm^{-1} to 5000 cm^{-1} is the one where the thermal emission from Mars and the reflected Solar energy are recorded. It represents the useful domain for scientific purpose. Below 1700 cm^{-1} there is no meaningful signal due to the low detector responsivity (see Fig. 15. in Giuranna et al. (2005b)), and this region is characterized only by ghosts of the continuum. We define the 0-5000 cm^{-1} as the signal domain.

At larger wavenumber than 5000 cm^{-1}, the signal to noise ratio is too low to expect any signal from Mars due to the detector low responsivity. This second domain, called laser line domain, is dominated by the laser line shape and its ghosts, directly and in aliasing. This domain will be used to test the coherence of the results. Since the laser has been switched off after orbit 662, it could not be used for the complete PFS archive (see section 2.3).

Using some mathematical reorganization and simplification, the analytical expression of mechanical vibration due to periodic misalignment and optical path errors can be written as a convolution products in complex form, see Eq. (13) in Shatalina et al. (2013). Assuming that the domain of wavenumber with significant signal I_{Mars} around $\sigma \sim 2000 - 3000$ cm^{-1} is constant ($\sigma_k \sim 2500$), the following Equation:

$$I_{PFS}(\sigma) = I_{Mars}(\sigma) + [\sigma.I_{Mars}(\sigma)] \star K(\sigma) \ , \tag{1}$$

simplifies to:

$$I_{PFS}(\sigma) = I_{Mars}(\sigma) \star [\delta(\sigma) + K(\sigma).\sigma_k] \ . \tag{2}$$

with $\delta()$,the dirac function.

By rewriting:

$$I_{PFS}(\sigma) = I_{Mars}(\sigma) \star K_{PFS}(\sigma) \ , \tag{3}$$

with $I_{PFS}(\sigma)$ the measured raw spectra, I_{Mars} the contribution of the raw spectra from Mars, K_{PFS} the kernel representing the mechanical vibration effects,

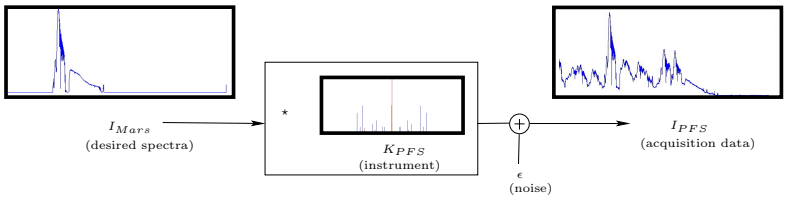


Figure 2: Model of acquisition by the PFS instrument

σ the wavenumber, and $K(\sigma)$ the non-normalized complex kernel (Shatalina et al., 2013).

From Shatalina et al. (2013), the kernel of all frequency of vibrations is:

$$K_{PFS}(\sigma) = \delta(\sigma) + A(\sigma)e^{i\varphi_A(\sigma)} + B(\sigma)e^{i\varphi_B(\sigma)} \ . \tag{4}$$

The quantities A, B, φ_A, φ_B are unknown and cannot be evaluated quantitatively due to the lack of knowledge about vibration amplitude and phase. In practice, the functions A, B, φ_A, φ_B are sparse over σ because the frequencies of vibrations are sparse. Please note that A, B, φ_A, φ_B are not symmetric around $\sigma = 0$ due to the relative phase. We propose to estimate those functions using an inversion procedure described in the next section.

The assumption of a reduced wavenumber domain is valid in first approximation due to the sensitivity of the detector and the typical Martian signal, leading to a misfit factor of x0.8 to x1.2 that is reasonable for this case. In addition, our strategy is to use semi-blind deconvolution algorithm in order to ensure the best fit any kind of spectra. This way, the wavenumber domain of significant signal has not to be defined explicitly.

Including to our model an additive noise ϵ which stands for the others sources of acquisition noise besides the mechanical vibrations and the error due to our PFS modeling by a convolution kernel K_{PFS}, PFS spectra in signal domain as illustrated in Fig. 2, are obtained through:

$$I_{PFS}(\sigma) = I_{Mars}(\sigma) \star K_{PFS}(\sigma) + \epsilon \ . \tag{5}$$

2.2. Inversion

From the direct model of the PFS instrument described above, see Eq. (5), we propose here a semi-blind deconvolution method to solve the inverse problem: estimation of the desired spectra I_{Mars} from the PFS spectra I_{PFS} although the convolution kernel K_{PFS} is unknown. We qualified our method as semi-blind because the only spectral a priori information is $\hat{I}^0_{Mars}$, known ab initio. We also used two a priori information : $\hat{I}_{Mars}$ is smooth and $\hat{K}_{PFS}$ is sparse. The notation $\hat{X}$,means the estimation of quantity X. A classical approach consists in introducing a cost function $\mathcal{C}$ whose minimum provides an estimation:

$$\hat{I}_{Mars}, \hat{K}_{PFS} = \underset{I_{Mars}, K_{PFS}}{\operatorname{argmin}} \; \mathcal{C}(I_{Mars}, K_{PFS}) \\ = \underset{I_{Mars}, K_{PFS}}{\operatorname{argmin}} \; \frac{1}{2}\|I_{PFS} - K_{PFS} \star I_{Mars}\|_2^2 + \lambda_K \|K_{PFS}\|_1 + \frac{\lambda_{Mars}}{2}\|D \star I_{Mars}\|_2^2 \; . \tag{6}$$

Three terms appear in $\mathcal{C}$

1. A data fit term $\frac{1}{2}\|I_{PFS} - K_{PFS} \star I_{Mars}\|_2^2$ that quantifies how well the estimated sources match the measured data. This term takes into account the characteristics of the noise supposed to be white and gaussian. This data match term is sensitive to high frequency noise and must be balanced with regularization term which corresponds to a mathematical prior on the expected solution (Idier, 2008).
2. A sparsity regularization term $\|K_{PFS}\|_1$ is chosen for the kernel, i.e. : the ℓ_1 norm (sum absolute value) of the kernel must be low. Indeed, the PFS kernel is supposed to be composed with few diracs at mechanical vibration frequencies.
3. A smooth regularization term is chosen for the Mars spectra : $\|D \star I_{Mars}\|_2^2$, where D is a discrete first-order derivation operator. This prior promotes smooth solution in order to avoid noise improvement.

All these terms are balanced with two hyperparameters λ_K and λ_{Mars} , both positive. The functional 6 is convex for each variables - convex in I_{Mars} when K_{PFS} is fixed and vice versa - but not from the couple (I_{Mars}, K_{PFS}). The strategy we choose here is a classical alternative procedure: from initial guesses $\hat{I}^0_{Mars}$, an iterative procedure updates successively at each iteration n, the new estimates $\hat{K}^{n+1}_{PFS}$ and $\hat{I}^{n+1}_{Mars}$.

2.2.1. Iterative procedure

At each iteration n we estimate successively the kernel $\hat{K}^{n+1}_{PFS}$ and the signal $\hat{I}^{n+1}_{Mars}$ until iteration N using the following steps:

1. First estimation of the kernel $\hat{K}^1_{PFS}$ from filtered $\hat{I}^0_{Mars}$ and I_{PFS} with L1 regularization
2. Iterative loop:
   (a) estimation of the Mars spectra $\hat{I}^{n+1}_{Mars}$ from unfiltered $\hat{K}^n_{PFS}$ and I_{PFS} with smooth regularization
   (b) estimation of the kernel $\hat{K}^{n+1}_{PFS}$ from unfiltered $\hat{I}^{n+1}_{Mars}$ and I_{PFS} with L1 regularization
3. Last estimation of the Mars spectra $\hat{I}^{final}_{Mars}$ from unfiltered $\hat{K}^{final}_{PFS}$ and I_{PFS}

For both estimations, a convex optimization algorithm converges to the solution defined by the minimum of a criteria made of a data match and a regularizations

terms. This means that the solution is unique and can be estimated either analytically or iteratively.

Since the first step of the iterative procedure is the estimation of the kernel $\hat{K}^1_{PFS}$, the only a priori information of this iterative procedure $\hat{I}^0_{Mars}$, estimated ab initio. Since $\hat{I}^0_{Mars}$, can only be estimated at large scale (all absorption lines may differ from spectra to spectra due to non-homogeneity of chemical compounds in the atmosphere/surface of Mars), the first iteration is done in a low-pass filtered space, as described in section 2.2.2.

Estimation of the PFS kernel. The estimation of the PFS kernel reduce to the following ℓ_1 regularized convex (non smooth) problem:

$$\hat{K}^{n+1}_{PFS} = \underset{K_{PFS}}{\operatorname{argmin}} \frac{1}{2}\|I_{PFS} - K_{PFS} \star \hat{I}^n_{Mars}\|_2^2 + \lambda_K \|K_{PFS}\|_1 \ , \tag{7}$$

where $\hat{I}^n_{Mars}$ is the estimation of the Mars spectra at the iteration number n. This problem is the well known Lasso (Tibshirani, 1996) or Basis-Pursuit Denoising (Chen et al., 1998) problem, and can be solved efficiently with the Fast Iterative/Thresholding Algorithm (FISTA) (Beck and Teboulle, 2009). Denoting by $\tilde{I}$ the adjoint of the kernel I and by S_λ the so-called soft-thresholding operator[1] the algorithm reads:

1. Let $i = 0$, $\tau^0 = 1$, $k = 1$, $Z^0 = K^n_{PFS}$ and $L = \|I_{Mars}\|^2$.
2. $K^i_{PFS} = S_{\lambda_K/L}\left(Z^i + \frac{1}{L}(I_{PFS} - Z^i \star \hat{I}^n_{Mars}) \star \tilde{\hat{I}}^n_{Mars}\right)$
3. $\tau^{i+1} = \frac{1+\sqrt{1+4\tau^{i^2}}}{2}$
4. $Z^{i+1} = K^i_{PFS} + \frac{\tau^i - 1}{\tau^{i+1}}(K^i_{PFS} - K^{i-1}_{PFS})$
5. $i = i + 1$
6. Go to 2 until $i = i_{max}$
7. $K^{n+1}_{PFS} = K^{i_{max}}_{PFS}$

From theoretical consideration, the kernel K_{PFS} must be a dirac-shape on zero, so we concentrate the energy around zero into a dirac to create the kernel estimation $\hat{K}^n_{PFS}$. We would like to emphasize that there is no analytical solution of eq. 7 so we solve this equation with an iterative procedure, initialized with the previous step K^n_{PFS}. For the first initialization K^0_{PFS}, we may use $\hat{K}^{approx}_{PFS}$ but any other guess (such zero) may apply when the laser line has been switch off. Nevertheless, closer the initialization, faster the convergence.

Estimation of the Mars spectra. For the Mars spectra, the estimation reduces to a classical Thikonov regularization (Idier, 2008):

$$\hat{I}^{n+1}_{Mars} = \underset{I_{Mars}}{\operatorname{argmin}} \|I_{PFS} - \hat{K}^{n+1}_{PFS} \star I_{Mars}\|_2^2 + \lambda_{Mars}\|D \star I_{Mars}\|_2^2 \tag{8}$$

[1] $S_\lambda(x) = \frac{x}{|x|}\max(|x| - \lambda, 0)$

Thanks to the fact that a convolution is diagonal in the Fourier domain, and the Parseval theorem, the solution reads:

$$\mathcal{F}(\hat{I}_{Mars}^{n+1}) = \underset{\mathcal{F}(I_{Mars})}{\operatorname{argmin}} \|\mathcal{F}(I_{PFS}) - \mathcal{F}(\hat{K}_{PFS}^{n+1}) \odot \mathcal{F}(I_{Mars})\|_2^2 + \lambda_{Mars} \|\mathcal{F}(D) \odot \mathcal{F}(I_{Mars})\|_2^2 \tag{9}$$

where $\odot$ is the Hadarmard element-wise product and $\mathcal{F}$ the Fourier transform. Then, the estimation of the Mars spectra at iteration $n+1$ is given in close form by :

$$\hat{I}_{Mars}^{n+1} = \mathcal{F}^{-1}\left(\mathcal{F}(I_{PFS}) \odot (\mathcal{F}(\hat{K}_{PFS}^{n+1})^{-2} - \lambda_{Mars}\mathcal{F}(D)^{-2})\right) \tag{10}$$

,

where $\mathcal{F}(\hat{K}_{PFS}^{n+1})^{-2}$ (resp. $\mathcal{F}(D)^{-2}$) represents the vector containing the inverted squared elements of the vector $\mathcal{F}(\hat{K}_{PFS}^{n+1})$ (resp. $\mathcal{F}(D)$).

We would like to emphasize that equation 10 is the analytical solution of eq 8 that did not require initialization.

2.2.2. Initial guesses of the Martian spectra and PFS kernel

Initial Mars spectra guess. We estimate the Martian spectra large scale feature (noted $\hat{I}_{Mars}^{0}$) by two Planck functions and the major absorption feature, representing (i) the Martian thermal emission and (ii) the solar energy reflected back by Mars and (iii) the 2200-2400 cm^{-1} gap, representing the CO_2 absorption band. The Martian temperature is estimated by fitting the 2500-3000 cm^{-1} domain, where the ghost seems to be less pronounced. The Planck function of the sun is scaled to the 3800-4200 cm^{-1} domain. We derive the raw spectra using the calibrations of detector responsivity and deep space measurements (Giuranna et al., 2005b). This initial guess is only valid at large scale because the absorption lines of major and minor gases may change, due to local pressure, atmospheric circulation, surface change and radiative transfer effects.

The phase of the initial guess is taken similar to the signal in the domain where the ghosts are absent and a constant extrapolation is proposed to the ghosted region.

Because the iterative procedure is sensitive to initialization, both PFS spectra I_{PFS} and mars initial guess $\hat{I}_{Mars}^{0}$ are filtered with a low-pass filter with a cut off frequency of $\frac{1}{20\triangle\sigma}$, where $\triangle\sigma = 1.02$ cm^{-1} is the spectral resolution, in order to keep the realistic features.

The initial guess $\hat{I}_{Mars}^{0}$ will force the initial step of the iterative procedure to find a local minimum around physical solution. Initializing the procedure with random or constant signal lead to non physical solutions.

Initial PFS Kernel guess. Thanks to the approximation from Shatalina et al., 2013, an estimation of the kernel $\hat{K}_{PFS}^{approx}$ from the laser line domain can be done (see section 2.3). Neither amplitudes, nor phases are precise but the frequencies

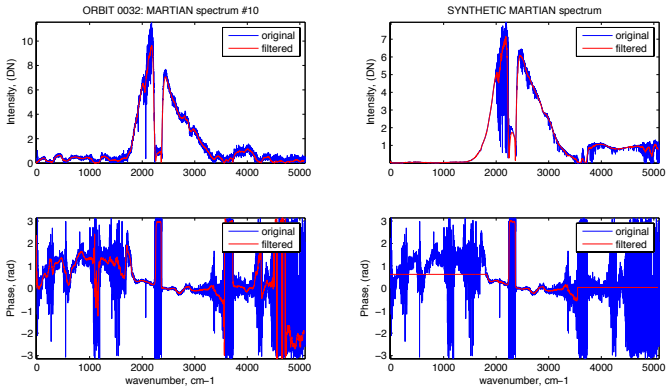


Figure 3: Raw measurements I_{PFS} (on left) and initial guess of the Martian signal $\hat{I}^0_{Mars}$ (on right) for the PFS measurement ORB0032, No 106.

should be well described by this methodology. This kernel is used as initial guess $\hat{K}^0_{PFS}$ to reach faster the convergence of the first kernel estimation $\hat{K}^1_{PFS}$. Unfortunately, only Mars Express orbit ¡ 634 are usable for this estimation. It represents 310 orbits out of 6255 orbits currently available i.e., less than 5% of the total current orbits.

2.3. Laser line domain (5000 to 8330 cm^{-1})

Knowing that laser line is almost dirac shaped, we could first hypothesize that the kernel K_{PFS} can be directly measured in the laser line domain. Unfortunately due to aliasing (laser line ghosts from left and right are superposed), from $I_{PFS}(\sigma)$ it is not possible to realize an inversion to estimate K_{PFS} because there are twice unknown variables in comparison to known variable. Under strong hypothesis, it is possible to estimate an approximation of $\hat{K}^{approx}_{PFS}$ (Shatalina et al., 2013).

Nevertheless, the recent analytical formulation of the mechanical effects on the laser line, allows us to compute the exact effect of the mechanical vibration on the laser line, knowing the vibration kernel K_{PFS} (see complex expression in Shatalina et al. (2013)). After the estimation of K_{PFS}, one simple test of coherence would be to compare the observed laser line ghost to the one predicted.

2.4. Quality of the results

We propose several criteria to estimate if the deconvolution is correct.

2.4.1. Distance between real and simulated PFS spectra

Because the only ground truth we could have is the real PFS spectra I_{PFS}, it should be as close as possible to the final simulated PFS spectra $\hat{I}^{final}_{PFS} =$

$\hat{I}^{final}_{Mars} \star \hat{K}^{final}_{PFS}$. We use the Root Mean Square distance (RMS) of $\hat{I}^{final}_{PFS} - I_{PFS}$. In this way, we evaluate at the same time the correctness of the estimated Mars spectra $\hat{I}^{final}_{Mars}$ and the instrument model $\hat{K}^{final}_{PFS}$.

2.4.2. Ghost removal in the signal domain (0 to 5000 cm^{-1})

In the 1 to 1530 cm^{-1} wavenumber domain, no signal is expected due to the very low signal to noise ratio but only the ghosts are present in the raw spectra. Thus, one simple criterion to estimate the efficiency of the correction is to measure the energy in this domain.

2.4.3. Ghosts in the laser line domain (5000 to 8330 cm^{-1})

The laser line modulated $\hat{I}^{final}_{LM}$ through filter, aliasing and vibrations effects can be computed from the estimated kernel $\hat{K}^{final}_{PFS}$ using the exact formulation of Shatalina et al., 2013. To check the quality of the results, we evaluate the distance between the actually measured signal and the predicted laser line modulated with its ghosts.

2.4.4. Distance to the approximated kernel

The estimation of the kernel $\hat{K}^{approx}_{PFS}$ from the laser line domain can be done. Neither amplitudes, nor phases are precise but the frequencies should well described by this methodology. The distance between $\hat{K}^{approx}_{PFS}$ and $\hat{K}^{final}_{PFS}$ is also a criteria of good results.

2.4.5. Comparison with vibration frequencies from MEx telemetry and technical specification

Several sources of vibrations are present in the MEx platform, mainly reaction wheels, Inertia Measurement Unit (IMU) dithering. PFS eigenmodes can also be exited and are considered as "source" of vibrations. Since, these vibrations are not unique onboard MEx (cryocooler, other instruments, ...) and the uncertainties on these vibrations frequencies are not known, it is not possible to have a supervised approach. One also have to note that all vibration frequencies may not be present in a PFS spectrum, depending the coupling with PFS. Nevertheless, a comparison between our blind estimation and the actual data is interesting.

From each vibration frequency f_d (in Hz), the perturbation is at wavenumber $\sigma = f_d/v_m$ (Saggin et al., 2007; Shatalina et al., 2013), with the pendulum speed $v_m = d_{zc}.f_{zc}$ where the zero-crossing frequencies f_{zc} is 2500 Hz and zero-crossing length d_{zc} is 1.2 microns for typical PFS measurements at Mars (Giuranna et al., 2005b).

Reaction wheels. Thanks to telemetry data from ESA, it is possible to estimate the frequencies of reaction wheels for ORB0032, spectra No 106 at 56.7 Hz, 33.3 Hz, 40.6 Hz and 30.3 Hz. Uncertainties are unknown.

IMU. Astrium technical specification of MEx (MEX.MMT.HO.2379) states that the IMU dithering onboard MEx are at 513.9 Hz, 564.3 Hz and 617.4 Hz. Uncertainties are unknown.

PFS eigenmodes. The PFS eigenmodes are around 135 Hz and 160 Hz. Uncertainties are unknown.

3. Results

Due to the stochastic character of the ghosts and especially their phase, few % of the PFS spectra in the archive, randomly distributed, present significant level of perturbations. In some lucky cases, the ghosts are absent but typical spectra contains few ghosts (Comolli and Saggin, 2010). We propose to illustrate our algorithm on the ORB0032, spectra No 106 of PFS, recorded in particularly high level of disturbances. This spectra contains several obvious ghosts (as shown by the arrows in fig. 5).

We find that the optimum inversion is reached with a loop of N=2, with special parameter for the first step due using the filtered initialization (λ_K=50) and then usual parameter (λ_{Mars}=0.001, λ_K=1) using the unfiltered spectra .

3.1. Mars spectra and kernel estimations obtained

For Mars spectra estimation, the final estimation of the signal $\hat{I}^{final}_{Mars}$ is presented in fig. 4 and 5. This figure presents the raw spectra, our corrected spectra in comparison with a synthetic spectra $\hat{I}^{0}_{Mars}$ (see section 2.2.2) and also the stack of 20 spectra. Our correction clearly removes the ghosts in the region at 0-1530 cm^{-1}, around 2700 cm^{-1}, around 3450 cm^{-1}, around 4150 cm^{-1} similar to the stacking method. The artifact at 2900 cm^{-1} persists, due to pollution of hydrocarbons in the telescope (Giuranna et al., 2005b). In the 4000-5000 cm^{-1} domain, our method improves the signal in comparison to the stacking method and partly correct the artificial decrease of the signal. The stacking clearly reduces the stochastic noise, that is not removed with our correction.

Figure 6 shows the evolution of the average spectra, when stacking 3, 5, 11 and 19 spectra. The plots clearly show that our method removes the ghosts contribution, already without stacking. In contrary, the stacking methods require ∼10 spectra to remove this effect. The signal to noise ratio at small scale, estimated by the standard deviation in the 0-1530 cm^{-1}, is not significantly changed between both methods.

The stack of ∼10 spectra correspond to ∼10 spots of around 7 km each, so that the spatial resolution can be improved by one order of magnitude. In term of temporal resolution improvement, it depends mainly on the location due to the very irregular observation density.

3.2. Quality of the results

As illustrated in Fig. 4, the lack of fit between the real PFS spectra I_{PFS} and the simulated one from our final guesses $\hat{I}^{final}_{PFS} = \hat{I}^{final}_{Mars} \star \hat{K}^{final}_{PFS}$ is very small ($\sim 10^{-5}$), showing that the solution is compatible with the observation.

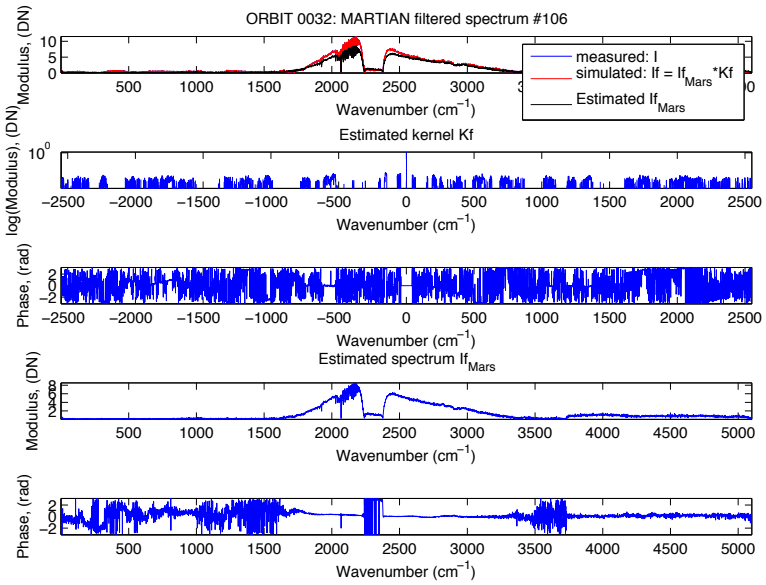


Figure 4: Final results of the spectra ORB0032 #106: at the top: modulus of measured I_{PFS} (blue) simulated $\hat{I}^{final}_{PFS} = \hat{I}^{final}_{Mars} \star \hat{K}^{final}_{PFS}$ PFS spectra (red) and the estimated Martian spectra $\hat{I}^{final}_{Mars}$ (black); Lack of fit between I_{PFS} and $\hat{I}^{final}_{PFS}$ is $1.8\ 10^{-5}$;in the middle: modulus (in log scale) and phase of the final estimated kernel $\hat{K}^{final}_{PFS}$; at the bottom: modulus and phase of the final estimated spectrum $\hat{I}^{final}_{Mars}$.

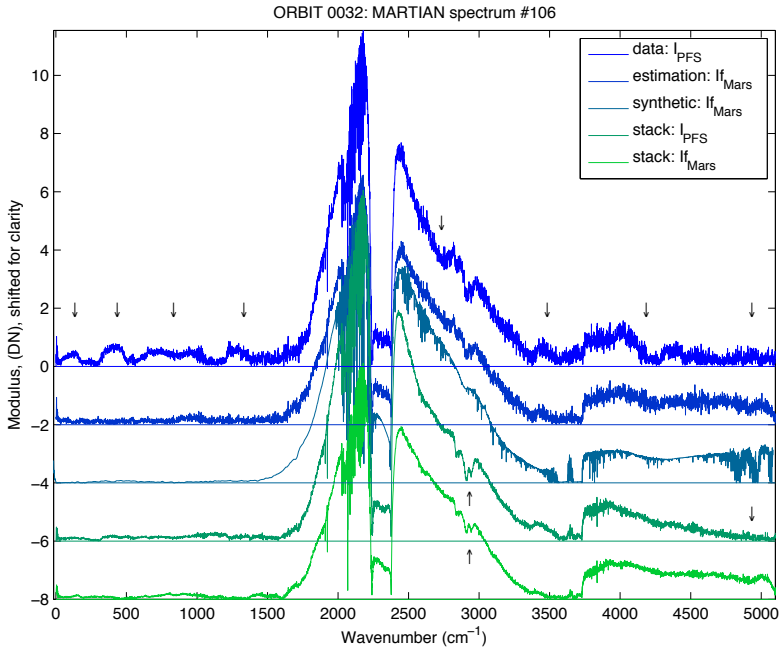


Figure 5: Final results of the spectra ORB0032 #106 as compared with stacking and synthetic measurements, from top to bottom : (i) raw PFS measurements, all arrows represents ghosts artifacts, (ii) estimated spectra from our algorithm, (iii) synthetic measurement of PFS, (iv) stack of 11 PFS spectra, (v) stack of 11 estimated spectra from our algorithm. The arrow at 2900 cm^{-1} represents the telescope contamination by hydrocarbons, the arrow at 4900 cm^{-1} represents an artifact of abnormal small signal, probably due to ghosts.

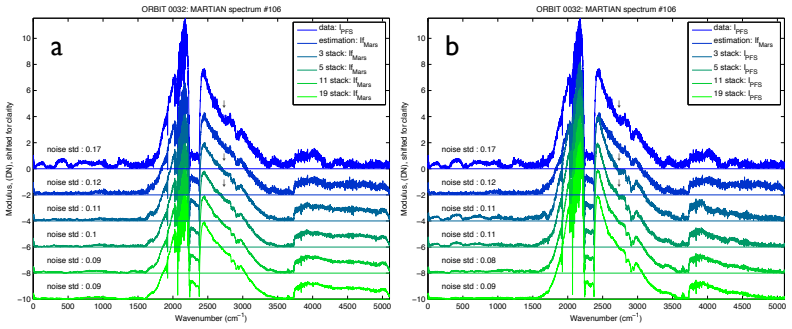


Figure 6: Comparison of our correction versus the stacking method : (a) Stacking of corrected spectra from our method (b) Stacking of PFS spectra. Noise standard deviation from the 0-1530 cm^{-1} are expressed for all spectra. Arrows at 2700 cm^{-1} represent significant difference in the signal domain due to ghosts, that persists for stacking of at least 5 PFS spectra but well corrected by our method.

The ghost removal in the 1 to 1530 cm^{-1} domain is efficient to remove the norm by a factor of ~ 2 (the RMS is 0.0093 for the raw spectra and to 0.0042 for the corrected spectra). The only signal left in $\hat{I}^{final}_{Mars}$ seems to be random, as expected (see Fig. 4). The theoretical value of noise standard deviation is about 0.1 using the estimated Signal to Noise ratio of about 100 in the 2000-2400 cm^{-1} Giuranna et al. (2005b). The estimated noise standard deviation of corrected spectra is in agreement with this value (see fig. 6).

The laser line modulated $\hat{I}^{final}_{LM}$ through filter, aliasing and vibration kernel $\hat{K}^{final}_{PFS}$ are compatible with the observation I_{LM} (see Fig. 7). The four mains peaks are estimated and also some smaller peaks. The distance is relatively small (~ 0.013).

The final kernel estimation $\hat{K}^{final}_{PFS}$ is close to the initial kernel guess $\hat{K}^{0}_{PFS} = \hat{K}^{approx}_{PFS}$ with a distance $\sim 10^{-5}$. As illustrated in Fig. 8, the main vibration frequencies estimated in $\hat{K}^{approx}_{PFS}$ are present in $\hat{K}^{final}_{PFS}$. The estimation of $\hat{K}^{approx}_{PFS}$ has been done under strong approximation. Especially the unconstrained amplitude may explain the differences. Also $\hat{K}^{final}_{PFS}$ presents a smooth signal due to the high frequencies filtering. Other methods without sparsity regularization doesn't succeed to get such a sparse kernel although we believe that the kernel is sparse due to limited vibrations in the mechanical environment of PFS onboard MEx (eigenmode of PFS, reaction wheels frequencies, inertia measurement unit dithering frequencies).

4. Discussion and conclusion

We described the approximated direct problem and an algorithm able to correct for the mechanical vibration of the PFS instrument. For the first time, we show that it is possible to reduce significantly the ghosts from the observed

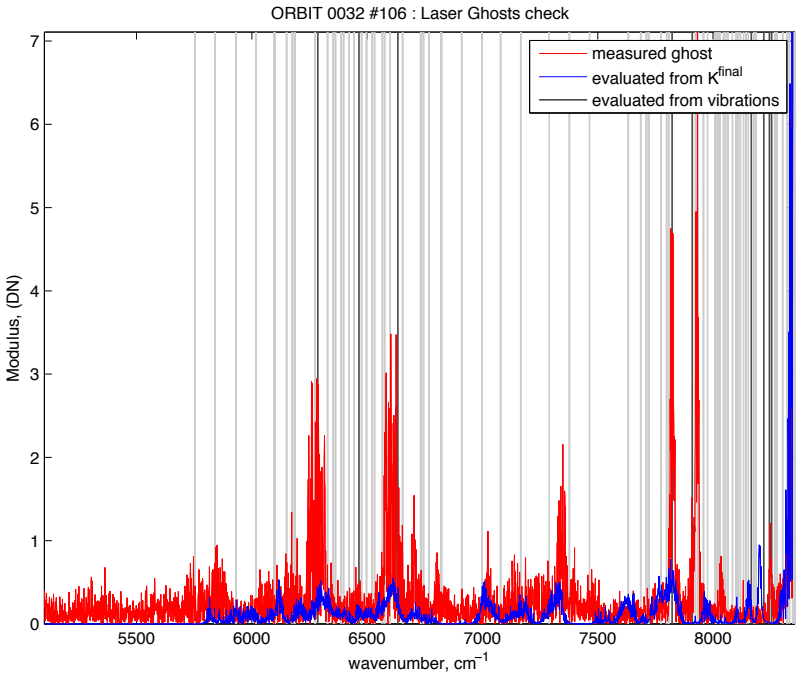


Figure 7: Modulus of the simulated laser line modulated $\hat{I}_{LM}^{final}$ through filter, aliasing and vibration kernel $\hat{K}_{PFS}^{final}$ (blue) and the observation I_{LM} (red). The lack of fit is 0.0270

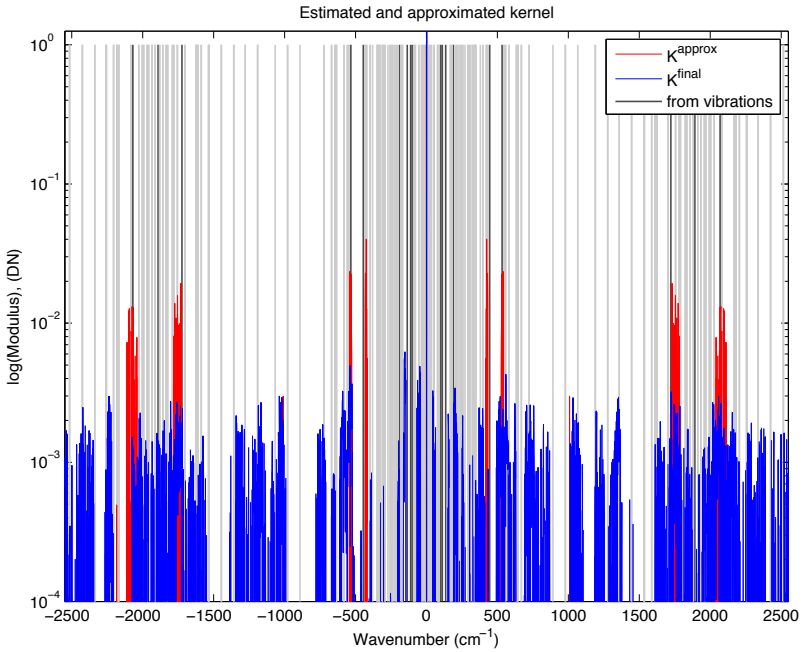


Figure 8: Modulus in log scale of the vibration kernel $\hat{K}_{PFS}^{final}$ (blue line), the approximated kernel $\hat{K}_{PFS}^{approx}$ (red line)and the reaction wheels vibration (dark grey line), and the combination of reaction wheels (light grey line). The lack of fit is3.2 10^{-4}.

signal using three coherent quantities: ghosts in the signal domain, laser line ghosts, distance to approximated kernel. Thus the global shape of PFS spectra can be corrected with our algorithm, allowing to better estimate temperature, and thermal profile on each PFS measurement, improving the few % of spectra with high χ^2 that could not be processed with current calibration (Grassi et al., 2005). Also, our correction may avoid the continuum removal step in the minor species retrieval (Sindoni et al., 2011). When the signal to noise ratio is high enough, our correction will also reduce the stacking procedure.

In the future, we would like to propose an algorithm to correct the complete archive that would require: efficient algorithm, timesaving implementation, and fully automatic procedure. Also, new correction procedure must be developed to treat the whole orbits currently available (6255 at the date of writing).

In order to correct any shaked FTS, semi-blind deconvolution is possible, knowing $\hat{I}^0_{Mars}$ (but without knowing $\hat{K}^{approx}_{PFS}$ from the "laser line domain") so that the "signal domain" only is required. Thus, any techniques of optical path measurement (laser line, mechanical, etc...) can be corrected with our technique. Nevertheless, the independent estimation of the kernel $\hat{K}^{approx}_{PFS}$ significantly improve the convergence of the algorithm. The only limitation to apply this method on other instruments is about the convolution equation. Convolution is true if the signal from the planet I_{Mars} has a significantly reduced wavenumber domain (as stated in eq. 1-3).

Acknowledgement

We acknowledge support from the "Institut National des Sciences de l'Univers" (INSU), the "Centre National de la Recherche Scientifique" (CNRS) and "Centre National d'Etude Spatiale" (CNES) and through the "Programme National de Planétologie". We also thank the European Space Agency' (ESA) for providing the reaction wheels speed of MEx.

References

Beck, A., Teboulle, M., 2009. A fast iterative shrinkage-thresholding algorithm for linear inverse problems. SIAM Journal on Imaging Sciences 2 (1), 183–202.

Chen, S., Donoho, D., Saunders, M., 1998. Atomic decomposition by basis pursuit. SIAM Journal on Scientific Computing 20 (1), 33–61.

Comolli, L., Saggin, B., Dec. 2005. Evaluation of the sensitivity to mechanical vibrations of an ir fourier spectrometer. Rev. Sci. Instrum. 76 (12), 123112–8. URL http://dx.doi.org/10.1063/1.2149009

Comolli, L., Saggin, B., Apr. 2010. Analysis of disturbances in the planetary fourier spectrometer through numerical modeling. Planetary and Space Science 58 (5), 864–874.
URL http://www.sciencedirect.com/science/article/B6V6T-4Y9CFBX-2/2/950f692b594101f9b0558dae213e3fc1

Formisano, V., Angrilli, F., Arnold, G., Atreya, S., Bianchini, G., Biondi, D., Blanco, A., Blecka, M., Coradini, A., Colangeli, L., Ekonomov, A., Esposito, F., Fonti, S., Giuranna, M., Grassi, D., Gnedykh, V., Grigoriev, A., Hansen, G., Hirsh, H., Khatuntsev, I., Kiselev, A., Ignatiev, N., Jurewicz, A., Lellouch, E., Lopez Moreno, J., Marten, A., Mattana, A., Maturilli, A., Mencarelli, E., Michalska, M., Moroz, V., Moshkin, B., Nespoli, F., Nikolsky, Y., Orfei, R., Orleanski, P., Orofino, V., Palomba, E., Patsaev, D., Piccioni, G., Rataj, M., Rodrigo, R., Rodriguez, J., Rossi, M., Saggin, B., Titov, D., Zasova, L., Aug. 2005. The planetary fourier spectrometer (pfs) onboard the european mars express mission. Planetary and Space Science 53 (10), 963–974.
URL http://www.sciencedirect.com/science/article/B6V6T-4G94HR4-2/2/c10c243741b6a0444b7d58665e9ec980

Giuranna, M., Formisano, V., Biondi, D., Ekonomov, A., Fonti, S., Grassi, D., Hirsch, H., Khatuntsev, I., Ignatiev, N., Malgoska, M., Mattana, A., Maturilli, A., Mencarelli, E., Nespoli, F., Orfei, R., Orleanski, P., Piccioni, G., Rataj, M., Saggin, B., Zasova, L., Aug. 2005a. Calibration of the planetary fourier spectrometer long wavelength channel. Planetary and Space Science 53 (10), 993–1007.
URL http://www.sciencedirect.com/science/article/B6V6T-4GCX0HK-1/2/9d8e4485b4eb45a54082fef03d4718a5

Giuranna, M., Formisano, V., Biondi, D., Ekonomov, A., Fonti, S., Grassi, D., Hirsch, H., Khatuntsev, I., Ignatiev, N., Michalska, M., Mattana, A., Maturilli, A., Moshkin, B., Mencarelli, E., Nespoli, F., Orfei, R., Orleanski, P., Piccioni, G., Rataj, M., Saggin, B., Zasova, L., Aug. 2005b. Calibration of the planetary fourier spectrometer short wavelength channel. Planetary and Space Science 53 (10), 975–991.
URL http://www.sciencedirect.com/science/article/B6V6T-4GCX1K5-2/2/a2f8e53774cbfb604eedcff6055edf4c

Grassi, D., Ignatiev, N., Zasova, L., Maturilli, A., Formisano, V., Bianchini, G., Giuranna, M., Aug. 2005. Methods for the analysis of data from the planetary fourier spectrometer on the mars express mission. Planetary and Space Science 53 (10), 1017–1034.
URL http://www.sciencedirect.com/science/article/pii/S0032063305000693

Idier, J. (Ed.), avr. 2008. Bayesian Approach to Inverse Problems. ISTE Ltd and John Wiley & Sons Inc.

Saggin, B., Comolli, L., Formisano, V., Aug. 2007. Mechanical disturbances in fourier spectrometers. Appl. Opt. 46 (22), 5248–5256.
URL http://ao.osa.org/abstract.cfm?URI=ao-46-22-5248

Shatalina, I., Schmidt, F., Saggin, B., Gac, N., Kowalski, M., Giuranna, M., Nhean, S., 2013. Combined microvibrations effects on Fourier Spectrometer. Aerospace Science and Technology submitted.

Sindoni, G., Formisano, V., Geminale, A., Feb. 2011. Observations of water vapour and carbon monoxide in the martian atmosphere with the swc of pfs/mex. Planetary and Space Science 59 (2-3), 149–162.
URL http://www.sciencedirect.com/science/article/B6V6T-51TGG5K-1/2/fdab0daa9bc5411b1c90cafa0ca13bae

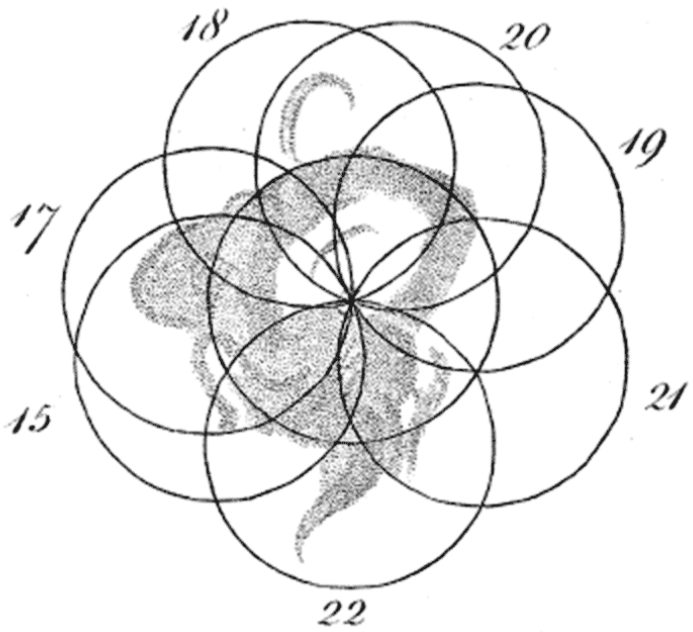
Tibshirani, R., 1996. Regression shrinkage and selection via the lasso. Journal of the Royal Statistical Society Serie B 58 (1), 267–288.

Deuxième partie

Echanges de volatils sur Mars

Chapitre 4

La calotte saisonnière sud de Mars



Première évidence de l'asymétrie de la calotte permanente sud (désaxée par rapport au pôle géographique) en 1784 par W. Herschel [128].

Les calottes polaires saisonnières de Mars signent une activité actuelle la plus visible de Mars. A l'échelle de la planète entière, cette activité a été observée depuis plus d'une centaine d'année. Aujourd'hui, grâce à des résolutions spatiales de plus en plus fines, de nombreux phénomènes d'activités ont été observés, dont certains sont liés aux variations saisonnières. Je me suis particulièrement intéressé à la calotte saisonnière sud de Mars car elle est majoritairement constituée de glace de CO_2 et de ce point de vue, plus facile à étudier que la calotte saisonnière nord, comportant à la fois du CO_2 et de l'eau.

Le premier sous-chapitre décrit les différents aspects de l'étude de la calotte sud de Mars, d'un point de vue historique, notre compréhension actuelle et ses incomplétudes. La synthèse des contributions de ma carrière sont détaillées au sous-chapitre 4.2 page 207. Plusieurs travaux spectroscopiques et de simulations sont en cours de développement dans la thèse de François Andrieu. Les perspectives sont décrites à la section 4.3 page 212.

4.1 Contexte

4.1.1 Histoire des observations des calottes martiennes

La première observation d'une calotte martienne, a été faite par C. Huygens durant l'opposition de septembre 1672. Certains historiens, exhibant un dessin de 1666, proposent d'attribuer la découverte à J.D. Cassini. La polémique réside dans le fait que ce schéma fait apparaître la calotte de la même couleur blanche que le limbe.
Néanmoins, la première mise en évidence de la calotte saisonnière a été produite par G.F. Maraldi, le neveu de J.D. Cassini. Ses observations, à l'Observatoire de Paris, montrent que la calotte saisonnière a complètement disparu en août et septembre 1719. Il prouve alors que les conditions physiques de la région polaire changent au cours du temps. Cependant, il n'avance aucune interprétation.

Il faut attendre 1784 et l'émergence d'une nouvelle génération de télescopes pour que W. Herschel, un allemand membre de la Royal Society of London, interprète ces observations comme étant de la neige d'eau au pôle [128].

> The analogy between Mars and the earth is, perhaps, by far the greatest in the whole solar system. The diurnal motion is nearly the same ; the obliquity of their respective ecliptics, on which the seasons depend, not very different ; of all the superior planets the distance of Mars from the sun is by far the nearest alike to that of the earth : nor will the length of the martial year appear very different from that which we enjoy, when compared to the surprising duration of the years of Jupiter, Saturn, and the Georgium Sidus. If, then, we find that the globe we inhabit has its polar regions frozen and covered with mountains of ice and snow, that only partly melt when alternately exposed to the sun, I may well be permitted to surmise that the same causes may probably have the same effect on the globe of Mars ; that the bright polar spots are owing to the vivid reflection of light from frozen regions ; and that the reduction of those spots is to be ascribed to their being exposed to the sun.

Herschel observe pour la première fois que la calotte permanente sud est désaxée par rapport au pôle géographique (voir page précédente). En 1877, quelques années avant la photographie, G.V. Schiaparelli dresse sa célèbre carte de Mars, à l'Observatoire de Brera, en Italie. Il utilise un vocabulaire biblique et mythologique pour nommer les lieux martiens. De la même manière que pour la Lune, les zones sombres sont désignées par des noms appartenant au champ sémantique de l'eau, comme : Mare Sirenum (Mer des Sirènes), Mare Cimmerium (Mer des Cimmériens),.... Les zones claires sont nommées par des termes désignant la terre, comme : Ausonia (Italie), Hellas (Grèce), ... Il ne prétend pas la portée universelle de sa classification :

> I do not ask that the [nomenclature] be approved by astronomers in general, nor do I request the honor of its universal acceptance. To the contrary, I am ready to accept as final whichever one is recognised by competent authority. Until then, however, grant me the

> chimera of these euphonic names, whose sounds awaken in the mind so many beautiful memories.

Utilisant une technique basée sur la persistance rétinienne, il parvient à dessiner des détails de la planète Mars. Malgré son daltonisme qui lui interdit de distinguer le rouge et le vert, il observe les détails photométriques avec une précision incomparable.
En 1877, Schiaparelli observe des formes linéaires sombres qu'il appelle *canali* ou canal. Cette nomenclature et les canaux vont induire une série d'interprétations qui paraissent aujourd'hui insensées (voir illustration page 265).

Les premiers arguments spectroscopiques datent des années 1860-1870. Notamment, le français Jules Janssen, relate en 1867 la détection de vapeur d'eau, d'après ses observations effectuées au mont Etna. Cependant, à l'époque, la correction des effets atmosphériques terrestres sur les spectres n'est pas très bonne.

En 1892, la récession de la calotte sud de Mars est à nouveau apparente. Percival Lowell observe une bande noire autour de la calotte brillante qui disparaît peu à peu. Il interprète cette figure comme un océan polaire en anneau. Embrassant les visions de Schiaparelli sur les canaux formés d'eau et celle de la végétation de Liais et Pickering, Lowell, astronome fondateur de l'Observatoire de Flagstaff, Arizona (USA), propose la théorie suivante. Mars serait une planète habitée en voie de désertification. La seule source d'eau liquide, nécessaire à ses habitants serait située au pôle, au moment où la glace fond. La forme de vie intelligente construit des canaux d'irrigation qui permettent de transporter la précieuse eau des pôles vers l'équateur. Le succès populaire de cette théorie lui vaut une renommée mondiale. Lowell écrira beaucoup de livres grand public [198]. L'astronome ira jusqu'à écrire que la température de Mars est "confortable comme le sud de l'Angleterre".

A l'Observatoire Lick du mont Hamilton en Californie, W.W. Campbell propose des observations spectroscopiques de Mars en 1894 [28]. Il montre que le comportement spectral de Mars est en tout point similaire à celui de la Lune. Il prétend que l'atmosphère martienne est très fine et que la détection d'eau n'est pas possible, car elle n'existe qu'en très petite quantité. Cependant, il ne doute pas que la calotte soit faite d'eau.

Au début du XXème siècle, se développe une théorie alternative sous l'impulsion notamment de A. R. Wallace qui critique sans égards le raisonnement de Lowell à propos de la température de Mars [334]. Dans la continuité A. C. Ranyard et G. J. Stoney emettent l'hypothèse que les calottes saisonnières de Mars soient faites de CO_2.

La première mesure quantitative de la température de Mars a été produite par deux équipes, à l'Observatoire Lowell à Flagstaff, avec D. H. Menzel, W. W. Coblentz, et C. O. Lampland, et d'autre part, au Mont Wilson en Californie du sud avec E. Petit et S. B. Nicholson. Les deux équipes ont utilisé un thermocouple et ont conclu à une température maximale atteignant 20°C à 30°C dans les régions sombres et une température minimale au pôle sud de -50°C à -70°C. Ces observations de 1924 suggèrent que la neige carbonique de CO_2 ne se condense pas sur Mars, à cause de la faible pression atmosphérique. Il faudrait une température maximale de -100°C. Ces équipes ont donc conforté l'hypothèse de glace d'eau comme constituant des calottes polaires.
En 1958, des nouvelles mesures spectroscopiques par Kuiper [173] établissent une présence plus probable de glace d'eau que de glace de CO_2.

Dans les années 1950-60, la conquête spatiale bat son plein. La première sonde à destination de Mars est russe : *"*Mars 1*"*, lancée en 1962 et perdue en 1963. En 1965, la première sonde américaine s'appelle : *"*Mariner 3*"*, perdue au lancement. En novembre 1965, la sonde "Mariner 4" est lancée par les Américains, suivi deux jours plus tard de la sonde russe *"*Zond 2". Seule la sonde américaine arrive à communiquer ces surprenants résultats : la surface de Mars est cratérisée et ancienne, semblable à celle de la Lune [186]. La première mesure de pression atmosphérique au sol est faite par transmission radar : la pression est incroyablement faible entre 4 et 6 mbar. Après *"*Mariner 4", Leighton et Murray remettent à jour l'hypothèse de la condensation/sublimation de CO_2 [187].

Les sondes suivantes Mariners 6 and 7, lancées et arrivées en 1969, se font voler la vedette par l'arrivée des premiers hommes sur la Lune. Mariner 7 prouve que la température de la calotte saisonnière

sud est de 145 K, proche de celle de la glace de CO_2 en équilibre avec son gaz pour ces faibles pressions atmosphériques [242, 243].
Herr et Pimentel confirment avec des arguments spectroscopiques à 3 microns que la calotte saisonnière est composée de glace de CO_2 [125]. La même équipe montre la présence de nuage de CO_2 dans la haute atmosphère [126] avec la bande à 4,3 microns.
Dans la foulée, le premier GCM martien, adapté d'un modèle terrestre, voit le jour [188]. Il comporte déjà le processus de condensation de CO_2.

A la suite de toutes ces observations, Murray et al. proposent de différencier la calotte saisonnière composée de glace de CO_2 et la calotte permanente vraisemblablement composée de glace d'eau [236].

En 1976, les landers au sol Viking 1 et 2 mesurent un cycle semi-annuel de pression atmosphérique avec deux minima de pression, à la fin des hivers nord et sud, confirmant les travaux de Leighton et Murray [129]. Les mesures thermiques confirment aussi que la calotte permanente nord est bien composée de glace d'eau [163].

Cet aperçu historique a été en partie établi d'après le livre suivant, disponible sur Internet [294], repris aussi dans mon manuscrit de thèse [283].

4.1.2 La calotte saisonnière sud de Mars

Une synthèse des connaissances actuelles a été dressée lors de ma thèse [283]. Cette section contient un résumé de cette synthèse, complétée des résultats scientifiques plus récents. Dans un premier temps, les observations et les modélisations seront décrites. Dans un second temps, nous détaillerons trois interrogations majeures concernant la calotte saisonnière sud de Mars.

4.1.2.1 Observations

La progression et la récession des dépôts saisonniers des images est l'observable majeure du cycle saisonnier de CO_2 sur Mars. La saison est exprimée en longitude sub-solaire (°Ls), c'est à dire en l'angle qui décrit la position de la planète sur son orbite : l'équinoxe de printemps Nord est à Ls=0°, le solstice d'été Nord à Ls=90°, etc, ...

Imagerie visible Il est possible de comparer les lignes crocus modélisées par les GCM et observées sur Mars, en moyennant en longitude [191]. La variable issue des GCM est la latitude équivalente, au delà de laquelle la surface est entièrement recouverte de dépôts saisonniers de CO_2. Elle est calculée pour des dépôts symétriques autour du pôle géographique, de manière à ce que la surface totale couverte de dépôts prédite par le GCM reste constante. La figure 4.1 page ci-contre montre l'adéquation entre les mesures de Viking [144] et le GCM développé en Europe [191]. Cependant, les images visibles ne distinguent pas de glaces de CO_2 et d'eau. Une première amélioration a été faite avec la température de surface, estimée grâce au flux thermique, mais surtout grâce aux spectro-images dans l'infra-rouge proche.

Imagerie infrarouge Les instruments Infrared Radiometer à bord de Mariner 6 et Mariner 7 ont mesuré pour la première fois la température des dépôts saisonniers à 148°K, indiquant la présence de glace de CO_2 [243]. Les imageurs infrarouges IRTM à bord de Viking [161], puis TES (3 km/pixel) à bord de MGS [165], ont permis de réaliser une cartographie des dépôts saisonniers dans les zones polaires. Des données d'infra-rouge thermiques, grâce à l'instrument PFS, ont aussi permis de tracer l'extension spatiale des glaces [103].

La *date crocus* pour un endroit donné, correspond à la date où la glace est en train de disparaître de la surface. Ce concept a été proposé par Kieffer et al. dans l'analyse des données TES [165]. Il correspond à la date d'inflexion du signal temporel de température (voir fig. 4.2 page suivante). Cette forme est modélisée par une fonction arctan sans justification physique.

La *ligne crocus* à une date donnée, correspond à l'extension spatiale des dépôts saisonniers. C'est la ligne reliant tous les points ayant une *date crocus* similaire. Par exemple, la figure 4.6 page 195 représente l'évolution de la ligne crocus au cours du temps (en °Ls).

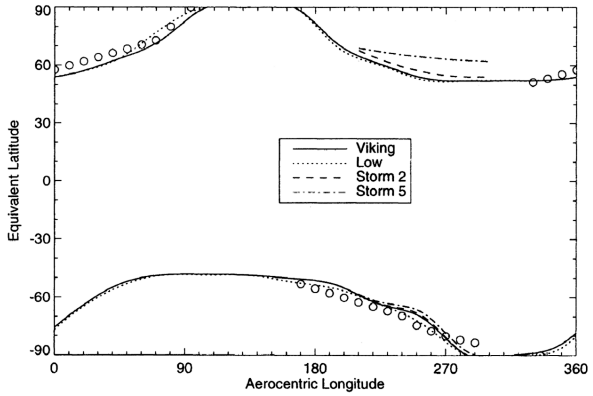


FIGURE 4.1: Comparaison de la surface couverte de dépôts saisonniers entre le GCM "Mars Climate Database" et les données Viking [144] (cercle). Les différentes lignes correspondent à la latitude équivalente pour plusieurs scenarii de profondeur optique de poussière (figure d'après [191]).

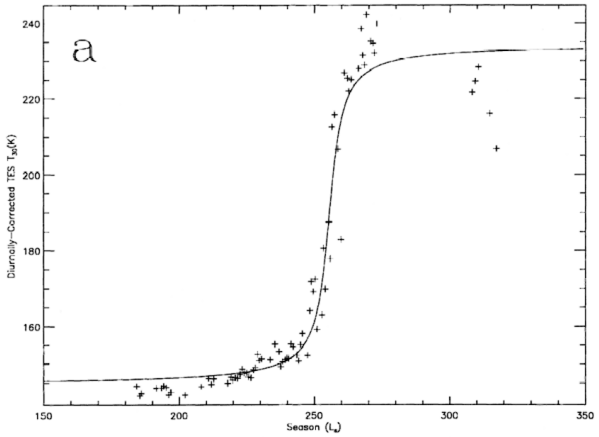


FIGURE 4.2: Définition de la *date crocus*. C'est le point d'inflexion dans le signal temporel de température de brillance (figure d'après [165]).

De plus, les interprétations des données TES indiquent que la calotte saisonnière sud a des comportements temporels complexes, impliquant du CO_2, de l'eau, des poussières [165]. Les données plus récentes de l'imageur infrarouge THEMIS (100 m/pixel) à bord de Mars Odyssey, ont identifié la présence d'un anneau d'eau dans la calotte saisonnière nord [333], et proposent des interprétations de la région cryptique au Sud [166]. Cependant, la distinction entre CO_2 et eau reste très difficile dans l'infrarouge thermique, car seule leur température de condensation permet de les distinguer. En cas de mélange au sein d'un pixel, il est difficile de distinguer les espèces chimiques volatiles.

Spectro-imagerie infra-rouge proche Les identifications spectroscopiques de glaces de CO_2 et d'eau ont pu se faire, dans l'infra-rouge proche, grâce à l'instrument OMEGA à bord MEx, puis CRISM à bord de MRO. D'après ces données, la calotte saisonnière sud est majoritairement constituée de glace de CO_2 avec quelques zones de fortes concentrations en eau [179], contrairement aux zones polaires nord relativement riches en eau [6]. Les données CRISM on été utilisées pour l'analyse de certaines zones spécifiques, notamment dans la région cryptique (voir section 4.1.3.2) [261, 262].

Grâce à la résolution spatiale des données OMEGA infra-rouge proche (~300m), j'ai proposé durant ma thèse une extension de la définition des limites de pôles : les *lignes crocus internes* et *externes* qui séparent le domaine de transition de la bordure de la calotte saisonnière dans laquelle une certaine proportion de surface est déjà nue car les dépôts saisonniers s'y sont sublimés. La *distance snowdrop* caractérise l'extension spatiale de cette zone de transition (voir figure 4.3). Les données OMEGA montrent

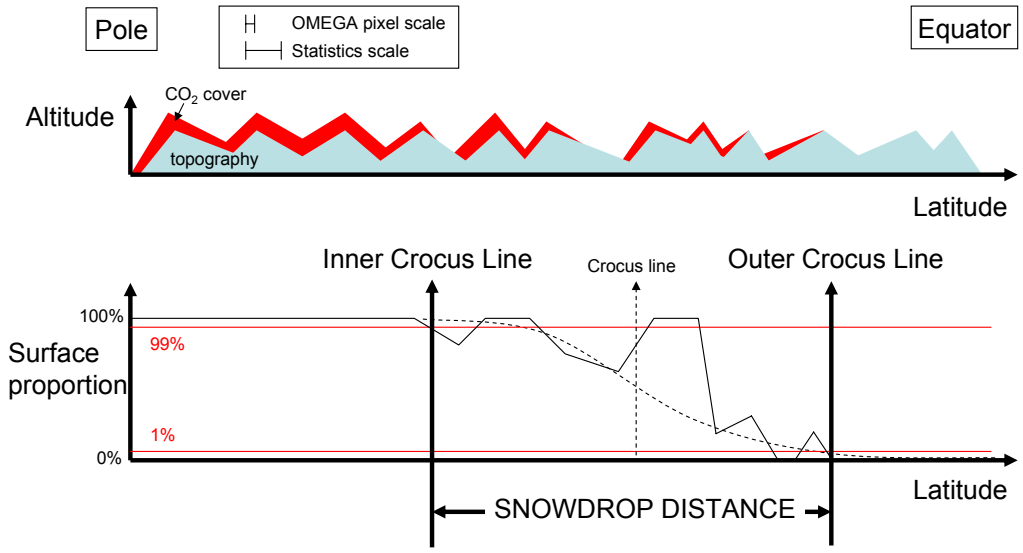


FIGURE 4.3: Définition de la *distance snowdrop*, des *lignes crocus internes* et *externes*. (figure d'après [285]).

clairement des variations spatiales et temporelles de cette zone de transitions (voir figure 4.4)

Pression Le signal de pression atmosphérique au sol, mesuré par Viking Lander 1 et 2, met en évidence plusieurs phénomènes à des échelles de temps différents [320, 134] (voir figure 4.5 a). A l'échelle journalière, l'effet des marées thermiques domine le signal. A l'échelle de quelques jours martiens, les ondes planétaires transitoires impriment leur passage. L'échelle annuelle comporte plusieurs phénomènes saisonniers imbriqués ayant une composante orographique et dynamique. La composante orographique est une variation horizontale de pression due aux différences d'altitude entre les deux hémisphères martiens. Tandis que la composante dynamique est due à l'équilibre géostrophique, responsable des fortes variations de pression en latitude.

Nuages de CO_2 Certaines observations des pôles pendant la nuit permanente, avec l'instrument IRTM de Viking Orbiter, ont mis en évidence des points "froids". Il s'agit de zones très localisées dans l'espace et dans le temps ayant des *températures de brillance* inférieures à 135 K alors que la température de condensation de la glace de CO_2 est de l'ordre de 145-148 K à l'équilibre de pression saturante [164]. Deux explications coexistent actuellement, impliquant de la glace de CO_2 à faible taille de grains, soit à la surface [113], soit dans l'atmosphère [91]. Ces scenarii produisent le même effet : un point froid, c'est à dire une zone de température de brillance anormalement basse. La distribution annuelle à l'échelle globale des points froids parfois est dû aux nuages mais majoritairement dû à de la neige fraîche au sol [139]. Aujourd'hui, les précipitations sont correctement modélisées par les GCM [54], en accord avec les observations de la structure atmosphérique, sursaturées à certains endroits, comme la région cryptique [105].

Récemment, des détections de nuages de CO_2 en haute altitude, dans la mésosphère, ont été découvertes [228, 204, 332], mais ils ne contribuent pas à une précipitation en surface.

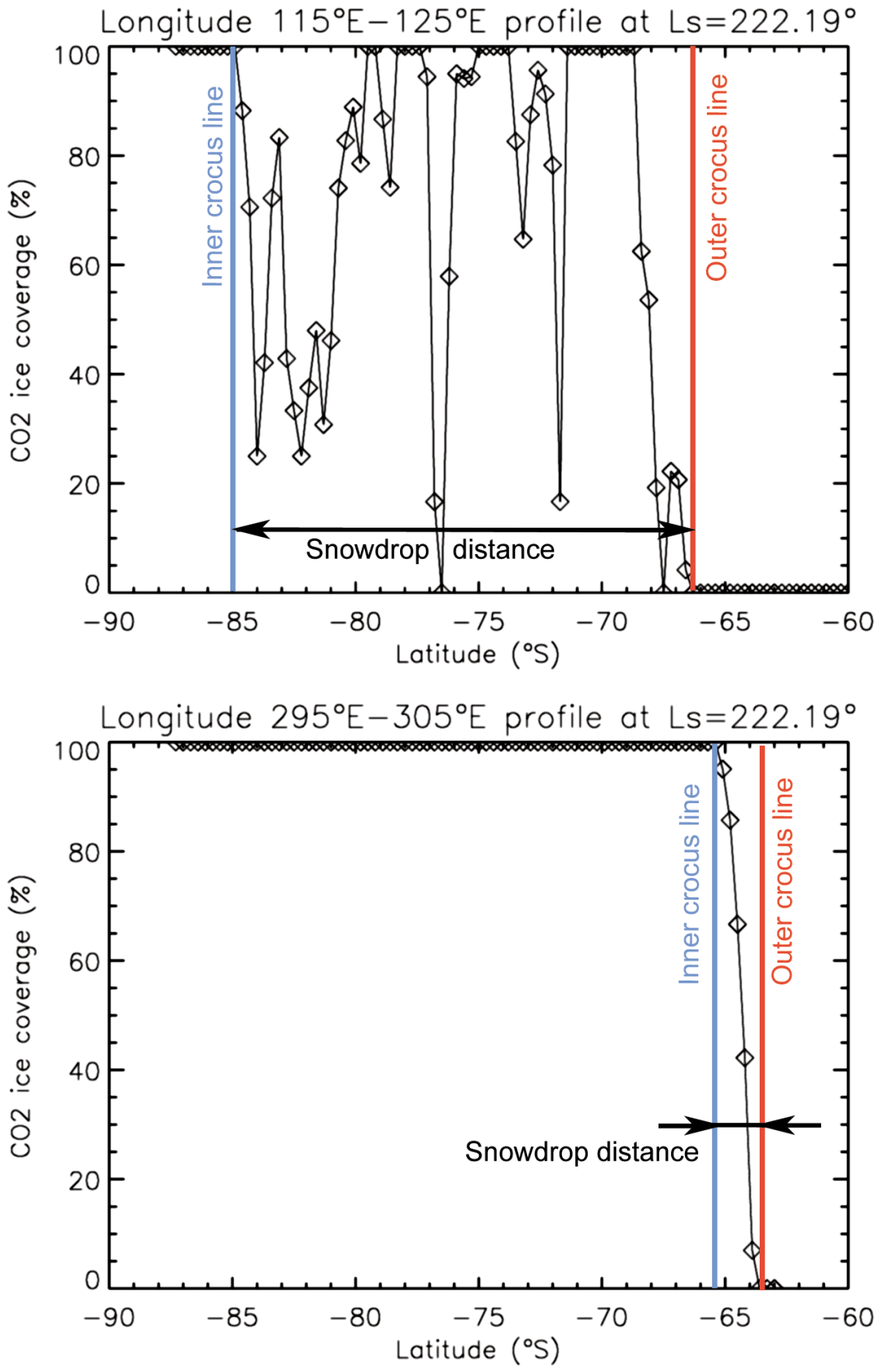
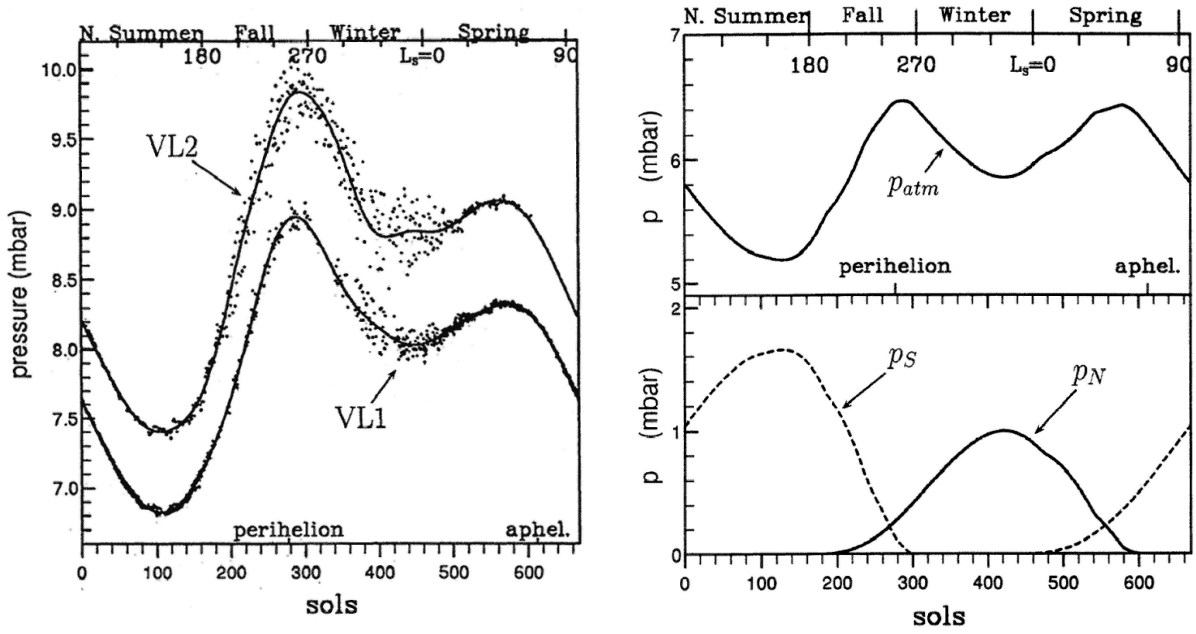


FIGURE 4.4: Exemples de distance snowdrop d'après OMEGA (figure d'après [285]).



(a) Viking (b) Modèle

FIGURE 4.5: Pression atmosphérique martienne : (a) pression au sol mesurée par Viking Lander 1 et 2 ; (b) en bas : pression atmosphérique équivalente stockée dans les calottes saisonnières ; (b) en haut : pression atmosphérique à l'altitude 0. Figure d'après Hourdin et al. [134].

Altitude L'étude des variations des altitudes[299] montre que l'amplitude des variations augmente linéairement avec la latitude entre 0 m à 60° de latitude et 1m au pôle. Une autre étude, basée sur la décomposition en série de Fourier du signal temporel, confirme que l'amplitude annuelle est d'un mètre [3].

Masse Les mesures de masse peuvent se faire par plusieurs techniques : déformation du géoïde [299, 341, 150], mesure par occultation du flux de neutrons [195, 196] et de gamma [155]. Tous sont globalement compatibles avec les GCM : 25% de la masse atmosphérique totale est impliquée dans le cycle saisonnier de condensation/sublimation.

En combinant les informations de masse, déduites de la déformation du géoïde, et les variations d'altitude, il est possible d'estimer une masse volumique pour les dépôts de 0,910±0,230 g.cm^{-3} [299]. En comparant avec les données de masse déterminées par les mesures du flux de neutrons, Aharonson propose une masse volumique plus réaliste de 0,5 g.cm^{-3}[3].

4.1.2.2 Modélisations

La quantité de masse de CO_2 qui se condense/sublime à la surface de Mars, est déduite des équations du bilan d'énergie et de conversion de chaleur latente, en explicitant les gains et les pertes d'énergie [90] :

$$\frac{\partial M_{CO_2}}{\partial t} = (F^{out}_{therm} - F^{in}_{Adv} - F_{cond} - W^{in}_{sun})\frac{1}{L_{CO_2}} \tag{4.1}$$

Avec F^{out}_{therm} la perte d'énergie par émission infrarouge thermique, F^{in}_{Adv} le gain d'énergie par advection atmosphérique, W^{in}_{sun} le gain d'énergie solaire, F_{cond} le bilan d'énergie échangée avec le sous-sol (ce terme peut être un gain ou une perte). $L_{CO_2} = 590.10^3$ [J.kg^{-1}] la chaleur latente de sublimation du CO_2, M_{CO_2} [kg.m^{-2}] la masse surfacique (intégrée sur l'épaisseur) de la couche de glace de CO_2.

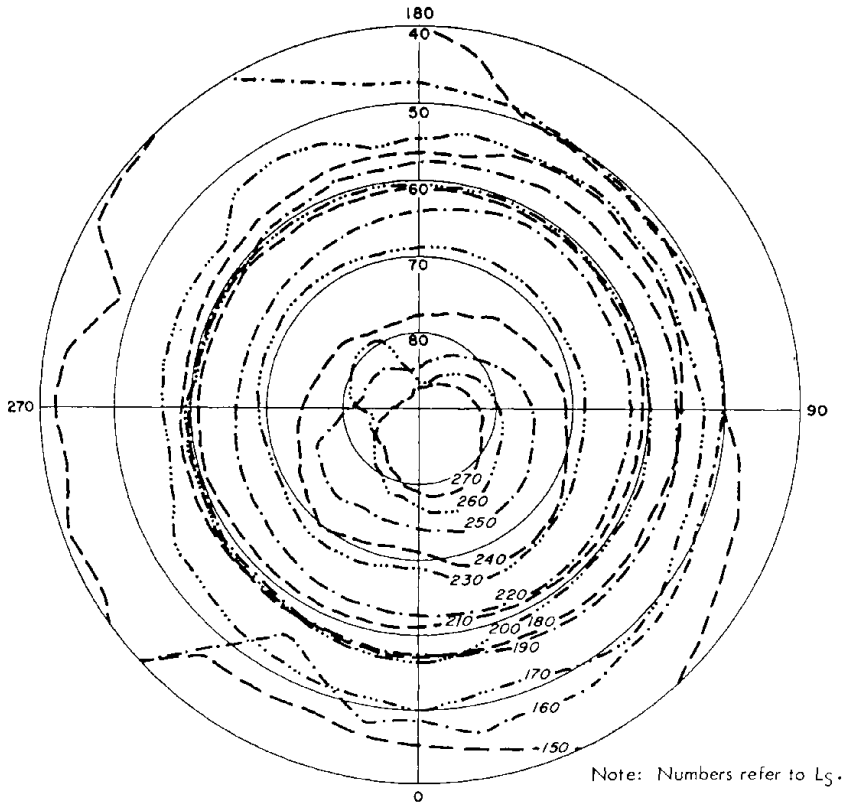


FIGURE 4.6: Récession de la calotte saisonnière sud observée depuis la Terre entre 1905 et 1965. Chaque cercle est une *ligne crocus* à une date notée en °Ls (d'après [87] repris dans [328]). Les longitudes sont notées en degrés croissants vers l'Ouest.

Cette modélisation a été intégrée à des études locales, comme celle développée durant ma thèse et mon post-doc (4.4.2 page 235) mais aussi dans les GCM [92, 190].

Malgré les récentes modélisations, basées sur les données d'albédo et de présence de glace les plus précises, il reste plusieurs incompréhensions autour des phénomènes contrôlant les dépôts saisonniers de Mars.

4.1.3 Incomplétudes

Cette section décrit trois incomplétudes majeures aux modélisations classiques de la calotte saisonnière sud de Mars, liées entre elles mais impliquant des études indépendantes.

4.1.3.1 Incomplétudes 1 : asymétrie de la récession

Les premières évidences de l'asymétrie de la récession de la calotte saisonnière sud apparaissent dès 1905 [87, 328] (voir figure 4.6). Malgré cette asymétrie, la récession est, au premier ordre, toujours identique d'une année martienne à une autre. Afin de comparer les différentes années et les différentes observations, James et al. proposent de modéliser l'extension géographique du dépôt saisonnier par un disque dans une projection stéréographique polaire sud [143]. Il s'agit d'ajuster deux paramètres : le centre et le rayon du disque. Les observations Viking [143], au sol [142, 141] ou MOC [15] montrent toujours une asymétrie de récession qui commence vers Ls=220°. Le méridien de longitude 120°E a une vitesse de récession plus rapide que le méridien opposé de longitude 60°W. Cette asymétrie a été confirmée par les observations TES [165] et OMEGA [179]. Elle est liée à la région cryptique (voir section 4.1.3.2), introduite par Kieffer, en 2000, à partir des analyses des données TES [165].

Cette vision simpliste du disque ne décrit pas correctement le détail de la zone couverte par les dépôts saisonniers (voir figure 4.4). Il existe des îlots clairs détachés du disque et des îlots sombres à l'intérieur du disque. De plus, le bord du disque a une géométrie complexe. Les montagnes de Mitchel forment l'îlot clair détaché le plus étendu et le plus connu. Il tient son nom du directeur de l'observatoire de Cincinatti qui l'a observé pendant l'opposition de 1845.

L'hypothèse avancée classiquement pour expliquer cette asymétrie de la récession est un effet d'altitude et de rugosité de surface [328]. Lors de ma thèse, j'ai testé et rejeté cette hypothèse. J'ai démontré que cette asymétrie de sublimation est due à une asymétrie d'albédo qui accélère la récession dans la zone la plus sombre [285] (article disponible à la section 4.4.1). Lors de mon post-doc, j'ai pu montrer qu'il existe néanmoins une légère asymétrie de condensation au bénéfice de la région cryptique [286] (article disponible à la section 4.4.2), probablement dû à une précipitation de neige préférentielle dans la région cryptique, en accord avec les prévisions des GCM [55] et les observations indirectes des nuages pendant la nuit polaire [105].

L'origine de l'asymétrie d'albédo est toujours débattue et sera discutée à la section suivante.

4.1.3.2 Incomplétudes 2 : Région cryptique

Le concept de région cryptique a été introduit par Kieffer, en analysant la récession de la calotte saisonnière sud avec l'instrument TES à bord de MGS [165]. Il s'agit d'une région qui comporte deux caractéristiques a priori contradictoires : un albédo faible (signant la présence de poussière) et une température proche de 140K (signant la présence de glace de CO_2). La région cryptique apparaît comme un îlot sombre à l'intérieur du disque (voir figure 4.7).

Une étude plus récente propose une définition plus précise de la région cryptique utilisant toujours les données TES [260]. Il s'agit de l'ensemble des îlots d'albédo inférieur à 0,38 et comportant une signature en température de glace de CO_2. Cette définition permet de dessiner les contours de la région cryptique au cours du temps. La "région cryptique union" est l'ensemble des points qui présentent des caractéristiques de crypticité à un moment donné pendant la récession de la calotte saisonnière (SSPC). La "région cryptique intersection" est l'ensemble des points qui présentent des caractéristiques de crypticité pendant toute la récession de la SSPC. Introduisons aussi la "région anticryptique" qui est le complémentaire de la "région cryptique union" dans le domaine des hautes latitudes.

Afin d'expliquer la contradiction apparente albédo/température de cette zone cryptique, deux hypothèses majeures ont été avancées :

1. La première explication est la présence d'une couche de glace à gros grains, très pure et suffisamment transparente pour que les photons visibles et proches infrarouges puissent atteindre le sol sous-jacent. Dans ce cas, la couche de glace de CO_2 imposerait bien une température de 140 K tandis que l'albédo serait contrôlé par le substrat [165]. Les interprétations spectroscopiques de TES sur la région cryptique montrent que les tailles de grains de CO_2 dans la région cryptique sont très grandes (> 1 cm) [165].
2. La seconde, plus simple, invoque de la poussière en contact avec de la glace sous-jacente [180]. La température de la couche de poussière superficielle serait contrôlée par le CO_2 sous-jacent, mais l'albédo de la couche supérieure resterait sombre. Il faut donc que la couche superficielle soit à la fois optiquement épaisse et non isolante thermiquement. D'après les données OMEGA, la région cryptique à Ls=220° est compatible avec de la glace transparente recouverte de poussière optiquement épaisse sur 70% de la surface [180]. Néanmoins, des zones de glaces transparentes ont été observées en divers endroits de la calotte [180, 278] (voir figure 4.8).

Plusieurs phénomènes peuvent être à l'origine de ces variations temporelles et spatiales d'albédo, de transparence et de quantité de poussières. Le plus discuté en ce moment est le modèle de geysers (voir section suivante), mais d'autres phénomènes ont aussi lieu :

- le métamorphisme [80, 81] qui tend à faire croître les tailles de grains.
- le mélange à une échelle sub-pixel, de zones entièrement nues et de zones glacées, qui pourra être en partie résolu grâce à l'instrument CRISM.

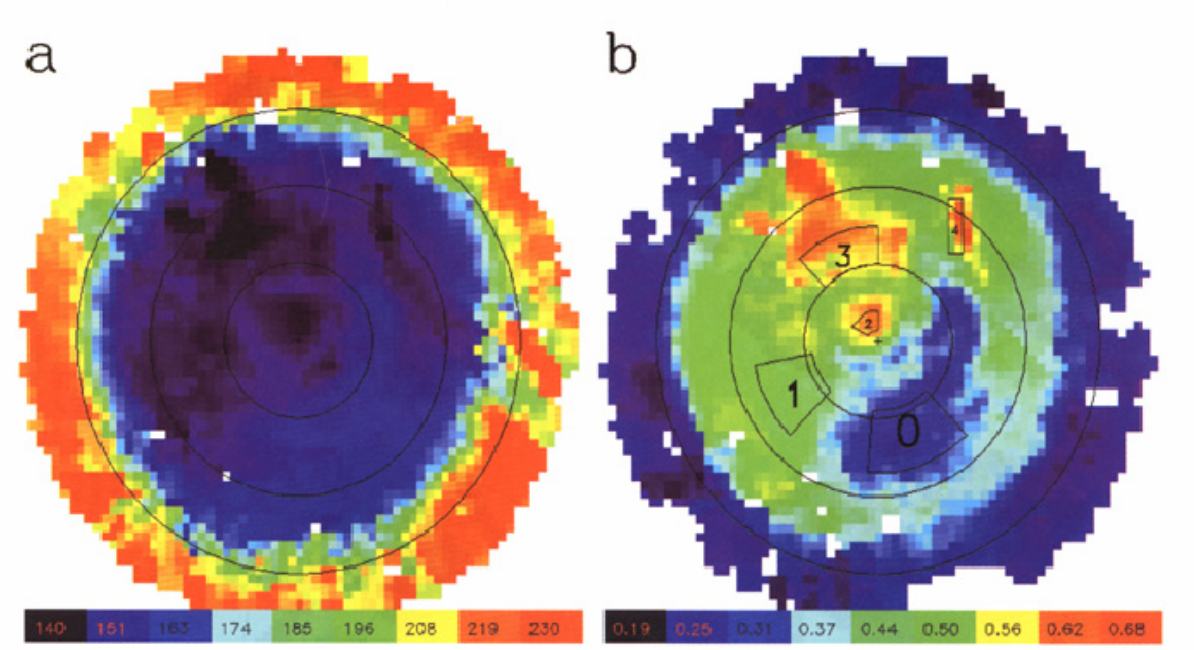


FIGURE 4.7: Propriétés a priori contradictoires de la région cryptique (notée 0) a Ls=220° d'après l'instrument TES : a) température de brillance (proche de 140K pour la zone 0), b) albédo (proche de 0.3 pour la zone 0) (d'après [165]).

- le mécanisme de dépôt par condensation/précipitation de neige qui peut déposer une fraction plus ou moins importante de grains fins en surfaces [54], en accord avec les observations de la structure atmosphérique, sursaturé à certains endroits [105]. L'origine de cette asymétrie est la présence des bassins d'Hellas et d'Argyre qui créent une asymétrie dans l'écoulement atmosphérique induisant plus de précipitations de neige dans la région cryptique.
- la précipitation de poussières éoliennes sur un substrat de glace, par exemple après une tempête de poussière ou plus localement autour d'un geyser (voir section suivante).
- un mécanisme de nettoyage, suggéré par une augmentation d'albédo de la glace au cours du temps [250, 165, 285]. Le nettoyage de la fraction fine peut-être dû à la saltation en présence de CO_2 [165], ou d'enfoncement des particules les plus grosses [265].
- un mécanisme d'ablation mécanique dû aux vents [21].

De nombreuses études et modélisations sont nécessaires pour à la fois améliorer les contraintes observationnelles (spectroscopie quantitative, géomorphologie quantitative) afin de comprendre/rejeter les phénomènes en compétition sur la calotte saisonnière sud de Mars.

4.1.3.3 Incomplétudes 3 : Spiders, geysers et écoulement sombre

Un unique mécanisme permet de concilier ces deux explications de couche de CO_2 transparente et de couverture de poussière : les geysers. Ce mécanisme consiste en un apport d'énergie basal au travers d'une couche de CO_2 transparente [165, 260, 166, 162]. Ce chauffage entraîne une sublimation du CO_2 sous la couche de glace. Le gaz ainsi produit monte en pression jusqu'à briser la couche de glace et se libérer, emportant avec lui la poussière présente dans le substratum. Ce modèle est schématisé dans la figure 4.9 et explique comment les hypothèses 1 et 2 peuvent avoir lieu. La partie droite du schéma correspond à la situation de la première hypothèse, tandis que la partie gauche correspond à la situation de la seconde.

Le scénario temporel de formation des spiders et geysers est illustré dans la figure 4.12. Ce modèle de geyser est conforté par l'observation de figures géomorphologiques très particulières : les "spiders" [260]. Il s'agit de formes ressemblant à des araignées creusées dans le sol minéral à l'échelle de moins

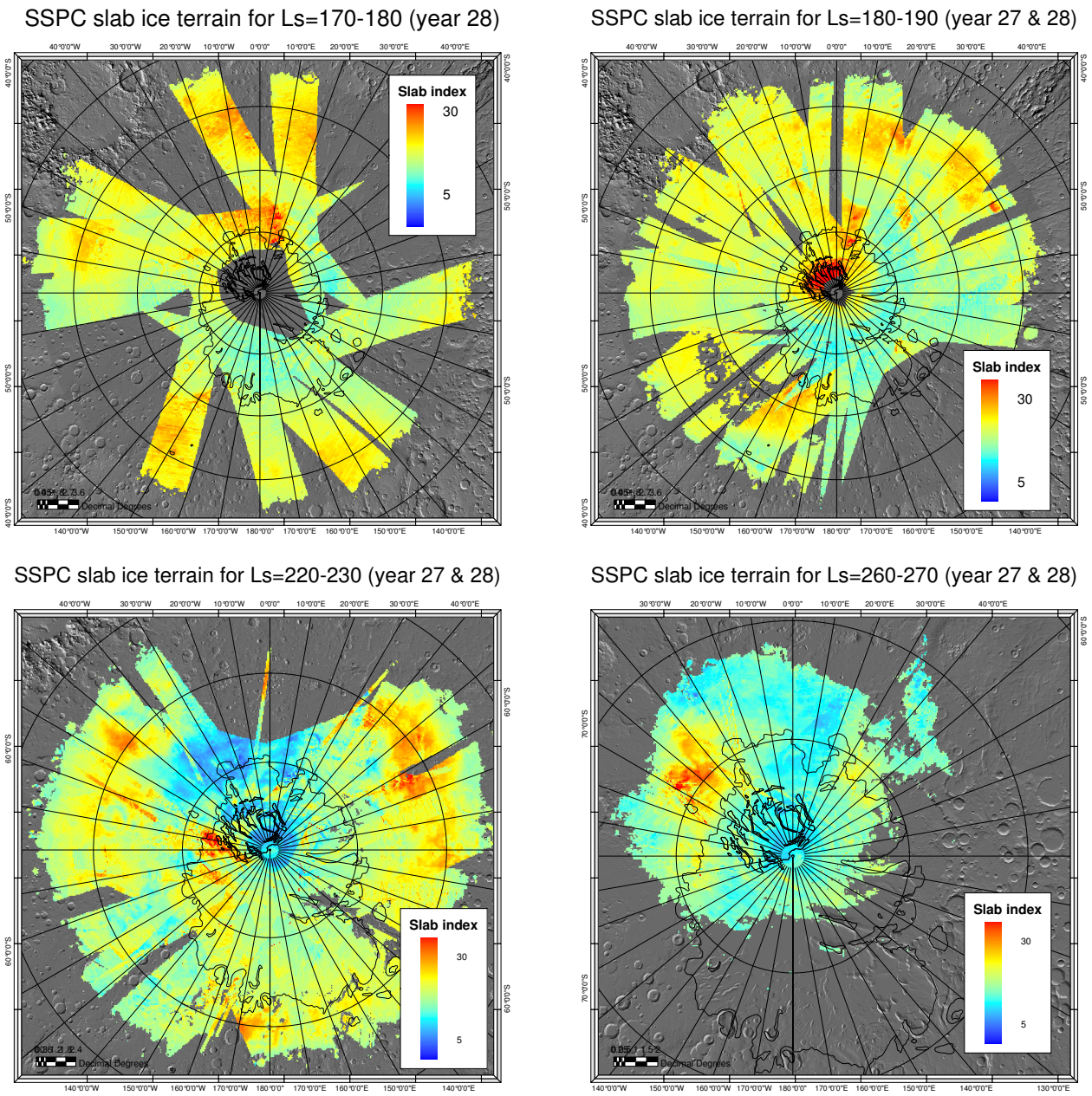


FIGURE 4.8: Variations de l'état de transparence de la glace observé par OMEGA (d'après [278]).

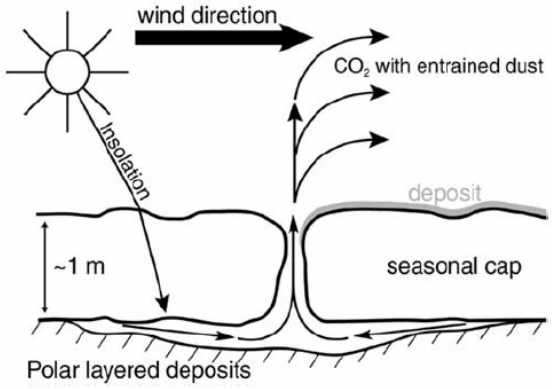


FIGURE 4.9: Schéma de la formation des geysers. D'après Piqueux et al. [260].

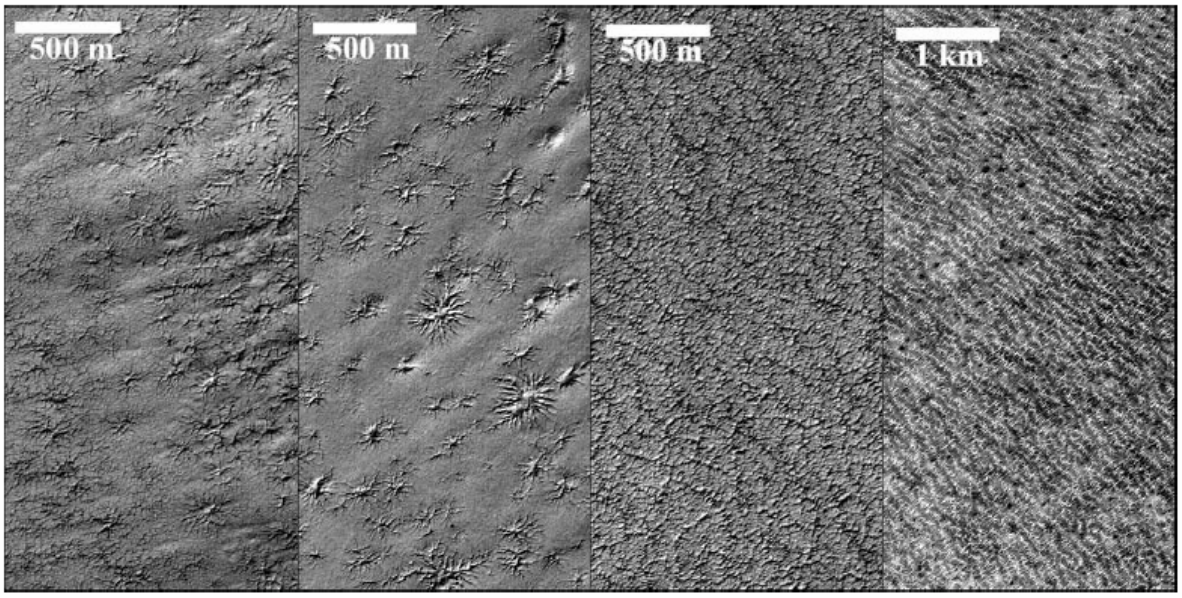


FIGURE 4.10: Observation MOC des Spiders. D'après Piqueux et al. [260].

d'un kilomètre (voir figure 4.10). Au printemps, les "spiders" sont recouverts de traînées sombres, vraisemblablement composées de poussières (voir figure 4.11) interprétées comme les traînées de poussières déposées par les geysers.

Plusieurs étapes sont nécessaires et ont été étudiés par plusieurs auteurs :

1. Dépôt de CO_2 par condensation/précipitation [54], puis nettoyage des poussières par enfoncement [265] ou saltation [165].
2. Etat de glace transparente, probablement après métamorphisme [80, 81]
3. Effet de serre à l'état solide, rupture mécanique et éjection de gaz et poussière.
   (a) Effet de serre à l'état solide dû au flux solaire qui pénètre dans la glace pour être absorbé dans le substratum. La glace étant opaque en infrarouge, les rayons sont donc piégés et absorbés en base de la couche transparente. L'énergie ainsi absorbée permet de sublimer la glace de CO_2 par le dessous. Des calculs thermiques ont montré qu'il est possible de réaliser cet effet de serre à l'état solide [265, 256]. Une étude expérimentale sur de la glace d'eau a bien montré la validité de ce phénomène [152]. Le terme de conduction de chaleur dans le sous-sol F_{cond} (voir eq. 4.1 page 194) dans le cas d'un sol d'une forte inertie thermique, a été proposé pour expliquer la présence très tôt des éjections [2]. Néanmoins, d'après une modélisation thermique plus complète [256], une forte inertie thermique tend à une condensation plus tardive et donc à une couche de CO_2 plus fine, mais aussi un chauffage plus difficile de la couche de poussière. Cette modélisation montre qu'une forte inertie thermique tend à retarder l'apparition des geysers.
   (b) La rupture mécanique du CO_2 intervient lorsque le seuil de contrainte est atteint. Cependant, aujourd'hui, les mesures de seuil d'élasticité de la glace de CO_2 ne sont pas connues. Deux géométries ont été proposées : (i) la couche de glace de CO_2 repose sur des bords, c'est à dire des endroits où la sublimation basale n'a pas eu lieu [265] (ii) la couche de CO_2 se décolle et lévite au dessus du sol [162]. Les flux de gaz sous la surface pourraient être à l'origine d'une remobilisation du substratum et à la formation des spiders [162].
   (c) L'éjection des gaz et poussières a été modélisée par des simulations d'écoulements fluides [314, 315]. Dans l'hypothèse d'un écoulement à l'équilibre (tout le gaz sublimé par le dessous sort par un tunnel dans la glace), le gaz sort à une vitesse d'éjection de 25 m/s, avec une accélération significative du gaz dans le voisinage de l'embouchure (<0.5 m), indiquant une

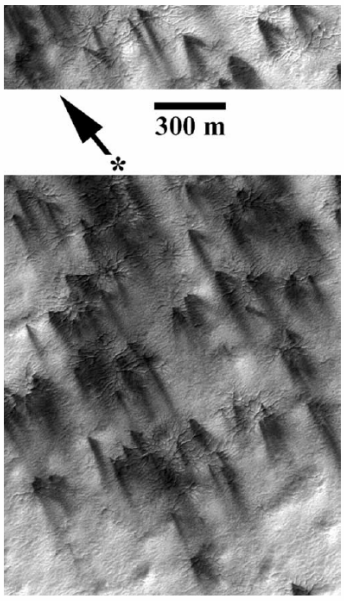


FIGURE 4.11: Observation MOC à Ls=208° des liens entre les "spiders" et geysers. Les traînées sombres de dépôt de poussière ont comme point d'origine les centres des "spiders". D'après Piqueux et al. [260].

érosion localisée autour du point d'éjection [314]. Une étude analogique a montré qu'il est possible de simuler des formes dendritiques convergentes en cas d'une éjection unique [65].

4. Dépôt des poussières entraînées par les geysers. D'après les observations HIRISE, les dépôts se font majoritairement le long de la pente, dus soit à des vents catabatiques, soit à la géométrie des conduits d'éjection [313]. Les simulations confirment qu'une forte pente permet une sublimation plus intense liée à une insolation intense et donc un entrainement de particules relativement plus grand alors que l'effet des vent locaux peut déplacer les fractions fines sur des distances importantes [315]. Ces simulations sont compatibles avec les observations de dépôts observées. Concernant la formation des halos clairs, l'hypothèse d'un refroidissement adiabatique lors de l'éjection des gaz, a été proposée [322] mais les simulations numériques d'écoulements montrent qu'il ne dure que 0.2 s et que les particules ainsi formées ne sont pas déposées [315]. En revanche, lors de la descente, les particules entraînent du gaz de CO_2 atmosphérique et amènerait à une surpression qui aboutirait à la condensation de particules de CO_2 [315]. Les données HiRISE suggèrent la formation de dépôts bleutés au centre des éjections qui seraient dus à des particules fines de CO_2. Tandis qu'à la limite extérieure, le halo bleuté pourrait provenir d'un enfoncement de la poussière [261]. Les premières analyses des données CRISM suggèrent une évolution complexe de l'eau et du CO_2, avec une sublimation précoce de l'eau et un nettoyage des poussières [261].
5. Sublimation totale de la glace et mise à jour des spiders. Les spiders sont les tranchées laissées par l'écoulement sous-glaciaire. Deux modèles persistent : les écoulements à l'équilibre [314, 315] impliquant des pressions maximum de 1 000 Pa, ou des écoulements sous la glace en lévitation [162] impliquant jusqu'à 4 000 Pa. Une étude analogique a montré qu'il est possible de simuler des formes dendritiques convergentes en cas d'une éjection unique [65]. Les observations sont compatibles avec un fluide gazeux car le conduit s'agrandit en remontant la pente [111].

Malgré ces différentes études, de nombreux points restent obscurs :

Localisation des spiders Initialement, les geysers, spiders et la région cryptique ont été mis en correspondance [260] : d'après ces auteurs, tous les spiders sont situés dans des lieux appartenant à la fois à la région cryptique union et à une unité géologique de terrains contenant de la poussière (SPLD pou South Polar Layered Deposit). La glace y est translucide au printemps ce qui assure le chauffage du sol et donc

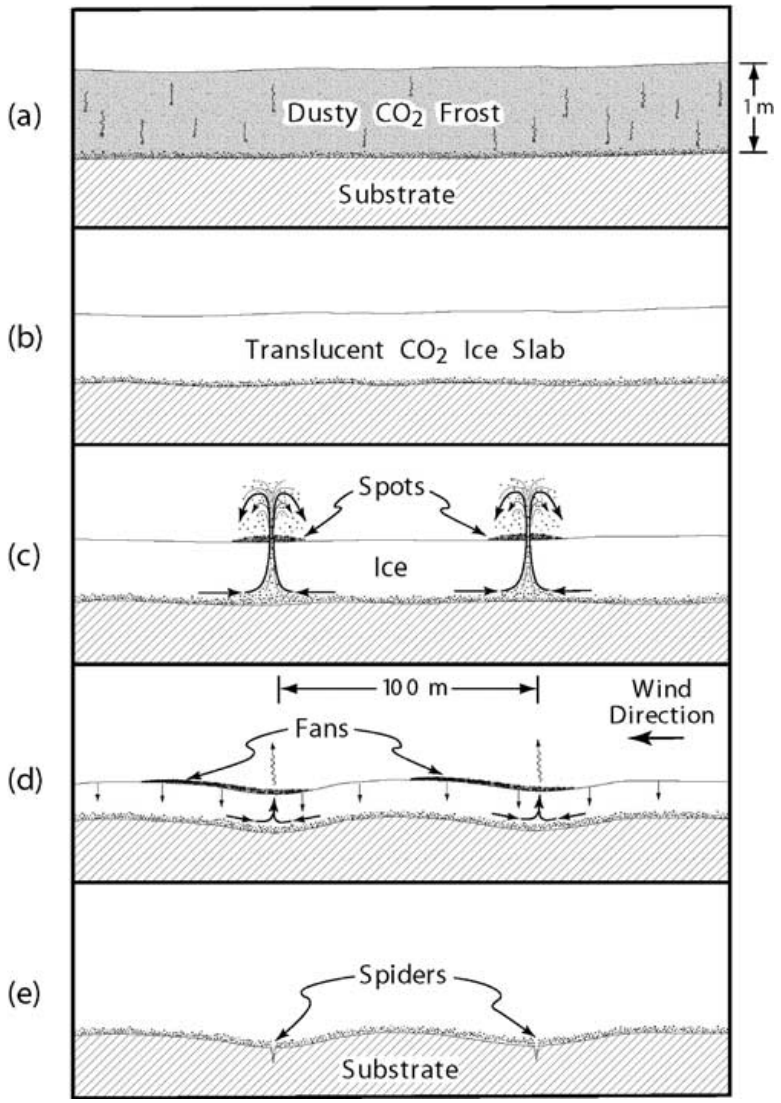


FIGURE 4.12: Schéma temporelle de la formation de la calotte saisonnière dans la région cryptique (d'après [166]).

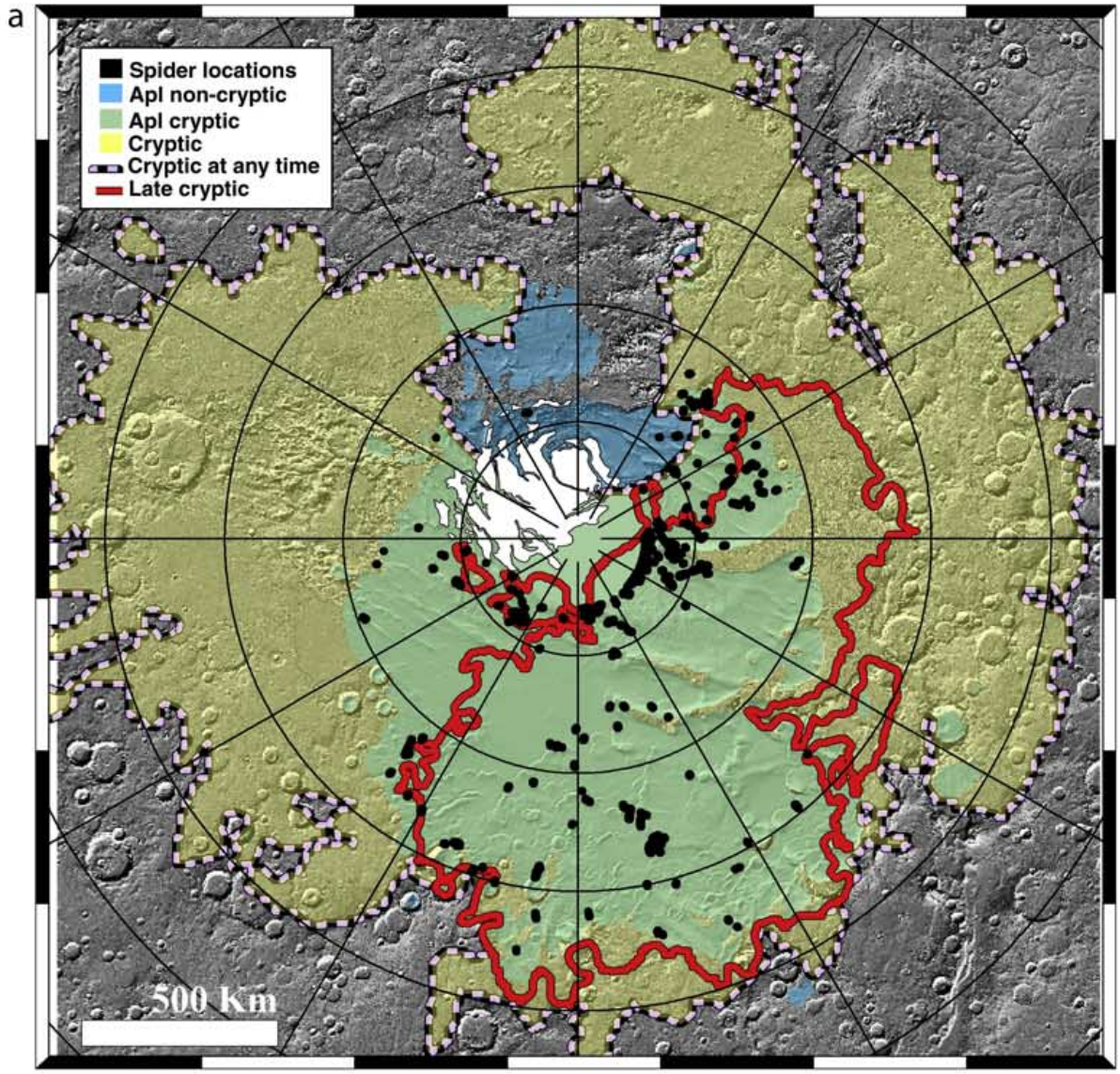


FIGURE 4.13: Localisation des spiders dans la zone polaire Sud de Mars (d'après [260]).

la formation de gaz sous pression. Les geysers résultants peuvent être matérialisés en surface et causer une contamination (voir figure 4.13).

A l'aide de Romain Dupire, stagiaire en M2, j'ai mené une étude plus complète comprenant la totalité des images MOC et des centaines d'image HiRISE, soit au total 5000 images (voir figure 4.14). Cette étude, en cours de rédaction pour publication montre que la corrélation n'est pas aussi bonne que présentée précédemment, puisqu'une part significative des spiders se trouve en dehors des SPLD.

Néanmoins, le maximum de contamination est observé par MOC [264] et OMEGA [180] à Ls=230°. D'autre part, la contamination vue par OMEGA est assez uniforme sur de grandes surfaces alors que la présence des spiders et des geysers est assez localisée.

Liens entre spiders et geysers D'après le modèle classique, le centre des spiders correspond au point d'éjection des geysers. Mais les images HiRISE à haute résolution (voir figure 4.15) montrent qu'au contraire les geysers sont situés sur les bords du spiders [313]. Dès lors, se pose la question du lien entre ces deux objets. Une possibilité serait le contrôle des geysers par l'insolation différentielle dû à la micro-topographie sur les pentes des tranchées du spider. Pour tester une telle hypothèse, un Modèle Numérique de Terrain (MNT) est nécessaire.

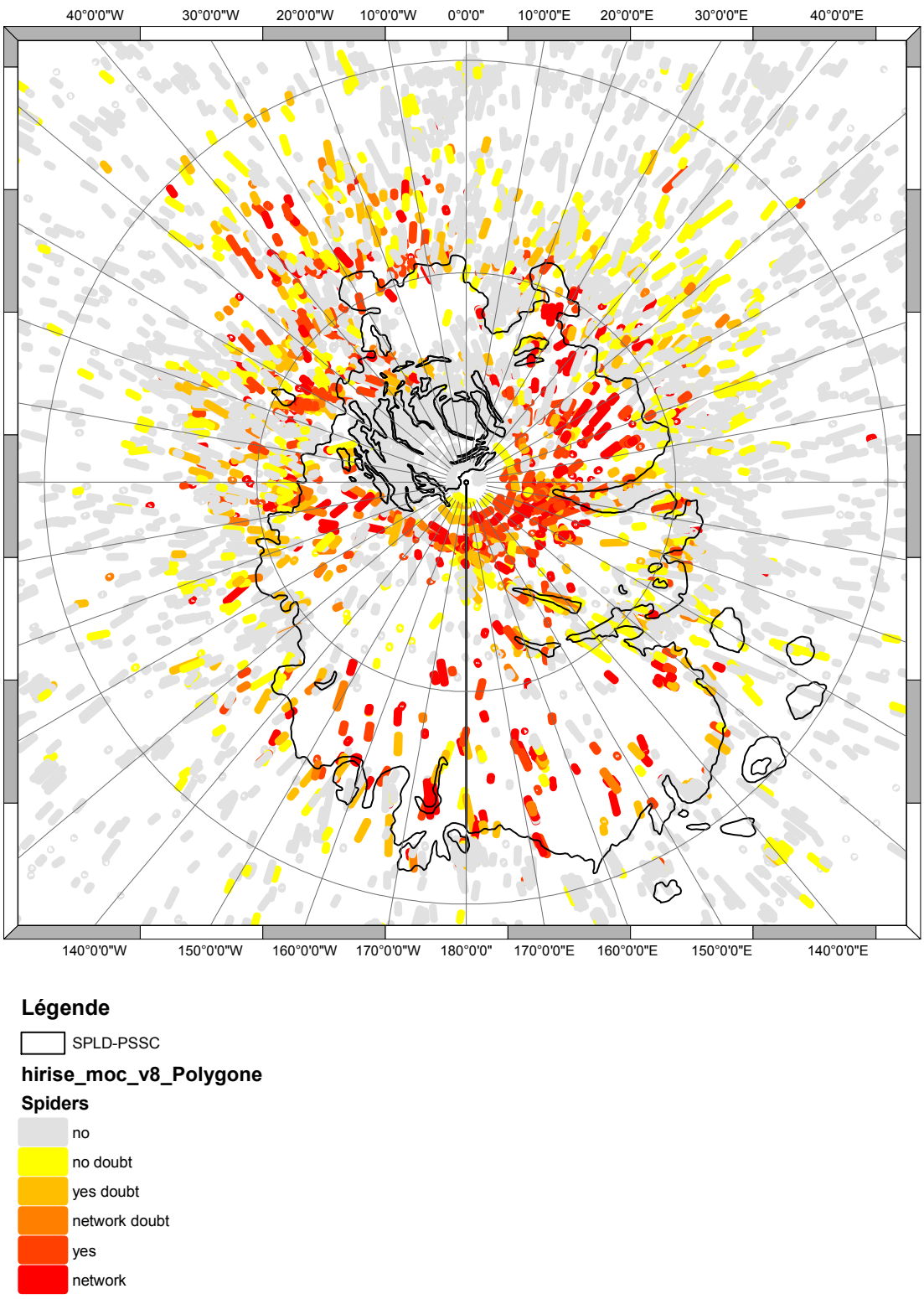


FIGURE 4.14: Localisation des spiders dans la zone polaire Sud de Mars (d'après [280, 281]).

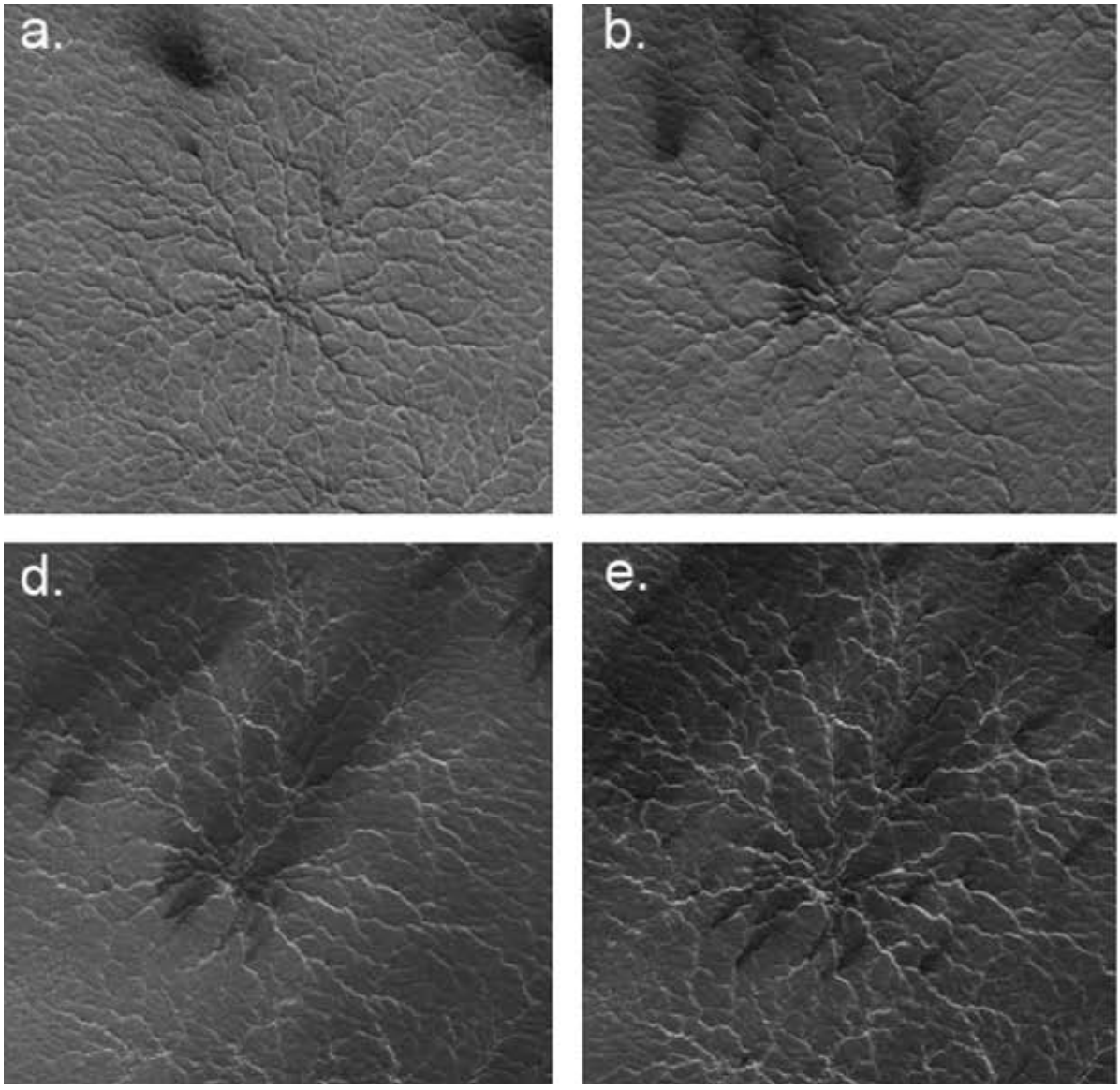


FIGURE 4.15: Liens entre geysers et spiders (d'après [313]).

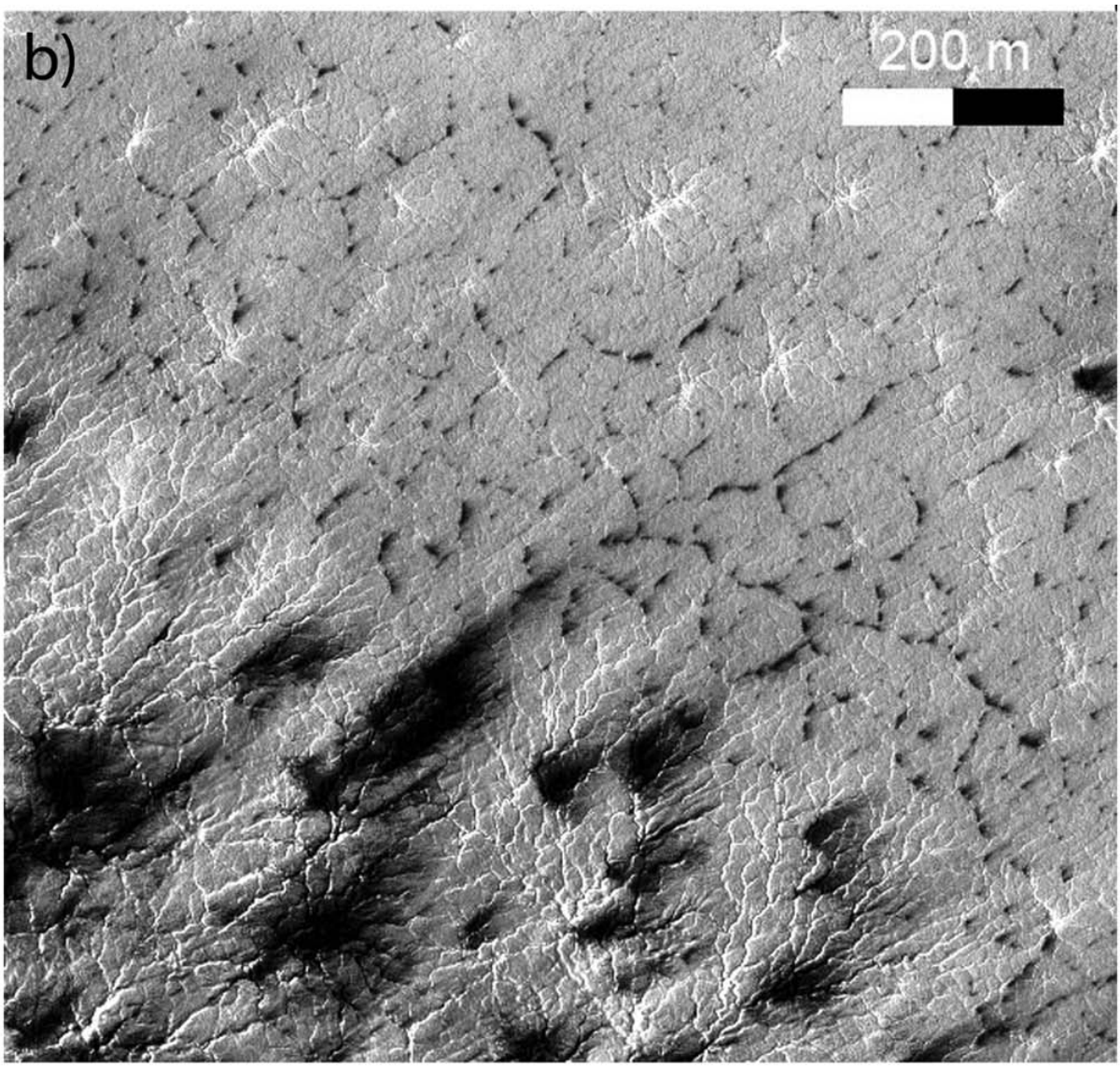


FIGURE 4.16: Geysers sous forme de cracks en réseau dans la partie Nord et sous forme de point dans la partie Sud (d'après [266]).

Ejections sous forme de cracks D'après le modèle classique, les geysers émanent d'un conduit unique mais les images HiRISE (voir figure 4.16) montrent que les éjections peuvent aussi provenir d'une zone fracturée [266]. Les cracks ne sont pas dans le substratum car ils sont différents d'une année martienne à l'autre [266]. Quelle est l'origine de ces différents mode de rupture ?

Liens entre geysers et glace transparente Le modèle classique et les calculs thermiques montrent que la présence de glace transparente conduit rapidement à la formation d'un geysers. Cependant, la mise en correspondance d'un indice de transparence de glace des données OMEGA et des geysers actifs (voir figure 4.17) ne montrent aucune corrélation évidente. Est-ce que les informations spectroscopiques de glace transparente sont cohérentes avec les données d'imagerie de présence de geysers ?

Activité très précoce de certains geysers Pour l'instant les premières images disponibles, juste après la nuit polaire, comportent déjà des geysers et il est donc très difficile de dater précisément la première apparition [313], par exemple avant Ls=174° à Inca City. Le terme de conduction de chaleur dans le sous-sol a été proposé pour expliquer la présence très tôt des éjections [2]. Mais finalement, un sol de

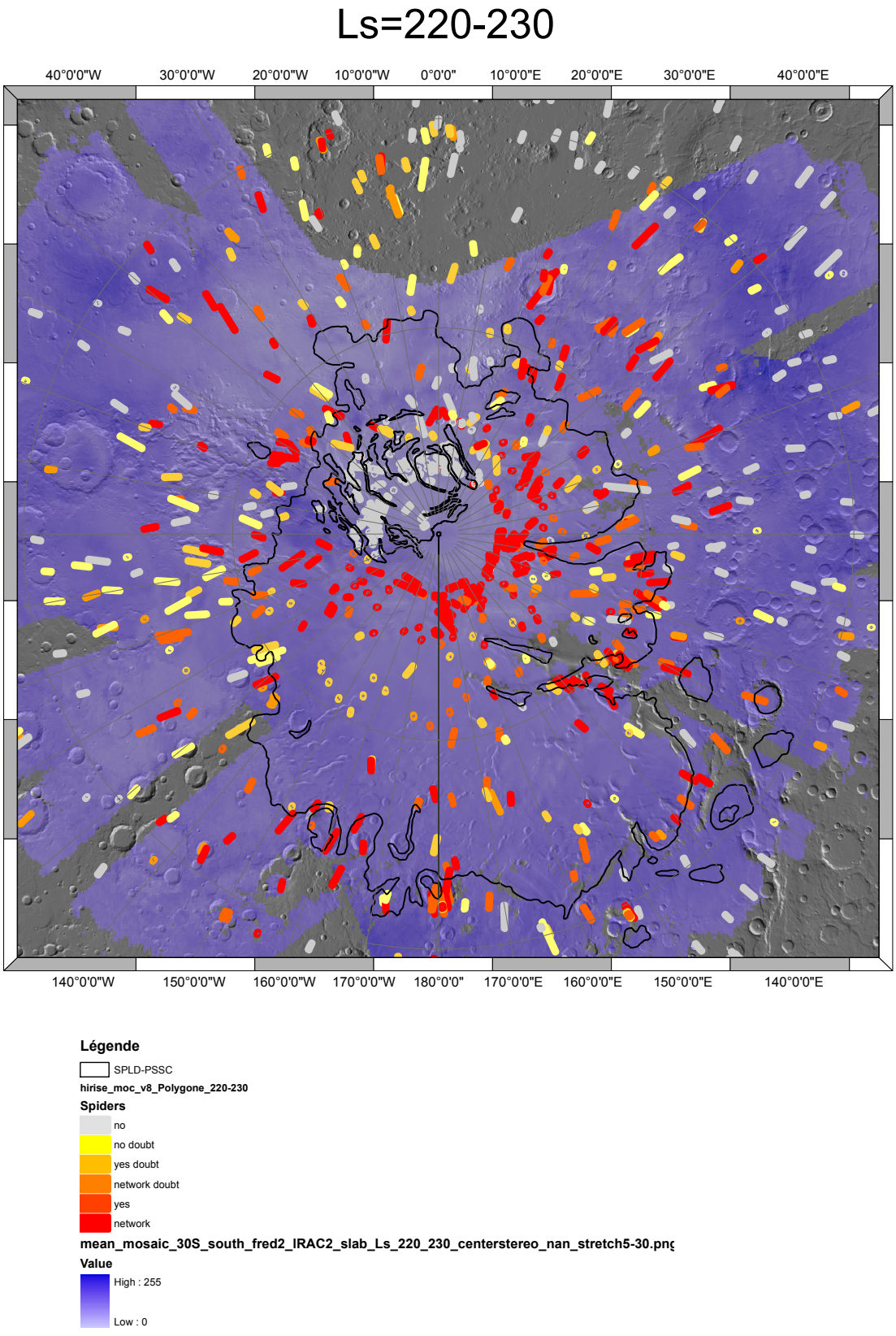


FIGURE 4.17: Localisation des geysers et de la glace transparente (d'après [281]).

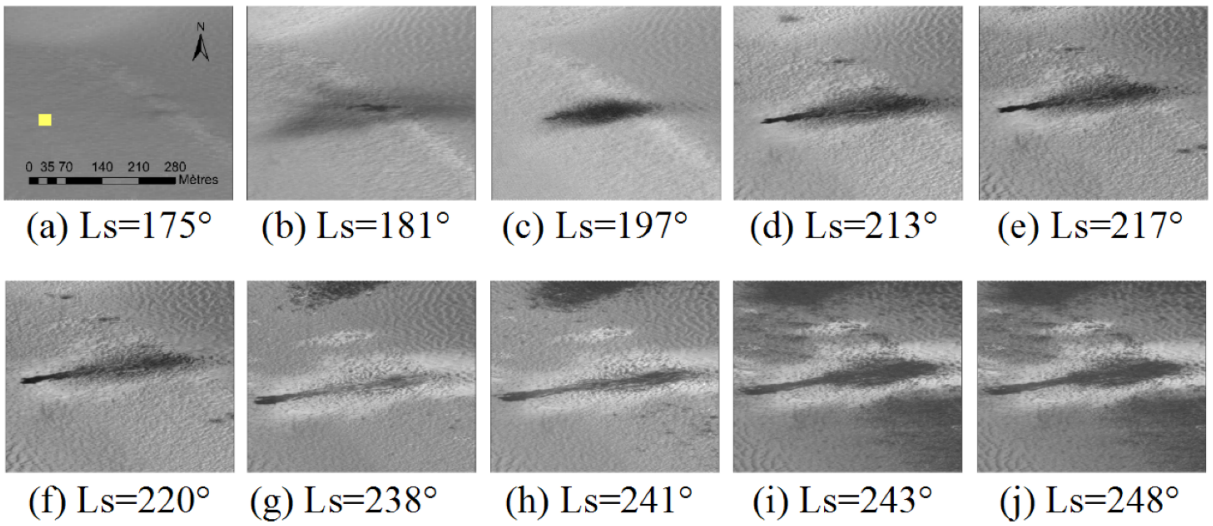


FIGURE 4.18: Ecoulement sombre dans la dune de Richardson (d'après [5]).

forte inertie thermique tend à retarder l'apparition des geysers [256]. Est-ce que le chauffage solaire seul peut expliquer les geysers précoces ?

Liens entre geysers, écoulement sombres Un lien entre les écoulements sur les dunes (voir illustration page 293) et le phénomène de geyser a été proposé sur la dune de Russel [99]. Depuis, plusieurs études ont montré la corrélation temporelle entre les écoulements et la présence de glace de CO_2 [78, 67, 110]. Certains auteurs ont proposé, un écoulement d'un film visqueux [240], de saumures [157] ou d'eau interfaciale [156]. Les travaux de thèse de François Andrieu en cours, concernent le cas de la dune de Richardson (voir figure 4.18). Sur cette zone, les premières étapes suggèrent la présence d'un geyser au sommet de la dune. Les étapes suivantes correspondent à un écoulement gravitaire. Ces morphologies sont aussi présentes sur les inter-dunes plates, connues sous le nom de "Dark Dune Spots". Même si certaines équipes proposent des hypothèses hasardeuses, comme par exemple des colonies de bactéries [133, 98], les liens entre geysers et écoulements sombres ne semblent pas encore compris. Est-ce que l'écoulement se fait sur le dessus ou sur le dessous ? Quel est le matériel qui s'écoule ?

De nombreuses questions restent en suspens car aucune observation directe d'un geyser n'a été possible jusqu'à présent [313]. Le phénomène de geyser et de formation des spiders est probablement le mécanisme majeur d'évolution morphologique sur Mars, le plus efficace pour la remobilisation des poussières sur Mars, 100 fois plus qu'une tempête de poussière globale [259, 111][259, 111]. La compréhension de ce phénomène est donc essentielle pour comprendre à la fois le climat actuel et passé de Mars, mais aussi son évolution géomorphologique.

4.2 Contributions

Mes recherches concernant la calotte saisonnière sud de Mars peuvent être découpées en plusieurs axes : la cartographie de présence de glace, la modélisation des échanges de glace de CO_2 en surface, caractérisation de la glace par la spectroscopie, caractérisation géomorphologique des processus de surface.

4.2.1 Cartographie de présence des glaces par spectro-imagerie

Lors de ma thèse, j'ai introduit des nouveaux concepts pour décrire l'extension spatiale de la calotte saisonnière : les lignes crocus internes et externes, ainsi que la distance snowdrop (voir figures 4.3 et 4.4).

J'ai sélectionné 544 observations OMEGA de l'année 2005–2006 (Année Martienne 27) de Ls=110° à Ls=320°, pour les latitudes 30° S jusqu'à 90°S. J'ai analysé ces images grâce à l'algorithme WAVANGLET (voir section 1.2.1) pour détecter la présence de glace au sol (voir figure 4.19). Puis, j'ai déterminé les lignes crocus internes et externes, ainsi que la distance snowdrop. Grâce à ces nouvelles observables, j'ai montré que l'asymétrie de sublimation est due à une asymétrie d'albédo qui accélère la récession dans la zone la plus sombre (région cryptique) [285].

Ce travail a été publié dans un article disponible à la section 4.4.1.

4.2.2 Modélisation des échanges de glace

Lors de mon post-doc, j'ai pu montrer qu'il existe néanmoins une légère asymétrie ($22 \pm 9\%$, voir figure 4.20) de condensation au bénéfice de la région cryptique [286] (article disponible à la section 4.4.2), probablement dû à une précipitation de neige préférentielle dans la région cryptique, en accord avec les prévisions des GCM [55] et les observations indirectes des nuages pendant la nuit polaire [105].

Ce travail a été publié dans un article, disponible à la section 4.4.2.

4.2.3 Spectroscopie

La question de la nature des écoulements sombres, décrit à la section 4.1.3.3, et de leur lien probable avec les geysers, est toujours ouverte. Au cours d'une collaboration avec A. Kereszturi, j'ai développé des arguments spectroscopiques pour tester la possibilité d'eau liquide. L'article présentant ce travail est disponible à la section 4.4.3.

Les écoulements sombres sur la pente, de taille de l'ordre de quelques mètres de large, ne sont pas directement observables sur un pixel CRIM de 18m. Nous avons donc choisi de s'intéresser aux phénomènes actifs situés sur la plaine inter-dune de Richardson (voir figure 4.21). Il s'agit de tâches sombres circulaires dont la croissance est radiale, souvent isotrope.

Les signatures de CO_2 sont dominantes sur les spectres CRISM. Grâce à l'outil de démélange linéaire FCLS (voir section 1.1.3.2 et 1.2.3), j'ai pu montrer qu'il n'y a aucune évidence spectroscopique de la présence d'eau sous forme liquide ou sous forme de saumures (voir figure 4.22). En revanche, la présence de glace d'eau est nécessaire pour expliquer les bandes d'absorption des spectres CRISM de la région. Les résultats montrent que la glace d'eau persiste plus longtemps que le CO_2, comme attendu d'après les modélisations climatiques [92]. En fin de sublimation, les conditions sont réunies pour créer une couche d'eau liquide interfaciale d'épaisseur 30 microns [159]. Le rôle de l'eau dans le mécanisme des écoulements n'est pas encore tout à fait compris.

D'autre part, j'ai contribué à développer une méthode permettant d'estimer la présence de glace transparente de CO_2 à partir des données OMEGA, grâce à la méthode GR-SIR [278]. Les résultats préliminaires sont représentés à la figure 4.17 et un article est en cours de préparation.

4.2.4 Géomorphologie

Durant le stage de Master 2ème année de Romain Dupire en 2010, nous avons abordé une cartographie exhaustive de la présence de spiders et geysers sur la totalité des images MOC et HiRISE disponibles à cette date (voir figure 4.14), venant en complément à des travaux similaires sur un nombre d'images très réduit [264] ou ayant un échantillonnage inconnu [260]. Ce travail d'analyse géomorphologique a été présenté à des congrès scientifiques internationaux Europlanet [279] et LPSC [281]. Nous avons pu montrer que les spiders étaient présents tout au long de l'année martienne, contrairement aux traces sombres, présentes majoritairement au printemps (voir figure 4.23). Aussi, la distribution spatiale des spiders est plus complexe que celle proposée initialement (uniquement sur l'unité "South Polar Layered Deposits") [260]. Aussi, nous avons souligné un manque de corrélation entre la présence de glace transparente et la formation des jets (voir figure 4.14).

Ce projet est en cours de rédaction pour une publication scientifique.

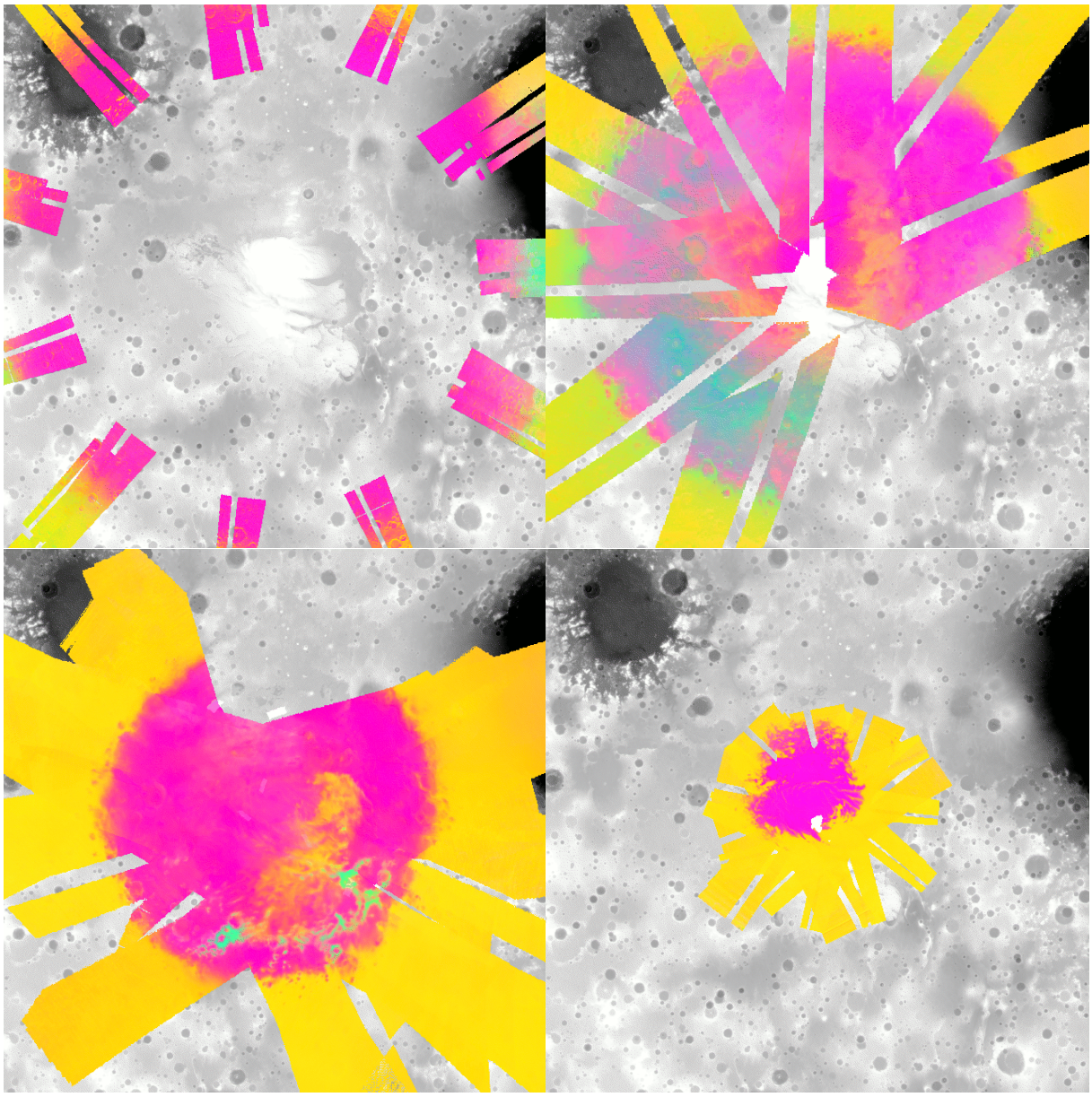


FIGURE 4.19: Evolution temporelle de la calotte saisonnière sud. Le fond en niveau de gris représente les altitudes MOLA. Les couleurs représentent les mosaïques des images hyperspectrales OMEGA : en jaune la poussière, en pourpre le CO_2 , en bleu l'eau (a) Ls=150-160° (b) Ls=180-190° (a) Ls=220-230° (a) Ls=275-280° (d'après [285]).

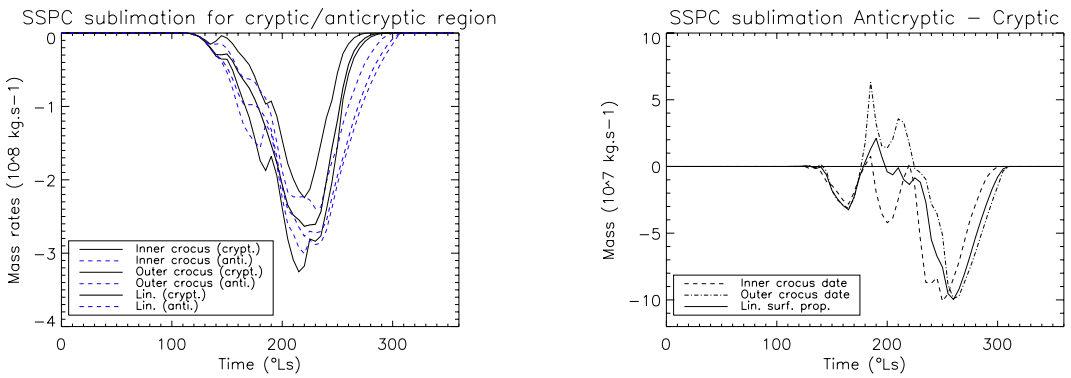


FIGURE 4.20: Flux de sublimation totales dans le demi-espace cryptique et anti-cryptique : à gauche, flux absolue, à droite flux relatif. Le flux anti-cryptique est légèrement dominant entre Ls=220° et 300° (d'après [286]).

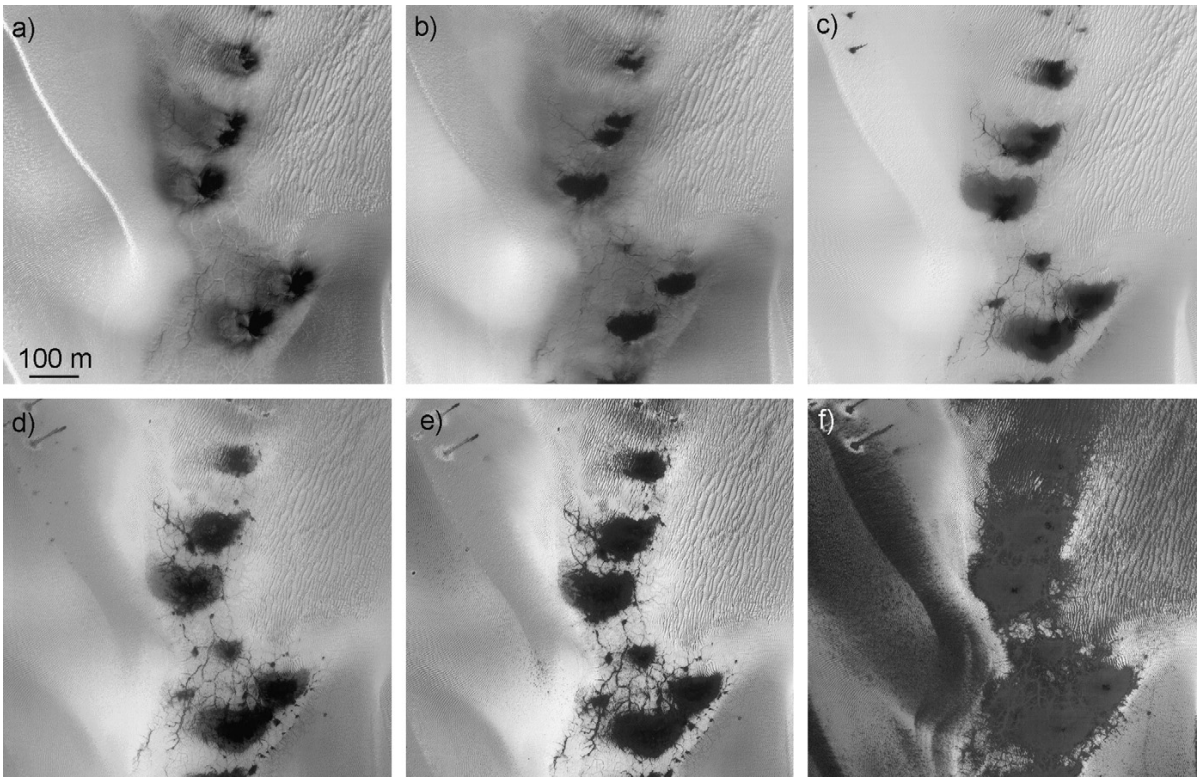


FIGURE 4.21: Evolution temporelle de l'inter-dune dans le cratère de Richardson entre Ls=166° et 218° (d'après [158]).

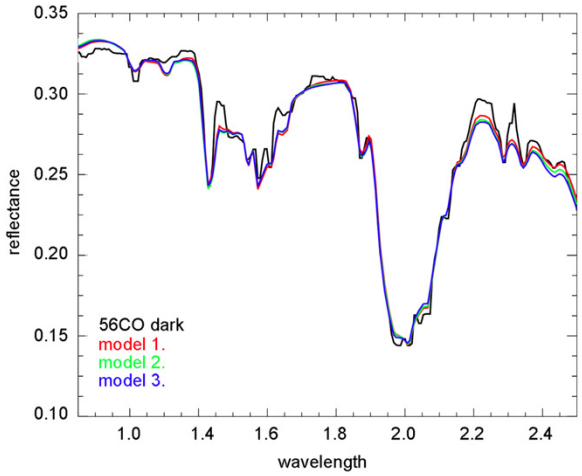


FIGURE 4.22: Modélisation d'un spectre du coeur sombre d'un dark spot. en noir : observation CRISM, modèle 1 : avec glaces uniquement, modèle 2 : avec glaces et eau liquide sans gypse, modèle 3 : avec glaces, gypse et eau liquide. Le RMS n'est pas significativement différent, signant la présence peu probable d'eau liquide (d'après [158]).

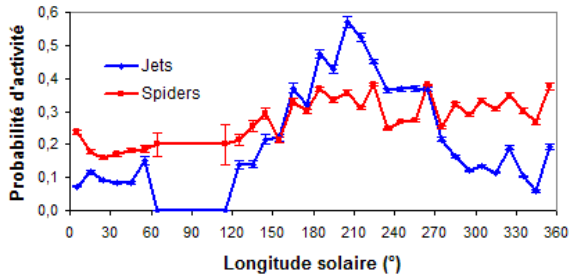


FIGURE 4.23: Probabilité d'occurrence des spiders et de geysers en fonction de la saison (d'après [279]).

D'autre part, j'ai contribué à l'étude en géomorphologie quantitative des gullies situés dans la dune de Russel pour montrer qu'ils se sont formés probablement dans un environnement périglaciaire, en présence d'une couche active (saturée en eau liquide) [149].

4.3 Perspectives

Cette thématique offre plusieurs perspectives de caractérisation des écoulements et d'identification des processus actifs liés à la sublimation de la glace de CO_2. Les enjeux principaux de ces travaux sont la compréhension du climat actuel de Mars mais aussi la compréhension de la dynamique des processus actuel sur Mars. Pour cela, il est nécessaire de bien établir la part des geysers dans les sources de poussière sur Mars. En effet, les poussières atmosphériques sont des noyaux de condensation des glaces mais aussi un agent important dans le bilan radiatif de la planète [227, 205]. D'autre part, il est nécessaire de mieux appréhender les mécanismes de surface (nettoyage, métamorphisme, ...) de la glace afin de les intégrer aux GCM pour simuler correctement le cycle climatique du CO_2, majeur de Mars. Aussi, il est important de mieux comprendre le rôle de la glace d'eau, à la fois traceur de la dynamique atmosphérique martienne actuelle mais également agent très important dans l'évolution géologique de Mars [210].

A mon sens, toutes les informations pertinentes des observations n'ont pas encore été extraites. En particulier, je souhaite réaliser une étude de spectroscopie fine, quantitative pour estimer l'évolution spatiale et temporelle des propriétés micro-physiques de la surface (taille de grains, transparence, rugosité, contenu en impureté, mode de mélange). Le but principal est de tester les différentes étapes du modèle de geyser, et en cas de validation, de proposer des données quantitatives fiables pour établir une modélisation physique des processus.

La thèse de François Andrieu en cours, se focalise sur l'étude des dark spots à petite échelle sur la dune de Richardson. Dans un premier temps, elle permettra de développer des outils méthodologiques pour estimer les caractéristiques de la surface, en utilisant la théorie de l'inversion bayésienne. Grâce à ces outils, les valeurs des paramètres et leurs incertitudes seront estimées de manière efficace pour l'ensemble des spectres des images hyperspectrales. Dans un second temps, une extension régionale de ce travail sur toute la zone sud de Mars me semble important, pour estimer des comportements d'évolutions globaux de la calotte.

D'autre part, je souhaite réaliser une étude géomorphologique quantitative d'après les images HiRISE à résolution de 50cm/pixel pour décrire finement l'évolution des écoulements, leur vitesse apparente, leur extension latérale,... L'idée est de coupler cette étude avec un modèle numérique de terrain pour connaître quantitativement la pente. Cette étude permettra de contraindre le mécanisme d'écoulement et de déstabilisation des reliefs martiens.

Enfin, je souhaite développer des modèles numériques et analogiques en chambre froide pour simuler les différents phénomènes macroscopiques (nettoyage des poussières, écoulements, ...), en complément des simulations thermodynamiques de l'IPAG (thèse de Florence Grisolle soutenue en 2013), en chambre froide à IDES, en chambre contrôlée à l'Open University de Londres. Il s'agira de réaliser des expériences simplifiées en laboratoire afin de tester et calibrer des simulations physiques qui pourront être transposées aux conditions martiennes actuelles. Seule la concordance entre expérimentations en laboratoire, simulations numériques et observations, pourra nous permettre de saisir les mécanismes en jeux sur Mars.

A plus long terme se tient l'enjeu de compréhension des cycles climatiques anciens et de l'évolution géologique de Mars. Je souhaite développer des outils de simulation pour étudier le phénomène majeur d'érosion martien dans les périodes passées. Il s'agirait de simuler le bilan de la déstabilisation des surfaces, en fonction de l'ensoleillement (dépendant à la fois de la saison, de la latitude et des pentes). A l'image des études sur la formation des calottes polaires [181] et du "mantle terrain" [189], existe-t'il la trace géologique des condensations de CO_2 et des phénomènes de geyser formées dans le passé de Mars ?

4.4 Publications

Co-encadrement de doctorant :
- F. Andrieu

Publications scientifiques :
- **Schmidt F.**, Douté S., Schmitt B., Vincendon, M., Langevin, Y., Bibring J.-P. and the OMEGA Team ; "Albedo control of the Seasonal South Polar Cap recession" ; Icarus, 2009, 200, 374-394 (voir section 4.4.1).
- **Schmidt F.**, Schmitt B., Douté S., Forget, F., Jeng, J.-J., Martin, P., Langevin, Y., Bibring J.-P. and the OMEGA Team ; "Sublimation of the Martian CO2 seasonal south Polar Cap", Planetary and Space Science, 2010, 58, 1129- 1138 (voir section 4.4.2 page 235).
- Kereszturi A., Vincendon M., **Schmidt F.**, "Water ice in the dark dune spots of Richardson crater on Mars", Planetary and Space Science, 2011, 59, 26-42 (voir section 4.4.3 page 246).
- Jouannic, G., Gargani, J., Costard, F., Ori, G. G., Marmo, C., **Schmidt, F.** and Lucas, A. (2012), "Morphological and mechanical characterization of gullies in a periglacial environment : The case of the Russell crater dune (Mars)", Planetary and Space Science, 71, 38-54
- **Schmidt F.** et al., "Dark spot in the South Polar Cap of Mars", in preparation

4.4.1 Asymétrie de la calotte saisonnière Sud de Mars

Cette section contient l'article suivant :

Schmidt F.**,** Douté S., Schmitt B., Vincendon, M., Langevin, Y., Bibring J.-P. and the OMEGA Team ; "Albedo control of the Seasonal South Polar Cap recession" ; Icarus, 2009, 200, 374-394

Icarus 200 (2009) 374–394

Contents lists available at ScienceDirect

Icarus

www.elsevier.com/locate/icarus

Albedo control of seasonal South Polar cap recession on Mars

Frédéric Schmidt [a,*], Sylvain Douté [a], Bernard Schmitt [a], Mathieu Vincendon [b], Jean-Pierre Bibring [b], Yves Langevin [b], The OMEGA Team

[a] *Laboratoire de Planétologie de Grenoble, Université de Grenoble, CNRS, INSU, BP 53, 38041 Grenoble Cedex 9, France*
[b] *Institut d'Astrophysique Spatiale, Université Paris XI, Bâtiment 121, 91405 Orsay cedex, France*

ARTICLE INFO

Article history:
Received 19 December 2007
Revised 9 October 2008
Accepted 1 December 2008
Available online 25 December 2008

Keywords:
Mars, surface
Mars, polar caps
Ices
Spectroscopy

ABSTRACT

Over the last few decades, General Circulation Models (GCM) have been used to simulate the current martian climate. The calibration of these GCMs with the current seasonal cycle is a crucial step in understanding the climate history of Mars. One of the main climatic signals currently used to validate GCMs is the annual atmospheric pressure cycle. It is difficult to use changes in seasonal deposits on the surface of Mars to calibrate the GCMs given the spectral ambiguities between CO_2 and H_2O ice in the visible range. With the OMEGA imaging spectrometer covering the near infra-red range, it is now possible to monitor both types of ice at a spatial resolution of about 1 km. At global scale, we determine the change with time of the Seasonal South Polar Cap (SSPC) crocus line, defining the edge of CO_2 deposits. This crocus line is not symmetric around the geographic South Pole. At local scale, we introduce the snowdrop distance, describing the local structure of the SSPC edge. Crocus line and snowdrop distance changes can now be used to calibrate GCMs. The albedo of the seasonal deposits is usually assumed to be a uniform and constant parameter of the GCMs. In this study, albedo is found to be the main parameter controlling the SSPC recession at both global and local scale. Using a defrost mass balance model (referred to as D-frost) that incorporates the effect of shadowing induced by topography, we show that the global SSPC asymmetry in the crocus line is controlled by albedo variations. At local scale, we show that the snowdrop distance is correlated with the albedo variability. Further GCM improvements should take into account these two results. We propose several possibilities for the origin of the asymmetric albedo control. The next step will be to identify and model the physical processes that create the albedo differences.

© 2009 Elsevier Inc. All rights reserved.

1. Introduction

A significant fraction of the martian atmosphere, mainly composed of CO_2, is trapped during winter on the planet's surface at high latitudes in the form of CO_2 frost. When the sunlight returns in spring, the frost radiative balance becomes positive and CO_2 sublimates and returns into the atmosphere. This main features of the martian seasonal cycle were revealed by the pioneering work of Leighton and Murray (1966).

The OMEGA imaging spectrometer confirmed that the Seasonal South Polar Cap (SSPC) of Mars, during its recession phase, is essentially composed of CO_2 ice. As discussed by Langevin et al. (2007), the H_2O ice signature, detected in the solar longitude range $Ls = 110°–193°$, is probably due to clouds in the atmosphere. Surface H_2O ice is present only at some specific locations over the range of $Ls = 220°–250°$. On the other hand, the seasonal North Polar cap involves both H_2O and CO_2 frosts (Schmitt et al., 2006). In this article, we will consider only CO_2 in the SSPC.

During the recession phase, different processes of energy loss/gain are involved in the defrost mass balance, namely latent heat consumption due to CO_2 frost sublimation, thermal emission, absorption of direct and indirect (scattered) sunlight, absorption of thermal emissions from the atmosphere and the surrounding terrain and conduction of thermal energy in the ground. Different parameters are involved in those processes, including albedo as suggested by Piqueux et al. (2003) and Colaprete et al. (2005), thermal emissivity as accurately modeled by Forget et al. (1998), slopes and surface roughness (Veverka and Goguen, 1973; Aharonson and Schorghofer, 2006), thermal inertia of the ground (Aharonson, 2004), annual surface pressure change, altitude and heat advection from the atmosphere.

Recent General Circulation Models (GCMs), integrating processes involved in the CO_2 cycle (including CO_2 snow formation and precipitation), are able to reproduce the Viking Lander 1 pres-

* Corresponding author. Presently at: ESA - ESAC, PO Box 78, E-28691 Villanueva de la Cañada Madrid, Spain. Fax: +34 91 81 31 325.
E-mail address: fschmidt@sciops.esa.int (F. Schmidt).

0019-1035/$ – see front matter © 2009 Elsevier Inc. All rights reserved.
doi:10.1016/j.icarus.2008.12.014

sure measurements (Forget et al., 1998, 1999), assuming a uniform and constant albedo value for the seasonal caps and no surface slope effects. Nevertheless, albedos observed by Viking (James et al., 1979) and more recently by MOC (James et al., 2001; Benson and James, 2005) and TES (Kieffer et al., 2000) and OMEGA (Langevin et al., 2007) are changing in space and time.

Current GCMs are able to reproduce the time evolution of the surface area covered by CO_2 frost (Lewis et al., 1999). In order to enhance our confidence in both present and past climate studies, the next generation of GCMs should reproduce the latitude of the so called "crocus line" at local scale as a function of longitude and time. For that purpose, they must take into account the changes in time and space of the parameters controlling the processes listed above.

The aim of this article is to determine the relative importance of these factors in controlling SSPC recession.

We will pursue the following objectives:

(1) Monitor the spatial distribution and albedo of H_2O and CO_2 ices in the SSPC as a function of time using a set of OMEGA observations for the time period ranging from $Ls = 110°$ to 320°. For that purpose, we use an automatic detection algorithm called Wavanglet (Schmidt et al., 2007). Concepts describing the structure of the SSPC edge ("inner crocus line," "outer crocus line" and "snowdrop time") are introduced, based on detection statistics inside latitudinal bins. The evolution of the latitude and structure of the SSPC edge as a function of time and longitude constitutes our main constraint (Section 2).
(2) Model, for an ice layer, the daily and cumulative CO_2 frost mass budget by integrating the radiative gains and losses from or toward space as well as the conductive heat coming from the ground. Special care will be taken in the modeling of the topographically induced shadows. The mass balance is calculated for individual facets with their own altitude and slope orientation based on MOLA DTM (Section 3).
(3) Perform a sensitivity study of the model regarding to its principal parameters, namely thermal inertia of the ground linked with subsurface heat release, altitude linked with the temperature of the CO_2 layer, surface roughness linked with shadowing effects and thus with absorption of solar light, emissivity linked with thermal emission of the ice (Section 4).
(4) Challenge the model with various measurements of the SSPC, including spatial and temporal distributions of the CO_2 ice occurrence as determined by OMEGA (see objective 1), spatial and temporal distributions of the CO_2 ice albedo as measured by OMEGA (see objective 1), total mass accumulation retrieved from neutron flux measurements by GRS and HEND. This analysis is done at two spatial scales:
   (a) global scale (i.e. flat South Polar region divided into two longitude sectors, cryptic and anti-cryptic). We show that the model is compatible with all measurements, using simple analytical laws for the visible and infrared albedo dependence with latitude and time (Section 4.1.8),
   (b) local scale (i.e. rough South Polar region, divided into facets at a resolution of 1 km). We demonstrate that the structure of the SSPC edge cannot be predicted by the model using the smooth albedo variation already used at global scale. We found a correlation between the structure of the SSPC edge and the distribution of albedo observed by OMEGA at the location of the transition zone, but more than 10 martian days before its passage (Section 4.2).
(5) Discussion of the processes that potentially govern the albedo global asymmetry between the cryptic and anti-cryptic sectors and that can explain the albedo variability at the lower spatial scale (Section 5).

2. Analyzing a sequence of OMEGA/MEX observations for monitoring CO_2 and H_2O ices

The aim of this section is to present how we monitor the SSPC during the recession phase, when ice sublimates.

2.1. Selection of OMEGA observations

The imaging spectrometer OMEGA on board Mars Express has acquired the most comprehensive set of observations to date in the near-infrared (0.93–5.1 μm) on the SSPC from winter solstice to the end of the recession at $Ls = 325°$ (Langevin et al., 2007). Monitoring the spatial distribution of CO_2 and H_2O ice requires their automatic detection due to the large number of images. For that purpose, we developed a method called "Wavanglet" (Schmidt et al., 2007) that is described briefly in the next section.

From $Ls = 110°$ to 320° of martian year 27 (early 2005 to mid 2006), we select a total of 605 OMEGA/MEX observations with a positive detection of CO_2 ice at high southern latitudes.

2.2. Wavanglet detection method

The detection is carried out by comparing each spectrum of an image with reference spectra of compounds we want to detect in an optimized subspace of wavelets. The correlation between the reduced observed and reference spectra is calculated and compared to a threshold in order to declare detection (1) or absence (0). After the processing of an OMEGA image, the Wavanglet algorithm provides one binary image with the same spatial dimensions—called the *detection mask*—for each reference compound (Schmidt et al., 2007).

We take into account the information about corrupted spectels and lines and we systematically remove spectra acquired with incidence angles higher than 85° and/or emergence angles higher than 70° (low signal to noise ratio). In this study we use four references, namely one synthetic (i.e. generated by a radiative transfer model) spectrum of CO_2 ice, one synthetic spectrum of H_2O ice, one endmember spectrum of dust extracted from an OMEGA image and one endmember spectrum of water ice clouds observed over Hellas.

2.3. Position and structure of the polar cap edge

Previous studies on the south seasonal cap recession in the visible range have been completed by several authors (James et al., 1979, 2000; Iwasaki et al., 1990; Benson and James, 2005). Other studies in the infrared range were conducted by Kieffer et al. (2000) using the TES instrument. These authors consider that a sudden rise of surface temperature, from around 145 K (the temperature of CO_2 ice in equilibrium with the atmosphere) to about 230 K (the temperature of the mineral bare ground) indicates the passage of the sublimation front. For a given location, fitting the temporal evolution of the temperature by an arctangent empirical law provides the crocus date which, by definition, coincides with the inflection of the curve. The crocus line is the set of locations, where the crocus dates are equal to a given *Ls*. In the visible range, another specific law is used to parametrize the decrease of albedo and evaluate the crocus date, assuming such event coincides with CO_2 disappearance. These studies already suggested that the edge of the seasonal cap is a transition zone where patches of CO_2 ice and dust coexist geographically over a certain spatial extent.

In this article, we propose to characterize the transition zone by defining "inner and outer crocus lines" using CO_2 detection by OMEGA in the near infrared. We define a *bin*, an element 0.3° by 10°, respectively in latitude and longitude, belonging to a geographical grid. Hundreds of OMEGA pixels usually fall into such

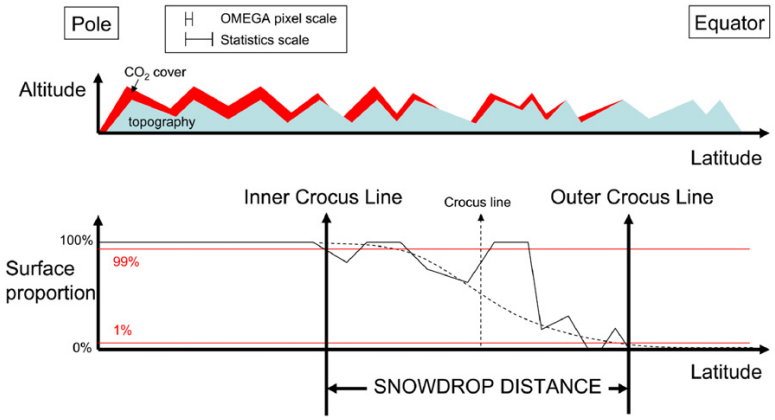


Fig. 1. Structure of the SSPC edge, definition of the inner/outer crocus lines and the snowdrop distance.

a bin making it possible to calculate statistics for different physical quantities. A *meridian profile* is the latitude sequence of values calculated for the bins falling into the same longitude range (see Appendix A).

First we segment all CO_2 detection masks (see Section 2.2) into bins. The OMEGA spatial resolution can change from 2 km to 700 m depending on observation conditions but the bin size is constant. The same grid is used to represent the model results (see Appendix A for definition of scales). For each bin, the CO_2 *ice coverage* indicator f_{CO_2} is the number of pixels with positive detection of CO_2 divided by the total number of pixels. In case of sub-pixel mixing, f_{CO_2} is an approximation of the real coverage.

Second, we build a meridian profile of CO_2 ice coverage for each individual OMEGA image corresponding to a given *Ls*. The bins that contain a border (border of the observation, border of corrupted portions of an image) are eliminated in order to prevent biases.

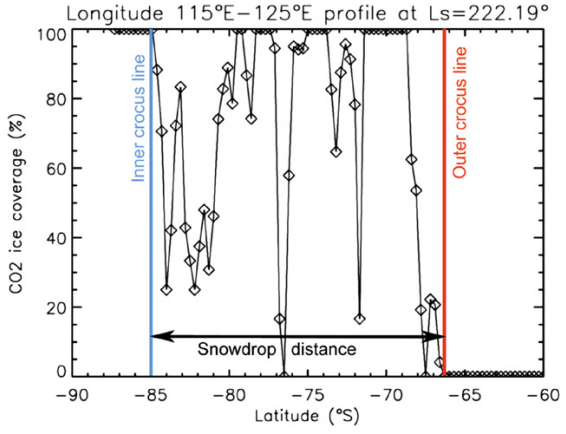
Third, from each meridian profile, we extract the inner/outer limits of the SSPC according to 3 rules:

- outer crocus line, i.e. the bin that contains a CO_2 ice coverage f_{CO_2} higher than 1% and that is the closest to the equator;
- inner crocus line, i.e. the bin that contains a CO_2 ice coverage f_{CO_2} lower than 99% and that is the closest to the pole;
- inner and outer crocus line, i.e. the bin that contains the inner/outer crocus line is valid only if its adjacent neighbor bins contain no image border.

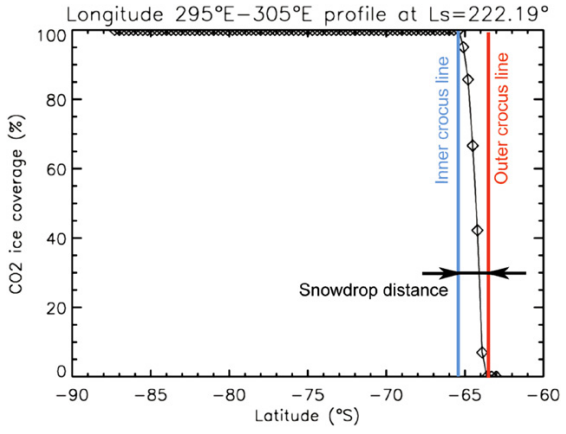
When treating our selection of OMEGA images, we determine the latitude of both crocus lines at discrete values of *Ls* (time) for 36 intervals 10° wide in longitude. At a given location, following the definition by Kieffer et al. (2000), we propose to name the date when the inner crocus line (respectively, outer crocus line) crosses that location the “inner crocus date” (respectively, the “outer crocus date”).

The latitudinal distance (resp. temporal gap) between the inner and outer crocus lines (resp. crocus date), that defines the width (resp. time) of the CO_2 snow drop, can be named SNOW-DROP. Incidentally, the term “snowdrop” also denotes a flower that grows through snow in spring on Earth. For convenience, and because we prefer flowers to inelegant acronyms, we propose the more simple term “snowdrop” (see Fig. 1).

At global scale, the position of the SSPC observed by OMEGA, described by the mean crocus line, is usually not symmetric around the geographic South Pole. At local scale, the structure of the SSPC edge, described by the snowdrop time, changes with time/latitude and longitude. The mean value of the snowdrop time is 15° *Ls*, but it can vary from a few degrees up to more than



(a) Cryptic sector



(b) Anti-cryptic sector

Fig. 2. Definition of the snowdrop distance at $Ls = 222.19°$ for two extreme cases: (a) meridian profile in the cryptic sector (longitude range 115°–125° E) where the transition zone of CO_2 ice coverage is wide and chaotic, and (b) meridian profile in the anti-cryptic sector (longitude range 195°–305° E) where the transition zone of CO_2 ice coverage is regular and narrow.

30° *Ls*. In some extreme situations, the snowdrop time can reach half of the total sublimation duration showing that this transition period can be very long. One goal of this paper is to understand these patterns and link them to processes and physical parameters.

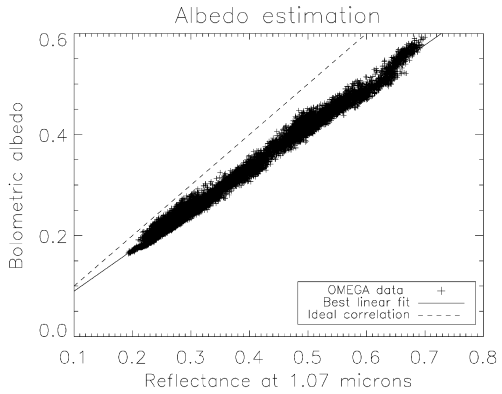


Fig. 3. Empirical relation between the reflectance $R^{O}_{1.07}$ measured by OMEGA at 1.07 μm and the bolometric albedo A^{O}_{vis} calculated (see Eq. (2)). The points represent the population of spectra of the observation ORB17886_1. We can find a regression line that fits the cloud of points with a chi-square of 1.41096. The same relation has been found for the observation ORB1868_1.

2.4. Monitoring the albedo with OMEGA

Calculating the instantaneous or integrated mass budget requires monitoring of the ice bolometric albedo, under the aerosols layer. Definition of the bolometric albedo $A_{dh,vis}$, spectrally integrated (weighted by the solar spectrum) and directional-hemispheric (dependent on the incidence direction and integrated on all emergence directions of the upper hemisphere) can be found in (Hapke, 1993).

Practically speaking, accurate evaluation requires either consecutive (Paige and Ingersoll, 1985) or simultaneous (for instance with the CRISM instrument by Murchie et al., 2004) multi-angular sampling of the bidirectional reflectance distribution function (BRDF) of the icy terrain. Multi-angular OMEGA data (EPF) that would allow us to constrain the BRDF prior to directional integration are very sparse in space and time. As a consequence, monitoring the bolometric albedo of the entire SSPC from OMEGA images lies outside the scope of this paper. We will suppose that the surface is lambertian.

For quantitative studies at global scale (see Section 4.1), we propose to estimate the bolometric albedo, noted A^{B}_{vis}, in a two step process. First, estimation of the CO_2 ice reflectance $R^{V}_{1.07}(\theta_i, \theta_e, \theta_a)$ at 1.07 μm in the continuum using Vincendon's approach to remove the contribution of aerosols (Vincendon et al., 2008). The use of this spectral channel was also proposed by Langevin et al. (2007) who argues that it combines a high signal to noise ratio, high radiometric accuracy and no absorption bands due to CO_2 ice, H_2O ice and CO_2 gas. We can note that, after $Ls = 220°$, water ice clouds are completely absent in the South Polar region. At 1.07 μm, dust aerosols significantly modify the apparent surface albedo, notably for bright icy surfaces which appear darker. Vincendon's method evaluates the contribution of the aerosol scattering and attenuation at all wavelengths from a narrow spectral region where the entire signal comes from the aerosols (saturated bands of CO_2 ice). Second, estimation of the spectrally integrated albedo from the reflectance $R^{V}_{1.07}(\theta_i, \theta_e, \theta_a)$ using an empirical law (see Fig. 3). Indeed we found a linear relationship between A_{vis} and $R_{1.07}$, on the one hand, by weighting and integrating the OMEGA visible and near IR channels and, on the other, using the lambertian hypothesis. As a first approximation, we suppose that the aerosol contribution always has the same spectral shape, such that the linear relationship is always valid. For global scale, the final relation is:

$$A_{dh,vis}(\theta_i) \simeq A^{B}_{vis} = 0.812 \times R^{V}_{1.07}(\theta_i, \theta_e, \theta_a) + 0.009. \quad (1)$$

For albedo studies at local scale (see Section 4.2), it is not possible to use Vincendon's method to estimate the aerosol contribution everywhere because the CO_2 ice absorption bands are not always saturated. As a crude approximation, we will use instead the reflectance $R^{O}_{1.07}$ measured by OMEGA in the continuum at 1.07 μm for a combination of incidence and emergence angles that vary weakly from pixel to pixel. We will assume that the local maximum of albedo variability, if constant over a long period of time, is more likely to be at the surface rather than in the atmosphere. For local scale, the final equation is:

$$A_{dh,vis}(\theta_i) \simeq A^{O}_{vis} = 0.812 \times R^{O}_{1.07}(\theta_i, \theta_e, \theta_a) + 0.009, \quad (2)$$

with θ_i the incidence angle, θ_e the emergence angle, and θ_a the azimuth.

In this study, we calculate the average and the variance of the "albedo" in each bin of the grid based on the pixels with positive detection of CO_2 (see Appendix A for definition of scales). Such quantity will be denoted A^{B}_{vis} and A^{O}_{vis}.

3. D-frost, the daily and cumulative CO_2 frost mass budget model

The aim of this section is to introduce the D-frost mass balance model used to solve the equations of a terrain facet (defined by location and slope) that is already covered by a layer of CO_2 ice.

3.1. Topography and roughness measured by MOLA

The MOLA topographic dataset covers the South Polar region at a resolution of 1/64 degree (available on line[1]). The dataset is interpolated where no data is recorded, especially near the geographic South Pole from latitude 90° S to 86° S. We use a map built according to a South Polar stereographic projection and a resolution of 920 m, comparable to the best OMEGA spatial resolution (≈700 m). Better spatial resolution is available but, in this case, the calculation time of our model would be too long (in excess of one month). We define each pixel of the MOLA dataset as a facet (see Appendix A for definition of scales).

3.1.1. MOLA topography

We calculate the local slope as a function of the geographic coordinates by differentiating the MOLA topography $h(x, y)$ with the following operator (see Appendix B for details):

$$\begin{cases} \dfrac{\partial}{\partial L} = \dfrac{2R\cos(\phi)}{1-\sin(\phi)}\left(-\sin(L)\dfrac{\partial}{\partial y} + \cos(L)\dfrac{\partial}{\partial x}\right), \\ \dfrac{\partial}{\partial \phi} = \dfrac{2R}{1-\sin(\phi)}\left(\cos(L)\dfrac{\partial}{\partial y} + \sin(L)\dfrac{\partial}{\partial x}\right), \end{cases} \quad (3)$$

L being the east increasing longitude, ϕ the latitude, R the radius of the planet and (x, y) the map coordinates.

This method has the advantage of producing a result for all points in this projection. Nevertheless, the errors due to the map projection and to the interpolation of several MOLA points are difficult to estimate.

3.1.2. MOLA roughness

Surface roughness is defined relatively to all scales higher than the facet size. Several statistical descriptors of this quantity can be found in the literature (Shepard et al., 2001; Aharonson et al., 2001), namely the standard deviation of the altitude $h(x, y)$ from the mean or more robustly from the median, interquartiles and the decorrelation length. Pioneer work on roughness as an instance of fractal distribution was done by Sayles and Thomas (1978). Such

[1] http://pds-geosciences.wustl.edu/missions/mgs/megdr.html.

description was applied for the north polar cap using MOLA data by Malamud and Turcotte (2001). They used wavelets to estimate roughness as the local value of the power law dependence of the power spectral density on frequency. They estimated the exponent $\beta \simeq 3.5$ for the south permanent cap and $\beta \simeq 2$ for the surrounding terrain. An alternative theory describes roughness as the local value of the exponent of the RMS slope as a function of baseline, i.e. the Hurst exponent H. Recently Aharonson and Schorghofer (2006) estimated a local value of H which is about 0.8 for both Mars as a whole and the region occupied by the seasonal South Polar cap. In this study, we use the Hurst exponent fractal description of the roughness because an adapted model of a self-shadowing function is provided by Shepard and Campbell (1998).

The study by Campbell et al. (2003) suggests that the MOLA dataset cannot be extrapolated for roughness scales lower than 15 m. In addition, no datasets are available for the complete South Polar region of Mars. In this article, the roughness at scales below the facet size are ignored.

3.2. Daily averaged radiation absorbed by frost

Computing the seasonal radiation budget is an important step in understanding the climate of the polar regions. From the parametrization of the "instantaneous" absorbed energy Q by Kieffer et al. (1977), Schorghofer and Aharonson (2005), Aharonson and Schorghofer (2006), we will compute the daily averaged absorbed radiation W at a given location on the surface of Mars using the integration method used by (Laskar et al., 1993). There are four sources, namely direct sunlight Q_{sun}, sunlight scattered by the atmosphere Q_{scat}, thermal emission by the atmosphere Q_{IR} and thermal emission by the neighboring facets Q_{floor}:

$$W = \int (Q_{\text{sun}} + Q_{\text{scat}} + Q_{\text{IR}} + Q_{\text{floor}})\, dt. \tag{4}$$

All these terms depend on local slope γ. We will use the following notation for three normalized vectors, that is $\overrightarrow{r_{\text{surf}}}(L,\phi)$ for the radius vector pointing at a location on the surface assuming a spherical planet, $\overrightarrow{r_{\text{sun}}}(\alpha,\delta)$ for the radius vector of the sub-solar point and $\overrightarrow{n_{\text{surf}}}(L_{\text{n}},\phi_{\text{n}})$ for the direction normal to the local surface. The coordinates are expressed in increasing east longitude (L, α, L_{n} are from 0 to 2π) and latitude ($\phi, \delta, \phi_{\text{n}}$ are from $-\frac{\pi}{2}$ to $\frac{\pi}{2}$). The local slope γ is defined as:

$$\gamma = \arctan\sqrt{\left(\frac{\partial topo}{\partial \phi}\right)^2 + \left(\frac{\partial topo}{\partial L}\right)^2}. \tag{5}$$

In order to simplify the equation, the integration of the "instantaneous" insolation is performed relative to longitude L instead of time as in Laskar et al. (1993), assuming that the relative orientation of the planet rotation axis and the sun direction is constant during a day, which is a reasonable assumption for planet Mars. The integration method is described in Appendix C.

Integration of the different contributions Q_{sun}, Q_{scat}, Q_{IR} and Q_{floor} are explicitly described below:

(1) Direct solar illumination

$$Q_{\text{sun}} = \frac{S_{\text{sun}}}{r_{\text{sun}}^2}(1-f)^{1/\max((\overrightarrow{r_{\text{surf}}}\bullet\overrightarrow{r_{\text{sun}}}),0.04)}(1-A_{\text{vis}}) \times (\overrightarrow{n_{\text{surf}}}\bullet\overrightarrow{r_{\text{sun}}})\Psi(\overrightarrow{r_{\text{surf}}}\bullet\overrightarrow{r_{\text{sun}}}, H, \gamma). \tag{6}$$

The first ratio is the solar constant at the heliocentric distance of Mars, the second factor expresses the absorption of radiation by the surface, the third represents the parametrized atmospheric attenuation (Kieffer et al., 1977; Schorghofer and Aharonson, 2005; Aharonson and Schorghofer, 2006), the fourth term expresses the geometrical effect and the fifth term Ψ quantifies the loss of illumination due to self-shadowing effects linked with roughness. In the following, these five factors will be noted F_1 to F_5. We use the empirical shadowing function for fractal surfaces $\Psi(\overrightarrow{r_{\text{surf}}}\bullet\overrightarrow{r_{\text{sun}}}, H, \gamma)$, truncated to the 6th term, determined by Shepard and Campbell (1998):

$$\Psi(\overrightarrow{r_{\text{surf}}}\bullet\overrightarrow{r_{\text{sun}}}, H, \gamma) = 1 - \frac{1}{2}\sum_{n=1}^{6}\frac{1}{2.3^{n-1}}\operatorname{erfc}\left(\frac{n^{1-H}}{\sqrt{2}\frac{\sqrt{1-(\overrightarrow{r_{\text{surf}}}\bullet\overrightarrow{r_{\text{sun}}})^2}}{(\overrightarrow{r_{\text{surf}}}\bullet\overrightarrow{r_{\text{sun}}})}\tan(\gamma)}\right). \tag{7}$$

We estimate the integral quantities using a Simpson numerical integration scheme (Press et al., 1986–1992).

(2) Indirect solar illumination by scattering in the atmosphere (half of the scattering lost in space) and absorbed by the surface according to Kieffer et al. (1977) and Aharonson and Schorghofer (2006):

$$Q_{\text{scat}} = \frac{S_{\text{sun}}}{r_{\text{sun}}^2} f_{\text{scat}} \frac{1}{2}(1-A_{\text{vis}})\cos^2\left(\frac{\gamma}{2}\right). \tag{8}$$

(3) Surface heating by thermal emission of the atmosphere according to Kieffer et al. (1977) and Aharonson and Schorghofer (2006):

$$Q_{\text{IR}} = \frac{S_{\text{sun}}}{r_{\text{sun}}^2} f_{\text{IR}}(1-A_{\text{IR}})\cos^2\left(\frac{\gamma}{2}\right)(\overrightarrow{r_{\text{surf}}}\bullet\overrightarrow{r_{\text{sun}}})_{\text{noon}}. \tag{9}$$

The cosine of the incidence angle at noon for a flat surface:

$$(\overrightarrow{r_{\text{surf}}}\bullet\overrightarrow{r_{\text{sun}}})_{\text{noon}} = (\overrightarrow{r_{\text{surf}}}\bullet\overrightarrow{r_{\text{sun}}})_{L=\alpha} = \sin\left(\frac{\pi}{2}+\phi-\delta\right). \tag{10}$$

(4) Surface heating by thermal emission of the surrounding soil, as in Kieffer et al. (1977) and Aharonson and Schorghofer (2006):

$$Q_{\text{floor}} = \varepsilon\sigma T^4(1-A_{\text{IR}})\sin^2\left(\frac{\gamma}{2}\right). \tag{11}$$

The parameter values used for the surface radiation budget are summarized in Appendix D.

3.3. Daily and cumulative defrost mass balance

3.3.1. Estimation of the "instantaneous" CO_2 defrost balance

We estimate the instantaneous CO_2 frost mass balance using the energy balance at the surface. We compute the daily radiation budget and neglect the heat advection from the atmosphere, which is a correct hypothesis for the sublimation phase as suggested by GCM studies (Forget, 1998). The flux of mass resulting from the energy balance is:

$$\frac{\partial M_{CO_2}}{\partial t} = \left(F_{\text{therm}}^{\text{out}} - W_{\text{sun}}^{\text{in}} - W_{\text{scat}}^{\text{in}} - W_{\text{IR}}^{\text{in}} - W_{\text{floor}}^{\text{in}} - F_{\text{cond}}^{\text{in}}\right)\frac{1}{L_{CO_2}}. \tag{12}$$

This equation can also be used for the daily balance assuming that the albedo and surface temperature of the facet do not change within the course of a day. A possible recondensation of CO_2 during the night on bare ground during the SSPC recession is not taken into account in this modeling. We neglect heat diffusion within the frost deposits by absorption and release of latent heat due to sublimation/recondensation and gas diffusion. We assume no metamorphism.

The different contributions of Eq. (12) are described below:

(1) Energy loss is the outgoing thermal flux from CO_2 frost at the surface. This term is estimated by a gray body emission as proposed by Warren et al. (1990):

$$F_{\text{therm}}^{\text{out}} = \varepsilon\sigma T_{\text{surf}}^4. \tag{13}$$

Surface temperature T_{surf} is determined assuming that CO_2 frost at the surface is in equilibrium with atmospheric CO_2 gas at surface pressure P_{surf}. We use the surface pressure calculated by the GCM of Forget et al. (1999) for a given date (season), location and altitude. This estimation takes into account the annual pressure cycle measured by Viking.
We use the empirical parametrized saturation curve proposed by Brown and Ziegler (1979) to convert P_{surf} into temperature T_{surf}. This method is correct only when CO_2 frost is already present on the facet.

(2) Energy gain is the absorbed radiative flux:

$$-W^{in}_{sun} - W^{in}_{scat} - W^{in}_{IR} - W^{in}_{floor}. \quad (14)$$

Those terms are estimated according to the method described in Section 3.2 (Eq. (4)).

(3) Energy gain is the conducted internal heat flux from planet Mars. It has two different origins.
   (a) Annual heat wave in the ground. This term can be neglected during the recession phase, as demonstrated in Section 4.1.3.
   (b) Geothermal heat flux. There is no direct measurement of the heat flux from planet Mars but several authors estimated it to be between 15 and 45 $mW\,m^{-2}$ on average (Shchuko et al., 2003). For comparison, on Earth the average value is around 80 $mW\,m^{-2}$. We assume that it is spatially and temporally constant:

$$F^{in}_{cond} = 40\ mW\,m^{-2}. \quad (15)$$

The order of magnitude of this flux is generally negligible in the cumulative frost balance when compared with the other terms. Nevertheless, for facets in the shadow, it could accelerate the occurrence of the crocus date by typically one martian day.

3.3.2. Cumulative mass loss during recession

We can estimate the cumulative mass loss of frost during the SSPC recession by integrating the "instantaneous" frost mass balance. We perform the integration between 2 dates T^M_{beg} and T^M_{end} expressed in solar longitude *Ls* with a time step of 5°. We start the calculation at $Ls = 90°$. The integration begins when the balance becomes negative, at a date noted T^M_{beg} (beginning of the recession as determined by the model M) that is, when the seasonal polar cap begins to sublimate. The date T^M_{beg} depends mainly on latitude, albedo and slope. T^M_{end} is the "mean" crocus date, the date of the end of the sublimation, T^M_{end}.

To convert Julian time expressed in seconds into time expressed in ° *Ls*, we use the J2000 relations which can be found in Allison and McEwen (2000).

The parameters used for modeling the defrost mass balance are summarized in Appendix E.

3.4. Latitudinal profiles of W and M_{CO_2}

We perform the calculation of the absorbed radiation W and of the frost mass balance M_{CO_2} for all the facets of the MOLA grid expressed in stereographic south projection. In order to compare both modeled and observed crocus lines, we arrange the facets inside the set of bins described in Section 2.4. For each bin, we calculate the mean and the variance of W and M_{CO_2}, both based on the population of facets within the bin. We present the results in the form of meridian profiles (see Section 2.3).

Both daily absorbed radiation and defrost mass are estimated every 5° *Ls* (almost 10 martian days). This time sampling interval is a compromise between accuracy and computational time (1 month for the M_{CO_2} on a bi-processor AMD Opteron 250, 64 bits, 2.4 GHz).

4. Results

At global scale, we show that the asymmetry of the SSPC crocus line is a consequence of a pre-existing asymmetry of the visible albedo. For both the cryptic and anti-cryptic sectors, we find that our sublimation model is compatible with the net accumulation measurements by HEND and GRS, as well as with the crocus line and albedo determined by OMEGA. At local scale, the SSPC snowdrop distance is controlled by the state of albedo distribution more than 5° *Ls* before the crossing of the inner crocus line.

We performed a sensitivity study that demonstrates that during the recession phase, the following effects/parameters have limited effects on CO_2 stability, namely heat exchange with the ground, altitude, surface roughness (slope and shadow), emissivity and albedo in the thermal infrared.

The high resolution accumulation field is difficult to estimate accurately because the only available measurements come from instruments with low spatial resolution. In addition, no accurate modeling of the SSPC CO_2 sublimation at such small scales is currently available (neither the temporal and spatial albedo variation, nor the effect of slope have been incorporated in the model). We assume in our calculations that the net accumulation has a smooth latitudinal dependency.

4.1. Recession at global scale

The global SSPC recession is not symmetric around the geographic South Pole as previously observed by Viking (James et al., 1979). Using TES data, Kieffer et al. (2000) define the *cryptic region* where CO_2 ice (at low temperature) has a low albedo. As seen in Fig. 4, this region recesses faster. This asymmetry is also observed with OMEGA data as mentioned by Langevin et al. (2007). We define the cryptic sector between longitude 60° E and 260° E, the anti-cryptic sector being the complementary, i.e. between longitude 100° W and 60° E.

In order to roughly describe the asymmetry, we estimate the mean OMEGA crocus line (or simply crocus line) for both sectors. We take the middle line between the inner and the outer crocus lines (Fig. 2) to ensure coherence with the definition by Kieffer et al. (2000). The crocus date can be noted T^O_{end}, as the date of the end of the recession observed by OMEGA. We estimate the crocus date for 4 latitudes that are also considered in a HEND study by Litvak et al. (2007). At latitude 65° S, the typical crocus date is $Ls = 220°$ for the cryptic sector and $Ls = 225°$ for the anti-cryptic sector. At latitude 85° S, the difference goes up to 20° *Ls*.

In the cryptic sector, some seemingly defrosted points (outliers) are present at latitudes higher than 70° S in the time period from $Ls = 180°$ to 230° (Fig. 4). This is due to the fact that some CO_2 deposits of the cryptic sector are covered by an optically thick mantle of dust as suggested by Langevin et al. (2006).

The near infrared view by OMEGA differs from the one offered by TES in the thermal infrared at 30 μm (see Fig. 4). The OMEGA crocus lines are at significantly lower latitudes compared to TES, even outside the interannual variability measured by TES for martian years 25, 26 and 27. This fact is probably due to subpixel mixing of ice and dust near the seasonal cap edge. The thermal infrared range is more sensitive to dust than the near infrared, according to the non-linearity of the thermal flux. In addition, the fact that the OMEGA inner crocus line is similar to the TES crocus line evolution suggests that the linear mixing occurs at a scale lower than OMEGA spatial resolution. An accurate comparison between different datasets is lies outside the scope of this paper, but would be interesting work in the future.

Now we discuss the origin of the SSPC recession asymmetry which we illustrate by two representative meridian profiles,

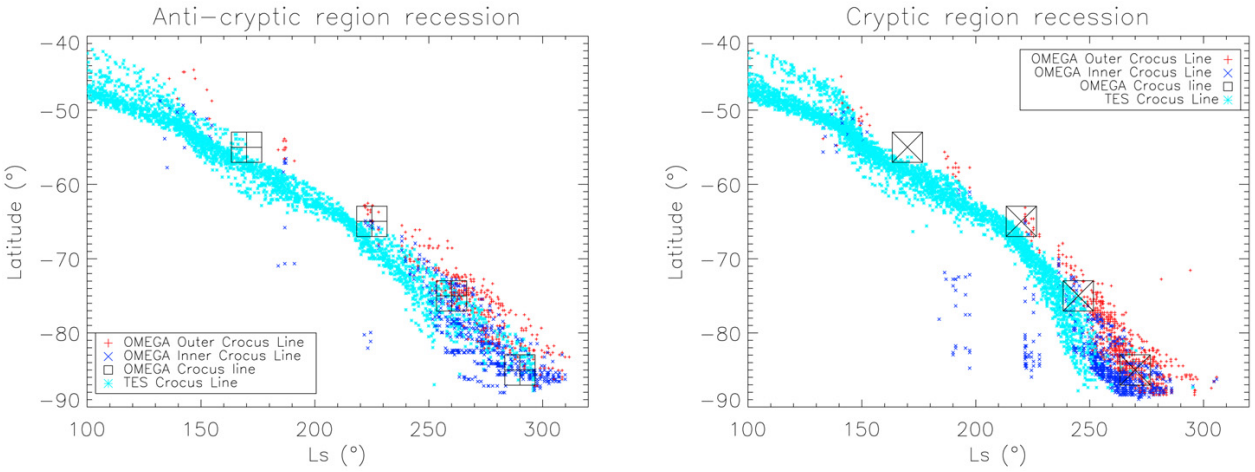


Fig. 4. SSPC recession for both the cryptic (between longitude 60° E and 260° E) and the anti-cryptic sectors (between longitude 100° W and 60° E). Small cross symbols represent the crocus line points respectively determined by OMEGA using our algorithm (+ and ×) (see Section 2.3) and by TES (∗) (Titus, 2005). Large symbols represent the average position of the OMEGA crocus line for four reference latitudes.

(a) within the cryptic sector (140°–150° E) and (b) within the anti-cryptic sector (270°–280° E).

For that purpose, we performed a sensitivity study of the defrost model, relative to the following effects/parameters on $\frac{\partial M_{CO_2}}{\partial t}$, namely annual heat wave in the ground, altitude, surface roughness, albedo and emissivity in the IR and finally albedo in the visible. We also discuss the degree of spatial asymmetry of accumulation $M_{CO_2/\mathrm{tot}}$ and the date of the beginning of sublimation T_{beg} as well as of the previous parameters.

4.1.1. CO_2 ice accumulation $M_{CO_2/tot}$

From a theoretical point of view, according to Forget (1998), the mass balance during the net accumulation phase is governed by this equation:

$$\frac{\partial M_{CO_2}}{\partial t} = \left(F^{\mathrm{out}}_{\mathrm{therm}} - F^{\mathrm{in}}_{\mathrm{adv}} - F^{\mathrm{in}}_{\mathrm{cond}} - W^{\mathrm{in}}_{\mathrm{sun}} - W^{\mathrm{in}}_{\mathrm{scat}} - W^{\mathrm{in}}_{\mathrm{IR}} - W^{\mathrm{in}}_{\mathrm{floor}}\right)\frac{1}{L_{CO_2}}. \quad (16)$$

The term $F^{\mathrm{out}}_{\mathrm{therm}}$ represents the thermal flux (Eq. (13)). It depends on emissivity ε and altitude via the CO_2 temperature. During the polar night, ε is estimated by $1 - BD_{25}$ with TES measurements by Eluszkiewicz and Moncet (2003). Before $Ls = 140°$, at latitude 87° S, they estimate that emissivity is around 0.9 for the cryptic sector and 0.75 for the anti-cryptic sector, leading to a lower accumulation mass in the latter. This difference in accumulation is in apparent contradiction with a longer recession time for the anti-cryptic sector. Section 4.1.4 shows that altitude can be considered as symmetric around the South Pole and thus the same is true for the equilibrium temperature.

Equation (16) is slightly different from Eq. (12) that expressed the defrost mass balance. The additional term $F^{\mathrm{in}}_{\mathrm{adv}}$ represents the heating due to internal, potential and kinetic energy advected by atmospheric motion. Pollack et al. (1990) shows that this term is no longer negligible because it can reach 40 $\mathrm{W\,m^{-2}}$ near the cap edge. This heating can be asymmetric due to the topographic forcing of Hellas and Argyre (Colaprete et al., 2005).

Moreover, the annual heat wave contribution $F^{\mathrm{in}}_{\mathrm{cond}}$ becomes one of the dominant sources of energy (Aharonson, 2004). On average, for the average SSPC, this term was estimated by Paige and Ingersoll (1985) to be up to 20–30 $\mathrm{W\,m^{-2}}$. An asymmetrical thermal inertia of the subsurface would lead to an asymmetrical accumulation. However, thermal inertia observed by TES is symmetrical around the pole (Putzig et al., 2005).

All radiation terms W are negligible because the main accumulation phase occurs during night time.

From an observational point of view, Viking, TES and OMEGA have observed that the SSPC is symmetric around the pole before $Ls = 220°$ at the end of the net accumulation phase (James et al., 1979; Kieffer et al., 2000; Langevin et al., 2007). Moreover a study by (Aharonson et al., 2004) using MOLA data reveals that the amplitude of the semi-annual cycle of elevation of the deposits shows no clear asymmetry in the accumulation phase. The HEND (Litvak et al., 2007) and the GRS (Kelly et al., 2006) instruments do not have enough spatial resolution to measure several meridian profiles of accumulation according to longitude.

We conclude that accumulation is likely symmetrical around the geographic South Pole.

4.1.2. Date of the beginning of sublimation T_{beg}

From a theoretical point of view, T_{beg} is the date when the balance expressed by the right hand side of Eq. (16) equals 0. Thus the asymmetry of T_{beg} depends on the asymmetry of all terms. The first three terms were previously discussed in the last section.

The radiation terms W are no longer negligible and will be discussed in Sections 4.1.5 to 4.1.7. The most likely parameter that can be asymmetric is the albedo, but the measurement by TES shows that albedo is symmetric from $Ls = 175°$ to 200° (Piqueux et al., 2003).

The date T_{beg} is difficult to evaluate by observation. The only direct measurement is by the HEND (Litvak et al., 2007) and the GRS (Kelly et al., 2006) instruments which do not have enough spatial resolution to measure T_{beg} as a function of longitude. Indirect measurement of altitude using MOLA data shows (Aharonson et al., 2004) no clear asymmetry.

Following the same argumentation as in the last section, we conclude that the date of the beginning of sublimation T_{beg} is likely symmetrical around the geographic South Pole. In the next models, T_{beg} will be a free parameter, fixed by the model itself.

4.1.3. Annual heat wave in the ground

As suggested by Aharonson (2004), the excess of heat absorbed by the ground during summer is partially released in winter. The amount of heat involved in this annual wave depends on the thermal inertia of the subsurface. We use the LMD 1D model (model

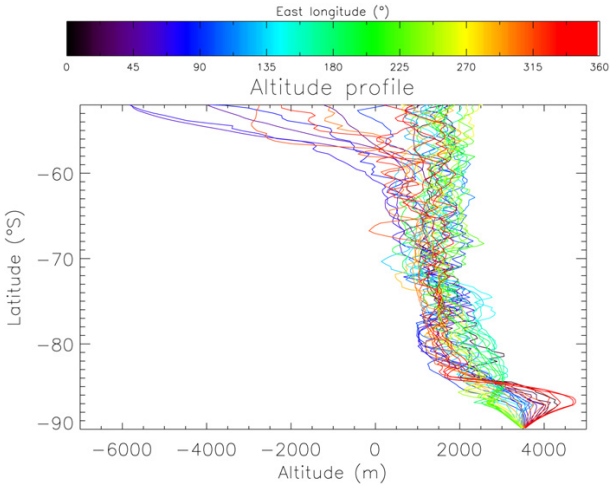


Fig. 5. Topography of the SSPC region expressed as a series of MOLA meridian profiles, each with its own color representing the longitude (see Appendix A).

M1), developed by Forget et al. (1999), to estimate the amount of energy that comes from the ground during the recession phase. We consider the cryptic and anti-cryptic sectors at four latitude points, 55° S, 65° S, 75° S and 85° S. Following the study by Aharonson (2004), the parameters of the bare soil are albedo $A_{\rm vis} = 0.29$, emissivity $\varepsilon = 0.99$. In the visible, the albedo of the frost is set to the equivalent albedo in the time independent scenario, model M2 (see Section 4.1.8). We compute the subsurface heat released during the net sublimation phase for two extreme thermal inertia values, 20 and 1000 $\mathrm{J\,m^{-2}\,s^{-1/2}\,K^{-1}}$, compatible with the range of apparent thermal inertia estimated for the South Polar region determined by Putzig et al. (2005). The integration is conducted from the $T^{\rm H}_{\rm beg}(L', \phi)$ date of the beginning of net sublimation as measured by HEND to $T^{\rm M1}_{\rm end}(L', \phi)$, the date of the total sublimation of the CO_2 ice layer computed by model M1. We run the model over three consecutive martian years to make it insensitive to the initial conditions. Subsurface heat is converted to an equivalent sublimated CO_2 mass.

The results are displayed in Table 4 for the cryptic sector and in Table 5 for the anti-cryptic sector. At maximum, 6% of the total mass sublimated is due to subsurface heat (at latitude 55° S), leading to a shift of the crocus date of less than 2° *Ls*. For comparison, the difference in crocus dates between the cryptic and anti-cryptic sectors is about 20° *Ls*.

In conclusion, this source of energy can be neglected in all calculations concerning the recession phase. Nevertheless, subsurface heat is one of the most important sources of energy during the polar night.

4.1.4. Altitude

Topography around the pole is quasi symmetric (Fig. 5). The maximum altitude difference between the anti-cryptic (orange-red profiles) and cryptic (blue-green profiles) sectors is ≈1000 m at latitudes higher than 84° S. Two particular regions depart from the general trend at latitudes lower that 60° S, namely the Hellas basin (between 40° E and 90° E) with a minimum altitude of less than −6000 m and the Argyre basin (between 300° E and 330° E) with a minimum altitude of −3000 m. Table 1 summarizes the reference altitude profiles taken for the model.

A difference in altitude produces a difference in equilibrium temperature that, in turns, leads to a difference in thermal emission and thus in defrost mass balance. We solve the equation of energy balance at the surface (see Section 3.3.1) for the cryptic and anti-cryptic sectors at four latitude points, 55° S, 65° S, 75° S and 85° S. We use the empirical law of time independent but latitude dependent albedo (model M2) as discussed in Section 4.1.8. Emissivity is set to 0.99 in order to maximize the effect of altitude on the defrost mass.

Table 1
Reference altitudes for both the cryptic and anti-cryptic sectors.

Latitude (° S)	55	65	75	85
Altitude cryptic sector (m)	1000	1000	2000	2500
Altitude anti-cryptic sector (m)	1000	1000	2000	3500

Table 2
Altitude effect on defrost mass balance at latitude 55° S. The defrost mass model is used for the SSPC anti-cryptic sector recession with the time independent albedo scenario (model M2) discussed in Section 4.1.8.

Altitude (m)	−6000	0	1000	2000
Defrost mass ($\mathrm{kg\,m^{-2}}$)	107	152	159	166

Table 3
Same as Table 2 at latitude 85° S.

Altitude (m)	1500	2500	3500
Defrost mass ($\mathrm{kg\,m^{-2}}$)	1214	1201	1189

At latitude 55° S (Table 2), a difference of ±1000 m in altitude leads to a difference in defrost mass of ±7 $\mathrm{kg\,m^{-2}}$ (±4.4% of the total mass sublimated during the recession phase) and thus a shift of the crocus date of ±1° *Ls*. At 85° S, the difference in defrost mass represents ±12 $\mathrm{kg\,m^{-2}}$, i.e. ±1.1% of the total mass, and thus a shift of the crocus date of ±0.6° *Ls* (Table 3). For comparison, the observed difference in crocus dates, which is about 20° of *Ls* at 85° S, corresponds to a defrost mass of 300 $\mathrm{kg\,m^{-2}}$.

In conclusion, the small altitude differences of ≈1000 m between the cryptic and anti-cryptic sectors cannot explain the SSPC recession asymmetry.

4.1.5. Radiation on a rough surface

This section presents a sensitivity study of our model regarding surface roughness. In order to estimate the effect of slope and shadow induced by surface roughness on the daily average absorbed radiation W (Eq. (4)), we compute it using the parametrization presented in Section 3.2. We choose the following configuration, $A_{\rm vis} = 0$, $A_{\rm IR} = 0.01$ and $\varepsilon = 0.99$ to maximize the effect of slope and shadow.

Fig. 6 represents the meridian profiles of W as a function of *Ls* for the cryptic and anti-cryptic ranges of longitudes. One can see that the spatio-temporal pattern of W is nearly identical for both sectors despite the fact that the distribution of the facets orientation as well as the roughness of the terrain could be different. This suggests that these factors do not play a role at a first order in the asymmetry.

4.1.6. Emissivity and albedo in the thermal infra-red

Emissivity and albedo are linked through the Kirchhoff law:

$$A_{\rm IR}(\theta, \lambda) = 1 - \varepsilon(\theta, \lambda), \tag{17}$$

with θ the zenith angle and λ the wavelength. The directional hemispheric albedo for a beam of light with incidence θ is noted $A_{\rm IR}(\theta, \lambda)$. The emissivity at the emergence angle θ is noted $\varepsilon(\theta, \lambda)$.

Neither the emissivity nor the albedo of the surface of Mars in the thermal infrared can be directly measured from space because of ambiguities with temperatures. Nevertheless, some estimation of emissivity with TES measurements using a band ratio of $\varepsilon = 1 - BD_{25}$ has been done by Eluszkiewicz and Moncet (2003). This

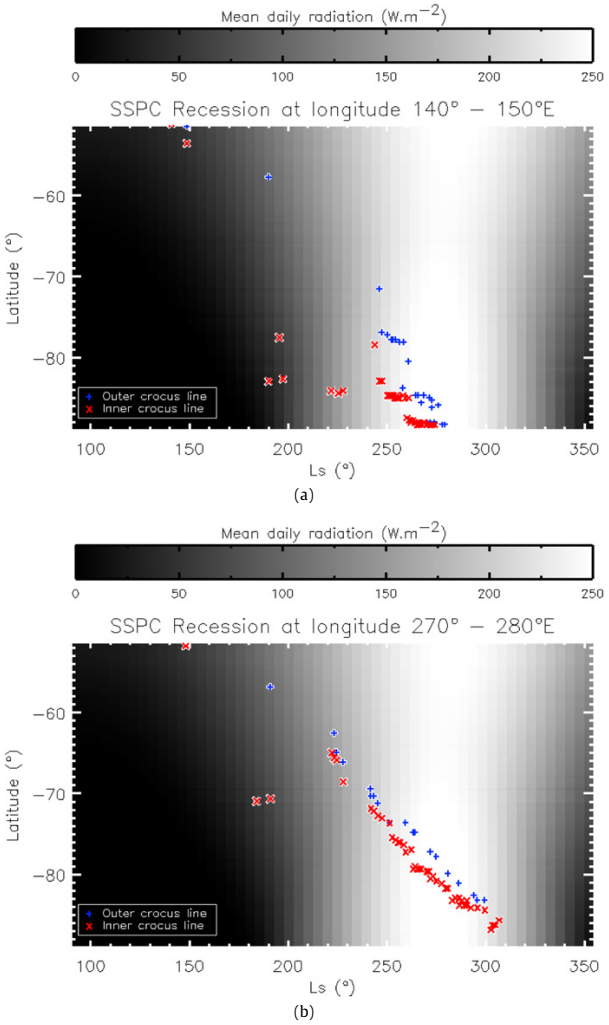


Fig. 6. SSPC crocus line points (+ and × symbols) for (a) one meridian profile of the cryptic sector (140°–150° E) and (b) for one the anti-cryptic sector (270°–280° E) compared to the spatio-temporal pattern of the mean daily absorbed radiation W (gray scale) for an albedo of 0.

study shows that, during the first year covered by MGS (martian year 25), the emissivity remains at levels higher than 0.9 for the polar region after $Ls = 140°$. A small asymmetry in emissivity is apparent at this date and then tends to disappear.

Theoretical studies or laboratory measurements provide some other clues. Warren et al. (1990) and more recently Hansen (1999) propose to model CO_2 ice spectral emissivity using the Mie theory applying the delta-Eddington approximation and using laboratory measured optical constants. In the first study Warren et al. (1990), emissivity is weighted by the Planck function for a temperature of 148 K, representative of the SSPC CO_2 frost temperature and averaged from 6 to 25 μm. This spectral domain contains only half of the black body energy, but no optical constants were available at wavelengths longer than 25 μm. For pure CO_2 ice, the emissivity increases with grain size, ranging from 0.29, for a grain size of 5 μm, to 0.91, for 2000 μm. As discussed by Langevin et al. (2007), the grain size of SSPC CO_2 observed by OMEGA ranges from a few millimeters to several dozens of centimeters, leading to an emissivity higher than 0.91. Warren et al. (1990), Hansen (1999) also shows that the presence of dust and water ice increase the emissivity. Local variability of grain size, water ice and dust content can lead to differences in emissivity from 0.91 (pure CO_2 ice with grain size of 2 mm) to 1.0 (maximum value).

We will use the range of emissivity from 0.91 to 0.99 in agreement with both TES measurements and theoretical considerations.

To estimate accurately the effect of emissivity, we simulate the cumulative frost sublimation mass, by solving the equation of energy balance at the surface (see Section 3.3.1) for the anti-cryptic sector at two extreme altitudes and latitude.

At 85° S, the cumulative defrosted mass with $\varepsilon = 0.99$ (resp. $\varepsilon = 0.91$) is 1213 kg m^{-2} (resp. 1242 kg m^{-2}). This difference represents 1.6% of the total mass sublimated during the recession phase and accelerates the crocus date by a shift of −1.6° Ls. At 55° S, the cumulative defrosted mass with $\varepsilon = 0.99$ (resp. $\varepsilon = 0.91$) is 159 kg m^{-2} (resp. 177 kg m^{-2}). This difference represents 13% of the total mass and should accelerate the crocus date by a shift of −2.4° Ls. These values are small compared to the difference in crocus dates of ≈20° between the cryptic and anti-cryptic sectors.

In conclusion, the effect of emissivity is negligible in the asymmetry of the SSPC recession.

4.1.7. Albedo in the visible range

As an approximation, we estimate the bolometric albedo A_{vis} in the visible range following the procedure exposed in Section 2.4. In that case, we implicitly assume that the variability of the albedo with the observation conditions (observation geometry, lighting condition) is weak compared to the variability linked with the surface physical properties.

In order to be compatible with our model, we average the observed OMEGA albedo for each bin, according to our reference grid (Section 3.4) with a integration time step of $Ls = 5°$. This albedo is noted A^{B}_{vis}.

Different investigations conducted in the visible and in the near IR have shown that the SSPC is asymmetric in albedo (James et al., 1979; Kieffer et al., 2000). Fig. 7 shows that OMEGA measurements confirm this conclusion. The A^{O}_{vis} of the cryptic sector is 20 to 60% lower than the albedo of the anti-cryptic sector. This leads to a sublimation rate that can be up to three times higher.

We observe that the crocus date at latitude 85° S occurs 29° Ls later at 270°–280° E longitude than at 140°–150° E. This seems to be very well correlated with the difference in observed albedo (Fig. 7). In addition, the divergence, between the cryptic and anti-cryptic sectors, of the albedo evolution and the crocus line recession occur nearly simultaneously at $Ls \approx 220°$ (see Section 4.1). Therefore, albedo seems to be a good candidate to explain the asymmetry in the SSPC recession. This qualitative result will be tested quantitatively in the next section. The origin of the albedo asymmetry, such as frost deposition, dust content, cleaning process and slab ice, will be discussed in Section 5.

4.1.8. Quantitative test

We tested the global coherence between the D-frost model (described in Sections 3.2 and 3.3), the mean latitudinal propagation of the crocus line with time $T^{O}_{end}(L', \phi)$ (see Fig. 4), the bolometric albedo A^{B}_{vis} estimated by OMEGA (see Section 2.4) and the GRS and HEND net CO_2 latitudinal accumulation curves $M^{H}_{CO_2/tot}(\phi)$ at the end of winter (Litvak et al., 2007; Kelly et al., 2006). As before, we consider two reference sectors of longitude (cryptic and anti-cryptic).

The albedo $A_{vis} = A_{vis}(L, \phi, Ls)$ is a field depending on longitude, latitude and time (expressed here in ° Ls) that is only sparsely sampled in space and time by our observations. As a consequence, we parametrize A_{vis} using simple laws for its dependencies with latitude and time, according to two basic scenarii:

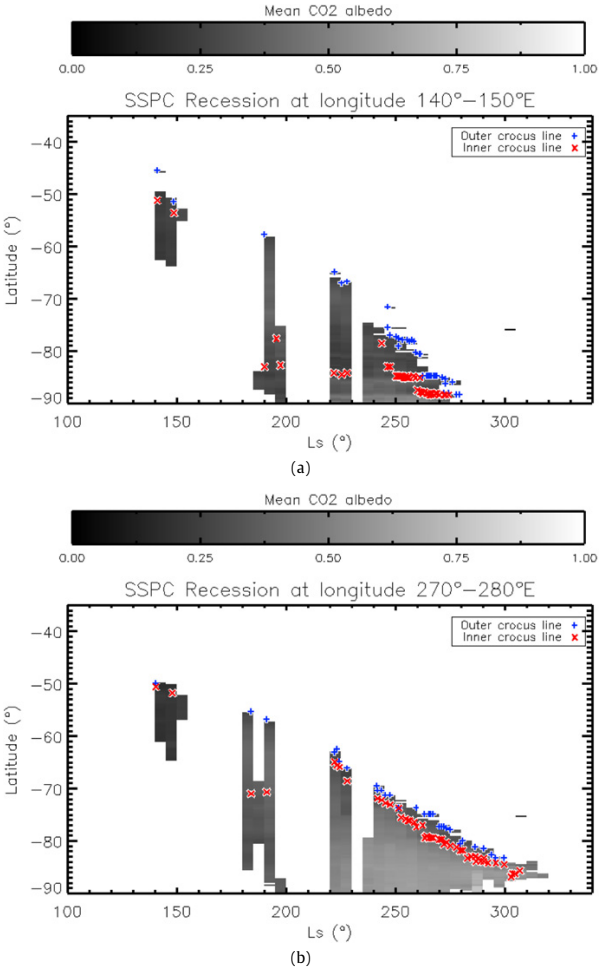


Fig. 7. SSPC crocus line points (+ and × symbols) compared to the spatio-temporal pattern of mean local albedo A^{O}_{vis} (grey scale) for two meridian profiles: (a) the cryptic (140°–150° E) and (b) anti-cryptic (270°–280° E) sectors.

- Time independent albedo (model M2), where $A_{vis}(L, \phi, Ls) = A^{M2}_{vis}(L', \phi)$. L' represents the considered longitude sector domain, cryptic or anti-cryptic, ϕ is the latitude. This scenario assumes that the seasonal polar cap has latitudinal variations of albedo that do not change with time (Ls). We reproduce different regression speeds of the crocus line by modulating the latitudinal distribution of energy absorbed by the frost since the beginning of the sublimation phase. For instance, an acceleration of the crocus line corresponds to the crossing of a region with a lower albedo than the adjacent regions at lower latitude.
- Latitude independent albedo (model M3), where $A_{vis}(L, \phi, Ls) = A^{M3}_{vis}(L', Ls)$. The same definition is used for L'. This scenario assumes that the seasonal polar cap has a constant latitudinal albedo that does change with time (Ls). We reproduce different regression speeds of the crocus line according to time and longitude by modulating the temporal repartition of the energy absorbed by the frost since the beginning of the sublimation phase. For instance, an acceleration of the crocus line corresponds to a simultaneous decrease of the albedo for the whole remaining cap.

In both cases we consider flat and horizontal surfaces, but use realistic altitudes.

4.1.8.1. Time independent albedo (model M2) For a given latitude ϕ, we compute the *equivalent albedo* $A^{M2}_{vis}(L', \phi)$ required to sublimate the CO_2 frost initial mass $M^{H}_{CO_2/tot}(\phi)$ measured by HEND/GRS, in the interval of time $[T^{M2}_{beg}(L', \phi), T^{O}_{end}(L', \phi)]$. The date $T^{M2}_{beg}(L', \phi)$ is the beginning of the net sublimation, when the local mass balance becomes negative in our model (Eq. (12)), whereas $T^{O}_{end}(L', \phi)$ is the crocus date determined by OMEGA (end of the sublimation phase, Fig. 4). The error bar on the equivalent albedo is mainly defined by the error bar on the initial mass. We use a high emissivity, $\varepsilon = 0.99$, and a low albedo in the thermal IR, $A_{IR} = 0.01$, in order to estimate the lower limit of the equivalent albedo. We show in Section 4.1.6 that the effect of emissivity in its realistic range of occurrence (between 0.91 and 1) is minor on the defrost mass and thus on the equivalent albedo.

We test the validity of the model by evaluating (i) the agreement between the equivalent albedo $A^{M2}_{vis}(L', \phi)$, estimated for the four latitudes at 85° S, 75° S, 65° S and 55° S in concordance with the HEND study (Litvak et al., 2007), and the observed albedo $A^{B2}_{vis}(L', \phi) = \langle A^{B}_{vis}(L', \phi, Ls) \rangle$, averaged over the whole recession period, (ii) the agreement between $T^{H}_{beg}(\phi)$, the date of the beginning of the net sublimation according to HEND, and this same date $T^{M2}_{beg}(L', \phi)$, according to the model.

The first evaluation (i) can be done by analyzing Fig. 8, showing albedo vs. latitude for the cryptic and anti-cryptic sectors.

For both sectors, there is a general agreement between $A^{M2}_{vis}(L', \phi)$ and the time averaged albedo $A^{B2}_{vis}(L', \phi)$ observed by OMEGA. Albedo increases with latitude, more strongly for the anti-cryptic sector than it does for the cryptic sector. The high dispersion of the albedo around 85° S in the cryptic sector is due to the high variability of ice type (slab ice, frost and mixing with dust) with time in this region (Kieffer et al., 2000; Piqueux et al., 2003; Langevin et al., 2006; Kieffer et al., 2006).

The second evaluation (ii) is done through the analysis of Tables 4 and 5. We can analyze the match between $T^{H}_{beg}(\phi)$ and $T^{M2}_{beg}(L', \phi)$ as an indicator of the validity of our scenario. The agreement is relatively good at low latitude ϕ for both sectors L'. The misfit increases as latitude increases. The effect of slope may be at the origin of this effect. For latitudes higher than 65° S, solar illumination becomes more grazing and the effect of slope may no longer be negligible. This effect does not affect the global defrosted mass, but changes the date of the beginning of sublimation for equator facing facets.

In conclusion, the model shows good consistency between the different datasets, i.e. albedos observed by OMEGA, crocus lines observed by OMEGA, net accumulation measured by HEND/GRS and altitudes measured by MOLA. Nevertheless, the low spatial resolution in latitude of the HEND/GRS measurements precludes the full testing of this model.

4.1.8.2. Latitude independent albedo (model M3) This second scenario (model M3) is based on a simple model of albedo $A^{M3}_{vis}(L', Ls)$, depending on longitude (cryptic/anti-cryptic) and time. It does not have the limitation of latitude resolution implied by the use of HEND/GRS data. Based on the OMEGA images, we determine two empirical laws of temporal evolution for the albedo of the cryptic and anti-cryptic sectors (Fig. 9). For the cryptic sector (longitudes between 60° and 260° E) is (mean = 0.0000; variance = 0.0012):

$$A^{M3}_{vis}(Ls) = -0.1967 + 0.0029 \times Ls. \quad (18)$$

For the anti-cryptic sector (longitude between 100° W and 60° E) (mean = −0.0067; variance = 0.0013):

$$A^{M3}_{vis}(Ls) = \min(-0.3920 + 0.0044 \times Ls, 0.63). \quad (19)$$

The albedo increases with time until $Ls = 230°$. The increase is much larger for the anti-cryptic sector than for the cryptic sec-

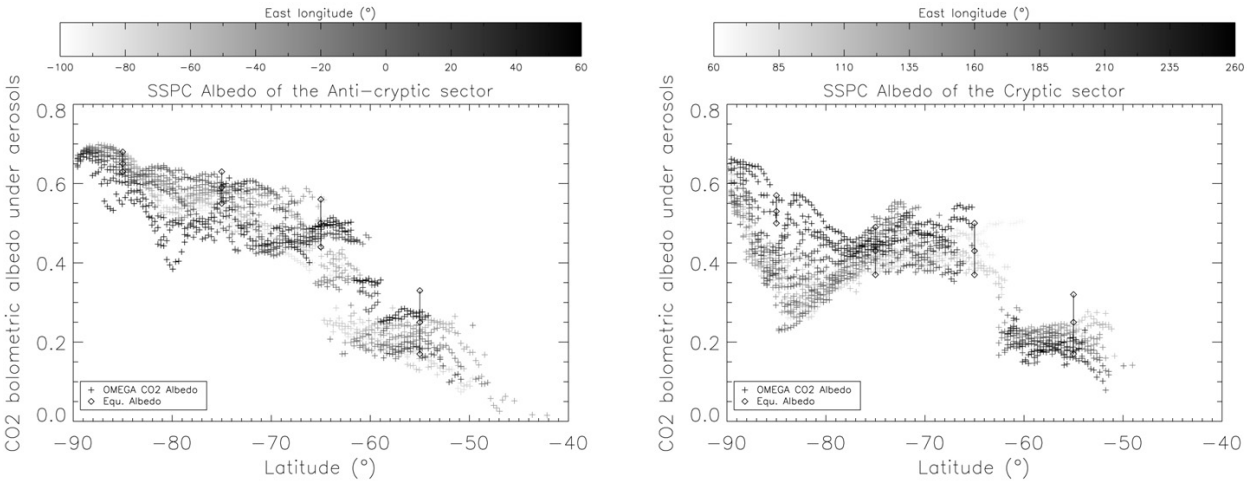


Fig. 8. Evaluation of the time independent scenario (model M2) for both cryptic and anti-cryptic sectors. Diamonds are equivalent albedo $A^{M2}_{vis}(L',\phi)$ required to sublimate the frost observed by HEND and GRS. Errors bars are due to the CO_2 thickness measurement uncertainties. Crosses are time averaged albedo $A^{B2}_{vis}(L',\phi)$ of CO_2 (gray scale represents the longitude) measured by OMEGA.

Table 4
Models for the SSPC recession in the cryptic sector. The first two lines are the measurements by HEND/GRS. The next three lines summarize the results of the time independent albedo scenario (model M2). The next two lines summarize the latitude independent albedo scenario (model M3). The last four lines show the heat released by the annual heat wave (model M1) as presented in Section 4.1.3.

	Latitude	55° S	65° S	75° S	85° S
HEND + GRS	Mass [kg m^{-2}] $M^{H}_{CO_2/tot}(\phi)$	180 ± 40	450 ± 80	750 ± 100	1050 ± 100
–	Sublimation duration [° *Ls*] $T^{H}_{beg}(\phi)/-$	140/–	160/–	170/–	180/–
Model M2	Sublimation duration [° *Ls*] $T^{M2}_{beg}(L',\phi)/T^{O}_{end}(L',\phi)$	135/170	165/220	185/245	200/270
–	Equivalent albedo [1] $A^{M2}_{vis}(L',\phi)$	0.25	0.43	0.43	0.53
–	Min/Max equ. albedo [1] $A^{M2}_{vis}(L',\phi)$	0.17/0.32	0.50/0.37	0.49/0.37	0.57/0.50
Model M3	Mass [kg m^{-2}] $M^{M3}_{CO_2/tot}(L',\phi)$	176	513	715	1118
–	Sublimation duration [° *Ls*] $T^{M3}_{beg}(L',\phi)/T^{O}_{end}(L',\phi)$	135/170	160/220	180/245	195/270
Model M1 ($I = 20$)	Subsurface heat [kg m^{-2}]	0.5	0.5	0.6	0.6
–	Sublimation duration [° *Ls*] $T^{H}_{beg}(\phi)/T^{M1}_{end}(L',\phi)$	140/185	160/235	170/260	180/280
Model M1 ($I = 1000$)	Subsurface heat [kg m^{-2}]	12	24	29	21
–	Sublimation duration [° *Ls*] $T^{H}_{beg}(\phi)/T^{M1}_{end}(L',\phi)$	140/155	160/215	170/245	180/265

Table 5
Same as Table 4, but for the SSPC recession models in the anti-cryptic sector.

	Latitude	55° S	65° S	75° S	85° S
HEND + GRS	Mass [kg m^{-2}] $M^{H}_{CO_2/tot}(\phi)$	180 ± 40	450 ± 80	750 ± 100	1050 ± 100
–	Sublimation duration [° *Ls*] $T^{H}_{beg}(\phi)/-$	140/–	160/–	170/–	180/–
Model M2	Sublimation duration [° *Ls*] $T^{M2}_{beg}(L',\phi)/T^{O}_{end}(L',\phi)$	135/170	170/225	190/260	205/290
–	Equivalent albedo [1] $A^{M2}_{vis}(L',\phi)$	0.25	0.5	0.59	0.65
–	Min/Max equ. albedo [1] $A^{M2}_{vis}(L',\phi)$	0.17/0.33	0.44/0.56	0.55/0.63	0.63/0.68
Model M3	Mass [kg m^{-2}] $M^{M3}_{CO_2/tot}(L',\phi)$	159	449	743	947
–	Sublimation duration [° *Ls*] $T^{M3}_{beg}(L',\phi)/T^{O}_{end}(L',\phi)$	135/170	165/225	185/260	205/290
Model M1 ($I = 20$)	Subsurface heat [kg m^{-2}]	0.5	0.6	0.7	0.5
–	Sublimation duration [° *Ls*] $T^{H}_{beg}(\phi)/T^{M1}_{end}(L',\phi)$	140/185	160/245	170/280	180/315
Model M1 ($I = 1000$)	Subsurface heat [kg m^{-2}]	12	27	29	27
–	Sublimation duration [° *Ls*] $T^{H}_{beg}(\phi)/T^{M1}_{end}(L',\phi)$	140/155	160/215	170/245	180/265

tor. Both laws fit well with the observed albedo $A^{B3}_{vis}(L',Ls) = \langle A^{B}_{vis}(L',\phi,Ls)\rangle$ averaged in latitude, as a function of time (Fig. 9).

We test the validity of this scenario by evaluating (i) the agreement between the sublimated CO_2 mass $M^{M3}_{CO_2/tot}(L',\phi)$ predicted by the model M3 and the mass $M^{H}_{CO_2/tot}(\phi)$ measured by GRS/HEND; (ii) the agreement between the date $T^{M3}_{beg}(L',\phi)$, the date of the beginning of the net sublimation according the model M3, and $T^{H}_{beg}(\phi)$, the same according to HEND.

We invite the reader to perform the first evaluation (i) by studying Tables 4 and 5. The mass $M^{M3}_{CO_2/tot}(L',\phi)$ predicted by the model fits well within the error-bar of the measured masses $M^{H}_{CO_2/tot}(\phi)$.

The second evaluation (ii) can be done using the same Tables 4 and 5. The agreement between $T^{H}_{beg}(L',\phi)$ and $T^{M3}_{beg}(L',\phi)$ is good at low latitudes for both sectors. However, the misfit increases as latitude increases. Again, the explanation is that the slope effect

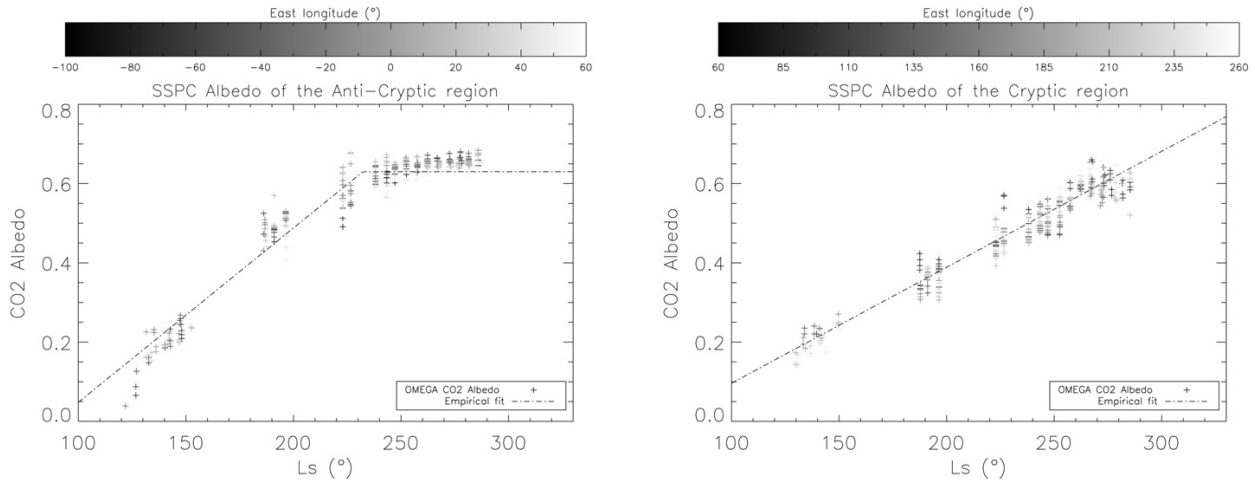


Fig. 9. Empirical law of albedo for the latitude independent scenario (model M3) for both cryptic and anti-cryptic sectors. The "+" symbols are latitude averaged albedo $A_{\text{vis}}^{\text{B3}}(L', Ls)$ of CO_2 ice (gray scale represents the longitude) measured by OMEGA. The dotted line is the empirical fit $A_{\text{vis}}^{\text{M3}}(L', Ls)$.

increases with latitude. At this point, the latitude independent scenario M3 is preferable compared to the time independent scenario M2 because it does not suffer from the coarse latitude resolution imposed by GRS.

In conclusion, confronting the model with the observations shows that the albedo is the most determinant parameter and that it increases globally during the recession for both (albeit differently) the cryptic and anti-cryptic sectors. The relative agreement between the model and the observations Langevin et al. (2006), in particular for the cryptic sector, suggests that all the solar energy absorbed by the mineral substrate underlying the CO_2 ice slab and/or the upper layer of dust contamination should be transferred efficiently to the CO_2 deposits for their sublimation. Future investigations should take into account the time and space variations of the albedo field, but this is not possible with OMEGA because the sampling is very sparse. Other datasets, such as MOLA or MOC, should help to achieve accurate modeling of the SSPC recession.

4.2. SSPC recession at local scale

Already at the end of the XIXth century, the irregular SSPC waning was noticed via telescopic observations by Campbell (1895). Using Mariner 9 photographs, Veverka and Goguen (1973) concluded that surface topography controls this irregularity. Here we characterize the edge structure of the SSPC by the snowdrop distance that we evaluate thanks to meridian profiles of CO_2 detection by OMEGA.

In Section 2.3, we define the inner and outer crocus lines for a given date (*Ls*) as well as the inner and outer crocus dates for a given latitude. The time elapsed between these two dates is the snowdrop time. According to OMEGA CO_2 ice detection, the snowdrop time ranges from a few ° *Ls* to more than 40° *Ls* depending on location and time. In this section, we will discuss the origin of this phenomenon.

We will address the following key questions. Is the local variability of snowdrop time due to local variations of accumulation? subsurface annual heat wave? CO_2 ice stability linked with altitude differences? radiation absorption controlled by roughness? difference in albedo in the visible range? difference in emissivity/albedo IR? These variations typically occur at spatial scales on the order of 1 km. For that purpose, we seek correlations between the variations of the snowdrop time and the previous parameters.

4.2.1. Statistical index

The inner and outer crocus lines are defined on the basis of spatial bins (see Fig. 1). The appearance of the first 1% of defrosted pixels defines the inner crocus date whereas the disappearance of the last 1% of frosted pixels defines the outer crocus date. Thus, the snowdrop time is a measure of the time elapsed between these two extreme defrost situations. In other words, the snowdrop time is an estimation of the distribution width of T_{end} inside the bin. Such a distribution is a function of three distributions, namely the initial CO_2 mass $M_{CO_2/\text{tot}}$, the date of the beginning of the sublimation T_{beg} and the mass flux of sublimation $\frac{\partial M_{CO_2}}{\partial t}$. If these distributions inside the bin are narrow, all facets will defrost at almost the same time and the snowdrop time will be short. On the contrary, if these distributions inside the bin are wide, all facets will defrost at different times and the snowdrop time will be long. In short, the snowdrop time must be correlated with a combination of the three distributions $M_{CO_2/\text{tot}}$, T_{beg} and $\frac{\partial M_{CO_2}}{\partial t}$.

We propose to describe the distribution width of the random variable X, with N occurrences named X_i, with the following statistical parameter:

$$\hat{P_{\text{stat}}}(\text{X}) = \frac{\sqrt{\hat{\sigma}}}{\hat{\mu}}. \tag{20}$$

$\hat{\mu}$ and $\hat{\sigma}$ being the usual estimators of the mean and variance:

$$\hat{\mu} = \frac{1}{N}\sum_{i=1}^{N} \text{X}_i, \tag{21}$$

$$\hat{\sigma} = \frac{1}{N-1}\sum_{i=1}^{N} (\text{X}_i - \hat{\mu})^2. \tag{22}$$

Now we define a statistical index $R_{\text{stat}}(\text{X})$ that describes the discrepancy between the lower and upper parts of the population of the distribution of X. Assuming that X is Gaussian, 32% of the population should be outside the range $[\hat{\mu} - \sqrt{\hat{\sigma}}, \hat{\mu} + \sqrt{\hat{\sigma}}]$, with 16% in the bottom wing and 16% in the top wing. The lower limit of the ratio between an occurrence of the upper population and an occurrence of the lower population is:

$$R_{\text{stat}} = \frac{\hat{\mu} + \sqrt{\hat{\sigma}}}{\hat{\mu} - \sqrt{\hat{\sigma}}} = \frac{1 + \hat{P_{\text{stat}}}}{1 - \hat{P_{\text{stat}}}}. \tag{23}$$

Assume that $M_{CO_2/\text{tot}}$ and T_{beg} take a unique value. If we estimate that $\hat{P_{\text{stat}}}$ for the defrost mass flux $\frac{\partial M_{CO_2}}{\partial t}$ inside a bin is

equal to 0.4, it means that 16% of the population (upper wing) will have a sublimation time duration T_{end} half of the other 16% (lower wing).

Now we must test the correlation, for a given latitude and longitude range, between the snowdrop time (distribution width of T_{end}) and the statistical index $\hat{P_{stat}}$ of (i) the initial accumulated mass $M_{CO_2/tot}$; (ii) the date of the beginning of the sublimation T_{beg}; (iii) the mass flux $\frac{\partial M_{CO_2}}{\partial t}$ or any physical parameter that controls it. In the special case of the albedo (that partly controls $\frac{\partial M_{CO_2}}{\partial t}$), we sort all pixels of the OMEGA observations from $Ls = 0°$ to 360° in the bins of our geographical grid (see Section 3.4) and by intervals of 5° *Ls*. Then we calculate for each bin containing pixels the mean $\hat{\mu}$, the variance $\hat{\sigma}$ and the statistical index $\hat{P_{stat}}$ of the albedo.

4.2.2. CO_2 ice accumulation $M_{CO_2/tot}$

The total CO_2 ice accumulation, previously discussed at global scale in Section 4.1.1, can vary at local scale.

According to Eq. (16), the local scale variation of accumulation depends on different terms which can have a local expression, namely (i) thermal emission controlled by temperature and emissivity; (ii) atmospheric heat advection; (iii) subsurface heat conduction which depends on slope, albedo and thermal inertia of the subsurface; (iv) absorbed radiation linked with the VIS and IR albedos, slope, and roughness.

The accurate modeling of accumulation at local scale, including atmospheric dynamic effects, lies outside the scope of this paper. Thermal inertia observed by TES is uniform near the South Pole (Putzig et al., 2005). In this study, we will assume that accumulation varies smoothly with latitude, as measured by HEND (Litvak et al., 2007). This apparent smoothness could be an effect of the large instrument footprint. Thus ambiguities between $M_{CO_2/tot}$, on the one hand, and T_{beg}, $\frac{\partial M_{CO_2}}{\partial t}$, on the other, will not be resolved properly in this work.

4.2.3. Date of the beginning of sublimation T_{beg}

As discussed in Section 4.1.2, T_{beg} is related to all terms of Eq. (16). In the next models, T_{beg} will be a free parameter, set by the model itself.

4.2.4. Annual heat wave in the ground

As previously discussed in Section 4.1.3, the maximum sublimated mass due to the annual heat wave in the ground represents 6% of the total sublimated mass (at latitude 55° S) leading to a shift of the crocus date of less than 2° *Ls*. For comparison, the maximum snowdrop time is more than 40° *Ls*. This energy source can thus be neglected at a first order in all discussions concerning the recession phase even at local scale.

4.2.5. Altitude

The effect of altitude, as previously discussed in Section 4.1.4, is very low at global scale. At local scale, the typical standard deviation of altitude inside a bin is between 10 m and 1000 m. We estimated the effect of a 1000 m difference in altitude for two extreme points of the anti-cryptic sector. At 85° S, an increase in altitude of 1000 m from the 2500 m level leads to a increase of defrosted mass of 13 $kg\,m^{-2}$ during the complete recession time. The corresponding snowdrop time delay is 0.5° *Ls*. At 55° S, from the 1000 m level, the defrosted mass increase represents 7 $kg\,m^{-2}$ and a snowdrop time delay of 1° *Ls*, much less than most observed snowdrop times. The altitude effect alone is not sufficient to explain the snowdrop time evolution in space and time.

4.2.6. Radiation budget on a rough surface

In order to estimate the effect of surface roughness on the local daily absorbed radiation W (Eq. (4)), we compute it using the model presented in Section 3.2. We set the albedos $A_{vis} = 0$, $A_{IR} = 0.01$ and the emissivity $\varepsilon = 0.99$, a configuration that maximizes the effect of slope and shadow on all radiation terms. Slope and altitude given by the MOLA database are at a resolution of 920 m. If roughness of the martian surface is the parameter that controls the recession at local scale, the snowdrop time and the local statistical index $\hat{P_{stat}}$ for the daily absorbed radiation must correlate. Fig. 10 represents the statistical index $\hat{P_{stat}}$ along two meridian profiles (a) 260°–270° E and (b) 270°–280° E.

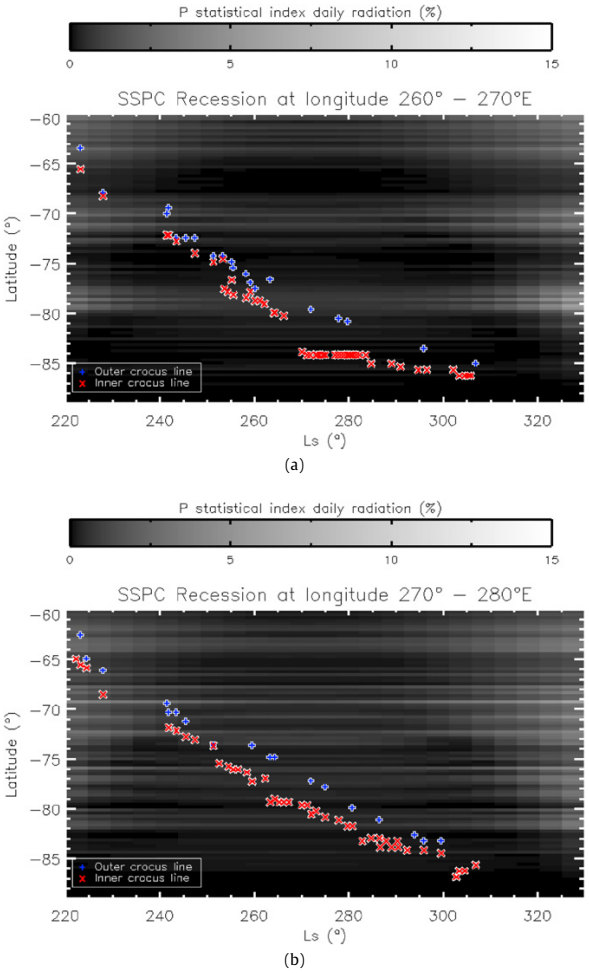


Fig. 10. SSPC recession compared to local radiation modulated by surface roughness for two meridian profiles in the longitude ranges (a) 260°–270° E and (b) 270°–280° E. Symbols + and × represent the outer and inner crocus lines respectively. The gray scale represent the statistical index $\hat{P_{stat}}$ (Eq. (20)) calculated for the local absorbed radiation W with a special configuration that maximizes the effect of surface roughness (see text).

In both Figs. 10a and 10b, we can note that the effect of slope distribution on the variability of absorbed radiation is particularly noticeable when the sun elevation at local noon is low. On profile (a), the maximum snowdrop time (about 30° *Ls*) occurs at latitude 85° S, but does not correlate with high values of the statistical index $\hat{P_{stat}}$. On profile (b), the snowdrop time is constant (about 10° *Ls*) despite the fact that the statistical index at the crocus line decreases with time. It seems that the snowdrop time is independent of the local absorbed radiation modulated by surface roughness. This result stands for all other directions around the geographic South Pole.

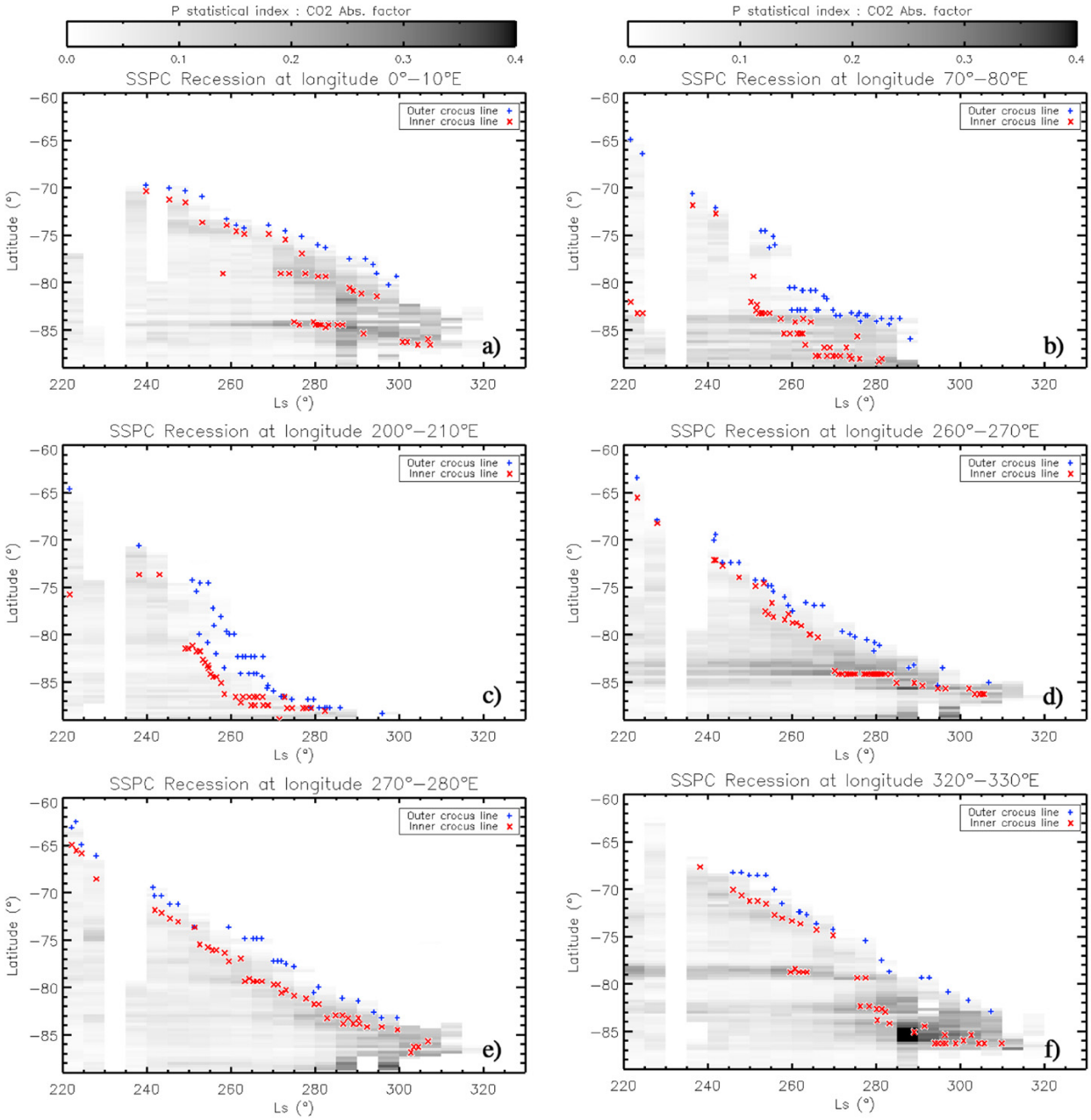


Fig. 11. SSPC recession compared to the albedo distribution observed by OMEGA for six meridian profiles in the longitude ranges (a) 0°–10° E, (b) 70°–80° E, (c) 200°–210° E, (d) 260°–270° E, (e) 270°–280° E and (f) 320°–330° E. Symbols + and × represent the outer and inner crocus lines respectively. The gray scale represents the statistical index $\hat{P}_{\text{stat}}$ (Eq. (20)) calculated for the local absorption factor Abs^{0}_{vis} inside each bin.

In order to completely reject the hypothesis of the surface roughness effect, the snowdrop time must be compared with the local distribution of defrost mass rather than with the radiation budget. Section 4.2.9 will discuss this point.

4.2.7. Emissivity and albedo in the thermal infra-red

As discussed in Section 4.1.6, emissivity likely ranges from 0.91 to 1.0 for CO_2 ice. Using the same calculation at both 85° S and 55° S, we can estimate the effect of emissivity distribution on snowdrop time. If emissivity is distributed between these two extreme values, the snowdrop time is increased by 1.6° *Ls* at 85° S and 2.4° *Ls* at 55° S. This is not enough to explain the local variations of snowdrop time. Emissivity cannot be the key parameter that controls the SSPC recession at local scale.

4.2.8. Albedo in the visible range

In order to estimate the effect of albedo on the snowdrop time, we estimate its distribution from our selection of OMEGA observations arranged into bins. We use the absorption factor $Abs_{\text{vis}} = 1 - A_{\text{vis}}$ that appears in Eq. (6). As an approximation, we estimate

the bolometric albedo A_{vis} with $A^{O}_{vis} = 1 - Abs^{O}_{vis}$ (see Eq. (2)). If the albedo is the parameter that controls the recession at local scale, snowdrop time and the local statistical index $\hat{P_{stat}}$ of Abs^{O}_{vis} must be correlated.

We choose to represent in Fig. 11 six typical meridian profiles to illustrate the test of our hypothesis, namely (a) 0°–10° E, (b) 70°–80° E, (c) 200°–210° E, (d) 260°–270° E, (e) 270°–280° E and (f) 320°–330° E. We restrict the time window of this investigation to $Ls = 220°–330°$ because, before $Ls = 220°$, pollution by atmospheric dust and water ice is likely (see Section 2.4) and their contribution to $R^{O}_{1.07}$ will affect its correspondence with surface albedo.

On profile (a), the snowdrop time is maximum (about 40° *Ls*) at 84° S and correlates with a high value of $\hat{P_{stat}}$ present at this latitude since $Ls = 255°$.

On profile (b), the snowdrop time is intermediate (about 15° *Ls*) from 75° S to 83° S, where $\hat{P_{stat}}$ is low. At latitudes between 83° S and the pole, the snowdrop time reaches 30° *Ls* and is well correlated with a local high $\hat{P_{stat}}$.

Profile (c) presents a uniform snowdrop time of about 10–15° *Ls* and the estimation of $\hat{P_{stat}}$ is low.

On profile (d), from latitude 84° S to 86° S and starting at $Ls = 220°$, albedo is very dispersed with high $\hat{P_{stat}}$ values. This is correlated with a very high snowdrop time of more than 30° *Ls*.

Profile (e) shows the most homogeneous snowdrop time (10° *Ls*) of all profiles around the south pole, in agreement with constantly low levels of $\hat{P_{stat}}$.

On profile (f), we note three very distinct regimes of albedo dispersion. At latitudes below 78° S, $\hat{P_{stat}}$ is close to zero. Between 78° S and 80° S, $\hat{P_{stat}}$ is higher than 20% starting at $Ls = 220°$. Between 82° S and 87° S, $\hat{P_{stat}}$ increases with time. This is correlated with a low snowdrop time for the first part (less than 10° *Ls*) and a high snowdrop time (more than 20° *Ls*) for the second as well as the third regimes.

Another phenomenon occurs on all profiles, as suggested by close examination of $\hat{P_{stat}}$. The albedo dispersion increases just before the transition zone. This is easily explained by the fact that subpixel mixing occurs at this time and that OMEGA sees pixels with various levels of sub-pixel mixing and thus various albedo, all with positive detection of CO_2. This is particularly obvious on profiles (a), (d), (e) and (f) where the global albedo level is high and the subpixel mixing can produce a high variance.

Local dispersions of albedo show a quasi-systematic correlation with the snowdrop time. This result is also valid for all other directions around the geographic South Pole. For the complete dataset, the correlation coefficient between the snowdrop time and the statistical parameter $\hat{P_{stat}}$ calculated for the 22.5–18.5° *Ls* albedo before the inner crocus date at a given location is 0.640 (see Fig. 12). We conclude that albedo is likely the key parameter that controls the SSPC recession at local scale.

4.2.9. Quantitative test

In Sections 4.2.4 to 4.2.8 we have shown that:

- local variations of subsurface heat flow, altitude and emissivity alone cannot control the snowdrop time for a given latitude since their influence on the cumulative mass of sublimated CO_2 is weak compared to the influence of other factors;
- the snowdrop time is well correlated with the local variability of albedo whereas it is not with the absorbed radiation variability due to the slope distribution alone.

In order to confirm the prevailing nature of the albedo, we perform a more detailed simulation of the cumulative mass of sublimated CO_2 frost for each facet of our geographical grid. We take the altitudes and slopes from the MOLA data at a resolution of

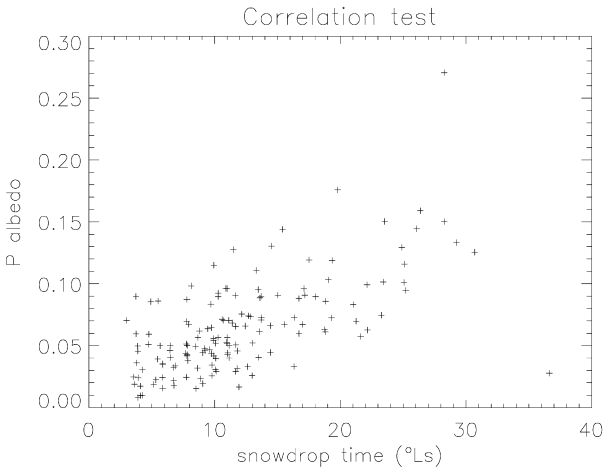


Fig. 12. Scatterplot to test the correlation between the snowdrop time and the statistical index $\hat{P_{stat}}$ calculated for the albedo, for all longitude ranges (correlation = 0.640). Albedo is taken to be 22.5 to 18.5° *Ls* before the inner crocus date.

920 m. Conversely, we ignore the local variation of the albedo by taking a homogeneous value that increases with time, i.e. the latitude independent scenario, model M3 (see Section 4.1.8) for the whole cap. At global scale, such a simplified model allowed us to reproduce the recession of the mean crocus line (Section 4.1.8). All the other parameters are set to the standard values given in Appendix E.

If surface roughness is the parameter that controls the recession at local scale, the snowdrop time and the local statistical index $\hat{P_{stat}}$ of the daily defrost mass $\frac{\partial M_{CO_2}}{\partial t}$ must be correlated.

In Fig. 13, we choose to represent the spatio-temporal behavior of $\hat{P_{stat}}$ for the six meridian profiles and the time window already considered in Section 4.2.8, namely (a) 0°–10° E, (b) 70°–80° E, (c) 200°–210° E, (d) 260°–270° E, (e) 270°–280° E and (f) 320°–330° E.

On profile (a), the snowdrop time is maximum (about 40° *Ls*) at 84° S and is well correlated with a high value of $\hat{P_{stat}}$ already present starting at $Ls = 220°$. There is also a correlation with a high dispersion of albedo (Section 4.2.8), but at 79° S, a high snowdrop time occurs with a low $\hat{P_{stat}}$.

On profile (b), the snowdrop time is intermediate (about 15° *Ls*) from 75° S to 83° S, when $\hat{P_{stat}}$ is latitude dependent. At latitudes above 83° S, the snowdrop time reaches 30° *Ls* and is anti-correlated with $\hat{P_{stat}}$.

From 80° S to 90° S, profile (c) presents a homogeneous intermediate snowdrop time of about 10–15° *Ls* corresponding to very low values of $\hat{P_{stat}}$.

On profile (d) from latitude 84° S to 86° S and starting at $Ls = 220°$, the defrosted mass is very uniform from place to place (low values of $\hat{P_{stat}}$). This is anti-correlated with a very high snowdrop time of more than 30° *Ls*.

Profile (e) shows the best constant snowdrop time (10° *Ls*) of all profiles around the South Pole despite the fact that the dispersion of defrosted mass $\hat{P_{stat}}$ strongly fluctuates with latitude.

On profile (f), no correlation between defrosted mass $\hat{P_{stat}}$ and snowdrop time appears. For instance, at latitudes between 78° S and 80° S, the snowdrop time is more than 20° *Ls* and $\hat{P_{stat}}$ is close to zero. Very close to latitude 84° S, the statistical index $\hat{P_{stat}}$ is always higher than 2%, but no increase of the snowdrop time is observed.

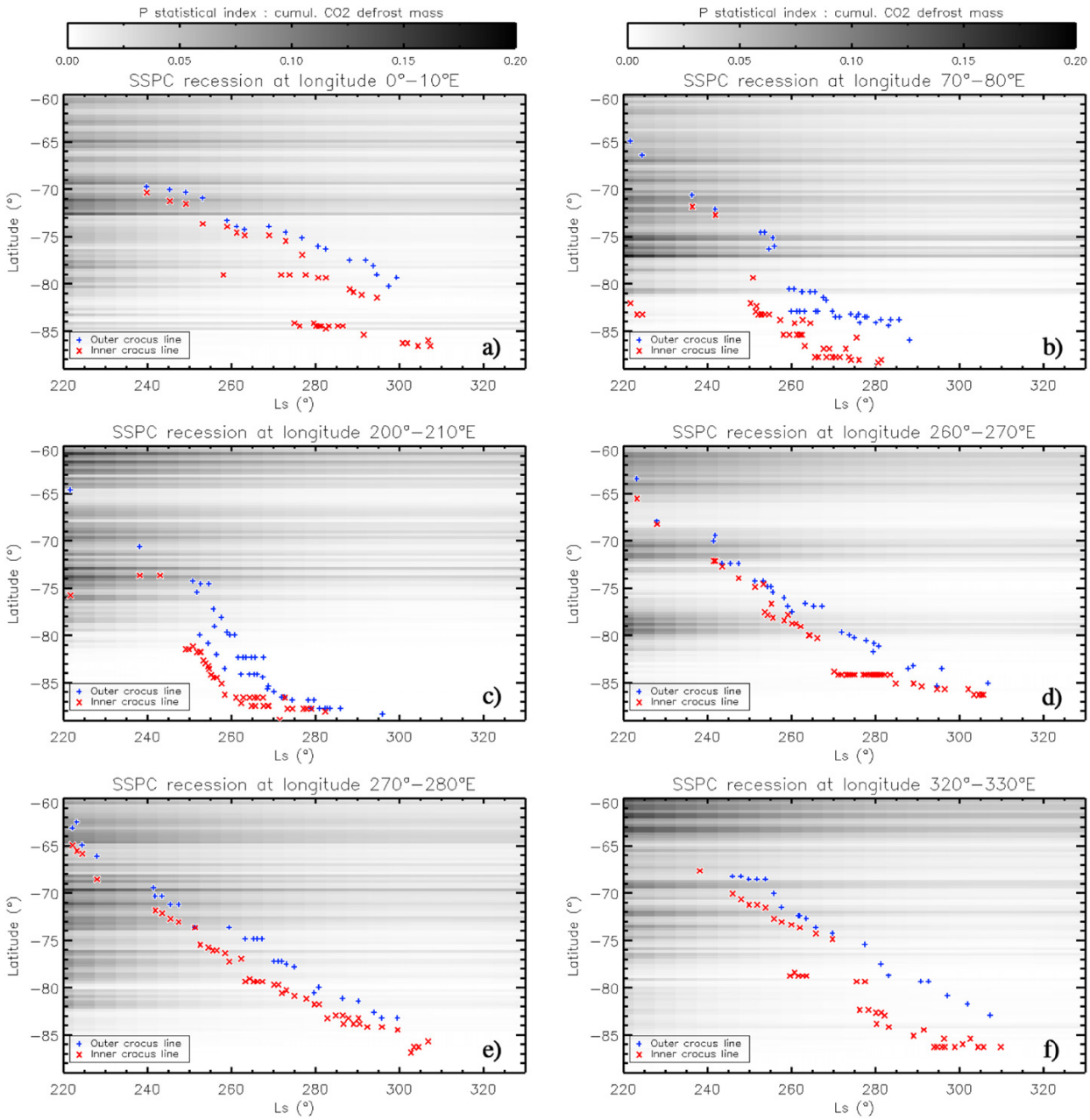


Fig. 13. SSPC recession compared to the sublimated CO_2 mass distribution computed for six meridian profiles in the longitude ranges (a) 0°–10° E, (b) 70°–80° E, (c) 200°–210° E, (d) 260°–270° E, (e) 270°–280° E and (f) 320°–330° E. Symbols + and × represent the outer and inner crocus lines respectively. The gray scale represents the statistical index P_{stat} (Eq. (20)) calculated for the local daily defrosted mass $\frac{\partial M_{CO_2}}{\partial t}$ inside each bin.

For the complete dataset, the correlation coefficient between the snowdrop time and the statistical parameter $\hat{P_{\text{stat}}}$ calculated for the daily defrost mass at 22.5–18.5° *Ls* before the inner crocus date at a given location is 0.358 (see Fig. 14).

This quantitative test confirms that the combined effects of altitude distribution, slope distribution and surface roughness on the defrost mass distribution are not sufficient to explain the variability of the snowdrop distance. Albedo remains the most pertinent parameter. This result stands for all other directions around the geographic South Pole.

5. Discussion

At global scale, the asymmetry of the SSPC recession around the geographic South Pole is due only to the albedo asymmetry. Indeed it can be reproduced by our defrost mass model with only two asymmetrical parameters, the mean crocus date and albedo with the latter increasing with time. In the model, the initial mass at the end of winter is symmetrical, in agreement with the measurements made via the loss of neutron flux (Litvak et al., 2007) or gamma rays (Kelly et al., 2006). Nevertheless, asymmetry in

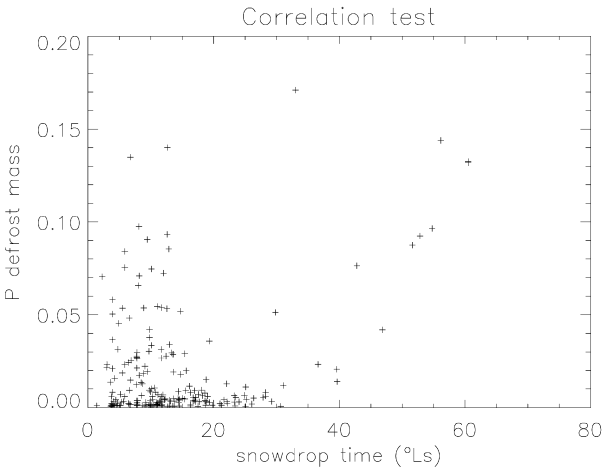


Fig. 14. Scatterplot to test the correlation between the snowdrop time and the statistical index $\hat{P}_{stat}$ calculated for the daily defrost mass with a homogeneous albedo and heterogeneous slopes, for all longitude ranges (correlation = 0.358). The modeled sublimed mass is taken to be 22.5 to 18.5° *Ls* before the inner crocus date.

the accumulation process remains an alternative possibility that our study cannot rule out completely. The time dependence of the equivalent albedo is in very good agreement with the OMEGA observations. This fact makes us confident that our model is valid at a first order. We have shown that neither the effect of the annual heat wave, nor the altitude, the surface roughness or the emissivity are important compared to the albedo effect. Thus albedo is the key parameter that controls the recession SSPC at global scale.

At local scale, we describe the fine structure of the SSPC edge with inner and outer crocus lines, the two being separated by the snowdrop distance. Since the SSPC recession involves space and time, all those indicators have an equivalent in the temporal domain, i.e. inner and outer crocus dates, snowdrop time. We concluded in Section 4.2 that the local albedo distribution which characterizes a region at a given latitude is the key parameter that controls the SSPC disappearance several weeks later.

The effect of surface roughness at a scale lower than the resolution of the MOLA data could be relevant, but is not tested in this work. The test may be done in the future trying to address the difficulties of extrapolating to the 1 m scale (Campbell et al., 2003).

At both global and local scales, albedo is the most pertinent parameter that controls the seasonal South Polar cap recession. Different physical parameters can induce asymmetry or variability in the albedo field.

- Subpixel mixing. Inside the footprint of the OMEGA instrument, a linear mixture as well as an intimate mixture of bright frost and dark rock/dust materials could occur. Such mixtures can produce an apparent albedo variability if quantities inside the pixel are variable.
- Grain size. As suggested by Warren et al. (1990), grain size significantly reduces albedo especially if the ice is slightly contaminated by a strong absorber. More recent calculations (Hansen, 1999; Douté et al., 2008; Douté et al., in preparation) using an optical constant of higher accuracy (Hansen, 1997; Schmitt et al., 1998) mitigate, but do not rule out this effect for pure ice. An extreme situation occurs when the SSPC deposits are made of a slab of pure CO_2 ice, so transparent that a large fraction of photons can reach the bottom and be absorbed by the dust substratum, thus producing a low visible albedo. This extreme scenario was suggested for the cryptic region from TES data (Kieffer et al., 2000). At this point, we should note that OMEGA observations also suggest the presence of slab ice outside the cryptic region (Langevin et al., 2006). For instance, at latitude 59° S in the anti-cryptic region (longitude 344° E) the albedo of the icy terrains is only 20%.
- Dust content. As suggested by Warren et al. (1990), dust within ice deposits significantly reduces albedo.
- Ice thickness. As suggested by Warren et al., 1990, the albedo of an optically thin CO_2 granular layer has a positive correlation with the snow depth.

Different processes can produce a global asymmetry and/or local variability of the previous physical parameters.

5.1. Subpixel mixing

The temperature of a completely defrosted terrain can go up to 300 K, a temperature which strongly increases its thermal emission, in particular towards the surrounding still frozen terrain, thus accelerating their sublimation.

Subpixel mixing should happen between the inner and outer crocus dates as suggested in Section 4.2.8. But subpixel mixing is not a good scenario for the whole SSPC because that would lead to a recession velocity much higher than observed. In the longitude sector 320°–330° E, the high albedo dispersion is present at least 40° *Ls* before the crossing of the inner crocus line (see Fig. 11).

5.2. Ice deposition process

During the phase of CO_2 frost accumulation, the SSPC is mainly formed by direct condensation, but some snow events can occur (Forget et al., 1998). GCM studies show that a topographic forcing by the Hellas basin creates an asymmetry in the mode of deposition. Precipitation events are more frequent for the anti-cryptic sector than for the cryptic sector (Colaprete et al., 2005; Giuranna et al., 2008). This suggests that the texture should be more granular (smaller grain sizes) for the former compared to the latter. This texture difference produces a relatively higher albedo in the anti-cryptic region.

Local topographic forcing could create local variability of snow precipitation (Colaprete and Toon, 2002), leading to a variability of grain size and ice thickness. No simulation has been done yet by GCM at local scale for the South Polar region, but this effect is a good candidate to explain the local variability of albedo.

During the SSPC recession, recondensation during the night can occur and the new condensate would cover dusty ices, enhancing the albedo. This process, that likely happens at local scale, tends to decrease albedo variability.

The usual defrost mass balance proposed in Section 3.3.1 can produce local differences of defrost mass due to slope orientation, shadows or altitude. However, the statistical index of these parameters is not correlated with that of albedo. Thus, slope orientation, shadows or altitude effects are not likely to produce relevant thickness distribution.

5.3. Metamorphism

Metamorphism tends to increase the optical mean free path within the ice through both grain growth and ice sintering, leading to an apparent grain size larger than the physical grain size (Eluszkiewicz, 1993). Thus, metamorphism tends to decrease albedo. This model shows that metamorphism is controlled by ice temperature, but could also be enhanced by the vertical distribution of solar energy absorption, boosting the internal vapor transport (sublimation, recondensation). At this time, there is a

lack of experimental results to constrain the CO_2 metamorphism regime on Mars.

Nevertheless, the differential boost by differential solar energy absorption, modulated by slopes and shadows, cannot explain either the asymmetry or the local variability of albedo. At global scale, both cryptic and anti-cryptic sectors undergo this effect with the same magnitude (Fig. 6). At local scale, there is no correlation between the snowdrop time and the radiation budget distribution (Figs. 10 and 11).

The differential boost may be relevant only if there is a difference in albedo, controlled for instance by grain size or dust load, leading to a difference in the amount of absorbed energy. There is a strong positive feedback between albedo and metamorphism. Lower albedo induces more solar energy absorbed, induces stronger metamorphism, induces higher grain size, induces lower albedo. Such a process can enhance small differences. For instance, metamorphism may be appropriate to enhance initial asymmetry due to grain size or initial local variability due to difference in dust load.

5.4. Dust precipitation

The dust content within the ice deposit can be incorporated during the accumulation phase or can be added later due to dust precipitation. Different scenarios could imply various dust sources such as the atmosphere or local geysers.

If dust particles have an aeolian origin, they can be deposited in variable amounts due to differential dust loading in the atmosphere. Furthermore, surface wind can reshuffle the dust on the ground, leading to local variability of albedo.

An alternative scenario, more likely to occur in the cryptic region (Piqueux et al., 2003; Kieffer et al., 2006), implies CO_2 geysers ejecting dust at the surface of the ice. Piqueux et al. (2003) suggest that this process is at the origin of the asymmetry in albedo at global scale. In addition, the detection of optically thick, but thermally thin dark materials, that would overlay a layer of CO_2 ice and thus would be kept at low temperatures, has been recently suggested by Langevin et al. (2006) for the cryptic region.

Moreover, there is a positive feedback involving albedo and dust content. More dust induces lower albedo, induces more solar energy absorbed, induces faster sublimation, induces less thickness, induces lower albedo. Such a mechanism tends to increase differences in albedo.

5.5. Cleaning process

Some authors found a correlation between albedo of the residual ice cap and insolation (Paige and Ingersoll, 1985; Kieffer et al., 2000) and claim that a cleaning process, controlled by insolation, progressively frees the ice from its dust. Different candidate processes can occur on the residual ice cap, but on the seasonal cap too, depending on the dust particle size. Dust can burrow through the ice or be ejected in the atmosphere (Kieffer et al., 2000; Portyankina et al., 2003). Such mechanisms increase the albedo by decreasing the dust content within the ice deposit.

However, these mechanisms alone cannot explain the asymmetry or the local variability of albedo. Both cryptic and anti-cryptic sectors should be cleaned with the same intensity if the initial dust load is identical (Fig. 6). At local scale, the snowdrop time and the radiation budget distribution, which would govern the magnitude of the cleaning process, are not correlated (Figs. 10 and 11).

However, differences of dust load/size/shape distribution at the top of the CO_2 ice layer associated with the cleaning process can be a clue to explain the variability of albedo. Nevertheless, there is a negative feedback between albedo and cleaning. Lower albedo induces more solar energy absorbed, induces stronger cleaning, induces higher albedo. Such a mechanism tends to smooth differences in albedo.

5.6. Mechanical ablation

A process of mechanical ablation of the ice deposits, caused by atmosphere turbulence, would decrease the ice thickness and the albedo. In this scenario, suggested on Earth for the formation of the blue ice area by catabatic winds in Antarctica (Bintanja, 1999), turbulence is linked with wind and surface roughness. Due to the low density of the atmosphere on Mars, this effect is likely only for small ice particles. Thomas et al. (1979) is of the opinion that some frost streaks have a wind origin.

6. Conclusions

We introduce and use a CO_2 ice sublimation model called D-frost and estimate its validity at global scale using (i) the accumulation estimated by GRS/HEND, (ii) the date of the end of sublimation estimated by OMEGA, (iii) the CO_2 ice albedo estimated by OMEGA. We propose two ways to test model consistency, namely time independent albedo (model M2) and latitude independent albedo (model M3). In both cases, albedo increases with time and the model matches the observations.

We also introduce the snowdrop time/distance to characterize the SSPC edge. This new quantity, complementary with the crocus date/line, is a new and promising observable to constrain efficiently the martian GCM.

We propose an efficient way to calculate the CO_2 ice sublimation mass using D-frost in a case of rough surfaces, taking into account statistically the shadow induced by the topography. We show that the snowdrop time is correlated with the albedo distribution. Also we estimate a very low level of correlation between (i) the snowdrop time and (ii) the sublimated mass distribution due to surface roughness estimated by the model. This suggests that the effect of topography can be neglected at a first order.

In conclusion, we show that the CO_2 ice sublimation in the SSPC is mainly controlled by albedo at both global and local scales, but additional investigations are required to point out the major processes controlling this quantity. One suggestion would be the use of other datasets, such as MOLA or MOC, to study in more detail the dependence of the increasing albedo trend with latitude, longitude and time. In addition, a modeling effort of ice cloud precipitation at local scale and geyser activity is necessary. Also, several experiments should be designed to measure the modalities and magnitude of CO_2 metamorphism, cleaning process and mechanical ablation. Finally, the physical analysis of the OMEGA and CRISM observations with surface radiative transfer models should produce quantitative maps of surface properties of the SSPC that will greatly help to understand the physical process acting to produce the observed albedo, crocus line and snowdrop distance.

Acknowledgments

This work is supported by a PhD grant from the 'Ministère délégué à l'Enseignement supérieur et à la Recherche' and by a contract with CNES through its 'Système Solaire' program. We thank the OMEGA team at IAS for support with sequencing and data download activities. We thank the OMEGA team at IAS for support with sequencing and data download activities. The authors also would like to thank Nicolas Jourdain for useful discussions, Shane Byrne and a anonymous reviewer for their suggestions.

Appendix A. Scales of interest

Bin: element of the geographical grid drawn regularly in longitude and latitude on the planetary surface. Sampling is 10° in

longitude (from 0° E to 360° E) and 0.3° in latitude (from 53° S to 90° S).

Meridian profile: sequence of values taken by a parameter along a meridian (constant longitude) for consecutive bins which span 10° in longitude. Latitudinal range covered is 53° S to 90° S for the model and from 30° S to 90° S for the OMEGA observations.

The bins are at a lower resolution than following objects:

Facet: pixel in MOLA data that is used for the calculation of the insolation modulated by roughness. Spatial resolution is 920 m in a South Polar stereographic projection;

Pixel: element of detection in the OMEGA observations, the spatial resolution can vary from 2 km to 700 m.

Appendix B. Slope in the stereographic South projection

The map and geographic coordinates are related by those formula:

$$x = \frac{2R\cos\phi\sin L}{1-\sin\phi}, \tag{B.1}$$

$$y = \frac{2R\cos\phi\cos L}{1-\sin\phi}. \tag{B.2}$$

The derivative are:

$$\frac{d}{dL} = \frac{2R\cos\phi}{1-\sin\phi}\cos L\frac{\partial}{\partial x} - \frac{2R\cos\phi}{1-\sin\phi}\sin L\frac{\partial}{\partial y}, \tag{B.3}$$

$$\frac{d}{d\phi} = \frac{2R}{1-\sin\phi}\sin L\frac{\partial}{\partial x} + \frac{2R}{1-\sin\phi}\cos L\frac{\partial}{\partial y}. \tag{B.4}$$

In order to use the dimensionless slope, we use $h' = \frac{h}{R}$ in radian instead of h in meter.

The slope calculation is:

$$\frac{\partial h'}{\partial x} = \frac{\partial h'}{\partial x'}\frac{1}{\Delta} = \frac{\partial h}{\partial x'}\frac{1}{R.\Delta} = \frac{h(x_{i+1}, y_i) - h(x_i, y_i)}{R.\Delta}, \tag{B.5}$$

$$\frac{\partial h'}{\partial y} = \frac{\partial h'}{\partial y'}\frac{1}{\Delta} = \frac{\partial h}{\partial y'}\frac{1}{R.\Delta} = \frac{h(x_i, y_{i+1}) - h(x_i, y_i)}{R.\Delta}. \tag{B.6}$$

Finally, we obtain both dimensionless slopes:

$$\frac{dh'}{dL} = \frac{2\cos\phi}{1-\sin\phi}\frac{1}{\Delta}\left(\cos L\frac{\partial h}{\partial x'} - \sin L\frac{\partial h}{\partial y'}\right), \tag{B.7}$$

$$\frac{dh'}{d\phi} = \frac{2}{1-\sin\phi}\frac{1}{\Delta}\left(\sin L\frac{\partial h}{\partial x'} + \cos L\frac{\partial h}{\partial y'}\right). \tag{B.8}$$

Appendix C. Integration of insolation

Unfortunately, the direct and indirect solar illumination Q_{sun} and Q_{scat} can be negative depending on L. Thus we multiply these two terms with a door function Π that bounds the integration of the absorbed energy to the interval of L values $[L_{\min}, L_{\max}]$ when it is positive (when the facet is illuminated).

$$\Pi_{L_{\min}}^{L_{\max}}(L) = \begin{cases} 1, & \text{for } L_{\min} < L < L_{\max} \text{ where } \overrightarrow{n_{\text{surf}}} \bullet \overrightarrow{r_{\text{sun}}} \geqslant 0, \\ 0, & \text{otherwise,} \end{cases} \tag{C.1}$$

$$\overrightarrow{r_{\text{surf}}} \bullet \overrightarrow{r_{\text{sun}}} = \sin(\phi)\sin(\delta) + \cos(\phi)\cos(\delta)\cos(L-\alpha), \tag{C.2}$$

$$\overrightarrow{n_{\text{surf}}} \bullet \overrightarrow{r_{\text{sun}}} = \sin(\phi_{\text{n}})\sin(\delta) + \cos(\phi_{\text{n}})\cos(\delta)\cos(L_{\text{n}}-\alpha). \tag{C.3}$$

The N/S slopes along a meridian are given by the following relations:

$$\phi_n = \begin{cases} \pi - \phi - \phi', & \text{for } \phi + \phi' > \frac{\pi}{2}, \\ -\pi - \phi - \phi', & \text{for } \phi + \phi' < -\frac{\pi}{2}, \\ \phi + \phi', & \text{otherwise,} \end{cases} \tag{C.4}$$

and the W/E slopes along a parallel by:

$$L_{\text{n}} = L + L' + L_{\text{c}} \begin{cases} L_{\text{c}} = 2\pi, & \text{for } L + L' < 0, \\ L_{\text{c}} = -2\pi, & \text{for } L + L' > 2\pi, \\ L_{\text{c}} = 0, & \text{otherwise.} \end{cases} \tag{C.5}$$

Using those relations:

$$\phi' = \arctan\left(-\frac{\partial topo}{\partial \phi}\right), \tag{C.6}$$

$$L' = \arctan\left(-\frac{\partial topo}{\partial L}\right). \tag{C.7}$$

We assume that insolation is null when the sun is on the opposite side of the facet. This condition corresponds to a virtual displacement of the considered surface point from its real longitude L to L_{n}.

Our assumption can be written:

$$\overrightarrow{n_{\text{surf}}} \bullet \overrightarrow{r_{\text{sun}}} \geqslant 0 \Leftrightarrow \cos(L_{\text{n}} - \alpha) \geqslant -\tan(\phi_{\text{n}})\tan(\delta). \tag{C.8}$$

There are 3 different solutions for the equations depending on latitude and slopes.

(1) The sun never rises:

$$\vec{n}_{\text{surf}} \bullet \overrightarrow{r_{\text{sun}}} < 0 \Leftrightarrow 1 < -\tan(\phi_{\text{n}})\tan(\delta), \tag{C.9}$$

$$W = \frac{1}{2\pi}\int_0^{2\pi} Q_{\text{sun}}\Pi_0^0 + Q_{\text{scat}}\Pi_0^0 + Q_{\text{IR}}\Pi_0^0 + Q_{\text{floor}}\Pi_0^{2\pi}\,dL. \tag{C.10}$$

(2) The Sun never sets:

$$\vec{n}_{\text{surf}} \bullet \overrightarrow{r_{\text{sun}}} > 0 \Leftrightarrow -1 > -\tan(\phi_{\text{n}})\tan(\delta), \tag{C.11}$$

$$W = \frac{1}{2\pi}\int_0^{2\pi} Q_{\text{sun}}\Pi_0^{2\pi} + Q_{\text{scat}}\Pi_0^{2\pi} + Q_{\text{IR}}\Pi_0^{2\pi} + Q_{\text{floor}}\Pi_0^{2\pi}\,dL. \tag{C.12}$$

(3) There is a sunrise and a sunset on the facet:

$$\overrightarrow{n_{\text{surf}}} \bullet \overrightarrow{r_{\text{sun}}} > 0 \Leftrightarrow -1 \leqslant -\tan(\phi_{\text{n}})\tan(\delta) \leqslant +1. \tag{C.13}$$

We can define H_{n0} the local horary angle on the facet:

$$\cos(H_{\text{n0}}) = -\tan(\phi_{\text{n}})\tan(\delta). \tag{C.14}$$

In this case, the Sun illuminates the facet only when:

$$\overrightarrow{n_{\text{surf}}} \bullet \overrightarrow{r_{\text{sun}}} > 0 \Leftrightarrow \alpha - H_{\text{n0}} < L_{\text{n}} < \alpha + H_{\text{n0}}. \tag{C.15}$$

Using Eq. (C.5), the condition for L is:

$$L_{\min} = \alpha - H_{\text{n0}} - L' - L_{\text{c}} < L < \alpha + H_{\text{n0}} - L' - L_{\text{c}} = L_{\max}, \tag{C.16}$$

$$W = \frac{1}{2\pi}\int_0^{2\pi} Q_{\text{sun}}\Pi_{L_{\min}}^{L_{\max}} + Q_{\text{scat}}\Pi_{L_{\min}}^{L_{\max}} + Q_{\text{IR}}\Pi_0^{2\pi} + Q_{\text{floor}}\Pi_0^{2\pi}\,dL. \tag{C.17}$$

Analytical integration The following integrals can be solved analytically:

$$W_{\text{scat}} = \frac{1}{2\pi}\int_0^{2\pi} Q_{\text{scat}}\Pi_0^{2\pi}\,dL = Q_{\text{scat}}, \tag{C.18}$$

$$W'_{\text{scat}} = \frac{1}{2\pi}\int_0^{2\pi} Q_{\text{scat}}\Pi_{L_{\min}}^{L_{\max}}\,dL = \frac{H_{\text{n0}}}{\pi}Q_{\text{scat}}, \tag{C.19}$$

$$W_{\text{IR}} = \frac{1}{2\pi}\int_0^{2\pi} Q_{\text{IR}}\Pi_0^{2\pi}\,dL = Q_{\text{IR}}, \tag{C.20}$$

$$W_{\text{floor}} = \frac{1}{2\pi}\int_0^{2\pi} Q_{\text{floor}} \Pi_0^{2\pi}\, dL = Q_{\text{floor}}. \tag{C.21}$$

Property Using Eqs. (C.2), (C.3), (C.5) and (7), we can see that Q_{sun} depends on L only through the scalar products:

$$Q_{\text{sun}} = F_1 \cdot F_2 \cdot F_3\big(\cos(L-\alpha)\big) \cdot F_4\big(\cos(L-\alpha+L'+L_c)\big) \cdot F_5\big(\cos(L-\alpha)\big), \tag{C.22}$$

$$W_{\text{sun}} = \frac{1}{2\pi}\int_{\alpha+C}^{\alpha+D} Q_{\text{sun}}(L)\, dL = \frac{1}{2\pi}\int_C^D \tilde{Q}_{\text{sun}}(\tilde{L})\, d\tilde{L}, \tag{C.23}$$

with $\tilde{L} = L-\alpha$, $C = -H_{n0} - L' - L_c$, $D = H_{n0} - L' - L_c$ and $\tilde{Q}_{\text{sun}} = F_1 \cdot F_2 \cdot F_3(\cos(\tilde{L})) \cdot F_4(\cos(\tilde{L}+L'+L_c)) \cdot F_5(\cos(\tilde{L}))$.

This shows that W_{sun} is independent of α, the longitude of the sub-solar point. We set this parameter to zero to estimate the integral (C.23).

Appendix D. Summary of the parameter values used for the surface radiation budget

Model parameters. Units are noted in brackets []; [1] denotes the absence of units.

$R = 3{,}386{,}200$ [m]	radius of the planet
h [m]	altitude
h' [radian]	normalized altitude
(x, y) [m]	map coordinates
(x', y') [1]	image coordinate in pixel
Δ [m]	pixel size (identical on x and y direction)
(L, ϕ) [radian]	East longitude (from 0 to 2π), latitude (from $-\frac{\pi}{2}$ to $\frac{\pi}{2}$)
γ [1]	local slope
Q_{sun} [W m^{-2}]	instantaneous absorbed energy from the direct sunlight
Q_{scat} [W m^{-2}]	instantaneous absorbed energy from the sunlight scattered by the atmosphere
Q_{IR} [W m^{-2}]	instantaneous absorbed energy from the thermal emission of the atmosphere
Q_{floor} [W m^{-2}]	instantaneous absorbed energy from the thermal emission of the neighboring facets
$\overrightarrow{r_{\text{surf}}}(L, \phi)$ [1]	normalized radius vector of a point at the surface assuming a spherical planet
$\overrightarrow{r_{\text{sun}}}(\alpha, \delta)$ [1]	normalized radius vector of the sub-solar point
$\overrightarrow{n_{\text{surf}}}(L_n, \phi_n)$ [1]	normalized vector of the direction normal to the local surface
$\Pi_{L_{\min}}^{L_{\max}}(L)$	door function
$S_{\text{sun}} = 589$ [W m^{-2}]	solar constant at the mean distance between Mars and the Sun $\langle d_{\text{sun}} \rangle$
r_{sun} [m]	ratio of mean distance between Mars and the Sun over the distance at time t $\langle d_{\text{sun}} \rangle / d_{\text{sun}}(t)$. We calculate this distance $d_{\text{sun}}(t)$ for any date t using the astronomical parameters determined by the celestial measurements of Pathfinder at J2000 by Allison and McEwen (2000).
A_{vis} [1]	bolometric albedo in the visible. We assume a lambertian surface $A_{\text{dh,vis}}(\theta_i) = A_{\text{vis}}$ and no dependence on the incidence angle (see Eq. (1)).
A_{IR} [1]	bolometric albedo in the thermal infra-red. We assume a lambertian surface $A_{\text{dh,IR}}(\theta_i) = A_{\text{IR}}$ and no dependence on the incidence angle. Albedo in the IR is linked to emissivity through $A_{\text{IR}} = 1 - \varepsilon$ (Warren et al., 1990).
$f = 0.06$	fraction of light attenuated by the atmosphere. This value was used in the modeling by Kieffer et al. (1977), Aharonson and Schorghofer (2006). $f \simeq f_{\text{scat}} + f_{\text{IR}}$.
$f_{\text{scat}} = 0.02$ [1]	fraction of the direct sunlight scattered by the atmosphere. This value was already used in the modeling by Kieffer et al. (1977), Aharonson and Schorghofer (2006).
$f_{\text{IR}} = 0.04$ [1]	equivalent fraction of noon time direct sunlight emitted by the atmosphere. This value, discussed by Haberle and Jakosky (1991), was already used in the modeling by Aharonson and Schorghofer (2006).
$H = 0.8$ [1]	Hurst exponent, describing the topographical roughness
ε [1]	thermal emissivity (see A_{IR})
$\sigma = 5.67 \times 10^{-8}$ [$\text{W m}^{-2}\,\text{K}^{-4}$]	Stefan Boltzmann constant
T [K]	temperature of the surrounding soil. This temperature is assumed to be the same as that for the considered facet. If the current facet is frosted and the surrounding ones are defrosted, Q_{floor} is underestimated.

Appendix E. Summary of the parameters used for modeling the defrost mass balance

In addition to the radiative parameters described in Appendix D, there are the parameters below.

$L_{CO_2} = 590 \times 10^3$ [J kg^{-1}]	latent heat for CO_2 sublimation
T_{surf} [K]	temperature of the facet
M_{CO_2} [kg m^{-2}]	CO_2 mass of the frost layer
t [s]	time

References

Aharonson, O., 2004. Sublimation at the base of a seasonal CO_2 slab on Mars. In: Mackwell, S., Stansbery, E. (Eds.), Proc. 35th Lunar Planet. Sci. Conf., p. 1918.

Aharonson, O., Schorghofer, N., 2006. Subsurface ice on Mars with rough topography. J. Geophys. Res. (E) 111. 11007.

Aharonson, O., Zuber, M.T., Rothman, D.H., 2001. Statistics of Mars' topography from the Mars Orbiter Laser Altimeter: Slopes, correlations, and physical models. J. Geophys. Res. (E) 106, 23723–23736.

Aharonson, O., Zuber, M.T., Smith, D.E., Neumann, G.A., Feldman, W.C., Prettyman, T.H., 2004. Depth, distribution, and density of CO_2 deposition on Mars. J. Geophys. Res. (E) 109. 5004.

Allison, M., McEwen, M., 2000. A post-Pathfinder evaluation of areocentric solar coordinates with improved timing recipes for Mars seasonal/diurnal climate studies. Planet. Space Sci. 48, 215–235.

Benson, J.L., James, P.B., 2005. Yearly comparisons of the martian polar caps: 1999–2003 Mars Orbiter Camera observations. Icarus 174, 513–523.

Bintanja, R., 1999. On the glaciological, meteorological, and climatological significance of antarctic blue ice areas. Rev. Geophys. 37, 337–360.

Brown, G.N.J., Ziegler, W.T., 1979. Vapor pressure and heats of vaporization and sublimation of liquids and solids of interest in cryogenics below 1-atm pressure. Adv. Cryogenic Eng. 25, 662–670.

Campbell, B.A., Ghent, R.R., Shepard, M.K., 2003. Limits on inference of Mars small-scale topography from MOLA data. Geophys. Res. Lett. 30. 15-1.

Campbell, W.W., 1895. The irregular waning of the South Polar cap of Mars. Publ. Astron. Soc. Pacific 7, 40–43.

Colaprete, A., Toon, O.B., 2002. Carbon dioxide snow storms during the polar night on Mars. J. Geophys. Res. (E) 107. 5-1.

Colaprete, A., Barnes, J.R., Haberle, R.M., Hollingsworth, J.L., Kieffer, H.H., Titus, T.N., 2005. Albedo of the south pole on Mars determined by topographic forcing of atmosphere dynamics. Nature 435, 184–188.

Douté, S., Schmidt, F., Schmitt, B., Langevin, Y., Vincendon, M., Bibring, J.-P., Omega Team, 2008. Physical characterization of the south seasonal cap of Mars during recession from OMEGA observations. Lunar Planet. Sci. 39, 1736.

Eluszkiewicz, J., 1993. On the microphysical state of the martian seasonal caps. Icarus 103 (1), 43–48.

Eluszkiewicz, J., Moncet, J.-L., 2003. A coupled microphysical/radiative transfer model of albedo and emissivity of planetary surfaces covered by volatile ices. Icarus 166 (2), 375–384.

Forget, F., 1998. Mars CO_2 ice polar caps. In: Schmitt, B., de Bergh, C., Festou, M. (Eds.), Solar System Ices. In: Astrophysics and Space Science Library, vol. 227. Kluwer, Dordrecht, pp. 477–507.

Forget, F., Hourdin, F., Talagrand, O., 1998. CO_2 snowfall on Mars: Simulation with a General Circulation Model. Icarus 131, 302–316.

Forget, F., Hourdin, F., Fournier, R., Hourdin, C., Talagrand, O., Collins, M., Lewis, S.R., Read, P.L., Huot, J.-P., 1999. Improved general circulation models of the martian atmosphere from the surface to above 80 km. J. Geophys. Res. (E) 104, 24155–24176.

Giuranna, M., Grassi, D., Formisano, V., Montabone, L., Forget, F., Zasova, L., 2008. Pfs/mex observations of the condensing CO_2 south polar cap of Mars. Icarus 197 (2), 386–402.

Haberle, R.M., Jakosky, B.M., 1991. Atmospheric effects on the remote determination of thermal inertia on Mars. Icarus 90, 187–204.

Hansen, G.B., 1997. The infrared absorption spectrum of carbon dioxide ice from 1.8 to 333 μm. J. Geophys. Res. (E) 102, 21569–21588.

Hansen, G.B., 1999. Control of the radiative behavior of the martian polar caps by surface CO_2 ice: Evidence from Mars Global Surveyor measurements. J. Geophys. Res. (E) 104, 16471–16486.

Hapke, B., 1993. Theory of reflectance and emittance spectroscopy. In: Topics in Remote Sensing. Cambridge Univ. Press, Cambridge, UK.

Iwasaki, K., Saito, Y., Nakai, Y., Akabane, T., Panjaitan, E., 1990. Martian south polar CAP 1988. J. Geophys. Res. (E) 95, 14751–14754.

James, P.B., Briggs, G., Barnes, J., Spruck, A., 1979. Seasonal recession of Mars' south polar CAP as seen by Viking. J. Geophys. Res. (E) 84, 2889–2922.

James, P.B., Cantor, B.A., Malin, M.C., Edgett, K., Carr, M.H., Danielson, G.E., Ingersoll, A.P., Davies, M.E., Hartmann, W.K., McEwen, A.S., Soderblom, L.A., Thomas, P.C., Veverka, J., 2000. The 1997 Spring regression of the martian south polar cap: Mars orbiter camera observations. Icarus 144, 410–418.

James, P.B., Cantor, B.A., Davis, S., 2001. Mars orbiter camera observations of the martian south polar cap in 1999–2000. J. Geophys. Res. (E) 106, 23635–23652.

Kelly, N.J., Boynton, W.V., Kerry, K., Hamara, D., Janes, D., Reedy, R.C., Kim, K.J., Haberle, R.M., 2006. Seasonal polar carbon dioxide frost on Mars: CO_2 mass and columnar thickness distribution. J. Geophys. Res. (E) 111, doi:10.1029/2006JE002678.

Kieffer, H.H., Martin, T.Z., Peterfreund, A.R., Jakosky, B.M., Miner, E.D., Palluconi, F.D., 1977. Thermal and albedo mapping of Mars during the Viking primary mission. J. Geophys. Res. (E) 82, 4249–4291.

Kieffer, H.H., Titus, T.N., Mullins, K.F., Christensen, P.R., 2000. Mars south polar spring and summer behavior observed by TES: Seasonal cap evolution controlled by frost grain size. J. Geophys. Res. (E) 105, 9653–9700.

Kieffer, H.H., Christensen, P.R., Titus, T.N., 2006. CO_2 jets formed by sublimation beneath translucent slab ice in mars' seasonal south polar ice cap. Nature 442, 793–796. 7104.

Langevin, Y., Douté, S., Vincendon, M., Poulet, F., Bibring, J.-P., Gondet, B., Schmitt, B., Forget, F., 2006. No signature of clear CO_2 ice from the 'cryptic' regions in Mars' south seasonal polar cap. Nature 442 (7104), 790–792.

Langevin, Y., Bibring, J.-P., Montmessin, F., Forget, F., Vincendon, M., Douté, S., Poulet, F., Gondet, B., 2007. Observations of the south seasonal cap of Mars during recession in 2004–2006 by the OMEGA visible/near-infrared imaging spectrometer on board Mars Express. J. Geophys. Res. (E) 112, doi:10.1029/2006JE002841.

Laskar, J., Joutel, F., Boudin, F., 1993. Orbital, precessional, and insolation quantities for the Earth from −20 Myr to +10 Myr. Astron. Astrophys. 270, 522–533.

Leighton, R.R., Murray, B.C., 1966. Behavior of carbon dioxide and other volatiles on Mars. Science 153, 136–144.

Lewis, S.R., Collins, M., Read, P.L., Forget, F., Hourdin, F., Fournier, R., Hourdin, C., Talagrand, O., Huot, J.-P., 1999. A climate database for Mars. J. Geophys. Res. (E) 104, 24177–24194.

Litvak, M.L., Mitrofanov, I.G., Kozyrev, A.S., Sanin, A.B., Tretyakov, V.I., Boynton, W.V., Kelly, N.J., Hamara, D., Saunders, R.S., 2007. Long-term observations of southern winters on Mars: Estimations of column thickness, mass, and volume density of the seasonal CO_2 deposit from HEND/Odyssey data. J. Geophys. Res. (E) 112, doi:10.1029/2006JE002841.

Malamud, B.D., Turcotte, D.L., 2001. Wavelet analyses of Mars polar topography. J. Geophys. Res. (E) 106, 17497–17504.

Murchie, S.L., and 42 colleagues, 2004. CRISM (Compact Reconnaissance Imaging Spectrometer for Mars) on MRO (Mars Reconnaissance Orbiter). In: Nardell, C.A., Lucey, P.G., Yee, J.-H., Garvin, J.B. (Eds.), Applications with Weather Satellites. II. Menzel, W.P., Iwasaki, T. (Eds.), Proc. of the SPIE, vol. 5660, pp. 66–77.

Paige, D.A., Ingersoll, A.P., 1985. Annual heat balance of martian polar caps—Viking observations. Science 228, 1160–1168.

Piqueux, S., Byrne, S., Richardson, M.I., 2003. Sublimation of Mars's southern seasonal CO_2 ice cap and the formation of spiders. J. Geophys. Res. (E) 108, doi:10.1029/2002JE002007.

Pollack, J.B., Haberle, R.M., Schaeffer, J., Lee, H., 1990. Simulations of the general circulation of the martian atmosphere. I. Polar processes. J. Geophys. Res. (E) 95, 1447–1473.

Portyankina, G., Markiewicz, W.J., 2003. Model for formation of spider patterns in the Cryptic region. In: Clifford, S., Doran, P., Fisher, D., Herd, C. (Eds.), Third Int. Conf. on Mars Polar Science and Exploration, p. 8026.

Press, W.H., Flannery, B.P., Teukolsky, S.A., Vetterling, W.T., 1986–1992. Numerical Recipes in Fortran 77: The Art of Scientific Computing. Cambridge Univ. Press. Chap. 4.4, pp. 110–114.

Putzig, N.E., Mellon, M.T., Kretke, K.A., Arvidson, R.E., 2005. Global thermal inertia and surface properties of Mars from the MGS mapping mission. Icarus 173, 325–341.

Sayles, R.S., Thomas, T.R., 1978. Surface topography as a nonstationary random process. Nature 271, 431–434.

Schmitt, B., Quirico, E., Trotta, F., Grundy, W.M., 1998. Optical properties of ices from UV to infrared. In: Schmitt, B., de Bergh, C., Festou, M. (Eds.), Solar System Ices. In: Astrophys. Space Sci. Libr., vol. 227. Kluwer, Dordrecht, pp. 199–240.

Schmitt, B., Schmidt, F., Douté, S., Langevin, Y., Forget, F., Bibring, J.-P., Gondet, B., Omega Team, 2006. Recession of the northern seasonal condensates on Mars by OMEGA/Mars Express. LPI Contributions 1323, 8050.

Schmidt, F., Douté, S., Schmitt, B., 2007. Wavanglet: An efficient supervised classifier for hyperspectral images. Geosci. Remote Sensing, IEEE Trans. 45 (5), 1374–1385.

Schorghofer, N., Aharonson, O., 2005. Stability and exchange of subsurface ice on Mars. J. Geophys. Res. (E) 110. 5003.

Shchuko, O.B., Kartashov, D.V., Picardi, G., Orosei, R., 2003. Martian underground water detection: Thermal model and simulations of radar signal propagation. J. Geophys. Res. (E) 108, doi:10.1029/2002JE001879.

Shepard, M.K., Campbell, B.A., 1998. Shadows on a planetary surface and implications for photometric roughness. Icarus 134, 279–291.

Shepard, M.K., Campbell, B.A., Bulmer, M.H., Farr, T.G., Gaddis, L.R., Plaut, J.J., 2001. The roughness of natural terrain: A planetary and remote sensing perspective. J. Geophys. Res. (E) 106, 32777–32796.

Thomas, P., Veverka, J., Campos-Marquetti, R., 1979. Frost streaks in the south polar CAP of Mars. J. Geophys. Res. (E) 84, 4621–4633.

Titus, T.N., Mar. 2005. Mars polar cap edges tracked over 3 full Mars years. In: Mackwell, S., Stansbery, E. (Eds.), 36th Annu. Lunar Planet. Sci. Conf. p. 1993.

Veverka, J., Goguen, J., 1973. The nonuniform recession of the south polar cap of Mars. J. Royal Astron. Soc. Canada 67, 273.

Vincendon, M., Langevin, Y., Poulet, F., Bibring, J., Gondet, B., Jouglet, D., the OMEGA Team, 2008. Dust aerosols above the south polar cap of Mars as seen by OMEGA. Icarus 196, 488–505.

Warren, S.G., Wiscombe, W.J., Firestone, J.F., 1990. Spectral albedo and emissivity of CO_2 in martian polar caps—Model results. J. Geophys. Res. (E) 95, 14717–14741.

4.4.2 Sublimation de la calotte saisonnière Sud de Mars

Cette section contient l'article suivant :

Schmidt F., Schmitt B., Douté S., Forget, F., Jeng, J.-J., Martin, P., Langevin, Y., Bibring J.-P. and the OMEGA Team ; "Sublimation of the Martian CO2 seasonal south Polar Cap", Planetary and Space Science, 2010, 58, 1129- 1138

Planetary and Space Science 58 (2010) 1129–1138

Contents lists available at ScienceDirect

Planetary and Space Science

journal homepage: www.elsevier.com/locate/pss

Sublimation of the Martian CO_2 Seasonal South Polar Cap

Frédéric Schmidt [a,b,*], Bernard Schmitt [c], Sylvain Douté [c], Francois Forget [d], Jeng-Jong Jian [e], Patrick Martin [a], Yves Langevin [f], Jean-Pierre Bibring [f], the OMEGA Team

[a] ESAC, PO Box 78, E-28691 Villanueva de la Canada, Madrid, Spain
[b] IDES, Université Paris-Sud 11, CNRS/INSU, Bâtiment 509, Université Paris-Sud, 91405 Orsay, France
[c] Laboratoire de Planétologie de Grenoble, Université de Grenoble, CNRS/INSU, BP 53, 38041 Grenoble Cedex 9, France
[d] Laboratoire de Météorologie Dynamique, Institut Pierre Simon Laplace, Université Paris VI, CNRS/INSU, BP99, 75252 Paris Cedex 05, France
[e] Institute of Astronomy, National Central University, 10F, No. 439, Dunhua Road, Beitun District, Taichung City 406, Taiwan
[f] Institut d'Astrophysique Spatiale, Université Paris-Sud 11, CNRS/INSU, Batiment 121, 91405 Orsay cedex, France

ARTICLE INFO

Article history:
Received 10 July 2009
Received in revised form
23 March 2010
Accepted 25 March 2010
Available online 3 April 2010

Keywords:
Mars
Ice
Atmosphere
Seasonal South Polar Cap
Cryptic region
Non-condensable gas

ABSTRACT

The polar condensation/sublimation of CO_2, that involve about one fourth of the atmosphere mass, is the major Martian climatic cycle. Early observations in visible and thermal infrared have shown that the sublimation of the Seasonal South Polar Cap (SSPC) is not symmetric around the geographic South Pole.

Here we use observations by OMEGA/Mars Express in the near-infrared to detect unambiguously the presence of CO_2 at the surface, and to estimate albedo. Second, we estimate the sublimation of CO_2 released in the atmosphere and show that there is a two-step process. From Ls=180° to 220°, the sublimation is nearly symmetric with a slight advantage for the cryptic region. After Ls=220° the anti-cryptic region sublimation is stronger. Those two phases are not balanced such that there is 22% ± 9 more mass the anti-cryptic region, arguing for more snow precipitation. We compare those results with the MOLA height measurements. Finally we discuss implications for the Martian atmosphere about general circulation and gas tracers, e.g. Ar.

© 2010 Elsevier Ltd. All rights reserved.

1. Introduction

The "cryptic region" is a dark region covered by ice in the South Polar Region of Mars (Kieffer et al., 2000; Titus et al., 2008). It appears to be a region where most of the "spiders" features are located (Piqueux et al., 2003; Kieffer, 2007). In order to simplify, we define in this article the cryptic region from longitude 50°E to 230°E (through longitude 90°E), and the anti-cryptic region from longitude 130°W to 50°E (the complementary sector, passing through longitude 0°E) (see Fig. 1).

During the phase of CO_2 frost accumulation, the Seasonal South Polar Cap (SSPC) is mainly formed by direct condensation, but some snow events can occur (Forget et al., 1998). GCM studies show that a topographic forcing by the Hellas basin creates an asymmetry in the mode of deposition. Precipitation events are more frequent for the anti-cryptic sector than for the cryptic sector (Colaprete et al., 2005; Giuranna et al., 2008). This suggests that the texture should be more granular (smaller grain sizes) for the former compared to the latter. This texture difference produces a relatively higher albedo in the anti-cryptic region and also possibly a higher accumulated mass.

The direct measurement of the sublimating CO_2 mass on Mars has been done only recently by three different techniques: gravity (Smith et al., 2001; Karatekin et al., 2006), neutron flux (Litvak et al., 2006) and gamma ray flux (Kelly et al., 2006). But the time and space resolutions of these methods prohibit any conclusion at the regional scale. At the present time, only direct measurements of the seasonal variations in altitude by MOLA are able to estimate the local CO_2 mass sublimation (Smith et al., 2001; Aharonson et al., 2004; Jian and Ip, 2009). But this impressive technique is limited by low signal to noise ratio because seasonal topographic variations are typically less that one meter. To enhance the climatic signal, Aharonson et al. (2004) use a Fourier transform and apply a filter on the MOLA time variation keeping only the annual period. Results show that the amplitude of this annual Fourier cycle is asymmetric, with a maximum in the anti-cryptic region (see Fig. 4(a) in Aharonson et al., 2004). This results lead to two different conclusions: (i) asymmetry in amplitude is actually related to asymmetry in accumulation and/or (ii) the annual period filtering may be not relevant to describe the real annual mass variation, so that the amplitude asymmetry may be an artefact related to the time of presence of CO_2. The second hypothesis is supported by the fact that the sublimation is much faster in the cryptic region (Kieffer et al., 2000; Langevin et al., 2007) leading to lower amplitude of the annual Fourier cycle. If this hypothesis is valid, the bi-annual cycle

* Corresponding author. Tel.: +33 1 69 15 61 52; fax: +33 1 69 16 48 82.
E-mail address: frederic.schmidt@u-psud.fr (F. Schmidt).

0032-0633/$ - see front matter © 2010 Elsevier Ltd. All rights reserved.
doi:10.1016/j.pss.2010.03.018

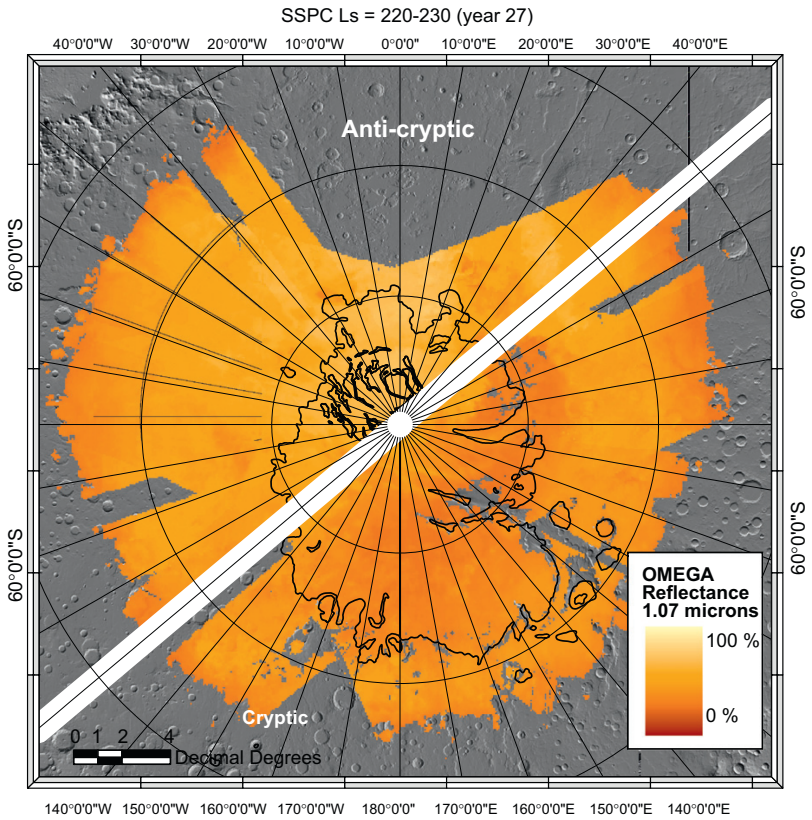


Fig. 1. Definition of the cryptic and anti-cryptic region within this article.

should be stronger for the cryptic region. More recently, Jian and Ip (2009) focus on the south polar region and show that cryptic and non-cryptic regions did not present any significant thickness difference.

Indirect measurement of the CO_2 mass has been performed for decades through modeling of: (i) the recession of the surface covered by ice observed by visible/infrared detectors (Leighton and Murray, 1966; Paige and Ingersoll, 1985; Lindner, 1993; Forget, 1998; Kieffer et al., 2000; Schmidt et al., 2009c), (ii) fitting the annual surface pressure cycle (Pollack et al., 1990; Wood and Paige, 1992; Hourdin et al., 1995). The first modeling methodology has the advantage to allow simple estimation of CO_2 ice sublimation mass at regional scale. It assumes that the CO_2 ice is in vapour-pressure equilibrium with the local atmosphere, and that the CO_2 mass balance at the surface is controlled by radiative balance. We propose to use this methodology using the latest OMEGA observation to estimate the local CO_2 mass balance in order to derive the difference in the cryptic/anti-cryptic region.

For each considered location on the map, the so-called crocus date is the date (Kieffer et al., 2000) when the surface deposit is completely gone. The crocus date is then a geophysical field of importance for atmospheric studies. Due to the fact that all instruments have a limited spatial resolution, Schmidt et al. (2009c) has introduced both inner and outer crocus date. Each location is defined by a super pixel with a spatial extent defined by the L_{stat} scale length (with a the pixel scale length $L_{pix} < L_{stat}$). The inner crocus date—respectively, outer crocus date—is the date when the first—resp. the last—pixels fails to exhibit any ice signature within the considered super pixel (see Fig. 2).

We will use the D-frost model (Schmidt et al., 2009c, 2008) to estimates the CO_2 frost mass balance. Several inputs are required: inner and outer crocus dates, albedo, altitude, slope. This model is able to calculate the total mass sublimated, from the date it becomes unstable (determined by the model itself), to the crocus date (determined by the observation). Thus the initial mass, before net sublimation, is not required as an input but will be determined by the model.

The aim of this work is to:

- estimate the main input fields, required for the D-frost model, from OMEGA observations: albedo, inner crocus/outer crocus date;
- calculate the sublimated mass of the SSPC using D-frost;
- derive the height variations, assuming a constant density, and compare to MOLA measurements;
- estimate the spatial asymmetry of the CO_2 mass release;
- derive potential effects on circulation at global scale, and on atmospheric gas tracers.

To avoid confusion about the sign of the "sublimation rate" of the SSPC, we adopt two natural conventions: surface convention with negative mass rates (sublimation of seasonal frosts); atmosphere convention, with positive mass rates (pump up of the atmosphere).

2. Methods

We propose to use the OMEGA imaging spectrometer (Bibring et al., 2004) on board Mars Express for simultaneously detect CO_2

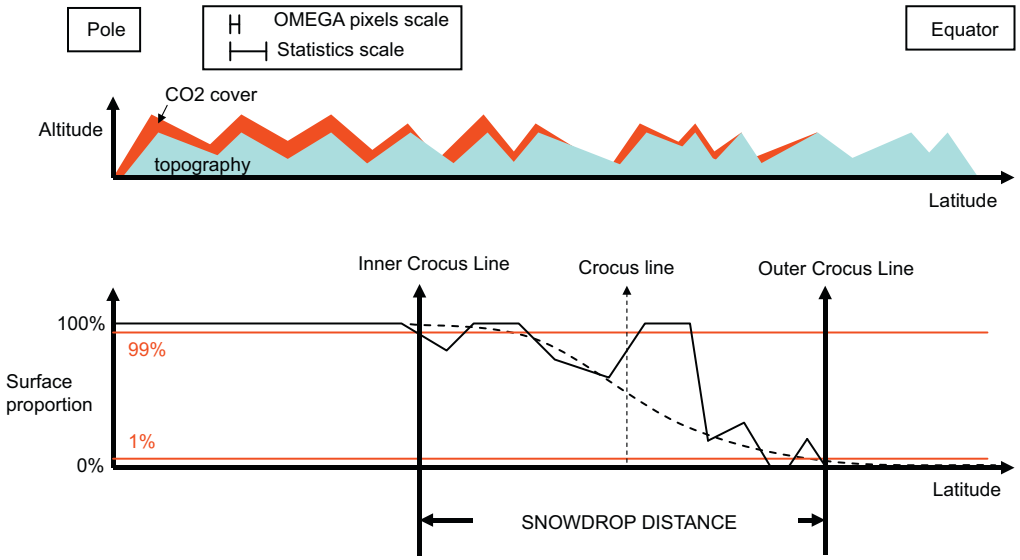


Fig. 2. Definition of inner crocus line, outer crocus line and snowdrop distance. Statistics scale length L_{stat} define the super pixel resolution, binning several OMEGA pixels. Black line represents the actual surface proportion covered by CO_2 ice for each super pixel. Doted lines represents the arctan model law (Kieffer et al., 2000). Crocus line is defined in the inflection point of the arctan law. Inner and Outer crocus lines are defined by the surface proportion of 99% and 1%.

ice on Mars and estimate the albedo under the aerosols layer. A compilation of all dataset available is out of the scope of this article but should be an interesting step for the future.

We use the following notation: latitude λ, longitude θ and time t. The spatial fields (inner and outer crocus dates) are sampled in a spatial grid of 0.3° latitude (200 steps from $\lambda=-90°$ to $-30°$) and 10° longitude (36 steps from $\theta=0°$ to 360°). The spatio-temporal fields (albedo and sublimated mass) are sampled in the same spatial grid and the temporal grid of 5°Ls (72 steps from $t=0°$ to 360°). Each element of the grid is called "bin". The succession of bins in latitude at constant longitude is called a "longitude sector". Respectively, a succession of bins in longitude at constant latitude is called a "latitude sector".

Due to the lack of the spatial/temporal cover we need to interpolate the measured crocus dates and albedo. The first two sections present our strategy. Each of these interpolation methods will be evaluated simply using the standard deviation of the difference between the actual data and the interpolated field.

2.1. Crocus dates field

For each bin with available OMEGA observation, we estimate the inner and outer crocus dates using previously described method in Schmidt et al. (2009c). This method uses WAVANGLET, an automatic detection algorithm (Schmidt et al., 2007), and a special algorithm to extract crocus lines. We use the OMEGA dataset in year 2005–2006 (Martian year 27) from Ls=110° to Ls=320° and selected 544 observations from latitude 30°S to 90°S.

We propose here the following methodology to get an interpolated map of both inner $t_{in}(\lambda,\theta)$ and outer $t_{out}(\lambda,\theta)$ crocus date.

2.1.1. Interpolation method

The crocus dates, binned into our grid (see Section 2), are re-estimated by a weighted sum of actually measured neighbouring values in order to interpolate the field in case of missing values. The weights depend on the distance and are chosen to be in a Gaussian shape. This operation is performed through a convolution product on the complete latitude/longitude grid with the Gaussian kernel:

$$t_{in}^{interp}(\lambda,\theta)=\iint t_{in}(\lambda,\theta)\cdot\frac{1}{2\pi\cdot\sigma_{lat}\cdot\sigma_{long}}\cdot\exp\left(\frac{(\lambda-\lambda')^2}{2\sigma_{lat}}+\frac{(\theta-\theta')^2}{2\sigma_{long}}\right)d\lambda'\,d\theta' \quad (1)$$

with:

- computation on the complete grid: latitude × longitude bins: 200 × 36;
- variance of the Gaussian in latitude × longitude bins: $\sigma_{lat}=41.66$ latitude bin (12.5° latitude), $\sigma_{long}=5$ longitude bin (50° latitude). The ratio of latitude and longitude variance is set to real average distance in our grid.

2.1.2. Results and evaluation

The interpolated crocus line field t_{in}^{interp}, average for the cryptic and anti-cryptic regions are drawn in Fig. 3(a). The recession is clearly symmetric before Ls=140° latitude 55°S. This symmetry can be biased by the interpolation, especially due to Hellas and Argyre basins where persistent CO_2 ice have been detected by Giuranna et al. (2007a). After Ls=190°, latitude 62°S, the cryptic region crocus lines are 20°Ls earlier than the anti-cryptic region. Two possible interpretations will be discussed in Section 3: lower accumulated CO_2 ice mass and/or lower albedo leading to higher absorption and sublimation.

To evaluate the quality of this interpolation, we analyze the difference between actual measurement and interpolated field. The standard deviation is quite large (14°Ls for outer crocus date and 17°Ls for inner crocus date) due to the sparseness and discontinuity of the dataset. Also it could be due to the sensitivity of daily variation in frost cover, ignored within our scheme. The mean snowdrop time is 15°Ls in agreement with the value measured by consecutive observations by Schmidt et al. (2009c).

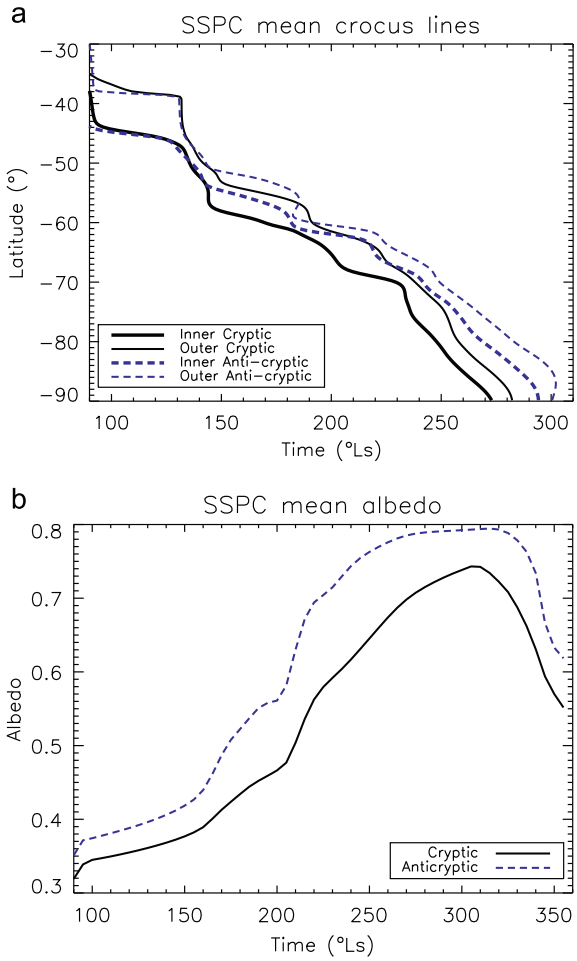


Fig. 3. Averaged fields interpolated from OMEGA observations for both cryptic and anti-cryptic regions: (a) crocus lines and (b) albedo under the aerosols. The interpolated fields are used as an input of the D-frost model.

2.2. Albedo field

Radiative balance requires the directional-hemispheric bolometric albedo of the surface *A*, or simply "albedo", that is an integrated quantity of the BRDF (bidirectional reflectance density function). It is dependent of the incidence direction (the solar direction) but integrated on all emergence directions of the top hemisphere and spectrally integrated—weighted by the solar spectrum. Definitions can be found in Hapke (1993).

This quantity can be estimated from space using the reflectance spectra in the visible/near infrared recorded by OMEGA, by removing the dust aerosols contribution that significantly modifies the apparent surface albedo, notably for bright icy surfaces that appear darker. Vincendon et al. (2008) propose a method to evaluate the contribution of the aerosol scattering and attenuation at all wavelengths from a narrow spectral region where the entire signal comes from the aerosols (saturated bands of CO_2 ice).

We use 265 images of the Martian year 27 from Ls=120° to 300° in the latitude range 52°S to 90°S. We average all estimations points where the method provided by Vincendon et al. (2008) can be applied to the corresponding bin. Then we perform an empirical spectral integration of the solar spectrum in the visible and near-IR as described in Schmidt et al. (2009c). Finally, we estimate the complete field of seasonal deposit albedo using the following empirical interpolation method. The main advance of this interpolation method compared to our previous study (Schmidt et al., 2009c) is to take into account both space and time evolution.

2.2.1. Interpolation method

The albedo, binned into our grid (see Section 2), are re-estimated by a weighted sum of actually measured neighbouring values in order to interpolate the field in case of missing values. The weights, depending on the distance in space and time, are chosen to be in a Gaussian shape. Albedo is interpolated in a similar strategy to crocus date (Section 2.1.1) with a convolution on the complete latitude/longitude/time grid with a Gaussian kernel. In order to keep in a realist situation, we apply a threshold on the resulting albedo and then smooth the results.

(1) Convolution with a Gaussian kernel on the complete latitude/longitude/time grid:

$$A^{interp1}(\lambda,\theta) = \iiint A(\lambda,\theta)\cdot\frac{1}{2\pi\cdot\sigma_{lat}\cdot\sigma_{long}\cdot\sigma_{time}} \times\exp\left(\frac{(\lambda-\lambda')^2}{2\sigma_{lat}}+\frac{(\theta-\theta')^2}{2\sigma_{long}}+\frac{(t-t')^2}{2\sigma_{time}}\right)d\lambda'\,d\theta'\,dt' \quad (2)$$

with:

- computation on the complete grid: latitude × longitude bins: 200 × 36 × 72;
- variance of the Gaussian in latitude × longitude × time bins: $\sigma_{lat}=41.66$ latitude bin (12.5° latitude), $\sigma_{long}=5$ longitude bin (50° latitude), $\sigma_{time}=4$ time bin (20°Ls). The ratio of latitude and longitude variance is set to the real average distance ratio in our grid.

(2) Application of a threshold on the albedo $A^{interp1}$ value in the range [0.3, 0.9] to get $A^{interp2}$ to remove noisy data.

(3) Convolution to smooth the threshold (same than Eq. (2)) using $A^{interp2}$ to get A^{interp}, with:

- computation on the local grid only to save computation time: 8 × 2 × 2;
- variance of the Gaussian in latitude × longitude × time bins: $\sigma_{lat}=8.3$ latitude bin (2.5° latitude), $\sigma_{long}=1$ longitude bin (10° latitude), $\sigma_{time}=1$ time bin (5°Ls). The ratio of latitude and longitude variance is set to the real average distance ratio in our grid.

2.2.2. Results and evaluation

The interpolated albedo field A^{interp}, average for the cryptic and anti-cryptic regions are shown in Fig. 3(b). Albedo increases in both region of the SSPC as previously noted (Paige and Ingersoll, 1985; Kieffer et al., 2000; Schmidt et al., 2009c). The anti-cryptic region has an albedo 0.03 higher than the cryptic in the beginning of the recession. The difference increase to reach 0.2 around Ls=220° and then decrease again. The main reasons for a lower albedo in the cryptic region, compared to the anti-cryptic region should be the following: (i) the fact that the ice is translucent and thus the low albedo is due to the underneath ground (Kieffer et al., 2000) (ii) the presence of the fans associated with the spiders (Piqueux et al., 2003; Kieffer et al., 2006; Kieffer, 2007), (iii) dust contamination close to the surface (Langevin et al., 2006), (iv) larger grain size in the case granular ice (Warren et al., 1990). Recent studies suggest that a slab ice is present in extensive position in the SSPC with a fast space and time

evolution (Schmidt et al., 2009a). We will discuss these points in an upcoming paper (Schmidt et al., 2009b).

This interpolation method is centred because the convolution with a Gaussian kernel is normalized. The standard deviation is 0.028 and is one order of magnitude lower than the mean interpolated albedo field (0.405). The resulting empirical interpolated albedo field is thus very close to the original measured dataset.

2.3. D-frost model: daily average sublimated mass model

We use the D-frost model to estimate the daily average CO_2 mass surface balance $dM = dM(\lambda,\theta,t)$ for each bin 0.3° latitude, 10° longitude and 5°Ls as described in introduction of Section 2. This method estimate the following radiative balance in the visible and IR range:

$$dM = (F^{out}_{therm} - W^{in}_{sun} - W^{in}_{scat} - W^{in}_{IR} - W^{in}_{floor} - F^{in}_{cond}) \frac{1}{L_{CO_2}} dt \quad (3)$$

F^{out}_{therm} represents the thermal energy flux from the surface; F^{in}_{sun} is the direct solar energy absorbed by the surface; W^{in}_{scat} is the solar energy scattered by the atmosphere and absorbed by the surface; W^{in}_{IR} represents the thermal energy emitted by the atmosphere and absorbed by the surface; W^{in}_{floor} is the thermal energy emitted by the neighbouring surface facets and absorbed by the surface; F^{in}_{cond} is the heat flux from the regolith; $L_{CO_2} = 590 \times 10^3\,\mathrm{J\,kg^{-1}}$ is the latent heat for CO_2 sublimation.

The thermal energy flux is estimated with the frost temperature determined by the local pressure of CO_2, based on the LMD GCM (Forget et al., 1999)—calibrated to Viking Lander pressure curves—scaled to MOLA elevation. The albedo in the thermal infrared domain is assumed to be constant at 0.1 and the emissivity is set to 0.99. Despite these parameters are actually changing in space and time (Eluszkiewicz and Moncet, 2003), a quantitative sensitivity test has shown that it should play a minor role (see Section 4.1.6. of Schmidt et al., 2009c). Also the annual heat wave is neglected to speed up the computation. This energy source has also been demonstrated to be negligible during the sublimation phase (see Section 4.1.3. of Schmidt et al., 2009c). More details about the computation scheme can be found in Schmidt et al. (2009c).

2.3.1. Ar description

We improve the D-frost model by including the effect of the non-condensable gas on the CO_2 partial pressure. We use the measurements of Ar by Sprague et al. (2007) to correct for the actual CO_2 pressure using the formula:

$$P_{CO_2} = P_{GCM} - P_{Ar} \quad (4)$$

In other words, we use P_{CO_2} instead of P_{GCM} in the estimation of surface temperature (see eq. 13 of Schmidt et al., 2009c).

We use the interpolated albedo field presented in the last section. Altitude and slopes are estimated for each bin averaging a map in stereographic south projection of MOLA data at a resolution of 920.8 m.

2.3.2. Time integration

The total mass sublimated M is estimated by this integral:

$$M = \int_{-30^\circ}^{-90^\circ} \int_{0^\circ}^{360^\circ} \int_{t_0}^{t_{end}} dM(\lambda,\theta,t)\, dS\, dt \quad (5)$$

where t_0 is the beginning of the sublimation (i.e. the first time when $dM < 0$), t_{end} is the crocus date (i.e. the time when all the CO_2 ice disappears).

We propose two extreme cases for t_{end}: the inner crocus date t_{in} and outer the crocus line t_{out}. A most realistic case is the decreasing of surface proportion $X = X(t)$ inside each bin from the inner to the outer crocus date. Then Eq. (5) becomes:

$$M = \int_{-30^\circ}^{-90^\circ} \int_{0^\circ}^{360^\circ} \int_{t_0}^{t_{end}} dM(\lambda,\theta,t)\, X(t)\, dS\, dt \quad (6)$$

We assume a linear decrease of $X(t)$ with time, from $X = 100\%$ at t_{in} to $X = 0\%$ at t_{out}. Thus the surface proportion can be written:

$$X(t) = \frac{t_{out} - t}{t_{out} - t_{in}} \quad (7)$$

In the following, this case will be referred to as "linear surface proportion".

2.4. MOLA height variation

The MOLA observations were performed from February 28, 1999 and June 30, 2001 in a time interval longer than one Martian year (MY 23 and MY24). In this study, we used MOLA data from orbit 10012 to 20327 (from Ls = 103° to 360° in MY23 and then to 190° in MY24). Between Ls = 344° in MY23 and Ls = 16° in MY24 there are no MOLA data acquired because solar conjunction. This time interval permits to investigate the height changes of the CO_2 polar deposits.

To determine the thickness of the CO_2 frost layer in different regions as a function of time, it is most important to compute the crossover residuals resulting from subtracting the altitude h of a certain location at some value of Ls to the reference altitude h_0 at the same location without frost. In this work about the south polar region, the no frost reference altitude is chosen at Ls = 300°. We have limited our consideration to a latitudinal band between 50°S and 85°S. Several small areas of about 0.1°–0.2° in longitude and 0.05° in latitude and with enough number of crossovers are then chosen. After computation of the average elevation value of each small area, we calculate the residuals by subtracting the average altitude h of a certain location at some value of Ls to the reference altitude h_0 at the same location.

3. Results

The total sublimated mass from latitude 50°S to 90°S during the year is about 5.9×10^{15} kg (Fig. 4). The two extreme cases (4.3×10^{15} kg for $t_{end} = t_{in}$ and 6.9×10^{15} for $t_{end} = t_{out}$) are considered as the error bar due to the main uncertainty on the crocus dates such that our estimation is $(5.6 \pm 1.3) \times 10^{15}$ kg.

Our estimation is compatible with gravity measurements of Karatekin et al. (2006) ($\sim 6 \times 10^{15}$ kg), GRS estimation from Kelly et al. (2006) (6×10^{15} kg) and HEND analysis provided by Litvak et al. (2007) ($((6.1 \pm 0.6) \times 10^{15}$ kg)). Since our calculations are done in the domain 50°S–90°S only and since we found the same numbers than other methods based on a global approach, it suggests that the CO_2 mass condensed at latitude lower than 50 S is negligible.

The GCM by Forget et al. (1999), calibrated by the pressure variation measurement from Viking, give also an estimate of the total SSPC of 6.9×10^{15} kg, slightly higher than our estimation. The pattern of the total sublimated mass M along time (Fig. 4) is compatible with the GCM (Forget et al., 1999) although the starting of sublimation seems to be slightly earlier for the D-frost model. Nevertheless, there is a good agreement about the end of sublimation: around Ls = 270°. The shift in the beginning of sublimation can be explained by the integration method. In this study, we integrate spatially the CO_2 mass that is subliming, independently of the condensation domain. In the GCM integrations (Forget et al., 1999), the whole SSPC spatial domain is covered: subliming and condensing CO_2. At Ls = 90°, the average

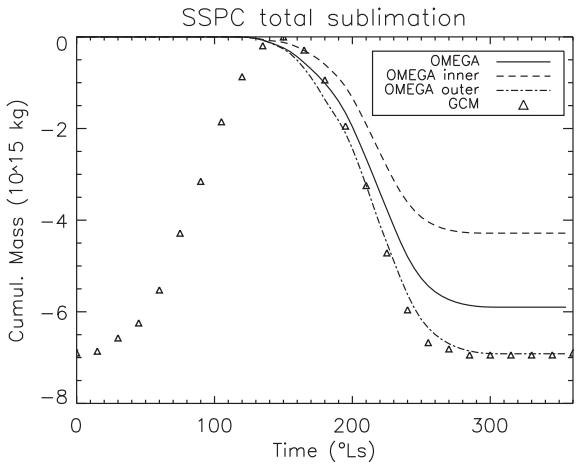


Fig. 4. Total cumulative sublimated mass estimated by the D-frost model using OMEGA inputs compared with GCM (Forget et al., 1999). Please note that a negative balance corresponds to surface mass loss (surface convention).

SSPC balance measured by the GCM is in accumulation due to the geographic polar region. Our integration shows already the sublimation that occurs at low latitude.

It is not possible to extend our calculation to the condensation domain because one energy source is missing: heat conducted in the soil (Haberle et al., 2008), which is no more negligible for the accumulation period (Schmidt et al., 2009c). Our estimation is limited in the domain latitude 50°S–90°S because for lower latitudes, CO_2 frost may be possible only with an apparent albedo below our threshold (0.3). Nevertheless, MOC observations shows seasonal frost at lower latitude suspected to be CO_2 ice (Schorghofer and Edgett, 2006). These condensates could be also predicted with D-frost using lower albedo and the shadowing effect at lower scale and would be an interesting point for the future. The good agreement between our mass balance and direct mass measurements suggests that the low latitude frost mass is negligible at first order.

If the Ar is well mixed in the south polar region, the effect on the temperature and thus on the total sublimated mass is below 1%.

Fig. 5 shows the integration of the SSPC sublimation for the two regions. The main conclusion is that despite the asymmetry of crocus lines and albedo, the sublimated mass seems to be symmetric around the geographic pole. The difference reach 20.5% (12.5% for $t_{end}=t_{in}$, 31.2% for $t_{end}=t_{out}$). To compile all errors, we estimate roughly that the mass difference is $22\% \pm 9$. This conclusion confirms that the condensation phases are not equivalent during the polar night for both cryptic and anti-cryptic sectors in contrary of our previous work (Schmidt et al., 2009c) argued only on four latitude points. There is a significant higher mass condensed in the anti-cryptic region, probably due to snow event, as previously suggested Colaprete et al. (2005), and Giuranna et al. (2008).

Assuming a density of 920 kg m^{-3} (as determined by Smith et al., 2001), the estimated maximum height from the D-frost model reach 0.32 m (0.21 m for $t_{end}=t_{in}$, 0.40 m for $t_{end}=t_{out}$) in the cryptic region and 0.41 m (0.31 m for $t_{end}=t_{in}$, 0.46 m for $t_{end}=t_{out}$) in the anti-cryptic region (see Fig. 5). We compile the errors to estimate the height 0.31 ± 0.10 m for the cryptic region and 0.38 ± 0.08 m for the anti-cryptic region. In comparison, the direct MOLA height measurements are 0.37 ± 0.08 m for the cryptic region and 0.35 ± 0.08 m for the anti-cryptic region at Ls=150°. At first order, absolute results from both methods are

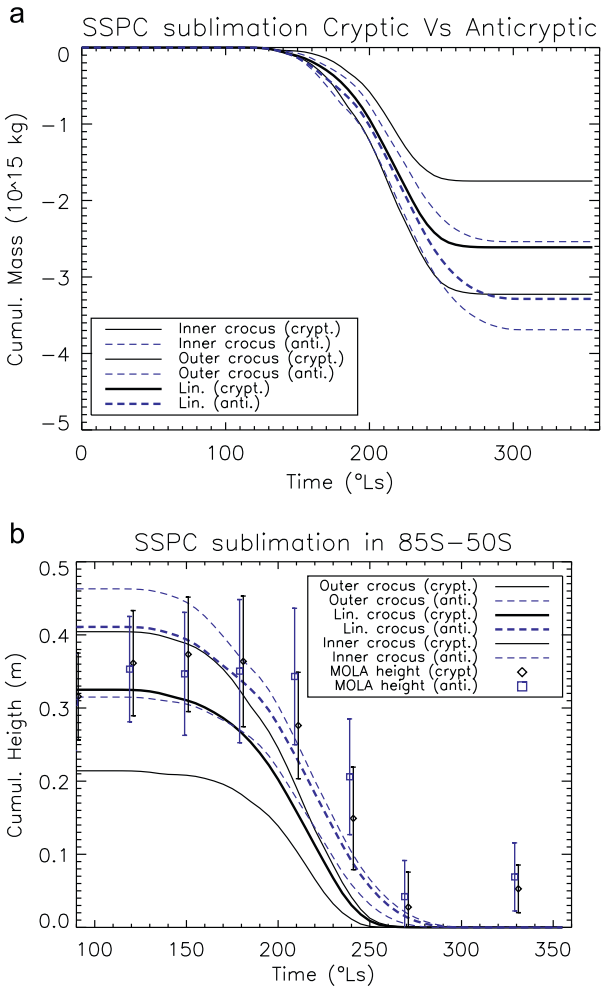


Fig. 5. Total sublimated CO_2 mass (a) and total sublimated mass CO_2 height (b) for both cryptic and anti-cryptic region (surface convention) assuming a density of 920 kg m^{-3} (as determined by Smith et al., 2001) compared to MOLA height change.

compatible with a difference below the error bar (see Fig. 5). The difference anti-cryptic/cryptic in the MOLA data is significant at Ls=210° and 240° in agreement with the D-frost model, when the mass ratio anti-cryptic/cryptic is the highest. At this time period, the MOLA height measurement is higher than the D-frost estimation probably due to a CO_2 bulk density lower than 920 kg m^{-3} as suggested by Aharonson et al. (2004), Giuranna et al. (2007b), Matsuo and Heki (2009).

During the first phase, the sublimation is nearly symmetric with a significant higher sublimation in the cryptic region for the time period Ls=180°–220° (see Figs. 6(a) and (b)). This corresponds to appearance of the low albedo cryptic region (Kieffer et al., 2000; Piqueux et al., 2003; Langevin et al., 2007) that absorbs and sublimates faster.

After Ls=220° the average anti-cryptic sector is subliming stronger with a maximum difference of 1.0×10^8 kg s^{-1} (see Figs. 6(a) and (b)) despite a maximum sublimation rate locally in the cryptic region. This is due to the fact that the effect of difference in surface cover is stronger than the effect of difference in albedo. At Ls=230, the ratio surface ratio is R_{surf}=*Surface anti-cryptic*/*Surface cryptic*=1.55 (see Fig. 3(a)) and the

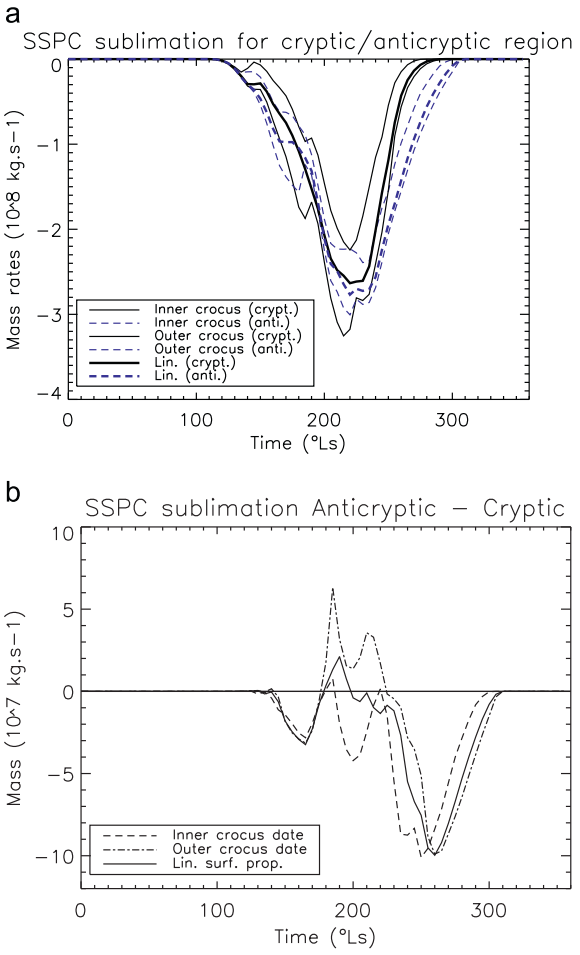


Fig. 6. Sublimated Mass and within the cryptic region and the anti-cryptic region. Note that the sublimated mass is a negative quantity so that when this difference is positive, the cryptic region is subliming faster than the anti-cryptic region (surface convention): (a) absolute sublimation rates, and (b) sublimation rates difference.

absorbance ratio is $R_{abs}=(1-Albedo\ \ anti\text{-}cryptic)/(1-Albedo\ cryptic)=0.71$ (see Fig. 3(b)). If we simplify Eq. (2) and only keep the direct sunlight term W^{in}_{sun}, the sublimation mass rates ratio can be estimated $R_{mass}=Mass\ anti\text{-}cryptic/Mass\ cryptic=R_{surf}\cdot R_{abs}=1.11$, in agreement with our results (see Figs. 6(a) and (b)). With this simple calculation, we demonstrate that after Ls=220° the anti-cryptic region is sublimating faster due to the fact that the SSPC recession is asymmetric, i.e.: the anti-cryptic region reaches the outer crocus line before the cryptic region.

Two phases are not balanced such that the total mass is different for both regions, with 20% more mass in the anti-cryptic region, arguing for more snow precipitation during winter time (Colaprete et al., 2005; Giuranna et al., 2008). If the resulting material in the anti-cryptic region, more concentrated in snow, has significant lower emissivity, it could also condensate slower. If this process occurs during the polar night, 20% is the minimum snow content. During winter time, "cold spots" has been observed since the 70's and been interpreted as clouds or fresh snow at the surface (Kieffer et al., 1977; Forget, 1998; Ivanov and Muhleman, 2001). Recent studies showed that the "cold spots" dynamic in thermal infrared range is as short as 5 Julian days (Cornwall and Titus, 2009; Cornwall and N, 2010) suggesting that metamorphism is very active and very fast on Mars. Thus the CO_2 emissivity is not likely to be lower than 0.9 during a significant period of time.

In conclusion, our estimates indicate that the sublimation flux is modulated by the local properties of the cryptic/anti-cryptic regions and in particular the crocus date. Schmidt et al. (2009c) conclusions are still valid: albedo is controlling the SSPC sublimation but once there is no CO_2 ice anymore it is obvious that the sublimation stops.

4. Ar dilution in the south polar vortex

Since SSPC is sublimating, the atmosphere is pumped up and rebalanced by mass transfer at global scale (Hourdin et al., 1995). This mass transfer lead also to a differential dilution of the minor non-condensable gas that acts like tracer of the phenomena. In addition to the sublimating SSPC, air mass coming from lower latitudes could enter the polar vortex and dilute the local air (Colaprete et al., 2008). Using a box modeling, we propose here to estimate the relevant quantity for this system: $\mathcal{F}$ the advection flux and compare it to Q the sublimation flux.

Modeling the geophysical system by boxes is a very convenient approach to understand the natural phenomena in a simple manner (Albarède, 2003). We propose to model the Martian atmosphere using 3 boxes: the south polar deposits (SSPC), the polar atmosphere and the Martian atmosphere as a whole (see Fig. 7).

4.1. CO_2 balance

We could write the mass balance of the polar atmosphere of CO_2 as

$$\frac{d\sigma_{pol}}{dt}=Q_{in}+\mathcal{F}_{in}-\mathcal{F}_{out} \tag{8}$$

with $\sigma_{pol}=M_{pol}/S_{pol}$ the mass of the polar atmosphere column by surface unit (in $kg\,m^{-2}$), the incoming flux from the sublimation $Q_{in}=dM$ estimated in the last section in atmosphere sign convention (in $kg\,m^{-2}\,s^{-1}$), $\mathcal{F}_{in}$ and $\mathcal{F}_{out}$ are, respectively, the incoming and outcoming advection fluxes (in $kg\,m^{-2}\,s^{-1}$).

We assume that the system is in steady state $d\sigma_{pol}/dt=0$ such that the incoming fluxes exactly compensate the outgoing flux: $Q_{in}+\mathcal{F}_{in}=\mathcal{F}_{out}$. In other terms, we suppose that the mass rebalance time of the atmosphere is much lower than the typical time of the non-condensable gas balance.

4.2. Non-condensable species balance

We could also write the mass balance of the minor non-condensable species, assuming that they are in homogeneous mixing within all boxes:

$$\sigma_{pol}\cdot\frac{dC_{pol}}{dt}=\mathcal{F}_{in}\cdot C_{mars}-\mathcal{F}_{out}\cdot C_{pol} \tag{9}$$

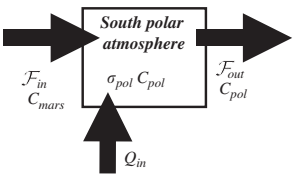


Fig. 7. Schema of the box modeling with $\mathcal{F}$ the advection flux, Q the sublimation flux, σ_{pol} the mass of the polar atmosphere column and C the mixing ratio of non- condensable gas, such Ar.

with C_{pol} and C_{mars}, the mixing ratio of the non-condensable gas in the polar region, respectively, in the whole Martian atmosphere. We solve this equation using the following numerical solution:

$$C_{pol}(t+\Delta t) = C_{pol}(t)\cdot\left(1-\frac{\mathcal{F}_{in}}{\sigma_{pol}}\cdot\Delta t-\frac{Q_{in}}{\sigma_{pol}}\cdot\Delta t\right)+C_{mars}\cdot\frac{\mathcal{F}_{in}}{\sigma_{pol}}\cdot\Delta t \qquad (10)$$

For the convenience, we use a time step $\Delta t = 1$ s.

Measurements of the Ar in the south polar atmosphere have been done by the GRS instrument (Sprague et al., 2004, 2007). During the time period of sublimation in the south polar region (Ls=110–350), we estimate the decrease of Ar using Eq. (10). We set the initial value of Ar abundance $C_{pol}(t=110^{\circ}\mathrm{Ls})=3.89\%$ as measured by GRS. We use the commonly used value of the Martian mixing ratio $C_{mars}=1.6\%$ in agreement with Viking Lander 2 measurements (Owen et al., 1977).

Minor species abundances evolution with time are plotted in Fig. 8, for different values of $\mathcal{F}_{in}$: 0, 4×10^{-6}, 8×10^{-6} and $20\times10^{-6}\,\mathrm{kg\,m^{-2}\,s^{-1}}$. The mixing ratio evolution decreases with time to reach a minimum around Ls=250 and then increases again. The first decrease is due to the sublimation of the seasonal frost, free of non-condensable gas. In addition, the advection flux dilutes Ar with a higher $\mathcal{F}_{in}$ leading to a faster dilution. The increase in second step is due to the injection of the Martian air, slightly enriched in Ar compared to the local polar air. The rate of increase is higher when $\mathcal{F}_{in}$ is faster.

By matching GRS data with our box model, we estimate that the flux $\mathcal{F}_{in}\simeq 4\times10^{-6}\,\mathrm{kg\,m^{-2}\,s^{-1}}$. This value has the same order of magnitude as the mean value of the sublimation flux $\langle Q_{in}\rangle = 6.7\times10^{-6}\,\mathrm{kg\,m^{-2}\,s^{-1}}$. This result suggests that the air mass entering the south polar vortex during the recession phase is of the same order than the sublimated mass. Thus the local difference in Q_{in} due to asymmetry should lead to non-negligible effect on the vortex dynamic, especially after Ls=220° (see Fig. 6).

Future studies using GCM or local climate model have to be conducted to study the actual dynamical effect of the asymmetry in sublimation. One particular attention should be drawn on the dilution factor regarding the dynamics in the cryptic vs anti-cryptic region. Some regional differences should be pointed out, as suggested by GRS (Sprague et al., 2007).

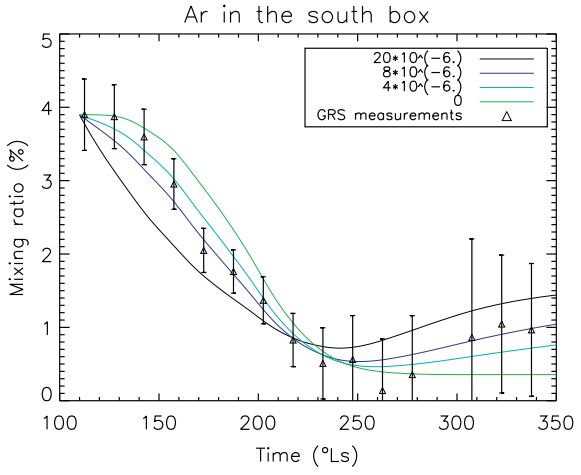


Fig. 8. Estimation of C_{pol} as a function of time in comparison with actual Ar measurements in the South Polar atmosphere. Lines represent the solution of our box modeling (Eq. (10)) for four cases: $\mathcal{F}_{in}=0$, 10^{-5}, 5×10^{-5} and 10^{-4} $\mathrm{kg\,m^{-2}\,s^{-1}}$. Triangles are Ar observations of the GRS instruments (Sprague et al., 2007) for the whole south polar region.

5. Conclusions

We estimate the CO_2 mass balance of the SSPC using the D-frost model and estimate the total sublimated mass to be around $(5.6\pm1.3)\times10^{15}$ kg which is compatible with gravity measurements (Karatekin et al., 2006), with measurements by gamma ray and neutron spectroscopy (Litvak et al., 2006; Kelly et al., 2006) and with previous GCM studies (Forget et al., 1999; Kelly et al., 2006). This agreement validates our current approach.

The effect of the Ar content, in the case of a well mixed atmosphere is below 1% on the total sublimated mass. A more realistic case of denser Ar enriched air in the bottom part of the atmosphere should be studied in the future.

We show that the SSPC is not symmetric in mass around the geographic pole, i.e.: the cryptic and anti-cryptic regions have an accumulated mass with a difference in order of $22\pm9\%$. in favour of the anti-cryptic region. Previous studies suggested that in addition to direct condensation, during the southern fall and winter seasons, snow precipitation is more intense in the anti-cryptic region than in the cryptic one (Colaprete and Toon, 2002; Giuranna et al., 2008). Our results show that, the actual mass deposited (possibly as snow) should be in order of 20%. This conclusion is still valid if the CO_2 emissivity has regional and/or temporal variations within the range 0.9–1 during the spring and summer, as observed by TES (Eluszkiewicz and Moncet, 2003) and supported by fast CO_2 metamorphism (Cornwall and N, 2010). The previous estimation on small regions of interests (ROI) by Kieffer et al. (2000) was $852\,\mathrm{kg\,m^{-1}}$ in the "cryptic" ROI and $841\,\mathrm{kg\,m^{-1}}$ in the "bright cap" ROI. The difference is probably due to the crocus date measurement that is delayed for OMEGA in comparison to TES. In case of subpixel mixing, due to the thermal emission dependence on the temperature at power four, bare soil is dominating in the thermal infrared. This effect is not present in near infrared domain and the mixing is really linear. Further studies should be done to precisely compare visible, near infrared and thermal infrared datasets.

From Ls=180°–220°, we point out that the cryptic region is sublimating slightly stronger than the anti-cryptic region. In the second phase, anti-cryptic region sublimation is dominating with a maximum difference in sublimation of $1.0\times10^{8}\,\mathrm{kg\,s^{-1}}$. This results is compatible with the MOLA height measurements difference that reach a maximum for Ls=210°–240°.

We use a simple box model to fit the GRS measurements of Ar and estimate that the atmosphere advection flux entering the south polar vortex is similar to the flux from the sublimating SSPC.

More precise studies on atmosphere dynamics and minor species concentration should be carried out with a GCM or a local scale climate model. At present time, SSPC albedo is a constant parameter in any GCM. Future studies should be done to include the SSPC asymmetry of albedo leading to an asymmetry of sublimation in order to simulate realistic dynamics and dilution factors. Those results will have to be compared to the atmospheric observations of pressure (for instance using the method proposed by Forget et al., 2007; Spiga et al., 2007) and minor species concentration (using gamma rays, i.e.: Sprague et al., 2004, optical measurements on the ground i.e: Encrenaz et al., 2005, or orbiters i.e.: Melchiorri et al., 2007).

In particular, future local climate studies should explain the actually asymmetric Ar enrichment (Sprague et al., 2004) that could play an indirect role in the stability of the SSPC itself. If the atmosphere is locally enriched in Ar, the partial pressure of CO_2 is lower and then CO_2 ice stability is lower (Forget et al., 2008).

Acknowledgments

This work has been supported by a contract with CNES through its 'Systeme Solaire' program. We thank the OMEGA and MOLA teams for data management. We also thank Mathieu Vincendon providing the SSPC reflectance map, under the aerosols. Finally, we are grateful to two anonymous reviewers for their helpful comments.

References

Aharonson, O., Zuber, M.T., Smith, D.E., Neumann, G.A., Feldman, W.C., Prettyman, T.H., 2004. Depth, distribution, and density of CO_2 deposition on Mars. Journal of Geophysical Research (Planets) 109 (5004–+).

Albarède, F., 2003. Geochemistry: An introduction. Cambridge University Press.

Bibring, J.-P., Soufflot, A., Berthé, M., Langevin, Y., Gondet, B., Drossart, P., Bouyé, M., Combes, M., Puget, P., Semery, A., Bellucci, G., Formisano, V., Moroz, V., Kottsov, V., Bonello, G., Erard, S., Forni, O., Gendrin, A., Manaud, N., Poulet, F., Poulleau, G., Encrenaz, T., Fouchet, T., Melchiori, R., Altieri, F., Ignatiev, N., Titov, D., Zasova, L., Coradini, A., Capacionni, F., Cerroni, P., Fonti, S., Mangold, N., Pinet, P., Schmitt, B., Sotin, C., Hauber, E., Hoffmann, H., Jaumann, R., Keller, U., Arvidson, R., Mustard, J., Forget, F., August 2004. OMEGA: Observatoire pour la Minéralogie, l'Eau, les Glaces et l'Activité. ESA SP-1240: Mars Express: the Scientific Payload, pp. 37–49.

Colaprete, A., Barnes, J.R., Haberle, R.M., Hollingsworth, J.L., Kieffer, H.H., Titus, T.N., 2005. Albedo of the south pole on Mars determined by topographic forcing of atmosphere dynamics. Nature 435, 184–188.

Colaprete, A., Barnes, J.R., Haberle, R.M., Montmessin, F., 2008. CO_2 clouds, cape and convection on mars: observations and general circulation modeling. Planetary and Space Science 56 (2), 150–180. URL ⟨http://www.sciencedirect.com/science/article/B6V6T-4PKXBT3-1/2/dfd675ef50bb83015599c6bd3c714ed6⟩.

Colaprete, A., Toon, O.B., 2002. Carbon dioxide snow storms during the polar night on Mars. Journal of Geophysical Research (Planets) 107, 1–5.

Cornwall, C., Titus, T.N., 2010. A comparison of Martain north and south polar cold spots and the long-term effects of the 2001 global dust storm. Journal of Geophysical Research, in press, doi:10.1029/2009JE003514.

Cornwall, C., Titus, T.N., 2009. Spatial and temporal distributions of Martian north polar cold spots before, during, and after the global dust storm of 2001. Journal of Geophysical Research (Planets) 114 (2003–+).

Eluszkiewicz, J., Moncet, J.-L., 2003. A coupled microphysical/radiative transfer model of albedo and emissivity of planetary surfaces covered by volatile ices. Icarus 166 (2), 375–384. URL ⟨http://www.sciencedirect.com/science/article/B6WGF-49V1DPH-3/2/12ed8d86bc224511b0d6f7ee29500ac6⟩.

Encrenaz, T., Bézard, B., Owen, T., Lebonnois, S., Lefèvre, F., Greathouse, T., Richter, M., Lacy, J., Atreya, S., Wong, A.S., Forget, F., 2005. Infrared imaging spectroscopy of Mars: H_2O mapping and determination of CO_2 isotopic ratios. Icarus 179, 43–54.

Forget, F., 1998. Mars CO_2 ice polar caps. In: Schmitt, B., de Bergh, C., Festou, M. (Eds.), Solar System Ices of Astrophysics and Space Science Library, vol. 227. Kluwer, pp. 477–507.

Forget, F., Hourdin, F., Fournier, R., Hourdin, C., Talagrand, O., Collins, M., Lewis, S.R., Read, P.L., Huot, J.-P., 1999. Improved general circulation models of the Martian atmosphere from the surface to above 80 km. Journal of Geophysical Research (Planets) 104, 24155–24176.

Forget, F., Hourdin, F., Talagrand, O., 1998. CO_2 snowfall on mars: simulation with a general circulation model. Icarus 131, 302–316.

Forget, F., Millour, E., Montabone, L., Lefevre, F., 2008. Non-condensable gas enrichment and depletion in the Martian polar regions. LPI Contributions 1447 (9106–+).

Forget, F., Spiga, A., Dolla, B., Vinatier, S., Melchiorri, R., Drossart, P., Gendrin, A., Bibring, J.-P., Langevin, Y., Gondet, B., 2007. Remote sensing of surface pressure on Mars with the Mars Express/OMEGA spectrometer: 1. Retrieval method. Journal of Geophysical Research (Planets) 112 (8–+).

Giuranna, M., Grassi, D., Formisano, V., Montabone, L., Forget, F., Zasova, L., 2008. Pfs/mex observations of the condensing CO_2 south polar cap of mars. Icarus 197 (2), 386–402. URL ⟨http://www.sciencedirect.com/science/article/B6WGF-4SPYKJM-1/2/61736d61880cf7c503ff493adcc83204⟩.

Giuranna, M., Formisano, V., Grassi, D., Maturilli, A., 2007a. Tracking the edge of the south seasonal polar cap of mars. Planetary and Space Science 55 (10), 1319–1327. URL ⟨http://www.sciencedirect.com/science/article/B6V6T-4MS9RGP-1/2/5e2cde3a3b8173badddefababaeaa1f0⟩.

Giuranna, M., Hansen, G., Formisano, V., Zasova, L., Maturilli, A., Grassi, D., Ignatiev, N., 2007b. Spatial variability, composition and thickness of the seasonal north polar cap of mars in mid-spring. Planetary and Space Science 55 (10), 1328–1345. URL ⟨http://www.sciencedirect.com/science/article/B6V6T-4ND0RT5-1/2/296230f162e6ab90e6d175919d2e324c⟩.

Haberle, R.M., Forget, F., Colaprete, A., Schaeffer, J., Boynton, W.V., Kelly, N.J., Chamberlain, M.A., 2008. The effect of ground ice on the Martian seasonal CO_2 cycle. Planetary and Space Science 56, 251–255.

Hapke, B., 1993. Theory of reflectance and emittance spectroscopy, Topics in Remote Sensing. Cambridge University Press, Cambridge, UK.

Hourdin, F., Forget, F., Talagrand, O., 1995. The sensitivity of the Martian surface pressure and atmospheric mass budget to various parameters: a comparison between numerical simulations and Viking observations. Journal of Geophysical Research (Planets) 100, 5501–5523.

Ivanov, A.B., Muhleman, D.O., 2001. Cloud reflection observations: results from the Mars orbiter laser altimeter. Icarus 154, 190–206.

Jian, J.-J., Ip, W.-H., 2009. Seasonal patterns of condensation and sublimation cycles in the cryptic and non-cryptic regions of the south pole. Advances in Space Research 43 (1), 138–142. URL ⟨http://www.sciencedirect.com/science/article/B6V3S-4SGD4WD-1/2/6db9a653ed786828772a3eb7a319b2d7⟩.

Karatekin, Ö., Van Hoolst, T., Dehant, V., 2006. Martian global-scale CO_2 exchange from time-variable gravity measurements. Journal of Geophysical Research (Planets) 111 (6003–+).

Kelly, N.J., Boynton, W.V., Kerry, K., Hamara, D., Janes, D., Reedy, R.C., Kim, K.J., Haberle, R.M., 2006. Seasonal polar carbon dioxide frost on Mars: CO_2 mass and columnar thickness distribution. Journal of Geophysical Research (Planets) 111 (3–+).

Kieffer, H.H., 2007. Cold jets in the Martian polar caps. Journal of Geophysical Research (Planets) 112 (8005–+).

Kieffer, H.H., Christensen, P.R., Titus, T.N., 2006. CO_2 jets formed by sublimation beneath translucent slab ice in mars' seasonal south polar ice cap. Nature 442 (7104), 793–796. URL ⟨http://dx.doi.org/10.1038/nature04945⟩.

Kieffer, H.H., Martin, T.Z., Peterfreund, A.R., Jakosky, B.M., Miner, E.D., Palluconi, F.D., 1977. Thermal and albedo mapping of Mars during the Viking primary mission. Journal of Geophysical Research (Planets) 82, 4249–4291.

Kieffer, H.H., Titus, T.N., Mullins, K.F., Christensen, P.R., 2000. Mars south polar spring and summer behavior observed by TES: seasonal cap evolution controlled by frost grain size. Journal of Geophysical Research (Planets) 105, 9653–9700.

Langevin, Y., Bibring, J.-P., Montmessin, F., Forget, F., Vincendon, M., Douté, S., Poulet, F., Gondet, B., 2007. Observations of the south seasonal cap of Mars during recession in 2004–2006 by the OMEGA visible/near-infrared imaging spectrometer on board Mars Express. Journal of Geophysical Research (Planets) 112 (8–+).

Langevin, Y., Douté, S., Vincendon, M., Poulet, F., Bibring, J.-P., Gondet, B., Schmitt, B., Forget, F., 2006. No signature of clear CO_2 ice from the 'cryptic' regions in mars' south seasonal polar cap. Nature 442 (7104), 790–792. URL ⟨http://dx.doi.org/10.1038/nature05012⟩.

Leighton, R.R., Murray, B.C., 1966. Behavior of carbon dioxide and other volatiles on Mars. Science 153, 136–144.

Lindner, B.L., 1993. The hemispherical asymmetry in the Martian polar caps. Journal of Geophysical Research (Planets) 98, 3339–3344.

Litvak, M.L., Mitrofanov, I.G., Kozyrev, A.S., Sanin, A.B., Tretyakov, V.I., Boynton, W.V., Kelly, N.J., Hamara, D., Saunders, R.S., 2007. Long-term observations of southern winters on Mars: estimations of column thickness, mass, and volume density of the seasonal CO_2 deposit from HEND/Odyssey data. Journal of Geophysical Research (Planets) 112 (3–+).

Litvak, M.L., Mitrofanov, I.G., Kozyrev, A.S., Sanin, A.B., Tretyakov, V.I., Boynton, W.V., Kelly, N.J., Hamara, D., Shinohara, C., Saunders, R.S., 2006. Comparison between polar regions of Mars from HEND/Odyssey data. Icarus 180, 23–37.

Matsuo, K., Heki, K., 2009. Seasonal and inter-annual changes of volume density of Martian CO_2 snow from time-variable elevation and gravity. Icarus 202 (1), 90–94. URL ⟨http://www.sciencedirect.com/science/article/B6WGF-4VS40BF-3/2/0b319f0d9c9fd76260beb2ea1164e0e8⟩.

Melchiorri, R., Encrenaz, T., Fouchet, T., Drossart, P., Lellouch, E., Gondet, B., Bibring, J.-P., Langevin, Y., Schmitt, B., Titov, D., Ignatiev, N., 2007. Water vapor mapping on Mars using omega/Mars express. Planetary and Space Science 55 (3), 333–342. URL ⟨http://www.sciencedirect.com/science/article/B6V6T-4KST3NG-5/2/408bf3ecd2f2bd46cccbc78575f37d45⟩.

Owen, T., Biemann, K., Biller, J.E., Lafleur, A.L., Rushneck, D.R., Howarth, D.W., 1977. The composition of the atmosphere at the surface of Mars. Journal of Geophysical Research (Planets) 82, 4635–4639.

Paige, D.A., Ingersoll, A.P., 1985. Annual heat balance of Martian polar caps—Viking observations. Science 228, 1160–1168.

Piqueux, S., Byrne, S., Richardson, M.I., 2003. Sublimation of Mars's southern seasonal CO_2 ice cap and the formation of spiders. Journal of Geophysical Research (Planets) 108, 5084–5093.

Pollack, J.B., Haberle, R.M., Schaeffer, J., Lee, H., 1990. Simulations of the general circulation of the Martian atmosphere. I—Polar processes. Journal of Geophysical Research (Planets) 95, 1447–1473.

Schmidt, F., Douté, S., Schmitt, B., 2007. Wavanglet: an efficient supervised classifier for hyperspectral images. IEEE Transactions on Geoscience and Remote Sensing 45 (5), 1374–1385.

Schmidt, F., Doute, S., Schmitt, B., Langevin, Y., Bibring, J.-P., the OMEGA Team, september 2009a. Slab ice in the seasonal south polar cap of Mars. In: European Planetary Science Congress (EuroPlanet), Potsdam, Germany, 13/09/09-18/09/09. vol. 4. EuroPlanet, ⟨http://www.europlanet-eu.org⟩, p. (electronic medium).

Schmidt, F., Douté, S., Schmitt, B., the OMEGA Team., 2009b. Physical state of CO_2 ice in the seasonal south polar cap. Icarus (in preparation).

Schmidt, F., Douté, S., Schmitt, B., Vincendon, M., Bibring, J.-P., Langevin, Y., 2009c. Albedo control of seasonal south polar cap recession on Mars. Icarus 200 (2), 374–394. URL ⟨http://www.sciencedirect.com/science/article/B6WGF-4V76270-1/2/60231d55061d19abebb5344bd9e40e2b⟩.

Schmidt, F., Schmitt, B., Douté, S., Forget, F., Langevin, Y., Bibring, J., 2008. Omega Team, 2008. Asymmetric release of CO_2 during southern spring. LPI Contributions 1447 (9003–+).

Schorghofer, N., Edgett, K.S., 2006. Seasonal surface frost at low latitudes on Mars. Icarus 180, 321–334.

Smith, D.E., Zuber, M.T., Neumann, G.A., 2001. Seasonal variations of snow depth on Mars. Science 294, 2141–2146.

Spiga, A., Forget, F., Dolla, B., Vinatier, S., Melchiorri, R., Drossart, P., Gendrin, A., Bibring, J.-P., Langevin, Y., Gondet, B., 2007. Remote sensing of surface pressure on Mars with the Mars Express/OMEGA spectrometer: 2. Meteorological maps. Journal of Geophysical Research (Planets) 112 (8–+).

Sprague, A.L., Boynton, W.i.V., Kerry, K.E., Janes, D.M., Kelly, N.J., Crombie, M.K., Nelli, S.M., Murphy, J.R., Reedy, R.C., Metzger, A.E., 2007. Mars atmospheric argon: tracer for understanding Martian atmospheric circulation and dynamics. Journal of Geophysical Research (Planets) 112 (15–+).

Sprague, A.L., Boynton, W.V., Kerry, K.E., Janes, D.M., Hunten, D.M., Kim, K.J., Reedy, R.C., Metzger, A.E., 2004. Mars' south polar Ar enhancement: a tracer for south polar seasonal meridional mixing. Science 306, 1364–1367.

Titus, T.N., Calvin, W.M., Kieffer, H.H., Langevin, Y., Prettyman, T.H., July 2008. Martian polar processes. pp. 578–+, (Chapter 25).

Vincendon, M., Langevin, Y., Poulet, F., Bibring, J.-P., Gondet, B., Jouglet, D., 2008. Dust aerosols above the south polar cap of mars as seen by omega. Icarus 196 (2), 488–505. URL 〈http://www.sciencedirect.com/science/article/B6WGF-4RV17PY-2/1/781d47cebdea184a353f89f9a98b3e35〉.

Warren, S.G., Wiscombe, W.J., Firestone, J.F., 1990. Spectral albedo and emissivity of CO_2 in Martian polar caps—model results. Journal of Geophysical Research (Planets) 95, 14717–14741.

Wood, S.E., Paige, D.A., 1992. Modeling the Martian seasonal CO_2 cycle 1. Fitting the viking lander pressure curves. Icarus 99 (1), 1–14. URL 〈http://www.sciencedirect.com/science/article/B6WGF-470F41G-7D/2/96bed1f6e592f4e45ce3720b8b0ecfd0〉.

4.4.3 Glace d'eau sur la dune de Richardson

Cette section contient l'article suivant :

Kereszturi A., Vincendon M., Schmidt F., "Water ice in the dark dune spots of Richardson crater on Mars", Planetary and Space Science, 2011, 59, 26-42

Planetary and Space Science 59 (2011) 26–42

Contents lists available at ScienceDirect

Planetary and Space Science

journal homepage: www.elsevier.com/locate/pss

Water ice in the dark dune spots of Richardson crater on Mars

A. Kereszturi [a,*], M. Vincendon [b], F. Schmidt [c]

[a] Collegium Budapest, Institute for Advanced Study, Szentháromsag u. 2, H-1014 Budapest, Hungary
[b] Department of Geological Sciences, Brown University, Providence, RI, USA
[c] IDES, Université Paris-Sud 11, CNRS/INSU, Bâtiment 509, Université Paris-Sud, 91405 Orsay, France

ARTICLE INFO

Article history:
Received 6 May 2010
Received in revised form
25 October 2010
Accepted 25 October 2010
Available online 3 November 2010

Keywords:
Mars
Polar
Ices
Dunes
Water

ABSTRACT

Interfacial liquid water has been hypothesized to form during the seasonal evolution of the dark dune spots observed in the high latitudes of Mars. In this study we assess the presence, nature and properties of ices – in particular water ice – that occur within these spots using HIRISE and CRISM observations, as well as the LMD Global Climate Model. Our studies focus on Richardson crater (72°S, 179°E) and cover southern spring and summer (L_S=175–341°). Three units have been identified of these spots: dark core, gray ring and bright halo. Each unit show characteristic changes as the season progress. In winter, the whole area is covered by CO_2 ice with H_2O ice contamination. Dark spots form during late winter and early spring. During spring, the dark spots are located in a 10 cm thick depression compared to the surrounding bright ice-rich layer. They are spectrally characterized by weak CO_2 ice signatures that probably result from spatial mixing of CO_2 ice-rich and ice-free regions within pixels, and from mixing of surface signatures due to aerosols scattering. The bright halo shaped by winds shows stronger CO_2 absorptions than the average ice-covered terrain, which is consistent with a formation process involving CO_2 re-condensation. According to spectral, morphological and modeling considerations, the gray ring is composed of a thin layer of a few tens of μm of water ice. Two sources/processes could participate to the enrichment of water ice in the gray ring unit: (i) water ice condensation at the surface in early fall (prior to the condensation of a CO_2-rich winter layer) or during wintertime (due to cold trapping of the CO_2 layer) and (ii) ejection of dust grains surrounded by water ice by the geyser activity responsible for the dark spot. In any case, water ice remains longer in the gray ring unit after the complete sublimation of the CO_2. Finally, we also looked for liquid water in the near-IR CRISM spectra using linear unmixing modeling but found no conclusive evidence for it.

© 2010 Elsevier Ltd. All rights reserved.

1. Introduction

The aim of this work is to study the presence, origins and properties of water ice in the dark spots observed at the surface of the polar regions of Mars during local spring. These spots can give rise to flow-like features (Horváth et al., 2001, 2009). Assessing the presence and properties of water ice there is an important step while studying the possible contribution of liquid water to the formation of these features. The polar regions of Mars undergo a strong and rapid warming during spring (Kieffer and Titus, 2001). Local dark, sunlight absorbing environments such as the dark spots could be favorable environments for the formation of ephemeral liquid water on Mars if water ice is present at those locations during spring. It is already known that water ice is present at the kilometer scale in the seasonal and perennial ice caps of both hemispheres (Kieffer et al., 1976; Titus et al., 2003; Bibring et al., 2004). In the northern hemisphere, a water-ice ring follows the receding edge of the shrinking CO_2 ice cap (Kieffer and Titus, 2001; Bibring et al., 2005; Schmitt et al., 2005, 2006), partly because it appears from below the sublimated carbon-dioxide seasonal cap and partly because it recondenses onto the perimeter of the remaining cold carbon-dioxide ice (Wagstaff et al., 2008). On the contrary, no similar water ice annulus was observed in the southern hemisphere: water ice there consist of smaller water ice patches (Titus, 2003, 2005, 2008; Bibring et al., 2004; Langevin et al., 2006), which appear at the perimeter of the receding carbon-dioxide cap, some of which remaining tens of kilometers away from the bright permanent CO_2 cap in summertime (Bibring et al., 2004). The high resolution imaging and spectroscopic dataset released by recent missions to Mars widen our ability to detect and study water ice in small, meter scaled environments such as the dark spots.

These dark dune spots, which we abbreviate as DDS (Horváth et al., 2001; Ganti et al., 2003; Pocs et al., 2003), are part of the great number of strange seasonal features that appear during local spring in the polar regions of Mars, such as spiders (Kieffer, 2000; Kieffer et al., 2000;

Abbreviations: CRISM, Compact Reconnaissance Imaging Spectrometer for Mars; DDS, dark dune spot; FCLS, fully constraint least square; HiRISE, High Resolution Imaging Science Experiment; L_S, solar longitude; rms, root-mean-square; LPG, Laboratoire de Planétologie de Grenoble; FCLS, fully constrained least square

* Corresponding author. Tel.: +36 06 30 3437 876; fax: +36 1 240 7708.
E-mail addresses: akos@colbud.hu, kru@mcse.hu (A. Kereszturi).

0032-0633/$ - see front matter © 2010 Elsevier Ltd. All rights reserved.
doi:10.1016/j.pss.2010.10.015

Ness and Orme, 2002; Piqueux et al., 2003; Christensen et al., 2005), dark spots (Malin et al., 1998; Malin and Edgett, 2001; Bridges et al., 2001; Zuber, 2003), flow-like features (Kieffer, 2003), Dalmatian spots (Kossacki and Kopystynski, 2004). Many of them could be the result of CO_2 gas outburst, but possibly other processes may also contribute like mass wasting (Hansen et al., 2010) or even flow of some liquid material (Möhlmann and Kereszturi, 2010). These phenomena potentially affect the CO_2 sublimation and may influence the climate at regional scale (Schmidt et al., 2009, 2010). We will present new observational evidence related to one of those phenomena, the dark dune spots, to further test and constrain the different proposed scenarios of formation for those features.

Recent observations and theoretical computations have suggested that ephemeral liquid water or brines could be present on Mars. Based on theoretical calculations, above around 180 K thin interfacial water layer (Mohlmann, 2004) and possible solid-state greenhouse warming may produce bulk brines (Mohlmann, 2010). At the polar landing site of Phoenix, not only solid ice was observed, but also spherical droplet-like features, slowly changing with time on the leg of the lander, that may be composed of dense salty solutions (Rennó et al., 2009a, b). Ephemeral flow-like features emanate from dark dune spots (DDSs) that could be formed by flowing brines or thin water layer lubricated grains have been recently studied in the northern and southern polar regions (Kereszturi et al., 2010a; Reiss et al., 2010)—although other interpretations, like dry mass wasting and avalanches could also be possible (Hansen et al., 2010). These flow-like features based on their appearance, dark color, and elevated temperatures are good candidates for the formation of liquid water.

Here we analyze dark spot-like features on the wintertime formed frost layer, which are called DDSs and which can give rise to flow-like features (Horváth et al., 2001, 2009), located in Richardson crater (72°S, 179°E). We study these features using CRISM (Compact Reconnaissance Imaging Spectrometer for Mars) and HiRISE data to argue whether water – ice or liquid – is present in some part of these spots. CO_2 ice, that form in the polar regions and may cold trap H_2O molecules and enhances their concentration, will also be studied in details. The high imaging performances of HiRISE (High Resolution Imaging Science Experiment, maximal spatial resolution 30 cm) are combined with the water detection capabilities of the near-IR CRISM experiment. Observational constraints about the nature and distribution of ice are compared to climate modeling predictions. A scenario is then proposed to explain the origin and evolution of water ice in this region.

2. Methods

This section contains the background information about the data acquired by the CRISM and HiRISE cameras onboard Mars Reconnaissance Orbiter, as well as a description of the modeling methods used to interpret them.

2.1. Observations

We analyzed CRISM spectral data (Murchie et al., 2007), with CAT-ENVI software (Morgan et al., 2009) in Richardson crater (72°S 179°E) using CRISM "FRT" observations, characterized by a high spatial and spectral resolution (18 m and 7 nm, respectively). Near-IR wavelengths that range between 1 and 4 μm were considered, and observations were corrected for photometry and atmospheric gas absorptions McGuire et al., 2009). A filtering method (Parente, 2008) is used to reduce noise. The interpretation of spectra measured by push-broom sensors may be influenced by the effect called "spectral smile": the mean wavelength of spectels and the spectral resolution can slightly change from one spatial pixel to the next (Ceamanos and Douté, 2009). We do not correct for the spectral smile because we take spectra near the center of the CRISM image where band shifts are lower than 0.002 μm (Murchie et al., 2007), which has a minor impact on large absorption bands. The list of CRISM observations analyzed in this study is indicated in Table 1.

The CRISM spectral data were complemented by the analysis of the higher spatial resolution HiRISE images. We selected the highest resolution images acquired under proper illumination conditions to study the thickness of surface features using shadows (see Table 2). We estimated absolute albedo values from HiRISE images, using the DN values of certain pixels from the RED channel images. We calculated the reflectivity with the formula $I/F=(\mathrm{DN}\times \mathrm{SCALING_FACTOR})+\mathrm{OFFSET}$, and divided it with $\cos i$, which gives an approach of lambertian albedo.

The study of the spatial and temporal distribution of H_2O and CO_2 ice is performed using band depth values, representing the absorption efficiency at certain wavelength region, characteristic

Table 1
CRISM images of Richardson crater analyzed in this paper.

CRISM image no.	L_S (deg.)	Date	Presence of CO_2 ice	Presence of H_2O ice
HRS0000411F _07_IF172L	175.5	2007.01.30	Yes	Yes
HRL000043A2_07_IF188L	181.67	2007.02.10	Yes	Yes
FRT000052BC_07_IF163L	213.61	2007.04.05	Yes	Yes
FRT000054E5_07_IF163L	217.5	2007.04.12	Yes	Yes
HRS000056C0_07_IF172L	220.96	2007.04.17	Yes	Yes
FRT00005AF7_07_IF163L	238.52	2007.05.15	Yes	Yes
FRT00005C94_07_IF163L	241.68	2007.05.20	Yes	Yes
FRT00005E38_07_IF163L	245.49	2007.05.26	Yes	Yes
FRT00005FF6_07_IF163L	248.72	2007.05.31	Yes	Yes
FRT00006102_07_IF165L	251.14	2007.06.04	Yes	Yes
FRT00006199_07_IF164L	252.41	2007.06.06	Yes	Yes
FRT0000630D_07_IF163L	255.58	2007.06.11	Uncertain	Yes
FRT000063FD_07_IF164L	258.12	2007.06.15	Uncertain	Yes
FRT00006516_07_IF163L	262.55	2007.06.22	No	No
FRT000066D0_07_IF163L	266.35	2007.06.28	No	No
FRT00006C56_07_IF163L	283.23	2007.07.25	No	No
FRT0000725F_07_iIF163L	296.86	2007.08.16	No	No
FRT000073b2_07_IF163L	299.67	2007.08.21	No	No
FRT00007a6a_07_IF163L	312.97	2007.09.13	No	No
FRT0000824E_07_IF163L	329.13	2007.10.11	No	No
FRT000085BD_07_IF163L	335.05	2007.10.22	No	No
FRT00008914_07_IF163L	340.51	2007.11.01	No	No

Table 2
HiRISE images of Richardson crater analyzed in this paper.

HiRISE image no.	L_S (deg.)	Date
PSP_002397_1080	172.5	2007.01.30
PSP_002542_1080	181.5	2007.02.10
PSP_002885_1080	197	2007.03.09
PSP_003175_1080	210.6	2007.03.31
PSP_003386_1080	220.7	2007.04.17
PSP_003597_1080	230.9	2007.05.07
PSP_003742_1080	238.1	2007.05.15
PSP_003808_1080	241.3	2007.05.20
PSP_003953_1080	248.5	2007.05.31

for certain molecules and minerals. The following parameters were used to analyze ices: "BD1500" (1.5 μm H_2O ice band depth), "BD 1435" (1.435 μm CO_2 ice band depth), and "ICER1" (CO_2 and H_2O ice band depth ratio) defined by Pelkey et al. (2007) (for detailed description of the calculation formulae see for the reference) on the basis of the parameters developed by Langevin et al. (2007). Very thin, micrometer thick layers of H_2O ice can be detected in near-IR spectra (Schmitt et al., 1998), for instance using the characteristic absorption feature at 1.5 μm (Bibring et al., 2004). The depth of this feature is measured by the "BD1500" spectral criteria.

2.2. Spectral unmixing modeling

The shape of the 1.5 μm band of H_2O ice is significantly controlled by temperature (Grundy and Schmitt, 1998) and grain size (Douté and Schmitt, 1998). Also, liquid water is spectrally distinct from water ice, with an absorption band at 1.5 μm shifted by 0.05 μm toward shorter wavelengths (Fig. 11). Other ubiquitous hydrated chemical species on Mars, such as sulfates, also have a band around 1.5 μm (Langevin et al., 2005; Bibring et al., 2006; Fishbaugh et al., 2007; Massé et al., 2010). The possible presence of water ice with different grain size, liquid water and gypsum are therefore considered while conducting the spectral analysis.

We applied a strategy of sparse linear unmixing using the Fully Constraint Least Square (FCLS) suitable to unmix spectral mixture in the case of an overcomplete reference database (Heinz and I-Chang, 2001). Each observed spectra Y_k (k is the index of wavelength) is decomposed into a weighted sum of all reference spectra S_{jk} (j is the index of the reference spectra, $j=1$ for CO_2, $j=2$ for H_2O at 1 μm grain size, etc.). The weight, or abundances, A_j are assumed to be *summed to one* – because the sum of surface proportion is one – and *sparse* – with a distribution of zeros and only few non-zeros values.

$$Y_k = SA_jS_{jk} \quad (1)$$

It means that if a spectrum is present in the database S but not present in the observed spectra Y, the method indicates zero abundance. This property is especially suitable for our case because we do not expect all grain size of water ice, liquid water and gypsum (see Section 3.5) appearing at the same time. Due to the sum-to-one constraint, we add a flat bright and a flat dark spectrum that can model at first order aerosol contribution and dust contamination at the surface, respectively. Abundances can be interpreted as surface proportion inside the pixel, if no non-linear mixing occurs. In a more likely case, intimate non-linear mixing should occur, leading to a significant shift between absolute abundances and actually estimated abundances with FCLS. Nevertheless, we will interpret the abundances A as "spectral abundances". Such methodology is valuable to interpret global tendencies and for detection, but not for precise quantification.

2.3. Climate modeling

Observations of water and CO_2 ice at Richardson crater are compared with the predictions of the Global Circulation Model developed at the *Laboratoire de Météorologie Dynamique de Jussieu*. This model is able to predict the water cycle of Mars and has been validated against available datasets (Forget et al., 1999, 2008; Montmessin et al., 2004). The model computes the seasonal meteorology, notably the variations in water vapor and water ice precipitations, with a spatial sampling of $5^\circ \times 5^\circ$ and a time step of half an hour. It is combined with a local energy balance code to predict the formation of ices on a given localized site with specific properties (Vincendon et al., 2010, in press).

3. Results

We first classify the observed features in Section 3.1 using HIRISE images. Then, we analyze the spatial and temporal change in the properties of ice on the basis of their spectral properties as reveled by CRISM band ratio in Section 3.2. In Section 3.3 we discuss how we assess the surface versus atmospheric origin of H_2O spectral signatures. HiRISE and CRISM data are correlated in Section 3.4. The results of the unmixing algorithm are discussed in Section 3.5. Modeling prediction of ice condensation based on climatologic and thermophysic considerations can be found in Section 3.6. Finally, we discuss the possible scenarios for the origin of the observed features in Section 3.7.

3.1. Classification of observed albedo features

There is a great number of various seasonal low albedo features on Mars in the polar region, including different dark spots (Malin et al., 1998; Malin and Edgett, 2000; Zuber, 2003; Kieffer et al., 2006; Kossacki et al., 2006), spider-like structures (Kieffer, 2000; Ness and Orme, 2002; Piqueux et al., 2003; Christensen et al., 2005) Dalmatian spots (Kossacki and Kopystynski, 2004), and dark dune spots (DDSs) (Horváth et al., 2001; Ganti et al., 2003; Pocs et al., 2003). Here we analyze only one group, called dark dune spots, and among them only the larger ones, which different sub-units could be resolved on CRISM images. There are various subsections of these spots, analyzed recently (Kereszturi et al., 2009, 2010) based on HiRISE images. Here we use the following classification:

- Dark features on the seasonal frost cover, with two groups (Fig. 1): (1) large spots (larger than about 20–40 m) are present only between the ridges of the dunes on horizontal surfaces, and (2) smaller spots, which are present on the dune ridges and between them also, and on the slopes where flow-like features emanate from them (Horváth et al., 2009; Kereszturi et al., 2010).
- Here we analyzed only the large spots, large enough (i.e. > 60 m) to identify the following different sub-units of them from CRISM data:
  - *Dark core*: A roughly isometric and darkest area in the center, with albedo between 0.15 and 0.26 when the feature was evident before $L_S=250^\circ$. After this date the features diminished and the terrain becomes homogeneous.
  - *Gray ring*: A wide ring-like feature that surrounds the core, its albedo is intermediate between the dark core and the undisturbed frost cover, with albedo values between 0.25 and 0.30.
  - *Bright halo (white collar)*: A region surrounding the spots brighter than the undisturbed average ice with albedo values between 0.37 and 0.24, somewhere elongated in downwind direction, possibly formed by refreezing process.

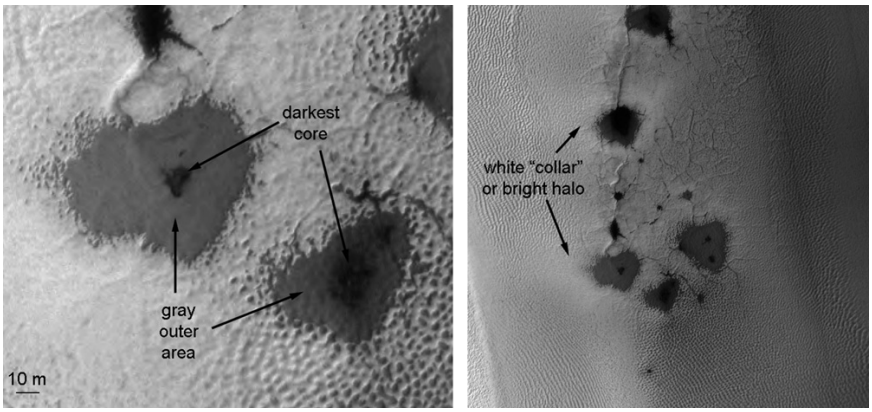


Fig. 1. The analyzed unit types of the spots in Richardson crater on the HiRISE image # PSP_003175_1080. Dark cores and gray outer rings are visible in the left subset, while elongated and probably wind-blown bright halos are present in the right subset.

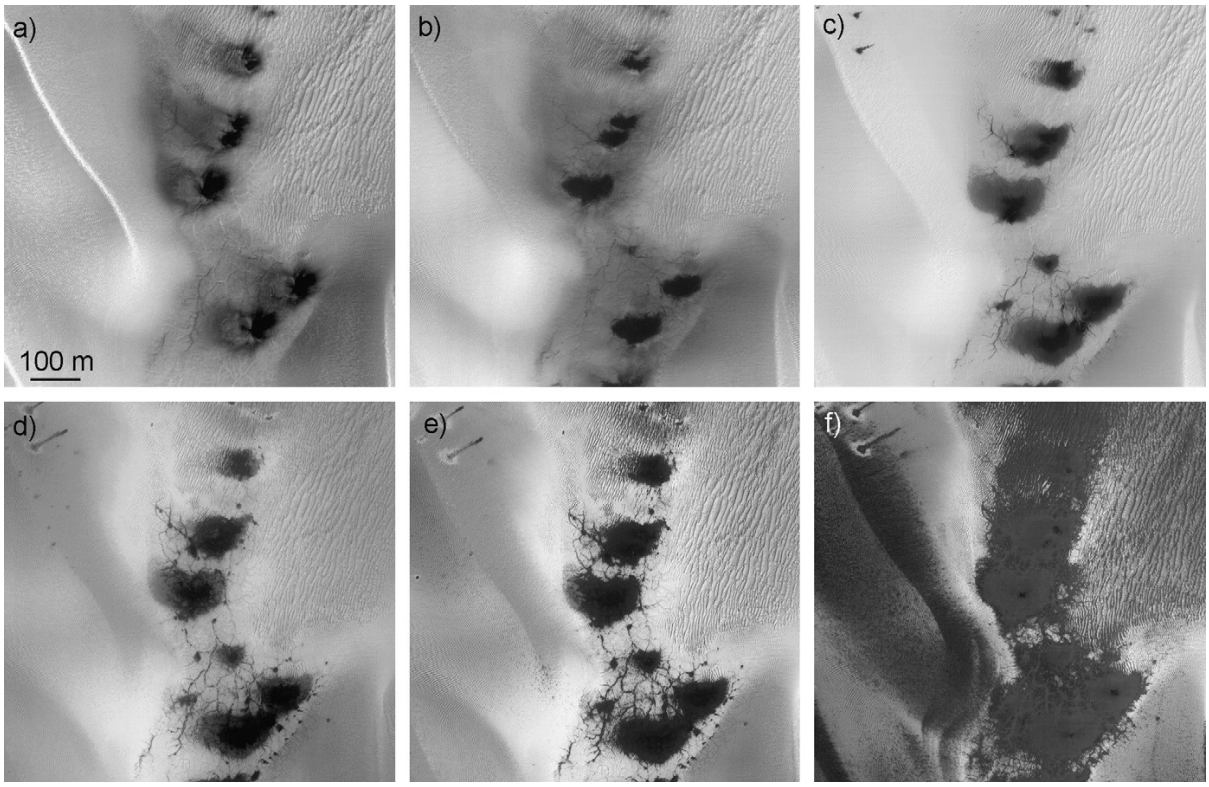


Fig. 2. Sequence of HiRISE images showing the temporal change of the same terrain with dark dune spots in Richardson crater. At the earliest phase (a, b) only dark cores are present and wind-blown dark streaks emanate from them toward the left, later the continuous gray ring forms around the dark cores (c, d), even later dark cores are expanding and gray rings contracting (d, e), finally only albedo differences are visible (f) but no ice is present based on CRISM data (image number and solar longitude values are: (a) PSP_002186_1080 (L_S=166.2°), (b) PSP_002397_1080 (L_S=172.5°), (c) PSP_002885_1080 (L_S=197.0°), (d) PSP_003597_1080 (L_S=230.9°), (e) PSP_003742_1080 (L_S=238.1°), (f) PSP_003953_1080 (L_S=248.1°)).

- The *undisturbed ice* terrain surrounding far away the spots was also analyzed for control measurement.

These features show characteristic changes: first the dark core appears with dark wind-blown features emanating from it; later gray rings develop, then bright halos appear and finally the whole terrain defrosts (Fig. 2).

3.2. Distribution and properties of ices from spectral analysis

Three typical spectral CRISM observations of the 4 units (dark core, gray ring, bright halo, and undisturbed ice) acquired during early to mid-spring are analyzed in Fig. 3. At that time near-IR H_2O ice signatures are observed at every location, even in the darkest cores, while based on the optical images no substantial surface ice

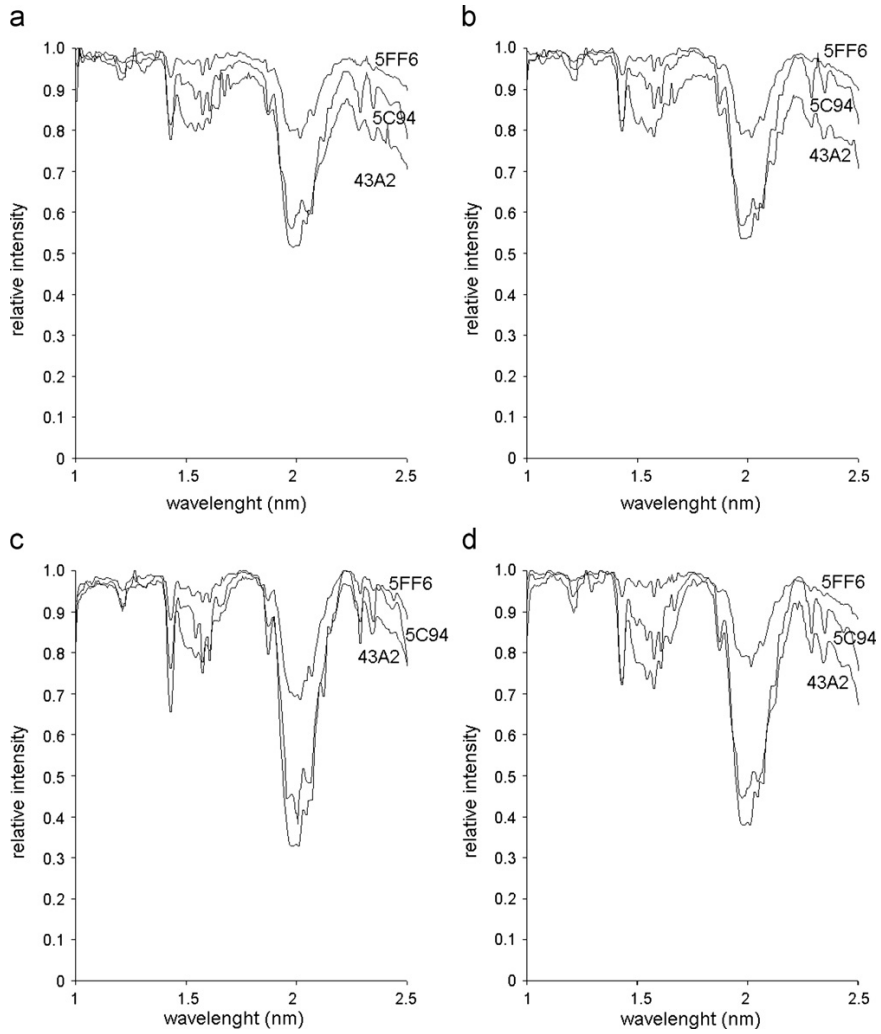


Fig. 3. Spectral shapes for three different periods (on images: 43a2, 5C94, 5FF6 at L_S=181.7°, 242.7°, 248.7°, marked with black, gray and light gray color, respectively) for the analyzed surface units (dark center, gray ring, bright halo, undisturbed ice), normalized to the continuum, between 1.0 and 2.6 μm. Carbon-dioxide and water ice signatures are present with decreasing band depth as the season progresses.

is present. Very small quantity of water ice (a few μm thick) could produce observable signatures in the spectra without visible effect in optical images, and thin water ice clouds may also contribute to the observed signature. Moreover, dust contamination within the ice (e.g., if ice as condensed on a dust nuclei) can significantly reduce the albedo of ice, making it barely detectable in the optical while clearly seen in the near-IR (Kieffer, 1990; Vincendon et al., 2007). CO_2 ice, detected on the basis of the 1.43 μm band depth, is also present everywhere at that time. It has been shown by Langevin et al. (2008) that aerosols scattering is responsible for a mixing of surface spectral properties when remotely observed, which could contribute to some of the signatures observed in this region characterized by high spatial variations of surface properties at the 10–100 s meters scale. This effect, often neglected, can however have a major impact on observations as surfaces surrounding a km size observed target could contribute to several 10 s of % of the observed signal (Langevin et al., 2008).

The spatial distribution of H_2O and CO_2 ices is outlined in Fig. 4. This figure contains small insets of HiRISE PSP_00307_1080 (1 column) and CRISM image FRT000052BC_07_IF163L (2–4 columns). Different rows are for different locations inside Richardson crater. The distribution of the water ice band depth (BD1500) in the second column shows that water ice is located in the gray outer ring area of spots. The CO_2 ice distribution is represented in the fourth column, showing that the darks spots are nearly CO_2 ice free, while the third column shows the areal distribution of the H_2O/CO_2 ice ratio (inverted ICER1 channel), which highlights that the outer gray ring is water ice rich. The ice ratio is a bit lower in the dark central core than in the ring, but here based on the optical images very small amount of ice could be present and the atmospheric dust scatter may have a strong impact in the spectra. Assessing changes in the composition of the ice mixtures from spectral analysis required the use of surface radiative transfer model (see e.g. Douté and Schmitt, 1998; Shkuratov et al., 1999; Hapke, 2008 and reference herein), observing change in the ice band depth provides a first order idea of change occurring on the ground, keeping in mind that such changes can be due to several factors including grain size, photometry, and mixture type. CO_2 ice is nearly always present together with H_2O ice, suggesting they could be mixed. But their ratio is changing, and

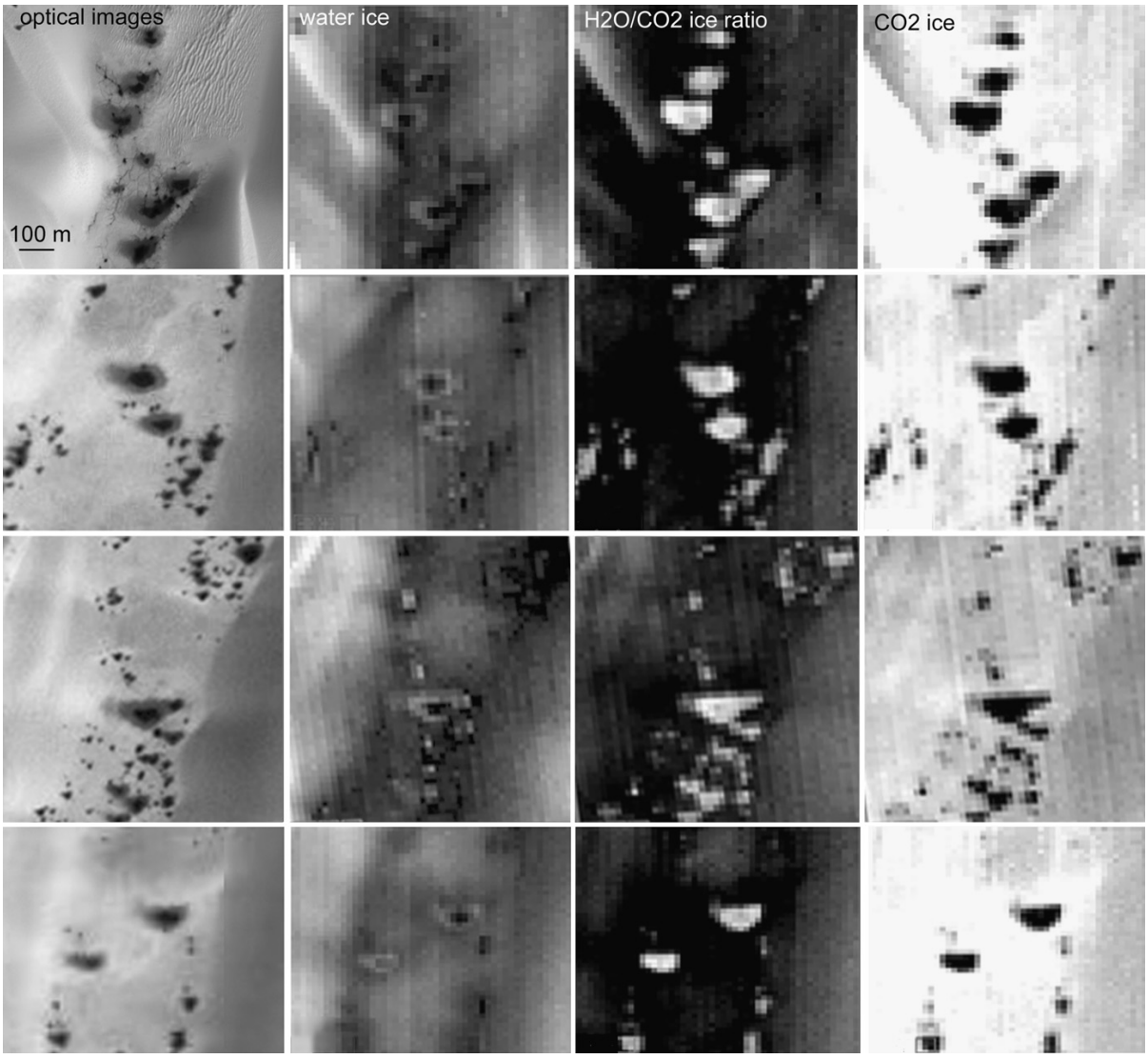


Fig. 4. Comparison of the distribution of water and CO_2 ice. The different rows show different locations in Richardson crater, and different columns are for: optical images (PSP_00307_1080 Column #1), water ice band depth image (BD1500 Column #2), image representing the ratio of H_2O/CO_2 ice (inverted ICER1 band Column #3), and CO_2 ice band depth images (BD1430 Column #4). The bright water ice rings in column #2 suggest surface H_2O ice is present in the gray ring unit.

could be correlated to the change in the appearance on visible images. CO_2 ice signatures are deeper in the bright halo and the undisturbed average icy surface, than in the darkest cores and the gray rings. The bright outer halo has the deepest CO_2 signatures compared to the average surface. The gray ring unit is relatively H_2O rich and CO_2 poor, comparing their ratio to other unit types.

We highlight in Fig. 5 the typical band depth change observed with time:

Changes of H_2O ice based on BD1500 values:

- The different surface units show the same trend during $L_S=170^\circ$ and 225°, except for the gray ring area.
- In the gray ring area the band depth increases from $L_S=180^\circ$ until 220°, which is not observed for the other surface types, where nearly constant values are present.
- The water ice band depth is significantly lower for the dark core and bright halo in comparison to undisturbed terrain.
- After $L_S=225^\circ$ there is a general decrease of the water ice band depth in all units which become spectrally similar.
- Water ice is confidently detected above the noise limit ($\sim$2%) until about $L_S=250^\circ$.

Changes of CO_2 ice based on BD1500 values:

- The depth of BD1430 increases from $L_S=170^\circ$ until 225°, and then decreases.
- The bright halo feature shows stronger CO_2 ice signal than the other features, suggesting some re-condensation happened there after $L_S=210^\circ$ (Titus et al., 2007).
- The CO_2 ice band depth is significantly lower for the dark core in comparison to undisturbed terrain.

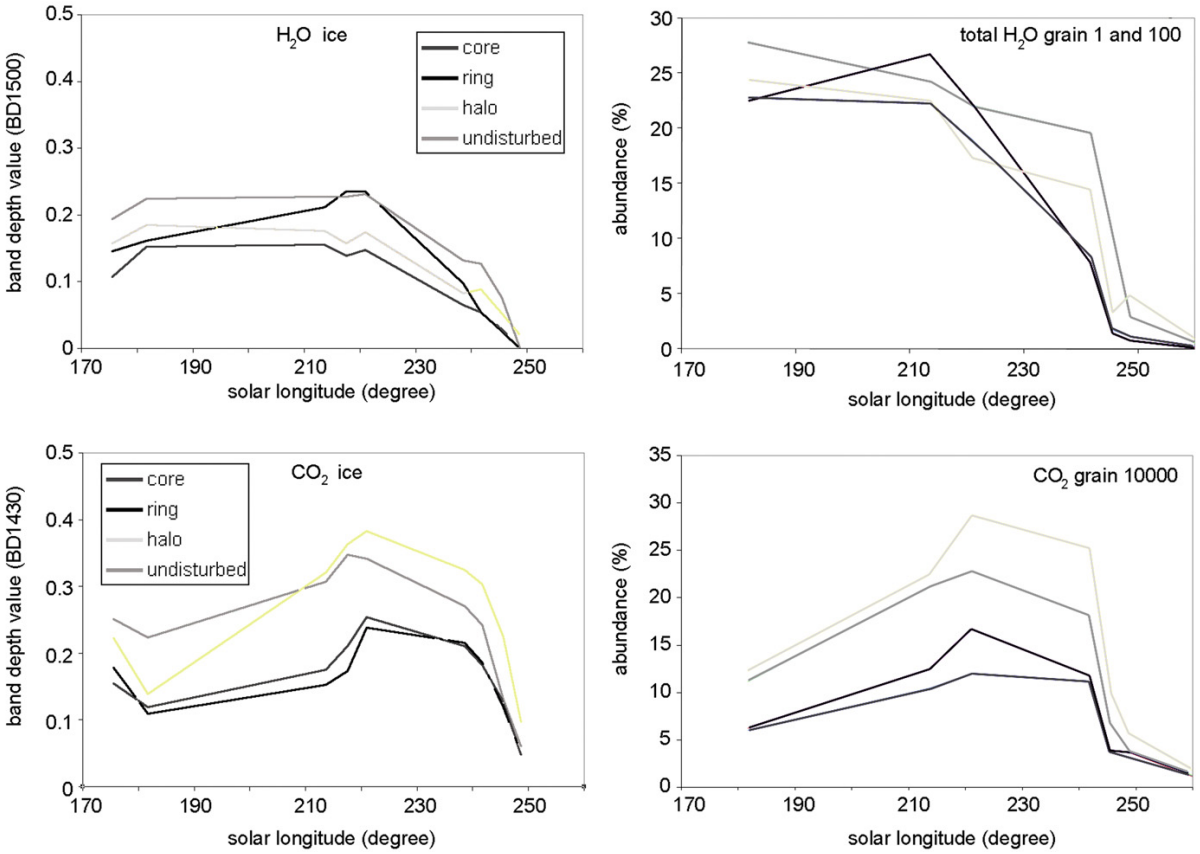


Fig. 5. Temporal changes of H_2O and CO_2 ice related band depth values (on left) and spectral abundances estimated with the linear unmixing method FCLS (on right, see Fig. 12 for more detailed explanation) for different units (core: blue, ring: pink, halo: yellow, undisturbed ice: blue). The top right panel shows the sum of the abundances of water ice at different grain size (only grain size of 1 and 100 μm are detected). The bottom right panel shows the abundance of CO_2 ice (only at 10 cm grain size). Top: H_2O ice. A general decrease can be seen, except for the gray ring, where an increase is present about $L_S=215^\circ$. Bottom: CO_2 ice. The amount of CO_2 ice increases during early spring, with a stronger increase seen during the formation of the bright halo feature (yellow). (For interpretation of the references to color in this figure legend, the reader is referred to the web version of this article.)

- The CO_2 ice band depth is lower than the noise after about $L_S=250^\circ$.

Between $L_S=210^\circ$ and 230°, the water ice band depth is higher relative to earlier and later periods in the gray ring unit. We discuss in the next section why this increase can be confidently attributed to surface bound ice.

3.3. Separation atmospheric and surface H_2O ice signatures

An important but difficult issue is to separate water ice spectral signature of the surface from those of ice crystals in the atmosphere. There are attempts to separate the two sources by spectral calculation using the size dependent spectral properties of water ice in the 3 μm range (Langevin et al., 2007; Carrozzo et al., 2009). However, no methods provide firm separation yet.

Another approach relies on the analysis of the spatial distribution of H_2O ice signatures. Localized increase of the ice signatures associated with specific tens of meters scale morphological features is indicative of a surface origin of the ice signature. While conducting this kind of analysis, one should however carefully consider the role of potential photometric effect: the apparent spectral signature of a widespread ice cloud can also change as a function of the surface type over which it is observed. For example, ice cloud signatures can be enhanced when observed above a tilted surface in shadow, as such a surface will be mainly illuminated by light scattered by the atmosphere, which contain the ice cloud signature. In Fig. 6, we show that the spectral signatures of H_2O ice observed in the gray ring area can be confidently attributed to the surface, as it localized, repetitively observed for each spot, not associated with lighting conditions, and as no suspicious trends with albedo are observed (both the darker and brighter areas around the gray ring show lower water signatures).

3.4. CRISM—HiRISE correlation

We analyzed in detail the HIRISE image PSP_003175_1080, which is characterized by a high spatial resolution, a low noise, and a low solar elevation above the horizon (to make long shadows). It has been obtained at $L_S=210^\circ$ (mid-spring). Although it is not easy to interpret the illumination based topography of the terrain with changing frost cover in springtime, we think a small topographic step along the perimeter of the gray ring is detectable in the image: the surrounding brighter ice is elevated, while the area of the gray ring (as well as the darkest core) is at lower topographic level. We are now going to detail the analysis of dark shadowed and bright illuminated sections of the terrain that lead to this result.

To find out the topography from illumination, both the intrinsic albedo of the surface material and the exposure of the

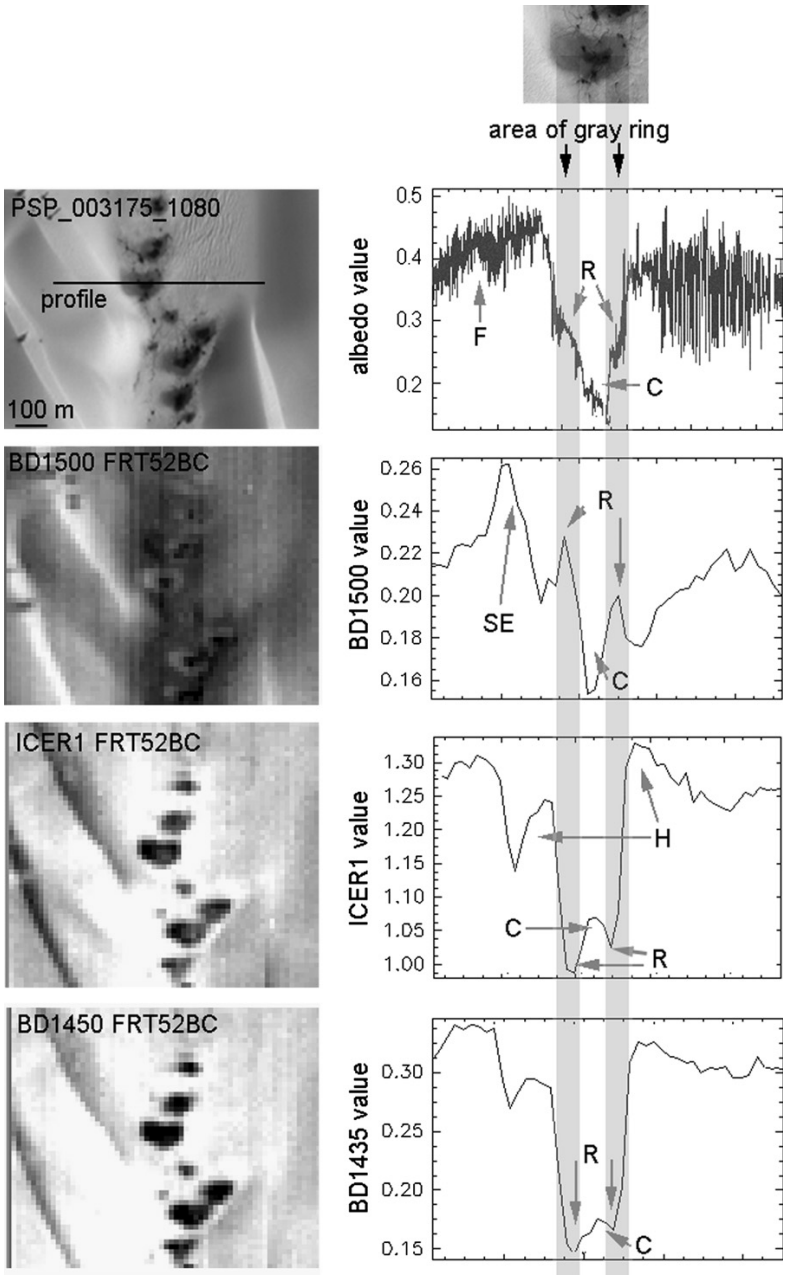


Fig. 6. Spatial changes on images (left) and graphs (right) along a spot for different parameters: (a) albedo (HiRISE), (b) water ice (BD1500), (c) ratio of CO_2/H_2O ice (ICER1) and (d) CO_2 ice (BD1430). The two gray columns on the right mark the location of the gray ring (R) area along the profile, showing a decreased CO_2 ice signature and an increased H_2O ice signature at this location. The magnified image of the analyzed spot is visible at the top right. The subsets show that the lowest albedo is found in the core (C), which is H_2O ice poor and shows some CO_2 ice signature (from atmospheric dust scattering of outer surfaces and/or from the surface). The outer ring (R) corresponds to a local minima in albedo with an elevated H_2O ice signature a low CO_2 ice signature. The high CO_2 signature of the bright halo (H) and the average frost covered terrain (F) is also marked, while slope effect (SE) is indicate the elevated value by a solar facing large slope.

surface slope toward the direction of solar insolation should be taken into account, as both may contribute to the observed brightness of any point of the images. We identified five surface unit types based on relative brightness differences, labeled from 1 (the brightest) to 5 (the darkest) (see Fig. 7). This analysis was realized on the above-mentioned PSP_003175_1080 image with good spatial resolution. The following brightness categories were identified:

1. *The brightest unit (DN values 600–530)*: This unit type covers only small part of the images and is located always right next to unit

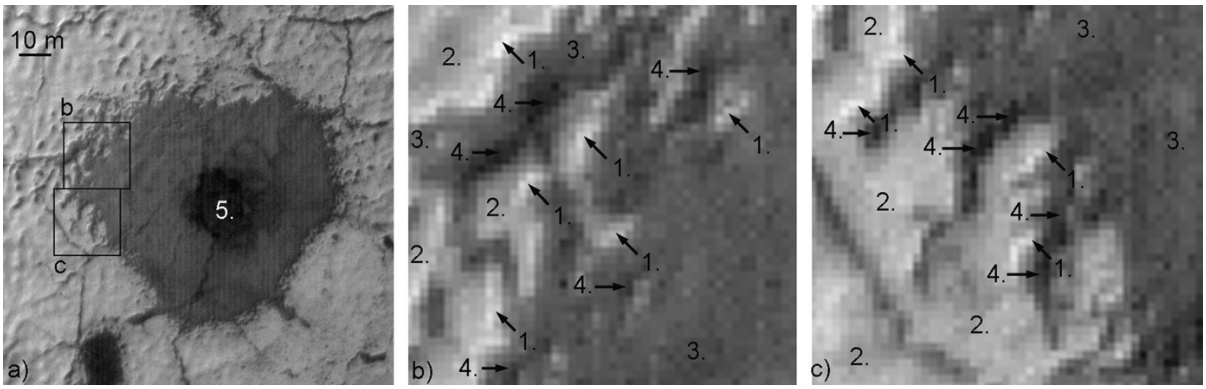


Fig. 7. Estimation of the topographic heights from shadow measurements (HiRISE image PSP_003175_1080). Five units are distinguished on the basis of their brightness (from 1 to 5). The context image (a) shows a dark dune spots with the locations of the magnified (b) and (c) subsets. In these subsets numbers arrows point toward examples for 4 of the 5 different units, while the darkest unit # 5 can be seen in the main image (a).

2 (see below). It is located along the perimeter of the spots. Members of this group are usually elongated roughly from the lower left to the upper right, in right angle to the direction of the solar illumination.

2. *Average brightness unit (DN values 580–460)*: This unit makes up most of the terrain surrounding the dark spots and probably consists of CO_2 ice.
3. *Moderately bright unit (DN values 440–300)*: It covers the outer gray ring of the DDS.
4. *Darker unit (DN values 460–240)*: Often elongated from the lower left to the upper right, also in right angle to the solar illumination. Besides the elongated ones this unit is also present on the left or top-left side of small, isolated and nearly isometric patches of unit 2.
5. *Darkest unit (DN values 130–40)*: It is present at the center of DDSs, where probably the barren, defrosted dark basaltic dune surface is visible.

We have derived the following conclusions based on the relative location of these brightness units:

- unit 1 and unit 3 frequently run parallel to each other on the right and left side of unit 2, respectively (Fig. 8a1, a2, b1). Such appearance is expected if they are the solar facing (1) and shadowed (3) units, respectively, produced by elevated and elongated CO_2 ice stripes;
- where units 1 and 2 form isolated, nearly isometric patches, unit 3 is also present at the left or top-left side of these brighter CO_2 "icebergs", also suggesting unit 3 is composed of shadows;
- unit 5 is only present in the center of DDSs, which represent a feature independent of the CO_2 ice cover, and probably show barren dark dune surface without any kind of ice;
- unit 4 covers only the outer ring of the DDSs where unit 1 or 2 are present, and is not present in the immediate surrounding of the unit 5. It also strengthens the possibility that it is the shadow of elevated CO_2 ice features.

To summarize, as unit 4 is always on the left or top-left side of unit 2, and it is also often elongated parallel to unit 1, unit 4 probably represents the shadow of thick CO_2 ice (Fig. 8a1, a2, b2). In this case the shadows could be used for the rough determination of thickness of CO_2 ice. For such measurement it is important to note that at some locations the elongated heights are composed of both the solid dune ripples below the CO_2 ice cover and the ice cover itself together (like Fig. 8a1, a2). In these cases the height measurement would show not only the thickness of CO_2 ice but also the height of the dune ripple. But there are many examples where small isolated heights (such as units 1 and 2) and their shadows (unit 3) are present together, and no ripple-like feature is visible in their surroundings (Fig. 8d1, d2, f1, f2). In these cases the heights are probably only the results of the unit 2 composed of CO_2 ice, and here the height estimation shows the thickness only of the CO_2 ice. It is also visible that bright units and darker shadows are present together close to the circular edge of dark spots, as one would expect if the CO_2 ice cover of the surrounding terrain begins here.

It is also possible that at some locations the surface albedo changes producing the difference in brightness, e.g. in the case of Fig. 8a1 where depressions on the left between dune ripples could be darker because of accumulated dark dust. But as the solar facing side of the bright unit is also present there, real topographic undulation should be present with solar facing bright slopes, and also with opposite facing shadowed slopes. And there are such cases (like Fig. 8b2, c1, d1, d2, f1, f2) where it is very improbable that dust accumulated only on the shadowed sides of isolated bright patches. More probable explanation is that these dark features are shadows.

The shadow-like unit 3 always surrounds small isometric or larger elongated heights and always elongated toward the left or top-left. During the acquisition of the image the Sun was 24° above the horizon toward the lower right. The shadows' average length is about 20–30 cm, so the bright ice layer covering the whole terrain except the spots is roughly about 10 cm high.

To exclude the effect that earlier formed and permanent depressions are visible in the images (and not annually reoccurring features) we compared images acquired before the spot development with later images contain dark spots. On the earlier images PSP_002186_1080 and PSP_003175_1080 of the same area, acquired during continuous CO_2 frost coverage (at L_S=166.20° and 210.6°, respectively) no spot or any topographic depression is visible. The lack of such depression suggests that the gray rings' area was covered originally with the layer that was at least 10 cm thick at that time, which disappeared later and formed the depression; the original thickness could have been even larger, as CO_2 ice may have already started to sublimate at the time of the shadow measurement. Unfortunately the earlier image's resolution is substantially lower than the analyzed one, and all later images showing summertime defrosted surface were acquired under bad illuminating conditions, and they cannot be used to analyze the topography in details. Fig. 9(a) shows the earlier image of a terrain in Richardson crater with complete CO_2 ice coverage, the (b) shows

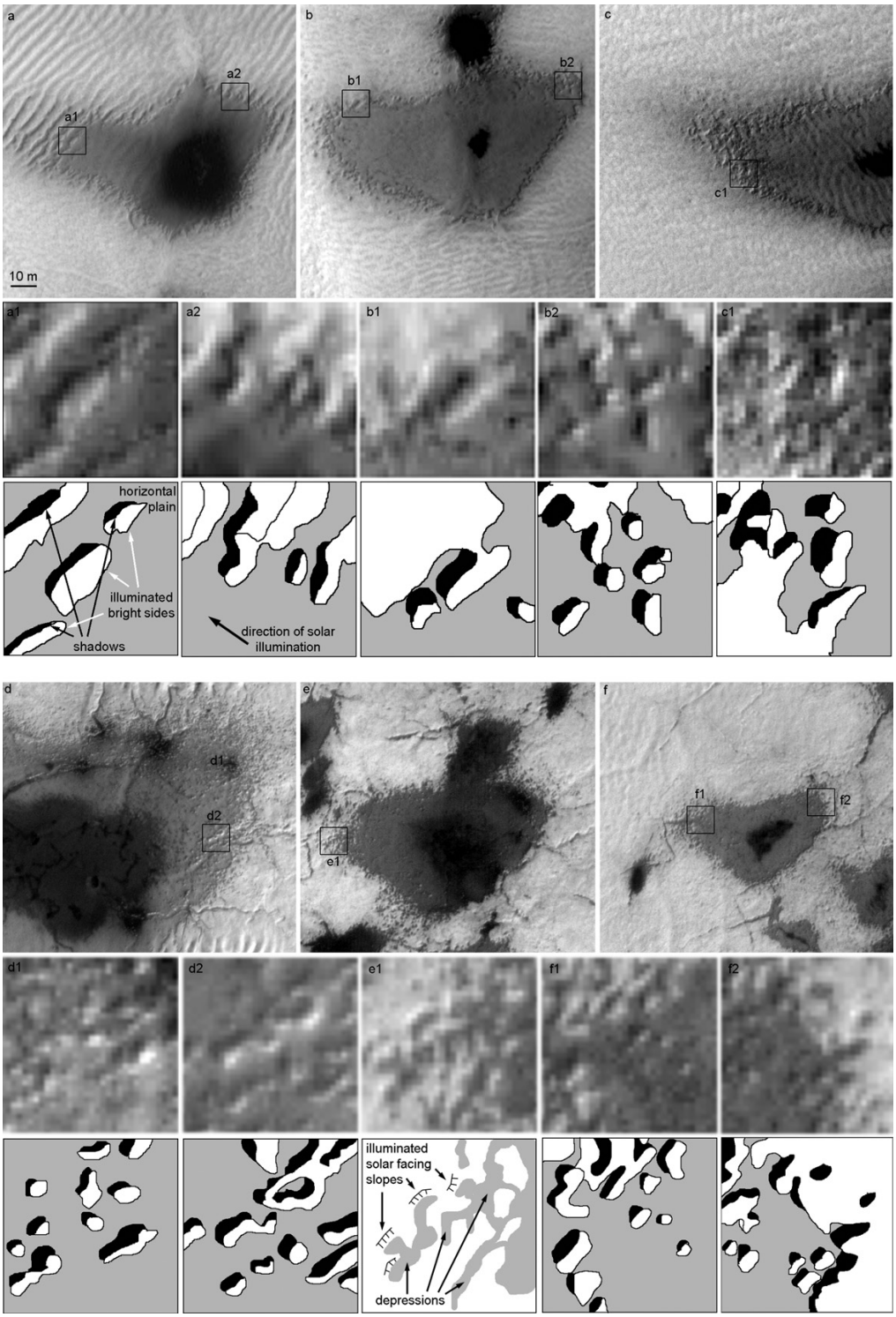


Fig. 8. Examples for the disappearing bright layer forming the depressed gray ring on the HiRISE image no. PSP_003175_1080. Six large spots are shown (largest images labeled a, b, c, d, e, f). Ten insets (10 m × 10 m) from these images are extracted (a1, a2, b1, b2, c1, d1, d2, e1, f1, f2). Outlines of these 10 insets have been produced to highlight the main features and the shadows. In the small inset images the bright ice layer casts shadows, somewhere shadow are present behind iceberg like heights. The Sun illuminates from the lower right, shadows are elongated to the upper left. The outlines show the solar facing and brighter slopes with white, the opposite slopes in shadow with dark, and the nearly horizontal plains (between or on the top of the heights composed of CO_2 ice) with gray color.

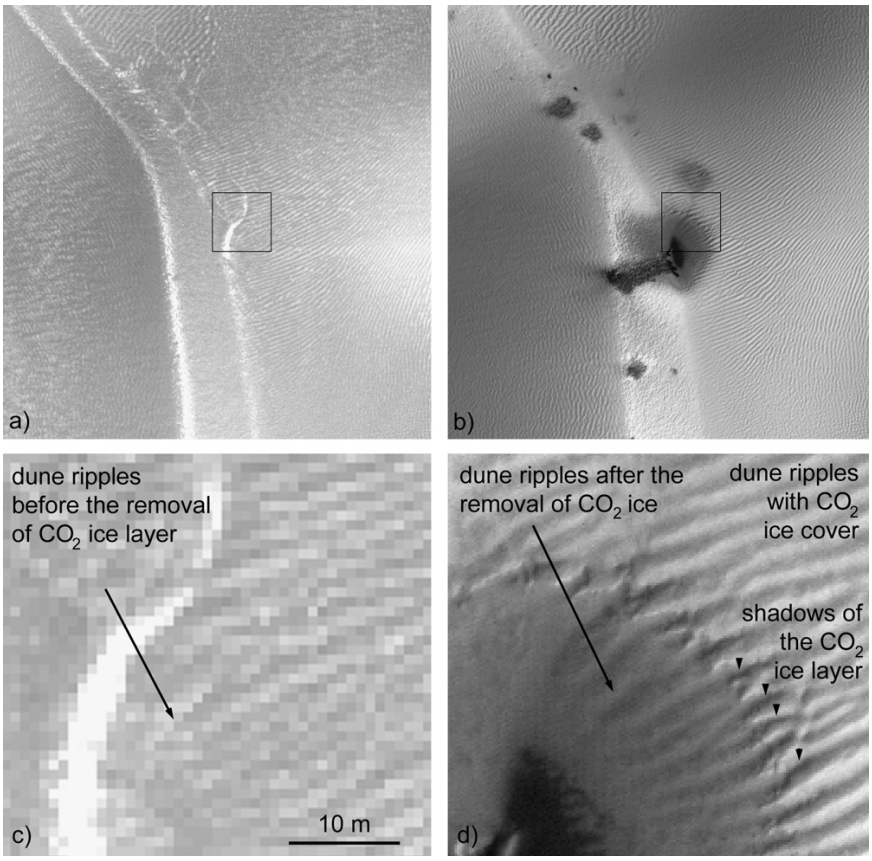


Fig. 9. An example area before and after the development of a spot in Richardson crater. The (a) and (b) image PSP_002252_1080 and PSP_003175_1080 were acquired at L_S=169.0°, 210.6°, respectively. The same small boxed areas are extracted below in (c) and (d) subsets. It can be seen that the depression of the gray ring (b, d) was not present earlier (a, c), in the previously CO_2 ice-covered area. Small dune ripples are present in the CO_2 ice-covered and CO_2 ice-free area also. In subset (d) the surface topography may contribute in producing the shadows, but the image suggests CO_2 ice contributed alone substantially in making the shadows, as it also can be seen from isolated CO_2 ice heights in Fig. 8.

the later image with several dark spots. The same boxed areas are magnified in (c) and (d) subsets. The continuous ice cover is visible in (c), while CO_2 ice free, but still H_2O ice-covered areas can be seen in the (d) subset. Arrows show dune ripples, which are present on the CO_2 ice-covered and in the CO_2 ice-free terrain too. The shadows by the CO_2 ice cover are marked with arrow heads in subset (d). It can be seen that even the topography of the ripples might affect the shadow length, the CO_2 ice layer definitely cast shadows. As it was shown earlier (see Fig. 8), there are such small, isolated, nearly isometric CO_2 heights, where no dune ripples below them affected the height of the CO_2 ice, and the thickness estimation based on shadows. The gray ring area is not barren dark opposite to the central core, suggesting some ice cover is still there. The gray layer is substantially thinner than the brighter CO_2 ice.

The location of the deepest H_2O ice signatures that could be confidently attributed to the surface (see Section 3.3) based on CRISM data coincides with the gray ring features seen in the HIRISE data (Fig. 10). In this area the small-scale dune ripples are also visible. This observation is compatible with the idea that condensed H_2O covers the surface there in a thin layer, which allows the topographic undulation of the surface to remain visible. The gray ring area also contains weaker CO_2 ice signatures. It has been shown by Langevin et al. (2008) that aerosols scattering are responsible for a mixing of surface spectral properties when remotely observed. In particular, an ice-free area of limited extent ($<$ km) surround by a widespread ice-rich area will contain ice signatures when seen from orbit as a result of the mixing of spectral properties by aerosols scattering. Surrounding icy areas will typically represent 10–30% of the observed signal (Langevin et al., 2008). As a consequence, the gray ring area could be free of CO_2 ice as it is of small extent, characterized by the weakest CO_2 signatures of the area (see Figs. 4 and 6) and surrounded by terrains with strong CO_2 ice signatures. Moreover, in Fig. 11 we show HiRISE images of the dark spots showing bright patch consistent with ice located within the dark spots. These cm-dm size patches are below the CRISM resolution. As a consequence, spatial mixing could also contribute to the CO_2 ice spectral signature seen by CRISM in the dark spots and gray ring, which could be mainly CO_2 ice free in mid-spring.

3.5. Spectral unmixing results

Using the FCLS linear unmixing method, we study the properties of this ice layer and we notably test the possible presence of liquid water in the four identified units. We consider 6 endmembers spectra (water ice with 3 grain size, CO_2 ice, liquid water and gypsum) which are representative of the expected potential surface components and which have a significant impact on the 1.5 μm spectral regions (see Fig. 12 and Section 2.1). CO_2 and H_2O ices have been modeled by a radiative transfer simulation (Douté and

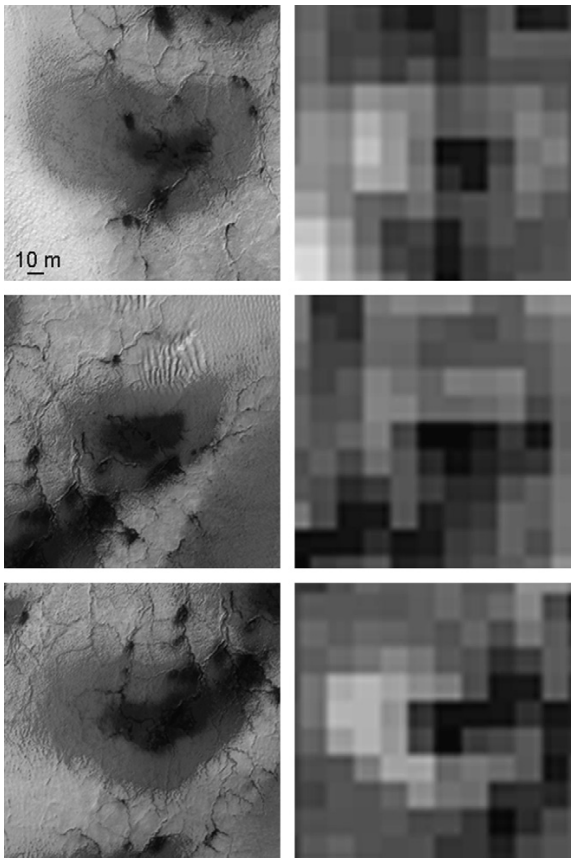


Fig. 10. Three examples for the spatial correlation between HiRISE image insets (left, from PSP_003175_1080 HiRISE image) and BD1500 values (right) from the CRISM image insets (FRT000052BC_07_IF163L). Despite the difference in spatial resolution we can see that the location of the strong BD1500 values (bright pixels on the right) coincide with the gray ring area (on the left).

Schmitt, 1998) using optical constant recorded in the laboratory (Schmitt et al., 1998). Both gypsum and liquid water have been acquired at Labotaroire de Planétologie de Grenoble (Schmitt and Pommerol, unpublished). These spectra will be soon available online at http://ghosst.obs.ujf-grenoble.fr. Two spectrally blank spectra are also considered to account for dust and aerosols. Also an atmosphere transmission spectrum has been added to take into account, small residue of the atmosphere removal.

We estimate the abundance of each reference spectra (see Fig. 12) for the CRISM images: 43A2 (L_S=181.7°), 52BC (L_S=213.7°), 56CO (L_S=221.0°), 5C94 (L_S=241.7°), 5E38 (L_S=245.5°), 5FF6 (L_S=248.7°) and 6516 (L_S=262.6°). We used the range 1.04–1.38 and 1.51–2.13 μm to remove the narrow CO_2 feature that could be affected by the spectral smile. We also weight by a factor of 5 the spectral range 1.50–1.53 μm, very sensitive to water ice, liquid water and gypsum. The root-mean-square (rms) is then computed without weight. All results for the model are shown in Appendix A.

The general trend of the total H_2O ice spectral abundance (sum of H_2O with grain size of 1 and 100 μm) is compatible with the band ratio (Fig. 5 top). Water ice at 1 cm grain size is never detected. The relative fraction of 1 μm grain size is plotted in Fig. 13. The dark core has the smallest mean grain size of the four units. The higher grain sizes are identified in the undisturbed terrain. Fig. 13 suggests a general trend with increasing grain size until L_S=220° and then decreasing until L_S=240°. These facts indicate that: (i) water ice is present with relative low grain size, consistent with seasonal ice; (ii) the grain size is evolving with time, which can be due to several mechanisms including resurfacing by sublimation, re-condensation during the night, sublimation or deposition by geyser activity, grain metamorphism.

The results show that the spectral abundance of CO_2 ice is decreasing from 10% to 3% in agreement with band ratio BD1430 (Fig. 5 bottom). Also, the fit of CO_2 ice bands is compatible with large grain size (10 cm) and possibly a translucent slab ice. The last observation 6516 shows an estimated abundance of 0.06%, probably due to atmospheric residue.

We have also included liquid water and gypsum – a mineral with a 1.5 μm band resembling that of liquid water – in our modeling procedure. In Fig. 14, we show one example of the model results for the dark spot of image 56CO for three linear unmixing scenarios: (1) without liquid nor gypsum (2) with liquid water only (3) with liquid water and gypsum. The rms is decreasing from model 1 to model 3 due to a slightly better fit of the 1.5 μm band (see Fig. 14). This tends to indicate that a spectral component with a water band shifted toward shorter wavelengths, such as gypsum or liquid water, could be present. Sulfates and/or liquid water have been detected in six over the seven images considered (i.e.: for all observation except the last one at L_S=262.6°) in the "dark center" region, while it is almost never detected in the average terrain or in the bright halo. However, retrieved abundances are low (< 3%, see Appendix A), and differences in modeled spectra are not significant given the first order method employed here (Fig. 14). Although the retrieval of a few % of species with a 1.45 μm band consistent with liquid water in the dark spots only is intriguing, no robust conclusions can be reached. Moreover, none of the ratio spectra show evidence for liquid water or gypsum (see Fig. 15). To assess more precisely the possible presence of liquid water and/or gypsum in CRISM spectra, a non-linear spectral inversion using radiative transfer model should be performed in the future.

3.6. Climate modeling results

The surface stability and presence of ices are analyzed at the latitude of Richardson crater as the season progresses from winter to summer using a climatic model (see Section 2 for details). Three modeling hypotheses concerning local surface properties are shown in Fig. 16: (A) diamonds for standard parameters (flat surface, moderately bright ices), (B) stars for condensation on a 15° pole facing slope (to estimate the effect of local favorable conditions), (C) triangles for "dark" ice (albedo of 0.25 for both H_2O and CO_2 ice, a rough attempt to assess the impact of dust contamination of ice). These modeling predictions are compared to the presence or absence of ices at Richardson crater as a function of season as constrained from CRISM data, which show a general good agreement between data and model.

Water ice accumulation starts before CO_2 ice at the beginning of fall, mainly due to snow precipitation of small grain size particles (more than 99% of the total water ice accumulation) that have condensed in the lower atmosphere according to the simulation (see also Forget et al., 2006). A thin layer of a few microns to a few 10 s of microns thick H_2O ice below the CO2 ice is expected according to model results, as noted by Schmitt et al. (2009). Then both ices condense simultaneously (H_2O inclusion within the CO_2 ice) 20–30° of L_S later. As a result we have a layered structure: only H_2O ice below, and CO_2 plus H_2O ice above. The ratio of H_2O ice in the upper layer depends on several factors, above all meteorological conditions and global atmospheric circulation, as during the CO_2 condensation in southern winter the average atmospheric vapor content reaches maximum supplied by the exposed northern permanent water ice cap. When cold CO_2 ice is present, it traps available water vapor. Ice

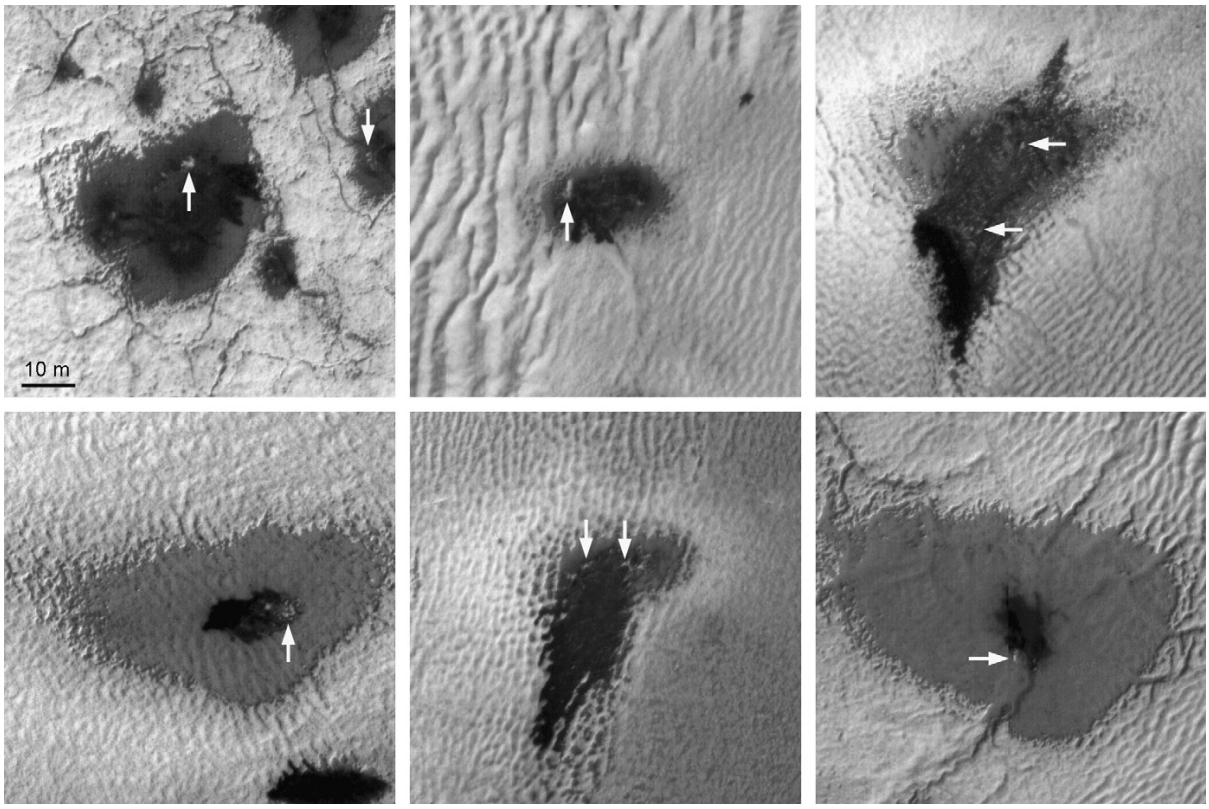


Fig. 11. Examples for small bright patches inside the spots (arrows) on HiRISE image PSP_003386_1080. These suggest, small CO_2 ice patches may still be present even at the darkest cores, which are below the spatial resolution of CRISM data, but may affect the spectra.

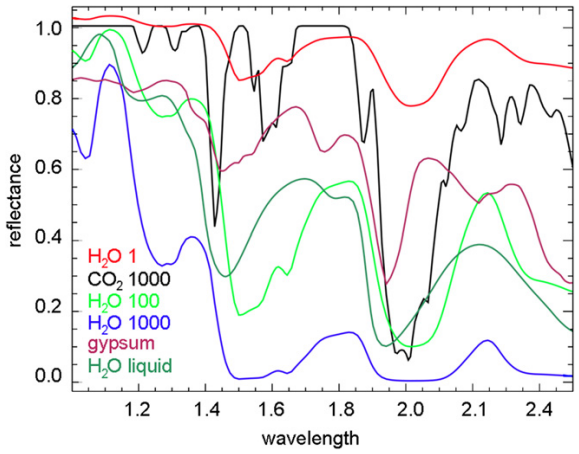


Fig. 12. Reference spectra used by FCLS to estimate the relative abundances for observed CRISM spectra. CO_2 ice at 10 cm grain size, H_2O ice at 1, 100 and 1000 μm have been modeled by a radiative transfer code (Douté and Schmitt, 1998) using optical constant recorded in the laboratory (Schmitt et al., 1998). Both gypsum and liquid water have been acquired at LPG (Schmitt and Pommerol, unpublished). These spectra will be soon available online at http://ghosst.obs.ujf-grenoble.fr.

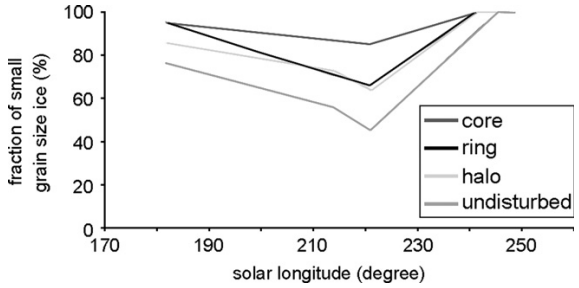


Fig. 13. Fraction of water ice spectra with 1 μm grain size from the total water ice content (grain size with 1 and 100 μm) as a function of time for the four units (see legend of Fig. 5). Dark core show the smaller grain size fraction. Gray ring and bright halo have intermediated grain size. Undisturbed terrains have the highest grain size. There is a general trend with increasing grain size from L_S=180° to 220° and then decreasing from L_S=220° to 240°.

disappears prior to the summer solstice even for favorable conditions. According to the model, water ice remains 5–10° of L_S later compared to CO_2. The contamination of ice by dust significantly decreases the stability of ice in spring, which sublimation is shifted by about 30° of L_S. According to the model, CO_2 ice disappears at L_S=220° for a moderately dark ice with a 0.25 albedo (Fig. 16). This is consistent with the morphological and spectral analyses conducted above, showing that at a similar period (L_S=210°, see Section 3.4) the gray ring is composed of an H_2O ice-rich thin layer while surrounding areas are still covered by a thicker layer of CO_2 ice.

3.7. Formation mechanisms of H_2O in the gray ring area

Based on the observations and modeling predictions presented in the previous sections, we propose the following scenario for the

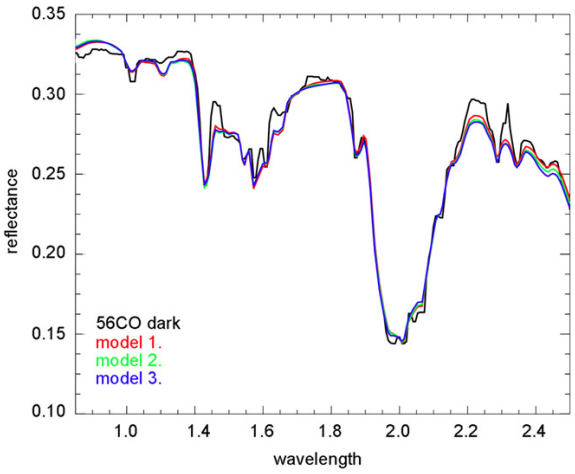


Fig. 14. Best synthetic spectra obtained by sparse linear mixture of reference database using FCLS algorithm versus observed spectra for the observation image no. 56CO dark core. Model 3 database include all spectra described in Fig. 12. In this case, liquid water is detected with an abundance of 0.04% and gypsum with an abundance of 1.57% (rms=0.0056). Model 2 represents the same inversion with liquid water (1.46%) but without gypsum (rms=0.0058). Model 1 represents the same inversion without gypsum, nor liquid water (rms=0.0059). CRISM signal to noise ratio is 300 and thus errors bars cannot be seen in this figure. The rms is slightly decreasing from model 1 to model 3, indicating the possible presence of liquid water or gypsum but non-linear radiative transfer inversion has to confirm this trend.

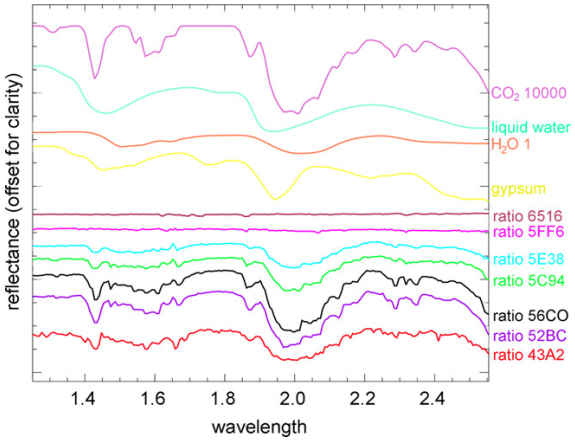


Fig. 15. The 4 first spectra at the top correspond to reference spectra (see Fig. 11) for CO_2 ice, water ice, liquid water and gypsum. Below ratio between undisturbed ice terrain divided by dark core for seven CRISM observations are visible: 43A2 (L_S=181.7°), 52BC (L_S=213.7°), 56CO (L_S=221.0°), 5C94 (L_S=241.7°), 5E38 (L_S=245.5°), 5FF6 (L_S=248.7°) and 6516 (L_S=262.6°). None of the ratio is compatible neither with gypsum nor with liquid water but with decreasing water ice and CO_2 ice compounds, strongly indicating that both water ice and CO_2 ice are present at the ground. The abundances of liquid water and gypsum, estimated by FCLS (model 3) on these ratio spectra, are always 0%. These results suggest that neither liquid water nor gypsum are enriched in the scene and therefore are presumably absent or in very small quantities.

formation of the observed surface H_2O ice in the dark dune spots of Richardson crater:

1. During early fall, H_2O deposits start to form at the surface. They are mainly composed of precipitations that have settled from the lower atmosphere. Several tens of μm of water ice accumulate at the surface (see Section 3.6).

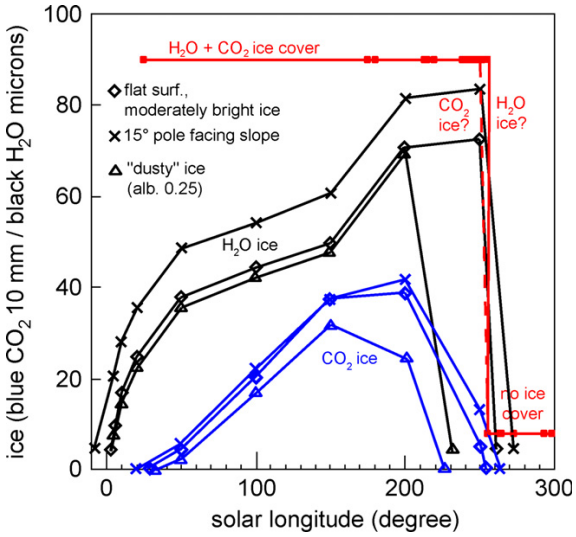


Fig. 16. Result of the model run on annual frost formation for H_2O ice (black) and CO_2 ice (blue), plus the observed presence of any kind of ice at the target location from CRISM data (red). It shows as a function of L_S (degree, horizontal axis) the cumulative thickness of CO_2 and H_2O ice condensed on the ground, on the vertical axis the thickness of H_2O and CO_2 are present using different scales, for CO_2 up to 40 cm and H_2O up to 80 μm thickness. Diamonds, triangles and crosses correspond to 3 hypotheses for model parameters related to ground properties (see text for details) (For interpretation of the references to color in this figure legend, the reader is referred to the web version of this article.)

2. During mid-fall, concomitant condensation of H_2O and CO_2 begin and form a layer of CO_2 ice contaminated by H_2O ice. Several tens of cm of frost, mainly composed of CO_2 ice, form in the whole area during that period according the earliest CRISM observations, the HiRISE observations of a 10 cm depression in mid-spring (Section 3.2) and the modeling predictions (see Section 3.6).
3. After the spring equinox, dark core are observed at Richardson crater. They probably result from the formation of CO_2 jets below the translucent ice (Kieffer, H.H., 2000), which carry along dune grains that settle about the jet. This scenario is in agreement with the results from the linear unmixing method: (i) detection of large CO_2 ice grain size; (ii) higher abundances of dark dust for the dark core and gray ring units (see Section 3.5). Around the dark core a "gray ring" is observed, which spectral composition during mid-spring is consistent with an enhanced amount of water ice (see Section 3.3) and probably no CO_2 ice. Two possible scenarios can then explain or contribute to the observed properties of this gray ring:
   (a) The presence of dark dust material fallen from the jet increases surface absorption and is responsible for ice sublimation. Ice sublimates faster at the dust covered area of the spot, which explain the depression observed in HiRISE images and the weak CO_2 ice bands observed in CRISM data for which spatial mixing of ice-free and ice-rich subpixel deposits, as well as aerosols scattering, is a probable explanation (see Section 3.4). In the outer gray area, albedo is higher and causes higher stability of water ice, as indicated by the model (see Fig. 15). The relative smaller water ice grain size could be due to the reappearance of the small grain size layer of snow precipitated in early fall.
   (b) The water ice, that is present between the sand substrate and the translucent CO_2 ice layer, is blown up with sand grains by geyser activity (Kieffer, 2000; Piqueux et al., 2003). Water ice grain falls on the top of the surface surrounding

the central dark core, contributing to the formation of the water ice-rich gray ring. The relative smaller water ice grain size could be due to the geyser activity.

4. Although no robust evidence for liquid water has been found in the spectra, the data are not inconsistent with the possible presence of small amount of liquid water in the dark core unit and, with an even lower probability, in the gray ring unit (see Section 3.5).

4. Conclusions

We have performed a study of the dark dune spots observed in Richardson crater using HiRISE and CRISM data. Our goal was to identify and analyze the presence of water ice within these features. It has been possible to analyze the largest spots using the 20 m spatial resolution of CRISM, which provided clues about the presence of water ice within these features. In particular, dark dune spots can give rise to flow-like feature and the role of liquid water in this process is the subject of ongoing research.

Based on the analysis of HiRISE images, we identified three characteristic sections of dark dune spots observed in Richardson crater during spring: dark core, gray ring and bright halo. We used time series of CRISM images between L_S=175.5° and 340.5° to analyze temporal changes of H_2O and CO_2 related band depth values. At the area of gray rings on HiRISE images the bright icy layer that surrounds the spots is missing. Based on shadow length measurements an about 10 cm deep horizontal depression is present there, measured relative to the top of surrounding bright ice cover. These depressions were not present in earlier images, suggesting they form due to the localized sublimation of the ice layer.

We identified H_2O and CO_2 ice at most locations during spring, but with significant spatial and seasonal variations in band depth and linear unmixing results. Spatial subpixel mixing, water ice cloud contribution, and aerosols scattering responsible for an apparent mixing of surface properties must be carefully considered while analyzing the apparent spectral properties in CRISM data. Enhanced water ice signature is observed during mid-spring at the gray ring area from BD1500 values. Based on the size of these ring features (20–30 m) and on the repeatability of these features from one spot to the next, the surface origin of this water ice has been confidently determined.

By analyzing CRISM images, HiRISE data and the result of a climate model, it has been possible to build a scenario for the formation and evolution of the ice layers in and around the dark dune spots of Richardson crater. During fall thin, tens of μm thick H_2O ice-rich layer forms at the surface. 30° of L_S later a layer of CO_2 ice with inclusions of H_2O ice forms on top of it, and reach a thickness of a few tens of cm. During late winter/early spring the dark spots form, probably by geysers activity (Kieffer, 2000) in agreement with the large CO_2 grain size detected by the linear unmixing. A bright halo-like feature surrounds the spot and show stronger CO_2 signature than the undisturbed average ice-covered surface, suggesting CO_2 was refrozen there. The dark spots and the gray rings are located in a 10 cm deep depression compared to the surrounding bright, ice-rich layer. The dark center spot is ice-free at some places (but contain ice signatures in CRISM images due to spatial mixing and aerosols scattering). At L_S=210–230°, the gray ring area is covered by an enhanced thin layer of H_2O ice. The origin of H_2O may be from two sources: (i) condensation on the surface in autumn (before the formation of CO_2 layer) or during wintertime (CO_2 layer acting as a clod trap) and exhumed by the differential sublimation of CO_2 and H_2O ice (ii) H_2O attached to the sand grains that are blown up by geyser activity and that fall at the surface around the spot.

We observed H_2O ice left behind the disappearance and/or reduction of CO_2 ice thickness in the gray ring area of dark dune spots. Resembling situation was observed as a shrinking H_2O ring during the recession of the northern seasonal cap (Appéré et al.,

Table A1
Numerical parameters and calculated values of the spectral analysis for various crystal sizes, and for the probability that gypsum or liquid water is in the spectra. First column shows the used CRISM image number and the analyzed surface feature type. See for more details the text around Figs. 12–14.

No. of CRISM image and area type	CO_2 grain 10000	H_2O grain 1	H_2O grain 100	H_2O grain 1000	Flat 1	Flat 0.001	Atmosphere	Gypsum	Liquid water	rms	L_S
43A2 average surface	0.1115	0.2127	0.0655	0	0	0.6102	0	0	0	0.0127	181.70
43A2 bright halo	0.1228	0.2086	0.0345	0	0	0.634	0	0	0	0.0142	181.70
43A2 dark center	0.0601	0.216	0.0113	0	0	0.6917	0	0.0209	0	0.0062	181.70
43A2 gray ring	0.062	0.2152	0.0101	0	0	0.6912	0	0.0215	0	0.0055	181.70
52BC average surface	0.2123	0.1363	0.1059	0	0	0.5455	0	0	0	0.0169	213.60
52BC bright halo	0.2245	0.164	0.0607	0	0	0.5508	0	0	0	0.0161	213.60
52BC dark center	0.1046	0.1934	0.0288	0	0	0.6613	0	0.0113	0.0006	0.0056	213.60
52BC gray ring	0.1244	0.1893	0.0779	0	0	0.6084	0	0	0	0.0127	213.60
56C0 average surface	0.2278	0.0994	0.1212	0	0	0.5516	0	0	0	0.0165	221.00
56C0 bright halo	0.2865	0.1096	0.0628	0	0	0.5411	0	0	0	0.0165	221.00
56C0 dark center	0.1199	0.1615	0.0282	0	0	0.671	0	0.0157	0.0037	0.0057	221.00
56C0 gray ring	0.167	0.1471	0.0747	0	0	0.6112	0	0	0	0.0109	221.00
5C94 average terrain	0.1817	0.181	0.0149	0	0	0.6139	0	0.0085	0	0.0109	241.70
5C94 bright halo	0.2529	0.1443	0	0	0	0.573	0.0299	0	0	0.0137	241.70
5C94 dark core	0.1122	0.084	0	0	0	0.6741	0.1038	0.0259	0	0.0056	241.70
5C94 gray ring	0.1181	0.0768	0	0	0	0.6567	0.1267	0.0216	0	0.0065	241.70
5E38 average surface	0.0665	0.1007	0	0	0	0.806	0.0266	0.0002	0	0.0053	245.50
5E38 bright halo	0.0983	0.0323	0	0	0	0.7833	0.086	0	0	0.008	245.50
5E38 dark center	0.0378	0.017	0	0	0.0014	0.8288	0.1041	0.0109	0	0.003	245.50
5E38 gray ring	0.0387	0.0148	0	0	0.0072	0.825	0.1031	0.0113	0	0.0037	245.50
5FF6 average surface	0.0377	0.0286	0	0	0.0943	0.7043	0.1254	0.0097	0	0.0038	248.70
5FF6 bright halo	0.0557	0.0482	0	0	0.0161	0.6831	0.1897	0.0071	0	0.0057	248.70
5FF6 dark center	0.0313	0.0111	0	0	0.0996	0.7017	0.1416	0.0146	0	0.0039	248.70
5FF6 gray ring	0.0368	0.0077	0	0	0.1017	0.701	0.1438	0.0089	0	0.0042	248.70
6516 average terrain	0.0068	0	0	0	0.1834	0.764	0.0458	0	0	0.0032	262.50
6516 bright halo	0.0087	0	0	0	0.198	0.7578	0.0355	0	0	0.0033	262.5
6516 dark center	0.0076	0	0	0	0.1779	0.7687	0.0458	0	0	0.0032	262.5
6516 gray ring	0.0055	0	0	0	0.1812	0.7618	0.0515	0	0	0.0031	262.5

2008; Wagstaff et al., 2008), and in some patches at the southern hemisphere too (Brown et al., 2010), but at substantially larger spatial scale.

The presence of water ice in physical contact with insolated dark dune material could lead to the formation of liquid water. Such environments are of interest while assessing the potential for habitability of present day Mars (Szathmary et al., 2007). In the gray ring area the water ice surrounds darker surface, where liquid interfacial water layer or brine (Mohlmann, 2004, 2009, 2010) may form. We found no firm evidence for the presence of liquid water in near-IR spectra, although linear unmixing results show that the data are not inconsistent with a possible slight contribution (a few %) of liquid water in the dark core unit.

The above-mentioned observations may have important impact on the explanation of other circumpolar features, showing water ice may be present in CO_2 ice-free regions at the southern hemisphere of Mars. We observed the presence of water ice in physical contact with relative dark dune grains in 100–200 m sized spots. In their surrounding of these spots in Richardson crater flow-like features are present emanate from resembling but smaller spots, which are too small to be resolved by CRISM. If resembling process happen there, such locations could be also interesting for the possible ephemeral presence of water ice, as well as other seasonal features should be analyzed in detail to search for water ice there.

Acknowledgments

The authors would like to thank Bernard Schmitt and Francois Forget for their help. This work was supported by the ESA ECS-project no. 98076. This work was also supported by the Centre National d'Etudes Spatiales (CNES). It is based on observations with CRISM embarked on MRO. We also acknowledge partial support from the Programme National de Planétologie (CNRS/INSU).

Appendix A

See Table A1.

References

Appéré, T., Schmitt, B., Pommerol, A., Douté, S., Beck, P., Forget, F., Schmidt, F., Langevin, Y., Bibring, J.-P., Gondet, B., 2008. Spatial and temporal distributions of the water ice annulus during recession of the northern seasonal condensates on Mars. In: Proceedings of the Third International Workshop on The Mars Atmosphere, Abstract, 9008.

Bibring, J.-P., Langevin, Y., Gendrin, A., Gondet, B., Poulet, F., Berthé, M., Soufflot, A., Arvidson, R., Mangold, N., Mustard, J., Drossart, P., 2005. the OMEGA team, 2005. Mars surface diversity as revealed by the OMEGA/Mars Express observations. Science 307, 1576–1581.

Bibring, J.-P., Langevin, Y., Poulet, F., Gendrin, A., Gondet, B., Berthé, M., Soufflot, A., Drossart, P., Combes, M., Bellucci, G., Moroz, V., Mangold, N., Schmitt, B., 2004. & the OMEGA team, 2004. Perennial water ice identified in the south polar cap of Mars. Nature 428, 627–630.

Bibring, J.-P., Langevin, Y., Mustard, J.F., Poulet, F., Arvidson, R., Gendrin, A., Gondet, B., Mangold, N., Pinet, P., Forget, F., the OMEGA teamBerthe, M., Bibring, J.-P., Gendrin, A., Gomez, C., Gondet, B., Jouglet, D., Poulet, F., Soufflot, A., Vincendon, M., Combes, M., Drossart, P., Encrenaz, T., Fouchet, T., Merchiorri, R., Belluci, G., Altieri, F., Formisano, V., Capaccioni, F., Cerroni, P., Coradini, A., Fonti, S., Korablev, O., Kottsov, V., Ignatiev, N., Moroz, V., Titov, D., Zasova, L., Loiseau, D., Mangold, N., Pinet, P., Doute, S., Schmitt, B., Sotin, C., Hauber, E., Hoffmann, H., Jaumann, R., Keller, U., Arvidson, R., Mustard, J.F., Duxbury, T., Forget, F., Neukum, G., 2006. Global mineralogical and aqueous Mars history derived from OMEGA/Mars Express data. Science 312, 400–404.

Bridges, N.T., Titus, T.N., Herkenhoff, K.E., Kieffer, H.H., Hecht, M.H., Mercer, C., 2001. Seasonal dark spots in Martian gullies and other terrains studied by TES and other data sets. Exploring Mars with TES: A Data Users Workshop, Arizona State University, Tempe, Arizona.

Brown, A.J., Calvin, W.M., McGuire, P.C., Murchie, S.L., 2010. Compact Reconnaissance Imaging Spectrometer for Mars (CRISM) south polar mapping: First Mars year of observations. Journal of Geophysical Research 115, E00D13. doi:10.1029/2009 JE003333.

Carrozzo, F.G., Bellucci, G., Altieri, F., D'Aversa, E., Bibring, J.-P., 2009. Mapping of water frost and ice at low latitudes on Mars. Icarus 203, 406–420.

Ceamanos, X., Douté, S., 2009. Spectral smile correction in CRISM hyperspectral images. In: Proceedings of the AGU'09—American Geophysical Union, Fall Meeting.

Christensen, P.R., Kieffer, H.H., Titus, T.N., 2005. Infrared and Visible Observations of South Polar Spots and Fans. American Geophysical Union, Fall Meeting, Abstract P23C-04.

Douté, S., Schmitt, B., 1998. A multi-layer bidirectional reflectance model for the analysis of planetary surface hyperspectral images at visible and near infrared wavelengths. Journal of Geophysical Research E103, 31,367–31,390.

Fishbaugh, K.E., Poulet, F., Chevrier, V., Langevin, Y., Bibring, J.-P., 2007. On the origin of gypsum in the Mars north polar region. Journal of Geophysical Research 112, E7 CiteID E07002.

Forget, F., Hourdin, F., Fournier, R., Hourdin, C., Talagrand, O., Collins, M., Lewis, S.R., Read, P., Huot, J.-P., 1999. Improved general circulation models of the Martian atmosphere from the surface to above 80 km. Journal of Geophysical Research 104 (E10), 24155–24176.

Forget, F., Haberle, R.M., Montmessin, F., Levrard, B., Head, J.W., 2006. Formation of Glaciers on Mars by atmospheric precipitation at high obliquity. Science 311, 368–371.

Forget, F., Millour, E., Madelaine, J., Lefevre, F., Montmessin, F., 2008. Simulation of the Mars water cycle with the LM Mars Global Climate model. The Mars Water Cycle Workshop, Paris, April 2008.

Ganti, T., Horvath, A., Berczi, Sz., Gesztesi, A., Szathmary, E., 2003. Dark Dune Spots: possible biomarkers on Mars? Origins of Life and Evolution of the Biosphere 33, 515–557.

Grundy, W., Schmitt, B., 1998. The temperature-dependent near-infrared absorption spectrum of hexagonal H_2O ice. Journal of Geophysical Research 103E, 25809–25822.

Hansen, C., Portyankina, G., Thomas, N., Byrne, S., McEwen, A., 2010. HiRISE images of spring on Mars. In: Proceedings of the 41th Lunar and Planetary Science Conference, Abstract 2029.

Hapke, B., 2008. Bidirectional reflectance spectroscopy: 6. Effects of porosity. Icarus 195, 918–926.

Heinz, D., I-Chang, C., 2001. Fully constrained least squares linear spectral mixture analysis method for material quantification in hyperspectral imagery. IEEE Transactions on Geosciences and Remote Sensing 39, 529–554.

Horváth, A., Ganti T., Gesztesi A., Berczi, Sz., Szathmary, E., 2001. Probable evidences of recent biological activity on Mars: appearance and growing of dark dune spots in the south polar region. In: Proceedings of the 32th Lunar Planetary Science Conference, Abstract 1543.

Horváth, A., Kereszturi, A., Bérczi, Sz., Sik, A., Pócs, T., Gánti, T., Szathmáry, E., 2009. Analysis of dark Albedo features on a Southern Polar Dune Field of Mars. Astrobiology 9 (1), 90–103.

Kereszturi, A., Möhlmann, D., Berczi, Sz., Ganti, T., Horvath, A., Kuti, A., Sik, A., Szathmary, E., 2010a. Indications of brine related local seepage phenomena on the northern hemisphere of Mars. Icarus 207, 149–164.

Kereszturi, A., Schmidt, F., Vincendon, M., 2010. Searching for water ice in the Dark Dune Spots of Mars using CRISM data. In: Proceedings of the 41th Lunar Planetary Science Conference, Abstract 1714.

Kereszturi, A., Möhlmann, D., Pócs, T., Bérczi, Sz., Horváth, A., Sik, A., 2009. Recent rheologic processes on dark polar dunes of Mars: driven by interfacial water? Icarus 201 492–503.

Kieffer, H.H., Chase, S.C., Martin, T.Z., Miner, E.D., Palluconi, F.D., 1976. Martian north pole summer temperatures: dirty water ice. Science 194, 1341–1344. doi:10.1126/science.194.4271.1341.

Kieffer, H.H., 1990. H_2O grain size and the amount of dust in Mars' residual north polar cap. Journal of Geophysical Research 95 (B2), 1481–1493.

Kieffer, H.H., 2000. Annual punctuated CO_2 slab-ice and jets on Mars. In: Proceedings of the International Conference on Mars Polar Science and Exploration, p. 93.

Kieffer, H.H., Christensen, P.R., Titus, T.N., 2006. CO_2 jets formed by sublimation beneath translucent slab ice in Mars' seasonal south polar ice cap. Nature 442, 793–796.

Kieffer, H.H., Titus, T.N., Mullins, K.F., Christensen, P.R., 2000. Mars south polar spring and summer behaviour observed by TES: seasonal cap evolution controlled by frost grain size. Journal of Geophysical Research 105, 9653–9700.

Kieffer, H.H., Titus, T.N., 2001. TES mapping of Mars' north seasonal cap. Icarus 154, 162–180.

Kieffer, H.H., 2003. Behaviour of CO_2 on Mars: real zoo [abstract 3158]. In: Proceedings of the Sixth International Conference on Mars, Lunar and Planetary Institute, Houston.

Kossacki, K.J., Markiewicz, W.J., Portyankina, G., Neukum, G., HRSC team, 2006. Conditions for water ice accumulation within craters on Mars. In: Proceedings of the Fourth Mars Polar Science Conference, Abstract 8016.

Kossacki, J.K., Kopystynski, L., 2004. Non-uniform seasonal defrosting of subpolar dune filed on Mars. Icarus 168, 201–204.

Langevin, Y., Poulet, F., Bibring, J.-P., Gondet, B., 2005. Sulfates in the North Polar Region of Mars detected by OMEGA/Mars Express. Science 307, 1584–1586.

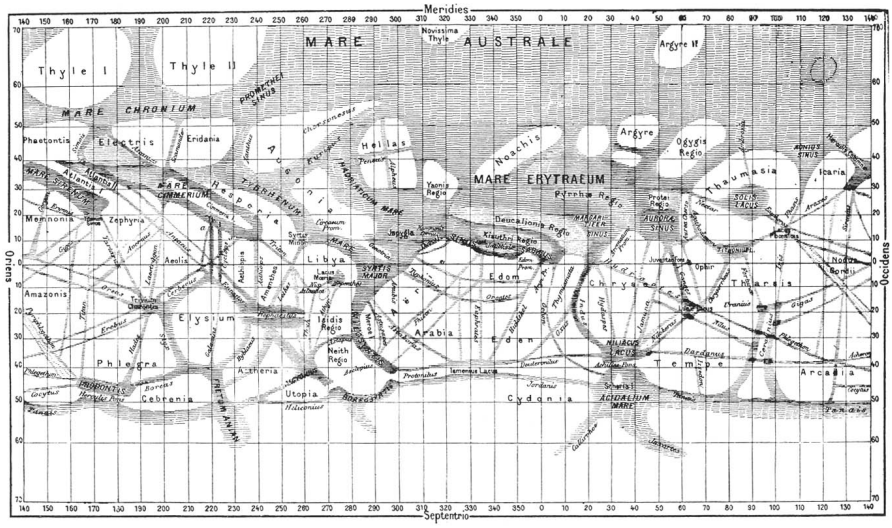
Langevin, Y., Bibring, J.P., Douté, S., Vincendon, M., Poulet, F., Gondet, B., Schmitt, B., Forget, F., Montmessin, F., and the OMEGA Team, 2006. CO_2 ice and H_2O ice in the seasonal caps of Mars during the spring retreat, phase. In: Proceedings of the Fourth Mars Polar Science Conference, Abstract 8091.

Langevin, Y., Bibring, J.-P., Montmessin, F., Forget, F., Vincendon, M., Doute, S., Poulet, F., Gondet, B., 2007. Observations of the south seasonal cap of Mars during recession in 2004–2006 by the OMEGA visible/near-infrared imaging

spectrometer on board Mars Express. Journal of Geophysical Research 112, E08S12. doi:10.1029/2006JE002841.
Langevin, Y., Vincendon, M., Poulet, F., Bibring, J.-P., Gondet, B., Douté, S., Encrenaz, T., 2008. Weak signatures of water ice at high northern latitudes: aerosols, frosts and ice outcrops. In: Proceedings of the 39th Lunar and Planetary Science Conference, Abstract 2134.
Malin, M.C., Carr, M.H., Danielson, G.E., Davies, M.E., Hartmann, W.K., Ingersoll, A.P., James, P.B., Masursky, H., McEwen, A.S., Soderblom, L.A., Thomas, P., Veverka, J., Caplinger, M.A., Ravine, M.A., Soulanille, T.A., Warren, J.L., 1998. Early views of the Martian Surface from the Mars Orbiter Camera of Mars Global Surveyor. Science 279, 1681–1685.
Malin, M.C., Edgett, K.S., 2000. Frosting and defrosting of Martian polar dunes. In: Proceedings of the 31th Lunar Planetary Science Conference, Abstract 1056.
Malin, M.C., Edgett, K.S., 2001. The Mars Global Surveyor Mars Orbiter camera: interplanetary cruise through primary mission. Journal of Geophysical Research 106, 23429–23570.
Massé, M., Bourgeois, O., Le Mouélic, S., Verpoorter, C., Le Deit, L., 2010. Origin of Martian circumpolar gypsum-bearing deposits. In: Proceedings of the 41th Lunar and Planetary Science Conference, Abstracts 1138.
McGuire, P.C., Bishop, J.L., Brown, A.J., Fraeman, A.A., Marzo, G.A., Morgan, M.F., Murchie, S.L., Mustard, J.F., Parente, M., Pelkey, S.M., Roush, T.L., Seelos, F.P., Smith, M.D., Wendt, L., Wolff, M.J., 2009. An improvement to the volcano-scan algorithm for atmospheric correction of CRISM and OMEGA spectral data. Planetary and Space Science 57, 809–815.
Mohlmann, D., 2004. Water in the upper Martian surface at mid- and low-latitudes: presence, state, and consequences. Icarus 168, 318–323.
Mohlmann, D., 2009. Temporary liquid water in upper snow/ice sub-surfaces on Mars? Icarus 207 140–148.
Mohlmann, D., 2010. The three types of liquid water in the surface of present Mars. International Journal of Astrobiology 9/1, 45–49.
Möhlmann, D., Kereszturi, A., 2010. Viscous liquid film flow on dune slopes of Mars. Icarus 207, 654–658. doi:10.1016/j.icarus.2010.01.002.
Montmessin, F., Forget, F., Rannou, P., Cabane, M., Haberle, R.M., 2004. Origin and role of water ice clouds in the Martian water cycle as inferred from a general circulation model. Journal of Geophysical Research 109, E10. doi: 10.1029/2004JE002284.
Morgan, F., Seelos, F., Murchie, S., 2009. CAT Tutorial. Presentation at the CRISM Workshop, The Woodlands, TX.
Murchie, S., Arvidson, R., Bedini, P., Beisser, K., Bibring, J.-P., Bishop, J., Boldt, J., Cavender, P., Choo, T., Clancy, R.T., Darlington, E.H., Des Marais, D., Espiritu, R., Fort, Green, R., Guinness, E., Hayes, J., Hash, C., Heffernan, K., Hemmler, J., Heyler, G., Humm, D., Hutcheson, J., Izenberg, N., Lee, R., Lees, J., Lohr, D., Malaret, E., Martin, T., McGovern, J.A., McGuire, P., Morris, R., Mustard, J., Pelkey, S., Rhodes, E., Robinson, M., Roush, T., Schaefer, E., Seagrave, G., Seelos, F., Silverglate, P., Slavney, S., Smith, M., Shyong, W.-J., Strohbehn, K., Taylor, H., Thompson, P., Tossman, B., Wirzburger, M., Wolff, M., 2007. Compact Reconnaissance Imaging Spectrometer for Mars (CRISM) on Mars Reconnaissance Orbiter (MRO). Journal of Geophysical Research 112, E05S03. doi:10.1029/2006JE002682.
Ness, P.K., Orme, G.M., 2002. Spider-ravine models and plant-like features on Mars—possible geophysical and biogeophysical modes of origin. Journal of the British Interplanetary Society 55 (3–4), 85–108.
Pelkey, S.M., Mustard, J.F., Murchie, S., Clancy, R.T., Wolff, M., Smith, M., Milliken, R., Bibring, J.-P., Gendrin, A., Poulet, F., Langevin, Y., Gondet, B., 2007. CRISM multi-spectral summary products: parameterizing mineral diversity on Mars from reflectance. Journal of Geophysical Research 112, E08S14. doi:10.1029/2006 JE002831.
Parente, M., 2008. A new approach to denoising CRISM images. In: Proceedings of the 39th Lunar and Planetary Science, Abstract 2528.
Piqueux, S., Byrbe, S., Richardson, M.I., 2003. Sublimation of Mars's Southern seasonal CO_2 ice cap and the formation of spiders. Journal of Geophysical Research 108, 5084.
Pocs, T., Horvath, A., Ganti, T., Berczi, Sz., Szathmary, E., 2003. Are the Dark Dune Spots Remnants of the Crypto-Biotic-Crust of Mars? Vernadsky/Brown Micro-symposium on Comparative Planetology 38.
Rennó, N.O., Bos, B.J., Catling, D., Clark, B.C., Drube, L., Fisher, D., Goetz, W., Hviid, S.,.F., Keller, H.U., Kok, J.F., Kounaves, S.P., Leer, K., Lemmon, M., Madsen, M.B., Markiewicz, W.J., Marshall, J., McKay, C., Mehta, M., Smith, M., Zorzano, M.P., Smith, P.H., Stoker, C., Young, S.,.M.M., 2009a. Possible physical and thermodynamical evidence for liquid water at the Phoenix landing site. Journal of Geophysical Research 114 (C10) CiteID E00E03.
Rennó, N.O., Mehta, M., Block, B.P., Braswell, S., 2009b. The discovery of liquid water on Mars and its implications for astrobiology. Instruments and Methods for Astrobiology and Planetary Missions XII. In: Proceedings of the SPIE, vol. 7441, pp. 74410C–74410C-12.
Reiss, D., Erkeling, G., Bauch, K.E., Hiesinger, H., 2010. Evidence for present day gully activity on the Russell crater dune field, Mars. Geophysical Research Letters 37, L06203. doi:10.1029/2009GL042192.
Schmidt, F., Douté, S., Schmitt, B., Vincendon, M., Bibring, J.-P., Langevin, Y., 2009. & the OMEGA Team, 2009. Albedo control of seasonal South Polar cap recession on Mars. Icarus 200, 374–394. doi:10.1016/j.icarus.2008.12.014.
Schmidt, F., Schmitt, B., Douté, S., Forget, F., Jian, J.-J., Martin, P., Langevin, Y., Bibring, J.-P., 2010. & the OMEGA Team, 2010. Sublimation of the Martian CO_2 Seasonal South Polar Cap Planetary and Space. Science 58, 1129–1138. doi:10.1016/j.pss. 2010.03.018.
Schmitt, B., Quirico, E., Trotta, F., Grundy, W.M., Schmitt, B., de Bergh, C., Festou, M. (Eds.), 1998. Optical Properties of Ices from UV to Infrared, Solar System Ices, 227. Kluwer, pp. 199–240.
Schmitt, B., Douté, S., Langevin, Y., Forget, F., Bibring, J.P., Gondet, B., 2005. and the OMEGA Team, 2005. Northern seasonal condensates on Mars by Omega/Mars Express. Lunar Planetary Science, 6 Abstract 2326.
Schmitt, B., Schmidt, F., Douté, S., Langevin, Y., Forget, F., Bibring, J.P., Gondet, B., and the OMEGA Team, 2006. Recession of the northern seasonal condensates on Mars by OMEGA/Mars Express. In: Proceedings of the Fourth Mars Polar Science Conference, Abstract 8050.
Schmitt, B., Appéré, T., Douté, S., Beck, P., Forget, F., Langevin, F.Y., Bibring, J.-P., 2009. Microphysical cycle of evolution of the northern Martian seasonal condensates. In: Proceedings of the Third International Workshop on Mars Polar Energy Balance and the CO_2 Cycle, Abstract 7027.
Shkuratov, Y., Starukhina, L., Hoffmann, H., Arnold, G., 1999. A Model of spectral albedo of particulate surfaces: implications for optical properties of the moon. Icarus 137, 235–246.
Szathmary, E., Ganti, T., Pocs, T., Horvath, A., Kereszturi, A., Berczi, Sz., Sik, A., 2007. Life in the dark dune spots of Mars: a testable hypothesis. In: Pudritz, Ralph, Higgs, Paul, Stone, Jonathan (Eds.), Planetary Systems and the Origin of Life. Cambridge University Press, pp. 241–262.
Titus, Timothy N., Kieffer, Hugh H., Christensen, Phillip R., 2003. Exposed water ice discovered near the South Pole of Mars. Science 299 (5609), 1048–1051.
Titus, T.N., 2005. Thermal infrared and visual observations of a water ice lag in the Mars southern summer. Geophysical Research Letters 32 (24), L24204. doi:10.1029/2005GL024211.
Titus, T.N., Kieffer, H.H., Langevin, Y., Murchie, S., Seelos, F., Vincendon, M., 2007. Bright Fans in Mars Cryptic Region Caused by Adiabatic Cooling of CO_2 Gas Jets. American Geophysical Union, Fall Meeting, Abstract #P24A-05.
Titus, T., 2008. Infrared observations of Mars south polar water ice. Mars Water Cycle Workshop, Paris.
Vincendon, M., Langevin, Y., Poulet, F., Bibring, J.-P., Gondet, B., 2007. Recovery of surface reflectance spectra and evaluation of the optical depth of aerosols in the near-IR using a Monte Carlo approach: application to the OMEGA observations of high-latitude regions of Mars. Journal of Geophysical Research 112, E08S13. doi:10.1029/2006JE002845.
Vincendon, M., Mustard, J., Forget, F., Kreslavsky, M., Spiga, A., Murchie, S., Bibring, J.-P., 2010. Near-tropical subsurface ice on Mars. Geophysical Research Letters 37, L01202. doi:10.1029/2009GL041426.
Vincendon, M., Forget, F., Mustard, J. Water ice at low to mid latitudes on Mars. Journal of Geophysical Research, in press, doi:10.1029/2010JE003584.
Wagstaff, K.L., Titus, T.N., Ivanov, A.B., Castaño, R., Bandfield, J.L., 2008. Observations of the north polar water ice annulus on Mars using THEMIS and TES. Planetary and Space Science 56, 256–265.
Zuber, M.T., 2003. Learning to think like Martians. Science 302, 1694–1695.

Chapitre 5

Les clathrates dans l'histoire de Mars



La carte de Mars dessinée par Schiaparelli en 1888.

La structure moléculaire de cage de molécule d'eau est appelée clathrate hydrate, parfois nommée simplement "clathrate" par commodité. Plusieurs structures de clathrate ont été décrites mais les plus communes sont les structures de type I et de type II. Dans celle de type I, la maille unitaire est formée de 46 molécules d'eau et contient 2 petites cages et 6 grandes cages. Dans la structure de type II, la maille consiste en 136 molécules d'eau et contient 16 petites cages et 8 grandes cages [26]. Chacune de ces cages peut contenir des molécules invitées qui stabilisent la structure (voir figure 5.1). Les clathrates ont été découverts sur Terre au XIXème siècle, mais leur présence est suspectée sur plusieurs corps du système solaire, les comètes, les satellites de glace mais aussi Mars.

La première section décrit l'état des discussions sur la possibilité de clathrate sur Mars, à la fois actuellement mais aussi dans le passé martien grâce aux traces géomorphologiques anciennes. La section 5.2 page 270 détaille mes contributions, dans le cadre d'une collaboration portée par Eric Chassefière. Enfin, les perspectives personnelles de ce travail seront exposées à la section 5.3 page 275.

5.1 Contexte

La présence de clathrate dans le passé de Mars est suspecté grâce à des indices géomorphologiques indirectes. Aussi l'existence de clathrates actuellement sur Mars a été suggéré sur des considérations de thermodynamiques et de géodynamiques. Depuis 1970, la possibilité de présence de clathrates sur les pôles de Mars a été évoquée [222]. En 1974, la déstabilisation des clathrates a été proposée pour expliquer l'origine des anciens chenaux de débâcle et les terrains chaotiques [223]. Les deux prochains chapitres argumentent ces hypothèses.

5.1.1 Indices géomorphologiques

Deux types de terrains majeurs nourrissent les suppositions de présence de clathrates sur Mars : les terrains chaotiques et vallées de débâcle associées, ainsi que les volcans de boues.

5.1.1.1 Terrains chaotiques et vallées de débâcle

Les terrains chaotiques sont les terrains de forme irrégulière, communément présents sur Mars à la fin de la période Hesperienne et Amazonienne, mais très rarement sur Terre (voir figure 5.2). Ils sont constitués par un ensemble de blocs angulaires de différentes tailles (du kilomètre à quelques dizaines de kilomètres), parfois séparés par des éléments linéaires, chaque bloc préservant la surface des hauts plateaux [291].

Les terrains chaotiques se sont vraisemblablement formés par l'effondrement localisé par l'érosion sous la surface de matière : glace, clathrates ou magma. Les terrains chaotiques sont reliés à de grands fossés et des chenaux de débâcles et sont situés généralement près de la dichotomie martienne. L'analogie entre ces gigantesques chenaux sur Mars et les inondations catastrophiques dans la région des Scablands (Etat de Washington) est basée sur la taille, le caractère anastomosé régional, la faible sinuosité, les collines et cratères profilés, l'escarpement en amont des obstacles à l'écoulement [11, 10]. Sur la base de cette analogie, le débit peut être estimé jusqu'à 10^9 m^3/s [31, 167] sur une échelle de temps de 10^3 à 10^6 ans [167]. Certaines analyses indiquent plusieurs étapes dans la formation du chaos, comme dans Xanthe Terra [272].

La dissociation catastrophique de clathrate de dioxyde de carbone a été proposée comme l'origine des inondations gigantesques sur Mars, ce qui explique à la fois les grands débits d'eau et le volume manquant des terrains chaotiques [223, 132]. La décomposition de 1 m^3 de clathrate hydrate produit ~ 164 m^3 de gaz (au condition standard) et 0,87 m^3 d'eau liquide [52]. Une autre possibilité pour la formation chaos serait la rupture d'un aquifère sous pression confiné par de la glace d'eau [31] et/ou des clathrates [213] ou un pergélisol [31]. La formation de Ganges Chaos a été interprétée comme une couche de glace/clathrate fragile sur un liquide de CO_2/H_2O qui en se déstabilisant, a créé une exsolution rapide de volatils [270]. Dans ce cas, l'eau de fonte était déjà présente dans le sous-sol en raison du flux de chaleur interne [31, 52] à une profondeur dépendante de la quantité de sel et de perchlorate [53]. En

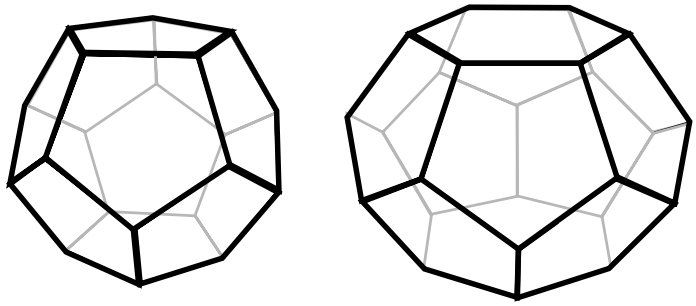


FIGURE 5.1: Schéma des petites cages de diamètre moyen 3.95 nm (à gauche) et grande cage de diamètre moyen 4.33 nm (à droite) présentes dans les clathrates hydrates, d'après [26]



FIGURE 5.2: Les terrains chaotiques sur Mars d'après une mosaïque Viking. Le chaos a un diamètre de 40 km et l'écoulement une section de 20 km. Figure d'après [31].

outre, la forme complexe du chaos peut s'expliquer par la fluidisation des matériaux lors de l'intense libération de gaz et la liquéfaction des sédiments [168].

La détection de petits volcans dans Hydrates Chaos indique que la déstabilisation a pu être produite par une intrusion magmatique [219], mais de nombreuses causes plausibles de déstabilisation ont été proposées, y compris le changement climatique [52], le flux interne de chaleur [52], la propagation de fracture [270], et l'activité sismique [245, 308]. Une autre possibilité serait la fonte de la glace du pergélisol le long de dykes [217]. Toutefois, le volume total de glace dans le sol de Mars semble être insuffisant pour rendre compte de l'ampleur des débits [52]. Max et Clifford (2001) ont fait valoir que seul un scénario d'aquifère est réaliste, avec possibilité de clathrates dans le pergélisol [213]. La présence d'une couche de clathrates est controversée, car la sublimation et la fonte de la glace peuvent entraîner des caractéristiques géomorphologiques similaires. Il existe de rares régions de chaos non connectées à une vallée de débâcle, impliquant que la phase liquide n'est pas nécessaire. Par exemple, Galaxia chaos a pu se former par sublimation de la glace sous la lave [253]. En outre, la décomposition de clathrates (avec une chaleur latente de fusion de ~73 kJ / mol) est plus difficile que la fusion de la glace (~ 6 kJ / mol) [52]. Enfin, le fluide à l'origine des chenaux de débâcle doit être stable pendant toute la durée de l'écoulement sur 1500 km de distance. Cela pourrait aussi remettre en question la présence d'eau liquide à cause des faibles pressions atmosphériques supposées.

5.1.1.2 Volcans de boue

Les volcans de boue sont présents sur Terre, sur les continents, les océans et en base des lacs (voir figure 5.3). Il s'agit d'édifice conique de taille métrique kilométriques avec des écoulements sporadiques de boue s'échappant du sommet [214]. Ils sont formés par des éjections de gaz, d'eau et de sédiments, depuis la subsurface, à cause des fortes pressions. Sur Terre, la déstabilisation des clathrates a souvent été proposée pour être à l'origine des volcans de boues sous-marins [221]. Les différents travaux d'analogie entre les terrains terrestres et martiens ont été synthétisés récemment [298, 169]. Les volcans de boues ont été proposés dans plusieurs régions comme Acidalia Planitia [85, 248], Chryse [307, 271], Cydonia Mensae [85].

5.1.2 Indices de clathrate actuel

La synthèse des observations et discussions de la détection actuelle de méthane sur Mars, hautement variable, enrichi dans la haute atmosphère, est exposée au chapitre 3.1.1 page 134. Notons simplement qu'une hypothèse de la présence de CH_4 actuel, serait sous forme de clathrate métastable dans l'atmosphère [38].

Les différentes hypothèses de formation de clathrate actuellement sur Mars ont été récemment compilées [43, 231]. Le méthane a pu se former en profondeur par serpentinisation, c'est à dire par altération aqueuse (hydrothermalisme) en présence de CO_2, et de minéraux ultra-mafiques (olivine fayalite, pyroxène riche en Fer) [249, 203]. Aussi, la serpentinisation produit du CH_4 qui pourrait être un puits additionnel de O, en accord avec l'échappement relatif de O et H [40]. Cette hypothèse est valide uniquement si l'échappement du H_2 par serpentinisation, entre 10 et 100 fois plus que celui du CH_4 est relativement ancien (âge >1000 ans), ce qui impliquerait la présence d'une couche tampon de CH_4 entre le lieu de l'hydrothermalisme en profondeur et la surface. Le clathrate de CH_4 pourrait jouer ce rôle. De plus, la serpentinisation conduit à un fort fractionnement isotopique de l'hydrogène et expliquerait que le rapport actuel D/H proviendrait du stockage sous forme de serpentine de grandes quantités d'eau, en accord avec la démagnétisation de la planète (couche globale équivalente d'eau de plusieurs centaines de mètres de profondeur) [42].

Une fois formé en profondeur, le méthane ainsi libéré remonte et peut être piégé à l'intérieur les cages de clathrate formé sous la cryosphère, comme représenté sur la figure 5.4 [43, 39], puis éventuellement être relargué en surface sous forme de gaz ou sous forme de clathrate métastable dans l'atmosphère [38]. Des études expérimentales montrent que cette hypothèse est possible [97]. Sous l'effet des changements d'obliquité, des couches à différentes attitudes ont pu se former et se déstabiliser [267].

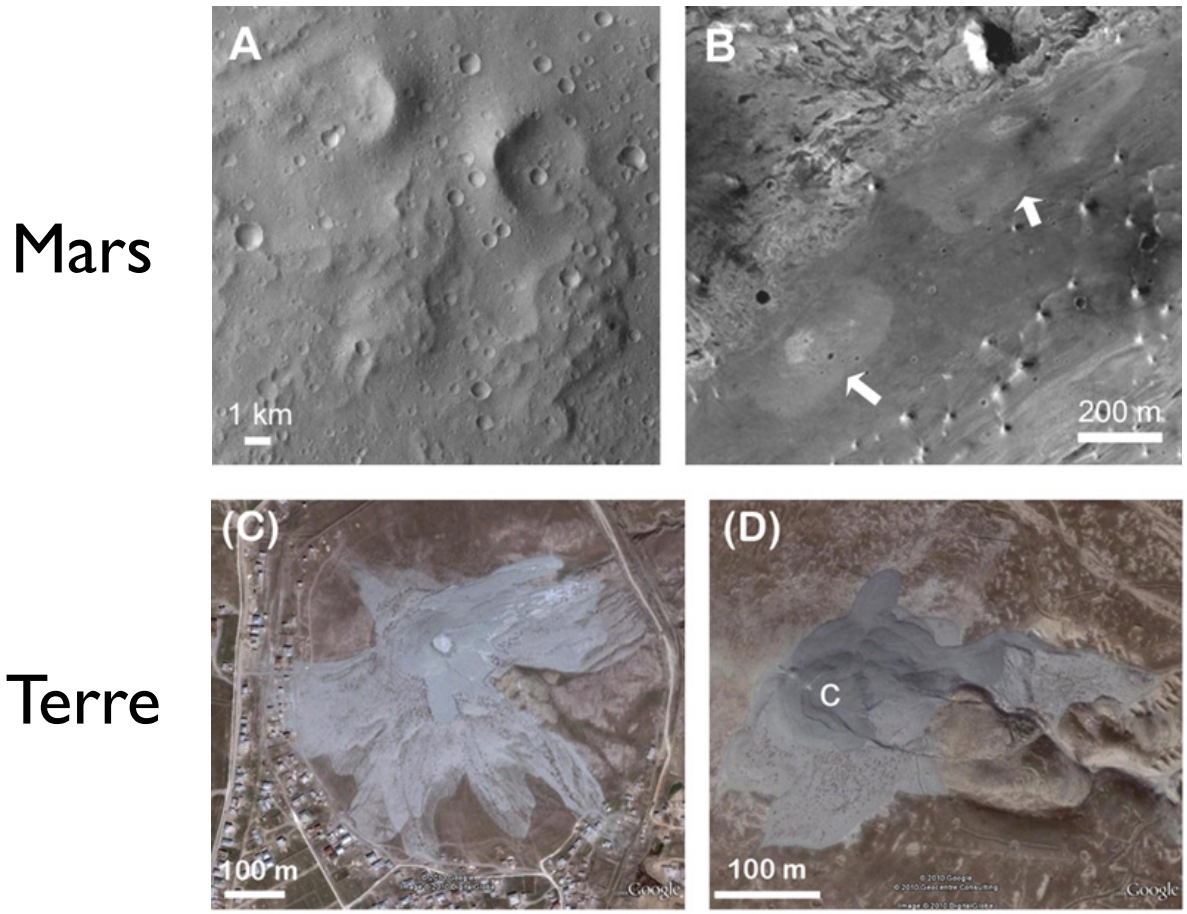


FIGURE 5.3: Analogie entre les volcans de boue Martiens et Terrestre. (A) Au Sud d'Utopia Planitia, d'après [298] (Image THEMIS visible V14113011). (B) Vernal Crater dans Arabia Terra (image HiRISE PSP_002812_1855) d'après [4] (C) Baku, Azerbadjian d'après [169] (Image Google Earth) (D) Baku, Azerbadjian un cratère sommital, noté (c) d'après [169] (image Google Earth)

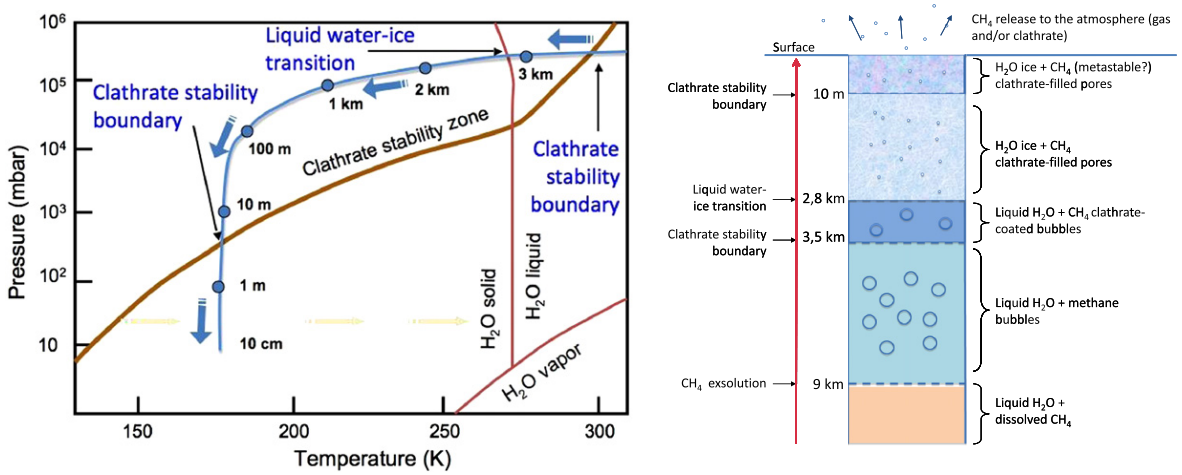


FIGURE 5.4: Schéma de principe de formation de clathrate dans la subsurface, d'après [43, 39]

Dans l'atmosphère, l'oxydation du CH_4 en CO_2 a dû produire des quantités de gaz du même ordre de grandeur que le dégazage volcanique, de l'ordre de 400 mbar chacun. Le CO_2 a pu précipiter sous forme de carbonate dans la croûte. Dans ce cas, les carbonates eux-même pourraient être la source de CO_2 pour la serpentinisation puisque la dissolution de ces carbonates serait à l'origine du C [39].

Aussi, la formation de clathrate de CO_2 en surface, incorporant le gaz atmosphérique (CO_2 à 95 %) est possible sur les calottes polaires, si la nucléation est suffisamment rapide [197]. Une autre étude montre que des clathrates de Ar, N_2 et CH_4 peuvent aussi se former en surface [127]. Les gaz piégés dans le clathrate hydrate sont significativement appauvri en méthane par rapport à la phase gazeuse d'un facteur 0.2, ce qui montre que ce mécanisme de formation ne joue pas un rôle majeur pour expliquer la présence de méthane sur Mars.

Dans le but d'identifier cette phase dans les milieux planétaires et astrophysiques par télédétection, plusieurs études expérimentales de spectroscopie ont été menées sur des clathrates de CH_4 [61], CO_2 [62, 246], H_2S [63], CO, [60].

Précisons néanmoins que pour l'instant **aucune** détection directe de présence de clathrate n'a pu être démontrée sur Mars par détection spectroscopique ou analyse in situ.

5.2 Contributions

Dans le passé de Mars, les clathrates de SO_2 ont pu jouer un rôle majeur dans le climat et la formation massive de souffre. Sur des arguments de thermodynamique et de géomorphologie, j'ai contribué à la discussion de la validité de cette hypothèse dont les aspects les plus importants sont décrits ci-après. Mon travail a constitué en une synthèse de travaux de plusieurs collaborateurs : des résultats théoriques sur l'enrichissement lors de la formation d'un clathrate mixte SO_2 et CO_2, des résultats de modèles climatiques et des observations géomorphologiques.

La figure 5.5 présente les résultats d'un modèle 1d de climat incorporant des processus photochimiques et microphysiques de SO_2 et CO_2 [319] et le diagramme de stabilité des clathrates de CO_2 [230]. Le CO_2 seul permet d'augmenter la température moyenne de 200K à 230K entre 0.001 bar et 3 bar. Mais la modélisation du climat montre que le SO_2 est un puissant gaz à effet de serre, qui peut augmenter fortement la température, par exemple de 10K dès une concentration de 1 ppmv (10^{-6}). Cette augmentation de température doit être très courte car sous l'effet photochimique, le SO_2 se condense sous forme de particules de S et de sulfate avec un fort pouvoir réfléchissant, ce qui réduit fortement la température de surface, de ~15K pour 1 ppmv de SO_2, soit un abaissement net de ~5K. Dans ce cas, la courbe d'équilibre des clathrates est franchie et la formation de clathrate de CO_2/SO_2 peut se faire en surface. Pour des valeurs de 10 ppmv de SO_2, l'effet radiatif global est un abaissement de température de plus de 30K, encourageant la condensation de clathrate mais aussi du CO_2 pure.

Dans le cas d'une précipitation intense de particule SO_2, sous l'effet de la pluie par exemple, de grande quantité de SO_2 gaz peuvent être stockée dans l'atmosphère dans un équilibre dynamique avec la précipitation, à haute température. En revanche, dès que l'arrêt de la pluie s'opère, l'effet refroidissant des particules reprend le dessus et la planète se refroidit fortement.

La figure 5.6 présente le même mécanisme sous forme d'un diagramme de température de surface en fonction de la concentration en SO_2. A 1.5 bar de CO_2, si l'atmosphère contient plus de 7 ppmv de SO_2, alors l'effet de refroidissement des aérosols induit une température de surface inférieure à 135K et les clathrates vont se condenser. Il en est de même à 1 bar (respectivement 0.5 bar), si la concentration est supérieure à 30 ppmv (respectivement 200 ppmv). Pour une pression de 3 bar de CO_2, le clathrate se forme naturellement, sans effet refroidissant du SO_2. Grâce à ce mécanisme, le clathrate se forme pendant toute la période de "haute concentration en SO_2".

Lors de la clathratisation de l'atmosphère de CO_2, les espèces minoritaires comme le SO_2 sont incorporés dans les cages. Les calculs thermodynamiques montrent que l'enrichissement du SO_2 peut se faire d'un facteur 100 à 10 000 en fonction des conditions de température et de concentration en SO_2 [41]. Dans ce cas, la clathratisation de l'atmosphère abaisse la concentration en SO_2, ce qui conduit à une boucle de rétro-action et un "équilibre tampon", entre la quantité de SO_2 dans l'atmosphère, la tem-

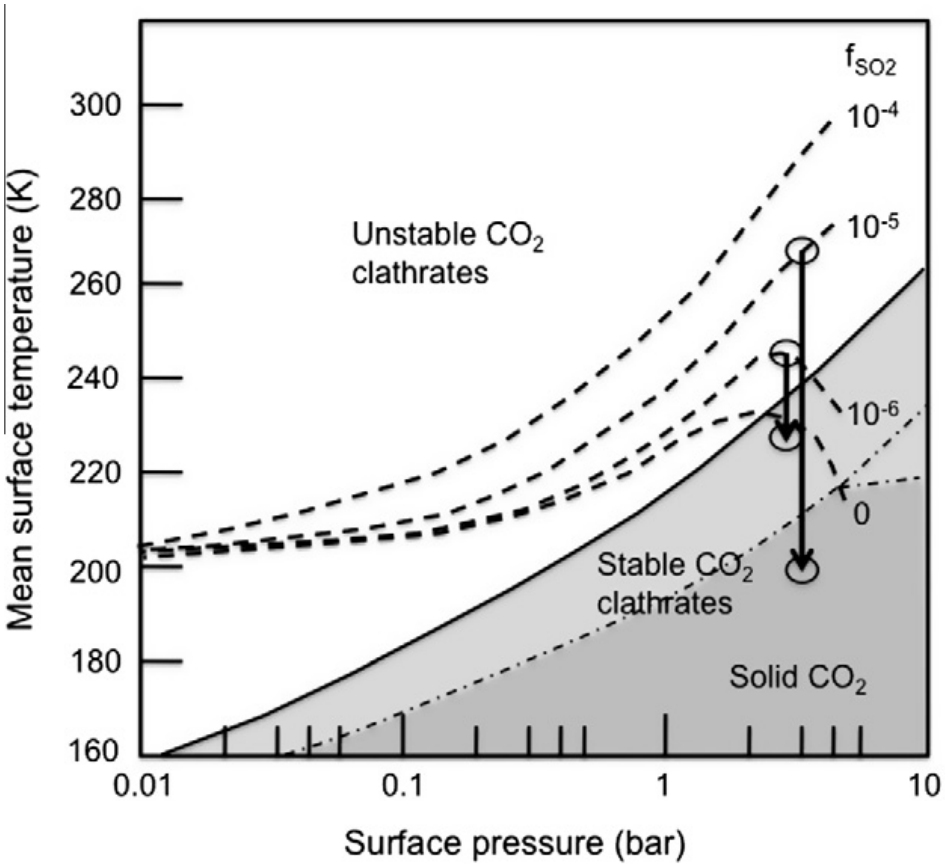


FIGURE 5.5: Diagramme de phase de présence de clathrate de SO_2 et CO_2, d'après un modèle photochimique de climat [319] : (a) en pointillé uniquement l'effet du gaz avec les concentrations volumiques ; (b) les flèches représentent l'effet réfléchissant et donc refroidissant des aérosols de S ; (c) le diagramme de stabilité des clathrates de CO_2 d'après [230]. Figure d'après [41]

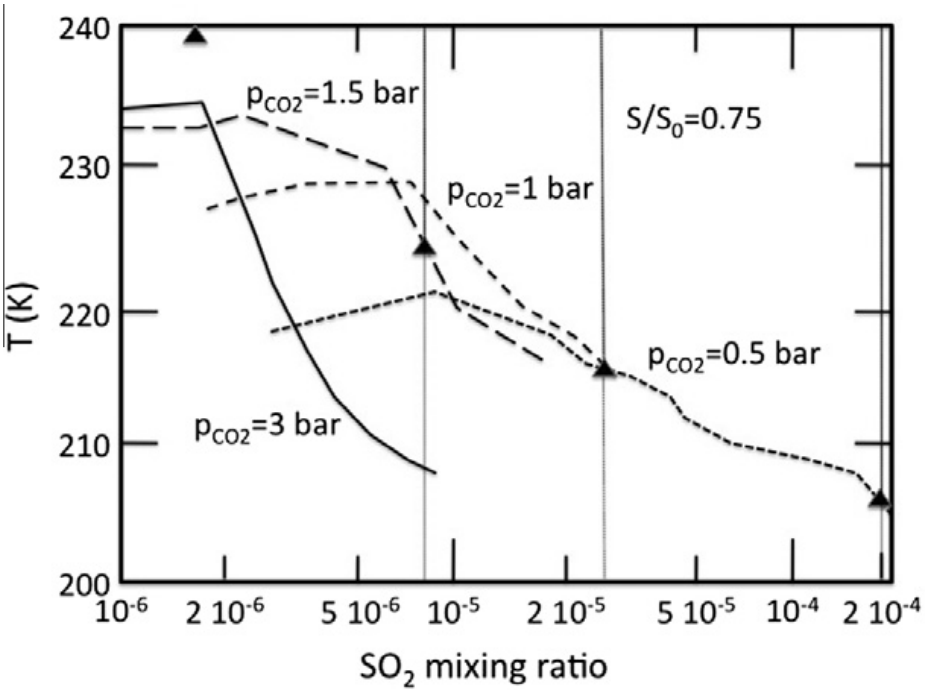


FIGURE 5.6: Température de surface en fonction de la quantité de SO_2 pour plusieurs pression atmosphérique de CO_2 d'après le modèle photochimique de climat dans des conditions de 75% du flux solaire actuelle. Les triangles représentent le point d'équilibre des clathrate. Figure d'après [41]

pérature de surface et le SO_2 stocké sous forme de clathrate. La figure 5.7 montre le même processus, en fonction des volumes éruptés. Par exemple à 1.5 bar, des volumes cumulés d'éruptions de plus de 1500 km^3 produiront une concentration de plus de 7 ppmv de SO_2 dans l'atmosphère qui induira un refroidissement de la planète et la formation de clathrate, jusqu'à l'équilibre à la valeur de 7 ppmv.

Une hypothèse forte de ce modèle est la présence d'eau disponible en surface, de manière à former les clathrates. Bien que les quantités totales d'eau sur Mars soient suffisantes, avec 35 m de réservoir apparent (pôle et glacier) [49], 500 m dans la cryosphère [53] et encore 500 m dans les aquifères sous la cryosphère [53], cette eau a dû se trouver toujours disponible en surface pour la formation de clathrate. De plus, on suppose que le temps de cinétique de formation des clathrates n'est pas limitant.

Finalement, ce scénario peut être appliqué à l'histoire climatique de Mars (voir figure 5.8). Durant toute l'histoire de Mars, la pression de CO_2 disponible en surface (atmosphère et proche surface) a diminué d'une valeur initiale de ~100 bar jusqu'à ~10 mbar aujourd'hui, soit par échappement, soit par carbonatation en profondeur. A un moment, la pression atmosphérique était inférieure à 2 bar et dans ce cas, l'équilibre tampon, décrit précédemment, s'est mis en place pour une surface à 230K. Depuis ce moment, toutes les éruptions volcaniques ont produit du SO_2 de manière à saturer l'atmosphère en SO_2 à la valeur donnée par la figure 5.7, et enrichir les clathrates en SO_2. Progressivement, la quantité de CO_2 en surface a diminué et le réservoir de clathrate de CO_2 s'est tari pour laisser place à un clathrate enrichi en SO_2. A la transition Noachien/Hespérien, la déstabilisation des clathrates majoritairement composés de SO_2 d'une épaisseur équivalente globale de 290-720 m, a permis un relargage massif du SO_2 dans l'atmosphère. Ce qui a induit une précipitation massive de particules de sulfate d'une épaisseur équivalent globale de 20-50 m en 40-1000 Ma. D'autre part, cette période de relargage massif de SO_2 est la période la plus propice pour un réchauffement temporaire par le mécanisme de pluie (voir figure 5.5), car la température et la pression sont les plus proches du point triple de l'eau. Aussi la concentration de SO_2 dans les réservoirs de proche surface et de l'atmosphère a dû être maximum dans cette période, et donc a pu induire un fort effet de serre.

Le scénario décrit précédemment est compatible avec plusieurs observations géomorphologiques :

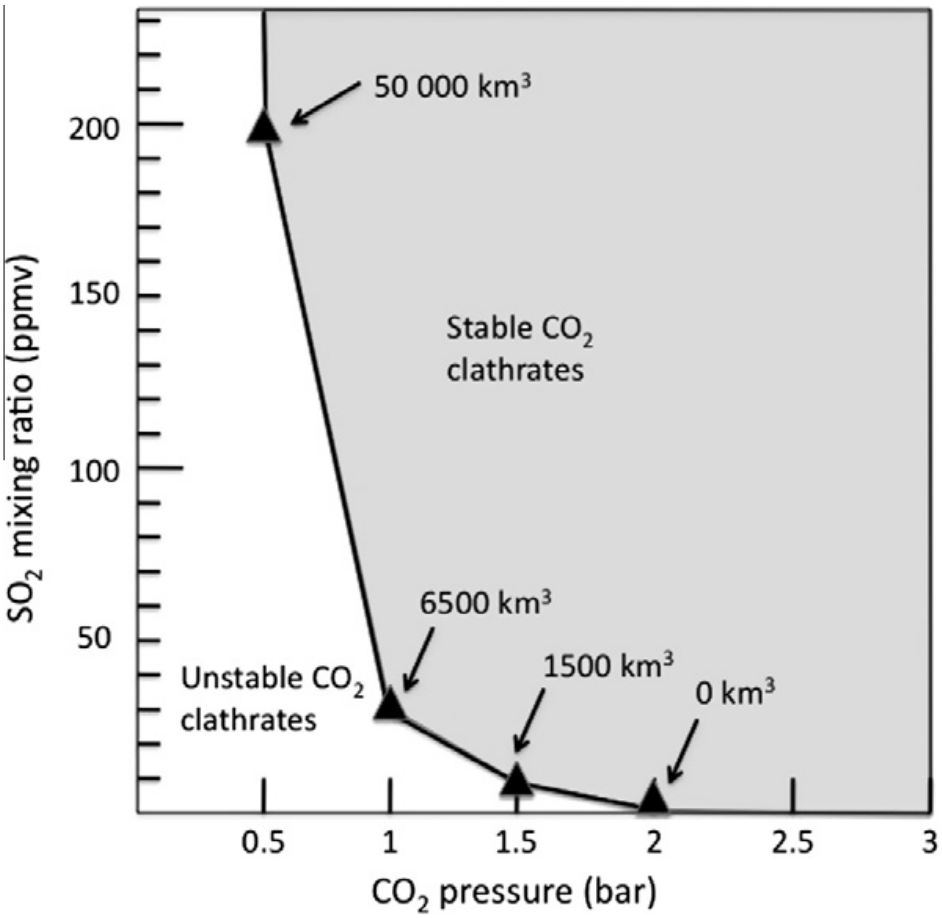


FIGURE 5.7: Concentration de SO_2 à l'équilibre en fonction de la pression en CO_2. Les chiffres correspondent aux volumes d'éruptions nécessaire à produire une quantité correspondante de SO_2. Figure d'après [41]

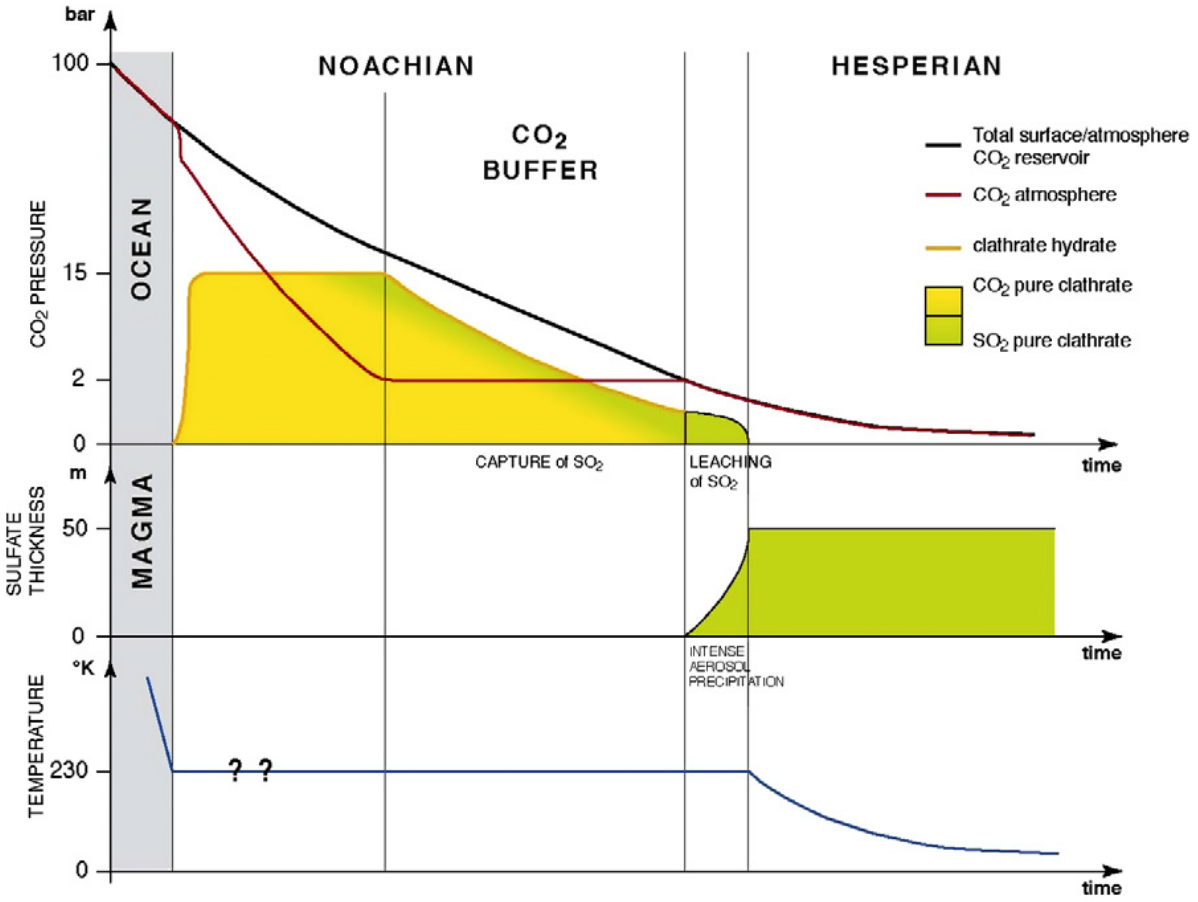


FIGURE 5.8: Histoire climatique de Mars d'après le scénario de formation des équilibre tampon de SO_2/CO_2. Figure d'après [41]

- La présence d'une couche de massive de sulfate à l'échelle de Mars à l'Hesperien, détectée sur Valles Marineris [20, 183, 338], Meridiani [304], Aram Chaos [211] et Syrtis Major [79]. Cette couche est présente sur des endroits très escarpés, comme les ILD au sommet de Valles Marineris, suggérant une formation par précipitation [220]. Les couches sont épaisses, de l'ordre de 5km pour les ILD [241], et formées rapidement en 400 Ma [268]
- La présence de terrain chaotique à l'Hesperien/Amazonien (voir section 5.1.1.1). Nous proposons que la couche de clathrate riche en SO_2 ait été déstabilisée en partie, par la baisse de pression atmosphérique sous 2 bar à la transition Hesperien. D'autre part, si l'on considère que 1/5 de la surface de Mars soit recouverte de ces clathrates, l'épaisseur estimée des clathrates de 1500-3500 m est compatible avec le dénivelé des chaos de l'ordre de ~3000 m.
- La présence de réseau de vallées dendritiques sur Mars d'âge majoritairement Noachien/Hespérien [210, 24][210, 24]. Ces réseaux impliquent la précipitation, au moins sporadique, d'un liquide à la surface de Mars, vraisemblablement de l'eau.

Pour plus de détails, l'article est disponible à la section 5.4.1

5.3 Perspectives

Une perspective intéressante pour estimer la validité de l'hypothèse de la déstabilisation de clathrate dans la formation des terrains chaotiques et des vallées de débâcle serait la modélisation numérique. Des travaux intéressants ont déjà montré que cette hypothèse est plausible [270, 151], en particulier parce que la conductivité thermique des clathrates est relativement faible, induisant une augmentation de température sous la couche. Ce travail consistera, dans un premier temps, en une étude géomorphologique détaillée des vallées de débâcle et des terrains chaotiques à partir des images récentes HiRISE, des données de topographie MOLA et de stéréoscopie HRSC et HiRISE. Quel est le lien entre ces deux unités ? Il s'agira aussi de réaliser une modélisation thermique, thermodynamique et mécanique de la déstabilisation de clathrates souterrains pour estimer si la formation de chaos/vallées de débâcle est possible, quels en sont les mécanismes (fluidisation ou fonte) et aussi pour déterminer les conditions nécessaires à cette formation.

Sur l'aspect de l'histoire du climat de Mars et de l'effet "équilibre tampon" du SO_2, nous avons proposé un schéma de principe (voir figure 5.8) de l'histoire martienne de type 0d. Il serait intéressant de développer un modèle plus réaliste en 1d, comportant une dimension latitudinale et une paramétrisation de la circulation atmosphérique et des échanges avec la subsurface, afin d'étudier les variations saisonnière en surface, à la manière de la modélisation de la présence de glace en subsurface dans les derniers millions d'années [289]. Ce type de modélisation nous permettra d'estimer comment la formation/déstabilisation de clathrate s'opère au cours de l'année, de la saison, et au cours des cycles astronomiques. Il s'agira de déterminer si la formation de couche de clathrate proche de l'équateur est possible, en accord avec les observations de chaos.

Une autre piste intéressante serait de combiner les cycles de SO_2 et CO_2, en reliant la précipitation de carbonate avec l'effet "équilibre tampon" du SO_2 pour proposer un mécanisme possible à la chute de pression atmosphérique de l'Hesperien. Pour l'instant, notre scénario (voir figure 5.8) propose comme condition au limite une diminution du réservoir glace/atmosphère de CO_2 en surface, mais l'échappement ne peut en aucun cas l'expliquer [37]. Un mécanisme possible pour expliquer cette diminution du CO_2 est la précipitation de carbonate, induite par le SO_2. Nous pouvons proposer deux processus :

- L'appauvrissement de la cryosphère en SO_2 lors de la phase de relargage massif, se traduirait par une baisse de l'acidité des eaux de fonte de la cryosphère dans des zones de chauffage interne génératrices d'hydrothermalisme, où peuvent se former les carbonates [41]. Le milieu étant moins acide, les carbonates vont se déposer plus facilement, résultant en une décroissance supplémentaire du CO_2. Ce mécanisme aurait une rétroaction positive conduisant à une chute brutale de la pression de CO_2, contemporaine au relargage de SO_2.
- De façon plus élaborée, un autre processus géochimique a été proposé [96], impliquant du SO_3 très acide (résultant de l'oxydation du CO_2) attaquant la roche et libérant des cations. En surface,

ce processus formerait des sulfates alors que le CO_2 resterait passif car il n'est pas consommé par l'altération. En profondeur SO_3 s'épuise, et le pH remonte suffisamment pour que le CO_2 puisse précipiter. Schématiquement, lorsque SO_2, donc SO_3, augmente dans l'atmosphère, le CO_2 est minéralisé en profondeur.

L'enjeu en est très important puisque, si ce processus se confirme, il fournira la seule explication existante à ce jour de la dissipation de l'atmosphère martienne à l'Hespérien.

5.4 Publications

Publications scientifiques :

- Mousis, O., Chassefière, E., Lasue, J., Chevrier, V., Elwood Madden, M., Lakhlifi, A., Lunine, J., Montmessin, F., Picaud, S., **Schmidt, F.** & Swindle, T. D. (2013), « Volatile Trapping in Martian Clathrates », Space Science Reviews, 174, 213-250
- Chassefière, E., Dartois, E., Herri, J.-M., Tian, F., **Schmidt, F.**, Mousis, O. & Lakhlifi, A. (2013), « CO_2-SO_2 clathrate hydrate formation on early Mars », Icarus, 223, 878-891 (voir section 5.4.1)

5.4.1 Clathrate de CO_2/SO_2 sur Mars

Cette section contient l'article suivant :

Chassefière, E., Dartois, E., Herri, J.-M., Tian, F., Schmidt, F., Mousis, O. & Lakhlifi, A. (2013), « CO_2-SO_2 clathrate hydrate formation on early Mars », Icarus, 223, 878-891

Icarus 223 (2013) 878–891

Contents lists available at SciVerse ScienceDirect

Icarus

journal homepage: www.elsevier.com/locate/icarus

CO_2–SO_2 clathrate hydrate formation on early Mars

Eric Chassefière [a,b,*], Emmanuel Dartois [c], Jean-Michel Herri [d], Feng Tian [e], Frédéric Schmidt [a,b], Olivier Mousis [f,g], Azzedine Lakhlifi [f]

[a] Univ Paris-Sud, Laboratoire IDES, UMR 8148, Université Paris-Sud, Bât. 504, Orsay F-91405, France
[b] CNRS, Orsay F-91405, France
[c] IAS, Université Paris-Sud, CNRS, France
[d] Centre SPIN, ENS des Mines de Saint-Etienne, France
[e] Center for Earth System Sciences, Tsinghua University, Beijing, China
[f] Institut UTINAM, UMR 6213, Université de Franche-Comté & OSU THETA de Franche-Comté, France
[g] Université de Toulouse, UPS-OMP, CNRS-INSU, IRAP, Toulouse, France

ARTICLE INFO

Article history:
Received 7 July 2012
Revised 20 November 2012
Accepted 2 January 2013
Available online 16 January 2013

Keywords:
Ices
Mars atmosphere
Mars climate
Mars surface
Volcanism

ABSTRACT

It is generally agreed that a dense CO_2-dominant atmosphere was necessary in order to keep early Mars warm and wet. However, current models have not been able to produce surface temperature higher than the freezing point of water. Most sulfate minerals discovered on Mars are dated no earlier than the Hesperian, despite likely much stronger volcanic activities and more substantial release of sulfur-bearing gases into martian atmosphere during the Noachian. Here we show, using a 1-D radiative–convective-photochemical model, that clathrate formation during the Noachian would have buffered the atmospheric CO_2 pressure of early Mars at ~2 bar and maintained a global average surface temperature ~230 K. Because clathrates trap SO_2 more favorably than CO_2, all volcanically outgassed sulfur would have been trapped in Noachian Mars cryosphere, preventing a significant formation of sulfate minerals during the Noachian and inhibiting carbonates from forming at the surface in acidic water resulting from the local melting of the SO_2-rich cryosphere. The massive formation of sulfate minerals at the surface of Mars during the Hesperian could be the consequence of a drop of the CO_2 pressure below a 2-bar threshold value at the late Noachian–Hesperian transition, which would have released sulfur gases into the atmosphere from both the Noachian sulfur-rich cryosphere and still active Tharsis volcanism. A lower value of the pressure threshold, down to ~0.5 bar, could have been sufficient to maintain middle and high latitude regions below the clathrate formation temperature during the Noachian and to make the trapping of SO_2 in clathrates efficient. Our hypothesis could allow to explain the formation of chaotic terrains and outflow channels, and the occurrence of episodic warm episodes facilitated by the release of SO_2 to the atmosphere. These episodes could explain the formation of valley networks and the degradation of impact craters, but remain to be confirmed by further modeling.

© 2013 Elsevier Inc. All rights reserved.

1. Introduction

Sulfur dioxide (SO_2) has been proposed as a possible greenhouse gas which worked together with CO_2 to raise the surface temperature of early Mars above the freezing point of water (Halevy et al., 2007; Johnson et al., 2008; Postawko and Kuhn, 1986), allowing liquid water to flow at the surface of the planet and carving the presently observed valley networks and outflow channels. However, the cooling from sulfur gases as a result of sulfate aerosol formation is an observational fact for the current atmosphere of Earth. On early Mars, the cooling effect of sulfate aerosols would also have counteracted efficiently the warming effect due to SO_2 greenhouse effect and sulfur outgassing. After a short period of warming, the presence of sulfate aerosols would have resulted in a colder surface, with a net cooling, instead of warming, of the planet (Tian et al., 2010). No mechanism to keep ancient Mars warm and wet through greenhouse effect has been generally accepted so far, suggesting a cold and wet early Mars. Much of the aqueous activity on Mars could have occurred in subsurface hydrothermal systems powered by magmatic or impact activity (Squyres and Kasting, 1994; Griffith and Shock, 1995; Segura et al., 2002, 2008), rather than at the surface of the planet.

Sulfur, under both oxidized (SO_2) and reduced (H_2S) forms, could have been released in large amount by volcanism during the Noachian. From several 100 millibar to around one bar of sulfur could have been outgassed along martian history, most of which during the Noachian and the Hesperian (see e.g. Craddock and Greeley, 2009; Gaillard and Scaillet, 2009). The reconstructed

* Corresponding author at: IDES, Université Paris-Sud, CNRS, France. Fax: +33 1 69 15 49 11.
E-mail address: eric.chassefiere@u-psud.fr (E. Chassefière).

0019-1035/$ - see front matter © 2013 Elsevier Inc. All rights reserved.
http://dx.doi.org/10.1016/j.icarus.2013.01.001

evolution of the cumulated amount of released SO_2 since the early Noachian, shortly after accretion, is shown in Fig. 1. It has been derived from both the CO_2 volcanic release rates calculated from a thermo-chemical evolution model of Mars (Grott et al., 2011) and a photogeological analysis of the martian surface (Craddock and Greeley (2009), referred to as CG09 in this paper). The ratio between SO_2 and CO_2 molar fractions in the volcanic gas f_{SO2}/f_{CO2} is typically in the range from 0.5 to ~1 (see Fig. 5 in Gaillard and Scaillet (2009)). The evolutions of the CO_2 partial pressure (denoted by p_{CO2} in the following) for two values (0.01 and 1) of the surface fraction covered by hot upwellings (f_p) are plotted on Fig. 4b in Grott et al. (2011). By applying the ratio f_{SO2}/f_{CO2} to Grott et al. curves, and taking into account the difference of molar mass between CO_2 (44 g/mol) and SO_2 (64 g/mol), we have plotted in Fig. 1 the corresponding evolutions of the cumulated amount of outgassed SO_2, expressed in pressure units, and the corresponding global equivalent layer (GEL) thickness of the sulfate mineral assuming that all the released sulfur is involved in anhydrite formation. The other plotted curve is obtained from a photogeological analysis of the martian surface yielding a cumulated lava extrusion volume of 0.7×10^8 km^3 (CG09), by assuming that basalts contain 7000 ppm sulfur by mass (an upper range according to Gaillard and Scaillet (2009)), that is 10 times more than assumed in CG09. This curve would be ~3 times lower assuming a lower range of 2500 ppm of S and four times higher assuming a lava extrusion volume of 3×10^8 km^3 (Gaillard and Scaillet, 2009). Both models and observations therefore suggest a cumulated pressure of outgassed SO_2 of typically ~1 bar, corresponding to a ~40 m thick sulfate GEL, within a factor of 3 both ways.

Interestingly, all sulfate minerals detected at the surface of Mars by OMEGA/Mars Express have been emplaced during the Hesperian, a relatively late epoch in martian history (Bibring et al., 2006). Later observations of CRISM on MRO have revealed additional sulfate deposits, a few of them under the form of interbedded phyllosilicate and sulfate layers in sediments of Noachian craters (Terra Sirenum) in the Southern hemisphere (Murchie et al., 2009). These intracrater deposits are relatively widespread, far from those mapped by OMEGA and at higher elevation, excluding that they have been transported from equatorial regions (Wray et al., 2011). Although a younger age for these sediments cannot be excluded, they are suspected to have formed by evaporitic processes in an acidic context at the Noachian. Such formations associating phyllosilicates and sulfates are also found in terrestrial acidic saline lake deposits (Baldridge et al., 2009). Most of sulfate deposits are observed in Hesperian terrains. They consist of several kinds of formations: (i) Hesperian layered sulfates under the form of extended deposits in Terra Meridiani, (ii) Interior Layered Deposits (ILD) throughout the Valles Marineris trough system consisting of massive mounds of layered material up to several kilometers thick, (iii) gypsum deposits in north polar dune field (Gaillard et al., 2013). Sulfur is also part of soil and dust at the global scale at an average level of ~6.8% (King and McLennan, 2010). It has been suggested that some sulfates could have been formed by evaporitic processes in the Valles Marineris region prior to Tharsis formation, then redistributed by fluvial transport to Meridiani Planum, where they are now observed, during the elevation of the Tharsis uplift (Fan et al., 2008). If so, sulfates detected in Hesperian terrains could have been formed in the Noachian. The question of the origin of sulfates is debated, and at least some of the observed deposits could have formed in the late Noachian. In the present paper, we make the hypothesis that most of the sulfates observed in equatorial regions (layered deposits, ILD) have been formed at the Hesperian (not excluding a start at the late Noachian), and propose an explanation for the scarcity of sulfates in Noachian terrains, and their apparently massive deposition at the Hesperian.

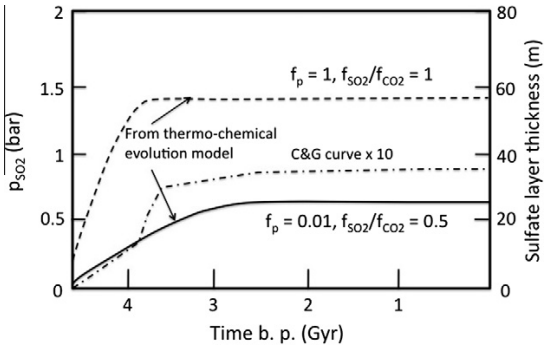


Fig. 1. Evolution of the cumulated amount of volcanically released sulfur in terms of SO_2 pressure (left vertical scale) and thickness of the corresponding sulfate mineral GEL (right vertical scale), assuming full conversion of sulfur into sulfate minerals. The "C&G" curve (dotted-dashed line) is obtained by multiplying by 10 the curve proposed in CG09 from a photogeological analysis of surface morphology (Greeley and Schneid, 1991). The two other curves are derived from CO_2 evolution curves proposed by Grott et al. (2011), as explained in the main text. These curves give the amount of CO_2 released from mantle carbon and do not include a possible contribution of superficial carbon (e.g. carbonates) to the volcanic CO_2.

The evolution of CO_2 on Mars is poorly constrained. Despite the discovery of carbonates in SNC meteorites and the recent orbital and in situ observations of carbonate rocks at some locations on the surface of Mars (see e.g. Niles et al., 2013), carbonates are not proved to be extensively present on Mars. The lack of global carbonate outcrops on Mars, which seems to contradict a massive presence of CO_2 in its early atmosphere, could be explained by either the action of sulfuric or sulfurous acids in large, standing bodies of water suppressing the formation of carbonates (Fairén et al., 2004; Halevy et al., 2007), or a rapid escape of early martian CO_2 atmosphere (Tian et al., 2009, referred to as T09 in this paper), or both.

According to an early Mars upper atmosphere model (T09), the timescale for 1 bar of CO_2 to be removed through thermal escape would have been ~1 Myr at 4.5 byr ago (Ga) and ~10 Myr at 4.1 Ga. Note that at first stages, during typically the first 100 Myr, carbon escape may have been slowed down by water hydrodynamic escape, which is not taken into account in T09. If Mars was endowed with amounts of CO_2 similar to those found on Venus and the Earth (~100 bar), and according to the model of T09, most of its initial CO_2 inventory would have been lost within the first 100 Myr after its formation. A mechanism that can possibly help Mars to keep its CO_2 inventory is carbonate formation through weathering of basalt (Pollack et al., 1987). The same authors proposed that a dense CO_2 atmosphere (1–5 bar) could have been maintained during the Noachian by constant recycling of CO_2 back into the atmosphere through rapid burial and thermal decomposition of carbonate minerals. They calculated a typical cycling time of CO_2 at 273 K of ~10 Myr, decreasing to ~1 Myr at larger temperatures of 300 K for a CO_2 pressure of 1 bar, a temperature easily achievable in the subsurface even if the surface was cold. If the formation of carbonate through weathering has occurred at a rate comparable to that of carbon thermal escape, substantial amounts of carbon could have been trapped in the format of carbonates and cycled through the subsurface-hydrosphere–atmosphere system. If so, a significant atmosphere of CO_2 could have survived until 4.1 Ga. The combination of a rapid formation of carbonate and a rapid thermal escape of carbon on Noachian Mars could have decreased the atmospheric pressure of Noachian Mars even more rapidly, resulting in shorter warm periods and longer, more frequent cold periods on Noachian Mars. It is important to note that the timescales of carbonate formation and their further destabilization are still poorly understood.

The present inventory of water on Mars is also poorly constrained. The total water content of the two perennial polar caps corresponds to a GEL of 16 m depth (Smith et al., 2001), and the ice deposits sequestered in the Dorsa Argentea Formation (DAF), near the south polar cap, could have represented a ~15 m thick GEL in the past (Head and Pratt, 2001). Nevertheless, only a fraction of the initial water could remain today in DAF reservoir, corresponding to a ~5–7.5 m thick GEL. Other reservoirs, expected to have been active during late Amazonian, could be present in tropical and mid-latitude regions (Head and Marchant, 2009). But they probably represent only a minor contribution to the global reservoir. The total inventory of the known reservoir, including near-surface stores that are distributed across middle to high latitudes, has been estimated to correspond to a 35 m thick GEL (Christensen, 2006). The mega-regolith capacity is large, with up to a ~500 m thick GEL potentially trapped in the cryosphere, and hypothetically several additional hundreds of meters GEL (up to ~500 m) of groundwater surviving at depth below the cryosphere (Clifford et al., 2010). It has been suggested that most of ground ice has been lost by sublimation at low latitudes, and that only small amounts of groundwater would survive today (Grimm and Painter, 2009), with therefore less water in the megaregolith. A ~500 m thick GEL is generally assumed to be required to explain the formation of outflow channels (Carr, 1987), and most of this water could be trapped today as water ice, and possibly deep liquid water, in the subsurface, as well as in subsurface hydrated minerals. Based on an analysis of the present Mars' atmospheric D/H ratio, it has been suggested that a water GEL of up to ~300–400 m depth could have been stored in crustal serpentine since the late Noachian due to hydrothermalism triggered by magmatic activity (Chassefière and Leblanc, 2011b).

In the present paper, we suggest that the formation of CO_2–SO_2 clathrate hydrates (indifferently written "clathrate hydrates" or "clathrates" in this article) in a potentially CO_2-dominant (a few bar) early atmosphere of Mars should have significantly decreased the atmospheric SO_2 and CO_2 contents and should have caused subsequent sulfur enrichment in early Mars cryosphere. As shown hereafter, for a CO_2 pressure above 2 bar, all volcanically released SO_2 and the fraction of atmospheric CO_2 in excess of 2 bar should have been converted to CO_2–SO_2 clathrates. In this way, the formation of sulfate particles in the atmosphere could have been inhibited and there would have been neither long term net cooling nor net warming from volcanic SO_2 eruptions. If atmospheric CO_2 pressure is between 1 and 2 bar, we show that a fraction of volcanically released SO_2 would have been converted to sulfate particles while the rest would have been trapped in clathrates. This mechanism would have resulted in a stabilization of the surface temperature at the clathrate equilibrium temperature after large volcanic events. At some time in the past, when the CO_2 pressure dropped below 1 bar, the formation of clathrates would have been totally inhibited and the sulfur injected by volcanism into the atmosphere would have been fully converted into atmospheric sulfate aerosols. Thus formation of sulfate minerals at the surface no earlier than at the Hesperian could be explained by a decrease in atmospheric CO_2 pressure below the 2 bar level occurring close to the late Noachian/Hesperian transition.

In the following section, we describe the potential impact of CO_2–SO_2 clathrate formation on the sulfur content in the atmosphere and the surface temperature. Then, we present an extrapolation to low temperature of the thermodynamic properties of CO_2–SO_2 clathrates. New calculations of the surface temperature of Mars in presence of sulfate particles for different values of the CO_2 pressure are made, and consequences on the climate of early Mars examined. After an assessment of the consequences of the presence of SO_2 on the trapping of noble gases in clathrates, we discuss the possible implications of the present results and measurements to be done by future missions to improve our understanding of the impact of sulfur on early Mars' climate.

2. Formation of CO_2–SO_2 clathrate hydrate at high CO_2 pressure and SO_2 mixing ratio

The cooling effect of sulfate aerosols on the early Mars climate has been recently pointed out through a detailed 1-D photochemical/microphysical model of ancient Mars' atmosphere (Tian et al., 2010, referred to as T10 in this paper). Under certain CO_2 pressure, the surface temperature increases only slightly with enhanced level of atmospheric SO_2 at first because of the greenhouse contribution from SO_2. At atmospheric SO_2 concentration which could lead to meaningful surface warming, photochemistry processes induce the formation of sulfate aerosols which can reflect sunlight and cause surface cooling. The surface temperature for various SO_2 mixing ratios (T10) together with the equilibrium temperature of CO_2 clathrate hydrate (Mousis et al., 2012), and CO_2 ice, are plotted in Fig. 2 as a function of the CO_2 pressure. At 3 bar atmospheric pressure and for a SO_2 mixing ratio of 10 ppmv, the amplitude of the cooling by sulfate aerosols is about 60 K (T10), resulting in a surface temperature low enough to allow the formation of CO_2 clathrate hydrates (and even CO_2 ice). For a lower SO_2 mixing ratio of 1 ppmv the cooling is smaller, of the order of 20 K, but sufficient to fall in the domain of stability of CO_2 clathrates (but not of CO_2 ice).

First, in a regime without sulfur, CO_2 clathrates are stable for $p_{CO2} > 2$ bar due to the cooling effect of the Rayleigh scattering (T10). As a consequence any CO_2 pressure in excess of 2 bar results in the formation of CO_2 clathrate hydrates until the atmospheric CO_2 pressure is reduced to ~2 bar, with a stabilization of p/T values close to 2 bar/230 K. Thus, the atmospheric CO_2 pressure could have been maintained at ~2 bar during most of the Noachian, if atmospheric escape is neglected. Because carbon escaped rapidly during the early Noachian, this regime is possible only if a few bar of carbon sequestered first in crustal carbonates was recycled to the atmosphere by volcanism during the Noachian, since the amount of carbon released from the mantle to the atmosphere during the late Noachian and at later epochs is rather modest, a few hundreds millibar according to existing models (Grott et al., 2011). The warming effect of CO_2 clouds by reflection of the IR

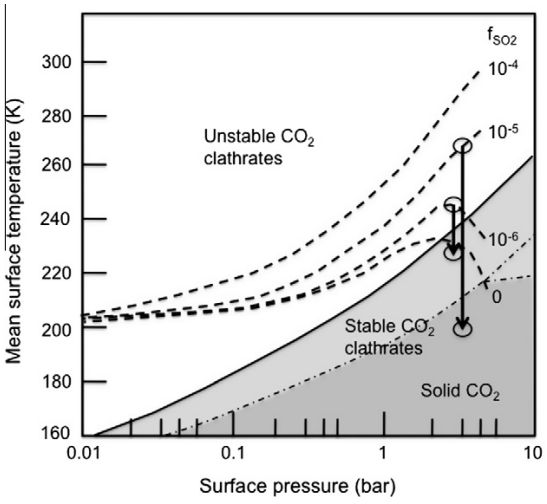


Fig. 2. Mean surface temperature as a function of the CO_2 pressure for SO_2 mixing ratios of 0, 1, 10 and 100 ppm show the cooling effect of SO_2 aerosols at $p_{CO2} = 3$ bar and mixing ratios of SO_2 of 1 ppm and 10 ppm. The equilibrium temperatures of CO_2 clathrate hydrate, and CO_2 ice, are plotted as a function of CO_2 pressure (from Mousis et al., 2012).

radiation emitted by the surface (Forget and Pierrehumbert, 1997) is not taken into account in this simulation. At p_{CO2} = 2 bar, the presence of CO_2 clouds may result in a surface temperature increase by ~5 K (Colaprete and Toon, 2003), somewhat increasing the temperature and pressure thresholds for the formation of CO_2 clathrates. Also, 1-D modeling provides only global average values and the local conditions may differ significantly from the average case. Formation of clathrates is expected to be more efficient in cold regions (polar caps) than at middle or lower latitudes. The possibility that a part of the CO_2 inventory may be stored under the form of clathrates has no significant impact on the discussion made in the previous section relative to the role of thermal escape. Indeed, any later decrease of the atmospheric CO_2 content following thermal escape would have resulted in the destabilization of CO_2 clathrates and a transfer to the atmosphere of an amount of CO_2 equal to that removed to space. In this regime, the CO_2 is buffering pressure and temperature around 2 bar/230 K until the total volatile CO_2 reservoir (ice, clathrate, and the atmosphere combined) decreased below 2 bar.

Second, the sporadic addition of SO_2 in the atmosphere by volcanic events into the previous regime would have had the following effects: (1) initial increase of the surface temperature by direct greenhouse effect, (2) rapid decrease of the surface temperature by formation of sulfate aerosols, in some cases below the equilibrium temperature of CO_2 clathrates (cf. Fig. 2). If the atmospheric SO_2, which is the source of sulfate aerosols, was trapped together with CO_2 in clathrates hydrates, the SO_2 atmospheric content would have been decreased, which would have slowed down or even inhibited the formation of sulfate aerosols and the subsequent cooling. Through this mechanism, the atmospheric mixing ratio of SO_2, following volcanic events, will stabilize close to the mixing ratio maintaining a surface temperature equal the CO_2–SO_2 clathrate equilibrium temperature. As an example, for p_{CO2} = 3 bar, this equilibrium mixing ratio is of the order of 0.1 ppm (Fig. 2). Any increase of the atmospheric SO_2 mixing ratio above this equilibrium value would have resulted in aerosol formation, cooling of the surface, formation of clathrates, and the removal of the remaining fraction of SO_2 gas from the atmosphere to clathrates. The higher the SO_2/CO_2 mixing ratio in the clathrates with respect to the gas, the more efficient this mechanism. If SO_2 is enriched with respect to CO_2 in the clathrates, formation of CO_2–SO_2 clathrates results in a decrease of the atmospheric SO_2 mixing ratio. If SO_2 is depleted in the solid phase, clathration results in an enrichment of SO_2 in the atmosphere. As shown in the next section, SO_2 is enriched by a factor of ~100–500 in the clathrate phase at ~220 K. The condensation of only 1% (or less) of the atmospheric CO_2 in clathrates, with therefore no significant change in p,T conditions, would have resulted in the removal of most atmospheric SO_2 to the cryosphere, implying that the proposed mechanism is highly efficient. Thus, once the regime described in the last paragraph is reached at p_{CO2} = 2 bar/230 K, any addition of atmospheric sulfur will be incorporated into CO_2–SO_2 clathrates.

The goal of the next section is to study the composition of CO_2–SO_2 clathrates as a function of gas composition, in particular the SO_2/CO_2 mixing ratio in the clathrate as a function of the gas mixing ratio to estimate the efficiency of CO_2–SO_2 clathrate formation in transferring SO_2 from the atmosphere to the cryosphere.

3. Thermodynamic modeling of CO_2–SO_2 clathrates in martian atmospheric conditions

3.1. Thermodynamical approach

The van der Waals and Platteeuw (1959) model describes the equilibrium of hydrate phases by means of a convergence between a statistical thermodynamics approach implementing Kihara parameters and a classical approach with a reference state parameters. In a recent publication (Herri and Chassefière, 2012), the Kihara parameters have been optimized to fit equilibrium data at low temperature concerning martian atmospheric components: carbon dioxide (95.3%), nitrogen (2.7%), Argon (2%) and methane (<50 ppb with an average at 15 ppb) (Owen et al., 1977; Mumma et al., 2009), using Handa and Tse (1986) reference state parameters. We observed that the stability of clathrate hydrate is firstly dependent on the partial pressure of carbon dioxide. However, the possible presence of SO_2 in the ancient Mars' atmosphere, a potential promoter for clathrate hydrate formation, could move the stability line for clathrate hydrate formation.

To test the influence of SO_2 we must implement in our models its Kihara parameters, retrieved from experimental data. Up to date, only few equilibrium data have been measured for sulfur dioxide. Above 0 °C there are 36 equilibrium data from Van Berkum and Diepen (1979) in the range of temperature (285.2–293.84 K) and the range of pressure (0.253–392.330 MPa), and 2 equilibrium data at (280.2 K, 0.101 MPa) and (273.2 K, 0.0396 MPa) from Von Stackelberg (1949). Below 0 °C Tamman and Krige (1925) measured the following experimental points: (261.15 K, 0.01695 MPa), (265.15 K, 0.01997 MPa), (269.15 K, 0.02597 MPa), (270.15 K, 0.02778 MPa), (271.15 K, 0.03051 MPa). Above 0 °C, the data cannot be easily used to constrain the Kihara parameters because it implies to describe the liquid phase in the presence of salts resulting from SO_2 dissolution (H_2SO_4, HSO_4^-, HSO_4^{2-}) and thus to model the speciation of the reaction as well as the activity coefficient of water. Below 0 °C the situation is easier, dealing with ice, simplifying the equations. From a practical point of view, the restricted range of available temperature and pressure measurements hampers the possibility of retrieving only one set of Kihara parameters, but only interdependent sets of values. Our aim is to test within these sets of constrained values the consequence on the composition of (CO_2–SO_2) clathrate hydrate under martian conditions.

The detailed description of the statistical–thermodynamic model and the strategy used for the retrieval of the SO_2 Kihara parameters required for the modeling are deferred to Appendix A. We, however, stress the importance of this aspect, defining the central parameters on which are based the scientific discussion outcomes in the following sections.

3.2. Extrapolation of experimental data to martian temperatures and kinetics of clathrate particle formation

We explored the minimization in the full 3D parameter space (see Appendix A) to deduce the minimum SO_2 enrichment during the formation of a mixed SO_2–CO_2 clathrate hydrate in contact with a CO_2 dominated atmosphere. Whatever the minimized set of Kihara parameters for SO_2, and exploring concentration ratios from 0.1 ppm to 1000 ppm of SO_2 in CO_2, the resulting mixed clathrate hydrate formed is always highly enriched in SO_2, by a factor above 60 with respect to gas phase, for all temperatures in the 170–240 K range (Fig. 3).

Falenty et al. (2011) performed experimental kinetics studies of CO_2 clathrate hydrate, monitoring the formation through the neutron diffraction pattern of hexagonal ice in the 185–195 K range. The data were extrapolated at low temperature through a model to compare with the actual polar frosts of Mars, at about 150 K, in order to show that the formation timescale for micron sized clathrates was longer than the typical seasonal variations regularly inducing the declathration. The nucleation rate depends not only on the temperature but on the ice grain sizes when nucleating pure clathrate hydrate from ice aerosol, as the nucleation proceeds in at least two steps: first surface nucleation followed by growth of the

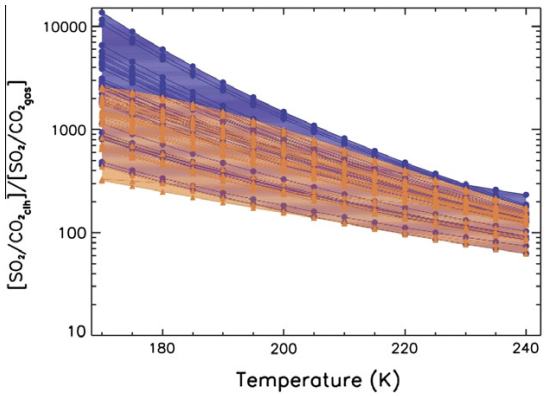


Fig. 3. Ratio of concentration in mixed SO_2–CO_2 clathrate hydrate with respect to gas phase one as a function of temperature using the different constrained extrapolated SO_2 Kihara parameters. Initial SO_2 concentrations are 0.1 ppm (circles, blue curves) and 1000 ppm (triangles, red curves), covering most of the expected range for martian conditions. (For interpretation of the references to colour in this figure legend, the reader is referred to the web version of this article.)

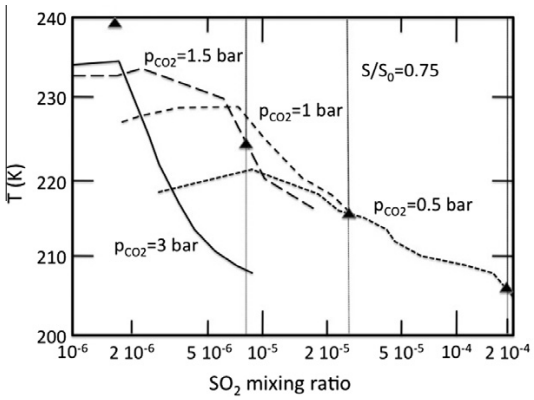


Fig. 4. Surface temperature as a function the SO_2 mixing ratio for different values of the CO_2 partial pressure: 3 bar, 1.5 bar, 1 bar, 0.5 bar. The black triangles correspond to the SO_2 mixing ratio for which the temperature is equal to the CO_2 clathrate equilibrium temperature.

hydrate crystal. At 195 K, for a distribution of ice particles of about 1.5 μm of mean equivalent sphere radius, the nucleation proceeds in about 1 day in the laboratory. Extrapolating at the higher temperatures considered in Fig. 3 for the ancient martian surface temperature, the nucleation rate for hydrate formation of similar size ice grains would be higher by a factor of 3 at 200 K to 2 orders of magnitude at 230 K. Precise nucleation timescale with an SO_2–CO_2 clathrate is difficult to extrapolate only based on these experiments, and will depend on the particular mechanism by which the aerosols or surface clathrate kinetic formation proceed (heterogeneous nucleation, diffusion controlled, etc.), but if we take the high rate of hydrate nuclei growth, it seems reasonable to grow grains as large as 100 μm in hours to days.

4. Modeling of the effects of SO_2 and sulfate aerosols on surface temperature and consequences of CO_2–SO_2 clathrate formation on early Mars climate

For modeling the effects of SO_2 and sulfate aerosols on surface temperature we used the 1-D radiative–convective climate model and the 1-D photochemical model in T10, which allows us to investigate the combined climate effect of CO_2, SO_2, and sulfate aerosols. Most of the model details are described in T10 and will not be repeated here. SO_2 in the early Mars atmosphere could have originated from volcanic outgassing, which is simulated by assuming different surface upward fluxes of SO_2 and H_2S. The ratio between the two species is kept at unity, and previous sensitivity tests (T10) showed that modifying this ratio does not change the results of the photochemical and climate calculations significantly. In this work the relative solar luminosity is set to $S/S_0 = 0.75$. The atmospheric pressure is set to the following levels: 1.5, 1, and 0.5 bar, in addition to the level of 3 bar already studied in T10, and Fig. 4 shows the relationship between surface temperature and atmospheric SO_2 concentration under different CO_2 pressures. As discussed in T10 the surface temperature increases with enhanced level of atmospheric SO_2 at first because of the greenhouse contribution from SO_2. Nevertheless, as atmospheric SO_2 concentration keeps increasing, photochemistry leads to the formation of sulfate aerosols which can reflect sunlight and cause surface cooling. The decrease of surface temperature with increasing atmospheric SO_2 is more dramatic under higher CO_2 pressure than under the lower CO_2 pressure because the sulfate aerosols fall slower in a denser atmosphere. It can be seen from Fig. 4 that the maximum surface temperatures from combined greenhouse effect of CO_2 and SO_2 in early martian atmosphere are 235, 235, 230, and 220 K under 3, 1.5, 1.0, and 0.5 bar CO_2 pressure respectively. Thus volcanic outgassing of SO_2 is not a solution to an early warm and wet Mars, consistent with the conclusion in T10.

For $p_{CO2} = 3$ bar, the curve is everywhere below the CO_2 clathrate equilibrium temperature. Black triangles in Fig. 4 correspond to the SO_2 mixing ratio for which the surface temperature is equal to the CO_2 clathrate equilibrium temperature. The same values are plotted as a function of p_{CO2} in Fig. 5. In the four cases ($p_{CO2} = 0.5$, 1, 1.5 and 3 bar), we have indicated the lava volumes required to give rise to the corresponding SO_2 mixing ratio (Wilson and Head, 2002; Hanna and Phillips, 2006). For a CO_2 pressure larger than 2 bar that may be reached sporadically due to seasonal/orbital effect or also to the CO_2 outgassing from the crust (volcanism and disruption of carbonates), CO_2 clathrates are stable whatever the SO_2 mixing

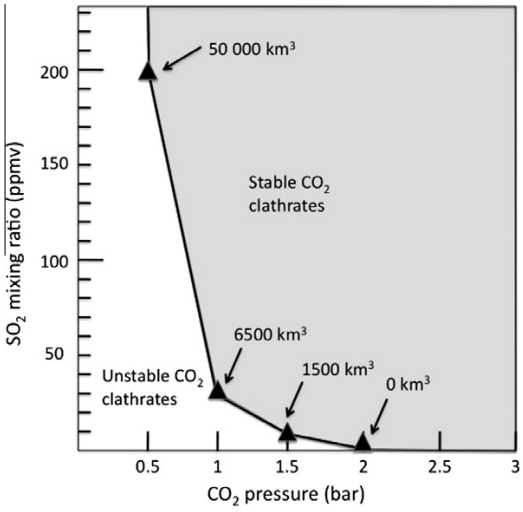


Fig. 5. Equilibrium SO_2 mixing ratio as a function of CO_2 pressure. The lava volumes required to give rise to the corresponding SO_2 mixing ratio, calculated by using the same conversion factor as in Johnson et al. (2008), are indicated on the figure.

ratio in the atmosphere, resulting in the trapping of the fraction of atmospheric CO_2 in excess of 2 bar in the cryosphere under clathrate form. Any atmospheric sulfur released by volcanism is trapped in the cryosphere under the form of CO_2–SO_2 clathrate. Occasionally an SO_2 mixing ratio of ~1 ppm may be reached since at this level, sulfur has no significant effect on the mean temperature. For higher values, the surface cooling down will result in CO_2–SO_2 clathration. Note that an ample reservoir of H_2O is available in polar caps (a several 10-m thick global equivalent layer in present conditions, probably much more during the Noachian) to feed the formation of clathrates. As soon as an atmospheric H_2O molecule is consumed in clathrate formation, it is replaced by a molecule sublimated from the polar caps, due to the short dynamical timescale of the atmosphere (a few weeks). In terms of reservoirs, the required quantities of H_2O (and CO_2) for all S released by volcanism during the Noachian to be stored in clathrates is discussed later in this section. H_2S either is converted into SO_2 within the atmosphere in a typical time of a couple of weeks (Wong et al., 2003), or is trapped directly in clathrates.

In the 0.5–2 bar p_{CO2} range, the SO_2 level in the atmosphere following a volcanic eruption can reach typically 10 ppm or so, the excess being trapped in the cryosphere. According to the estimate of the characteristic growth time of a clathrate particle in the atmosphere made in Section 3 (a few hours to days for a 100 μm size particle), trapping occurs rapidly, simultaneously with the radiative cooling of the atmosphere due to sulfate particle formation, which occurs within a few months after SO_2 outgassing. After large volcanic events, the surface temperature is therefore stabilized at the CO_2–SO_2 clathrate equilibrium temperature (~220 K, see Fig. 2) within a few months. Some of the SO_2 trapped in the cryosphere at previous times when p_{CO2} > ~2 bar (if it ever occurred) may similarly be released to the atmosphere. Also, the release of a few thousand cubic kilometers of lava may have happened frequently during Tharsis formation (Johnson et al., 2008, and references therein). During this period, the atmosphere could have been rich in SO_2 and sulfate particles (often at equilibrium condition described in Fig. 5) and the SO_2-rich cryosphere could have lost part of its SO_2.

For a CO_2 pressure below 0.5 bar, there is no more formation of CO_2–SO_2 clathrates for SO_2 mixing ratio <200 ppm and all the released sulfur is converted to sulfates. A 200 ppm level of SO_2 in the atmosphere corresponds to the most important eruption supposed to have taken place on Mars, with a lava volume of 50,000 km^3 (Wilson and Head, 2002).

The potential consequences of CO_2–SO_2 clathrate formation on early Mars climate are multiple. Let assume that the CO_2 pressure has been buffered at 2 bar during most of the Noachian. Whereas, during the time when p_{CO2} > ~2 bar, there is no SO_2 in the atmosphere and a progressive storing of SO_2 in the cryosphere, the drop of the CO_2 pressure below 2 bar results in the appearance of SO_2 and sulfate aerosols in the atmosphere, due to both episodic volcanism and continuous release of SO_2 previously stored in the cryosphere, with the subsequent acidification and formation of sulfate minerals at the surface. The cryosphere is progressively depleted in SO_2. At this time, if a significant level of the SO_2 mixing ratio is maintained in the atmosphere, including during the periods between volcanic eruptions due to the continuous SO_2 release from the SO_2-rich cryosphere, the surface temperature is stabilized close to the CO_2 clathrate equilibrium temperature of ~220 K (210–230 K in the p_{CO2} range from 1 to 2 bar). Interestingly, the time when the CO_2 pressure dropped below 2 bar, resulting in sulfate precipitation at the surface, subsequent acidification of the surface and formation of sulfate minerals, could coincide with the age of sulfate minerals observed by OMEGA/Mars Express (Bibring et al., 2006). If so, the CO_2 pressure had to be of the order of 2 bar at the late Noachian/Hesperian transition.

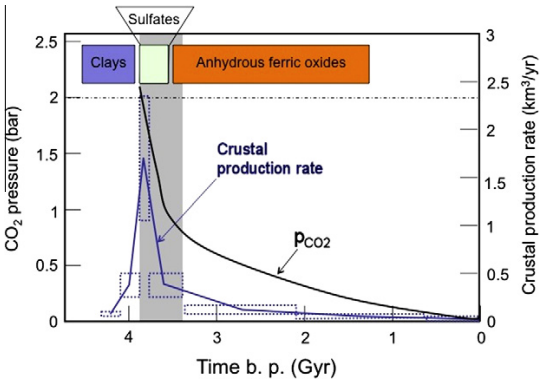


Fig. 6. CO_2 evolution profile scaled on the Chassefière and Leblanc (2011a) profile to fit a 2 bar value at 3.8 Gyr b.p. (solid line). Blue rectangles with dotted lines and blue "average" dotted curve represent the evolution of the crust production rate derived from photogeological analysis (Greeley and Schneid, 1991). The chronology of clays, sulfates and ferric oxides proposed by Bibring et al. (2006) is shown at the top. The vertical gray band corresponds to the time interval when volcanic activity was significant according to Greeley and Schneid estimates. (For interpretation of the references to colour in this figure legend, the reader is referred to the web version of this article.)

The chronology of clays, sulfates and ferric oxides proposed by Bibring et al. (2006) is shown in Fig. 6. We have scaled the CO_2 evolution profile calculated by Chassefière and Leblanc (2011a) by multiplying p_{CO2} by 2.5, in such a way to fit a pressure of ~2 bar at the end of the Noachian, just before sulfate minerals observed by OMEGA were emplaced. The estimated time profile of the crust production rate is also shown (Greeley and Schneid, 1991). The vertical gray band corresponds to the time interval when volcanic activity was significant according to Greeley and Schneid estimates. If the CO_2 pressure dropped below 2 bar at the end of the Noachian, the high volcanic activity during the first half of the Hesperian, when observed sulfate minerals formed, together with the release of SO_2 trapped in the cryosphere during Noachian volcanic events, should have resulted in the precipitation of large amounts of sulfate aerosols, with subsequent acidification of the surface and formation of sulfate minerals. The transformation of the volatile SO_2 from accessible near-surface clathrate reservoir, stored in the Noachian 2-bar regime, to sulfate sediment reservoir is not reversible since there is no efficient sediment recycling on Mars due to plate tectonics. However, martian impacts may have contributed to recycling. The drop down of surface pressure has permitted the destabilization mechanism to be more and more efficient. The onset of sulfate mineral formation would have been triggered by the drop in CO_2 pressure below 2 bar. The end of sulfate mineral formation would be due to the sharp decrease of volcanic activity at the end of the Hesperian, and the total transformation from CO_2–SO_2 clathrate to sediment.

The origin of a possible CO_2 pressure drop at the end of the Noachian is unclear. Non-thermal escape is not expected to have removed more than ~10 mbar during the last 4 Gyr (Chassefière and Leblanc, 2011a). The sink for CO_2 is necessarily within the crust and formation of carbonates in subsurface hydrothermal systems may seem a good candidate (Griffith and Shock, 1995; Chassefière and Leblanc, 2011a). The reason for a stage of intense hydrothermalism at the early Hesperian could be the occurrence of a global scale episode of fissural volcanism between 3.8 and 3.6 Ga (Ody et al., 2012). The olivine-rich magma could have reached the surface through fractures and cracks in the basement rock caused by impacts during the late heavy bombardment (Ody et al., 2013). Such a context, with a highly fractured upper crust filled with both magma and liquid water from the melting

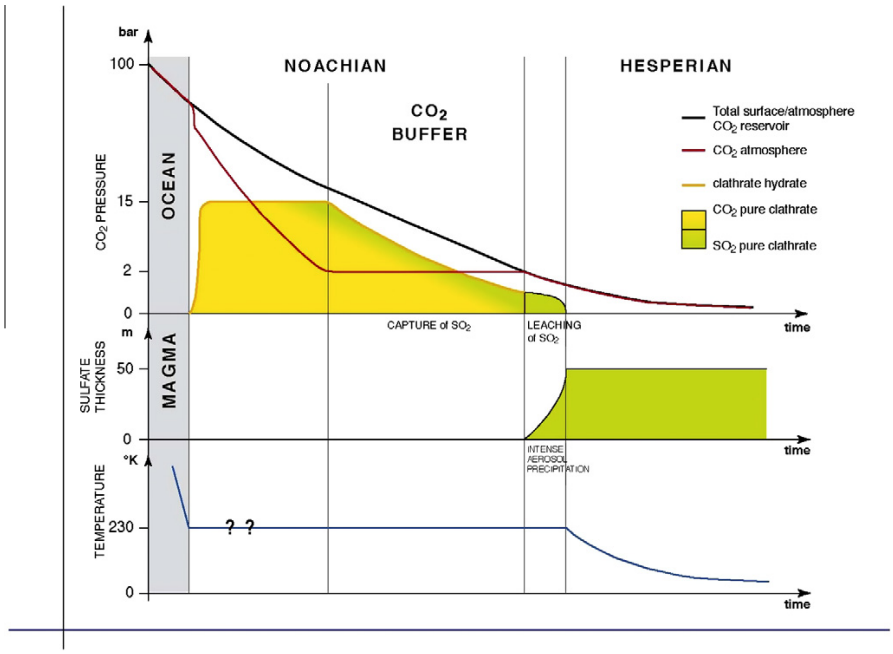


Fig. 7. Schematic representation of sulfur and CO_2 reservoir during the Noachian and Hesperian periods. The total volatile surface/atmosphere CO_2 reservoir is decreasing due to thermal escape and possible formation of carbonates in the subsurface, from an initial budget ~100 bar. After magma ocean crystallization, CO_2 and water condense in form of clathrate (15 bar of CO_2 at maximum can be stored in form of clathrate when reacting with the total martian water content of 1000 m GEL). After volcanic release of S, atmospheric SO_2 is systematically enriched in the condensating clathrate, triggered either by climatic changes or by global cooling due to aerosol formation. The CO_2 clathrate acts as an atmospheric buffer when the atmospheric pressure reaches 2 bar. After the complete consumption of CO_2 clathrate, the atmospheric pressure can drop below 2 bar and massive release of SO_2 from the clathrate induces the condensation of aerosols and precipitation as a Mars-wide sulfate layer (50 m represent the total SO_2 outgassed from Tharsis formation). This scenario represents the equilibrium state of surface/atmosphere but significant departure may have happened due to large impacts.

cryosphere, may have favored the circulation of CO_2-rich hot waters in the subsurface and the deposition of carbonates in crustal cold water pools (Chassefière and Leblanc, 2011a). This episode could also be responsible for the trapping of large amounts of water in the crust by serpentinization (Chassefière and Leblanc, 2011b; Ehlmann et al., 2013). Because in the same time, according to the massive sulfur precipitation scenario, the cryosphere would have lost most of its SO_2, less and less acidic conditions would have prevailed in the subsurface hydrosphere, making more and more efficient the precipitation of carbonates. These hypotheses remain to be confirmed by further studies.

Assuming (i) 2×10^{21} to 5×10^{21} g as the total sulfur degassed in the Noachian by the Tharsis province (Gaillard and Scaillet, 2009), (ii) an equilibrium flux of S outgassing and sulfate precipitation in the range from 2×10^9 to 2×10^{10} molecule cm^{-2} s^{-1} for an atmospheric SO_2 mixing ratio in the range from 1 to 200 ppm (T10), we can estimate that the complete S content from the clathrate reservoir is released in a time range from 40 to 1000 Myr. The cryosphere in the Noachian 2-bar regime has to be quite rich in SO_2. Assuming for example a SO_2/CO_2 ratio in the clathrate of 20%, the required water GEL thickness is in the range from 250 to 630 m, for a CO_2 global equivalent pressure in the range from 3 to 7.5 bar. A twice lower ratio of 10% results in twice higher H_2O and CO_2 inventories (500–1300 m/6–15 bar). A twice larger ratio of 40% results in twice lower H_2O and CO_2 inventories (125–315 m/1.5–3.7 bar). These orders of magnitude estimates are reasonable for the global inventory of martian volatiles, as described in Section 1, implying a SO_2/CO_2 ratio in the clathrates of several tens percents. If the sulfate is deposited in form of anhydrite (Gaillard and Scaillet, 2009) at 136 g mol^{-1}, it will precipitate in a 20–50 m global layer.

Two majors geomorphological units are compatible with our scenario:

(1) The presence of a thick Mars-wide sedimentary formation of sulfate, including in very uncommon places at high topography, such the Interior Layer Deposit (ILD) at the top of Valles Marineris. Eolian deposition was proposed from geomorphological arguments (Michalski and Niles, 2011). For ILD in Valles Marineris, the formation as thick as 5 km (Nedell et al., 1987) must be done in 400 Myr, after the tectonic opening at 3.9 Ga and the formation of the floor 3.5 Ga (Quantin et al., 2004). In our scenario, 20–50 m GEL sulfur particle could have precipitated directly from atmosphere in 40–1000 Myr, in agreement with the observation. The sedimentary formation of sulfate seems to be at very large scale (Bibring et al., 2006) since it has been detected in different places on Mars such as Valles Marineris (Bibring et al., 2007; Le Deit et al., 2008), Meridiani Planum (Squyres et al., 2004), Aram Chaos (Massé et al., 2008) and Syrtis Major (Ehlmann and Mustard, 2012).

(2) The chaotic terrains, at equatorial region, could have been formed by disruption of the CO_2 clathrate in the past at the late Hesperian/Amazonian period. This interpretation is compatible with our scenario since the formation of clathrate must have been global during the Noachian, it should also affect equatorial region. The reason for such a disruption has been debated, including climatic change (Clifford and Parker, 2001), internal heat flux (Clifford and Parker, 2001), fracture propagation (Rodriguez et al., 2006), and seismic activity (Nummedal and Prior, 1981; Tanaka, 1999). We propose here that the disruption may be due to

the pressure decrease below 2 bar. In our scenario, a GEL of CO_2–SO_2 clathrate ranging from 290 m to 720 m depth has been destabilized. Scaling this volume to the province of the chaos (1/10 surface of Mars) is compatible with the typical height loss in chaos ~3000 m. A schematic representation of the evolution of early Mars' under the effect of CO_2–SO_2 clathrate formation and destabilization is shown in Fig. 7.

As previously stated, the surface temperature of ~230 K proposed to have prevailed during the Noachian is a global average value due to the use of a 1-D model. In the real martian surface, there are places where the temperature is higher than 230 K, and clathrates do not form, for instance near the equator at low obliquity. They form only in the locations where the temperature reach 230 K, for instance at the pole at low obliquity. Due to the large variations of the obliquity of Mars on typical time periods of 10^5–10^6 year (Laskar et al., 2002; Levrard et al., 2004), the colder regions of the planet regularly become warmer, and vice versa. We do not know if variations of orbital parameters similar to those calculated for the last 10 Myr occurred on early Mars. This is still unknown, especially under the scenario of giant planet migration (Gomes et al., 2005; Morbidelli et al., 2007). Some chaotic variations of obliquity may have occurred at the Noachian (before giant planet migration) in specific dynamical conditions, but in other conditions obliquity may have remained stable (Brasser and Walsh, 2011). Making the hypothesis that early Mars obliquity changed in a similar fashion as it does today, a coming and going of ice deposits, including CO_2–SO_2 clathrates, between high latitude (at low obliquity) and low latitude (at high obliquity) regions through alternate sequences of sublimation and condensation should have occurred. On the recent Mars (last 10 Myr), the typical timescale for ice migration during a transition of the mean obliquity, like that which occurred 4 Myr ago, is ~1 Myr (Levrard et al., 2007). On ancient Mars, where water was more abundant and the CO_2 pressure higher, this time should have been larger. Assuming that the residence time of SO_2 in the atmosphere with respect to clathrate formation on the cold trap is 1 yr (see below), and that the equivalent of 1 bar of SO_2 is transferred in 1 Myr, the average SO_2 mixing ratio in a 2-bar atmosphere during an obliquity transition is 0.5 ppm. For an ice migration time of 10 Myr, and an amount of transferred SO_2 of 0.2 bar, the average SO_2 mixing ratio during obliquity transition is 10^{-2} ppm. These values are small, with no expected effect on climate. An important question is to know if, during its transfer through the atmosphere, SO_2 is preserved from forming aerosols and being removed from the atmosphere–cryosphere system. The residence time of SO_2 in the atmosphere, before being removed by aerosol deposition, is 10^2–10^3 year (Johnson et al., 2009, T10). The global mixing time of Mars atmosphere is ≈0.5 year (Krasnopolsky, 2005), of the same order as the Earth troposphere mixing time (≈1 year). The lifetime of a SO_2 molecule with respect to trapping in clathrates is therefore 2–3 orders of magnitude smaller than the time of SO_2 removal by aerosol deposition. SO_2 is therefore expected to survive ice migrations, making possible the preservation of a SO_2-rich cryosphere during the whole Noachian.

It must be emphasized that the threshold pressure value of 2 bar is obtained by using the 1-D model. The mean annual surface temperature is not uniform, decreasing from the equator to the poles. On Mars today, regions above 45° latitude in both hemispheres have an annual surface temperature lower by more than 10 K than the global average temperature (see e.g. Mellon et al., 2004). As shown on Fig. 2, the difference between the mean global temperature and the CO_2 clathrate formation temperature is smaller than ≈10 K in the range 0.5–2 bar. By analogy with present

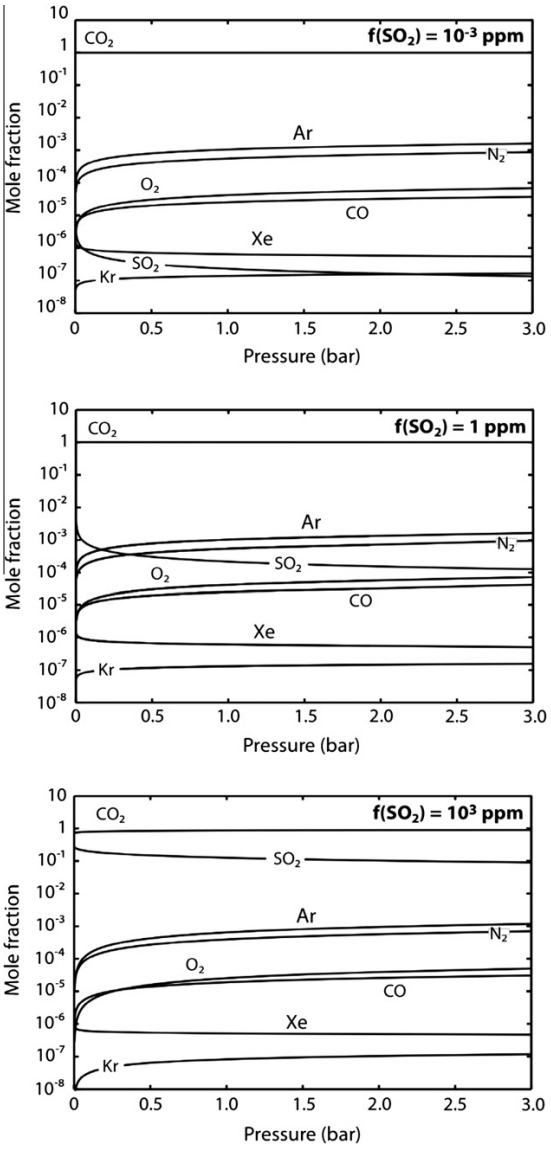


Fig. 8. Mole fraction of volatiles encaged in clathrates calculated as a function of the surface pressure of CO_2 in the cases of, from top to bottom, SO_2 atmospheric abundances equal to 10^{-3}, 1 and 10^3 ppm.

Mars, it results that even with a CO_2 pressure of only 0.5 bar, regions above 45° latitude could have been below the clathrate formation temperature in annual average. If so, it may be thought that the cold trap formed by middle and high latitude regions may have been efficient enough to remove most of the SO_2 released to the atmosphere (including in equatorial regions) by volcanism. More accurate 2-D or 3-D models are required to precisely define the value of the pressure threshold, which could be smaller than 2 bar and even possibly 1 bar. Such a lower threshold value would be in better agreement with a strong carbon hydrodynamic escape ruling out a dense martian atmosphere until the late Noachian (Tian et al., 2009), and the recent estimate of <1 bar obtained from the constraint provided by the $^{40}Ar/^{36}Ar$ ratios of trapped gases within martian meteorite ALH 84001 (Cassata et al., 2012).

5. Influence of the presence of SO_2 on the trapping of argon, krypton and xenon in clathrates

Mousis et al. (2012) found recently that it was possible to account for the two orders of magnitude drop existing between the measured atmospheric abundances of non-radiogenic argon, krypton and xenon in Earth versus Mars (see Pepin, 1991) by invoking the trapping of these noble gases in clathrate deposits incorporated into the current martian cryosphere. In their scenario, these authors estimated that masses of xenon, krypton and argon equivalent to those found on Earth could be incorporated into clathrates if one assumes the simultaneous trapping of at least 2.3 bar of CO_2. This value is quite close to the maximum value of 2 bar imposed by the CO_2 clathrate saturation law, as previously explained, and is therefore compatible with constraints derived from the present work. Mousis et al. (2012) also considered the presence of atmospheric SO_2 on the clathrate composition. In order to quantify the influence of this species on the noble gas trapping in CO_2-dominated clathrate, they used approximate combination rules allowing them to retrieve a set of interaction potential parameters for SO_2–H_2O interactions. They then deduced that this species was a poor clathrate former in the presence of a CO_2-dominated gas and concluded that it has zero influence on the trapping efficiencies of other minor species, including noble gases.

The set of potential parameters determined for SO_2–H_2O interactions in the present work supersedes the exploratory one used by Mousis et al. (2012) and suggests that the mole fraction of SO_2 can be strongly enriched in CO_2-dominated clathrate compared to that existing in the gas phase. This implies that the question of the influence of this species on the noble gas trapping in CO_2-dominated clathrate remains open. Here we use a gas phase composition similar to the one defined by Mousis et al. (2012), in which the mole fraction of SO_2 is varied between 10^{-3}, 1 and 10^3 ppm, in order to investigate the influence of SO_2 on the trapping of other minor species. Abundances of CO_2, N_2, O_2, CO, Ar, Kr and Xe derive from Moroz (1998). In each of the three cases, the abundance of CO_2 is adjusted to allow the normalization to 1 of the sum of the mole fractions.

A set of SO_2–H_2O interaction parameters, which is representative of the range of solutions determined in Section 2 and Appendix A, has been selected ($a = 0.75$ Å, $\varepsilon/K = 258.91$ K and $\sigma = 2.7$ Å). These parameters correspond to a mean enrichment factor of 100 of the SO_2 mole fraction in clathrate compared to the atmospheric one at a surface pressure of 1 bar, irrespective of the considered SO_2 abundance (10^{-3}, 1 and 10^3 ppm). Fig. 8 represents the clathrate composition computed in the three cases of the SO_2 abundance for atmospheric pressures up to 3 bar, allowing us to encompass all the plausible values discussed in the literature. At each pressure considered, the temperature used in our computations is the equilibrium temperature of CO_2-dominated clathrate. The figure shows that the mole fractions of minor species are not altered when considering SO_2 atmospheric abundances ranging from 10^{-3} to 1 ppm. At a SO_2 atmospheric abundance of 10^3 ppm, the trapping efficiencies of Ar and Kr are decreased by a factor of 10 and that of Xe is almost unchanged.

Our calculations imply that the conclusions of Mousis et al. (2012) remain valid if one assumes that the SO_2 atmospheric abundance ranges between 10^{-3} and 1 ppm. However, for higher mixing ratios such as those estimated in the Noachian (see Section 4), the efficient clathration of SO_2 implies the trapping of up to several dozens of bar of atmospheric CO_2 if one wants to account for the losses or Ar and Kr via their clathration in the cryosphere. Because these values are implausible, it seems that the scenario proposing that the noble gas deficiency of the martian atmosphere is due to their efficient sequestration in clathrates present in the cryosphere is not consistent with the one proposed here for SO_2.

6. Discussion

We suggested in the present study that the formation of CO_2–SO_2 clathrates at Noachian and Hesperian times could have played an important role in controlling and stabilizing the level of volcanic sulfur in the atmosphere, as well as the level of atmospheric CO_2 for earliest times. If the CO_2 pressure exceeded a threshold of $p_0 = 2$ bar (possibly less: 0.5–1 bar, which remains to be confirmed from more sophisticated 3D models) due to an efficient Noachian volcanism, the CO_2 in excess of p_0 (assumed to be ~2 bar for the discussion) could have been stored in the cryosphere under the form of CO_2 clathrates. Indeed, due to the increasing albedo of the atmosphere through Rayleigh scattering for increasing CO_2 pressure above 1 bar, the surface temperature induced by a $p > \sim 2$ bar CO_2 atmosphere is smaller than the equilibrium temperature of clathrates, resulting in a saturation of CO_2 and its condensation under the form of clathrates. Such a clathrate buffer would have maintained the CO_2 pressure close to ~2 bar, and the surface temperature close to 230 K, resulting in a cold Mars at the Noachian. The cryosphere would have trapped all the sulfur released by volcanism under the form of sulfur-rich (enriched by a factor ~100–500 with respect to the gas phase) CO_2–SO_2 clathrates.

Because the thermal conductivity of clathrates is low, smaller than that of water ice on the order of 5–6 times (Mellon, 1996), the formation of clathrate deposits should result in a higher thermal gradient, with an accumulation of heat beneath the clathrate layer. It has been suggested that, on present Mars, no more than a global equivalent atmospheric pressure of 112 mbar of CO_2, in a 4-km thick polar deposit, may be contained in the polar caps. For a larger amount of deposited CO_2, the warming at the base of the clathrate layer results in the liquefaction of CO_2, essentially precluding the stability of the system. On early Mars, the deposition of large amounts of CO_2 clathrates, assuming an atmospheric content larger than 2 bar, could have led to this kind of instability. But if clathrates were deposited on an extended fraction of the surface, much larger than the present caps, the maximum admissible value of the global equivalent atmospheric pressure of CO_2 trapped in clathrates could be much larger than 112 mbar. This phenomenon should have to be taken into account in any detailed modeling of massive clathrate deposition in the Noachian cryosphere.

For a surface pressure smaller than 2 bar and progressively decreasing, atmospheric sulfur is no longer trapped in clathrates, and an increasing fraction of the atmospheric SO_2, up to 10 ppm at $p_{CO2} = 1.5$ bar, and 30 ppm at $p_{CO2} = 1$ bar, can remain in the atmosphere. If the amount of atmospheric SO_2 exceeds these thresholds, the cooling effect of sulfate aerosols results in a decrease of surface temperature below the clathrate equilibrium temperature and the condensation of the SO_2 in excess in CO_2–SO_2 clathrates. During this period, significant amount of SO_2 (and H_2S rapidly converted in SO_2 by atmospheric photochemistry) was converted into sulfate aerosols, which further settled down to the surface and possibly led to the formation of sulfate minerals. This sulfur may have been released, not only by volcanoes but also (and more continuously) by the SO_2-rich cryosphere formed when $p_{CO2} > \sim 2$ bar. Through this mechanism, the cryosphere may have lost at this stage some of the volcanic SO_2 stored at earlier times, released back to the atmosphere. In this time range (2–1 bar p_{CO2} range), the surface temperature has been buffered, during and after episodes of sulfur release, at a temperature from 230 K ($p_{CO2} = 2$ - bar) to 210 K ($p_{CO2} = 1$ bar). For $p_{CO2} < 1$ bar, all the released SO_2 remains in the atmosphere, with no more trapping in clathrates.

We proposed the hypothesis that the formation of sulfate minerals, which have been observed from orbit and are formed during the Hesperian (Bibring et al., 2006), could have been triggered by a fall of early Mars atmosphere pressure below 2 bar and that this change occurred close to the late Noachian/Hesperian transition. This hypothesis requires that the total amount of CO_2 in both the atmosphere and the cryosphere during the Noachian has been greater than the content of a 2 bar atmosphere as a result of substantial volcanic outgassing and/or rapid carbonate formation, which might have been efficient enough to keep some CO_2 on early Mars despite rapid carbon escape. This constraint could be alleviated if further 3D-modeling shows that a pressure threshold value of 0.5–1 bar is sufficient to keep most of the released SO_2 trapped under clathrate form in the Noachian cryosphere. According to our hypothesis, Mars' cryosphere would have stored under the form of CO_2–SO_2 clathrates a significant amount of the sulfur outgassed during the whole Noachian (from the magma ocean crystallization to the 2-bar transition). At the transition between Noachian and Hesperian, this reservoir would have been released back into the atmosphere through clathrate disruption that may be at the origin of the chaotic terrains. Then sulfur has precipitated in the form of aerosols, creating a large-scale sulfate deposit, in agreement with several in situ and orbital observations. Today, the sulfate layer is not present everywhere but observed in some places such Valles Marineris (Bibring et al., 2007; Le Deit et al., 2008), Meridiani Planum (Squyres et al., 2004), Aram Chaos (Massé et al., 2008) and Syrtis Major (Ehlmann and Mustard, 2012). First, the net aerosols precipitation flux in the ancient Mars should be controlled by local winds and topography in an analogous manner than snow precipitation (Forget et al., 2006). Second, the erosion may have removed significant part of the initial layer, especially because sulfate is highly transportable in soluble phase, such kieserite.

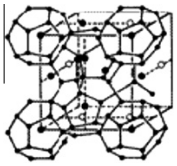
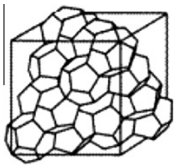
According to our scenario, the formation of carbonates should have been inhibited (at least in the superficial cryosphere) during most of the Noachian, although probably not at earliest times when the cryosphere was still SO_2-free, due to the acidification of water resulting from the local melting of the SO_2-rich cryosphere. Such fluid can precipitate sulfate phase locally in the subsurface but the cryosphere may be SO_2-rich enough (it can potentially store the complete SO_2 degassed from volcanism, see Section 4) implying unlikely conditions for carbonates precipitation. As previously mentioned it may be thought that during the massive release of SO_2 to the atmosphere after the end of the 2-bar stage at the Noachian–Hesperian transition, and the subsequent sequestration of sulfur in sediments, a less acidic cryosphere allowed the formation of carbonates, relatively deep in the subsurface due to cold and acidic surface conditions. Because the trapping of CO_2 in carbonates results in a decrease of the atmospheric pressure, and therefore a release of SO_2 to the atmosphere and its further sequestration in sediments, a positive feedback could have occurred. The removal of CO_2 in carbonates would have allowed SO_2 to be released and trapped in sulfate sediments, decreasing the acidity of the cryosphere and allowing more carbonates to be formed. Such a runaway process could be one of the reasons for the sharp decrease of atmospheric CO_2 during the Hesperian, simultaneously with the formation of large sediment deposits, but remains a hypothesis to be further explored.

According to our scenario in the pre-Noachian and Noachian periods, the massive presence of sulfur in the cryosphere/atmosphere has kept low global temperature (near 230 K), in agreement with the results of clay minerals observations (Ehlmann et al., 2011). Under such conditions, clays may have been formed by alteration of the crust in the locally warmer region, where no SO_2–CO_2 clathrate can condense (equator during low obliquity). The low atmospheric SO_2 gas content may lead to acidic pH preventing carbonate from precipitating but permitting clay formation near the surface. More detailed modeling are required to discuss these implications.

Interestingly, the massive presence of sulfur in the pre-Noachian and Noachian cryosphere could have favored the occurrence of warm episodes, with liquid water at the surface and a global hydrological cycle. Such a warm episode, or series of warm episodes, with a typical duration of 10^5–10^7 years, could have allowed the formation of valley networks observed in the southern hemisphere (Hoke et al., 2011), and formed close to the late Noachian/Hesperian transition. Similar episodes seem to be required at the middle Noachian to explain the high degree of degradation of ancient craters (Mangold, personal communication, 2012). It has been suggested that SO_2, in addition to CO_2, could have played a major role in maintaining water in a liquid state at the surface of Mars for significant periods of time, with an ocean and a global hydrological cycle, and that such an episode could have been controlled by a well-developed SO_2 cycle (Halevy et al., 2007). The major objection in our scenario is that, starting from a cold state, any release of SO_2 to the atmosphere is followed by the formation of sulfate aerosols and a subsequent cooling of the atmosphere (T10). But any catastrophic event such as a giant asteroid impact or a massive volcanic SO_2 release or a large-scale destabilization of methane clathrate from a highly magmatically active subsurface, might have been able to melt the superficial cryosphere and release huge amounts of SO_2 and H_2O (and possibly CO_2) into the atmosphere. Provided such a catastrophic event was able to trigger a global hydrological cycle, even for a short time of a few years or 100 years, the SO_2 (and CO_2) released at the same time from the melting cryosphere could have taken the relay and driven a somewhat longer period of warm and wet Mars, according to Halevy et al. scenario. Episodes of huge methane release from clathrates present on oceanic floors occurred during the history of Earth. At the Paleocene–Eocene transition, 55.5 Myr ago, massive dissociation of oceanic methane hydrate led to a warming of 5–6 °C during ~1000 yr (see e.g. Higgins and Schrag, 2006). The injection of CH_4 into early Mars atmosphere with a mixing ratio of a few percents, that is partial pressure of a few tens millibar, may have possibly raised the surface temperature above 0 °C (Kasting, 1997), but further calculations by Tian (unpublished) do not confirm that CH_4, even at several percent level, is able to bring surface temperature close to the freezing point of water. Understanding if massive methane injections in the atmosphere of Mars, and/or giant impacts, have been able to initiate a SO_2 cycle-driven episode of warm and wet Mars (Halevy et al., 2007), breaking the background cold Noachian climate, is of prime interest to progress in our understanding of early Mars climate.

Whatever the precise triggering mechanisms of such possible warm episodes favored by the release of massive amounts of SO_2 together with CO_2 to the atmosphere may have been, our hypothesis may potentially explain the occurrence of outflow channels, valley networks and the degradation of impact craters. In Section 4, we suggested that the destabilization of clathrates when p_{CO2} dropped below 2 bar could be at the origin of chaotic terrains, and it may therefore as well explain the formation of outflow channels, provided sufficient amounts of water were present in the subsurface. Valley networks, formed at the late Noachian and which ended relatively sharply at the beginning of the Hesperian (Fasset and Head, 2011), could be the result of warm episodes occurring when the CO_2 pressure was still close to 2 bar, and the temperature relatively "high" (230 K). Such episodes could explain the formation of some sulfate deposits during the Noachian. The postulated drop in pressure at the Noachian/Hesperian transition resulted in a general cooling of the planet from 230 K to 220 K (for p_{CO2} = 1 bar), then 210 K (for p_{CO2} = 0.5 bar) (see Fig. 2). Provided this drop was sharp enough, the cooling of the planet by ≈20 K during the Hesperian could have rapidly inhibited warm episodes possibly at the

Table A1
Structure of SI and SII gas hydrates.

	SI		SII	
				
Cavity	5^{12}	$5^{12}6^2$	5^{12}	$5^{12}6^4$
Type of cavity (j: indexing number)	1	2	1	3
Number of cavities (m_j)	2	6	16	8
Average cavity radius (nm) (1)	0.395	0.433	0.391	0.473
Variation in radius (%) (2)	3.4	14.4	5.5	1.73
Co ordination number	20	24	20	28
Number of water molecules	42		136	
Cell parameters (nm)	a = 1.1956(3)		a = 1.7315(4)	
Cell volume (nm^3)	1.709(3)		5.192(4)	

(1) From Sloan (1998, p. 33).
(2) Variation in distance of oxygen atoms from center of cages (from Sloan, 1998, p. 33).
(3) For ethane hydrate (from Udachin et al., 2002).
(4) For tetrahydrofuran hydrate (from Udachin et al., 2002).

Table A2
Reference state parameters.

	Unit	Structure I	Structure II
$\Delta\mu_w^{L-\beta,0}$	J/mol	1287	1068
$\Delta h_w^{L-\beta,0}$	J/mol	931	764
$\Delta v_w^{L-\beta}\vert_{T^o}$	10^{-6} m^3/mol	4.5959	4.99644
$\Delta c_{p,w}^{L-\beta,0}$	J/(mol K^{-1})	−38.12	−38.12
$b_{p,w}^{L-\beta}$	J/(mol K^{-2})	0.141	0.141

$\Delta\mu_w^{L-\beta,0}$, $\Delta h_w^{L-\beta,0}$: Handa and Tse (1986).
$\Delta v_w^{L-\beta}\vert_{T^o}$, $\Delta c_{p,w}^{L-\beta,0}$, $b_{p,w}^{L-\beta}$: Sloan (1998).

origin of valley networks. A recent study shows that the degradation of impact craters experienced a sharp transition at 3.7 Ga (Mangold et al., 2012). This transition between a period of substantial erosion due to a significant global fluvial activity (late Noachian) and a period of more regional and sporadic warming episodes (Hesperian) may be the result of the suggested drop in pressure, resulting in both a general cooling of the planet and episodes of massive SO_2–CO_2 release. The necessarily sporadic nature of clathrate destabilization during the Hesperian could be at the origin of the degradation of Hesperian craters, showing no relationship between age and degradation state (Mangold et al., 2012). In order to confirm these views, it will be necessary to build reliable scenarios of such warming episodes, possibly triggered by specific events (impacts, massive methane release, obliquity variations, etc.) and favored by massive SO_2 release together with CO_2. If these events are intense enough, liquid water precipitation (rain) may incorporate atmospheric SO_2 so that the SO_2 aerosol deposition time could be shorter than in our arid model (SO_2 aerosols precipitation), implying a reduced cooling effect of aerosols, not sufficient to counteract the warming effect of SO_2 and other greenhouse gases. These extreme events provide also SO_2 precipitation before the Noachian–Hesperian boundary that could explain observed geological units. Also, clays may have been formed during such favorable climatic excursions (see e.g. Fan et al., 2008; Murchie et al., 2009; Wray et al., 2011).

Our results are based on extrapolations to low temperatures of the results obtained in Earth's laboratory conditions. In order to progress in our understanding of the role of the sulfur cycle in the early evolution of Mars, experimental measurements devoted to the measurements of CO_2–SO_2 clathrates thermodynamical and kinetic properties in martian conditions would be necessary. Future space missions to Mars could also bring new results. Search for SO_2 plumes associated with outgassing from surviving buried cryospheric SO_2 clathrate-rich reservoirs by the Exomars TGO mission in 2016, and mapping of SO_2 (if detected), could help in characterizing a possible residual activity of sulfur in the martian crust. SO_2 has never been detected in the martian atmosphere, with a measured upper limit at 2σ of 1 ppb (Krasnopolsy, 2005). Nevertheless, if some SO_2 has been trapped at depth in long life time clathrate layers, an episodic release due to tectonic or subsurface thermal events triggering the destabilization of clathrates cannot be ruled out. The dielectric constants of clathrates are too close to that of water ice to allow to them to be easily distinguished at radar wavelengths (Mousis et al., 2013), which makes subsurface clathrate layers hardly detectable from orbit. Buried reservoirs of SO_2 and H_2S clathrate–hydrates could be searched for through drilling from future landers on Mars. If some sulfur clathrate deposits survived close to some volcanoes, a concentric structure might be observed, like e.g. around the Hakon Mosby mud volcano in Marmara Sea where concentric layers of gas hydrates are observed, with a maximum concentration of clathrates in the sediment of 10–20% at about 500 m of the volcano (Fig. II.17 in Bourry, 2008). In a similar way, although in quite different conditions (subaerial volcanism, larger space and timescales), concentric deposits of CO_2–SO_2–H_2S clathrates could have been formed on Mars around volcanoes, with concentrations and composition expected to depend on the distance to the outgassing plume. The possibility for such deposits to have survived a long time is of course highly speculative, and we do not know at which depth they could have been preserved.

Acknowledgments

E. Chassefière, E. Dartois, A. Lakhlifi and F. Schmidt thank the interdisciplinary EPOV program of CNRS. O. Mousis acknowledges support from CNES. We feel indebted to the referees, M. Mischna and A. Fairén, for their constructive comments that allowed to significantly improve the quality of this paper. We thank L. Daumas for the drawing of Fig. 7.

Appendix A

A.1. Description of the statistical–thermodynamic model

Three main clathrate hydrate structures have been identified: SI, SII and SH. They differ by their crystallographic structure in which water is organized in a three dimensional network. It liberates internal cavities of different polyhedral types called 5^{12}, $5^{12}6^2$, $5^{12}6^4$, $4^35^66^3$ and $5^{12}6^8$ (e^f describes a polyhedron: e is the number of edges of the face, and f is the number of faces with e edge). In Table A1 are described more precisely the SI and SII structures, the major ones to be formed due to the composition of martian gases.

In the case of clathrate hydrates in thermodynamic equilibrium, below the water freezing point, the equality of chemical potentials of water in the ice phase and in the hydrate phase can be written, by introducing a hypothetical reference state (phase β) corresponding to a hydrate with empty cavities:

$$\Delta\mu_w^{H-\beta} - \Delta\mu_w^{I-\beta}, \quad (1)$$

where $\Delta\mu_w^{H-\beta}$ and $\Delta\mu_w^{I-\beta}$ are the differences of the chemical potentials between water in hydrate (H) or ice (I) and water in the reference phase (β), respectively.

A.1.1. Modeling of $\Delta\mu_w^{H-\beta}$

$\Delta\mu_w^{H-\beta}$ is then determined from statistical thermodynamics whereas $\Delta\mu_w^{l-\beta}$ is determined by means of relations from classical thermodynamics that can be expressed as a function of the fugacity f_j of the gas j as:

$$\Delta\mu_w^{H-\beta} = RT\sum_i v_i \ln\left(1-\sum_j \theta_j^i\right) - RT\sum_i v_i \ln\left(1-\sum_j C_j^i f_j(T,P)\right) \quad (2)$$

where v_i is the number of cavities of type i, C_j^i is the Langmuir constant of component j in the cavity i describing the interaction potential between the encaged guest molecule and the surrounding water molecules, evaluated by assuming a spherically symmetrical cage and associated potential:

$$C_j^i = \frac{4\pi}{kT}\int_0^\infty \exp\left(-\frac{w(r)}{kT}\right) r^2 dr, \quad (3)$$

where w is the radial interaction potential between the guest molecule and the water molecules forming the structure. The interaction potential, when described by a Kihara model (Mckoy and Sinagoglu, 1963), can be expressed as:

$$w(r) = 2z\varepsilon\left[\frac{\sigma^{12}}{\bar{R}^{11} r}\left(\delta^{10} + \frac{a}{\bar{R}}\delta^{11}\right) - \frac{\sigma^6}{\bar{R}^5 r}\left(\delta^4 + \frac{a}{\bar{R}}\delta^5\right)\right] \quad (4)$$

$$\delta^N = \frac{1}{N}\left[(1 - r/\bar{R} - a/\bar{R})^{-N} - (1 + r/\bar{R} - a/\bar{R})^{-N}\right] \quad (5)$$

The gas parameters ε, σ and a are the Kihara parameters describing the potential we seek for and can be calculated from experimental data by fitting the model equations to corresponding hydrate equilibrium experimental data. The interaction potential takes into account the geometrical properties of the cavities (coordination number z and average mean radius $\bar{R}$, given in Table A1).

The equations that can be used to evaluate $\Delta\mu_w^{l-\beta}$, the difference in chemical potential between ice and the reference state T_0 = 273.15 K and the pressure P_0 = 1 bar are summarized in chapter 5 and in particular in Table 5.9 of Sloan and Koh (2008) and Table 4.3.1 of Herri et al. (2011). The corresponding values of the reference state parameters used in the model are given in Table A2.

A.1.2. Equilibrium

A simultaneous minimization of the three Kihara parameters (sigma, core radius and epsilon/k) on the clathrate hydrate model

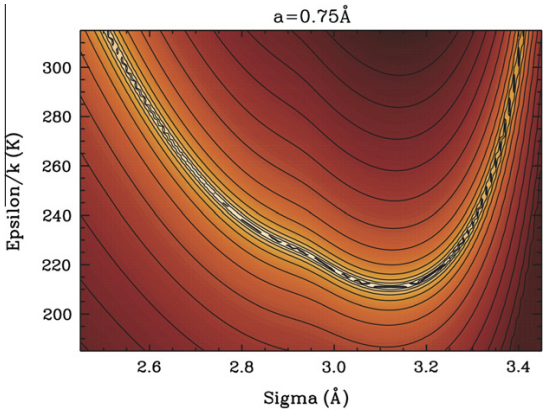


Fig. A1. Pearson's chi square test contour plot of the minimized ε/k versus σ for SO_2 Kihara parameters, with core radius a fixed at 0.75 Å. Contour levels are spaced in powers of 3 of the best-regressed value. Pressure and temperature equilibrium data for SO_2 hydrate are taken from Tamman and Krige (1925).

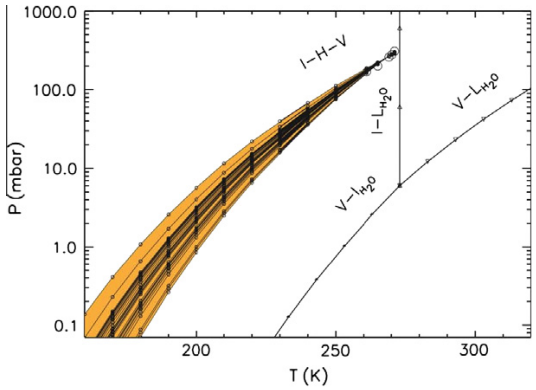


Fig. A2. Range of pressure and temperature extrapolated equilibrium for SO_2 clathrate hydrate using our model (small dots, colored range). The input Kihara parameters are obtained in the 3D {ε/k, σ, a} parameter space regression on experimental data by setting the core radius in the $a \in [0.55, 0.95]$ range, then regressing the degenerate Kihara parameters as shown in Fig. 3. Original data from Tamman and Krige (1925) (large circle) are displayed as well as water phase diagram limits.

faces a high level of degeneracy, an issue amplified by the paucity of available equilibrium data in the sulfur dioxide case. In a rather well defined and measured system the degeneracy remains an issue (Herri et al., 2011). This is somehow already reflected in the distinct Kihara parameters deduced in the literature. Kihara parameters for pure substances can be evaluated from measurement of the viscosity, or can be calculated from the second virial coefficient, or from a combination of measurements (Tee et al., 1996). Also, they can be evaluated from Henry constants (Uno et al., 1975). The principle is to retrieve the Kihara parameters over experimental data with a limited number of pure substances. The authors propose a correlation to estimate the Kihara parameters for all kinds of gases. The optimization strategy we adopt to reduce the degeneracy is to set one of the parameters before to deduce the corresponding two others by minimization, as suggested in e.g. Mehta and Sloan (1996). They propose to fix the Kihara a value. Based on the parameterization by Tee et al. (1966) and Uno et al. (1975) for SO_2, the core radius a value is estimated to lie close to a = 0.75 Å, that we further set to explain the analysis performed.

Then, for a given set of Kihara parameters ε_j and σ_j, and a given temperature (resp. a given pressure), the calculated equilibrium pressure P_{calc} (resp. the calculated equilibrium temperature T_{calc}) corresponds to the value such as $\Delta\mu_w^{H-\beta} - \Delta\mu_w^{l-\beta}$. Then the calculated pressure and temperature are compared to the experimental ones P_{exp} and T_{exp}, and a deviation function can be defined as:

$$F(\varepsilon_j,\sigma_j) = \sum_{i=1}^{N}\left|\frac{P_{calc}}{P_{exp}} - 1\right| \rightarrow \min\left(\text{resp.}F(\varepsilon_j,\sigma_j) = \sum_{l=1}^{N}\left|\frac{T_{calc}}{T_{exp}} - 1\right| \rightarrow \min\right) \quad (6)$$

The summation is performed over all N data of the set.

In the work of Herri and Chassefière (2012), the Kihara parameters for CO_2 clathrate hydrate were retrieved with such a scheme, with ε/k = 178.21 K, a = 0.6805 Å and σ = 2.873 Å. By using the same method, the present work aims at retrieving the Kihara parameters for SO_2 hydrate.

A.2. Retrieving the SO_2 Kihara parameters

We focus on the value of a = 0.75 Å, but the minimization was performed over a broader range of a values. Then, the ε and σ

can be optimized from experimental results. Using the Tamman and Krige (1925) data, the minimized ε and σ values dependencies are shown in Fig. A1, following a valley of minima all satisfying the available experimental data. Using another core radius value would give rise to another satisfying correlation. With the limited data available, covering only the range of temperature from 261.15 K to 271.15 K, corresponding pressure and temperature SO_2 clathrate hydrate equilibria at lower temperatures are shown in Fig. A2 (in this case the core radius was explored over a larger range). Nevertheless, taking into account the regression uncertainties, significant constraints can be set in the martian context as shown in the next section.

References

Baldridge, A.M. et al., 2009. Contemporaneous deposition of phyllosilicates and sulfates: Using Australian acidic saline lake deposits to describe geochemical variability on Mars. Geophys. Res. Lett. 36, L19201. http://dx.doi.org/10.1029/2009GL040069.

Bibring, J.-P. et al., 2006. Global mineralogical and aqueous Mars history derived from OMEGA/Mars Express data. Science 312 (5772), 400–404.

Bibring, J.-P. et al., 2007. Coupled ferric oxides and sulfates on the martian surface. Science 317, 1206–1210.

Bourry, C., 2008. Caractérisation physique et géochimique d'hydrates de gaz d'environnements géologiques différents. PhD thesis, University of Brest, France.

Brasser, R., Walsh, K.J., 2011. Stability analysis of the martian obliquity during the Noachian era. Icarus 213, 423–427.

Carr, M., 1987. Water on Mars. Nature 326, 30–35.

Cassata, W.S., Shuster, D.L., Renne, P.R., Weiss, B.P., 2012. Trapped Ar isotopes in meteorite ALH 84001 indicate Mars did not have a thick ancient atmosphere. Icarus 221, 461–465.

Chassefière, E., Leblanc, F., 2011a. Methane release and the carbon cycle on Mars. Planet. Space Sci. 59, 207–217.

Chassefière, E., Leblanc, F., 2011b. Constraining methane release due to serpentinization by the D/H ratio on Mars. Earth Planet. Sci. Lett. 310, 262–271.

Christensen, P., 2006. Water at the poles and in permafrost regions of Mars. Elements 2, 151–155.

Clifford, S.M., Parker, T.J., 2001. The evolution of the martian hydrosphere: Implications for the fate of a primordial ocean and the current state of the northern plains. Icarus 154, 40–79.

Clifford, S.M., Lasue, J., Heggy, E., Boisson, J., McGovern, P., Max, M.D., 2010. Depth of the martian cryosphere: Revised estimates and implications for the existence and detection of subpermafrost groundwater. J. Geophys. Res. 115, E07001. http://dx.doi.org/10.1029/2009JE003462.

Colaprete, A., Toon, O.B., 2003. Carbon dioxide clouds in an early dense martian atmosphere. J. Geophys. Res. 108, 5025. http://dx.doi.org/10.1029/2002JE001967.

Craddock, R.A., Greeley, R., 2009. Minimum estimates of the amount and timing of gases released into the martian atmosphere from volcanic eruptions. Icarus 204, 512–526.

Ehlmann, B.L., Mustard, J.F., 2012. An in situ record of major environmental transitions on early Mars at Northeast Syrtis Major. Geophys. Res. Lett. 39, L11202.

Ehlmann, B.L. et al., 2011. Subsurface water and clay mineral formation during the early history of Mars. Nature 479, 53. http://dx.doi.org/10.1038/nature10582.

Ehlmann, B.L. et al., 2013. Geochemical Consequences of Widespread Clay Mineral Formation in Mars' Ancient Crust. Space Sci. Rev. 174 (1–4), 329–364.

Fairén, A.G. et al., 2004. Inhibition of carbonate synthesis in acidic oceans on early Mars. Nature 431, 423–426.

Falenty, A., Genov, G., Hansen, Th.C., Kuhs, W.F., Salamatin, A.N., Falenty, 2011. Kinetics of CO_2 hydrate formation from water frost at low temperatures: Experimental results and theoretical model. J. Phys. Chem. C 115, 4022–4032.

Fan, C., Schulze-Makuch, D., Fairén, A.G., Wolff, J.A., 2008. A new hypothesis for the origin and redistribution of sulfates in the equatorial region of western Mars. Geophys. Res. Lett. 35, L06201. http://dx.doi.org/10.1029/2007GL033079.

Fasset, C.I., Head, J.W., 2011. Sequence and timing of conditions on early Mars. Icarus 211, 1204–1214.

Forget, F., Pierrehumbert, R.T., 1997. Warming early Mars with carbon dioxide clouds that scatter infrared radiation. Science 278, 1273–1276.

Forget, F., Haberle, R.M., Montmessin, F., Levrard, B., Head, J.W., 2006. Formation of glaciers on mars by atmospheric precipitation at high obliquity. Science 311, 368–371.

Gaillard, F., Scaillet, B., 2009. The sulfur content of volcanic gases on Mars. Earth Planet. Sci. Lett. 279 (1–2), 34–43.

Gaillard, F., Michalski, J., Berger, G., McLennan, S., Scaillet, B., 2013. Geochemical reservoirs and timing of sulphur cycling on Mars. Space Sci. Rev. 174 (1–4), 251–300.

Gomes, R., Levison, H., Tsiganis, K., Morbidelli, A., 2005. Origin of the cataclysmic late heavy bombardment period of the terrestrial planets. Nature 435, 466–469.

Greeley, R., Schneid, B.D., 1991. Magma generation on Mars – Amounts, rates, and comparisons with Earth, Moon, and Venus. Science 254 (1991), 996–998.

Griffith, L.L., Shock, E.L., 1995. A geochemical model for the formation of hydrothermal carbonates on Mars. Nature 377, 406–408.

Grimm, R.E., Painter, S.L., 2009. On the secular evolution of groundwater on Mars. Geophys. Res. Lett. 36 (24) (CiteID L24803).

Grott, M. et al., 2011. Volcanic outgassing of CO_2 and H_2O on Mars. Earth Planet. Sci. Lett. 308, 391–400.

Halevy, I., Zuber, M.T., Schrag, D.P., 2007. A sulfur dioxide climate feedback on early Mars. Science 318 (5858), 1903–1907.

Handa, Y.P., Tse, J.S., 1986. Thermodynamic properties of empty lattices of structure I and structure II clathrate hydrates. J. Phys. Chem. 23, 5917–5921.

Hanna, J.C., Phillips, R.J., 2006. Tectonic pressurization of aquifers in the formation of Mangala and Athabasca valles, Mars. J. Geophys. Res. 111, E03003. http://dx.doi.org/10.1029/2005JE002546.

Head, J.W., Marchant, D.R., 2009. Inventory of ice-related deposits on mars: evidence for burial and long-term sequestration of ice in non-polar regions and implications for the water budget and climate evolution. Lunar Planet. Sci. 40. id.1356.

Head, J.W., Pratt, S., 2001. Extensive Hesperian-aged south polar ice sheet on Mars: Evidence for massive melting and retreat, and lateral flow and ponding of meltwater. J. Geophys. Res. 106 (E6), 12275–12300.

Herri, J.M., Chassefière, E., 2012. Carbon dioxide, argon, nitrogen and methane clathrate hydrates: Thermodynamic modelling, investigation of their stability in martian atmospheric conditions and variability of methane trapping. Planet. Space Sci. 73 (1), 376–386.

Herri, J.-M., Bouchemoua, A., Kwaterski, M., Fezoua, A., Ouabbas, Y., Cameirao, A., 2011. Gas hydrate equilibria from CO_2–N_2 and CO_2–CH_4 gas mixtures – Experimental studies and thermodynamic modelling. Fluid Phase Equilib. 301, 171–190.

Higgins, J.A., Schrag, D.P., 2006. Beyond methane: Towards a theory for the Paleocene–Eocene thermal maximum. Earth Planet. Sci. Lett. 245, 523–537.

Hoke, M.R.T., Hynek, B.M., Tucker, G.E., 2011. Formation timescales of large martian valley networks. Earth Planet. Sci. Lett. 312, 1–12.

Johnson, S.S., Mischna, M.A., Grove, T.L., Zuber, M.T., 2008. Sulfur-induced greenhouse warming on early Mars. J. Geophys. Res. 113, E8 (CiteID E08005).

Johnson, S.S., Pavlov, A.A., Mischna, M.A., 2009. Fate of SO_2 in the ancient martian atmosphere: Implications for transient greenhouse warming. J. Geophys. Res. 114, E11011. http://dx.doi.org/10.1029/2008JE003313.

Kasting, J.F., 1997. Warming early Earth and Mars. Science 276, 1213–1215.

King, P.P., McLennan, S.M., 2010. Sulfur on Mars. Elements 6, 107–112.

Krasnopolsky, V.A., 2005. A sensitive search for SO_2 in the martian atmosphere: Implications for seepage and origin of methane. Icarus 178, 487–492.

Laskar, J., Levrard, B., Mustard, J.F., 2002. Orbital forcing of the martian polar layered deposits. Nature 419, 375–377.

Le Deit, L. et al., 2008. Ferric oxides in East Candor Chasma, Valles Marineris (Mars) inferred from analysis of OMEGA/Mars Express data: Identification and geological interpretation. J. Geophys. Res. 113 (E7) (CiteID E07001).

Levrard, B., Forget, F., Montmessin, F., Laskar, J., 2004. Recent ice-rich deposits formed at high latitude on Mars by sublimation of unstable equatorial ice during low obliquity. Nature 431 (7012), 1072–1075.

Mangold, N., Adeli, S., Conway, S., Ansan, V., Langlais, B., 2012. A chronology of early Mars climatic evolution from impact crater degradation. J. Geophys. Res. 117, E04003. http://dx.doi.org/10.1029/2011JE004005.

Massé, M. et al., 2008. Mineralogical composition, structure, morphology, and geological history of Aram Chaos crater fill on Mars derived from OMEGA Mars Express data. J. Geophys. Res. 113 (E12) (CiteID E12006).

Mckoy, V., Sinagoglu, O.J., 1963. Theory of dissociation pressures of some gas hydrates. J. Chem. Phys. 38, 2946–2956.

Mehta, A.P., Sloan, E.D., 1996. Improved thermodynamic parameters for prediction of structure H hydrate equilibria. Aiche J. 42 (7), 2036–2046.

Mellon, M.T., 1996. Limits on the CO_2 content of the martian polar deposits. Icarus 124, 268–279.

Mellon, M.T., Feldman, W.C., Prettyman, T.H., 2004. The presence and stability of ground ice in the southern hemisphere of Mars. Icarus 169, 324–340.

Michalski, J., Niles, P.B., 2011. Origin of martian sulfates and interior layered deposits (ILDs) in the Valles Marineris by atmospherically driven processes. EPSC-DPS Joint Meeting 2011, p. 1752.

Morbidelli, A., Tsiganis, K., Crida, A., Levison, H., Gomes, R., 2007. Dynamics of the giant planets of the Solar System in the gaseous protoplanetary disk and their relationship to the current orbital architecture. Astron. J. 134, 1790–1798.

Moroz, V.I., 1998. Chemical composition of the atmosphere of Mars. Adv. Space Res. 22, 449–457.

Mousis, O., Lunine, J.I., Chassefière, E., Montmessin, F., Lakhlifi, A., Picaud, S., Petit, J.-M., Cordier, D., 2012. Mars cryosphere: A potential reservoir for heavy noble gases? Icarus 218, 80–87.

Mousis, O. et al., 2013. Volatile trapping in martian clathrates. Space Sci. Rev. 174 (1–4), 213–250.

Mumma, M.J. et al., 2009. Strong release of methane on mars in northern summer 2003. Science 323, 1041–1045.

Murchie, S.L. et al., 2009. A synthesis of martian aqueous mineralogy after 1 Mars year of observations from the Mars Reconnaissance Orbiter. J. Geophys. Res. 114, E00D06. http://dx.doi.org/10.1029/2009JE003342.

Nedell, S.S., Squyres, S.W., Andersen, D.W., 1987. Origin and evolution of the layered deposits in the Valles Marineris, Mars. Icarus 70, 409–441.

Niles, P.B. et al., 2013. Geochemistry of carbonates on Mars: Implications for climate history and nature of aqueous environments. Space Sci. Rev. 174 (1–4), 301–328.

Nummedal, D., Prior, D.B., 1981. Generation of martian chaos and channels by debris flows. Icarus 45, 77–86.
Ody, A. et al., 2013. Global investigation of olivine on Mars: Insights into crust and mantle composition. J. Geophys. Res., in press. http://dx.doi.org/10.1029/2012JE004149.
Owen, T., Biemann, K., Rushneck, D.R., Biller, J.E., Howarth, D.W., LaFleur, A.L., 1977. The composition of the atmosphere at the surface of Mars. J. Geophys. Res. 82, 4635–4639.
Pepin, R.O., 1991. On the origin and early evolution of terrestrial planet atmospheres and meteoritic volatiles. Icarus 92, 2–79.
Pollack, J.B., Kasting, J.F., Richardson, F.M., Poliakoff, K., 1987. The case for a wet, warm climate on early Mars. Icarus 71, 203–224.
Postawko, S.E., Kuhn, W.R., 1986. Effect of the greenhouse gases (CO_2, H_2O, SO_2) on martian paleoclimate. In: 60th Proc. Lunar Planet. Sci. Conf. J. Geophys. Res., 91, D431.
Quantin, C., Allemand, P., Mangold, N., Delacourt, C., 2004. Ages of Valles Marineris (Mars) landslides and implications for canyon history. Icarus 172 (2), 555–572.
Rodriguez, J.A.P. et al., 2006. Headward growth of chasmata by volatile outbursts, collapse, and drainage: Evidence from Ganges chaos, Mars. Geophys. Res. Lett. 33 (18) (CiteID L18203).
Segura, T.L., Toon, O.B., Colaprete, A., Zahnle, K., 2002. Environmental effects of large impacts on Mars. Science 298 (5600), 1977–1980.
Segura, T.L., Toon, O.B., Colaprete, A., 2008. Modeling the environmental effects of moderate-sized impacts on Mars. J. Geophys. Res. 113 (E11) (CiteID E11007).
Sloan, E.D., 1998. Clathrate Hydrates of Natural Gases, second ed. Marcel Decker, New York.
Sloan, E.D., Koh, C.A., 2008. Clathrate Hydrates of Natural Gases, third ed. CRC Press.
Smith, D.E. et al., 2001. Mars Orbiter Laser Altimeter: Experiment summary after the first year of global mapping of Mars. J. Geophys. Res. 106 (E10), 23689–23722.
Squyres, S.W., Kasting, J.F., 1994. Early Mars: How warm and how wet? Science 265 (5173), 744–749.
Squyres, S.W. et al., 2004. In situ evidence for an ancient aqueous environment at Meridiani Planum, Mars. Science 306, 1709–1714.
Tamman, G., Krige, G.J., 1925. Equilibrium pressures of gas hydrates. Zeit. Anorg. Und Algem. Chem. 146, 179–195.
Tanaka, K.L., 1999. Debris-flow origin for the Simud/Tiu deposit on Mars. J. Geophys. Res. 104, 8637–8652.
Tee, L.S., Gotoh, S., Stewart, W.E., 1996. Molecular parameters of normal fluids: the Kihara potential with special core. Ind. Eng. Fundam. 5, 363.
Tian, F., Kasting, J.F., Solomon, S.C., 2009. Thermal escape of carbon from the early martian atmosphere. Geophys. Res. Lett. 36 (2) (CiteID L02205).
Tian, F. et al., 2010. Photochemical and climate consequences of sulfur outgassing on early Mars. Earth Planet. Sci. Lett. 295, 412–418.
Udachin, K.A., Ratcliffe, C.I., Ripmeester, J.A., 2002. Single crystal diffraction studies of structures I, II and H hydrates: Structure, cage occupancy and composition. J. Supra Mol. Chem. 2, 405–408.
Uno, K. et al., 1975. Application of the perturbation theory to the calculation of Henry's constants for normal fluids. J. Chem. Eng. Japan 8 (3), 201–206.
Van Berkum, J.G., Diepen, G.A.M., 1979. Phase equilibria in $SO_2 + H_2O$: The sulfur dioxide gas hydrate two liquid phases, and the gas phase in the temperature range 273 to 400 K and at pressures up to 400 MPa. J. Chem. Thermodyn. 11, 317–334.
Van der Waals, J.∼H., Platteeuw, J.∼C., 1959. Clathrate solutions. In: Advances in Chemical Physics, vol. 2. Interscience, New York, 1–57.
Von Stackelberg, M., 1949. Solid gas hydrates. Die Naturwissenschaften 36 (12), 359–362.
Wilson, L., Head III, J.W., 2002. Tharsis-radial graben systems as the surface manifestation of plume-related dike intrusion complexes: Models and implications. J. Geophys. Res. 107 (E8), 5057. http://dx.doi.org/10.1029/2001JE001593.
Wong, A.-S., Atreya, S.K., Encrenaz, Th., 2003. Chemical markers of possible hot spots on Mars. J. Geophys. Res. 110 (E4), 5026. http://dx.doi.org/10.1029/2002JE002003.
Wray, J.J., Murchie, S.L., Squyres, S.W., Seelos, F.P., Tornabene, L.L., 2011. Diverse aqueous environments on ancient Mars revealed in the southern highlands. Geology 37 (11), 1043–1046. http://dx.doi.org/10.1130/G30331A.1.

Troisième partie

Projet de recherche

Chapitre 6

Projet de recherche : interaction surface-atmosphère

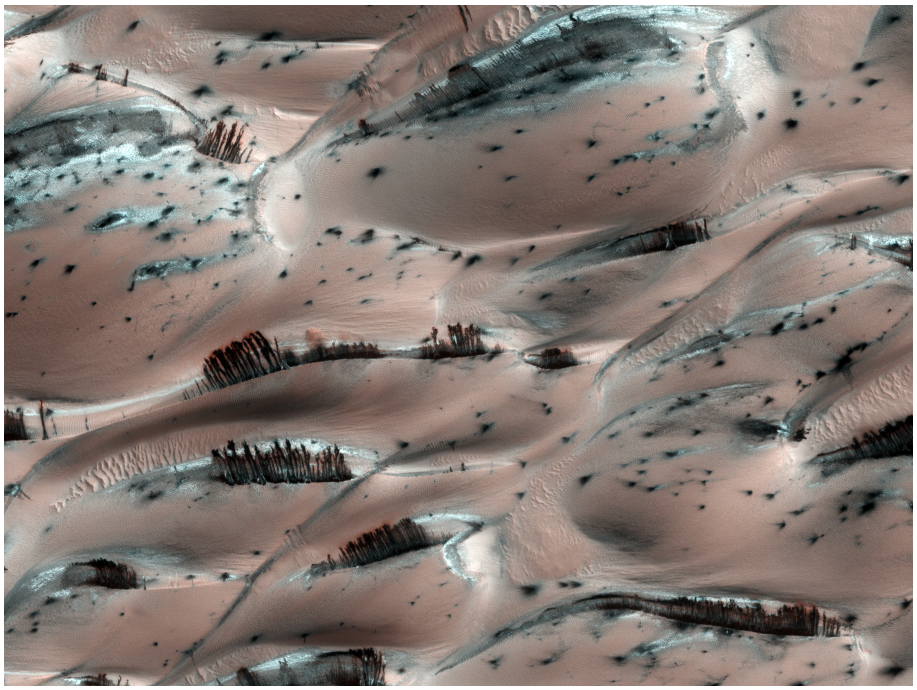


Image HiRISE des écoulements sombres

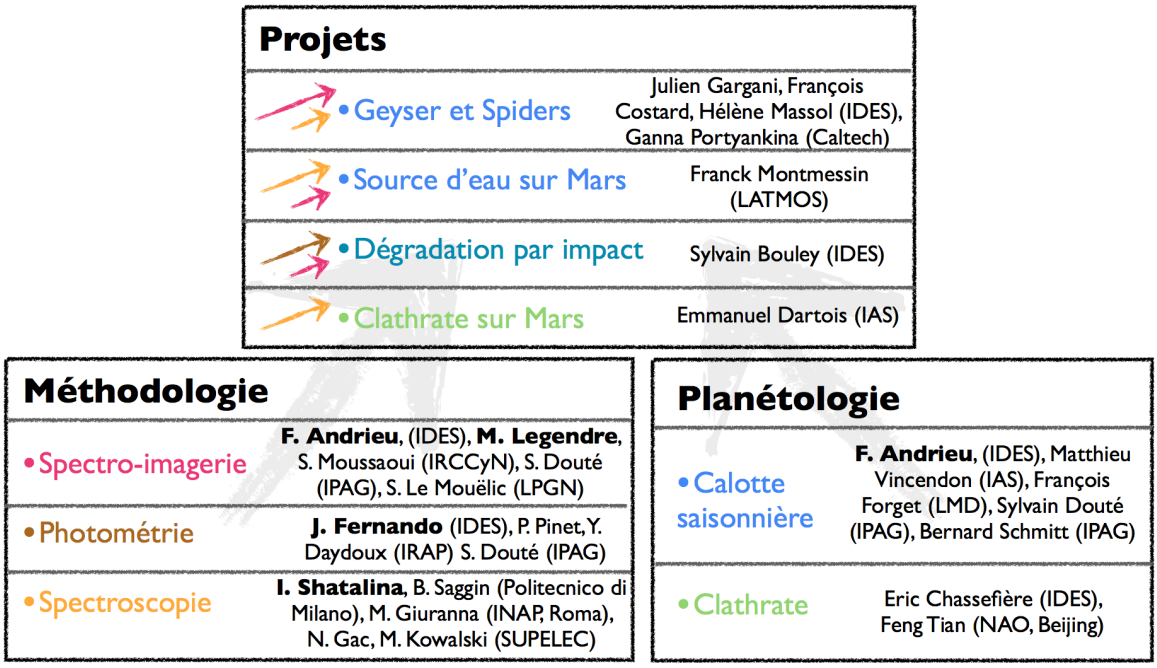


FIGURE 6.1: Bilan des collaborations et des projets. Les étudiants en thèse que j'ai co-encadrés ou suivis sont en gras.

Pour comprendre les échanges de volatils sur plusieurs échelles de temps et d'espace, je souhaite étudier les interactions surface-atmosphère à travers plusieurs exemples :

- les geysers et spiders sur Mars, avec échanges de glace, activité actuelle à l'échelle de quelques semaines sur quelques dizaines de mètres
- la source d'eau atmosphérique actuelle Martienne dans la calotte permanente nord de Mars, activité actuelle à l'échelle de quelques mois sur quelques millions de km^2
- la dégradation des surfaces par photométrie, sous l'effet du bombardement météoritique/éolien, activité récente à l'échelle de quelques centaines d'années à quelques millions d'années, sur des mètres à km
- les clathrates sur Mars actuellement et dans le passé martien, à l'échelle de l'année jusqu'au milliard d'années, sur quelques millions de km^2

Ces quarte projets sont issus de mes travaux antérieurs, à la fois des parties méthodologique et planétologique. La figure 6.1 présente les liens entre ces différents programmes de recherche ainsi que les collaborateurs principaux.

6.1 Geysers et spiders

Les spiders et les geysers ont été découverts initialement d'après les images MOC [206]. Il s'agit de structures dendritiques, présentes sur la surface sud de Mars, souvent associées à des formes sombres allongées. La section 4.1.3.3 page 197 décrit les observations, le modèle et les incompréhensions actuelles. Les perspectives ont été développées dans cette section 4.3 page 212.

La localisation spatiale des spiders et geysers à l'échelle du pôle sud n'a pas trouvé d'explication plausible. D'autre part, le lien entre spiders et geyser n'est pas tout à fait établi, puisqu'ils existent indépendamment l'un de l'autre. De plus, la formation de cracks dans la glace de CO_2 reste encore méconnue. Le modèle n'est pas tout à fait compatible avec les premières analyses spectroscopiques et géomorphologiques car de la glace transparente est présente sur des zones non recouvertes de geysers [180, 278]. Le modèle peine aussi à expliquer l'activité très précoce de certains geysers. Enfin, le lien entre geyser et écoulement sombre n'est pas bien compris. Rappelons que de nombreuses questions

restent en suspens, car aucune observation directe d'un geyser n'a été possible jusqu'à présent [313].

L'enjeu majeur est une meilleure description du cycle de CO_2 martien actuel pour la compréhension de ces phénomènes, le cycle de CO_2 ayant une place prédominante dans le climat de la planète rouge. Ces mécanismes de geysers diminuent fortement l'albédo du CO_2, impliquant une augmentation de la sublimation à grande échelle et donc une modification des pressions et de l'écoulement atmosphériques. Leurs modélisations devraient améliorer sensiblement la validité des modèles de climat globaux (GCM) actuel, mais aussi permettront de mieux appréhender les variations climatiques anciennes sur Mars. En effet, l'histoire de l'effet de serre et de la température à la surface de Mars est fortement liée au CO_2. Il est possible que les spiders aient joué un rôle majeur dans le passé, notamment à haute obliquité dans des régions à plus basse latitude.

L'autre enjeu primordial est la compréhension du cycle des poussières et des phénomènes éoliens sur Mars. En l'absence d'eau, les phénomènes éoliens sont une source majeure de l'abrasion des surfaces martiennes. Les phénomènes de geysers et de formation des spiders constituent le mécanisme d'évolution morphologique le plus efficace sur Mars, puisqu'il est 100 fois plus efficace qu'une tempête de poussière globale [259, 111].

Je souhaite développer plusieurs approches pour étudier ces phénomènes. Dans un premier temps, il s'agit de réaliser des inversions rapides de modélisation spectroscopique fine (de type transfert radiatif) sur les données d'images hyperspectrales. Ces perspectives méthodologiques ont été développées dans la section 1.3.1 page 18 et font l'objet de la thèse de doctorat de François Andrieu.

Aussi, je souhaite réaliser des études géomorphologiques quantitatives sur les données HiRISE à haute résolution spatiale afin de décrire les changements morphologiques pour contraindre les phénomènes en jeux. Des Modèles Numériques de Terrain (MNT) seront utiles dans cette tâche. Par exemple, il serait pertinent de discuter la vitesse de l'écoulement sombre au regard de la pente des dunes.

En complément aux études observationnelles de spectro-imagerie et de géomorphologie, il est nécessaire de créer des modélisations numériques et des modélisations analogiques en laboratoire, afin de tester quantitativement la véracité des phénomènes proposés. Durant cette étape, il s'agira de réaliser des expériences simplifiées de différents phénomènes macroscopiques (nettoyage des poussières, écoulement, ...) dans des conditions s'approchant de celle de Mars. Des modélisations physiques permettront à la fois de transposer les conditions de laboratoire à celle de Mars mais aussi de tester la pertinence de ces phénomènes de manière générale.

6.2 Source d'eau atmosphérique sur Mars

La condensation locale et la sublimation du CO_2 et H_2O est le cycle climatique principal actuellement. Il implique un quart de l'atmosphère martienne. Les dépôts saisonniers de l'hémisphère sud sont essentiellement composés de glace de CO_2 [179] et leur sublimation est contrôlée par leur albédo [285]. Les dépôts saisonniers nord sont plus déroutants car ils mélangent CO_2 et H_2O [104, 6].

L'origine de cette dichotomie entre les calottes saisonnières nord et sud, semble être la présence de glace d'eau uniquement au sommet de la calotte nord PNPC (Permanent North Polar Cap). Tandis que la calotte permanente sud PSPC (Permanent South Polar Cap) est recouverte en permanence d'une couche de CO_2 qui empêche l'injection d'eau dans l'atmosphère au pôle sud. Les mesures TES [301] et les modélisations GCM [227] suggèrent que la majorité de l'eau dans l'atmosphère actuelle martienne provient du PNPC pendant l'été.

En outre, l'analyse des données OMEGA suggère que la glace d'eau du PNPC évolue au cours de l'été [178] en raison du métamorphisme. L'énergie solaire absorbée dans le PNPC peut être soit (i) convertie à sublimer la glace H_2O pour enrichir l'atmosphère martienne (ii) convertie en chaleur pour augmenter la température de l'eau et le métamorphisme de glace. La proportion relative entre sublimation et métamorphisme, et plus généralement la microphysique de la surface du PNPC, reste une question ouverte. L'enjeu de cette étude est de déterminer la contribution globale de l'eau dans le climat martien à l'heure actuelle, mais aussi pour le passé, dans des conditions différentes d'obliquité.

Pour déterminer l'évolution temporelle du PNPC, mon objectif est de réaliser une étude spectroscopique fine à l'aide d'une inversion de transfert radiatif dans le but de mesurer à la fois les paramètres de surface (compacité, taille de grains, ...), mais aussi la température de vibration de la glace d'eau par spectroscopie [287] . Cette étude ne peut se faire qu'à haute résolution spectrale, comme disponible avec l'instrument PFS. Le chapitre 3 page 133 décrit ma contribution dans l'amélioration de la calibration de l'instrument. Aussi, les perspectives de cet instrument sont développées dans la section 3.3 page 141.

6.3 Dégradation des surfaces planétaires par étude photométrique

La photométrie est l'étude de l'intensité lumineuse provenant des surfaces planétaires sous plusieurs géométries d'acquisition (directions d'incidence et d'émergence). Elle consiste à mesurer et interpréter la réflectance bi-directionnelle (BRDF), comme exposée au chapitre 2 page 75. En utilisant les données d'un corps entier, il est possible de donner la courbe de phase moyenne pour le corps (réflectance en fonction de l'angle de phase, simplification de la BRDF) , par exemple, la Lune globale grâce à des observations télescopiques [324] et spatiale par SELENE [342]. Une synthèse des observations et interprétations lunaires a été publiée très récemment [296]. Aussi, des études ont pu être menées à l'échelle globale sur Mercure, grâce à des observations télescopiques [336] et spatiales par MESSENGER [72]. Sur Mars, une estimation globale a très récemment été réalisée après correction atmosphérique [331]. Connaître la courbe photométrique d'une région donnée est beaucoup plus difficile car elle nécessite plusieurs observations de la même zone. Les études locales ont été possibles sur la Lune grâce aux dernières missions d'exploration CLEMENTINE UVVIS [172], SMART-1 AMIE [153], LUNAR RECONNAISSANCE ORBITER NAC [154]. Sur Mars, l'instrument HRSC [145], OMEGA [257] et maintenant CRISM [35, 86] permettent de faire une acquisition de données de la même zone, pour plusieurs géométries en une seule acquisition et d'en estimer la BRDF. Le mode pointage OMEGA a été réalisé pour quelques sites, celui de HRSC ne comporte que 9 géométries (de + /- 18,9° d'émergence) et l'instrument CRISM réalise en routine 11 observations (de +/- 60° d'émergence) quasi instantanément de la même zone, dans le but d'échantillonner la BRDF. Il n'existe malheureusement pas d'instrument équivalent pour la Lune, mais la BRDF peut être estimée en fusionnant plusieurs observations à des géométries différentes.

Sous l'effet du bombardement solaire et météorique (space weathering), les surfaces subissent des changements spectraux largement étudiés dans la littérature scientifique [120]. Aussi, des changements photométriques sont attendus [114] mais peu d'études observationnelles n'ont pu le montrer jusqu'à présent, car les études photométriques locales ne sont disponibles que depuis très récemment. L'étude de ces changements photométriques permettrait de contraindre les paramètres micro-physiques des régolites planétaires, comme la taille de grains, la rugosité, la compacité qui sont modifiés par le "space weathering". Sur Mars, les effets atmosphériques de dégradations mécaniques éolienne et chimique (notamment par la présence de volatils) viennent s'ajouter au "space weathering". Cependant, les impacts de météorites sont fréquents à la surface, car l'atmosphère est très ténue [207, 64].

L'enjeu de cette étude est de déterminer, par comparaison entre Mars et la Lune, la part de la dégradation des surfaces dû aux phénomènes atmosphériques et celle dû au "space weathering".

Je propose de réaliser une étude observationnelle pour caractériser et comprendre les processus de dégradation des cratères d'impact dans deux environnements différents sur Mars et la Lune. Aussi, je souhaite mener une étude expérimentale pour étudier les limites de validité des modèles de transferts radiatifs. Ce projet est en cours de développement grâce à la thèse de Jennifer Fernando. Des perspectives ont déjà été dressées à la section 2.3 page 84.

6.3.1 Observation

6.3.1.1 Mars

La section 2.2 page 81 présente les détails de la méthode. Mars-ReCO a été développé au cours de la thèse de Jennifer Fernando, en collaboration avec Sylvain Douté et Xavier Ceamanos de l'IPAG, ainsi que

Patrick Pinet et Yves Daydou de l'IRAP. Cette méthode permet de corriger l'effet des aérosols martiens et d'estimer la BRDF de la surface depuis le sommet de l'atmosphère [35]. Dans un premier temps, Mars-ReCO consiste en une correction atmosphérique rapide utilisant le formalisme de Green, en connaissant les propriétés optiques de l'atmosphère. Mars-ReCO permet de réaliser une correction atmosphérique en supposant que la surface est non-lambertienne, en cohérence avec une BRDF quelconque contrairement aux autres méthodes [329, 340, 293]. La seconde étape réside dans l'estimation des paramètres du modèle photométrie de Hapke [86], pour chacun des pixels de la surface à une résolution de 500 m. Cette méthode a été validée par une étude numérique [35] et par la comparaison des données des rovers Martiens Spirit et Opportunity [86].

Dans un premier temps, nous souhaitons déterminer une zone d'étude martienne comportant plusieurs cratères de différents âges et différentes tailles. Il s'agira ensuite d'appliquer l'outil d'estimation de la BRDF et de montrer une évolution photométrique associée à la dégradation des cratères. L'obstacle majeur de cette étude martienne est la présence potentielle d'une couche très récente en surface issue des dépôts des "dust devil" ou des tempêtes de poussière. Une sélection méticuleuse de la zone d'étude devra être conduite.

6.3.1.2 Lune

Sur la Lune, l'absence d'effets atmosphériques rend à la fois l'observation de la BRDF plus aisée, mais aussi son interprétation, car il n'y a pas de phénomènes éoliens. En revanche, aucun instrument dédié à la mesure de la BRDF n'est disponible. Le seul moyen est de fusionner des observations ayant des géométries différentes.

Nous souhaitons déterminer une zone d'étude lunaire comportant les meilleures conditions géométriques d'observation pour déterminer la photométrie dans le cadre de la dégradation des cratères. Les observations des instruments NAC et WAC Lunar Reconnaissance Orbiter disponibles en ligne seront privilégiées, notamment à cause de leur résolution spatiale de 50 cm. Des observations à l'échelle de 100 m ont déjà montré des évidences de variations photométriques sur les impacts de cratères frais [172, 153, 154]. D'autre part, la photométrie des dépôts pyroclastiques du cratère Lavoisier suggère des processus d'homogénéisation de la BRDF [303] qu'il serait intéressant de déterminer.

6.3.2 Expérience de laboratoire

L'interprétation des variations photométriques est une entreprise très difficile car la physique du transfert radiatif dans les milieux granulaires denses est encore à ses balbutiements [226]. Depuis 30 ans, plusieurs avancées ont permis de construire des modèles photométriques efficaces basés sur l'équation du transfert radiatif avec des arrangements concernant des effets spécifiques de compacité, d'opposition et de rugosité [117, 73, 225]. Les effets photométriques sont nécessaires pour réaliser des estimations quantitatives non biaisées, comme illustrés par les études expérimentales sur les abondances relatives de mélanges de poudres analogues aux régolites planétaires [237]. L'étude expérimentale de référence de la photométrie des grains individuels a permis de montrer que les propriétés de diffusion peuvent être décrites, par une fonction de Henyey-Greenstein à deux lobes, permettant de classer les grains en fonction de leur rugosité [215]. Récemment une étude expérimentale a confirmé ces tendances sur des poudres de matériaux naturels terrestres [302]. Aussi, des poudres de matériaux synthétiques ont été mesurées pour montrer l'effet de la compacité et de l'albédo [295]. Enfin, une autre étude s'est focalisée sur des poudres de météorites [14] dans le but d'une comparaison avec les astéroïdes.

Nous souhaitons réaliser une étude photométrique de laboratoire sur des échantillons synthétiques commerciaux et analogues naturels, dont les propriétés sont connues et caractérisées par ailleurs. Nous souhaitons nous focaliser sur un paramètre d'intérêt majeur qui n'a pour l'instant pas encore été étudié en détail : la rugosité des grains. Notre apport sera de tester sur un matériau artificiel uniquement les variations de la rugosité des grains, toute chose égale par ailleurs dans la mesure du possible, afin de compléter les études sur des matériaux naturels [302] et sur des grains isolés [215]. L'effet du bombardement mais aussi ceux des processus éoliens ont tendance à changer la rugosité des grains, il nous

apparaît essentiel d'étudier en détail ce paramètre pour comprendre la dégradation des cratères. A plus long terme, d'autres caractéristiques micro-physiques pourront être étudiés, comme la composition ou la compacité des matériaux granulaires.

6.4 Clathrate sur Mars

6.4.1 Clathrate de CH_4 actuel

Le méthane a été détecté dans l'atmosphère de Mars à un niveau moyen de 10-20 ppb par plusieurs études [171, 93, 234, 89]. Une des caractéristiques les plus surprenantes de méthane observée est sa variabilité temporelle et spatiale apparente, ce qui implique une vie photochimique de 200 jours [185], beaucoup plus courte que la durée de vie actuellement admise de 300 ans, sur la base de modèles photochimiques existants. Un autre aspect intéressant est la corrélation globale trouvée entre le méthane et la vapeur l'eau. Pour expliquer cette corrélation, certains auteurs ont suggéré que le méthane est libéré à partir de couches de clathrate de subsurface sous la forme de particules de clathrate métastables [38]. Ces particules pourraient se décomposer dans l'atmosphère sous l'effet de la condensation de la vapeur d'eau et ainsi libérer du méthane en phase gazeuse. Le puits de méthane est inconnu et pourrait être en surface ou dans l'atmosphère. Il a été suggéré que le méthane serait oxydé dans le sous-sol, soit par un oxydant puissant, comme H_2O_2, produit dans l'atmosphère et absorbé dans le proche sous-sol, ou par réaction chimique avec les surfaces oxydées des grains et des roches dans le régolite superficiel [40].

La section 3.1.1 page 134 décrit l'état actuel des connaissances à propos du méthane sur Mars et la section 5.1.2 page 268 détaille la possibilité de clathrate et les enjeux autour de cette thématique.

L'objectif scientifique principal de ce projet est de valider ou d'invalider la présence de méthane sur Mars, d'après les mesures de spectroscopie à haute résolution PFS. Il s'agit de reprendre les données, grâce à notre nouvelle méthode de calibration des données PFS, permettant de corriger les effets des micro-vibrations, comme exposé à la section 3.2 page 138.

Aussi, l'hypothèse de la libération de méthane sous forme de particules de clathrates métastables peut être testée par la recherche de signatures spectrales de clathrate. Les propriétés spectrales des clathrates dans l'infrarouge ont été déterminées expérimentalement [61]. Les raies d'absorption du méthane piégé dans les clathrates sont élargies et décalées vers le rouge par quelques dizaines cm^{-1}. Bien que ces raies d'absorption ne soient pas très bien marquées, une analyse statistique approfondie des données PFS permettrait éventuellement de les détecter.

La formation des clathrates binaire CO_2-CH_4 sur les calottes polaires saisonnières pourrait être thermodynamiquement possible, et la signature spectrale de clathrates doit aussi être recherchée sur les calottes polaires. A l'échelle locale, une anticorrélation entre les concentrations de méthane gazeux et solide est prévue, si les particules de clathrates sont rapidement converties à la phase gazeuse en présence de condensation de la vapeur d'eau [38].

Si cette détection est validée, je souhaite réaliser une cartographie des clathrates de méthane, afin d'améliorer notre connaissance du cycle atmosphérique du méthane. Dans ce cas, la question des puits locaux de méthane sera ouverte et il faudra déterminer les espèces chimiques impliquées.

Notre deuxième objectif scientifique consiste à identifier ces puits de méthane. On attend une anticorrélation entre les signatures de méthane gazeux et les signatures des espèces oxydantes tuant le méthane. Selon V. Formisano, certaines raies non identifiés sont présentes sur les spectres lorsque le méthane n'est pas détecté, notre réanalyse permettrait de les identifier.

6.4.2 Clathrates passés

La section 5.3 page 275 décrit les perspectives de la présence de clathrate dans le passé martien. Il s'agit, dans un premier temps, d'estimer la validité de l'hypothèse de la déstabilisation de clathrate, pour la formation à l'Hesperien/Amazonien, des terrains chaotiques et de vallées de débâcle. L'enjeu de cette étude est la compréhension des mécanismes à l'origine de la plus importante décharge d'eau du système solaire, estimée à 10^9 m^3/s [31, 167]. Cette étude nécessitera une modélisation thermique,

thermodynamique et mécanique de la déstabilisation des clathrates afin de déterminer si les conditions nécessaires à ce mécanisme ont pu être réalisées dans le passé de Mars. D'autre part, ce programme de recherche devra être compléter par une modélisation géomorphologique en comparaison avec les observations issues des nouvelles données HiRISE à haute résolution spatiale, notamment les modèles numériques de terrains.

L'autre objectif scientifique concerne l'effet tampon dû au SO_2 et CO_2, décrit à la section 5.2 page 270. Ce mécanisme, bien que simple, explique plusieurs observations majeures martiennes, dont le changement climatique à la transition Noachien/Hespérien, la présence d'une couche massive de sulfate, la présence des terrains chaotiques. L'enjeu de ce projet est la compréhension de l'histoire géologique de Mars. Je souhaite développer l'hypothèse de l'effet tampon en réalisant des modélisations climatiques en fonction de la latitude, pour modéliser de manière plus réaliste au cours du premier milliard d'années de Mars. Aussi, je souhaite améliorer la modélisation de l'effet tampon en ajoutant une boucle de rétro-action entre le relargage de SO_2 et la formation de carbonate, afin d'expliquer la perte CO_2 atmosphérique au cours de l'histoire de Mars. Enfin, une modélisation plus précise d'un hypothétique cycle de l'eau actif dans le cadre de l'effet tampon serait très intéressant pour valider/invalider cette hypothèse face aux observations géomorphologiques des réseaux de vallées.

Conclusion

Mes travaux d'étude des échanges de volatils entre la surface et l'atmosphère de Mars sont à la frontière entre plusieurs disciplines : géomorphologie, spectroscopie et climatologie. Mon approche principale est l'analyse de différents types de données avec des outils de traitement du signal innovants dans le but d'extraire les informations pertinentes. Certains défis méthodologiques ont été levés grâce au développement d'outils novateurs permettant la détection automatique des corps chimiques à la surface de Mars, mais aussi tendant vers une description quantitative de la surface de Mars (taille de grain, mode de mélange, rugosité,...). Grâce à ces outils, j'ai effectué des interprétations de l'évolution des échanges de volatils sur la calotte saisonnière sud. D'autre part, j'ai développé un modèle numérique de bilan de masse de CO_2 pour la calotte saisonnière sud de Mars, et un modèle conceptuel d'échange de CO_2/SO_2 pour l'effet tampon dû aux clathrates. Ces modèles contribuent à mieux saisir les liens entre ces échanges et les unités géomorphologiques actuelles (geysers, spiders) et passées (vallée de débâcle, terrains chaotiques). Cependant, de nombreuses perspectives se dressent pour mieux comprendre le climat de Mars et les échanges de volatils dans l'histoire de la planète rouge.

A court terme, il s'agit d'appliquer mes outils à plusieurs problèmes, comme (i) la détection automatiques de glace et minéraux sur un large jeu de données OMEGA et CRISM, (ii) l'estimation des paramètres microphysiques de la glace de la calotte saisonnière sud, (iii) la réalisation de carte spectrophotométrique sur plusieurs zones typiques des terrains martiens, (iv) la recalibration complète des données PFS. Les thèses de Jennifer Fernando, de François Andrieu et de Maxime Legendre, que je co-encadre, permettront de réaliser en grande partie ces applications. D'autre part, la thèse d'Irina Shatalina, que j'ai suivi pendant cinq mois à IDES, a permis de mettre au point un outil de recalibration des données PFS.

A moyen terme, il s'agira à la fois d'améliorer les outils existants mais aussi de réaliser les études des processus d'échanges de volatils sur les quatre exemples choisis : les geysers et spiders, la source d'eau atmosphérique, la déstabilisation photométrique et les implications de la présence de clathrates sur Mars. Ces études feront l'objet de demandes de financement localement au laboratoire Interactions et Dynamique des Environnement de Surface (IDES) et à l'Université Paris Sud, à l'Institut National des Sciences de l'Univers (INSU), au Programme National de Planétologie (PNP), au Centre National d'Etude Spatial (CNES) mais aussi sur des programmes de type Agence National de la Recherche (ANR) ou European Research Council (ERC).

A plus long terme, je souhaite développer des outils numériques, à la fois de modélisation directe et d'inversion pour l'analyse des données, mais aussi des outils analogiques et numériques de simulation des échanges de volatils. L'objectif poursuivit est de comprendre l'histoire du climat de Mars et plus généralement l'histoire des régolites planétaires. Ce programme de recherche s'inscrit naturellement dans le contexte des prochaines missions spatiales sur Mars, comme ExoMars Trace Gas Orbiter, Mars 2020 et sur les satellites de glaces, comme JUICE.

Quatrième partie

Annexes

Chapitre 7

Annexe 1 : Curriculum Vitae detaillé

7.1 Emplois dans la recherche :

- depuis Septembre 2009 : Maître de Conférence section 35, IDES, Orsay.
- Janvier 2008- Août 2009 : Post-doc ESA, ESAC, Madrid
- Octobre 2007- Décembre 2007 : Post-doc CNRS, IPAG (ex LPG), Grenoble
- Octobre 2004 - Septembre 2007 : Doctorat, IPAG (ex LPG), Grenoble

7.2 Enseignements :

- Maître de Conférence : 150 h/an en 2009-2011 , puis 200 h /an depuis 2011
  - L2 STU, Planétologie : Notions d'orbitographie, Le principe du télescope, Les corps telluriques.
  - L2 STU, Photo-interprétation : Notions de bases de télédétection, Hydrographie, Volcanisme, Géomorphologie structurale, Glaciologie, Reliefs Eoliens, Formation des reliefs complexes, TD d'application sous Google Earth.
  - L3 IUT Pro GEDEP, Topographie : La topographie, Les instruments de mesure de la toporgraphie, TP Nivellement, TP Cartographie
  - M1 STU, Surface et Intérieurs Planétaires : Orbitographie, Principe du Télescope
  - M1 STU, Télédétection : Notions de bases, Format numérique, Physique du rayonnement, Transfert radiatif, Traitement d'image, Classification, TD d'application informatique sous SCILAB.
  - M2 STU Génie Géologique, Cartographie Géologique : TD
  - M2 STU Planétologie, Physiographie des Planètes : Introduction, Topographie, Isostasie, Volcanisme, Tectonique, Satellite de glace, Impact et cratères.
  - M2 STU Planétologie, Informatique : Méthodes d'inversions
- Doctorat 2004-2007 : vaccation 140 h
  - sujet : géodynamique, géophysique, cartographie, terrain et pétrographie

7.3 Jury et commission de recrutement :

- Commission de recrutement du poste 35 MCF 357 (2012) : Analyse géomorphologique et minéralogique des surfaces planétaires, UPSUD.
- Examinateur de la thèse de doctorat d'Amer AL KWATLI, soutenu le 10 Juin 2010 : Evolution volcano-tectonique du nord de la plaque arabique (Syrie) : cadre géodynamique, géochronologie K-Ar, caractères géochimiques et éléments de cartographie (SIG et Télédétection), UPSUD
- Master 2 STU spécialité Planétologie depuis 2010-2011 : Oraux et écrits

7.4 Encadrement d'étudiants :

- Doctorat :
  - Jennifer Fernando (Septembre 2011 - Septembre 2014) (co-encadrement 50%, avec F. Costard (50%))
  - Maxime Legendre (Janvier 2012 - Janvier 2015) (co-encadrement 30% avec S. Mousssaoui (30%) et J. Idier (40%))
  - François Andrieu (Septembre 2012 - Septembre 2015) (co-encadrement 50% avec E. Chassefière (50%))
  - Irina Shatalina (invité à IDES Avril-Août 2012) : Signal Treatment for Planetary Fourier Spectrometer, *Doctorante du Politecnico Di Milano*
- Stage Post-Master :
  - Luca Capriotti (Septembre-Décembre 2012) : GPU Implementation of OMEGA unmixing, *ESA, ESAC, Madrid*
- Master 2ème année :
  - Jennifer Fernando (Avril-Juin 2011) : PROPRIÉTÉS PHYSIQUES DE LA SURFACE DANS LE CRATÈRE GUSEV AU MOYEN DES OBSERVATIONS CRISM (Compact Reconnaissance Imaging Spectrometer for Mars) À BORD DE LA SONDE MRO (Mars Reconnaissance Orbiter), M2 STU Planétologie, UPMC
  - Romain Dupire (Avril-Juin 2010) : Etude des spiders et activité des jets de gaz sur Mars, M2 STU Planétologie, UPMC
  - Maël GUIHENEUF (Avril-Octobre 2009) : PARALLELIZATION OF ICA MATLAB ALGORITHM - PROFILING : MEMORY & COMPUTATION, ESA, ESAC
  - Hafrùn Hauksdóttir (Mars-Juin 2006) : On the Decomposition of Mars Hyperspectral Data by ICA and Bayesian Positive Source Separation, *GIPSA-LAB, INPG Grenoble*
- Master 1ère année :
  - Antony Lagain (Mai-Juin 2013) : Etude des propriétés physiques de la surface de Mars par l'analyse des observations multi-angulaires CRISM (Compact Reconnaissance Imaging Spectrometer for Mars) à bord de la sonde MRO (Mars Reconnaissance Orbiter) : exemple du cratère Holden, M1 STU, UPSUD
  - Batiste Rousseau (Mai-Juin 2013) : La saltation dans le cadre des « dark spots » martiens, étude par l'expérience, M1 STU, UPSUD
  - Nicolas Ligier (Mai-Juin 2012) : Dark Spot des hautes latitudes Sud de Mars, M1 STU, UPSUD
  - Kevin Angeli (Mai-Juin 2012) : Géométrie des observations CRISM pour l'étude photométrique de la surface de Mars, M1 STU, UPSUD
  - Maximilien Verdier (Mai-Juin 2012) : Comparaison des algorithmes de traitement des images hyperspectrales CRISM et OMEGA, *M1 STEP Teledetection & techniques spatiales, Univ. Paris Diderot*
  - Laura Fernandez (Avril-Juin 2011) : LA SUBLIMATION DU DIOXYDE DE CARBONE SUR MARS, *Master 1 Physique et Applications, Univ. Pierre et Marie Curie*
  - Samsophath Nhean (Avril-Juillet 2011) : Traitement des données spectrales de l'instrument Planetary Fourier Spectrometer de la sonde Mars Express, *M1 Physique Appliquée et Mécanique, UPSUD*
  - Ottaviano Ruesch (Mai-Juin 2010) : Analyses spectrales et morphologiques de lave sur Mars, M1 STU, UPSUD
  - Jennifer Fernando (Mai-Juin 2010) : LA CONTRIBUTION DE L'ATMOSPHÈRE DANS LA RÉPONSE PHOTOMÉTRIQUE DE SURFACE (INSTRUMENT CRISM) - ÉTUDE DES PROPRIÉTÉS PHOTOMÉTRIQUES DES POUSSIÈRES ET SPIDERS DANS LA CALOTTE POLAIRE SUD DE MARS, *M1 STEP Géologie, Univ. Pierre et Marie Curie*
- Licence 3ème année :
  - Alain Gilbert (Juin-Juillet 2011) : Traitement des données Hyperspectrale OMEGA, L3 STU, UPSUD

  - Anthony Lethuillier (Juin 2011) : Phobos et Phobos Grunt, L3 STU, UPSUD
  - Erika Bonhoure (Juin 2010) : Géomorphologie martienne : jets et spiders, L3 STU, UPSUD
- Licence 2ème année :
  - Rémi Navarre (Juin 2012) : Traitements de données spectrales de Mars, *DUT Génie électrique, IUT Cachan*

7.5 Instruments spatiaux :

- Co-Investigator OMEGA (Mars Express, ESA) depuis 2009
- Co-Investigator PFS (Mars Express, ESA) depuis 2010

7.6 Responsabilité :

- Représentant invité OSUPS depuis 2013.
- Elu à la CCSU section 35-36 depuis 2010.
- Responsable Master 2 STU, spécialité Planétologie à UPSUD depuis 2010-2011.

7.7 Expert pour les revues suivantes :

- IEEE Transaction on Geosciences and Remote Sensing
- Planetary and Space Science
- Earth and Planetary Science Letters
- Journal of Geophysical Research

7.8 Financements :

Classés par programme, puis par date décroissante :

- Co-Investigator OMEGA (Mars Express, ESA), financement CNES depuis 2009 (responsable : F. Schmidt).
- Co-Investigator PFS (Mars Express, ESA), financement CNES depuis 2010 (responsable : F. Schmidt et E. Chassefière).
- Contributeur HRSC (Mars Express, ESA), financement CNES depuis 2009 (responsable : F. Costard).
- Laboratoire IDES depuis 2009 : BQR Jeune Chercheur, BQR Interne (responsable : F. Schmidt)
- Equipement de Recherche Mutualisé 2013, Université Paris Sud (responsable : G. Lagache) : Plate-forme de calcul haute performance pour la production intensive de données, l'exploitation de codes aboutis, l'étude de nouvelles applications à cette plate-forme ainsi que l'optimisation de cette ressource
- INSU/Programme National de Planétologie 2013 (responsable : S. Bouley) : Caractérisation de la dégradation des cratères d'impact
- INSU/Programme National de Planétologie 2012 (responsable : F. Costard) : Processus saisonniers à la surface de Mars
- INSU/Programme National de Planétologie 2011 (responsable : F. Schmidt) : Processus glaciaires et périglaciaires Martiens
- INSU/Programme National de Planétologie 2010 (responsable : F. Schmidt) : Origine et évolution des formations périglaciaires sur Mars - Développement d'outils d'analyse topographique
- PIR Environnements Planétaires et Origines de la Vie 2011 (responsable : E. Chassefière) : MÉTHANE MARTIEN : ORIGINE, RÉSERVOIRS, OBSERVATIONS, IMPLICATIONS POUR L'ÉVOLUTION DE MARS

- PID Environnements Planétaires et Origines de la Vie 2010 (responsable : E. Chassefière) : MÉTHANE MARTIEN : ORIGINE, RÉSERVOIRS, OBSERVATIONS, IMPLICATIONS POUR L'ÉVOLUTION DE MARS
- ANR Blanc International II France-Chine 2012 (responsable : S. Douté et B. Luo) : I2-Mars : Interprétation et indexation d'images orbitales multi-modales de la planète Mars.
- ARISTEIA 2012 ("Excellence" en grec, équivalent du programme ANR en Grèce) (responsable : Thanasis Rontogiannis) : Advancing hyperspectral image processing for planetary mineral exploration and thematic mapping : the case of planet Mars
- Bourse Ministère de l'Enseignement Supérieur et de la Recherche (2011-2014) : financement thèse Jernifer Fernando (IDES, Orsay), encadrant : F. Costard, co-encadrant : F. Schmidt
- Bourse ESA-Région Pays de la Loire (2011-2014) : financement thèse de Maxime Legendre (IRCCyN, Ecole Centrale de Nantes), encadrant : J. Idier (40%), co-encadrant : S. Moussaoui (30%) et F. Schmidt (30 %)
- Bourse Ecole Normale Supérieure de Cachan (2012-2015) : financement thèse de François Andrieu (IDES, Orsay), encadrant : E. Chassefière, co-encadrant : F. Schmidt

7.9 Publications

7.9.1 Publications de rang A :

14 publications dont 5 en premier auteur (dont 1 avec un doctorant encadré en premier auteur)
2 articles soumis (dont 1 en premier auteur)

- **Schmidt F.** ; Douté S. & Schmitt B., "WAVANGLET : an efficient supervised classifier for hyperspectral images" ; IEEE Transactions on Geoscience and Remote Sensing, 2007, 45, 1374-1385
- Moussaoui, S. ; Hauksdóttir, H. ; **Schmidt, F.** ; Jutten, C. ; Chanussot, J. ; Brie, D. ; Douté, S. & Benediktsson, J., "On the Decomposition of Mars Hyperspectral data by ICA and Bayesian positive source separation" ; Neurocomputing, Neurocomputing for Vision Research ; Advances in Blind Signal Processing, 2008, 71, 2194-2208
- **Schmidt F.**, Douté S., Schmitt B., Vincendon, M., Langevin, Y., Bibring J.-P. & the OMEGA Team ; "Albedo control of the Seasonal South Polar Cap recession" ; Icarus, 2009, 200, 374-394
- **Schmidt F.**, Schmitt B., Douté S., Forget, F., Jeng, J.-J., Martin, P., Langevin, Y., Bibring J.-P. & the OMEGA Team ; "Sublimation of the Martian CO2 seasonal south Polar Cap", Planetary and Space Science, 2010, 58, 1129- 1138
- **Schmidt, F.** ; Schmidt, A. ; Tréguier, E. ; Guiheneuf, Maël and Moussaoui, S. & Dobigeon, N., "Implementation strategies for hyperspectral unmixing using Bayesian source separation", IEEE Transaction on Geoscience and Remote Sensing, 2010, 48, 4003-4013
- Kereszturi A., Vincendon M. & **Schmidt F.**, "Water ice in the dark dune spots of Richardson crater on Mars", Planetary and Space Science, 2011, 59, 26-42
- Ceamanos, X. ; Douté ;, S. ; Luo, B. ; **Schmidt, F.** ; Jouannic, G. & Chanussot, J., "Intercomparison and Validation of Techniques for Spectral Unmixing of Hyperspectral Images : A Planetary Case Study", IEEE Transaction on Geoscience and Remote Sensing, 2011, 49, 4341-4358
- Themelis, K. E. ; **Schmidt, F.** ; Sykioti, O. ; Rontogiannis, A. A. ; Koutroumbas, K. D. & Daglis, I. A., "On the unmixing of MEx/OMEGA hyperspectral data", Planetary and Space Science, 2012, 68, 34-41
- Jouannic, G., Gargani, J., Costard, F., Ori, G. G., Marmo, C., **Schmidt, F.** & Lucas, A., "Morphological and mechanical characterization of gullies in a periglacial environment : The case of the Russell crater dune (Mars)", Planetary and Space Science, 2012, 71, 38-54
- Mousis, O., Chassefière, E., Lasue, J., Chevrier, V., Elwood Madden, M., Lakhlifi, A., Lunine, J., Montmessin, F., Picaud, S., **Schmidt, F**. & Swindle, T. D. , "Volatile Trapping in Martian Clathrates", Space Science Reviews, 2013, 174, 213-250
- Chassefière, E., Dartois, E., Herri, J.-M., Tian, F., **Schmidt, F.**, Mousis, O. & Lakhlifi, A. (2013),

"CO2- SO2 clathrate hydrate formation on early Mars", Icarus, 223, 878-891

- Ceamanos, X., Doute, S., Fernando, J., **Schmidt, F.**, Pinet, P. & Lyapustin, A. (2013), "Surface reflectance of Mars observed by CRISM/MRO : 1. Multi-angle Approach for Retrieval of Surface Reflectance from CRISM Observations (MARS-ReCO)", Journal of Geophysical Research, 118, 1-20
- **Fernando, J., Schmidt, F.**, Ceamanos, X., Pinet, P., Douté, S. & Daydou, Y. (2013), "Surface reflectance of Mars observed by CRISM/MRO : 2. Estimation of surface photometric properties in Gusev Crater and Meridiani Planum", Journal of Geophysical Research, 118, 1-26
- **Schmidt, F.**, **Shatalina, I.**, Kowalski, M., Gac, N., Saggin, B. & Giuranna, M. (2014), "Toward a numerical deshaker for PFS", accepté dans Planetary and Space Science

7.9.2 Résumé de congrès :

52 résumé dont 29 avec acte (EPSC, WHISPERS, MOMA, Mars Atmo, Traitement du signal).

7.9.3 Autres publications :

- François Costard et **Frédéric Schmidt**, Chronique d'un monde glacé, Géochronique, 2013
- Vincent Chevrier, Derek Sears, Megan Elwood Madden, Essam Heggy, **Frédéric Schmidt**, Laboratory Measurements in Support of Present and Future Missions to Mars, White paper to NASA Planetary Science Decadal Planning Group
- **Frédéric Schmidt**, Spiders in the cryptic region of Mars, ESA News, 2009

Bibliographie

[1] *VIRTIS : The Visible and Infrared Thermal Imaging Spectrometer*, volume 1295 of *ESA Special Publication*, December 2007.

[2] O. Aharonson. Sublimation at the Base of a Seasonal CO_2 Slab on Mars. In S. Mackwell and E. Stansbery, editors, *Lunar and Planetary Institute Conference Abstracts*, pages 1918–+, March 2004.

[3] O. Aharonson, M. T. Zuber, D. E. Smith, G. A. Neumann, W. C. Feldman, and T. H. Prettyman. Depth, distribution, and density of CO_2 deposition on Mars. *Journal of Geophysical Research (Planets)*, 109 :5004–+, May 2004. doi : 10.1029/2003JE002223.

[4] Carlton C Allen and Dorothy Z Oehler. A case for ancient springs in arabia terra, mars. *Astrobiology*, 8(6) :1093–1112, 2008. doi : 10.1089/ast.2008.0239.

[5] F. Andrieu, M. Nachon, F. Schmidt, J. Gargani, and S. Doute. Co2 ice state at the martien dark spots. In *EPSC (Madrid, 23-28 September 2012)*, 2012. URL http://meetingorganizer.copernicus.org/EPSC2012/EPSC2012-892-1.pdf.

[6] T. Appéré, B. Schmitt, Y. Langevin, S. Douté, A. Pommerol, F. Forget, A. Spiga, B. Gondet, and J.-P. Bibring. Winter and spring evolution of northern seasonal deposits on mars from omega on mars express. *J. Geophys. Res.*, 116(E5) :E05001–, May 2011. ISSN 0148-0227. URL http://dx.doi.org/10.1029/2010JE003762.

[7] Raymond E. Arvidson, James L. Gooding, and Henry J. Moore. The martian surface as imaged, sampled, and analyzed by the viking landers. *Rev. Geophys.*, 27(1) :39–60, February 1989. ISSN 1944-9208. URL http://dx.doi.org/10.1029/RG027i001p00039.

[8] Sushil K. Atreya, Paul R. Mahaffy, and Ah-San Wong. Methane and related trace species on mars : Origin, loss, implications for life, and habitability. *Planetary and Space Science*, 55(3) :358–369, February 2007. ISSN 0032-0633. URL http://www.sciencedirect.com/science/article/B6V6T-4KPNB0K-4/2/578f9aa76915b1fc7b6ad91039985cc8.

[9] Sushil K. Atreya, Olivier Witasse, Vincent F. Chevrier, Francois Forget, Paul R. Mahaffy, P. Buford Price, Christopher R. Webster, and Richard W. Zurek. Methane on mars : Current observations, interpretation, and future plans. *Planetary and Space Science*, 59(2-3) :133–136, February 2011. ISSN 0032-0633. URL http://www.sciencedirect.com/science/article/B6V6T-51CVG1G-1/2/1ddb27d8cd3630732f4ecdffcdf0d7da.

[10] Victor R. Baker. The channeled scabland : A retrospective. *Annual Review of Earth and Planetary Sciences*, 37(1) :393–411, May 2009. ISSN 0084-6597. URL http://dx.doi.org/10.1146/annurev.earth.061008.134726.

[11] Victor R. Baker and Daniel J. Milton. Erosion by catastrophic floods on mars and earth. *Icarus*, 23(1) :27 – 41, 1974. ISSN 0019-1035. doi : 10.1016/0019-1035(74)90101-8. URL http://www.sciencedirect.com/science/article/pii/0019103574901018.

[12] J. L. Bandfield, V. E. Hamilton, and P. R. Christensen. A Global View of Martian Surface Compositions from MGS-TES. *Science*, 287 :1626–1630, March 2000.

[13] M. Bartoszek, M. Wecks, G. Jakobs, and D. Möhlmann. Photochemically induced formation of mars relevant oxygenates and methane from carbon dioxide and water. *Planetary and Space Science*, 59(2-3) :259–263, February 2011. ISSN 0032-0633. URL http://www.sciencedirect.com/science/article/B6V6T-511C022-3/2/a922e90932ae51105efa6ce642b1c962.

[14] P. Beck, A. Pommerol, N. Thomas, B. Schmitt, F. Moynier, and J.-A. Barrat. Photometry of meteorites. *Icarus*, 218(1) :364–377, March 2012. ISSN 0019-1035. URL http://www.sciencedirect.com/science/article/pii/S0019103511004702.

[15] J. L. Benson and P. B. James. Yearly comparisons of the martian polar caps : 1999-2003 Mars Orbiter Camera observations. *Icarus*, 174 :513–523, April 2005. doi : 10.1016/j.icarus.2004.08.025.

[16] J.-P. Bibring, M. Combes, Y. Langevin, A. Soufflot, C. Cara, P. Drossart, Th. Encrenaz, S. Erard, O. Forni, B. Gondet, L. Ksanfomalfty, E. Lellouch, Ph. Masson, V. Moroz, F. Rocard, J. Rosenqvist, and C. Sotin. Results from the ism experiment. *Nature*, 341(6243) :591–593, October 1989. URL http://dx.doi.org/10.1038/341591a0.

[17] J.-P. Bibring, A. Soufflot, M. Berthé, Y. Langevin, B. Gondet, P. Drossart, M. Bouyé, M. Combes, P. Puget, A. Semery, G. Bellucci, V. Formisano, V. Moroz, V. Kottsov, G. Bonello, S. Erard, O. Forni, A. Gendrin, N. Manaud, F. Poulet, G. Poulleau, T. Encrenaz, T. Fouchet, R. Melchiori, F. Altieri, N. Ignatiev, D. Titov, L. Zasova, A. Coradini, F. Capacionni, P. Cerroni, S. Fonti, N. Mangold, P. Pinet, B. Schmitt, C. Sotin, E. Hauber, H. Hoffmann, R. Jaumann, U. Keller, R. Arvidson, J. Mustard, and F. Forget. *OMEGA : Observatoire pour la Minéralogie, l'Eau, les Glaces et l'Activité*, pages 37–49. ESA SP-1240 : Mars Express : the Scientific Payload, August 2004.

[18] J.-P. Bibring, Y. Langevin, A. Gendrin, B. Gondet, F. Poulet, M. Berthé, A. Soufflot, R. Arvidson, N. Mangold, J. Mustard, and P. Drossart. Mars Surface Diversity as Revealed by the OMEGA/Mars Express Observations. *Science*, 307 :1576–1581, March 2005. doi : 10.1126/science.1108806.

[19] J.-P. Bibring, R. E. Arvidson, A. Gendrin, B. Gondet, Y. Langevin, S. Le Mouelic, N. Mangold, R. V. Morris, J. F. Mustard, F. Poulet, C. Quantin, and C. Sotin. Coupled Ferric Oxides and Sulfates on the Martian Surface. *Science*, 317(5842) :1206–1210, 2007. doi : 10.1126/science.1144174. URL http://www.sciencemag.org/cgi/content/abstract/317/5842/1206.

[20] Jean-Pierre Bibring, Yves Langevin, John F. Mustard, Francois Poulet, Raymond Arvidson, Aline Gendrin, Brigitte Gondet, Nicolas Mangold, P. Pinet, F. Forget, the OMEGA team, Michel Berthe, Jean-Pierre Bibring, Aline Gendrin, Cecile Gomez, Brigitte Gondet, Denis Jouglet, Francois Poulet, Alain Soufflot, Mathieu Vincendon, Michel Combes, Pierre Drossart, Therese Encrenaz, Thierry Fouchet, Riccardo Merchiorri, GianCarlo Belluci, Francesca Altieri, Vittorio Formisano, Fabricio Capaccioni, Pricilla Cerroni, Angioletta Coradini, Sergio Fonti, Oleg Korablev, Volodia Kottsov, Nikolai Ignatiev, Vassili Moroz, Dimitri Titov, Ludmilla Zasova, Damien Loiseau, Nicolas Mangold, Patrick Pinet, Sylvain Doute, Bernard Schmitt, Christophe Sotin, Ernst Hauber, Harald Hoffmann, Ralf Jaumann, Uwe Keller, Ray Arvidson, John F. Mustard,

Tom Duxbury, Francois Forget, and G. Neukum. Global mineralogical and aqueous mars history derived from omega/mars express data. *Science*, 312(5772) :400–404, April 2006. URL http://www.sciencemag.org/cgi/content/abstract/312/5772/400.

[21] R. Bintanja. On the glaciological, meteorological, and climatological significance of antarctic blue ice areas. *Reviews of Geophysics*, 37 :337–360, 1999. doi : 10.1029/1999RG900007.

[22] J.M. Bioucas-Dias, A. Plaza, N. Dobigeon, M. Parente, Qian Du, P. Gader, and J. Chanussot. Hyperspectral unmixing overview : Geometrical, statistical, and sparse regression-based approaches. *Selected Topics in Applied Earth Observations and Remote Sensing, IEEE Journal of*, 5(2) :354–379, 2012. ISSN 1939-1404.

[23] J.W. Boardman, F. A. Kruse, and R. O. Green. Mapping target signatures via partial unmixing of AVIRIS data : in Summaries. In *Fifth JPL Airborne Earth Science Workshop, JPL Publication 95-1*, volume 1, pages 23–26, March 1995.

[24] S. Bouley, R.A. Craddock, N. Mangold, and V. Ansan. Characterization of fluvial activity in parana valles using different age-dating techniques. *Icarus*, 207(2) :686–698, June 2010. ISSN 0019-1035. URL http://www.sciencedirect.com/science/article/B6WGF-4Y646NS-1/2/d404d0aceb2f388c554f1d8e5dbe1659.

[25] R. Brown, K. Baines, G. Bellucci, J.-P. Bibring, B. Buratti, F. Capaccioni, P. Cerroni, R. Clark, A. Coradini, D. Cruikshank, P. Drossart, V. Formisano, R. Jaumann, Y. Langevin, D. Matson, T. Mccord, V. Mennella, E. Miller, R. Nelson, P. Nicholson, B. Sicardy, and C. Sotin. The cassini visual and infrared mapping spectrometer (vims) investigation. In *The Cassini-Huygens Mission*, pages 111–168, 2004. URL http://dx.doi.org/10.1007/1-4020-3874-7_3.

[26] Bruce A. Buffett. Clathrate hydrates. *Annual Review of Earth & Planetary Sciences*, 28(1) :477–, May 2000. ISSN 00846597. URL http://search.ebscohost.com/login.aspx?direct=true&db=aph&AN=5371416&lang=fr&site=ehost-live.

[27] Peter Camillo. A canopy reflectance model based on an analytical solution to the multiple scattering equation. *Remote Sensing of Environment*, 23(3) :453–477, December 1987. ISSN 0034-4257. URL http://www.sciencedirect.com/science/article/pii/0034425787901015.

[28] W. W. Campbell. The Spectrum of Mars. *Publications of the Astronomical Society of the Pacific*, 6 :228–+, August 1894.

[29] J.-F. Cardoso. Infomax and maximum likelihood for blind source separation. *Signal Processing Letters, IEEE*, 4(4) :112–114, 1997. ISSN 1070-9908.

[30] R. W. Carlson, P. R. Weissman, W. D. Smythe, and J. C. Mahoney. Near-infrared mapping spectrometer experiment on galileo. *Space Science Reviews*, 60(1) :457–502, May 1992. URL http://dx.doi.org/10.1007/BF00216865.

[31] Michael H. Carr. Formation of martian flood features by release of water from confined aquifers. *J. Geophys. Res.*, 84(B6) :2995–3007, 1979. ISSN 0148-0227. URL http://dx.doi.org/10.1029/JB084iB06p02995.

[32] J. Carter, F. Poulet, S. Murchie, and J.P. Bibring. Automated processing of planetary hyperspectral datasets for the extraction of weak mineral signatures and applications to {CRISM} observations of hydrated silicates on mars. *Planetary and Space Science*, 76(0) :53 – 67, 2013. ISSN 0032-0633. doi : 10.1016/j.pss.2012.11.007. URL http://www.sciencedirect.com/science/article/pii/S0032063312003625.

[33] X. Ceamanos and S. Doute. Spectral smile correction of crism/mro hyperspectral images. *Geoscience and Remote Sensing, IEEE Transactions on DOI - 10.1109/TGRS.2010.2064326*, 48(11) : 3951–3959, 2010. ISSN 0196-2892.

[34] X. Ceamanos, S. Doute, B. Luo, F. Schmidt, G. Jouannic, and J. Chanussot. Intercomparison and validation of techniques for spectral unmixing of hyperspectral images : A planetary case study. *Geoscience and Remote Sensing, IEEE Transactions on DOI - 10.1109/TGRS.2011.2140377*, 49 (11) :4341–4358, 2011. ISSN 0196-2892. doi : http://dx.doi.org/10.1109/TGRS.2011.2140377.

[35] X. Ceamanos, S. Douté, J. Fernando, F. Schmidt, P. Pinet, and A. Lyapustin. Surface reflectance of Mars observed by CRISM/MRO : 1. Multi-angle Approach for Retrieval of Surface Reflectance from CRISM observations (MARS-ReCO). *Journal of Geophysical Research (Planets)*, 118 : 514–533, March 2013. doi : 10.1029/2012JE004195.

[36] S. Chandrasekhar. *Radiative transfer*. New York : Dover, 1960, 1960.

[37] E. Chassefiere and F. Leblanc. The Impact of Subsurface Sources and Sinks on the Evolution of Early Atmospheric CO2, CH4, and D/H. In *Third Conference on Early Mars : Geologic, Hydrologic, and Climatic Evolution and the Implications for Life*, volume 1680, page 7002, May 2012. held May 21-25, 2012, in Lake Tahoe, Nevada. LPI Contribution No. 1680, id.7002.

[38] Eric Chassefière. Metastable methane clathrate particles as a source of methane to the martian atmosphere. *Icarus*, 204(1) :137–144, November 2009. ISSN 0019-1035. URL http://www.sciencedirect.com/science/article/pii/S0019103509002620.

[39] Eric Chassefière and François Leblanc. Methane release and the carbon cycle on mars. *Planetary and Space Science*, 59(2-3) :207–217, February 2011. ISSN 0032-0633. URL http://www.sciencedirect.com/science/article/B6V6T-511K3WN-1/2/11b7daa19f27afe67cdb4919841a7628.

[40] Eric Chassefière and François Leblanc. Explaining the redox imbalance between the h and o escape fluxes at mars by the oxidation of methane. *Planetary and Space Science*, 59(2-3) :218–226, February 2011. ISSN 0032-0633. URL http://www.sciencedirect.com/science/article/B6V6T-512VTKJ-3/2/35cef661d63122f8eeb58a1d74a042db.

[41] Eric Chassefière, Emmanuel Dartois, Jean-Michel Herri, Feng Tian, Frédéric Schmidt, Olivier Mousis, and Azzedine Lakhlifi. Co2-so2 clathrate hydrate formation on early mars. *Icarus*, 223 (2) :878–891, April 2013. ISSN 0019-1035. doi : 10.1016/j.icarus.2013.01.001. URL http://www.sciencedirect.com/science/article/pii/S0019103513000080.

[42] Eric Chassefière, Benoit Langlais, Yoann Quesnel, and François Leblanc. The fate of early mars's lost water : The role of serpentinization. *J. Geophys. Res. Planets*, 118(5) :1123–1134, May 2013. ISSN 2169-9100. URL http://dx.doi.org/10.1002/jgre.20089.

[43] Brendon K. Chastain and Vincent Chevrier. Methane clathrate hydrates as a potential source for martian atmospheric methane. *Planetary and Space Science*, 55(10) :1246–1256, July 2007. URL http://www.sciencedirect.com/science/article/B6V6T-4N4J321-3/2/29afc0d886d00d6bc4feb2ecdc34266c.

[44] Serge D. Chevrel, Patrick C. Pinet, and James W. Head. Gruithuisen domes region : A candidate for an extended nonmare volcanism unit on the moon. *Journal of Geophysical Research : Planets*, 104(E7) :16515–16529, 1999. ISSN 2156-2202. doi : 10.1029/1998JE900007. URL http://dx.doi.org/10.1029/1998JE900007.

[45] E. Chouzenoux, M. Legendre, S. Moussaoui, and J. Idier. Fast constrained least squares spectral unmixing using primal-dual interior-point optimization. *Selected Topics in Applied Earth Observations and Remote Sensing, IEEE Journal of*, 7(1) :59–69, 2014. ISSN 1939-1404. doi : 10.1109/JSTARS.2013.2266732.

[46] Emilie Chouzenoux, Said Moussaoui, and Jerome Idier. Algorithme primal-dual de points interieurs pour l'estimation penalisee des cartes d'abondances en imagerie hyperspectrale. In *Actes de GRETSI 2011*, page ID290, Bordeaux, France, September 2011. URL http://hal.archives-ouvertes.fr/hal-00625893.

[47] Emilie Chouzenoux, Saïd Moussaoui, Maxime Legendre, and Jérôme Idier. Algorithme primal-dual de points intérieurs pour l'estimation pénalisée des cartes d'abondances en imagerie hyperspectrale. *Traitement du Signal*, 30(1-2) :35–59, 2013. URL http://hal.archives-ouvertes.fr/hal-00808278.

[48] P. R. Christensen, J. L. Bandfield, V. E. Hamilton, S. W. Ruff, H. H. Kieffer, T. N. Titus, M. C. Malin, R. V. Morris, M. D. Lane, R. L. Clark, B. M. Jakosky, M. T. Mellon, J. C. Pearl, B. J. Conrath, M. D. Smith, R. T. Clancy, R. O. Kuzmin, T. Roush, G. L. Mehall, N. Gorelick, K. Bender, K. Murray, S. Dason, E. Greene, S. Silverman, and M. Greenfield. Mars global surveyor thermal emission spectrometer experiment : Investigation description and surface science results. *Journal of Geophysical Research : Planets*, 106(E10) :23823–23871, 2001. ISSN 2156-2202. doi : 10.1029/2000JE001370. URL http://dx.doi.org/10.1029/2000JE001370.

[49] Philip R. Christensen. Water at the poles and in permafrost regions of mars. *Elements*, 2(3) : 151–155, June 2006. URL http://elements.geoscienceworld.org/content/2/3/151.abstract.

[50] Philip R. Christensen, Donald L. Anderson, Stillman C. Chase, Roger N. Clark, Hugh H. Kieffer, Michael C. Malin, John C. Pearl, James Carpenter, Nuno Bandiera, F. Gerald Brown, and Steven Silverman. Thermal emission spectrometer experiment : Mars observer mission. *Journal of Geophysical Research : Planets*, 97(E5) :7719–7734, 1992. ISSN 2156-2202. doi : 10.1029/92JE00453. URL http://dx.doi.org/10.1029/92JE00453.

[51] R. T. Clancy, M. J. Wolff, and P. R. Christensen. Mars aerosol studies with the MGS TES emission phase function observations : Optical depths, particle sizes, and ice cloud types versus latitude and solar longitude. *Journal of Geophysical Research (Planets)*, 108 :2–1, September 2003. doi : 10.1029/2003JE002058.

[52] Stephen M. Clifford and Timothy J. Parker. The evolution of the martian hydrosphere : Implications for the fate of a primordial ocean and the current state of the northern plains. *Icarus*, 154 (1) :40–79, November 2001. ISSN 0019-1035. URL http://www.sciencedirect.com/science/article/pii/S0019103501966710.

[53] Stephen M. Clifford, Jeremie Lasue, Essam Heggy, Joséphine Boisson, Patrick McGovern, and Michael D. Max. Depth of the martian cryosphere : Revised estimates and implications for the existence and detection of subpermafrost groundwater. *J. Geophys. Res.*, 115(E7) :E07001–, July 2010. ISSN 0148-0227. URL http://dx.doi.org/10.1029/2009JE003462.

[54] A. Colaprete and O. B. Toon. Carbon dioxide snow storms during the polar night on Mars. *Journal of Geophysical Research (Planets)*, 107 :5–1, July 2002. doi : 10.1029/2001JE001758.

[55] A. Colaprete, J. R. Barnes, R. M. Haberle, J. L. Hollingsworth, H. H. Kieffer, and T. N. Titus. Albedo of the south pole on Mars determined by topographic forcing of atmosphere dynamics. *Nature*, 435 :184–188, May 2005. doi : 10.1038/nature03561.

[56] J.-P. Combe, S. Le Mouélic, C. Sotin, A. Gendrin, J. F. Mustard, L. Le Deit, P. Launeau, J.-P. Bibring, B. Gondet, Y. Langevin, P. Pinet, and the OMEGA Science team. Analysis of OMEGA/Mars Express data hyperspectral data using a Multiple-Endmember Linear Spectral Unmixing Model (MELSUM) : Methodology and first results. *Planetary and Space Science*, 56 : 951–975, May 2008. doi : 10.1016/j.pss.2007.12.007.

[57] L. Comolli and B. Saggin. Evaluation of the sensitivity to mechanical vibrations of an ir fourier spectrometer. *Rev. Sci. Instrum.*, 76(12) :123112–8, December 2005. URL http://dx.doi.org/10.1063/1.2149009.

[58] Lorenzo Comolli and Bortolino Saggin. Analysis of disturbances in the planetary fourier spectrometer through numerical modeling. *Planetary and Space Science*, 58(5) :864–874, April 2010. ISSN 0032-0633. URL http://www.sciencedirect.com/science/article/B6V6T-4Y9CFBX-2/2/950f692b594101f9b0558dae213e3fc1.

[59] A Coradini, F Capaccioni, P Drossart, A Semery, G Arnold, U Schade, F Angrilli, M.A Barucci, G Bellucci, G Bianchini, J.P Bibring, A Blanco, M Blecka, D Bockelee-Morvan, R Bonsignori, M Bouye, E Bussoletti, M.T Capria, R Carlson, U Carsenty, P Cerroni, L Colangeli, M Combes, M Combi, J Crovisier, M Dami, M.C DeSanctis, A.M DiLellis, E Dotto, T Encrenaz, E Epifani, S Erard, S Espinasse, A Fave, C Federico, U Fink, S Fonti, V Formisano, Y Hello, H Hirsch, G Huntzinger, R Knoll, D Kouach, W.H Ip, P Irwin, J Kachlicki, Y Langevin, G Magni, T McCord, V Mennella, H Michaelis, G Mondello, S Mottola, G Neukum, V Orofino, R Orosei, P Palumbo, G Peter, B Pforte, G Piccioni, J.M Reess, E Ress, B Saggin, B Schmitt, ; Stefanovitch, A Stern, F Taylor, D Tiphene, and G Tozzi. Virtis : an imaging spectrometer for the rosetta mission. *Planetary and Space Science*, 46(9-10) :1291–1304, October 1998. ISSN 0032-0633. URL http://www.sciencedirect.com/science/article/B6V6T-3W1R5DR-N/2/1cde0964222ad97e19c477f78f637aed.

[60] E. Dartois. Co clathrate hydrate : Near to mid-ir spectroscopic signatures. *Icarus*, 212(2) :950–956, April 2011. ISSN 0019-1035. URL http://www.sciencedirect.com/science/article/pii/S0019103510004604.

[61] E. Dartois and D. Deboffle. Methane clathrate hydrate FTIR spectrum. Implications for its cometary and planetary detection. *Astronomy and Astrophysics*, 490 :L19–L22, November 2008. doi : 10.1051/0004-6361:200810926.

[62] E. Dartois and B. Schmitt. Carbon dioxide clathrate hydrate FTIR spectrum. Near infrared combination modes for astrophysical remote detection. *Astronomy and Astrophysics*, 504 :869–873, September 2009. doi : 10.1051/0004-6361/200911812.

[63] E. Dartois, Ph. Duret, U. Marboeuf, and B. Schmitt. Hydrogen sulfide clathrate hydrate ftir spectroscopy : A help gas for clathrate formation in the solar system ? *Icarus*, 220(2) :427–434, August 2012. ISSN 0019-1035. URL http://www.sciencedirect.com/science/article/pii/S0019103512002035.

[64] I.J. Daubar, A.S. McEwen, S. Byrne, M.R. Kennedy, and B. Ivanov. The current martian cratering rate. *Icarus*, 225(1) :506–516, July 2013. ISSN 0019-1035. URL http://www.sciencedirect.com/science/article/pii/S0019103513001693.

[65] S. de Villiers, A. Nermoen, B. Jamtveit, J. Mathiesen, P. Meakin, and S. C. Werner. Formation of martian araneiforms by gas-driven erosion of granular material. *Geophys. Res. Lett.*, 39(13) :L13204–, July 2012. ISSN 0094-8276. URL http://dx.doi.org/10.1029/2012GL052226.

[66] Robert E. Dickinson, Bernard Pinty, and Michel M. Verstraete. Relating surface albedos in gcm to remotely sensed data. *Agricultural and Forest Meteorology*, 52(1-2) :109–131, August 1990. ISSN 0168-1923. doi : 10.1016/0168-1923(90)90103-D. URL http://www.sciencedirect.com/science/article/pii/016819239090103D.

[67] Serina Diniega, Shane Byrne, Nathan T. Bridges, Colin M. Dundas, and Alfred S. McEwen. Seasonality of present-day martian dune-gully activity. *Geology*, 38(11) :1047–1050, November 2010. URL http://geology.gsapubs.org/cgi/content/abstract/38/11/1047.

[68] Nicolas Dobigeon, Saïd Moussaoui, Jean-Yves Tourneret, and Cédric Carteret. Bayesian separation of spectral sources under non-negativity and full additivity constraints. *Signal Processing*, 89(12) :2657–2669, December 2009. ISSN 0165-1684. URL http://www.sciencedirect.com/science/article/B6V18-4W9XDSW-2/2/f3d4b6f457b91e5ccfcce8ffcf41bb18.

[69] A. Dollfus. Propriétés photométriques des contrées désertiques sur la planète mars. *C.R. Seances Acad. Sci. Paris*, 244 :162–164, 1957.

[70] A. Dollfus. Étude de la planète Mars de 1954 à 1958. *Annales d'Astrophysique*, 28 :722, February 1965.

[71] Audouin Dollfus and Marc Deschamps. Grain-size determination at the surface of mars. *Icarus*, 67(1) :37–50, July 1986. ISSN 0019-1035. doi : 10.1016/0019-1035(86)90172-7. URL http://www.sciencedirect.com/science/article/pii/0019103586901727.

[72] Deborah L. Domingue, Faith Vilas, Gregory M. Holsclaw, Johan Warell, Noam R. Izenberg, Scott L. Murchie, Brett W. Denevi, David T. Blewett, William E. McClintock, Brian J. Anderson, and Menelaos Sarantos. Whole-disk spectrophotometric properties of mercury : Synthesis of messenger and ground-based observations. *Icarus*, 209(1) :101–124, September 2010. ISSN 0019-1035. doi : 10.1016/j.icarus.2010.02.022. URL http://www.sciencedirect.com/science/article/pii/S0019103510000965.

[73] S. Douté and B. Schmitt. A multilayer bidirectional reflectance model for the analysis of planetary surface hyperspectral images at visible and near-infrared wavelengths. *Journal of Geophysical Research*, 103 :31367–31390, December 1998. doi : 10.1029/98JE01894.

[74] S. Douté, E. Deforas, F. Schmidt, R. Oliva, and B. Schmitt. A Comprehensive Numerical Package for the Modeling of Mars Hyperspectral Images. In *Lunar and Planetary Institute Conference Abstracts*, volume 38 of *Lunar and Planetary Institute Conference Abstracts*, pages 1836–+, March 2007.

[75] S. Douté, B. Schmitt, Y. Langevin, J.-P. Bibring, F. Altieri, G. Bellucci, B. Gondet, F. Poulet, and the MEX OMEGA team. South Pole of Mars : Nature and composition of the icy terrains from Mars Express OMEGA observations. *Planetary and Space Science*, 55 :113–133, January 2007. doi : 10.1016/j.pss.2006.05.035.

[76] S. Douté, X. Ceamanos, and T. Appéré. Retrieving Atmospheric Dust Opacity on Mars by Imaging Spectroscopy at Large Angles. *ArXiv e-prints*, February 2013.

[77] Sylvain Douté. *Modélisation numérique de la réflectance spectrale des surfaces glacées du Système Solaire. Application Ã l'analyse de spectres de Triton et Pluton et au traitement d'images hyperspectrales NIMS de Io.* PhD thesis, Université Joseph Fourier - Grenoble I, 1998.

[78] Colin M. Dundas, Alfred S. McEwen, Serina Diniega, Shane Byrne, and Sara Martinez-Alonso. New and recent gully activity on mars as seen by hirise. *Geophys. Res. Lett.*, 37(7) :L07202–, April 2010. ISSN 0094-8276. URL http://dx.doi.org/10.1029/2009GL041351.

[79] Bethany L. Ehlmann and John F. Mustard. An in-situ record of major environmental transitions on early mars at northeast syrtis major. *Geophys. Res. Lett.*, 39(11) :L11202–, June 2012. ISSN 0094-8276. URL http://dx.doi.org/10.1029/2012GL051594.

[80] Janusz Eluszkiewicz and Jean-Luc Moncet. A coupled microphysical/radiative transfer model of albedo and emissivity of planetary surfaces covered by volatile ices. *Icarus*, 166(2) :375–384, December 2003. URL http://www.sciencedirect.com/science/article/B6WGF-49V1DPH-3/2/12ed8d86bc224511b0d6f7ee29500ac6.

[81] Janusz Eluszkiewicz, Jean-Luc Moncet, Timothy N. Titus, and Gary B. Hansen. A microphysically-based approach to modeling emissivity and albedo of the martian seasonal caps. *Icarus*, 174(2) :524–534, April 2005. URL http://www.sciencedirect.com/science/article/B6WGF-4FGX7XV-8/2/4bc82512b24af99cca6629d85eea7b73.

[82] S. Erard. A spectro-photometric model of Mars in the near-infrared. *Geophysical Research Letters*, 28 :1291–1294, April 2001. doi : 10.1029/2000GL012347.

[83] S. Erard, P. Drossart, and G. Piccioni. Multivariate analysis of visible and infrared thermal imaging spectrometer (virtis) venus express nightside and limb observations. *J. Geophys. Res.*, 114 :–, January 2009. URL http://dx.doi.org/10.1029/2008JE003116.

[84] Stephane Erard and Wendy Calvin. New composite spectra of mars, 0.4 microns. *Icarus*, 130(2) : 449–460, December 1997. ISSN 0019-1035. URL http://www.sciencedirect.com/science/article/pii/S0019103597958309.

[85] William H. Farrand, Lisa R. Gaddis, and Laszlo Keszthelyi. Pitted cones and domes on mars : Observations in acidalia planitia and cydonia mensae using moc, themis, and tes data. *J. Geophys. Res.*, 110(E5) :E05005–, May 2005. ISSN 0148-0227. URL http://dx.doi.org/10.1029/2004JE002297.

[86] J. Fernando, F. Schmidt, X. Ceamanos, P. Pinet, S. Douté, and Y. Daydou. Surface reflectance of Mars observed by CRISM/MRO : 2. Estimation of surface photometric properties in Gusev Crater and Meridiani Planum. *Journal of Geophysical Research (Planets)*, 118 :534–559, March 2013. doi : 10.1029/2012JE004194. URL http://arxiv.org/abs/1303.4549.

[87] G. E. Fischbacher, L. J. Martin, and W. A. Baum. Seasonal behavior of the Martian polar caps. *Publications of the Astronomical Society of the Pacific*, 81 :538–+, 1969.

[88] E. Flamini, F. Capaccioni, L. Colangeli, G. Cremonese, A. Doressoundiram, J.L. Josset, Y. Langevin, S. Debei, M.T. Capria, M.C. De Sanctis, L. Marinangeli, M. Massironi, E. Mazzotta Epifani, G. Naletto, P. Palumbo, P. Eng, J.F. Roig, A. Caporali, V. Da Deppo, S. Erard, C. Federico, O. Forni, M. Sgavetti, G. Filacchione, L. Giacomini, G. Marra, E. Martellato, M. Zusi, M. Cosi, C. Bettanini, L. Calamai, M. Zaccariotto, L. Tommasi, M. Dami, J. Ficai Veltroni, F. Poulet, and Y. Hello. Simbio-sys : The spectrometer and imagers integrated observatory system for the bepicolombo planetary orbiters. *Planetary and Space Science*, 58(1-2) :125 – 143, 2010. ISSN 0032-0633. doi : http://dx.doi.org/10.1016/j.pss.2009.06.017. URL http://www.sciencedirect.com/science/article/pii/S0032063309001652. Comprehensive Science Investigations of Mercury : The scientific goals of the joint ESA/JAXA mission BepiColombo.

[89] S. Fonti and G. A. Marzo. Mapping the methane on mars. *A&A*, 512 :–, March 2010. URL http://dx.doi.org/10.1051/0004-6361/200913178.

[90] F. Forget. Mars CO_2 ice polar caps. In B. Schmitt, C. de Bergh, and M. Festou, editors, *Solar System Ices*, volume 227 of *Astrophysics and Space Science Library*, pages 477–507. Kluwer, 1998.

[91] F. Forget, G. B. Hansen, and J. B. Pollack. Low brightness temperatures of Martian polar caps : CO_2 clouds or low surface emissivity ? *Journal of Geophysical Research*, 100 :21219–21234, 1995. doi : 10.1029/95JE02378.

[92] F. Forget, F. Hourdin, R. Fournier, C. Hourdin, O. Talagrand, M. Collins, S. R. Lewis, P. L. Read, and J.-P. Huot. Improved general circulation models of the Martian atmosphere from the surface to above 80 km. *Journal of Geophysical Research*, 104 :24155–24176, October 1999. doi : 10.1029/1999JE001025.

[93] V. Formisano, S. Atreya, T. Encrenaz, N. Ignatiev, and M. Giuranna. Detection of Methane in the Atmosphere of Mars. *Science*, 306 :1758–1761, December 2004. doi : 10.1126/science.1101732.

[94] V. Formisano, F. Angrilli, G. Arnold, S. Atreya, G. Bianchini, D. Biondi, A. Blanco, M.I. Blecka, A. Coradini, L. Colangeli, A. Ekonomov, F. Esposito, S. Fonti, M. Giuranna, D. Grassi, V. Gnedykh, A. Grigoriev, G. Hansen, H. Hirsh, I. Khatuntsev, A. Kiselev, N. Ignatiev, A. Jurewicz, E. Lellouch, J. Lopez Moreno, A. Marten, A. Mattana, A. Maturilli, E. Mencarelli, M. Michalska, V. Moroz, B. Moshkin, F. Nespoli, Y. Nikolsky, R. Orfei, P. Orleanski, V. Orofino, E. Palomba, D. Patsaev, G. Piccioni, M. Rataj, R. Rodrigo, J. Rodriguez, M. Rossi, B. Saggin, D. Titov, and L. Zasova. The planetary fourier spectrometer (pfs) onboard the european mars express mission. *Planetary and Space Science*, 53(10) :963–974, August 2005. ISSN 0032-0633. URL http://www.sciencedirect.com/science/article/B6V6T-4G94HR4-2/2/c10c243741b6a0444b7d58665e9ec980.

[95] O. Forni, F. Poulet, J.-P. Bibring, S. Erard, C. Gomez, Y. Langevin, B. Gondet, and The Omega Science Team. Component Separation of OMEGA Spectra with ICA. In S. Mackwell and E. Stansbery, editors, *36th Annual Lunar and Planetary Science Conference*, pages 1623–+, March 2005.

[96] Fabrice Gaillard, Joseph Michalski, Gilles Berger, ScottM. McLennan, and Bruno Scaillet. Geochemical reservoirs and timing of sulfur cycling on mars. 174(1-4) :251–300–, 2013. ISSN 0038-6308. URL http://dx.doi.org/10.1007/s11214-012-9947-4.

[97] S.R. Gainey and M.E. Elwood Madden. Kinetics of methane clathrate formation and dissociation under mars relevant conditions. *Icarus*, 218(1) :513–524, March 2012. ISSN 0019-1035. URL http://www.sciencedirect.com/science/article/pii/S0019103511005008.

[98] T. Gánti, A. Horváth, S. Bérczi, A. Gesztesi, and E. Szathmáry. Dark Dune Spots : Possible Biomarkers on Mars ? *Origins of Life and Evolution of the Biosphere*, 33 :515–557, October 2003.

[99] E. Gardin, P. Allemand, C. Quantin, and P. Thollot. Defrosting, dark flow features, and dune activity on mars : Example in russell crater. *J. Geophys. Res.*, 115(E6) :E06016–, June 2010. ISSN 0148-0227. URL http://dx.doi.org/10.1029/2009JE003515.

[100] A. Geminale, V. Formisano, and M. Giuranna. Methane in martian atmosphere : Average spatial, diurnal, and seasonal behaviour. *Planetary and Space Science*, 56(9) :1194–1203, July 2008. ISSN 0032-0633. URL http://www.sciencedirect.com/science/article/B6V6T-4S62RPB-2/2/1d51df2872f8120606c66846602d624f.

[101] M. Giuranna, V. Formisano, D. Biondi, A. Ekonomov, S. Fonti, D. Grassi, H. Hirsch, I. Khatuntsev, N. Ignatiev, M. Malgoska, A. Mattana, A. Maturilli, E. Mencarelli, F. Nespoli, R. Orfei, P. Orleanski, G. Piccioni, M. Rataj, B. Saggin, and L. Zasova. Calibration of the planetary fourier spectrometer long wavelength channel. *Planetary and Space Science*, 53(10) :993–1007, August 2005. ISSN 0032-0633. URL http://www.sciencedirect.com/science/article/B6V6T-4GCX0HK-1/2/9d8e4485b4eb45a54082fef03d4718a5.

[102] M. Giuranna, V. Formisano, D. Biondi, A. Ekonomov, S. Fonti, D. Grassi, H. Hirsch, I. Khatuntsev, N. Ignatiev, M. Michalska, A. Mattana, A. Maturilli, B.E. Moshkin, E. Mencarelli, F. Nespoli, R. Orfei, P. Orleanski, G. Piccioni, M. Rataj, B. Saggin, and L. Zasova. Calibration of the planetary fourier spectrometer short wavelength channel. *Planetary and Space Science*, 53(10) :975–991, August 2005. ISSN 0032-0633. URL http://www.sciencedirect.com/science/article/B6V6T-4GCX1K5-2/2/a2f8e53774cbfb604eedcff6055edf4c.

[103] M. Giuranna, V. Formisano, D. Grassi, and A. Maturilli. Tracking the edge of the south seasonal polar cap of mars. *Planetary and Space Science*, 55(10) :1319–1327, July 2007. URL http://www.sciencedirect.com/science/article/B6V6T-4MS9RGP-1/2/5e2cde3a3b8173badddefababaeaa1f0.

[104] M. Giuranna, G. Hansen, V. Formisano, L. Zasova, A. Maturilli, D. Grassi, and N. Ignatiev. Spatial variability, composition and thickness of the seasonal north polar cap of mars in mid-spring. *Planetary and Space Science*, 55(10) :1328–1345, July 2007. URL http://www.sciencedirect.com/science/article/B6V6T-4ND0RT5-1/2/296230f162e6ab90e6d175919d2e324c.

[105] M. Giuranna, D. Grassi, V. Formisano, L. Montabone, F. Forget, and L. Zasova. Pfs/mex observations of the condensing co2 south polar cap of mars. *Icarus*, 197(2) :386–402, October 2008. URL http://www.sciencedirect.com/science/article/B6WGF-4SPYKJM-1/2/61736d61880cf7c503ff493adcc83204.

[106] Timothy D. Glotch and Philip R. Christensen. Geologic and mineralogic mapping of aram chaos : Evidence for a water-rich history. *J. Geophys. Res.*, 110(E9) :E09006–, September 2005. ISSN 0148-0227. URL http://dx.doi.org/10.1029/2004JE002389.

[107] Cécile Gomez. *Potentiels des données de télédétection mutlisources pour la cartographie géologique : Application Ã la région de Rehoboth (Namibie)*. PhD thesis, Université Claude Bernard - Lyon 1, 2004.

[108] Robert O Green, Michael L Eastwood, Charles M Sarture, Thomas G Chrien, Mikael Aronsson, Bruce J Chippendale, Jessica A Faust, Betina E Pavri, Christopher J Chovit, Manuel Solis, Martin R Olah, and Orlesa Williams. Imaging spectroscopy and the airborne visible/infrared imaging spectrometer (aviris). *Remote Sensing of Environment*, 65(3) :227–248, September 1998. ISSN 0034-4257. URL http://www.sciencedirect.com/science/article/pii/S0034425798000649.

[109] W. M. Grundy, S. Douté, and B. Schmitt. A Monte Carlo ray-tracing model for scattering and polarization by large particles with complex shapes. *Journal of Geophysical Research*, 105 : 29291–29314, December 2000. doi : 10.1029/2000JE001276.

[110] C. J. Hansen, M. Bourke, N. T. Bridges, S. Byrne, C. Colon, S. Diniega, C. Dundas, K. Herkenhoff, A. McEwen, M. Mellon, G. Portyankina, and N. Thomas. Seasonal erosion and restoration of mars' northern polar dunes. *Science*, 331(6017) :575–578, February 2011. URL http://www.sciencemag.org/content/331/6017/575.abstract.

[111] C.J. Hansen, N. Thomas, G. Portyankina, A. McEwen, T. Becker, S. Byrne, K. Herkenhoff, H. Kieffer, and M. Mellon. Hirise observations of gas sublimation-driven activity in mars' southern polar regions : I. erosion of the surface. *Icarus*, 205(1) :283–295, January 2010. ISSN 0019-1035. URL http://www.sciencedirect.com/science/article/B6WGF-4WW2SPC-6/2/f9e99877d29cdba494c9721e0f297b61.

[112] G. Hansen, M. Giuranna, V. Formisano, S. Fonti, D. Grassi, H. Hirsh, N. Ignatiev, A. Maturilli, P. Orleanski, G. Piccioni, M. Rataj, B. Saggin, and L. Zasova. PFS-MEX observation of ices in the residual south polar cap of Mars. *Planetary and Space Science*, 53 :1089–1095, August 2005. doi : 10.1016/j.pss.2004.12.011.

[113] G. B. Hansen. Control of the radiative behavior of the Martian polar caps by surface CO_2 ice : Evidence from Mars Global Surveyor measurements. *Journal of Geophysical Research*, 104 : 16471–16486, July 1999. doi : 10.1029/1998JE000626.

[114] B. Hapke. Effects of a Simulated Solar Wind on the Photometric Properties of Rocks and Powders. *Annals of the New York Academy of Sciences*, 123 :711–721, November 1965.

[115] B. Hapke. Bidirectional reflectance spectroscopy. III - Correction for macroscopic roughness. *Icarus*, 59 :41–59, July 1984. doi : 10.1016/0019-1035(84)90054-X.

[116] B. Hapke. Bidirectional reflectance spectroscopy. IV - The extinction coefficient and the opposition effect. *Icarus*, 67 :264–280, August 1986. doi : 10.1016/0019-1035(86)90108-9.

[117] B. Hapke. *Theory of reflectance and emittance spectroscopy*. Topics in Remote Sensing, Cambridge, UK : Cambridge University Press, 1993.

[118] B. Hapke. Bidirectional Reflectance Spectroscopy5. The Coherent Backscatter Opposition Effect and Anisotropic Scattering. *Icarus*, 157 :523–534, June 2002. doi : 10.1006/icar.2002.6853.

[119] Bruce Hapke. Bidirectional reflectance spectroscopy 1. theory. *J. Geophys. Res.*, 86 :–, 1981. URL http://dx.doi.org/10.1029/JB086iB04p03039.

[120] Bruce Hapke. Space weathering from mercury to the asteroid belt. *J. Geophys. Res.*, 106 (E5) :10039–10073, 2001. ISSN 0148-0227. URL http://dx.doi.org/10.1029/2000JE001338.

[121] Bruce Hapke. Bidirectional reflectance spectroscopy : 6. effects of porosity. *Icarus*, 195(2) : 918–926, June 2008. URL http://www.sciencedirect.com/science/article/B6WGF-4RR8YWH-2/1/a50020f57fb3b60836f4511a299f1e1a.

[122] Bruce W. Hapke, Michael K. Shepard, Robert M. Nelson, William D. Smythe, and Jennifer L. Piatek. A quantitative test of the ability of models based on the equation of radiative transfer to predict the bidirectional reflectance of a well-characterized medium. *Icarus*, 199(1) :210–218, January 2009. ISSN 0019-1035. URL http://www.sciencedirect.com/science/article/B6WGF-4TMSNWP-4/2/e453e1a339899062eedb00bcd2fa27d0.

[123] D.C. Heinz and Chein-I-Chang. Fully constrained least squares linear spectral mixture analysis method for material quantification in hyperspectral imagery. *Geoscience and Remote Sensing, IEEE Transactions on*, 39(3) :529 –545, mar 2001. ISSN 0196-2892. doi : 10.1109/36.911111.

[124] L. G. Henyey and J. L. Greenstein. Diffuse radiation in the Galaxy. *Astrophysical Journal*, 93 : 70–83, January 1941. doi : 10.1086/144246.

[125] K. C. Herr and G. C. Pimental. Infrared absorptions near three microns recorded over the polar CAP of mars. *Science*, 166 :496–499, October 1969.

[126] K. C. Herr and G. C. Pimentel. Evidence for Solid Carbon Dioxide in the Upper Atmosphere of Mars. *Science*, 167 :47–49, January 1970.

[127] Jean-Michel Herri and Eric Chassefière. Carbon dioxide, argon, nitrogen and methane clathrate hydrates : Thermodynamic modelling, investigation of their stability in martian atmospheric conditions and variability of methane trapping. *Planetary and Space Science*, 73(1) :376–386, December 2012. ISSN 0032-0633. URL http://www.sciencedirect.com/science/article/pii/S0032063312002358.

[128] W. Herschel. On the remarkable appearances at the polar regions of the planet mars, the inclination of its axis, the position of its poles, and its spheroidical figure ; with a few hints relating to its real diameter and atmosphere. by william herschel, esq. f. r. s. *Philosophical Transactions of the Royal Society of London (1776-1886)*, 74 :233–273, January 1784. URL http://www.journals.royalsoc.ac.uk/openurl.asp?genre=article&id=U2738806008362M5.

[129] S. L. Hess, R. M. Henry, and J. E. Tillman. The seasonal variation of atmospheric pressure on Mars as affected by the south polar CAP. *Journal of Geophysical Research*, 84 :2923–2927, June 1979.

[130] R. Heylen, D. Burazerovic, and P. Scheunders. Fully constrained least squares spectral unmixing by simplex projection. *Geoscience and Remote Sensing, IEEE Transactions on*, 49(11) :4112–4122, 2011. ISSN 0196-2892. doi : 10.1109/TGRS.2011.2155070.

[131] H. Hiesinger and J. Helbert. The mercury radiometer and thermal infrared spectrometer (mertis) for the bepicolombo mission. *Planetary and Space Science*, 58(1-2) :144 – 165, 2010. ISSN 0032-0633. doi : http://dx.doi.org/10.1016/j.pss.2008.09.019. URL http://www.sciencedirect.com/science/article/pii/S0032063308003127. Comprehensive Science Investigations of Mercury : The scientific goals of the joint ESA/JAXA mission BepiColombo.

[132] Nick Hoffman. White mars : A new model for mars' surface and atmosphere based on co2. *Icarus*, 146(2) :326–342, August 2000. ISSN 0019-1035. URL http://www.sciencedirect.com/science/article/pii/S001910350096398X.

[133] A. Horváth, T. Gánti, A. Gesztesi, S. Bérczi, and E. Szathmáry. Probable Evidences of Recent Biological Activity on Mars : Appearance and Growing of Dark Dune Spots in the South Polar Region. In *Lunar and Planetary Institute Conference Abstracts*, volume 32 of *Lunar and Planetary Institute Conference Abstracts*, pages 1543–+, March 2001.

[134] F. Hourdin, F. Forget, and O. Talagrand. The sensitivity of the Martian surface pressure and atmospheric mass budget to various parameters : A comparison between numerical simulations and Viking observations. *Journal of Geophysical Research*, 100 :5501–5523, March 1995.

[135] A. Huck, M. Guillaume, and J. Blanc-Talon. Minimum dispersion constrained nonnegative matrix factorization to unmix hyperspectral data. *Geoscience and Remote Sensing, IEEE Transactions on DOI - 10.1109/TGRS.2009.2038483*, 48(6) :2590–2602, 2010. ISSN 0196-2892.

[136] A. Hyvarinen and E. Oja. Independent component analysis : algorithms and applications. *Neural Networks*, 13(4-5) :411–430, June 2000. URL http://www.sciencedirect.com/science/article/B6T08-43X2MFY-2/2/e16b1ec17aa9eec8247cd937c631e846.

[137] A. Hyvärinen, J. Karhunen, and E. Oja. *Independent component analysis*. Adaptive and Learning Systems for Signal Processing, Communications, and Control. John Wiley, New York, 2001.

[138] Jérôme Idier. *Bayesian Approach to Inverse Problems*. ISTE Ltd and John Wiley & Sons Inc, avr. 2008.

[139] A. B. Ivanov and D. O. Muhleman. Cloud Reflection Observations : Results from the Mars Orbiter Laser Altimeter. *Icarus*, 154 :190–206, November 2001. doi : 10.1006/icar.2001.6686.

[140] Hironobu Iwabuchi. Efficient monte carlo methods for radiative transfer modeling. *Journal of the Atmospheric Sciences*, 63(9) :2324–2339, September 2006. URL http://dx.doi.org/10.1175%2FJAS3755.1.

[141] K. Iwasaki, Y. Saito, Y. Nakai, T. Akabane, and E. Panjaitan. Martian south polar CAP 1988. *Journal of Geophysical Research*, 95 :14751–14754, August 1990.

[142] P. B. James and K. Lumme. Martian south polar CAP boundary - 1971 and 1973 data. *Icarus*, 50 :368–380, June 1982. doi : 10.1016/0019-1035(82)90130-0.

[143] P. B. James, G. Briggs, J. Barnes, and A. Spruck. Seasonal recession of Mars' south polar CAP as seen by Viking. *Journal of Geophysical Research*, 84 :2889–2922, June 1979.

[144] P. B. James, K. M. Malolepszy, and L. J. Martin. Interannual variability of Mars' south polar CAP. *Icarus*, 71 :298–305, August 1987. doi : 10.1016/0019-1035(87)90154-0.

[145] A. Jehl, P. Pinet, D. Baratoux, Y. Daydou, S. Chevrel, F. Heuripeau, N. Manaud, A. Cord, C. Rosemberg, G. Neukum, K. Gwinner, F. Scholten, H. Hoffman, and T. Roatsch. Gusev photometric variability as seen from orbit by hrsc/mars-express. *Icarus*, 197(2) :403–428, October 2008. ISSN 0019-1035. URL http://www.sciencedirect.com/science/article/B6WGF-4STB0J6-3/2/7d905531eed585267c03cc94b4a3e60f.

[146] Jeffrey R. Johnson, Randolph Kirk, Laurence A. Soderblom, Lisa Gaddis, Robert J. Reid, Daniel T. Britt, Peter Smith, Mark Lemmon, Nicolas Thomas, James F. Bell, Nathan T. Bridges, Robert Anderson, Ken E. Herkenhoff, Justin Maki, Scott Murchie, Andreas Dummel, Ralf Jaumann, Frank Trauthan, and Gabriele Arnold. Preliminary results on photometric properties of materials at the sagan memorial station, mars. *J. Geophys. Res.*, 104(E4) :8809–8830, April 1999. ISSN 2156-2202. URL http://dx.doi.org/10.1029/98JE02247.

[147] Jeffrey R. Johnson, William M. Grundy, Mark T. Lemmon, James F. Bell, Miles J. Johnson, Robert Deen, R. E. Arvidson, W. H. Farrand, E. Guinness, Alexander G. Hayes, K. E. Herkenhoff, F. Seelos, J. Soderblom, and S. Squyres. Spectrophotometric properties of materials observed by pancam on the mars exploration rovers : 2. opportunity. *J. Geophys. Res.*, 111(E12) :E12S16–, December 2006. ISSN 2156-2202. URL http://dx.doi.org/10.1029/2006JE002762.

[148] Jeffrey R. Johnson, William M. Grundy, Mark T. Lemmon, James F. Bell, Miles J. Johnson, Robert G. Deen, Raymond E. Arvidson, William H. Farrand, Edward A. Guinness, Alexander G. Hayes, Ken E. Herkenhoff, Frank Seelos, Jason Soderblom, and Steve Squyres. Spectrophotometric properties of materials observed by pancam on the mars exploration rovers : 1. spirit. *J. Geophys. Res.*, 111(E2) :E02S14–, February 2006. ISSN 2156-2202. URL http://dx.doi.org/10.1029/2005JE002494.

[149] Gwenaël Jouannic, Julien Gargani, François Costard, Gian G. Ori, Chiara Marmo, Frédéric Schmidt, and Antoine Lucas. Morphological and mechanical characterization of gullies in a periglacial environment : The case of the russell crater dune (mars). *Planetary and Space Science*, 71(1) :38–54, October 2012. ISSN 0032-0633. doi : 10.1016/j.pss.2012.07.005. URL http://www.sciencedirect.com/science/article/pii/S0032063312001997.

[150] Ö. Karatekin, T. Van Hoolst, and V. Dehant. Martian global-scale CO_2 exchange from time-variable gravity measurements. *Journal of Geophysical Research (Planets)*, 111 :6003–+, June 2006. doi : 10.1029/2005JE002591.

[151] Jeffrey S. Kargel, Roberto Furfaro, Olga Prieto-Ballesteros, J. Alexis P. Rodriguez, David R. Montgomery, Alan R. Gillespie, Giles M. Marion, and Stephen E. Wood. Martian hydrogeology sustained by thermally insulating gas and salt hydrates. *Geology*, 35(11) :975–978, November 2007. doi : 10.1130/G23783A.1. URL http://geology.gsapubs.org/content/35/11/975.abstract.

[152] Erika Kaufmann, Norbert I. Komle, and Gunter Kargl. Laboratory simulation experiments on the solid-state greenhouse effect in planetary ices. *Icarus*, 185(1) :274–286, November 2006. URL http://www.sciencedirect.com/science/article/B6WGF-4KV3Y29-4/2/33d6a87cbe48f24cfd9bba61b9da0d9d.

[153] V. Kaydash, M. Kreslavsky, Yu. Shkuratov, S. Gerasimenko, P. Pinet, J.-L. Josset, S. Beauvivre, and B. Foing. Photometric anomalies of the lunar surface studied with smart-1 amie data. *Icarus*, 202(2) :393–413, August 2009. ISSN 0019-1035. doi : 10.1016/j.icarus.2009.03.018. URL http://www.sciencedirect.com/science/article/pii/S0019103509001262.

[154] Vadym Kaydash, Yuriy Shkuratov, Viktor Korokhin, and Gorden Videen. Photometric anomalies in the apollo landing sites as seen from the lunar reconnaissance orbiter. *Icarus*, 211(1) :89–96, January 2011. ISSN 0019-1035. doi : 10.1016/j.icarus.2010.08.024. URL http://www.sciencedirect.com/science/article/pii/S0019103510003404.

[155] N. J. Kelly, W. V. Boynton, K. Kerry, D. Hamara, D. Janes, R. C. Reedy, K. J. Kim, and R. M. Haberle. Seasonal polar carbon dioxide frost on Mars : CO_2 mass and columnar thickness distribution. *Journal of Geophysical Research (Planets)*, 111 :3–+, December 2006. doi : 10.1029/2006JE002678.

[156] A. Kereszturi, D. Möhlmann, Sz. Berczi, T. Ganti, A. Kuti, A. Sik, and A. Horvath. Recent rheologic processes on dark polar dunes of mars : Driven by interfacial water ? *Icarus*, 201(2) :492–503, June 2009. ISSN 0019-1035. URL http://www.sciencedirect.com/science/article/B6WGF-4VH4DKM-1/2/b68ca3c303a3b26e1a0fd2c9ab657813.

[157] A. Kereszturi, D. M'ohlmann, Sz. Berczi, T. Ganti, A. Horvath, A. Kuti, A. Sik, and E.¨ Szathmary. Indications of brine related local seepage phenomena on the northern hemisphere of mars. *Icarus*, 207(1) :149–164, May 2010. ISSN 0019-1035. doi : 10.1016/j.icarus.2009.10.012. URL http://www.sciencedirect.com/science/article/pii/S001910350900428X.

[158] A. Kereszturi, M. Vincendon, and F. Schmidt. Water ice in the dark dune spots of richardson crater on mars. *Planetary and Space Science*, 59(1) :26–42, January 2011. ISSN 0032-0633. doi : 10.1016/j.pss.2010.10.015. URL http://www.sciencedirect.com/science/article/B6V6T-51CVG1G-4/2/2a48ecf880299ffeaf715c5a27ddd24d.

[159] Akos Kereszturi and Edgard G. Rivera-Valentin. Locations of thin liquid water layers on present-day mars. *Icarus*, 221(1) :289–295, September 2012. ISSN 0019-1035. doi : 10.1016/j.icarus.2012.08.004. URL http://www.sciencedirect.com/science/article/pii/S0019103512003235.

[160] N. Keshava. Distance metrics and band selection in hyperspectral processing with applications to material identification and spectral libraries. *Geoscience and Remote Sensing, IEEE Transactions on*, 42(7) :1552–1565, 2004. ISSN 0196-2892.

[161] H. H. Kieffer. Mars south polar spring and summer temperatures - A residual CO2 frost. *Journal of Geophysical Research*, 84 :8263–8288, December 1979.

[162] H. H. Kieffer. Cold jets in the Martian polar caps. *Journal of Geophysical Research (Planets)*, 112 :8005–+, August 2007. doi : 10.1029/2006JE002816.

[163] H. H. Kieffer, T. Z. Martin, S. C. Chase, Jr., E. D. Miner, and F. D. Palluconi. Martian north pole summer temperatures - Dirty water ice. *Science*, 194 :1341–1344, December 1976.

[164] H. H. Kieffer, T. Z. Martin, A. R. Peterfreund, B. M. Jakosky, E. D. Miner, and F. D. Palluconi. Thermal and albedo mapping of Mars during the Viking primary mission. *Journal of Geophysical Research*, 82 :4249–4291, September 1977.

[165] H. H. Kieffer, T. N. Titus, K. F. Mullins, and P. R. Christensen. Mars south polar spring and summer behavior observed by TES : Seasonal cap evolution controlled by frost grain size. *Journal of Geophysical Research*, 105 :9653–9700, April 2000. doi : 10.1029/1999JE001136.

[166] Hugh H. Kieffer, Philip R. Christensen, and Timothy N. Titus. Co_2 jets formed by sublimation beneath translucent slab ice in mars' seasonal south polar ice cap. *Nature*, 442(7104) :793–796, August 2006. ISSN 0028-0836. URL http://dx.doi.org/10.1038/nature04945.

[167] M. G. Kleinhans. Flow discharge and sediment transport models for estimating a minimum timescale of hydrological activity and channel and delta formation on mars. *J. Geophys. Res.*, 110 (E12) :E12003–, December 2005. ISSN 0148-0227. URL http://dx.doi.org/10.1029/2005JE002521.

[168] G. Komatsu, J. S. Kargel, V. R. Baker, R. G. Strom, G. G. Ori, C. Mosangini, and K. L. Tanaka. A Chaotic Terrain Formation Hypothesis : Explosive Outgas and Outlow by Dissociation of Clathrate on Mars. In *Lunar and Planetary Institute Science Conference Abstracts*, volume 31 of *Lunar and Planetary Inst. Technical Report*, pages 1434–+, March 2000.

[169] Goro Komatsu, Gian Gabriele Ori, Marco Cardinale, James M. Dohm, Victor R. Baker, David A. Vaz, Ryo Ishimaru, Noriyuki Namiki, and Takafumi Matsui. Roles of methane and carbon dioxide in geological processes on mars. *Planetary and Space Science*, 59(2-3) :169–181, February 2011. ISSN 0032-0633. URL http://www.sciencedirect.com/science/article/B6V6T-50GJ2P7-2/2/59196fca8ea4dcad295a25670c4c1e69.

[170] V. A. Krasnopolsky, G. L. Bjoraker, M. J. Mumma, and D. E. Jennings. High-resolution spectroscopy of mars at 3.7 and 8 microns : A sensitive search for h2o2, h2co, hcl, and ch4, and detection of hdo. *J. Geophys. Res.*, 102(E3) :6525–6534, March 1997. ISSN 2156-2202. URL http://dx.doi.org/10.1029/96JE03766.

[171] Vladimir A. Krasnopolsky, Jean Pierre Maillard, and Tobias C. Owen. Detection of methane in the martian atmosphere : evidence for life ? *Icarus*, 172(2) :537–547, December 2004. ISSN 0019-1035. URL http://www.sciencedirect.com/science/article/pii/S0019103504002222.

[172] M. A. Kreslavsky and Y. G. Shkuratov. Photometric anomalies of the lunar surface : Results from clementine data. *J. Geophys. Res.*, 108(E3) :5015–, March 2003. ISSN 0148-0227. URL http://dx.doi.org/10.1029/2002JE001937.

[173] G. P. Kuiper. Visual Observations of Mars, 1956. *Astrophysical Journal*, 125 :307–+, March 1957.

[174] C. Kwan, B. Ayhan, G. Chen, Jing Wang, Baohong Ji, and Chein-I Chang. A novel approach for spectral unmixing, classification, and concentration estimation of chemical and biological agents. *Geoscience and Remote Sensing, IEEE Transactions on*, 44(2) :409–419, 2006. ISSN 0196-2892.

[175] J.L. Lacoume, P.O. Amblard, and P. Comon. *Statistiques d'Ordre Supérieur pour le Traitement du Signal*. Masson, 1997.

[176] David A. Landgrebe. *Signal Theory Methods in Multispectral Remote Sensing*. John Wiley and Sons, 2003.

[177] Y. Langevin, F. Poulet, J.-P. Bibring, and B. Gondet. Sulfates in the North Polar Region of Mars Detected by OMEGA/Mars Express. *Science*, 307 :1584–1586, March 2005. doi : 10.1126/science.1109091.

[178] Y. Langevin, F. Poulet, J.-P. Bibring, B. Schmitt, S. Douté, and B. Gondet. Summer Evolution of the North Polar Cap of Mars as Observed by OMEGA/Mars Express. *Science*, 307 :1581–1584, March 2005. doi : 10.1126/science.1109438.

[179] Y. Langevin, J.-P. Bibring, F. Montmessin, F. Forget, M. Vincendon, S. Douté, F. Poulet, and B. Gondet. Observations of the south seasonal cap of Mars during recession in 2004-2006 by the OMEGA visible/near-infrared imaging spectrometer on board Mars Express. *Journal of Geophysical Research (Planets)*, 112 :8–+, July 2007. doi : 10.1029/2006JE002841.

[180] Yves Langevin, Sylvain Douté, Mathieu Vincendon, Francois Poulet, Jean-Pierre Bibring, Brigitte Gondet, Bernard Schmitt, and F. Forget. No signature of clear co_2 ice from the 'cryptic' regions in mars' south seasonal polar cap. *Nature*, 442(7104) :790–792, August 2006. ISSN 0028-0836. URL http://dx.doi.org/10.1038/nature05012.

[181] J. Laskar, B. Levrard, and J. F. Mustard. Orbital forcing of the martian polar layered deposits. *Nature*, 419 :375–377, September 2002.

[182] Charles L. Lawson and Richard J. Hanson. *Solving Least Squares Problems*. SIAM (Society for Industrial and Applied Mathematics), July 1995. URL http://link.aip.org/link/?SIR/18/518/1.

[183] Laetitia Le Deit, Stéphane Le Mouélic, Olivier Bourgeois, Jean-Philippe Combe, Daniel Mège, Christophe Sotin, Aline Gendrin, Ernst Hauber, Nicolas Mangold, and Jean-Pierre Bibring. Ferric oxides in east candor chasma, valles marineris (mars) inferred from analysis of omega/mars express data : Identification and geological interpretation. *J. Geophys. Res.*, 113 :–, July 2008. URL http://dx.doi.org/10.1029/2007JE002950.

[184] Daniel D. Lee and H. Sebastian Seung. Learning the parts of objects by non-negative matrix factorization. *Nature*, 401(6755) :788–791, October 1999. ISSN 0028-0836. URL http://dx.doi.org/10.1038/44565.

[185] Franck Lefevre and Francois Forget. Observed variations of methane on mars unexplained by known atmospheric chemistry and physics. *Nature*, 460(7256) :720–723, August 2009. ISSN 0028-0836. URL http://dx.doi.org/10.1038/nature08228.

[186] R. B. Leighton, B. C. Murray, R. P. Sharp, J. Denton Allen, and R. K. Sloan. Mariner IV Photography of Mars : Initial Results. *Science*, 149 :627–630, August 1965.

[187] R. R. Leighton and B. C. Murray. Behavior of carbon dioxide and other volatiles on Mars. *Science*, 153 :136–144, July 1966.

[188] C. Leovy and Y. Mintz. Numerical simulation of atmospheric circulation and climate of mars. *Journal of the Atmospheric Sciences*, 26(6) :1167–1190, Nov. 1969.

[189] B. Levrard, F. Forget, F. Montmessin, and J. Laskar. Recent ice-rich deposits formed at high latitudes on Mars by sublimation of unstable equatorial ice during low obliquity. *Nature*, 431 : 1072–1075, October 2004. doi : 10.1038/nature03055.

[190] S. R. Lewis. Mars : atmosphere : Modelling the martian atmosphere. *Astronomy and Geophysics*, 44 :6–+, August 2003. doi : 10.1046/j.1468-4004.2003.44406.x.

[191] S. R. Lewis, M. Collins, P. L. Read, F. Forget, F. Hourdin, R. Fournier, C. Hourdin, O. Talagrand, and J.-P. Huot. A climate database for Mars. *Journal of Geophysical Research*, 104 :24177–24194, October 1999. doi : 10.1029/1999JE001024.

[192] X. Li and A.H. Strahler. Geometric-optical bidirectional reflectance modeling of the discrete crown vegetation canopy : effect of crown shape and mutual shadowing. *Geoscience and Remote Sensing, IEEE Transactions on DOI - 10.1109/36.134078*, 30(2) :276–292, 1992. ISSN 0196-2892.

[193] Shunlin Liang and Alan H. Strahler. An analytic radiative transfer model for a coupled atmosphere and leaf canopy. *J. Geophys. Res.*, 100(D3) :5085–5094, 1995. ISSN 0148-0227. URL `http://dx.doi.org/10.1029/94JD03249`.

[194] S. Liangrocapart and M. Petrou. A two-layer model of the bidirectional reflectance of homogeneous vegetation canopies. *Remote Sensing of Environment*, 80(1) :17–35, April 2002. ISSN 0034-4257. URL `http://www.sciencedirect.com/science/article/pii/S0034425701002644`.

[195] M. L. Litvak, I. G. Mitrofanov, A. S. Kozyrev, A. B. Sanin, V. I. Tret'yakov, W. V. Boynton, C. Shinohara, D. Hamara, S. Saunders, and D. M. Drake. Seasonal Carbon Dioxide Depositions on the Martian Surface as Revealed from Neutron Measurements by the HEND Instrument Onboard the 2001 Mars Odyssey Spacecraft. *Solar System Research*, 38 :167–177, May 2004. doi : 10.1023/B:SOLS.0000030856.83622.17.

[196] M. L. Litvak, I. G. Mitrofanov, A. S. Kozyrev, A. B. Sanin, V. I. Tretyakov, W. V. Boynton, N. J. Kelly, D. Hamara, C. Shinohara, and R. S. Saunders. Comparison between polar regions of Mars from HEND/Odyssey data. *Icarus*, 180 :23–37, January 2006. doi : 10.1016/j.icarus.2005.08.009.

[197] J. Longhi. Phase equilibrium in the system CO_2-H_2O : Application to Mars. *Journal of Geophysical Research (Planets)*, 111 :6011–+, June 2006. doi : 10.1029/2005JE002552.

[198] P. Lowell. *Mars and Its Canals*. Macmillan, New York, 1906.

[199] W. Lucht, C.B. Schaaf, and A.H. Strahler. An algorithm for the retrieval of albedo from space using semiempirical brdf models. *Geoscience and Remote Sensing, IEEE Transactions on DOI - 10.1109/36.841980*, 38(2) :977–998, 2000. ISSN 0196-2892.

[200] K. Lumme and E. Bowell. Radiative transfer in the surfaces of atmosphereless bodies. I - Theory. *Astronomical Journal*, 86 :1694–1721, November 1981. doi : 10.1086/113054.

[201] A. Lyapustin and Y. Knyazikhin. Green s Function Method for the Radiative Transfer Problem. I. Homogeneous non-Lambertian Surface. *Applied Optics*, 40 :3495–3501, July 2001.

[202] Alexei Lyapustin, John Martonchik, Yujie Wang, Istvan Laszlo, and Sergey Korkin. Multiangle implementation of atmospheric correction (maiac) : 1. radiative transfer basis and look-up tables. *J. Geophys. Res.*, 116(D3) :D03210–, February 2011. ISSN 0148-0227. URL `http://dx.doi.org/10.1029/2010JD014985`.

[203] James R. Lyons, Craig Manning, and Francis Nimmo. Formation of methane on mars by fluid-rock interaction in the crust. *Geophys. Res. Lett.*, 32 :–, July 2005. URL `http://dx.doi.org/10.1029/2004GL022161`.

[204] A. Maattanen, F. Montmessin, B. Gondet, F. Scholten, H. Hoffmann, F. González-Galindo, A. Spiga, F. Forget, E. Hauber, G. Neukum, J.-P. Bibring, and J.-L. Bertaux. Mapping the mesospheric co2 clouds on mars : Mex/omega and mex/hrsc observations and challenges for atmospheric models. *Icarus*, 209(2) :452–469, October 2010. ISSN 0019-1035.

URL http://www.sciencedirect.com/science/article/B6WGF-506W6TM-4/2/c5c5a059645305213a7edbc60fa26616.

[205] J.-B. Madeleine, F. Forget, E. Millour, L. Montabone, and M. J. Wolff. Revisiting the radiative impact of dust on mars using the lmd global climate model. *J. Geophys. Res.*, 116 (E11) :E11010–, November 2011. ISSN 0148-0227. URL http://dx.doi.org/10.1029/2011JE003855.

[206] M. C. Malin, M. H. Carr, G. E. Danielson, M. E. Davies, W. K. Hartmann, A. P. Ingersoll, P. B. James, H. Masursky, A. S. McEwen, L. A. Soderblom, P. Thomas, J. Veverka, M. A. Caplinger, M. A. Ravine, T. A. Soulanille, and J. L. Warr En. Early Views of the Martian Surface from the Mars Orbiter Camera of Mars Global Surveyor. *Science*, 279(5357) :1681–1685, March 1998. doi : 10.1126/science.279.5357.1681.

[207] Michael C. Malin, Kenneth S. Edgett, Liliya V. Posiolova, Shawn M. McColley, and Eldar Z. Noe Dobrea. Present-Day Impact Cratering Rate and Contemporary Gully Activity on Mars. *Science*, 314(5805) :1573–1577, 2006. doi : 10.1126/science.1135156.

[208] Frank S. Marzano and Giancarlo Ferrauto. Generalized eddington analytical model for azimuthally dependent radiance simulation in stratified media. *Appl. Opt.*, 44(28) :6032–6048, October 2005. URL http://ao.osa.org/abstract.cfm?URI=ao-44-28-6032.

[209] M. Massé, O. Bourgeois, S. Le Mouélic, C. Verpoorter, A. Spiga, and L. Le Deit. Wide distribution and glacial origin of polar gypsum on mars. *Earth and Planetary Science Letters*, 317 ?318 (0) :44–55, February 2012. ISSN 0012-821X. URL http://www.sciencedirect.com/science/article/pii/S0012821X11007035.

[210] Philippe Masson, Michael H. Carr, FranÃ§ois Costard, Ronald Greeley, Ernst Hauber, and Ralf Jaumann. Geomorphologic evidence for liquid water. *Space Science Reviews*, 96(1) :333–364, April 2001. URL http://dx.doi.org/10.1023/A:1011913809715.

[211] M. Massé, S. Le Mouélic, O. Bourgeois, J.-P. Combe, L. Le Deit, C. Sotin, J.-P. Bibring, B. Gondet, and Y. Langevin. Mineralogical composition, structure, morphology, and geological history of aram chaos crater fill on mars derived from omega mars express data. *J. Geophys. Res.*, 113 (E12) :E12006–, December 2008. ISSN 0148-0227. URL http://dx.doi.org/10.1029/2008JE003131.

[212] M. Massé, O. Bourgeois, S. Le Mouélic, C. Verpoorter, L. Le Deit, and J.P. Bibring. Martian polar and circum-polar sulfate-bearing deposits : Sublimation tills derived from the north polar cap. *Icarus*, 209(2) :434–451, October 2010. ISSN 0019-1035. URL http://www.sciencedirect.com/science/article/B6WGF-4YYGH4P-3/2/5011c4af102b555c2357bea0bd8de6a2.

[213] Michael D. Max and Stephen M. Clifford. Initiation of martian outflow channels : Related to the dissociation of gas hydrate ? *Geophys. Res. Lett.*, 28(9) :1787–1790, 2001. ISSN 0094-8276. URL http://dx.doi.org/10.1029/2000GL011606.

[214] A. Mazzini. Mud volcanism : Processes and implications. *Marine and Petroleum Geology*, 26(9) : 1677–1680, November 2009. ISSN 0264-8172. URL http://www.sciencedirect.com/science/article/pii/S0264817209000981.

[215] Audrey F. McGuire and Bruce W. Hapke. An experimental study of light scattering by large, irregular particles. *Icarus*, 113(1) :134–155, January 1995. URL http://www.sciencedirect.com/science/article/B6WGF-45NJJC1-4K/2/c537f8ccc1ab93b678085ab6fbb1a9ab.

[216] Patrick C. McGuire, Janice L. Bishop, Adrian J. Brown, Abigail A. Fraeman, Giuseppe A. Marzo, M. Frank Morgan, Scott L. Murchie, John F. Mustard, Mario Parente, Shannon M. Pelkey, Ted L. Roush, Frank P. Seelos, Michael D. Smith, Lorenz Wendt, and Michael J. Wolff. An improvement to the volcano-scan algorithm for atmospheric correction of crism and omega spectral data. *Planetary and Space Science*, 57(7) :809–815, June 2009. ISSN 0032-0633. URL http://www.sciencedirect.com/science/article/B6V6T-4W0SK35-1/2/25b4e9e1b70bd07ce6bff7187b54c473.

[217] Dan McKenzie and Francis Nimmo. The generation of martian floods by the melting of ground ice above dykes. *Nature*, 397(6716) :231–233, January 1999. ISSN 0028-0836. URL http://dx.doi.org/10.1038/16649.

[218] R. Melchiorri, P. Drossart, T. Fouchet, B. Bézard, F. Forget, A. Gendrin, J.P. Bibring, and N. Manaud. A simulation of the omega/mars express observations : Analysis of the atmospheric contribution. *Planetary and Space Science*, 54(8) :774–783, August 2006. ISSN 0032-0633. URL http://www.sciencedirect.com/science/article/pii/S0032063306000687.

[219] Sandrine Meresse, FranÃ§ois Costard, Nicolas Mangold, Philippe Masson, and Gerhard Neukum. Formation and evolution of the chaotic terrains by subsidence and magmatism : Hydraotes chaos, mars. *Icarus*, 194(2) :487–500, April 2008. ISSN 0019-1035. URL http://www.sciencedirect.com/science/article/pii/S001910350700509X.

[220] Joseph Michalski and Paul B. Niles. Atmospheric origin of martian interior layered deposits : Links to climate change and the global sulfur cycle. *Geology*, 40(5) :419–422, May 2012. URL http://geology.gsapubs.org/content/40/5/419.abstract.

[221] A.V Milkov. Worldwide distribution of submarine mud volcanoes and associated gas hydrates. *Marine Geology*, 167(1-2) :29–42, June 2000. ISSN 0025-3227. URL http://www.sciencedirect.com/science/article/pii/S0025322700000220.

[222] Stanley L. Miller and William D. Smythe. Carbon dioxide clathrate in the martian ice cap. *Science*, 170(3957) :531–533, October 1970. URL http://www.sciencemag.org/content/170/3957/531.abstract.

[223] Daniel J. Milton. Carbon dioxide hydrate and floods on mars. *Science*, 183(4125) :654–656, 1974. doi : 10.1126/science.183.4125.654. URL http://www.sciencemag.org/content/183/4125/654.abstract.

[224] M. Minnaert. The reciprocity principle in lunar photometry. *Astrophysical Journal*, 93 :403–410, May 1941.

[225] M. I. Mishchenko, Z. M. Dlugach, E. G. Yanovitskij, and N. T. Zakharova. Bidirectional reflectance of flat, optically thick particulate layers : an efficient radiative transfer solution and applications to snow and soil surfaces. *Journal of Quantitative Spectroscopy and Radiative Transfer*, 63 : 409–432, December 1999.

[226] Michael I. Mishchenko. Directional radiometry and radiative transfer : A new paradigm. *Journal of Quantitative Spectroscopy and Radiative Transfer*, 112(13) :2079–2094, September 2011. ISSN 0022-4073. URL http://www.sciencedirect.com/science/article/pii/S0022407311001634.

[227] F. Montmessin, F. Forget, P. Rannou, M. Cabane, and R. M. Haberle. Origin and role of water ice clouds in the Martian water cycle as inferred from a general circulation model. *Journal of Geophysical Research (Planets)*, 109 :10004–+, October 2004. doi : 10.1029/2004JE002284.

[228] F. Montmessin, J.-L. Bertaux, E. Quémerais, O. Korablev, P. Rannou, F. Forget, S. Perrier, D. Fussen, S. Lebonnois, A. Rébérac, and E. Dimarellis. Subvisible CO_2 ice clouds detected in the mesosphere of Mars. *Icarus*, 183 :403–410, August 2006. doi : 10.1016/j.icarus.2006.03.015.

[229] K. Mosegaard and A. Tarantola. Monte Carlo sampling of solutions to inverse problems. *Journal of Geophysical Research*, 100 :12431–12448, July 1995. doi : 10.1029/94JB03097.

[230] Olivier Mousis, Jonathan I. Lunine, Eric Chassefière, Franck Montmessin, Azzedine Lakhlifi, Sylvain Picaud, Jean-Marc Petit, and Daniel Cordier. Mars cryosphere : A potential reservoir for heavy noble gases ? *Icarus*, 218(1) :80–87, March 2012. ISSN 0019-1035. URL http://www.sciencedirect.com/science/article/pii/S0019103511004726.

[231] Olivier Mousis, Eric Chassefière, Jérémie Lasue, Vincent Chevrier, MeganE. Elwood Madden, Azzedine Lakhlifi, JonathanI. Lunine, Franck Montmessin, Sylvain Picaud, Frédéric Schmidt, and Timothy D. Swindle. Volatile trapping in martian clathrates. *Space Science Reviews*, 174(1-4) : 213–250, 2013. ISSN 0038-6308. doi : 10.1007/s11214-012-9942-9. URL http://dx.doi.org/10.1007/s11214-012-9942-9.

[232] S. Moussaoui, D. Brie, A. Mohammad-Djafari, and C. Carteret. Separation of non-negative mixture of non-negative sources using a bayesian approach and mcmc sampling. *Signal Processing, IEEE Transactions on [see also Acoustics, Speech, and Signal Processing, IEEE Transactions on]*, 54(11) :4133–4145, 2006. ISSN 1053-587X.

[233] S. Moussaoui, H. Hauksdóttir, F. Schmidt, C. Jutten, J. Chanussot, D. Brie, S. Douté, and J.A. Benediktsson. On the decomposition of mars hyperspectral data by ica and bayesian positive source separation. *Neurocomputing*, 71(10-12) :2194–2208, June 2008. doi : 10.1016/j.neucom.2007.07.034. URL http://www.sciencedirect.com/science/article/B6V10-4RV17HX-4/1/739950d227add850ec0720718c1c2362.

[234] Michael J. Mumma, Geronimo L. Villanueva, Robert E. Novak, Tilak Hewagama, Boncho P. Bonev, Michael A. DiSanti, Avi M. Mandell, and Michael D. Smith. Strong release of methane on mars in northern summer 2003. *Science*, 323(5917) :1041–1045, February 2009. URL http://www.sciencemag.org/cgi/content/abstract/323/5917/1041.

[235] S. Murchie, R. Arvidson, P. Bedini, K. Beisser, J.-P. Bibring, J. Bishop, J. Boldt, P. Cavender, T. Choo, R. T. Clancy, E. H. Darlington, D. Des Marais, R. Espiritu, D. Fort, R. Green, E. Guinness, J. Hayes, C. Hash, K. Heffernan, J. Hemmler, G. Heyler, D. Humm, J. Hutcheson, N. Izenberg, R. Lee, J. Lees, D. Lohr, E. Malaret, T. Martin, J. A. McGovern, P. McGuire, R. Morris, J. Mustard, S. Pelkey, E. Rhodes, M. Robinson, T. Roush, E. Schaefer, G. Seagrave, F. Seelos, P. Silverglate, S. Slavney, M. Smith, W.-J. Shyong, K. Strohbehn, H. Taylor, P. Thompson, B. Tossman, M. Wirzburger, and M. Wolff. Compact reconnaissance imaging spectrometer for mars (crism) on mars reconnaissance orbiter (mro). *J. Geophys. Res.*, 112(E5) :E05S03–, May 2007. ISSN 0148-0227. URL http://dx.doi.org/10.1029/2006JE002682.

[236] Bruce C. Murray, Laurence A. Soderblom, James A. Cutts, Robert P. Sharp, Daniel J. Milton, and Robert B. Leighton. Geological framework of the south polar region of mars. *Icarus*, 17(2) :328–345, October 1972. URL http://www.sciencedirect.com/science/article/B6WGF-473119B-50/2/53cfed7eede443a93225271173b17ec7.

[237] John F. Mustard and Carle M. Pieters. Photometric phase functions of common geologic minerals and applications to quantitative analysis of mineral mixture reflectance spectra. *J. Geophys. Res.*, 94 :–, 1989. URL http://dx.doi.org/10.1029/JB094iB10p13619.

[238] John F. Mustard, S. L. Murchie, S. M. Pelkey, B. L. Ehlmann, R. E. Milliken, J. A. Grant, J.-P. Bibring, F. Poulet, J. Bishop, E. Noe Dobrea, L. Roach, F. Seelos, R. E. Arvidson, S. Wiseman,

R. Green, C. Hash, D. Humm, E. Malaret, J. A. McGovern, K. Seelos, T. Clancy, R. Clark, D. D. Marais, N. Izenberg, A. Knudson, Y. Langevin, T. Martin, P. McGuire, R. Morris, M. Robinson, T. Roush, M. Smith, G. Swayze, H. Taylor, T. Titus, and M. Wolff. Hydrated silicate minerals on mars observed by the mars reconnaissance orbiter crism instrument. *Nature*, 454(7202) :305–309, July 2008. ISSN 0028-0836. URL http://dx.doi.org/10.1038/nature07097.

[239] A. Määttänen, T. Fouchet, O. Forni, F. Forget, H. Savijärvi, B. Gondet, R. Melchiorri, Y. Langevin, V. Formisano, M. Giuranna, and J.-P. Bibring. A study of the properties of a local dust storm with mars express omega and pfs data. *Icarus*, 201(2) :504–516, June 2009. ISSN 0019-1035. URL http://www.sciencedirect.com/science/article/B6WGF-4VKDMYP-2/2/8435537a0c01939cd5c49a2408f7c468.

[240] Diedrich Möhlmann and Akos Kereszturi. Viscous liquid film flow on dune slopes of mars. *Icarus*, 207(2) :654–658, June 2010. ISSN 0019-1035. URL http://www.sciencedirect.com/science/article/B6WGF-4Y6454S-1/2/bacdef88950bb73ef83c15d4596e8769.

[241] Susan S. Nedell, Steven W. Squyres, and David W. Andersen. Origin and evolution of the layered deposits in the valles marineris, mars. *Icarus*, 70(3) :409–441, June 1987. ISSN 0019-1035. doi : 10.1016/0019-1035(87)90086-8. URL http://www.sciencedirect.com/science/article/pii/0019103587900868.

[242] G. Neugebauer, G. Munch, S. C. Chase, Jr., H. Hatzenbeler, E. Miner, and D. Schofield. Mariner 1969 : Preliminary Results of the Infrared Radiometer Experiment. *Science*, 166 :98–99, October 1969.

[243] G. Neugebauer, G. Miinch, H. Kieffer, S. C. Chase, Jr., and E. Miner. Mariner 1969 Infrared Radiometer Results : Temperatures and Thermal Properties of the Martian Surface. *Astronomical Journal*, 76 :719–+, October 1971.

[244] J.M. Norman, J.M. Welles, and E.A. Walter. Contrasts among bidirectional reflectance of leaves, canopies, and soils. *Geoscience and Remote Sensing, IEEE Transactions on DOI - 10.1109/TGRS.1985.289384*, GE-23(5) :659–667, 1985. ISSN 0196-2892.

[245] Dag Nummedal and David B. Prior. Generation of martian chaos and channels by debris flows. *Icarus*, 45(1) :77–86, January 1981. ISSN 0019-1035. URL http://www.sciencedirect.com/science/article/pii/0019103581900075.

[246] Adriana Oancea, Olivier Grasset, Erwan Le Menn, Olivier Bollengier, Lucile Bezacier, Stéphane Le Mouélic, and Gabriel Tobie. Laboratory infrared reflection spectrum of carbon dioxide clathrate hydrates for astrophysical remote sensing applications. *Icarus*, 221(2) :900–910, November 2012. ISSN 0019-1035. doi : 10.1016/j.icarus.2012.09.020. URL http://www.sciencedirect.com/science/article/pii/S0019103512003934.

[247] Maureen E. Ockert-Bell, James F. Bell, James B. Pollack, Christopher P. McKay, and François Forget. Absorption and scattering properties of the martian dust in the solar wavelengths. *J. Geophys. Res.*, 102(E4) :9039–9050, April 1997. ISSN 2156-2202. URL http://dx.doi.org/10.1029/96JE03991.

[248] Dorothy Z. Oehler and Carlton C. Allen. Evidence for pervasive mud volcanism in acidalia planitia, mars. *Icarus*, 208(2) :636–657, August 2010. ISSN 0019-1035. URL http://www.sciencedirect.com/science/article/pii/S0019103510001405.

[249] Christopher Oze and Mukul Sharma. Have olivine, will gas : Serpentinization and the abiogenic production of methane on mars. *Geophys. Res. Lett.*, 32 :–, May 2005. URL http://dx.doi.org/10.1029/2005GL022691.

[250] D. A. Paige and A. P. Ingersoll. Annual heat balance of Martian polar caps - Viking observations. *Science*, 228 :1160–1168, June 1985.

[251] M. Parente, J.T. Clark, A.J. Brown, and J.L. Bishop. End-to-end simulation and analytical model of remote-sensing systems : Application to crism. *Geoscience and Remote Sensing, IEEE Transactions on DOI - 10.1109/TGRS.2010.2050000*, 48(11) :3877–3888, 2010. ISSN 0196-2892.

[252] J.S. Pearlman, P.S. Barry, C.C. Segal, J. Shepanski, D. Beiso, and S.L. Carman. Hyperion, a space-based imaging spectrometer. *Geoscience and Remote Sensing, IEEE Transactions on*, 41 (6) :1160–1173, 2003. ISSN 0196-2892.

[253] G.B.M. Pedersen and J.W. Head III. Chaos formation by sublimation of volatile-rich substrate : Evidence from galaxias chaos, mars. *Icarus*, 211(1) :316–329, January 2011. ISSN 0019-1035. URL http://www.sciencedirect.com/science/article/B6WGF-511K3YH-2/2/fbfc82e1d0891895370c5c99ccf94247.

[254] S. M. Pelkey, J. F. Mustard, S. Murchie, R. T. Clancy, M. Wolff, M. Smith, R. Milliken, J.-P. Bibring, A. Gendrin, F. Poulet, Y. Langevin, and B. Gondet. CRISM multispectral summary products : Parameterizing mineral diversity on Mars from reflectance. *Journal of Geophysical Research (Planets)*, 112 :8–+, July 2007. doi : 10.1029/2006JE002831.

[255] Carle M Pieters, Joseph Boardman, Bonnie Buratti, Alok Chatterjee, Roger Clark, Tom Glavich, Robert Green, James Head III, Peter Isaacson, Erick Malaret, et al. The moon mineralogy mapper (m3) on chandrayaan-1. *Curr. Sci*, 96(4) :500–505, 2009.

[256] C. Pilorget, F. Forget, E. Millour, M. Vincendon, and J.B. Madeleine. Dark spots and cold jets in the polar regions of mars : New clues from a thermal model of surface co2 ice. *Icarus*, 213(1) :131–149, May 2011. ISSN 0019-1035. URL http://www.sciencedirect.com/science/article/B6WGF-5241FFF-1/2/d652c7548d5201ab931b833d742cb887.

[257] P. C. Pinet, Y. Daydou, A. Cord, S. C. Chevrel, F. Poulet, S. Erard, J.-P. Bibring, Y. Langevin, R. Melchiorri, G. Bellucci, F. Altieri, R. E. Arvidson, and OMEGA Co-Investigator Team. Derivation of Mars Surface Scattering Properties from OMEGA Spot Pointing Observations. In S. Mackwell and E. Stansbery, editors, *36th Annual Lunar and Planetary Science Conference*, volume 36 of *Lunar and Planetary Institute Science Conference Abstracts*, page 1694, March 2005.

[258] Bernard Pinty, Michel M. Verstraete, and Robert E. Dickinson. A physical model of the bidirectional reflectance of vegetation canopies 2. inversion and validation. *J. Geophys. Res.*, 95(D8) :11767–11775, 1990. ISSN 0148-0227. URL http://dx.doi.org/10.1029/JD095iD08p11767.

[259] S. Piqueux and P. R. Christensen. North and south subice gas flow and venting of the seasonal caps of Mars : A major geomorphological agent. *Journal of Geophysical Research (Planets)*, 113 : 6005–+, June 2008. doi : 10.1029/2007JE003009.

[260] S. Piqueux, S. Byrne, and M. I. Richardson. Sublimation of Mars's southern seasonal CO_2 ice cap and the formation of spiders. *Journal of Geophysical Research (Planets)*, 108 :5084, August 2003. doi : 10.1029/2002JE002007.

[261] A. Pommerol, G. Portyankina, N. Thomas, K.-M. Aye, C. J. Hansen, M. Vincendon, and Y. Langevin. Evolution of south seasonal cap during martian spring : Insights from high-resolution observations by hirise and crism on mars reconnaissance orbiter. *J. Geophys. Res.*, 116(E8) :E08007–, August 2011. ISSN 0148-0227. URL http://dx.doi.org/10.1029/2010JE003790.

[262] A. Pommerol, T. Appéré, G. Portyankina, K.-M. Aye, N. Thomas, and C.J. Hansen. Observations of the northern seasonal polar cap on mars iii : Crism/hirise observations of spring sublimation. *Icarus*, 225(2) :911–922, August 2013. ISSN 0019-1035. URL http://www.sciencedirect.com/science/article/pii/S0019103512003582.

[263] Antoine Pommerol and Bernard Schmitt. Strength of the h2o near-infrared absorption bands in hydrated minerals : Effects of measurement geometry. *J. Geophys. Res.*, 113(E12) :E12008–, December 2008. ISSN 2156-2202. URL http://dx.doi.org/10.1029/2008JE003197.

[264] G. Portyankina, W. J. Markiewicz, M. Garcia-Comas, H. U. Keller, J.-P. Bibring, and G. Neukum. Simulations of Geyser-type Eruptions in Cryptic Region of Martian South Polar Cap. *LPI Contributions*, 1323 :8040–+, October 2006.

[265] Ganna Portyankina, Wojciech J. Markiewicz, Nicolas Thomas, Candice J. Hansen, and Moses Milazzo. Hirise observations of gas sublimation-driven activity in mars' southern polar regions : Iii. models of processes involving translucent ice. *Icarus*, 205(1) :311–320, January 2010. ISSN 0019-1035. URL http://www.sciencedirect.com/science/article/B6WGF-4X908W3-1/2/d9ac846781af1d6e4215b59bd8a677e9.

[266] Ganna Portyankina, Antoine Pommerol, Klaus-Michael Aye, Candice J. Hansen, and Nicolas Thomas. Polygonal cracks in the seasonal semi-translucent co2 ice layer in martian polar areas. *J. Geophys. Res.*, 117(E2) :E02006–, February 2012. ISSN 0148-0227. URL http://dx.doi.org/10.1029/2011JE003917.

[267] Olga Prieto-Ballesteros, Jeffrey S. Kargel, Alberto G. Fairen, A. G.n, David C. Fernandez-Remolar, James M. Dohm, and Ricardo Amils. Interglacial clathrate destabilization on mars : Possible contributing source of its atmospheric methane. *Geology*, 34(3) :149–152, March 2006. URL http://geology.gsapubs.org/content/34/3/149.abstract.

[268] C. Quantin, P. Allemand, N. Mangold, and C. Delacourt. Ages of valles marineris (mars) landslides and implications for canyon history. *Icarus*, 172(2) :555–572, December 2004. ISSN 0019-1035. doi : 10.1016/j.icarus.2004.06.013. URL http://www.sciencedirect.com/science/article/pii/S001910350400212X.

[269] Hafizur Rahman, Michel M. Verstraete, and Bernard Pinty. Coupled surface-atmosphere reflectance (csar) model 1. model description and inversion on synthetic data. *J. Geophys. Res.*, 98(D11) :20779–20789, 1993. ISSN 0148-0227. URL http://dx.doi.org/10.1029/93JD02071.

[270] J. A. P. Rodriguez, Jeffrey Kargel, David A. Crown, III Bleamaster, Leslie F., Kenneth L. Tanaka, Victor Baker, Hideaki Miyamoto, James M. Dohm, Sho Sasaki, and Goro Komatsu. Headward growth of chasmata by volatile outbursts, collapse, and drainage : Evidence from ganges chaos, mars. *Geophys. Res. Lett.*, 33(18) :L18203–, September 2006. ISSN 0094-8276. URL http://dx.doi.org/10.1029/2006GL026275.

[271] Jose Alexis Palmero Rodriguez, Kenneth L. Tanaka, Jeffrey S. Kargel, James M. Dohm, Ruslan Kuzmin, Alberto G. Fairen, Sho Sasaki, Goro Komatsu, Dirk Schulze-Makuch, and Yan Jianguo. Formation and disruption of aquifers in southwestern chryse planitia, mars. *Icarus*, 191(2) : 545–567, November 2007. ISSN 0019-1035. URL http://www.sciencedirect.com/science/article/pii/S0019103507002382.

[272] Jose A.P. Rodriguez, Sho Sasaki, Ruslan O. Kuzmin, James M. Dohm, Ken L. Tanaka, Hideaki Miyamoto, Kei Kurita, Goro Komatsu, A.G. FairÃ©n, and Justin C. Ferris. Outflow channel sources, reactivation, and chaos formation, xanthe terra, mars. *Icarus*, 175(1) :36–57, May 2005. ISSN 0019-1035. URL http://www.sciencedirect.com/science/article/pii/S0019103504003896.

[273] A. D. Rogers, J. L. Bandfield, and P. R. Christensen. Global spectral classification of Martian low-albedo regions with Mars Global Surveyor Thermal Emission Spectrometer (MGS-TES) data. *Journal of Geophysical Research (Planets)*, 112 :2004–+, February 2007. doi : 10.1029/2006JE002726.

[274] J. K. Ross. *The Radiation Regime and Architecture of Plant Stands*. Kluwer academic publisher, The Hague, Netherlands, 1981.

[275] Jean-Louis Roujean, Marc Leroy, and Pierre-Yves Deschamps. A bidirectional reflectance model of the earth's surface for the correction of remote sensing data. *J. Geophys. Res.*, 97(D18) :20455–20468, 1992. ISSN 0148-0227. URL http://dx.doi.org/10.1029/92JD01411.

[276] Bortolino Saggin, Lorenzo Comolli, and Vittorio Formisano. Mechanical disturbances in fourier spectrometers. *Appl. Opt.*, 46(22) :5248–5256, August 2007. URL http://ao.osa.org/abstract.cfm?URI=ao-46-22-5248.

[277] M.C. Sanctis, A. Coradini, E. Ammannito, G. Filacchione, M.T. Capria, S. Fonte, G. Magni, A. Barbis, A. Bini, M. Dami, I. Ficai-Veltroni, and G. Preti. The vir spectrometer. *Space Science Reviews*, 163(1-4) :329–369, 2011. ISSN 0038-6308. doi : 10.1007/s11214-010-9668-5. URL http://dx.doi.org/10.1007/s11214-010-9668-5.

[278] F. Schmidt, S. Doute, B. Schmitt, Y. Langevin, J.-P. Bibring, and the OMEGA Team. Slab ice in the seasonal south polar cap of Mars. In *European Planetary Science Congress (EuroPlanet), Potsdam, Germany, 13/09/09-18/09/09*, volume 4, page (electronic medium), http ://www.europlanet-eu.org, septembre 2009. EuroPlanet.

[279] F. Schmidt, R. Dupire, S. Doute, and G. Portyankina. Active jets and slab ice in the seasonal south polar cap of mars. In *European Planetary Science Congress (EuroPlanet), Roma, Italy, 19/09/10 - 24/09/10*, volume 4, page (electronic medium), http ://www.europlanet-eu.org, septembre 2010. EuroPlanet. doi : http://meetingorganizer.copernicus.org/EPSC2010/EPSC2010-560.pdf.

[280] F. Schmidt, R. Dupire, S. Douté, and G. Portyankina. Jets actifs, glace transparente dans la calotte saisonnière sud de mars. In *Congrès du Programme National de Planétologie, Brest*, 2010.

[281] F. Schmidt, R. Dupire, S. Doute, and G. Portyankina. Active Jets and Slab Ice in the Seasonal South Polar Cap of Mars. In *Lunar and Planetary Institute Science Conference Abstracts - LPSC Houston 07-11 March 2011*, volume 42 of *Lunar and Planetary Inst. Technical Report*, pages 1942–+, March 2011.

[282] F. Schmidt, I. Shatalina, M. Kowalski, N. Gac, B. Saggin, and M. Giuranna. Toward a numerical deshaker for pfs. *Planetary and Space Science*, 91(0) :45–51, February 2014. ISSN 0032-0633. doi : 10.1016/j.pss.2013.11.012. URL http://www.sciencedirect.com/science/article/pii/S0032063313003243.

[283] Frédéric Schmidt. *CLASSIFICATION DE LA SURFACE DE MARS PAR IMAGERIE HYPERSPECTRALE OMEGA. SUIVI SPATIO-TEMPOREL ET ÉTUDE DES DÉPÔTS SAISONNIERS DE CO2 ET H2O.* PhD thesis, UNIVERSITE JOSEPH FOURIER - GRENOBLE I, 2007.

[284] Frédéric Schmidt, Sylvain Douté, and Bernard Schmitt. Wavanglet : An efficient supervised classifier for hyperspectral images. *Geoscience and Remote Sensing, IEEE Transactions on*, 45(5) : 1374–1385, 2007. ISSN 0196-2892. doi : 10.1109/TGRS.2006.890577.

[285] Frédéric Schmidt, Sylvain Douté, Bernard Schmitt, Mathieu Vincendon, Jean-Pierre Bibring, and Yves Langevin. Albedo control of seasonal south polar cap recession on mars. *Icarus*, 200(2) :374–394, April 2009. ISSN 0019-1035. doi : 10.1016/j.icarus.2008.12.014. URL http://www.sciencedirect.com/science/article/B6WGF-4V76270-1/2/60231d55061d19abebb5344bd9e40e2b.

[286] Frédéric Schmidt, Bernard Schmitt, Sylvain Douté, Francois Forget, Jeng-Jong Jian, Patrick Martin, Yves Langevin, and Jean-Pierre Bibring. Sublimation of the martian co2 seasonal south polar cap. *Planetary and Space Science*, 58(10) :1129–1138, August 2010. ISSN 0032-0633. doi : 10.1016/j.pss.2010.03.018. URL http://www.sciencedirect.com/science/article/B6V6T-4YS4WC4-1/2/9aa719d355d28b1cde9dccfa2742e980.

[287] B. Schmitt, E. Quirico, F. Trotta, and W. M. Grundy. Optical Properties of Ices from UV to Infrared. In B. Schmitt, C. de Bergh, and M. Festou, editors, *Solar System Ices*, volume 227 of *Astrophysics and Space Science Library*, pages 199–240. Kluwer, 1998.

[288] B. Schmitt, S. Douté, Y. Langevin, F. Forget, J.-P. Bibring, B. Gondet, and The Omega Team. Northern Seasonal Condensates on Mars by OMEGA/Mars Express. In S. Mackwell and E. Stansbery, editors, *36th Annual Lunar and Planetary Science Conference*, volume 36 of *Lunar and Planetary Institute Conference Abstracts*, pages 2326–+, March 2005.

[289] Norbert Schorghofer. Dynamics of ice ages on mars. *Nature*, 449(7159) :192–194, September 2007. ISSN 0028-0836. URL http://dx.doi.org/10.1038/nature06082.

[290] H. Seeliger. Zur theorie der beleuchtung der grossen *planeten, insbesondere des saturn. *Abh. Bayer. Akad. Wiss. 2 Kl.*, 16 :405–516, 1887.

[291] Robert P. Sharp. Mars : Fretted and chaotic terrains. *J. Geophys. Res.*, 78(20) :4073–4083, 1973. ISSN 0148-0227. URL http://dx.doi.org/10.1029/JB078i020p04073.

[292] Irina Shatalina, Frederic Schmidt, Bortolino Saggin, Nicolas Gac, Matthieu Kowalski, Marco Giuranna, and Samsophath Nhean. Analytical expression of combined microvibrations effects on fourier spectrometer. *Aerospace Science and Technology*, submitted, 2013.

[293] Amy Shaw, M. J. Wolff, F. P. Seelos, S. M. Wiseman, and S. Cull. Surface scattering properties at the opportunity mars rover's traverse region measured by crism. *J. Geophys. Res. Planets*, 118(8) : 1699–1717, August 2013. ISSN 2169-9100. URL http://dx.doi.org/10.1002/jgre.20119.

[294] William Sheehan. *The Planet Mars : A History of Observation and Discovery*. The University of Arizona Press, Tucson, 1996.

[295] Michael K. Shepard and Paul Helfenstein. A laboratory study of the bidirectional reflectance from particulate samples. *Icarus*, 215(2) :526–533, October 2011. ISSN 0019-1035. URL http://www.sciencedirect.com/science/article/pii/S0019103511003058.

[296] Y. Shkuratov, V. Kaydash, V. Korokhin, Y. Velikodsky, N. Opanasenko, and G. Videen. Optical measurements of the moon as a tool to study its surface. *Planetary and Space Science*, 59(13) : 1326–1371, October 2011. ISSN 0032-0633. URL http://www.sciencedirect.com/science/article/pii/S0032063311001954.

[297] Y. Shkuratov, V. Kaydash, V. Korokhin, Y. Velikodsky, D. Petrov, E. Zubko, D. Stankevich, and G. Videen. A critical assessment of the hapke photometric model. *Journal of Quantitative Spectroscopy and Radiative Transfer*, 113(18) :2431–2456, December 2012. ISSN 0022-4073. doi : 10.1016/j.jqsrt.2012.04.010. URL http://www.sciencedirect.com/science/article/pii/S0022407312001926.

[298] James A. Skinner Jr. and Adriano Mazzini. Martian mud volcanism : Terrestrial analogs and implications for formational scenarios. *Marine and Petroleum Geology*, 26(9) :1866–1878, November 2009. ISSN 0264-8172. URL http://www.sciencedirect.com/science/article/pii/S0264817209000336.

[299] D. E. Smith, M. T. Zuber, and G. A. Neumann. Seasonal Variations of Snow Depth on Mars. *Science*, 294 :2141–2146, December 2001. doi : 10.1126/science.1066556.

[300] M. D. Smith, J. L. Bandfield, and P. R. Christensen. Separation of atmospheric and surface spectral features in Mars Global Surveyor Thermal Emission Spectrometer (TES) spectra. *Journal of Geophysical Research*, 105 :9589–9608, April 2000. doi : 10.1029/1999JE001105.

[301] Michael D. Smith. Interannual variability in tes atmospheric observations of mars during 1999-2003. *Icarus*, 167(1) :148–165, January 2004. URL http://www.sciencedirect.com/science/article/B6WGF-4B1SGYB-1/2/913198761c55214891ba8734e92d04da.

[302] A.L. Souchon, P.C. Pinet, S.D. Chevrel, Y.H. Daydou, D. Baratoux, K. Kurita, M.K. Shepard, and P. Helfenstein. An experimental study of hapke's modeling of natural granular surface samples. *Icarus*, 215(1) :313–331, September 2011. ISSN 0019-1035. URL http://www.sciencedirect.com/science/article/pii/S0019103511002405.

[303] A.L. Souchon, S. Besse, P.C. Pinet, S.D. Chevrel, Y.H. Daydou, J.-L. Josset, L. D ?Uston, and J. Haruyama. Local spectrophotometric properties of pyroclastic deposits at the lavoisier lunar crater. *Icarus*, 225(1) :1–14, July 2013. ISSN 0019-1035. URL http://www.sciencedirect.com/science/article/pii/S0019103513001127.

[304] S. W. Squyres, J. P. Grotzinger, R. E. Arvidson, J. F. Bell, W. Calvin, P. R. Christensen, B. C. Clark, J. A. Crisp, W. H. Farrand, K. E. Herkenhoff, J. R. Johnson, G. Klingelhöfer, A. H. Knoll, S. M. McLennan, H. Y. McSween, R. V. Morris, J. W. Rice, R. Rieder, and L. A. Soderblom. In Situ Evidence for an Ancient Aqueous Environment at Meridiani Planum, Mars. *Science*, 306 : 1709–1714, December 2004. doi : 10.1126/science.1104559.

[305] K. Stamnes, S.-C. Tsay, K. Jayaweera, and W. Wiscombe. Numerically stable algorithm for discrete-ordinate-method radiative transfer in multiple scattering and emitting layered media. *Appl. Opt.*, 27 :2502–2509, June 1988. doi : 10.1364/AO.27.002502.

[306] Gwynn H. Suits. The calculation of the directional reflectance of a vegetative canopy. *Remote Sensing of Environment*, 2(0) :117–125, 1971. ISSN 0034-4257. URL http://www.sciencedirect.com/science/article/pii/003442577190085X.

[307] Kenneth L. Tanaka. Sedimentary history and mass flow structures of chryse and acidalia planitiae, mars. *J. Geophys. Res.*, 102(E2) :4131–4149, 1997. ISSN 0148-0227. URL http://dx.doi.org/10.1029/96JE02862.

[308] Kenneth L. Tanaka. Debris-flow origin for the simud/tiu deposit on mars. *J. Geophys. Res.*, 104(E4) :8637–8652, 1999. ISSN 0148-0227. URL http://dx.doi.org/10.1029/98JE02552.

[309] D. Tanre, M. Herman, P. Y. Deschamps, and A. de Leffe. Atmospheric modeling for space measurements of ground reflectances, including bidirectional properties. *Applied Optics*, 18 :3587–3594, November 1979.

[310] A. Tarantola and B. Valette. Inverse Problems = Quest for Information. *Journal of Geophysics*, 50 :159–170, 1982.

[311] Konstantinos E. Themelis, Frederic Schmidt, Olga Sykioti, Athanasios A. Rontogiannis, Konstantinos D. Koutroumbas, and Ioannis A. Daglis. On the unmixing of mex/omega hyperspectral data. *Planetary and Space Science*, 68(1) :34–41, August 2012. ISSN 0032-0633. doi : 10.1016/j.pss.2011.11.015. URL http://www.sciencedirect.com/science/article/pii/S0032063311003497.

[312] Kostas Themelis and Athanasios A. Rontogiannis. A soft constrained map estimator for supervised hyperspectral signal unmixing. *Proceedings of European Signal Processing Conference, EUSIPCO'08.*, 2008. URL http://www.eurasip.org/Proceedings/Eusipco/Eusipco2008/papers/1569104584.pdf.

[313] N. Thomas, C.J. Hansen, G. Portyankina, and P.S. Russell. Hirise observations of gas sublimation-driven activity in mars' southern polar regions : Ii. surficial deposits and their origins. *Icarus*, 205(1) :296–310, January 2010. ISSN 0019-1035. URL http://www.sciencedirect.com/science/article/B6WGF-4WHFD8Y-1/2/a6d5976260af3d6791b76c4abfac9213.

[314] N. Thomas, G. Portyankina, C. J. Hansen, and A. Pommerol. Sub-surface co2 gas flow in mars' polar regions : Gas transport under constant production rate conditions. *Geophys. Res. Lett.*, 38(8) :L08203–, April 2011. ISSN 0094-8276. URL http://dx.doi.org/10.1029/2011GL046797.

[315] N. Thomas, G. Portyankina, C.J. Hansen, and A. Pommerol. Hirise observations of gas sublimation-driven activity in mars' southern polar regions : Iv. fluid dynamics models of co2 jets. *Icarus*, 212(1) :66–85, March 2011. ISSN 0019-1035. URL http://www.sciencedirect.com/science/article/B6WGF-51SWG5S-4/2/dcc2e9308b94faafaf6dce35f08a1936.

[316] D.R. Thompson, L. Mandrake, M.S. Gilmore, and R. Castaño. Superpixel endmember detection. *Geoscience and Remote Sensing, IEEE Transactions on DOI - 10.1109/TGRS.2010.2070802*, 48 (11) :4023–4033, 2010. ISSN 0196-2892.

[317] Thomas E. Thorpe. Mariner 9 photometric observations of mars from november 1971 through march 1972. *Icarus*, 20(4) :482–489, December 1973. ISSN 0019-1035. URL http://www.sciencedirect.com/science/article/pii/0019103573900213.

[318] Thomas E. Thorpe. Viking orbiter photometric observations of the mars phase function july through november 1976. *J. Geophys. Res.*, 82(28) :4161–4165, September 1977. ISSN 2156-2202. URL http://dx.doi.org/10.1029/JS082i028p04161.

[319] Feng Tian, Mark W. Claire, Jacob D. Haqq-Misra, Megan Smith, David C. Crisp, David Catling, Kevin Zahnle, and James F. Kasting. Photochemical and climate consequences of sulfur outgassing on early mars. *Earth and Planetary Science Letters*, 295 :412–418, July 2010. ISSN 0012-821X. URL http://www.sciencedirect.com/science/article/pii/S0012821X10002542.

[320] J. E. Tillman, N. C. Johnson, P. Guttorp, and D. B. Percival. The Martian annual atmospheric pressure cycle - Years without great dust storms. *Journal of Geophysical Research*, 98 :10963–+, June 1993.

[321] Victor P. Tishkovets, Elena V. Petrova, and Michael I. Mishchenko. Scattering of electromagnetic waves by ensembles of particles and discrete random media. *Journal of Quantitative Spectroscopy and Radiative Transfer*, 112(13) :2095–2127, September 2011. ISSN 0022-4073. URL http://www.sciencedirect.com/science/article/pii/S0022407311001683.

[322] T. N. Titus, H. H. Kieffer, Y. Langevin, S. Murchie, F. Seelos, and M. Vincendon. Bright Fans in Mars Cryptic Region Caused by Adiabatic Cooling of CO2 Gas Jets. In *AGU Fall Meeting Abstracts*, page A5, December 2007.

[323] G. Vane, R. O. Green, T. G. Chrien, H. T. Enmark, E. G. Hansen, and W. M. Porter. The Airborne Visible/Infrared Imaging Spectrometer (AVIRIS). *Remote Sensing of Environment*, 44 :127–143, June 1993.

[324] Yu.I. Velikodsky, N.V. Opanasenko, L.A. Akimov, V.V. Korokhin, Yu.G. Shkuratov, V.G. Kaydash, G. Videen, Sh.A. Ehgamberdiev, and N.E. Berdalieva. New earth-based absolute photometry of the moon. *Icarus*, 214(1) :30–45, July 2011. ISSN 0019-1035. doi : 10.1016/j.icarus.2011.04.021. URL http://www.sciencedirect.com/science/article/pii/S0019103511001564.

[325] W. Verhoef. Light scattering by leaf layers with application to canopy reflectance modeling : The sail model. *Remote Sensing of Environment*, 16(2) :125–141, October 1984. ISSN 0034-4257. URL http://www.sciencedirect.com/science/article/pii/0034425784900579.

[326] E. Vermote and D. Tanré. Analytical expressions for radiative properties of planar rayleigh scattering media, including polarization contributions. *Journal of Quantitative Spectroscopy and Radiative Transfer*, 47(4) :305–314, April 1992. ISSN 0022-4073. URL http://www.sciencedirect.com/science/article/B6TVR-46DFNDC-87/2/4b60b7bf72c3e9b6b182205bbeef87f6.

[327] Michel M. Verstraete, Bernard Pinty, and Robert E. Dickinson. A physical model of the bidirectional reflectance of vegetation canopies 1. theory. *J. Geophys. Res.*, 95(D8) :11755–11765, 1990. ISSN 0148-0227. URL http://dx.doi.org/10.1029/JD095iD08p11755.

[328] J. Veverka and J. Goguen. The Nonuniform Recession of the South Polar Cap of Mars. *Journal of the Royal Astronomical Society of Canada*, 67 :273–+, December 1973.

[329] M. Vincendon, Y. Langevin, F. Poulet, J.-P. Bibring, and B. Gondet. Recovery of surface reflectance spectra and evaluation of the optical depth of aerosols in the near-IR using a Monte Carlo approach : Application to the OMEGA observations of high-latitude regions of Mars. *Journal of Geophysical Research (Planets)*, 112 :E08S13, 1–12, July 2007. doi : 10.1029/2006JE002845.

[330] M. Vincendon, Y. Langevin, F. Poulet, J.-P. Bibring, B. Gondet, and D. Jouglet. Dust aerosols above the south polar cap of mars as seen by omega. *Icarus*, 196(2) :488–505, August 2008. URL http://www.sciencedirect.com/science/article/B6WGF-4RV17PY-2/2/20b2c4bacf5da32200f8904a149ba5e3.

[331] Mathieu Vincendon. Mars surface phase function constrained by orbital observations. *Planetary and Space Science*, 76(0) :87 – 95, 2013. ISSN 0032-0633. doi : 10.1016/j.pss.2012.12.005. URL http://www.sciencedirect.com/science/article/pii/S0032063312003820.

[332] Mathieu Vincendon, Cedric Pilorget, Brigitte Gondet, Scott Murchie, and Jean-Pierre Bibring. New near-ir observations of mesospheric co2 and h2o clouds on mars. *J. Geophys. Res.*, 116 :E00J02–, November 2011. ISSN 0148-0227. URL http://dx.doi.org/10.1029/2011JE003827.

[333] Kiri L. Wagstaff, Timothy N. Titus, Anton B. Ivanov, Rebecca Castaño, and Joshua L. Bandfield. Observations of the north polar water ice annulus on mars using themis and tes. *Planetary and Space Science*, 56(2) :256–265, February 2008. ISSN 0032-0633. URL http://www.sciencedirect.com/science/article/B6V6T-4PJCYDS-2/2/3549fd86b0687e11f611c817c575d46a.

[334] A. R. Wallace. *Is Mars Habitable ?* Macmillan, London, 1907.

[335] W. Wanner, X. Li, and A. H. Strahler. On the derivation of kernels for kernel-driven models of bidirectional reflectance. *J. Geophys. Res.*, 100(D10) :21077–21089, 1995. ISSN 0148-0227. URL http://dx.doi.org/10.1029/95JD02371.

[336] J. Warell and C. Bergfors. Mercury's integral phase curve : Phase reddening and wavelength dependence of photometric quantities. *Planetary and Space Science*, 56(15) :1939–1948, December 2008. ISSN 0032-0633. doi : 10.1016/j.pss.2008.09.002. URL http://www.sciencedirect.com/science/article/pii/S0032063308002754.

[337] Christopher R. Webster, Paul R. Mahaffy, Sushil K. Atreya, Gregory J. Flesch, Kenneth A. Farley, and the MSL Science Team. Low upper limit to methane abundance on mars. *Science*, pages – , September 2013. URL http://www.sciencemag.org/content/early/2013/09/18/science.1242902.abstract.

[338] Lorenz Wendt, Christoph Gross, Thomas Kneissl, Mariam Sowe, Jean-Philippe Combe, Laetitia LeDeit, Patrick C. McGuire, and Gerhard Neukum. Sulfates and iron oxides in ophir chasma, mars, based on omega and crism observations. *Icarus*, 213(1) :86–103, May 2011. ISSN 0019-1035. doi : 10.1016/j.icarus.2011.02.013. URL http://www.sciencedirect.com/science/article/pii/S0019103511000716.

[339] Michael E. Winter. N-findr : an algorithm for fast autonomous spectral end-member determination in hyperspectral data. In *Proc. SPIE 3753, Imaging Spectrometry V*, pages 266–275, October 27, 1999 1999. doi : 10.1117/12.366289. URL http://dx.doi.org/10.1117/12.366289.

[340] M. J. Wolff, M. D. Smith, R. T. Clancy, R. Arvidson, M. Kahre, F. Seelos, S. Murchie, and H. Savijärvi. Wavelength dependence of dust aerosol single scattering albedo as observed by the compact reconnaissance imaging spectrometer. *J. Geophys. Res.*, 114(E2) :E00D04–, February 2009. ISSN 2156-2202. URL http://dx.doi.org/10.1029/2009JE003350.

[341] C. F. Yoder, A. S. Konopliv, D. N. Yuan, E. M. Standish, and W. M. Folkner. Fluid Core Size of Mars from Detection of the Solar Tide. *Science*, 300 :299–303, April 2003. doi : 10.1126/science.1079645.

[342] Yasuhiro Yokota, Tsuneo Matsunaga, Makiko Ohtake, Junichi Haruyama, Ryosuke Nakamura, Satoru Yamamoto, Yoshiko Ogawa, Tomokatsu Morota, Chikatochi Honda, Kazuto Saiki, Kenichi Nagasawa, Kohei Kitazato, Sho Sasaki, Akira Iwasaki, Hirohide Demura, Naru Hirata, Takahiro Hiroi, Rie Honda, Yuichi Iijima, and Hitoshi Mizutani. Lunar photometric properties at wavelengths 0.5-1.6 ?m acquired by selene spectral profiler and their dependency on local albedo and latitudinal zones. *Icarus*, 215(2) :639–660, October 2011. ISSN 0019-1035. doi : 10.1016/j.icarus.2011.07.028. URL http://www.sciencedirect.com/science/article/pii/S0019103511003009.

[343] Kevin Zahnle, Richard S. Freedman, and David C. Catling. Is there methane on mars ? *Icarus*, 212(2) :493–503, April 2011. ISSN 0019-1035. URL http://www.sciencedirect.com/science/article/B6WGF-51P9X12-1/2/f4bbcf68e60d62834eaf651f9e08db0d.

Table des figures

1.1 Principe d'acquisition des spectro-imageurs 8
1.2 Schéma d'un cube hyperspectral. 9
1.3 Sélection des coefficients d'ondelettes utiles (sous-espace utile) pour la séparation des trois spectres de références. (a)-(d) Représentation des coefficients d'ondelette des échelles 1 à 5 (voir article pour le détail de la méthode de représentation), (e) spectre typique de poussière et de contenu atmosphérique (f) spectre synthétique de glace de CO_2 (g) spectre synthétique de glace d'eau. La figure est issue de l'article de Schmidt et al. [284]. 15
1.4 Comparaison entre l'estimation des sources d'après la méthode BPSS avec pré-sélection JADE. Les figures sont issues de l'article de Moussaoui et al. [233]. 15
1.5 Comparaison entre l'estimation des méthodes de séparation de source en aveugle sur les données CRISM (au milieu) et la carte de classification HiRISE (en haut). Le tableau représente la corrélation r et l'erreur ε entre les deux, pour les différentes méthodes. Les figures sont issues de l'article de Ceamanos et al. [34]. 17
1.6 Précision de la détection pour plusieurs algorithmes sur un jeu de données de 1000 spectres synthétiques simulant Mars pour différentes valeurs de contenu en aérosols. Les ronds représentent les bonnes détections, les carrés les fausses détections. "slope" signifie avec l'ajout des spectres additionnels de la stratégie LinMin (en haut, à gauche) algorithme IPLS (en haut, à droite) algorithme BIICE (en bas à gauche) détection des 71 spectres contenant de l'olivine forsterite uniquement en utilisant IPLS et le rapport de bande (en bas à gauche). Détection des 59 spectres d'olivine fayalite uniquement en utilisant IPLS et le rapport de bande (voir l'article disponible à la section 1.4.3 page 45). 19

2.1 Définition des angles en photométrie : angle solide d'incidence $d\omega$ dans la direction s, angle solide d'émergence $d\omega'$ dans la direction s', direction normale à la surface z, angle d'incidence θ, angle d'émergence θ', angle de phase g, angle d'azimut d'incidence Φ par rapport à la direction du Nord, angle d'azimut d'émergence Φ' par rapport à la direction du Nord, angle d'azimut relatif ϕ (figure d'après [77]). 76
2.2 Géométrie d'observation de l'instrument CRISM en mode FRT (figure d'après [35]). . . 77
2.3 Schéma du transfert radiatif : (a) pas d'atmosphère (b) atmosphère non diffusante (c) atmosphère diffusante 1-d plan parallèle 80
2.4 Exemple de résultats de Mars-ReCO d'après [35]. A gauche : la BRDF de surface, généré d'après le modèle de Hapke. Au centre : l'estimation de la BRDF de surface avec Mars-ReCO, dans le cas de $\tau = 0.5$. A droite : l'erreur, exprimé en % 82
2.5 Exemple de résultats de l'inversion bayésienne pour les 6 paramètres de Hapke, dans le cas d'une seule observation CRISM (10 géométries en bleu) et de la fusion de 3 observations CRISM (27 géométries en rouge) 84

3.1 Schéma optique de l'instrument PFS d'après [94] 136

3.2 Exemple de fantôme (ghost) sur une observation PFS SWC en unité DN (non calibré en radiance) d'après [282] . . . 136
3.3 Effet de la vitesse d'acquisition de l'interferogramme sur les artefacts de PFS SWC, d'après [102] . . . 137
3.4 Comparaison entre simulation d'artefact (extrême en rouge) et les données réelles (points de couleurs), et la moyenne (en noir), d'après [58] . . . 138
3.5 Schéma de l'effet d'une fréquence pure de vibration sur le spectre PFS, d'après[292]. . . 139
3.6 Comparaison du traitement entre notre algorithme (à gauche) et la méthode du stacking (à droite), d'après [282]. . . . 141
3.7 Comparaison entre le noyau de vibration K_{PFS} : d'après notre algorithme en bleu, d'après une méthode approximée basée sur le signal laser de référence en rouge, d'après les données ab initio de la sonde Mars Express en gris foncé, les combinaison des fréquences de vibrations ab initio en gris clair (figure d'après [282]) . . . 142

4.1 Comparaison de la surface couverte de dépôts saisonniers entre le GCM "Mars Climate Database" et les données Viking [144] (cercle). Les différentes lignes correspondent à la latitude équivalente pour plusieurs scenarii de profondeur optique de poussière (figure d'après [191]). . . . 191
4.2 Définition de la *date crocus*. C'est le point d'inflexion dans le signal temporel de température de brillance (figure d'après [165]). . . . 191
4.3 Définition de la *distance snowdrop*, des *lignes crocus internes* et *externes*. (figure d'après [285]). . . . 192
4.4 Exemples de distance snowdrop d'après OMEGA (figure d'après [285]). . . . 193
4.5 Pression atmosphérique martienne : (a) pression au sol mesurée par Viking Lander 1 et 2 ; (b) en bas : pression atmosphérique équivalente stockée dans les calottes saisonnières ; (b) en haut : pression atmosphérique à l'altitude 0. Figure d'après Hourdin et al. [134]. . 194
4.6 Récession de la calotte saisonnière sud observée depuis la Terre entre 1905 et 1965. Chaque cercle est une *ligne crocus* à une date notée en °Ls (d'après [87] repris dans [328]). Les longitudes sont notées en degrés croissants vers l'Ouest. . . . 195
4.7 Propriétés a priori contradictoires de la région cryptique (notée 0) a Ls=220° d'après l'instrument TES : a) température de brillance (proche de 140K pour la zone 0), b) albédo (proche de 0.3 pour la zone 0) (d'après [165]). . . . 197
4.8 Variations de l'état de transparence de la glace observé par OMEGA (d'après [278]). . . 198
4.9 Schéma de la formation des geysers. D'après Piqueux et al. [260]. . . . 198
4.10 Observation MOC des Spiders. D'après Piqueux et al. [260]. . . . 199
4.11 Observation MOC à Ls=208° des liens entre les "spiders" et geysers. Les traînées sombres de dépôt de poussière ont comme point d'origine les centres des "spiders". D'après Piqueux et al. [260]. . . . 200
4.12 Schéma temporelle de la formation de la calotte saisonnière dans la région cryptique (d'après [166]). . . . 201
4.13 Localisation des spiders dans la zone polaire Sud de Mars (d'après [260]). . . . 202
4.14 Localisation des spiders dans la zone polaire Sud de Mars (d'après [280, 281]). . . . 203
4.15 Liens entre geysers et spiders (d'après [313]). . . . 204
4.16 Geysers sous forme de cracks en réseau dans la partie Nord et sous forme de point dans la partie Sud (d'après [266]). . . . 205
4.17 Localisation des geysers et de la glace transparente (d'après [281]). . . . 206
4.18 Ecoulement sombre dans la dune de Richardson (d'après [5]). . . . 207
4.19 Evolution temporelle de la calotte saisonnière sud. Le fond en niveau de gris représente les altitudes MOLA. Les couleurs représentent les mosaïques des images hyperspectrales OMEGA : en jaune la poussière, en pourpre le CO_2 , en bleu l'eau (a) Ls=150-160° (b) Ls=180-190° (a) Ls=220-230° (a) Ls=275-280° (d'après [285]). . . . 209

4.20 Flux de sublimation totales dans le demi-espace cryptique et anti-cryptique : à gauche, flux absolue, à droite flux relatif. Le flux anti-cryptique est légèrement dominant entre Ls=220° et 300° (d'après [286]). 210
4.21 Evolution temporelle de l'inter-dune dans le cratère de Richardson entre Ls=166° et 218° (d'après [158]). 210
4.22 Modélisation d'un spectre du coeur sombre d'un dark spot. en noir : observation CRISM, modèle 1 : avec glaces uniquement, modèle 2 : avec glaces et eau liquide sans gypse, modèle 3 : avec glaces, gypse et eau liquide. Le RMS n'est pas significativement différent, signant la présence peu probable d'eau liquide (d'après [158]). 211
4.23 Probabilité d'occurrence des spiders et de geysers en fonction de la saison (d'après [279]). 211

5.1 Schéma des petites cages de diamètre moyen 3.95 nm (à gauche) et grande cage de diamètre moyen 4.33 nm (à droite) présentes dans les clathrates hydrates, d'après [26] . 267
5.2 Les terrains chaotiques sur Mars d'après une mosaïque Viking. Le chaos a un diamètre de 40 km et l'écoulement une section de 20 km. Figure d'après [31]. 267
5.3 Analogie entre les volcans de boue Martiens et Terrestre. (A) Au Sud d'Utopia Planitia, d'après [298] (Image THEMIS visible V14113011). (B) Vernal Crater dans Arabia Terra (image HiRISE PSP_002812_1855) d'après [4] (C) Baku, Azerbadjian d'après [169] (Image Google Earth) (D) Baku, Azerbadjian un cratère sommital, noté (c) d'après [169] (image Google Earth) 269
5.4 Schéma de principe de formation de clathrate dans la subsurface, d'après [43, 39] 269
5.5 Diagramme de phase de présence de clathrate de SO_2 et CO_2, d'après un modèle photochimique de climat [319] : (a) en pointillé uniquement l'effet du gaz avec les concentrations volumiques ; (b) les flèches représentent l'effet réfléchissant et donc refroidissant des aérosols de S ; (c) le diagramme de stabilité des clathrates de CO_2 d'après [230]. Figure d'après [41] 271
5.6 Température de surface en fonction de la quantité de SO_2 pour plusieurs pression atmosphérique de CO_2 d'après le modèle photochimique de climat dans des conditions de 75% du flux solaire actuelle. Les triangles représentent le point d'équilibre des clathrate. Figure d'après [41] 272
5.7 Concentration de SO_2 à l'équilibre en fonction de la pression en CO_2. Les chiffres correspondent aux volumes d'éruptions nécessaire à produire une quantité correspondante de SO_2. Figure d'après [41] 273
5.8 Histoire climatique de Mars d'après le scénario de formation des équilibre tampon de SO_2/CO_2. Figure d'après [41] 274

6.1 Bilan des collaborations et des projets. Les étudiants en thèse que j'ai co-encadrés ou suivis sont en gras. 294

Liste des tableaux

1.1 Liste des instruments spectro-imageurs hyperspectraux (plus d'une centaine de canaux spectraux) majeurs, terrestres et en Planétologie en vol et sélectionné, avec leur couverture spectrale totale et leur nombre totale de longueurs d'ondes. Les autres caractéristiques de ces instruments sont disponibles dans les références. 7
1.2 Caractéristiques spectrales de l'instrument OMEGA à bord de Mars Express. 9
1.3 Caractéristiques spectrales de l'instrument CRISM à bord de Mars Reconnaissance Orbiter. 10

RÉSUMÉ : L'étude de Mars a été profondément modifiée par les dernières générations d'instruments spatiaux : les spectro-imageurs, les spectro-imageurs-photomètres et les spectroscopes à haute résolution spectrale. Ils permettent un suivi spatial et temporel des propriétés optiques des sols et de l'atmosphère. Le premier objectif de cette thèse d'Habilitation à Diriger des Recherches est méthodologique et consiste à proposer des outils permettant de traiter la grande quantité de données afin d'aborder des problématiques planétologiques. Plusieurs types d'outils d'analyse des images hyperspectrales, notamment celles produites par les instruments OMEGA (Mars Express/ESA) et CRISM (Mars Reconnaissance Orbiter/NASA), ont été proposés : (i) WAVANGLET, une méthode rapide de détection des corps chimiques au sol basée sur la transformée en ondelette, (ii) BPSS, une méthode de séparation de source en aveugle qui détecte des corps chimiques sans a priori, (iii) des méthodes de dé-mélanges linéaires supervisées rapides utilisant la stratégie LinMin. Aussi des outils de correction atmosphérique couplés à des méthodes d'inversion bayésienne de modèle photométrique de surface ont été développés pour l'instrument CRISM. Enfin, une méthode de correction des effets de vibrations par déconvolution semi-aveugle a été développée pour PFS (Mars Express/ESA).

Les régions polaires de Mars sont le siège d'un cycle climatique annuel d'échange de CO_2 entre atmosphère et surface. Pendant la nuit polaire, le CO_2 atmosphérique se condense au sol, tandis qu'il se sublime à nouveau, dès les premiers rayons du soleil. Ce cycle a été mis à jour depuis les années 1960 mais aujourd'hui encore, la microphysique d'interaction surface/atmosphère demeure inconnue. Des observations d'imagerie à haute résolution spatiale (50 cm) par HiRISE (Mars Reconnaissance Orbiter/NASA) ont montré une multitude de phénomènes actifs associés à la sublimation. Le second objectif de cette thèse est d'établir un modèle de sublimation des dépôts saisonniers, à la fois par simulation du bilan de masse mais aussi par étude géomorphologique et spectroscopique. Les résultats montrent que la sublimation de la calotte saisonnière sud de Mars est contrôlée majoritairement par son albédo mais des travaux plus détaillés seront nécessaires pour déterminer les mécanismes à l'origine des variations d'albedo.

Le troisième objectif de cette thèse est de discuter les implications de la présence de clathrate hydrate en surface dans l'histoire climatique de Mars. Un scénario impliquant la formation de clathrate hydrate mixte de soufre et CO_2 est proposé au regard des traces géomorphologiques du paysage martien.

MOTS CLEFS : Mars, régolite, pôle, glace de CO_2, glace d'eau, clathrate hydrate, soufre, télédétection, hyperspectral, spectroscopie, photométrie, climat, dépôts saisonniers, récession de la calotte saisonnière sud, bilan de masse, OMEGA, CRISM, PFS, Mars Express, Mars Reconnaissance Orbiter, grande base de données, fouille de données, inversion bayesienne, Monte-Carlo, Chaine de Markov, déconvolution, démélange linéaire, séparation de source en aveugle, classification, détection, supervisée, non-supervisée, calcul parallèle, GPU

SUMMARY : Imaging spectrometer, Imaging spectro-photometer and high resolution spectrometer constitute the last generation of space instruments that strongly modified the study of planetary bodies. Such instruments allow us to follow the soil and atmospheric optical properties through space and time. The first objective of this Habilitation thesis is to propose some tools to analyze a huge amount of data in planetological perspectives. Three types of methods are introduced to examine the hyperspectral data acquired by OMEGA (Mars Express/ESA) and CRISM (Mars Reconnaissance Orbiter/NASA) instruments : (i) WAVANGLET, a fast detection algorithm based on wavelets to identify the presence of chemical species at the ground, (ii) BPSS, a blind source separation method that is able to detect chemical species without a priori, (iii) supervised unmixing algorithm using LinMin strategy. Also atmospheric correction methods, coupled to Bayesian inversion of photometric model, allow us to deal with the full CRISM photometric dataset. Finally, a method of micro-vibrations correction has been proposed in order to improve the quality of the PFS instrument (Mars Express/ESA) using semi-blind deconvolution.

The Martian annual cycle of CO_2 consists of an exchange between surface and atmosphere, which is particularly relevant in polar regions. During the polar night, atmospherical CO_2 condensates at the ground, whereas it starts to sublimate again during the spring, when the solar light bring energy to the surface. This major climatic cycle has been identified in the 1960th but even today, the microphysic of interaction between surface and atmosphere is still unknown. Recent images at high spatial resolution (50 cm) from HiRISE (Mars Reconnaissance Orbiter/NASA) instrument show many active processes associated to sublimation. The second objective of this thesis is to build a model of the seasonal deposits sublimation, by simulating the mass balance but also by geomorphological and spectroscopic studies. Results show that the seasonal south polar cap sublimation is mainly controlled by its albedo. Further studies must determine the exact mechanisms in the origin of this albedo variability.

The third objective of this thesis is to discuss the possibility of clathrate hydrate in the climatic history of Mars. A scenario, implying formation of clathrate hydrate of S and CO_2 is examined in comparison with geomorphological clues of the Martian surface.

KEY WORD : Mars, regolith, pole, CO_2 ice, H_2O ice, water, clathrate hydrate, sulphur, remote sensing, hyperspectral, spectroscopy, photometry, climate, seasonal deposits, seasonal south polar cap recession, mass balance, OMEGA, CRISM, PFS, Mars Express, Mars Reconnaissance Orbiter, mass data, data clustering, Bayesian inversion, Monte Carlo, Markov Chain, blind deconvolution, linear unmixing, blind source separation, classification, detection, supervised, unsupervised, parallel computing, GPU